Spatial variability of Arctic sea ice algae

Dissertation

with the Aim of Achieving a Doctoral Degree in Natural Science

at the Faculty of Mathematics, Informatics and Natural Sciences

Department of Biology of Universität Hamburg

Submitted by

Benjamin Allen Lange

M.Sc. Earth and Atmospheric Sciences
B.Sc. Environmental Sciences

Hamburg 2016

PhD thesis defense date: 08 February 2017

PhD thesis defense committee members:

1. Chair **Prof. Dr. Inga Hense**
Universität Hamburg, Biozentrum Grindel und Zoologisches Museum,
Martin-Luther King-Platz 3, 20146 Hamburg

2. Evaluator **Prof. Dr. Angelika Brandt**
Universität Hamburg, Biozentrum Grindel und Zoologisches Museum,
Martin-Luther King-Platz 3, 20146 Hamburg

3. Evaluator **Prof. Dr. Christian Möllmann**
Universität Hamburg, Biozentrum Grindel und Zoologisches Museum,
Martin-Luther King-Platz 3, 20146 Hamburg

4. Evaluator **Dr. Hauke Flores**
Alfred Wegener Institute for Polar and Marine Research
Department of Polar Biological Oceanography
Am handelshafen 12, 27570, Bremerhaven, Germany

5. Evaluator **Prof. Dr. Christiam Haas**
Alfred Wegener Institute for Polar and Marine Research
Section Head: Department of Sea Ice Physics
Bussestrasse 24, 27570, Bremerhaven, Germany

Evaluators of the written PhD dissertation:

1. Evaluator **Prof. Dr. Angelika Brandt**
Universität Hamburg, Biozentrum Grindel und Zoologisches Museum,
Martin-Luther King-Platz 3, 20146 Hamburg

2. Evaluator **Dr. Hauke Flores**
Alfred-Wegner-Institut Helmholtz-Zentrum für Polar- und Meeresforschung,
Am Handelshafen 12, 27570 Bremerhaven

3. Evaluator **Anonymous**

Table of Contents

I dedicate this thesis to my son,
Jari Matis Gordon,
and in memory of my grandparents:
Else and Werner Lange, and
Gordon Rule

Summary

The most pronounced effects of global climate change have been experienced in the Arctic region. In particular, Arctic sea ice decline and volume loss have emphasized the impeding threat of continued climate change, and have been center stage in the public eye for over a decade. Many of the observed changes in the Arctic are related to the physical system because these parameters, such as sea ice extent and thickness, are more easily observed from space and airborne platforms. The linkage between ecosystem function and its physical environment is clear from all well investigated systems. This undoubtedly means that the observed changes to the physical system have had an equally dramatic impact on the Arctic ecosystem. Our understanding of the Arctic marine ecosystem, however, is severely limited due to the methodological and logistical constraints of monitoring ecological properties. This has caused significant seasonal and geographical knowledge gaps, particularly in the high (> 80ºN) and central Arctic Ocean.

Over the past decades a disproportional emphasis has been put on the importance of primary production (PP) and the availability of food in the water column. Observations have indicated an overall increase in Arctic-wide net primary production (NPP) as a result of a thinning and declining sea ice cover, and increasing duration of the phytoplankton growth season. This increased biomass may suggest a corresponding increase in the biomass of consumers and higher trophic levels. This premise, however, neglects the rather important role that the sea ice environment and sea ice algae play in the Arctic food web. The timing, duration and spatial availability of ice algae are drastically different compared to pelagic phytoplankton. Therefore, it is only by first gaining a better understanding of the base of the Arctic food web that we can start to understand the rest of the food web.

Throughout this thesis, we aimed to assess how sea ice algae biomass availability and habitat will be affected by continued changes to the sea ice habitat, and what consequences can be expected for the Arctic food web. This was accomplished by developing novel methodologies and approaches to characterize and quantify the spatial variability of sea ice algae-biomass, -primary production and –habitat. Subsequently, we used this toolset to assess the implications of a rapidly changing sea ice habitat in relation to spatial variability of sea ice algae carbon availability and carbon demand by ice-associated organisms.

In Chapter 2, we developed a methodological toolbox to process environmental sensor array observations acquired from under-ice profiling platforms (e.g., Remotely Operated Vehicle – ROV, and the Surface and Under-Ice Trawl – SUIT), which included novel mathematical and statistical approaches to representatively capture the spatial variability of sea ice and under-ice physical-biological properties. We showed that our developed approaches produced observations, which could capture the spatial variability better than traditional point location characterizations of environmental properties. Specifically, the insufficient spatial representativeness of sea ice-algal biomass can cause biases in large-scale ice algal biomass and PP estimates.

In Chapter 3, we further developed upon Chapter 2 methodologies by introducing a new approach to estimate primary production on floe-scales (meters to kilometers), further justifying the need for representative ice-algae biomass and PP estimates. We also showed that the sea ice environment and under-ice water properties played an important role in structuring the under-ice community. Furthermore, we indicated that ecological key species of the central Arctic Ocean thrived significantly on carbon synthesized by ice algae. These results highlighted the key role of sea ice as a habitat and as a feeding ground within the Arctic Ocean.

In Chapter 4, we aimed to compare the physical-biological properties of multi-year sea ice (MYI) and first-year sea ice (FYI) to provide some insight into how the Arctic will change with the continued

replacement of MYI by FYI. We developed and confirmed the hypothesis that thick MYI hummocks do have the potential to host substantial ice algae biomass and identified hummocks as common and permanent features, which represent a reliable habitat for sea ice algae due to the typically thin or absent snow cover. We developed key physical-biological relationships to classify the springtime spatial variability of sea ice algae habitat for both FYI and MYI. We applied this classification to pan-Arctic ice thickness and snow observations, and showed that MYI is substantially under-estimated in terms of suitable habitat. Furthermore, we identified thick sea ice features, such as MYI hummocks and sea ice ridges, as potentially high biomass regions with great ecological value. We also indicated that the thicker sea ice, which remains in late-summer, has reduced melt-induced algal losses.

In conclusion, we developed a robust and novel approach to representatively quantify sea ice environmental properties, and sea ice algae biomass and PP at floe-scales. These estimates resulted in more accurate estimates of overall carbon biomass availability and production, which we used to improve the spatial variability of the ice-algae derived carbon budget. We concluded that there was a large mis-match between ice-algal primary produced carbon and ice-algal carbon demand by dominant species. This mis-match was also accompanied by large regional variability. This was expected during our sampling period since production was shutting down. Taking a different approach, we showed that the standing stocks of ice-algal carbon were quite substantial. These results suggest that during late-summer, when primary production shuts down, the remaining ice-algal biomass in high latitude regions may represent a crucial food source to sustain ice associated organisms during the onset of polar night.

Altogether, the continued thinning and loss of thicker sea ice features may result in the loss of a reliable carbon supply, in the form of sea ice algae carbon, at key times of the year when other carbon sources are severely limited.

Zusammenfassung

In der Arktis sind die Auswirkungen des globalen Klimawandels so deutlich spürbar wie in nur wenigen anderen Regionen der Welt. Insbesondere Rückgang und Volumenverlust des Meereises stehen schon seit über einer Dekade im Mittelpunkt des öffentlichen Interesses. Viele der beobachtenden Veränderungen in der Arktis beziehen sich auf das physikalische System, da Parameter wie Meereisausdehnung und-dicke leichter aus dem All und aus Flugzeugen abgeschätzt werden können. Die physikalischen Veränderungen können sich ohne Zweifel auf ebenso drastische Weise auch auf das Arktische Ökosystem auswirken. Unser Wissen über das Arktische marine Ökosystem ist jedoch lückenhaft, da die methodischen und logistischen Möglichkeiten zur Erfassung wichtiger ökologischer Parameter eingeschränkt sind. So existieren auch heute noch erhebliche Wissenslücken in den hoch-arktischen Regionen (> 80°N) des zentralen Arktischen Ozeans.

In jüngerer Zeit stand vor allem die Bedeutung der Primärproduktion (PP) und der Nahrungsverfügbarkeit in der Wassersäule im Fokus der ökologischen Forschung in der Arktis. Aus Beobachtungen wurde eine allgemeine Zunahme der Nettoprimärproduktion (NPP) in der gesamten Arktis abgeleitet, welche aus dem Rückgang der Dicke und Ausdehnung des Meereises bei gleichzeitiger Verlängerung der Wachstumsperiode des Phytoplanktons resultiert. Diese erhöhte PP könnte eine ebenfalls gesteigerte Sekundärproduktion der höheren trophischen Ebenen bewirken. Diese Annahme lässt jedoch die wichtige Rolle der Meereisalgen für das Arktische Nahrungsnetz außer Acht. Zeitpunkt, Dauer und regionale Verfügbarkeit von Eisalgenbiomasse unterscheiden sich deutlich vom pelagischen Phytoplankton. Deshalb ist es wichtig, die Basis des Arktischen Nahrungsnetzes unter Berücksichtigung des Beitrages von Eisalgen zu charakterisieren, um die Folgen von Veränderungen für das Ökosystem abschätzen zu können.

Das Ziel dieser Arbeit ist es, zu erforschen, wie die Verfügbarkeit und die Lebensbedingungen von Eisalgen von den kontinuierlichen Veränderungen des Meereishabitats beeinflusst werden, und welche Konsequenzen sich daraus für das Arktische Ökosystem ergeben. Hierfür wurden neuartige Methoden und Ansätze für die Beschreibung und Quantifizierung der räumlichen Variabilität der Eisalgenbiomasse, Eisalgen-PP und des Eisalgenhabitats entwickelt. Anschließend nutzten wir diese Methoden, um die Auswirkungen sich schnell verändernder Meereishabitate in Bezug auf die räumliche Variabilität des von Eisalgen produzierten Kohlenstoffs und des Kohlenstoffbedarfs eis-assoziierter Organismen abzuschätzen.

In Kapitel 2 entwickelten wir einen Ansatz, der es ermöglicht, Umweltdaten von Sensoren auf Untereis-Drohnen (Remotely Operated Vehicle, ROV) und Untereis-Schleppnetzen (Surface and Under-Ice Trawl, SUIT) zu prozessieren. Dieser Ansatz beinhaltete neuartige mathematische Methoden für die repräsentative Darstellung der räumlichen Variabilität von Meereis-Umweltparametern. Wir konnten zeigen, dass die entwickelten Methoden die räumliche Variabilität dieser Parameter besser erfassen als traditionelle Punktmessungen. Insbesondere konnte gezeigt werden, dass die korrekte Wiedergabe der räumlichen Variabilität von Meereis-Umweltparametern und Eisalgenbiomasse kritisch ist für eine realistische Abschätzung von Eisalgenbiomasse und PP auf regionalen und pan-arktischen Skalen.

In Kapitel 3 entwickelten wir die in Kapitel 2 eingeführten methodischen Ansätze weiter, indem wir einen neuen Ansatz für die Schätzung der PP entwickelten, der die räumliche Variabilität von Eisalgenbiomasse und Meereis-Umweltparametern in Größenordnungen von 0,1 bis 5 km berücksichtigt. Wir demonstrierten weiterhin, dass die Eigenschaften der Meereisumgebung und des Habitats unter dem Eis eine wichtige Rolle für die Strukturierung der eis-assoziierten Lebensgemeinschaft spielten. Außerdem konnten wir zeigen, dass ökologische Schlüsselarten des zentralen Arktischen Ozeans einen Großteil ihres Kohlenstoffbedarfs mit eisalgen-produzierten Kohlenstoff decken. Diese Ergebnisse unterstreichen die Schlüsselrolle des Meereises als Habitat und Kohlenstoffquelle im Arktischen Ökosystem.

In Kapitel 4 vergleichen wir die physikalisch-biologischen Eigenschaften von mehrjährigem Meereis (Multi-Year Ice, MYI) und einjährigem Meereis (First-Year Ice, FYI), um Erkenntnisse darüber zu gewinnen, wie sich die Arktis verändern wird, wenn MYI zunehmend durch FYI ersetzt wird. Wir entwickelten und bestätigten die Hypothese, dass dicke MYI-Hügel das Potential haben, große Mengen Eisalgen zu beherbergen. Wir identifizierten diese Eishügel als dauerhafte Ausformungen des Eises, die aufgrund der typischerweise geringen Schneebedeckung zuverlässige Habitate für Eisalgen darstellen. Wir erstellten physikalisch-biologische Beziehungen für die Einordnung der räumlichen Variabilität des Eisalgenhabitats in MYI und FYI im Frühjahr. Diese Klassifizierung wurde dann auf die Eisdicke und Schneedickenmessungen der gesamten Arktis angewendet und zeigte, dass MYI als Habitat für Eisalgen bisher womöglich deutlich unterschätzt wurde. Weiterhin identifizierten wir Merkmale dicken Eises, wie Eishügel in mehrjährigem Eis und Presseisrücken, als potentielle Orte hoher Biomassen mit hohem ökologischem Wert. Wir konnten außerdem ermitteln, dass dickeres Eis, welches im Spätsommer bestehen bleibt, geringere schmelz-bedingte Algenverluste aufweist als dünnes FYI.

Zusammenfassend entwickelten wir eine robuste und neuartige Methodik für die repräsentative Quantifizierung der ökologischen Eigenschaften des Meereises, der Eisalgenbiomasse und PP in der räumlichen Größenordnung von typischen Eisschollen (0,1 – 5 km). Diese Schätzungen ermöglichten akkuratere Abschätzungen der Verfügbarkeit und Produktion von Eisalgen-Kohlenstoff für das Arktische Nahrungsnetz. Daraus schlossen wir, dass ein großes Missverhältnis zwischen der Menge eisalgen-produzierten Kohlenstoffs und der Nachfrage dominanter Arten bestand. Dieses Missverhältnis wurde von einer starken regionalen Variabilität begleitet. Mit einem anderen Ansatz zeigten wir hingegen, dass am Ende der Wachstumsphase der Vorrat an Eisalgenbiomasse noch beträchtlich ist. Diese Ergebnisse deuten darauf hin, dass während des Spätsommers, wenn die PP dem Ende zugeht, die verbleibenden Eisalgenbestände in den hohen Breitengraden eine essentielle Nahrungsquelle bieten können, um eisassoziierte Organismen während des Beginns der Polarnacht zu versorgen.

Zusammengefasst könnte das kontinuierliche Ausdünnen des Eises und der Verlust des dicken Meereises zum Verlust einer verlässlichen Kohlenstoffquelle in Form von eisalgen-produzierten Kohlenstoffs während wichtiger Perioden des Jahres führen, wenn die Verfügbarkeit anderer Kohlenstoffquellen stark limitiert ist.

Abbreviations

CAO	central Arc tic Ocean
chl *a*	chlorophyll *a*
C	carbon
EOF	empirical orthogonal function
NDI	normalized difference index
ROV	remotely operated vehicle
SUIT	surface and under-ice trawl
PP	primary production
NPP	net primary production
PAR	photosynthetically active radiation
FYI	first-year sea ice
MYI	multi-year sea ice

Chapter 1: Introduction

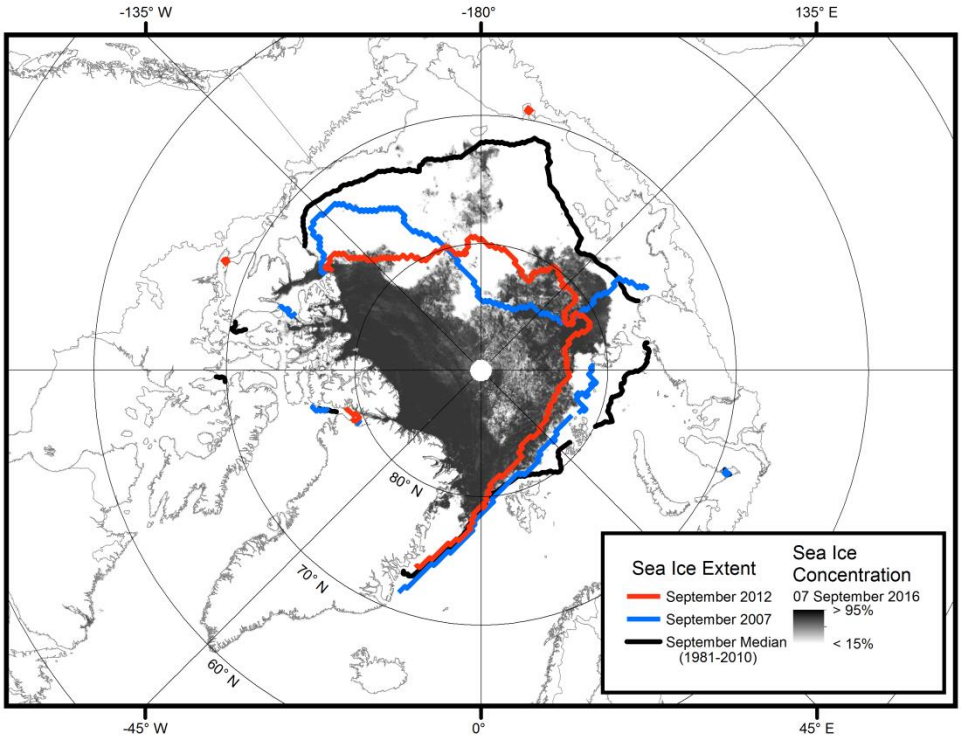

Figure 1. Map of the Arctic Ocean summarizing the recent decline in sea ice extent. Sea ice extent data are the September monthly means for 2007, 2012 and the median for the period 1981 to 2012 (extent data acquired from NSIDC according to algorithms in Fetterer et al., 2002, udpated 2011). Daily sea ice concentration data were acquired on 07 September 2016, from www.meereisportal.de according to algorithms in Spreen et al. (2008).

1.1 A brief history of Arctic sea ice

Many of the most pronounced changes in the Arctic Ocean have been observed in the physical sea ice environment, as these properties are easily monitored using large-scale remote sensing platforms. These changes to the Arctic sea ice cover are likely to continue unabated into the future, having profound global ecological consequences (AMAP, 2011; IPCC, 2013).

Sea ice melt and growth season length are good indicators of Arctic climate change, however, they vary spatially and temporally, making it difficult to characterize these variables. Markus et al. (2009) demonstrated that the melt season for the entire Arctic has increased by 20 days during the period 1979-2007. Furthermore, Markus et al. (2009) showed that the largest increases in melt season were recorded for the Hudson Bay and the Chukchi/Beaufort, Laptev/East Siberian and East Greenland seas. Howell et al. (2009) also demonstrated a significant positive trend in the duration of the melt season within the Canadian Arctic Archipelago. Regions with a lengthening melt season coincided with regions that have experienced the largest decline in ice extent and concentration (Stroeve et al., 2011).

Sea ice areal coverage is an important property, in terms of energy balance, as sea ice has a high albedo, reflecting large amounts of short-wave solar radiation away from the Earth's surface (Budyko, 1969; Perovich et al., 2007). The sea ice cover in turn limits the availability of photosynthetically active radiation (PAR) for autotrophic organisms living within the sea ice and water column (Cota & Horne, 1989). Since the beginning of the satellite observation record (1979) there has been a declining

trend in sea ice extent (SIE) for all months with the largest decline during the end of the melt season in September (Serreze et al., 2007b; Stroeve et al., 2012). In September 2012, a new record Arctic sea ice extent minimum was set, far exceeding the previous record minimum of 2007 (Figure 1), which was itself a remarkable decline from previous years (IPCC, 2013; Parkinson & Comiso, 2013). As of 07 September 2016, it appears that a new record sea ice extent minimum may be reached before the end of September 2016 (Figure 1).

The decline in SIE has resulted in more open water and therefore more solar radiation being absorbed due to the lower albedo of water (Perovich et al., 2011; Perovich et al., 2008). This process is the main driving force in the "snow/ice-albedo" feedback system, where continued decline of SIE will continue to increase absorption of solar radiation and further increase temperatures (air and ocean), which in turn will cause further reductions in SIE (Budyko, 1969; Johannessen et al., 2004; Perovich et al., 2011; Perovich et al., 2007). The albedo feedback system, and its influence on the global energy balance has and will play a major role in Arctic sea ice processes, however, additional mechanisms also have an important role in recent Arctic changes.

The negative trend in SIE can best be explained by the interplay of rising atmospheric greenhouse gas concentrations (GHG) and variations in air temperature and atmospheric and oceanic circulation (Serreze et al., 2007a; Serreze et al., 2007b; Stroeve et al., 2012). Wind is the primary driving force of sea ice drift in the Arctic Ocean, which is dominated by two main circulation patterns (Figure 2) (Rigor et al., 2002). The Beaufort Gyre (BG) is characterized by anticyclonic circulation and high pressure over the Beaufort Sea and Western Arctic Ocean; and the Transpolar Drift Stream (TDS), which is characterized by cyclonic circulation and low pressure over the Eurasian sector of the Arctic Ocean (Figure 2) (Rigor et al., 2002). The strength and location of these two pressure systems largely determines sea ice drift and amount of ice exported from the Arctic Ocean (Rigor et al., 2002).

The general circulation patterns of the BG and TDS result in sea ice being transported from the Siberian sectors of the Arctic Ocean, across the North Pole and either exported through the Fram Strait or pushed up against the Northern coasts of the Canadian Arctic Archipelago (CAA) and Greenland. The ice north of Canada and Greenland can then be re-circulated into the Arctic Ocean, which results in the formation of thicker multi-year sea ice (MYI; Figure 2). The large internal stresses experienced by sea ice as it is forced against the coast results in vast shear zones and deformation (ridging & rafting), producing the thickest ice in the Arctic along the northern coast of the CAA (Figure 2) (Haas et al., 2006; Kwok et al., 2010). Sea ice export through the Fram Strait corresponds to the largest annual export flux from the Arctic Ocean (Kwok, 2009; Serreze et al., 2006). Although no trends were observed over the long term, seasonally high flux rates were observed in summers of 2005 and 2007, contributing to the reductions of sea ice and record minima sea ice coverage (Kwok, 2009).

The declining trend of Arctic SIE has not only affected the areal coverage of sea ice, but has resulted in a dramatic shift in the ice composition from being dominated by MYI to being dominated by FYI and large amounts of open water during summer (Kwok, 2007; Kwok & Cunningham, 2010). Over the period 1980-2010, ice age distributions have demonstrated a flushing of very old MYI (10+ years), commencing in the late 1980s and continuing into the early 1990s, with a relatively stable period from 1995-2000 and then a continued decline of MYI from 2001 to 2011 (Maslanik et al., 2007; Maslanik et al., 2011).

The loss of thick, old MYI has also resulted in pronounced thinning within the central Arctic basin. Winter mean ice thickness derived from submarine ULS was 3.64 m in 1980 compared to the 1.89 m winter mean during 2008 derived from ICESat observations, (Kwok & Rothrock, 2009). The highest rates of decline during the submarine record were -0.08 m/yr, observed during 1990 (period of accelerated export of old MYI in the Arctic), and highest rates of decline for the 2003-2008 ICESat record were trends of -0.10/-0.20 m per year (winter/summer), with negative trends for all regions of the Arctic (Kwok & Rothrock, 2009). Furthermore, there was a ~0.6 m thinning and net winter volume loss of 6300 km^3 (> 40 %) of Arctic MYI during the 4 year ICESat observation period 2005-2008 (Kwok et al., 2009).

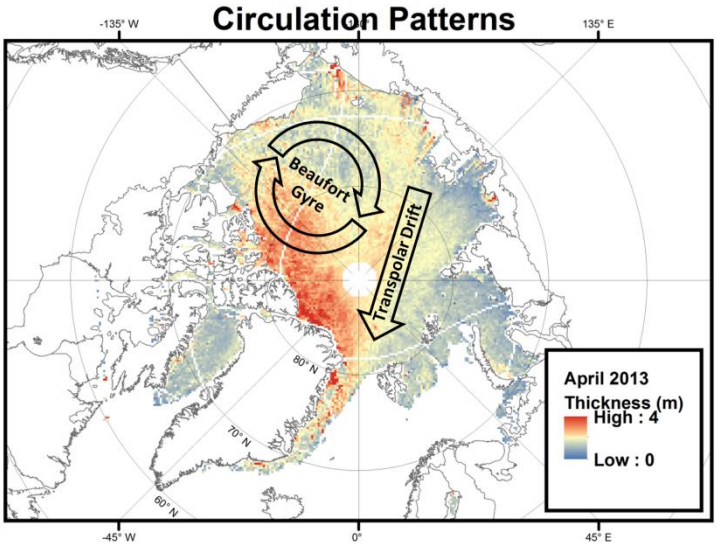

Figure 2. General sea ice circulation patterns in the Arctic Ocean, following Rigor et al. (2002). Ice thickness data were acquired by Cryosat-2 and retrieved www.meereisportal.de according to algorithms described by Ricker et al. (2014).

The decline in older MYI and a general thinning of the Arctic ice pack can only partially be attributed to warming (Rothrock et al., 2003), and is better explained by a regime shift in circulation patterns (Rigor & Wallace, 2004; Rigor et al., 2002). The regime shift coincided with the period of anomalous export of old MYI from the Arctic (Maslanik et al., 2007; Maslanik et al., 2011) and a period (1990) of rapid thinning over the central Arctic (Kwok & Rothrock, 2009). This resulted in the pre-conditioning of the Arctic ice pack for further thinning and reductions of MYI (Lindsay & Zhang, 2005; Ogi et al., 2008; Serreze et al., 2007b), which is supported by more recent ice thickness measurements from satellites (Kwok et al., 2009; Laxon et al., 2013) and airborne observations (Haas et al., 2010; Haas et al., 2008). Following on the premise that thinner, younger ice melts more easily, the larger proportion of thinner FYI in the Arctic has resulted in decreased survivability of the ice pack (Kwok, 2007). This has introduced another feedback system, where less MYI leaves the ice pack even more susceptible to melt, further decreasing the survivability and fraction of MYI in the Arctic. The survivability of MYI is heavily dependent on level ice thickness, whereby ice that is thicker than the typical summer melt rate will survive (Notz, 2009). Therefore, Arctic Sea ice may arrive at a thickness that is thinner than the summer melt rate, at which point the Arctic will be mostly seasonally ice-free.

Sea ice decline, thinning of Arctic sea ice, and the loss of MYI have resulted in reduced Arctic-wide sea ice albedo (Riihela et al., 2013), and more light reaching the under-ice environment in summer (Nicolaus et al., 2012). Furthermoe, the rapid loss of sea ice represents an equally rapid change in habitat for sea ice algae, protists, and ice-associated fauna with important ecological consequences.

1.2 The sea ice-associated ecosystem

A unique feature of sea ice is the formation of brine channels within the ice matrix. These features form due to the rejection of salts during freezing, which results in the formation of brine pockets and channels with very high salinities (Eicken, 2003; Weeks & Ackley, 1986). It is the presence of these interstitial brine channels, full of nutrients, that allows for the formation of a unique ice associated ecosystem (Figure 3). Organisms are initially incorporated into the sea ice matrix from the water column during ice formation. During later stages of sea ice growth or melt, the in-ice organism can also be exchanged with organisms from the underlying sea water by wave fields that exchange or pump water between the environments (Horner et al., 1992). Arctic sea ice inhabitants include microalgae, bacteria, protists, and invertegrate metazoans. Autotrophic microalgae are dominated by diatoms, which represent the base of the Arctic food web (Gradinger et al., 1999; Melnikov et al.,

2002). Most sea ice bacteria are heterotrophic and likely represent an important component in terms of nutrient recycling (Rysgaard et al., 2008). Heterotrophic protists represent the main consumers of microalgae and are dominated by ciliates and flagellates (e.g., Michel et al., 2002; Rat'kova et al., 2004), see also review in Arrigo (2014). Furthermore, cnidarians, turbellarians, annelids, and arthropods can be found within the ice (e.g., Bluhm et al., 2007; Gradinger et al., 2005), cnidarians, ctenophores, copepods, amphipods and fish are typically found living at the ice-water interface (David et al., 2015; Gradinger & Bluhm, 2004) (Werner, 1997). These sympagic metazoans (dominant representatives of the "under-ice fauna" compartment in Figure 3) represent a particularly important component of the Arctic food web in terms of carbon transfer from the in-ice microalgae (hereafter referred to as sea ice algae) to the pelagic realm and upper trophic levels, such as zooplankton, fish, seals, whales and polar bears (Budge et al., 2008; Kohlbach et al., 2016; Wang et al., 2015; Wang et al., 2016).

Organisms living under the sea ice or within the ice can live their entire life cycle or only part of it in association with the sea ice environment (Arndt & Swadling, 2006). In both cases, this requires the ability to adapt their life cycles to strong seasonality of the sea ice environment. Ice-associated organisms can use the ice for feeding, reproduction and/or as a refuge. The under-ice topography provides a wide range of advantageous micro-habitats. For example, polar cod (*Boreogadus saida*) reside in ice wedges along the ice floe edge to avoid access by predators (Gradinger & Bluhm, 2004); and ice meiofauna and under-ice amphipods seeking shelter at sea ice ridges during advanced melt (Gradinger et al., 2010). Perhaps most important though is the fact that sea ice algae represent a high quality and critical food source for many organisms (Kohlbach et al., 2016; Søreide et al., 2006; Søreide et al., 2010; Wang et al., 2015; Wang et al., 2016). Furthermore, sea ice algae may represent a more cost-effective food resource in comparison to pelagic phytoplankton floating in the water column. Grazing sea ice algae or hunting for ice algae grazers could be accomplished with low energy expenditure while being attached or scanning a two-dimensional bottom-ice surface, in comparison to the energy requirements of swimming and searching for prey or phytoplankton in a three-dimensional water column.

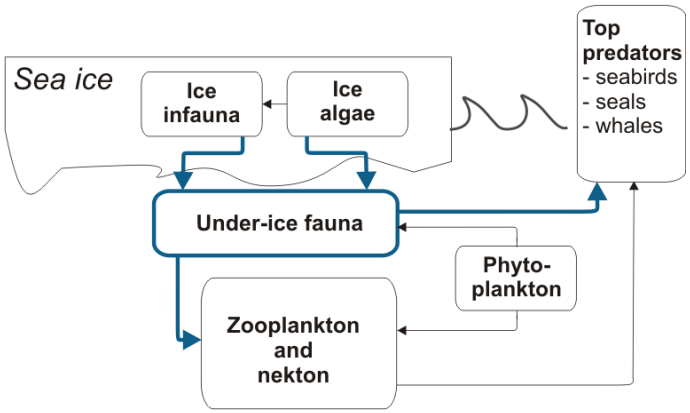

Figure 3. Conceptual overview of the ice associated foodweb with the flux of carbon represented by arrows (reproduced from H. Flores, 2009).

1.3 Ecological implications of a changing Arctic sea ice environment

There is mounting evidence for an overall increase in Arctic-wide net primary production (NPP) as a result of the declining sea ice cover and increasing duration of the phytoplankton growth season (Arrigo & van Dijken, 2011; Arrigo & van Dijken, 2015; Fernández-Méndez et al., 2015). It remains uncertain, how sea ice algae NPP will respond to continued changes of the sea ice environment. It has been suggested that a thinning Arctic sea ice cover and increased light transmittance will result in increased sea ice algae primary production (PP) rates due to more available photosynthetically active radiation (PAR) (Nicolaus et al., 2012).

Kosobokova and Hirche (2009) suggested, based on the limited studies of PP estimates for the high central Arctic that the lower PP rates, and hence, lower food availability, were the reason for the lower zooplankton biomass. This may be correct, however, the estimates for PP available at that time either did not include ice-algal PP or had a limited spatial-temporal coverage. Ice-algae represent one of the dominant carbon producers within the CAO (Fernández-Méndez et al., 2015; Gosselin et al., 1997), and therefore should be quantified representatively in order to assess the true estimate of the ice-algal derived carbon budget. Focusing on pelagic production, Kosobokova and Hirche (2009) suggested higher food availability and thus potentially higher zooplankton biomass as a result of sea ice decline. This prediction, however, neglects the important role of sea ice algae in the diet of key Arctic zooplankton and top predators (Budge et al., 2008; Kohlbach et al., 2016; Wang et al., 2015; Wang et al., 2016).

Lavoie et al. (2010) and Leu et al. (2015) argued that ice algal growth and production will likely be hampered due to a combination of earlier snow melt and increased precipitation in the Arctic. The small-scale variability of the snow cover on both FYI and MYI is a commonly overlooked factor when assessing the future of Arctic sea ice algae. Not only is the overall snow depth and mass balance important, but how this snow is (re)distributed on the surface is one of the most important factors controlling the atmosphere-ice-ocean heat flux (Sturm et al., 2002) and the transmission of light (Grenfell & Maykut, 1977; Perovich, 1996).

During the SEDNA drift study, Melnikov et al. (2002) showed an ice algal peak in late-July during a period of no- or low-snow with an overall mean snow depth of only 3 cm by the end of June (Sturm et al., 2002). This indicated a different seasonal progression of sea ice algal growth within the central Arctic Ocean, showing an ice-algal biomass peak around 100 days later than all other documented seasonal studies reviewed in Leu et al. (2015), albeit conducted in regions characterized by seasonal sea ice. This suggests some clear differences between sea ice algal growth in regions characterized by seasonal sea ice compared to the central and high (>80ºN) Arctic Ocean, and that these differences should be considered when assessing the future of a changing Arctic system.

1.4 Sea ice algae biomass and primary production

The development of sea ice algae communities is influenced by sea ice microstructure (e.g., salinity and temperature, which influence permeability), nutrient supply, and transmitted irradiance (see recent reviews by Arrigo, 2014; Vancoppenolle et al., 2013). During spring, the main influences on under-ice irradiance are the snow depth distribution (Hamre et al., 2004; Järvinen & Leppäranta, 2011; Maykut & Grenfell, 1975; Thomas, 1963), and to a lesser extent ice thickness (Grenfell & Maykut, 1977; Light et al., 2008; Nicolaus et al., 2010; Thomas, 1963). Initial growth of sea ice algae, during early spring is primarily controlled by the snow distribution, which is typically evident by a negative relationship between chlorophyll *a* (chl *a*) and snow depth (e.g., Campbell et al., 2014a; Mundy et al., 2007). During the progression of melt, light transmission increases due to changes in the optical properties of snow and ice (Nicolaus et al., 2010; Perovich, 1996). Consequently, ice algal growth increases and shifts to a more nutrient-limited system, which can be accompanied by a combination of other limiting factors such as: self-shading, diurnal light patterns, or ice ablation (Cota & Smith, 1991; Gosselin et al., 1990; Lavoie et al., 2005). In some instances, when light transmission increases faster than algal communities can adapt, the increased light field can reduce activity and biomass of algal communities due to photoinhibition (Barlow et al., 1988; Michel et al., 1988). Ice algal growth and the bloom period are terminated during advanced and rapid melt or nutrient depletion (Lavoie et al., 2005).

The high spatial and temporal variability of sea ice algae, in addition to sparse sampling, results in poorly constrained sea ice-algal biomass and PP estimates for the central Arctic Ocean (Miller et al., 2015). Large-scale estimates of sea ice algal biomass and PP are limited to modelling studies, as satellites are unable to observe the underside of sea ice. Lee et al. (2015) demonstrated that pelagic phytoplankton PP models for the Arctic Ocean were highly sensitive to uncertainties in chlorophyll *a* (chl a) and performed best with *in situ* chl *a* data. *In situ* ice algal chl *a* used in models, however, are

typically based on a small number of ice core observations, and may therefore not correctly represent the true spatial variability of ice algal biomass (e.g., Fernández-Méndez et al., 2015).

Furthermore, Miller et al. (2015) reviewed the different methods for primary production measurements with spatial sampling resolution on the order of 0.01 m for ice coring-based *in vitro* incubations (e.g., Fernández-Méndez et al., 2015; Gosselin et al., 1997; Gradinger, 2009) or *in situ* incubations (e.g., Gradinger, 2009; Mock & Gradinger, 1999). At larger scales the under-ice eddy covariance method integrates primary production over an area of 100 m^2 (Long et al., 2012). Thus, there is a large gap in spatial coverage between the 0.01 to 100 m^2 scales, which is not resolved by these methods. It is within this spatial range that many environmental properties can vary. This can have a large influence on light availability, ice melt and growth, and the spatial distribution of ice algae. Typical patch sizes of snow have been reported in the range from 20 to 25 m (Gosselin et al., 1986; Steffens et al., 2006). Surface properties such as albedo have patch sizes of approximately 10 m (Katlein et al., 2015; Perovich et al., 1998), and sea ice draft can vary at scales of around 15 m (Katlein et al., 2015).

1.5 Logistical and methodological constraints of Arctic sea ice research

It is apparent from the previous review of literature that there are significant seasonal and geographical knowledge gaps of the Arctic ecosystem, particularly in the high (>80ºN) and central Arctic Ocean (Wassmann, 2011; Wassmann et al., 2011). This lack of observations can be attributed to methodological and logistical constraints of sea ice research. First of all, the seasonal and regional variability of environmental conditions results in sampling biases, which limit the seasonal and temporal coverage of studies within the Arctic Ocean. During the early-spring to summer transition period, the majority of ecologically focused studies are conducted within the peripheral seas and coastal regions of the Arctic Ocean (Leu et al., 2015; Wassmann et al., 2011). During this time of year, ship-based campaigns are severely limited in terms of access to vast regions of the central Arctic Ocean due to the difficulty in breaking through the thick snow and sea ice cover (Figure 4). Furthermore, the sea ice season is generally shorter in the lower latitude, coastal regions and therefore sea ice focused studies in these regions are also limited to the early-spring to summer transition, because beyond this period, sea ice does not exist or is not safe to work on (Figure 4). Although these studies may capture the full season of ice algal growth, the seasonal progression and general environmental conditions are drastically different compared to the high and central Arctic Ocean. This imposes limitations when making pan-Arctic assessments based on information from lower latitude studies conducted in regions characterized by seasonal sea ice. This means that in order to assess the future fate of the central Arctic ecosystem, we need observations from the central Arctic.

Furthermore, monitoring sea ice ecosystems remains a challenge due to the difficulty of remotely sensing biological processes in and under the ice cover. Multi-scale sea ice algae observations are of particular interest in order to address potential changes to the sea ice ecosystem. There is growing interest in extending sea ice algal observations by developing larger-scale observation systems and methodologies that can capture the spatial distribution of sea ice algae at multiple scales. Although sea ice coring will remain an essential method for any ice-related research, point measurement coring is time consuming, making it an unlikely candidate for large-scale ice-algal observation systems. Other devices such as the slurp-gun (Gosselin et al., 1990) or underwater pulse-amplitude-modulated fluorometer (Diving-PAM; Rysgaard et al., 2001) have shown promise, however, they require the deployment by divers, which is also logistically demanding and time intensive.

New developments of Autonomous Underwater and Remotely Operated Vehicles (AUV/ROV) give promising new opportunities to study the underside of ice (Wadhams, 2012). Currently these platforms have mainly been used to observe physical (e.g., Katlein et al., 2015; Nicolaus & Katlein, 2013; Nicolaus et al., 2012) and biological processes (e.g., Ambrose et al., 2005; Katlein et al., 2014a) within and under the ice at larger scales and with relatively minimal logistical requirements, in terms of spatial coverage compared to other methods (e.g., 8 hours for 100 to 500 m transects). ROVs deployed with mounted digital imagery systems have been used to document the distribution of sub-ice algal aggregates (e.g., Ambrose et al., 2005; Gutt, 1995; Katlein et al., 2014a). Digital imagery is

limited to two-dimensional space and therefore abundance estimates may have high uncertainty. Using image analysis, Katlein et al. (2014a) showed that ice-algal aggregate distribution is mainly controlled by under-ice topography with the accumulation of aggregates along the edges of ridges and in dome-shaped ice features.

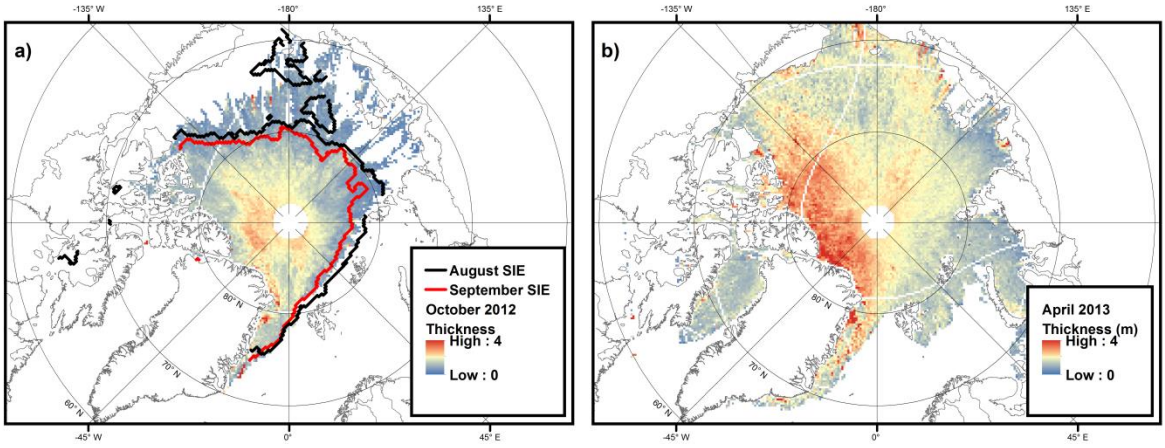

Figure 4. Sea ice conditions for the Arctic Ocean during a) late-summer/autumn 2012; and b) spring 2013. Ice thickness data were acquired during a) October 2012 and b) April 2013 by Cryosat-2 and retrieved www.meereisportal.de according to algorithms described by Ricker et al. (2014). Sea ice extent correspond to monthly means during August and September for 2012 (extent data acquired from NSIDC, Fetterer et al. (2002, udpated 2011)).

Under-ice spectral measurements can be used to derive chl *a* and other pigment concentrations in sea ice and the water column using different bio-optical approaches (Campbell et al., 2014b; Craig et al., 2012; Melbourne-Thomas et al., 2015; Mundy et al., 2007; Taylor et al., 2013). Until now, however, these models have not been applied to larger scale under-ice ROV spectral measurements. ROVs have recently been deployed, with mounted spectral radiometers, to measure under-ice spectral irradiance (e.g., Katlein et al., 2015; Katlein et al., 2014b; Nicolaus & Katlein, 2013; Nicolaus et al., 2012), but focused primarily on physical processes and energy budgets. Spectral radiometers have also been mounted on the Surface and Under-Ice Trawls (SUIT;van Franeker et al., 2009), a potential horizontal profiling platform for monitoring ice algal concentration in combination with the abundance of under-ice grazers over profiles up to 3 km in length (e.g., David et al., 2015). The development of under-ice horizontal profiling platforms for observing spectral properties of sea ice, among other properties, has resulted in and will continue to result in larger amounts of under-ice spectra. These spectral observations, both from the past and future, could be used to estimate the temporal evolution and spatial variability of ice-algal chl *a* and primary production. However, this requires the development of robust and reliable methodologies that can be applied to datasets with variable temporal and spatial coverage, and with a large range of environmental conditions.

1.6 Significance of this study

Our current understanding of the Arctic marine ecosystem has been limited due to methodological and logistical constraints. These constraints have caused significant seasonal and geographical knowledge gaps, particularly in the high (> 80ºN) and central Arctic Ocean (Wassmann, 2011; Wassmann et al., 2011). There is mounting evidence for an overall increase in Arctic-wide net primary production (NPP) as a result of a thinning and declining sea ice cover, and increasing duration of the phytoplankton growth season (Arrigo & van Dijken, 2011; Arrigo & van Dijken, 2015; Fernández-Méndez et al., 2015). It remains uncertain, however, how sea ice algae related primary production and biomass availability will respond to continued changes of the sea ice environment. In the central Arctic Ocean, sea-ice algae has been documented to contribute for up to ~ 60% of the NPP during summer (Fernández-Méndez et al., 2015; Gosselin et al., 1997). Overall, however, sea ice-related NPP is relatively low, accounting for 1 to 10 % of total NPP in the Arctic Ocean (Arrigo & van Dijken, 2015; Dupont, 2012). Regardless of the overall low contribution of ice-related NPP, sympagic

(ice-associated) organisms, pelagic organisms and top-predators showed high dependency on ice-algae produced carbon in many regions of the Arctic Ocean (Budge et al., 2008; Kohlbach et al., 2016; Wang et al., 2015; Wang et al., 2016). The key role of sea ice algae in Arctic food webs, particularly in terms of reproduction and growth of key Arctic organisms (Leu et al., 2011; Michel et al., 1996; Søreide et al., 2010), highlights the importance of timing and duration of ice algal growth, and the availability of algal biomass throughout different times of the year. In order to assess the impact of a changing Arctic sea ice environment on this important food source, we must characterize the spatial-temporal variability of sea ice algae to representatively estimate ice-algal carbon biomass availability and primary production at multiple spatial and temporal scales (Miller et al., 2015).

1.7 Scientific Questions and Objectives

In this thesis, we aimed to address a key overarching question in Arctic ecology, which encompasses both spatial and seasonal aspects of sea ice ecology:

> **How will sea ice algae biomass and habitat be affected by continued sea ice decline and the replacement of MYI by FYI, and what consequences can be expected for Arctic food webs?**

In order to address this main question, we needed to first fill some important methodological and knowledge gaps concerning the variability of sea ice algae, specifically:

1. **Can we improve the spatial representativeness of key environmental sea ice and under-ice water parameters by developing new methodological approaches?** What observation systems are available to address the spatial variability of key environmental sea ice and under-ice water parameters, and how can we improve these systems and methods?
2. Is it important for large-scale estimates and ecological models to **capture the spatial variability of environmental properties** such as: sea ice thickness, ice algal-biomass and -primary production (PP), and under-ice water chl *a* biomass, PP, salinity and temperature?
3. **How do larger-scale observations of sea ice algal –biomass, –PP, and suitable habitat compare to traditional and smaller-scale observation systems**, particularly ice coring, of which up-scaled estimates assume spatial representativeness?
4. What are the large-scale patterns in sea ice algae-biomass and -habitat? Specifically, are there differences between MYI and FYI (or between ice types/classes)?

To answer these questions, this thesis aimed to develop novel methodologies and approaches to characterize and quantify the spatial variability of sea ice algae-biomass, -primary production and -habitat. Furthermore, we applied these approaches to larger-scale remotely sensed observations and assessed the spatial variability of these parameters at multiple scales. Because a full dataset was only available during summer for this thesis, we assessed the implications of a rapidly changing sea ice habitat in relation to summertime spatial variability of sea ice algae carbon availability and carbon demand by ice-associated organisms. To accomplish this I addressed the following objectives:

i) Develop a methodological toolbox to characterize the variability of sea ice habitat properties at the floe size scale (meters to kilometers), using mobile under-ice profiling platforms;
ii) Estimate the floe-scale variability of ice algal biomass using hyper-spectral profiles from mobile under-ice sensor platforms and compare its representativeness with traditional (ice core-based) methods;
iii) Assess the impact of using improved floe scale-based estimates of sea ice properties and ice algal biomass on pan-Arctic scale estimates and models
iv) Investigate the factors controlling the spatial variability of ice algal biomass, such as ice thickness, ridges and hummocks;
v) Study the potential of MYI for ice algal biomass distribution, and expected changes in the future
vi) Unravel the relationship between the spatial distribution of ice algae, sea ice associated grazers and carbon flux.

1.8 Thesis Overview and Publications Outline

This cumulative dissertation presents a comprehensive summary of the major scientific contributions accomplished throughout my PhD project. My PhD was conducted from July 2012 to September 2017 (with ~10 months of total parental leave from March 2015 to December 2015). My PhD project was a component of the Helmholtz Association Young Investigators Group *Iceflux*: Ice-ecosystem carbon flux in polar oceans (VH-NG-800) with Dr. Hauke Flores as the principal investigator as well as my main supervisor. The thesis begins with a general introduction (already presented here in Chapter 1) into the Arctic Ocean and its physical-ecological status. Chapters 2, 3 and 4 include my main scientific contributions accomplished during my PhD, which include published papers, papers currently under review or manuscripts in preparation for submission. The thesis is finalized in Chapter 5 with a synoptic discussion of all the papers, with the addition of preliminary datasets and analysis.

Chapter 2: *Methodological advancements of ecologically relevant sea ice observations*

In Chapter 2, we developed a methodological toolbox to process environmental sensor array observations acquired from under-ice profiling platforms (e.g., ROV and SUIT), which included novel mathematical and statistical approaches to representatively capture the spatial variability of sea ice and under-ice physical-biological properties.

Paper 1

Title: *The Surface and Under-Ice Trawl (SUIT)-mounted environmental sensor array*

in preparation for submission to: *Deep-Sea Research Part I: Oceanographic Research Papers*

Author list: **Benjamin A. Lange**, Giulia Castellani, Jan Andries van Franeker and Hauke Flores

Author contributions: This study, the SUIT and sensor array were designed and developed by **B. A. Lange,** H. Flores J.A. van Franeker. Data were acquired by **B. A. Lange** and H. Flores. Data processing and protocols were developed by **B.A. Lange** with contributions from G. Castellani**.** Protocols were developed by **B. A. Lange,** G. Castellani and H. Flores. The analysis of the data was conducted by **B. A. Lange**. The manuscript first draft was written by **B. A. Lange** with contributions from all authors on the final version.

Paper 2

Title: *Spectrally-derived sea ice-algal chlorophyll a concentrations using under-ice horizontal profiling platforms*

paper currently under review in *Journal of Geophysical Research: Oceans*

Author list: **Benjamin A. Lange**, Christian Katlein, Marcel Nicolaus, Ilka Peeken, and Hauke Flores

Author contributions: This study was designed by **B. A. Lange**, M. Nicolaus, I. Peeken and H. Flores. ROV data were acquired by M. Nicolaus and C. Katlein. Data processing of ROV spectra were conducted by **B. A. Lange,** M. Nicolaus and C. Katlein. SUIT sensor data were acquired and processed by **B. A. Lange,** M. Nicolaus and H. Flores. Ice core sampling and processing were conducted by **B. A. Lange** and I. Peeken. Bio-optical statistical model development was realized by **B. A. Lange**. Data analyses were conducted by **B. A. Lange** with support from C. Katlein and H. Flores. The manuscript was written by **B. A. Lange** with contributions from all authors.

Below are additional publications not included in this thesis, which have made use of the methodological advancements presented in Chapter 2 and have incorporated the environmental data as essential components of their studies:

David, C., **B. Lange**, T. Krumpen, F. Schaafsma, J. A. van Franeker, and H. Flores (2015), Under-ice distribution of polar cod *Boreogadus saida* in the central Arctic Ocean and their association with sea-ice habitat properties, *Polar Biol.*, doi:10.1007/s00300-015-1774-0.

David, C., F. L. Schaafsma, J. A. van Franeker, **B. Lange**, A. Brandt, and H. Flores (2016), Community structure of under-ice fauna in relation to winter sea-ice habitat properties from the Weddell Sea, *Polar Biol.*, doi:10.1007/s00300-016-1948-4.

Schaafsma, F. L., C. David, E. A. Pakhomov, B. P. V. Hunt, **B. A. Lange**, H. Flores, and J. A. van Franeker (2016), Size and stage composition of age class 0 Antarctic krill (*Euphausia superba*) in the ice–water interface layer during winter/early spring, *Polar Biol.*, doi:10.1007/s00300-015-1877-7.

Chapter 3: *Linking sea ice algae spatial variability to summertime carbon demand*

In Chapter 3, we combined the developed toolbox from Chapter 2 with additional biological data, such as: photosynthetic parameters, under-ice fauna distributions, and under-ice fauna carbon demand, in order to develop robust ecological models for the ice-associated ecosystem. Furthermore, as an essential step in developing robust ecological models, we assessed the spatial variability of ice algae carbon production and availability at multiple scales (e.g., local to regional scales), and identified important relationships with community structure and sea ice-associated carbon demand.

Paper 3

Title: *On improving the spatial representativeness of sea ice algae chlorophyll a biomass and primary production estimates*

in preparation for submission to: *Geophysical Research Letters*

Author list: **Benjamin A. Lange**, Christian Katlein, Giulia Castellani, Mar Fernández-Méndez, Marcel Nicolaus, Ilka Peeken, and Hauke Flores

Author contributions: This study was designed by **B. A. Lange** and H. Flores. ROV data were acquired by M. Nicolaus and C. Katlein. Data processing of ROV spectra were conducted by **B. A. Lange,** M. Nicolaus and C. Katlein. SUIT sensor data were acquired and processed by **B. A. Lange,** M. Nicolaus and H. Flores. Ice core sampling and processing were conducted by **B. A. Lange**, M Fernández-Méndez and I. Peeken. Photosynthetic parameters and ice core PP rates were determined by M Fernández-Méndez. Bio-optical statistical model and PP up-scaling approach were developed by **B. A. Lange**. Data analyses were conducted by **B. A. Lange** with support from C. Katlein, M Fernández-Méndez and H. Flores. The manuscript was written by **B. A. Lange** with contributions from all authors.

Paper 4

Title: *Community structure of under-ice fauna in the Eurasian central Arctic Ocean in relation to environmental properties of sea-ice habitats*

published in *Marine Ecology Progress Series* (2015) 522:15-32

Author list: Carmen David, **Benjamin A. Lange**, Benjamin Rabe, Hauke Flores

Author contributions: This study was designed by C. David, H. Flores and **B. A. Lange**. Field sampling was performed by C. David, H. Flores and **B. A. Lange**. Species identification and counting was performed by C. David. Sensor data were processed by **B. A. Lange** H. Flores. Oceanographic data were provided by B. Rabe. The analysis of data was performed by C. David with support from **B. A. Lange** and H. Flores. Writing of the manuscript was realized by C. David with contribution from all authors.

Paper 5

Title: *The importance of ice algae-produced carbon in the central Arctic Ocean ecosystem: food web relationships revealed by lipid and stable isotope analyses*

Published in: *Limnology and Oceanography*, doi:10.1002/lno.10351

Author list: Doreen Kohlbach, Martin Graeve, **Benjamin A. Lange**, Carmen David, Ilka Peeken, and Hauke Flores

Author contributions: Field sampling for this study was performed by **B. A. Lange**, H. Flores, C. David and I. Peeken. Taxonomic classification was conducted by H. Flores and C. David. Laboratory analyses were accomplished by D. Kohlbach and M. Graeve. Data analyses were performed by D. Kohlbach with support from **B. A. Lange** and H. Flores. The manuscript was written by D. Kohlbach with contribution from all authors.

Chapter 4: *Assessing springtime spatial variability of sea ice algal habitat: MYI vs. FYI*

In Chapter 4, we conducted a detailed comparison of the physical-biological properties between multi-year sea ice (MYI) and first-year sea ice (FYI). In addition, we developed key physical-biological relationships to characterize springtime spatial variability of sea ice algae habitat for both FYI and MYI. We demonstrated a useful approach to use physical-biological relationships to parameterize a simple sea ice model, and for up-scaling sea ice algae habitat to satellite-based sea ice thickness and climatology-based snow depth observations.

Paper 6

Title: *Comparing springtime ice-algal chlorophyll a and physical properties of multi-year and first-year sea ice from the Lincoln Sea*

published in: *PLoS One*, 10(4), e0122418, doi:10.1371/journal.pone.0122418

Author list: **Benjamin A. Lange,** Christine Michel, Justin F. Beckers, J. Alec Casey, Hauke Flores, Ido Hatam, Guillaume Meisterhans, Andrea Niemi, Christian Haas

Author contributions: This study was designed by **B. A. Lange**, C. Michel and C. Haas. Field sampling was performed by **B. A. Lange,** I. Hatam, J. F. Beckers, J.A. Casey and C. Haas. Sample processing was conducted **B. A. Lange**, C. Michel, G. Meisterhans and A. Niemi. Data analyses were conducted by **B. A. Lange,** J. F. Beckers, J. A. Casey, H. Flores. The manuscript was written by **B. A. Lange** with contributions from all authors.

Paper 7

Title: *Suitable ice-algal habitat and biomass are largely underestimated over multi-year sea ice*

in preparation for submission to: *Progress in Oceanography*

Author list: **Benjamin A. Lange**, Hauke Flores, Christine Michel, Justin Beckers, Anne Bublitz, J. Alec Casey, Giulia Castellani, Ido Hatam, Anke Reppchen, Svenja A. Rudolph, Christian Haas

Author contributions: This study was designed by **B. A. Lange**, C. Michel and C. Haas. Field sampling was performed by **B. A. Lange**, I. Hatam, J. F. Beckers, J.A. Casey, A. Bublitz and C. Haas. Sample processing was conducted **B. A. Lange**, A. Reppchen and C. Michel. Data and statistical analyses were conducted by **B. A. Lange**, J. F. Beckers, J. A. Casey, H. Flores, A. Reppchen, S.A. Rudolph and C. Michel. The manuscript was written by **B. A. Lange** with contributions from all authors.

Complete list of peer-reviewed publications completed during my PhD project:

Lange, B. A., C. Michel, J. F. Beckers, J. A. Casey, H. Flores, I. Hatam, G. Meisterhans, A. Niemi, and C. Haas (2015), Comparing springtime ice-algal chlorophyll a and physical properties of multi-year and first-year sea ice from the Lincoln Sea, *PLoS One*, *10*(4), e0122418, doi:10.1371/journal.pone.0122418.

Hatam, I., **B. Lange**, J. Beckers, C. Haas, and B. Lanoil (2016), Bacterial communities from Arctic seasonal sea ice are more compositionally variable than those from multi-year sea ice, *The ISME journal*, doi:10.1038/ismej.2016.4.

David, C., **B. Lange**, T. Krumpen, F. Schaafsma, J. A. van Franeker, and H. Flores (2015a), Under-ice distribution of polar cod Boreogadus saida in the central Arctic Ocean and their association with sea-ice habitat properties, *Polar Biology*, doi:10.1007/s00300-015-1774-0.

David, C., **B. Lange**, B. Rabe, and H. Flores (2015b), Community structure of under-ice fauna in the Eurasian central Arctic Ocean in relation to environmental properties of sea-ice habitats, *Marine Ecoogy Progress Series*, *522*, 15-32, doi:10.3354/meps11156.

Kohlbach, D., M. Graeve, **B. A. Lange**, C. David, I. Peeken, and H. Flores (2016), The importance of ice algae-produced carbon in the central Arctic Ocean ecosystem: food web relationships revealed by lipid and stable isotope analyses, *Limnology and Oceanography*, doi: 10.1002/lno.10351.

David, C., F. Schaafsma, J. A. van Franeker, **B. Lange**, Brandt, A., and H. Flores (2016), Community structure of under-ice fauna in relation to winter sea-ice habitat properties from the Weddell Sea, *Polar Biology*, doi: 10.1007/s00300-016-1948-4

Schaafsma, F. L., C. David, E. A. Pakhomov, B. P. V. Hunt, **B. A. Lange**, H. Flores, and J. A. van Franeker (2016), Size and stage composition of age class 0 Antarctic krill (Euphausia superba) in the ice–water interface layer during winter/early spring, *Polar Bioogy.*, doi:10.1007/s00300-015-1877-7.

Stecher, A., S. Neuhaus, **B. Lange**, S. Frickenhaus, B. Beszteri, P. G. Kroth, and K. Valentin (2015), rRNA and rDNA based assessment of sea ice protist biodiversity from the central Arctic Ocean, *European Journal of Phycology*, 1-16, doi:10.1080/09670262.2015.1077395.

Hatam, I., R. Charchuk, **B. Lange**, J. Beckers, C. Haas, and B. Lanoil (2014), Distinct bacterial assemblages reside at different depths in Arctic multiyear sea ice, *FEMS Microbiology Ecology*, 1-11, doi:10.1111/1574-6941.12377.

Backs, J., J. Bottoms, S. P. Khaligh, **B. Lange**, and S. Williamson (**2013**), AlbertaSat-1: Greenhouse Gas Monitoring for Industrial and Environmental Improvement, in *Innovative Ideas for Micro/Nano-satellite Missions*, edited by R. Sandau, S. Nakasuka, R. Kawashima and J. J. Sellers, pp. 40 - 62, International Academy of Astronautics.

References:

AMAP, 2011. Snow,water, ice and permafrost in the Arctic (SWIPA): Climate change and the cryosphere. Gaustadalléen 21, N-0349 Oslo, Norway (www.amap.no).

Ambrose, W.G., von Quillfeldt, C., Clough, L.M., Tilney, P.V.R., Tucker, T., 2005. The sub-ice algal community in the Chukchi sea: large- and small-scale patterns of abundance based on images from a remotely operated vehicle. *Polar Biology*, 28, 784-795.

Arndt, C.E., Swadling, K.M., 2006. Crustacea in Arctic and Antarctic Sea Ice: Distribution, Diet and Life History Strategies. In A.J. Southward, D.W. Sims (Eds.), *Advances in Marine Biology*, Vol. 51 (p. 119). San Diego, California 92101-4495, USA: Elsevier.

Arrigo, K.R., 2014. Sea Ice Ecosystems. *Annual Review of Marine Science*, 6, 439-467.

Arrigo, K.R., van Dijken, G.L., 2011. Secular trends in Arctic Ocean net primary production. *Journal of Geophysical Research*, 116, C09011.

Arrigo, K.R., van Dijken, G.L., 2015. Continued increases in Arctic Ocean primary production. *Progress in Oceanography*, 136, 60-70.

Barlow, R.G., Gosselin, M., Legendre, L., Therriault, J.C., Demers, S., Mantoura, R.F.C., Llewellyn, C.A., 1988. Photoadaptive strategies in sea-ice microalgae. *Marine Ecology Progress Series*, 45, 145-152.

Bluhm, B.A., Gradinger, R., Piraino, S., 2007. First record of sympagic hydroids (Hydrozoa, Cnidaria) in Arctic coastal fast ice. *Polar Biology*, 30, 1557-1563.

Budge, S.M., Wooller, M.J., Springer, A.M., Iverson, S.J., McRoy, C.P., Divoky, G.J., 2008. Tracing carbon flow in an arctic marine food web using fatty acid-stable isotope analysis. *Oecologia*, 157, 117-129.

Budyko, M.I., 1969. The effect of solar radiation variations on the climate of the earth. *Tellus*, 21, 611-619.

Campbell, K., Mundy, C.J., Barber, D.G., Gosselin, M., 2014a. Characterizing the sea ice algae chlorophyll a–snow depth relationship over Arctic spring melt using transmitted irradiance. *Journal of Marine Systems*, , in press.

Campbell, K., Mundy, C.J., Barber, D.G., Gosselin, M., 2014b. Remote Estimates of Ice Algae Biomass and Their Response to Environmental Conditions during Spring Melt. *Arctic*, 67, 375.

Cota, G.F., Horne, E.P.W., 1989. Physical Control of Arctic Ice Algal Production. *Marine Ecology Progress Series*, 52, 111-121.

Cota, G.F., Smith, R.E.H., 1991. Ecology of bottom ice algae: III. Comparative physiology. *Journal of Marine Systems*, 2, 297-315.

Craig, S.E., Jones, C.T., Li, W.K.W., Lazin, G., Horne, E., Caverhill, C., Cullen, J.J., 2012. Deriving optical metrics of coastal phytoplankton biomass from ocean colour. *Remote Sensing of Environment*, 119, 72-83.

David, C., Lange, B., Rabe, B., Flores, H., 2015. Community structure of under-ice fauna in the Eurasian central Arctic Ocean in relation to environmental properties of sea-ice habitats. *Marine Ecology Progress Series*, 522, 15-32.

Dupont, F., 2012. Impact of sea-ice biology on overall primary production in a biophysical model of the pan-Arctic Ocean. *Journal of Geophysical Research*, Vol. 117.

Eicken, H., 2003. From the microscopic, to the macroscopic, to the regional scale: growth, microstructure and properties of sea ice. *Sea ice—an introduction to its physics, biology, chemistry and geology. Blackwell Science, London, England* (pp. 22–81).

Fernández-Méndez, M., Katlein, C., Rabe, B., Nicolaus, M., Peeken, I., Bakker, K., Flores, H., Boetius, A., 2015. Photosynthetic production in the Central Arctic during the record sea-ice minimum in 2012. *Biogeosciences Discussions*, 12, 2897-2945.

Fetterer, F., Knowles, K., Meier, W., Savoie, M., 2002, udpated 2011. Sea Ice Index. Boulder, CO: National Snow and Ice Data Center. Digital Media.

Gosselin, M., Legendre, L., Therriault, J.-C., Demers, S., 1990. Light and nutrient limitation of sea-ice microalgae (Hudson Bay, Canadian Arctic). *Journal of Phycology*, 26, 220-232.

Gosselin, M., Legendre, L., Therriault, J.C., Demers, S., Rochet, M., 1986. Physical control of the horizontal patchiness of sea-ice microalgae. *Marine Ecology Progress Series*, 29, 289-298.

Gosselin, M., Levasseur, M., Wheeler, P.A., Horner, R.A., Booth, B.C., 1997. New measurements of phytoplankton and ice algal production in the Arctic Ocean. *Deep Sea Research Part II: Topical Studies in Oceanography*, 44, 1623-1644.

Gradinger, R., 2009. Sea-ice algae: Major contributors to primary production and algal biomass in the Chukchi and Beaufort Seas during May/June 2002. *Deep Sea Research Part II: Topical Studies in Oceanography*, 56, 1201-1212.

Gradinger, R., Bluhm, B., 2004. In-situ observations on the distribution and behavior of amphipods and Arctic cod (Boreogadus saida) under the sea ice of the High Arctic Canada Basin. *Polar Biology*, 27.

Gradinger, R., Bluhm, B., Iken, K., 2010. Arctic sea-ice ridges—Safe heavens for sea-ice fauna during periods of extreme ice melt? *Deep Sea Research Part II: Topical Studies in Oceanography*, 57, 86-95.

Gradinger, R., Friedrich, C., Spindler, M., 1999. Abundance, biomass and composition of the sea ice biota of the Greenland Sea pack ice. *Deep Sea Research Part II: Topical Studies in Oceanography*, 46, 1457-1472.

Gradinger, R., Meiners, K., Plumley, G., Zhang, Q., Bluhm, B.A., 2005. Abundance and composition of the sea-ice meiofauna in off-shore pack ice of the Beaufort Gyre in summer 2002 and 2003. *Polar Biology*, 28, 171-181.

Grenfell, T.C., Maykut, G.A., 1977. The optical properties of ice and snow in the Arctic Basin. *Journal of Glaciology*, 18, 445-463.

Gutt, J., 1995. The occurrence of sub-ice algal aggregations off northeast Greenland. *Polar Biology*, 15, 247-252.

Haas, C., Hendricks, S., Doble, M., 2006. Comparison of the sea-ice thickness distribution in the Lincoln Sea and adjacent Arctic Ocean in 2004 and 2005. *Annals of Glaciology*, 44, 247-252.

Haas, C., Hendricks, S., Eicken, H., Herber, A., 2010. Synoptic airborne thickness surveys reveal state of Arctic sea ice cover. *Geophysical Research Letters*, Vol. 37 (p. L09501).

Haas, C., Pfaffling, A., Hendricks, S., Rabenstein, L., Etienne, J.-L., Rigor, I., 2008. Reduced ice thickness in Arctic Transpolar Drift favors rapid ice retreat. *Geophysical Research Letters*, Vol. 35 (p. L17501).

Hamre, B., Winther, J.-G., Gerland, S., Stamnes, J.J., Stamnes, K., 2004. Modeled and measured optical transmittance of snow-covered first-year sea ice in Kongsfjorden, Svalbard. *Journal of Geophysical Research*, 109, C10006.

Horner, R., Ackley, S., Dieckmann, G., Gulliksen, B., Hoshiai, T., Legendre, L., Melnikov, I., Reeburgh, W., Spindler, M., Sullivan, C., 1992. Ecology of sea ice biota. *Polar Biology*, 12, 417-427.

Howell, S.E.L., Duguay, C.R., Markus, T., 2009. Sea ice conditions and melt season duration variability within the Canadian Arctic Archipelago: 1979–2008. *Geophysical Research Letters*, Vol. 36 (p. L10502).

IPCC, 2013. Climate Change 2013: The Physical Science Basis. Contribution of Working Group I to the Fifth Assessment Report of the Intergovernmental Panel on Climate Change. In T.F. Stocker, D. Qin, G.-K. Plattner, M. Tignor, S.K. Allen, J. Boschung, A. Nauels, Y. Xia, V. Bex and P.M. Midgley (eds.) (Ed.) (p. 1535). Cambridge, United Kingdom and New York, NY, USA.

Järvinen, O., Leppäranta, M., 2011. Transmission of solar radiation through the snow cover on floating ice. *Journal of Glaciology*, 57, 861-870.

Johannessen, O.M., Bengtsson, L., Miles, M.W., Kuzmina, S.I., Semenov, V.A., Alekseev, G.V., Nagurnyi, A.P., Zakharov, V.F., Bobylev, L.P., Pettersson, L.H., Hasselmann, K., Cattle, H.P., 2004. Arctic climate change: observed and modelled temperature and sea ice variability. *Tellus* 56A, 328-341.

Katlein, C., Arndt, S., Nicolaus, M., Perovich, D.K., Jakuba, M.V., Suman, S., Elliott, S., Whitcomb, L.L., McFarland, C.J., Gerdes, R., Boetius, A., German, C.R., 2015. Influence of ice thickness and surface properties on light transmission through Arctic sea ice. *Journal of Geophysical Research: Oceans*, 120, 5932-5944.

Katlein, C., Fernández-Méndez, M., Wenzhöfer, F., Nicolaus, M., 2014a. Distribution of algal aggregates under summer sea ice in the Central Arctic. *Polar Biology*.

Katlein, C., Nicolaus, M., Petrich, C., 2014b. The anisotropic scattering coefficient of sea ice. *Journal of Geophysical Research*, 119, 842-855.

Kohlbach, D., Graeve, M., Lange, B.A., David, C., Peeken, I., Flores, H., 2016. The importance of ice algae-produced carbon in the central Arctic Ocean ecosystem: food web relationships revealed by lipid and stable isotope analyses. *Limnol. Oceanogr*.

Kosobokova, K., Hirche, H.-J., 2009. Biomass of zooplankton in the eastern Arctic Ocean – A base line study. *Progress in Oceanography*, 82, 265-280.

Kwok, R., 2007. Near zero replenishment of the Arctic multiyear sea ice cover at the end of 2005 summer. *Geophysical Research Letters*, Vol. 34 (p. L05501).

Kwok, R., 2009. Outflow of Arctic Ocean Sea Ice into the Greenland and Barents Seas: 1979–2007. *Journal of Climate*, 22, 2438-2457.

Kwok, R., Cunningham, G., 2010. Contribution of melt in the Beaufort Sea to the decline in Arctic multiyear sea ice coverage: 1993–2009. *Geophysical Research Letters*, Vol. 37 (p. L20501).

Kwok, R., Cunningham, G.F., Wensnahan, M., Rigor, I., Zwally, H.J., Yi, D., 2009. Thinning and volume loss of the Arctic Ocean sea ice cover: 2003–2008. *Journal of Geophysical Research*, Vol. 114 (p. C07005).

Kwok, R., Rothrock, D.A., 2009. Decline in Arctic sea ice thickness from submarine and ICESat records: 1958–2008. *Geophysical Research Letters*, Vol. 36 (p. L15501).

Kwok, R., Toudal Pedersen, L., Gudmandsen, P., Pang, S., 2010. Large sea ice outflow into the Nares Strait in 2007. *Geophysical Research Letters*, Vol. 37 (p. L03502).

Lavoie, D., Denman, K., Michel, C., 2005. Modeling ice algal growth and decline in a seasonally ice-covered region of the Arctic (Resolute Passage, Canadian Archipelago). *Journal of Geophysical Research*, 110, C11009.

Lavoie, D., Denman, K.L., Macdonald, R.W., 2010. Effects of future climate change on primary productivity and export fluxes in the Beaufort Sea. *Journal of Geophysical Research C: Oceans*, 115.

Laxon, S.W., Giles, K.A., Ridout, A.L., Wingham, D.J., Willatt, R., Cullen, R., Kwok, R., Schweiger, A., Zhang, J., Haas, C., Hendricks, S., Krishfield, R., Kurtz, N., Farrell, S., Davidson, M., 2013. CryoSat-2 estimates of Arctic sea ice thickness and volume. *Geophysical Research Letters*, 40, 732-737.

Lee, Y.J., Matrai, P.A., Friedrichs, M.A.M., Saba, V.S., Antoine, D., Ardyna, M., Asanuma, I., Babin, M., Bélanger, S., Benoît-Gagné, M., Devred, E., Fernández-Méndez, M., Gentili, B., Hirawake, T., Kang, S.-H., Kameda, T., Katlein, C., Lee, S.H., Lee, Z., Mélin, F., Scardi, M., Smyth, T.J., Tang, S., Turpie, K.R., Waters, K.J., Westberry, T.K., 2015. An assessment of phytoplankton primary productivity in the Arctic Ocean from satellite ocean color/in situ chlorophyll-a based models. *Journal of Geophysical Research: Oceans*, 120, 6508-6541.

Leu, E., Mundy, C.J., Assmy, P., Campbell, K., Gabrielsen, T.M., Gosselin, M., Juul-Pedersen, T., Gradinger, R., 2015. Arctic spring awakening – Steering principles behind the phenology of vernal ice algal blooms. *Progress in Oceanography*, 139, 151-170.

Leu, E., Søreide, J.E., Hessen, D.O., Falk-Petersen, S., Berge, J., 2011. Consequences of changing sea-ice cover for primary and secondary producers in the European Arctic shelf seas: Timing, quantity, and quality. *Progress in Oceanography*, 90, 18-32.

Light, B., Grenfell, T.C., Perovich, D.K., 2008. Transmission and absorption of solar radiation by Arctic sea ice during the melt season. *Journal of Geophysical Research*, 113, C03023.

Lindsay, R., Zhang, J., 2005. The thinning of Arctic sea ice, 1988-2003: have we passed a tipping point? *Journal of Climate*, 18, 4879-4894.

Long, M.H., Koopmans, D., Berg, P., Rysgaard, S., Glud, R.N., Søgaard, D.H., 2012. Oxygen exchange and ice melt measured at the ice-water interface by eddy correlation. *Biogeosciences*, 9, 1957-1967.

Markus, T., Stroeve, J.C., Miller, J., 2009. Recent changes in Arctic sea ice melt onset, freezeup, and melt season length. *Journal of Geophysical Research*, Vol. 114 (p. C12024).

Maslanik, J.A., Fowler, C., Stroeve, J., Drobot, S., Zwally, J., Yi, D., Emery, W., 2007. A younger, thinner Arctic ice cover: Increased potential for rapid, extensive sea-ice loss. *Geophysical Research Letters*, Vol. 34 (p. L24501).

Maslanik, J.A., Stroeve, J.C., Fowler, C., Emery, W., 2011. Distribution and trends in Arctic sea ice age through spring 2011. *Geophysical Research Letters*, Vol. 38 (p. L13502).

Maykut, G.A., Grenfell, T.C., 1975. Spectral Distribution of Light beneath 1st-Year Sea Ice in Arctic Ocean. *Limnology and Oceanography*, 20, 554-563.

Melbourne-Thomas, J., Meiners, K.M., Mundy, C.J., Schallenberg, C., Tattersall, K.L., Dieckmann, G.S., 2015. Algorithms to estimate Antarctic sea ice algal biomass from under-ice irradiance spectra at regional scales. *Marine Ecology Progress Series*, 536, 107-121.

Melnikov, I.A., Kolosova, E.G., Welch, H.E., Zhitina, L.S., 2002. Sea ice biological communities and nutrient dynamics in the Canada Basin of the Arctic Ocean. *Deep Sea Research Part I: Oceanographic Research Papers*, 49, 1623-1649.

Michel, C., Legendre, L., Demers, S., Therriault, J., 1988. Photoadaptation of sea-ice microalgae in springtime: Photosynthesis and carboxylating enzymes. *Marine Ecology Progress Series*, 50, 177-185.

Michel, C., Legendre, L., Ingram, R.G., Gosselin, M., Levasseur, M., 1996. Carbon budget of sea-ice algae in spring: Evidence of a significant transfer to zooplankton grazers. *Journal of Geophysical Research: Oceans*, 101, 18345-18360.

Michel, C., Nielsen, T.G., Nozais, C., Gosselin, M., 2002. Significance of sedimentation and grazing by ice micro-and meiofauna for carbon cycling in annual sea ice (northern Baffin Bay). *Aquatic Microbial Ecology*, 30, 57-68.

Miller, L.A., Fripiat, F., Else, B.G.T., Bowman, J.S., Brown, K.A., Collins, R.E., Ewert, M., Fransson, A., Gosselin, M., Lannuzel, D., Meiners, K.M., Michel, C., Nishioka, J., Nomura, D., Papadimitriou, S., Russell, L.M., Sørensen, L.L., Thomas, D.N., Tison, J.-L., van Leeuwe, M.A., Vancoppenolle, M., Wolff, E.W., Zhou, J., 2015. Methods for biogeochemical studies of sea ice: The state of the art, caveats, and recommendations. *Elementa: Science of the Anthropocene*, 3, 000038.

Mock, T., Gradinger, R., 1999. Determination of Arctic ice algal production with a new in situ incubation technique. *Marine Ecology Progress Series*, 177, 15-26.

Mundy, C.J., Ehn, J.K., Barber, D.G., Michel, C., 2007. Influence of snow cover and algae on the spectral dependence of transmitted irradiance through Arctic landfast first-year sea ice. *Journal of Geophysical Research*, 112, C03007.

Nicolaus, M., Gerland, S., Hudson, S.R., Hanson, S., Haapala, J., Perovich, D.K., 2010. Seasonality of spectral albedo and transmittance as observed in the Arctic Transpolar Drift in 2007. *Journal of Geophysical Research*, 115, C11011, doi:11010.11029/12009JC006074.

Nicolaus, M., Katlein, C., 2013. Mapping radiation transfer through sea ice using a remotely operated vehicle (ROV). *The Cryosphere*, 7, 763-777.

Nicolaus, M., Katlein, C., Maslanik, J., Hendricks, S., 2012. Changes in Arctic sea ice result in increasing light transmittance and absorption. *Geophysical Research Letters*, 39, 2699–2700.

Notz, D., 2009. The future of ice sheets and sea ice: Between reversible retreat and unstoppable loss. *Proceedings of the National Academy of Sciences*, Vol. 106 (pp. 20590-20595).

Ogi, M., Rigor, I.G., McPhee, M.G., Wallace, J.M., 2008. Summer retreat of Arctic sea ice: Role of summer winds. *Geophysical Research Letters*, Vol. 35 (p. L24701).

Perovich, D.K., 1996. The Optical Properties of Sea Ice. Cold Regions Research and Engineering Laboratory.

Perovich, D.K., Jones, K.F., Light, B., Eicken, H., Markus, T., Stroeve, J., Lindsay, R., 2011. Solar partitioning in a changing Arctic sea-ice cover. *Annals of Glaciology*, 52, 192-196.

Perovich, D.K., Light, B., Eicken, H., Jones, K.F., Runciman, K., Nghiem, S.V., 2007. Increasing solar heating of the Arctic Ocean and adjacent seas, 1979–2005: Attribution and role in the ice-albedo feedback. *Geophysical Research Letters*, Vol. 34 (p. L19505).

Perovich, D.K., Richter-Menge, J.A., Jones, K.F., Light, B., 2008. Sunlight, water, and ice: Extreme Arctic sea ice melt during the summer of 2007. *Geophysical Research Letters*, Vol. 35 (p. L11501).

Perovich, D.K., Roesler, C.S., Pegau, W.S., 1998. Variability in Arctic sea ice optical properties. *Journal of Geophysical Research: Oceans*, 103, 1193-1208.

Rat'kova, T., Sazhin, A., Kosobokova, K., 2004. Unicellular inhabitants of the White Sea underice pelagic zone during the early spring period. *Oceanology*, 44, 240-246.

Ricker, R., Hendricks, S., Helm, V., Skourup, H., Davidson, M., 2014. Sensitivity of CryoSat-2 Arctic sea-ice freeboard and thickness on radar-waveform interpretation. *The Cryosphere*, 8, 1607-1622.

Rigor, I.G., Wallace, J.M., 2004. Variations in the age of Arctic sea-ice and summer sea-ice extent. *Geophysical Research Letters*, Vol. 31 (p. L09401).

Rigor, I.G., Wallace, J.M., Colony, R.L., 2002. Response of Sea Ice to the Arctic Oscillation. *Journal of Climate*, 15, 2648-2663.

Rothrock, D.A., Zhang, J., Yu, Y., 2003. The arctic ice thickness anomaly of the 1990s: A consistent view from observations and models. *Journal of Geophysical Research*, Vol. 108 (p. 3083).

Rysgaard, S., Glud, R.N., Sejr, M.K., Blicher, M.E., Stahl, H.J., 2008. Denitrification activity and oxygen dynamics in Arctic sea ice. *Polar Biology*, 31, 527-537.

Rysgaard, S., Kühl, M., Glud, R.N., Hansen, J.W., 2001. Biomass, production and horizontal patchiness of sea ice algae in a high-Arctic fjord (Young Sound, NE Greenland). *Marine Ecology Progress Series*, 223, 15-26.

Serreze, M.C., Barrett, A.P., Slater, A.G., Steele, M., Zhang, J., Trenberth, K.E., 2007a. The large-scale energy budget of the Arctic. *Journal of Geophysical Research*, Vol. 112 (p. D11122).

Serreze, M.C., Barrett, A.P., Slater, A.G., Woodgate, R.A., Aagaard, K., Lammers, R.B., Steele, M., Moritz, R., Meredith, M., Lee, C.M., 2006. The large-scale freshwater cycle of the Arctic. *Journal of Geophysical Research*, Vol. 111 (p. C11010).

Serreze, M.C., Holland, M.M., Stroeve, J., 2007b. Perspectives on the Arctic's shrinking sea-ice cover. *Science*, 315, 1533-1536.

Søreide, J.E., Hop, H., Carroll, M.L., Falk-Petersen, S., Hegseth, E.N., 2006. Seasonal food web structures and sympagic–pelagic coupling in the European Arctic revealed by stable isotopes and a two-source food web model. *Progress in Oceanography*, 71, 59-87.

Søreide, J.E., Leu, E.V.A., Berge, J., Graeve, M., Falk-Petersen, S., 2010. Timing of blooms, algal food quality and Calanus glacialis reproduction and growth in a changing Arctic. *Global Change Biology*, Vol. 16 (pp. 3154–3163).

Spreen, G., Kaleschke, L., Heygster, G., 2008. Sea ice remote sensing using AMSR-E 89-GHz channels. *Journal of Geophysical Research*, 113, C02S03.

Steffens, M., Granskog, M., Kaartokallio, H., Kuosa, H., Luodekari, K., Papadimitriou, S., Thomas, D., 2006. Spatial variation of biogeochemical properties of landfast sea ice in the Gulf of Bothnia, Baltic Sea. *Annals of Glaciology*, 44, 80-87.

Stroeve, J.C., Kattsov, V., Barrett, A., Serreze, M., Pavlova, T., Holland, M., Meier, W.N., 2012. Trends in Arctic sea ice extent from CMIP5, CMIP3 and observations. *Geophysical Research Letters*, 39, L16502.

Stroeve, J.C., Serreze, M.C., Holland, M.M., Kay, J.E., Malanik, J., Barrett, A.P., 2011. The Arctic's rapidly shrinking sea ice cover: a research synthesis. *Climatic Change* (pp. 1-23).

Sturm, M., Holmgren, J., Perovich, D.K., 2002. Winter snow cover on the sea ice of the Arctic Ocean at the Surface Heat Budget of the Arctic Ocean (SHEBA): Temporal evolution and spatial variability. *Journal of Geophysical Research*, Vol. 107 (p. 8047).

Taylor, B.B., Taylor, M.H., Dinter, T., Bracher, A., 2013. Estimation of relative phycoerythrin concentrations from hyperspectral underwater radiance measurements—A statistical approach. *Journal of Geophysical Research: Oceans*, 118, 2948-2960.

Thomas, C.W., 1963. On the transfer of visible radiation through sea ice and snow. *Journal of Glaciology*, 4, 481-484.

van Franeker, J.A., Flores, H., van Dorssen, M., 2009. The surface and under ice trawl (SUIT). Frozen desert alive—the role of sea ice for pelagic macrofauna and its predators. *PhD thesis, University of Groningen,Groningen*.

Vancoppenolle, M., Meiners, K.M., Michel, C., Bopp, L., Brabant, F., Carnat, G., Delille, B., Lannuzel, D., Madec, G., Moreau, S., 2013. Role of sea ice in global biogeochemical cycles: emerging views and challenges. *Quaternary science reviews*, Vol. 79 (pp. 207-230).

Wadhams, P., 2012. The use of autonomous underwater vehicles to map the variability of under-ice topography. *Ocean Dynamics*, 62, 439-447.

Wang, S.W., Budge, S.M., Iken, K., Gradinger, R.R., Springer, A.M., Wooller, M.J., 2015. Importance of sympagic production to Bering Sea zooplankton as revealed from fatty acid-carbon stable isotope analyses. *Marine Ecology Progress Series*, 518, 31-50.

Wang, S.W., Springer, A.M., Budge, S.M., Horstmann, L., Quakenbush, L.T., Wooller, M.J., 2016. Carbon sources and trophic relationships of ice seals during recent environmental shifts in the Bering Sea. *Ecological Applications*, 26, 830-845.

Wassmann, P., 2011. Arctic marine ecosystems in an era of rapid climate change. *Progress in Oceanography*, Vol. 90 (pp. 1-17).

Wassmann, P., Duarte, C.M., Agusti, S., Sejr, M.K., 2011. Footprints of climate change in the Arctic marine ecosystem. *Global Change Biology*, Vol. 17 (pp. 1235-1249).

Weeks, W.F., Ackley, S.F., 1986. The growth, structure, and properties of sea ice. In N. Untersteiner (Ed.), *The geophysics of sea ice. NATO ASI Series. Series B, Physics vol. 146.* (pp. 9-164). Plenum, New York: Springer.

Werner, I., 1997. Grazing of Arctic under-ice amphipods on sea-ice algae. *Marine Ecology Progress Series*, Vol. 160 (pp. 93-99).

Chapter 2: Methodological Advancements of Ecologically Relevant Sea Ice Observations

The Surface and Under-Ice Trawl (SUIT) towed behind the *RV Polarstern* within Arctic sea ice.

Paper 1. The Surface and Under-Ice Trawl (SUIT)-mounted environmental sensor array

in preparation for submission to: *Deep-Sea Research Part I: Oceanographic Research Papers*

NOTE: Supplementary Material for this paper is found in Appendix A1 & A2

Benjamin A. Lange, Giulia Castellani, Jan Andries van Franeker and Hauke Flores

Key Points

- Observed large horizontal variability in ice thickness, and surface water chl *a* and salinity
- SUIT sensor array represented the spatial variability better than traditional point location characterizations of environmental properties
- SUIT sensor array is an essential contribution to accurately and representatively model the ice associated ecosystem

Abstract

In order to accurately characterize relationships between a community and its physico-biogeochemical surrounding, it is particularly important to representatively characterize the associated environmental properties. The Surface and Under-ice Trawl (SUIT) is a relatively new net, which can catch organisms residing in close proximity to the sea ice underside. Since sea ice is a highly inhomogeneous habitat, it is essential to characterize the spatial variability of this environment coincident to the under-ice trawl's in order to representatively assess and model relationships between the community and its environment. Here we presented a detailed description of the newly developed SUIT-mounted environmental sensor array, which can measure key environmental properties such as: sea ice thickness, salinity, temperature, water chlorophyll *a* (chl *a*), under-ice light, and ice-algal chl *a*. Furthermore, we provided detailed descriptions of data processing and calculations of all parameters. Our results indicated large horizontal variability in ice thickness, and surface water chl *a* and salinity, whereas temperature was rather homogeneous within hauls. A comparison with nearby ship-based and ice station observations showed that the SUIT sensor array represented the spatial variability better than these traditional point location characterizations of the under-ice environmental properties. We showed that the SUIT-mounted sensor array is an essential contribution in order to accurately and representatively model the ice associated ecosystem.

1.1 Overview of SUIT and sensor array

The surface and under-ice trawl (SUIT; Figure 1) was developed by IMARES (The Netherlands) to address a key issue in polar ecology regarding representative sampling of the under-ice environment. The SUIT has been extensively used in the Southern Ocean (e.g., David et al., 2016; Flores et al., 2011; Flores et al., 2012; Schaafsma et al., 2016) and was not deployed within the ice covered Arctic Ocean until more recently (e.g., David et al., 2015a; David et al., 2015b; Kohlbach et al., 2016).

Previous studies using the SUIT have described in detail the ecological and biological aspects of the catch and distribution of organisms in both Polar Regions. A detailed description of the SUIT operation and physical schematics is provided in (van Franeker et al., 2009). Studies conducted before 2012, included only qualitative assessments (e.g., human observations) of the sampled ice and under-ice environment and/or used nearby ship-based CTD casts to describe the environmental setting. Therefore, an environmental sensor array was developed in order to conduct coincident quantitative observations of the ice and under-ice water environments (Figure 1 c). This sensor array was previously described, albeit briefly, in (David et al., 2015b). Therefore, a more detailed description of data processing and calculations of all parameters is warranted and described here.

Not only does the sensor array provide coincident quantitative observations but it allows investigations of the horizontal variability of key environmental parameters, which are likely crucial in structuring the under-ice communities and are not possible with qualitative observations or point location vertical CTD casts. In addition to the methodological description, we provided a brief overview of the results and compare the SUIT observations to nearby ship-based and ice station-based observations in order to assess the representativeness of using nearby observations (i.e., not-coincident) to characterize the environmental setting.

Throughout the development of this sensor array we compiled detailed protocols for SUIT deployments. These protocols are found in Appendix A-1 and provide detailed instructions on:

i) preparing the sensors before deployment, including configuring the sensors using specific manufacturer software;
ii) data retrieval after deployments, also using manufacturer software; and
iii) formatting data to be suitable for the processing described in this paper.

Furthermore, processing scripts were developed using R software (R-Development-Core-Team, 2012), which in addition to data processing provide extensive plotting, data summary, and data inspection functionality. These scripts were developed to be user-friendly and thus can easily be applied by additional users, albeit with a relatively good knowledge of R programming. This compilation of R scripts is available upon request.

Figure 1. The Surface and Under-Ice Trawl (SUIT): a) in the water being towed by the RV Polatstern; b) laying on its side on the deck of the Polarstern; and c) depicted in a simplified diagram showing a side view with mounted locations of the sensors (not to scale).

1.2 Data and Methods

1.2.1 Data Processing

Here we presented processing and results of the environmental sensor data acquired from 15 SUIT hauls deployed during the *RV Polarstern* cruise PS80.3 (*IceArc*) to the central Arctic Ocean from 4 August to 8 October 2012 (Figure 2). The environmental sensor array enabled measurements of:

i) *water inflow speed* and *direction*, *pitch* and *roll* angles, and *pressure* (i.e., depth) using an Acoustic Doppler Current Profiler (ADCP; Nortek Aquadopp® Profiler) with three acoustic beams, which allowed 3-dimensional measurements of current velocities, at frequency of 2 MHZ, and a sampling interval of 1s;

ii) *water temperature*, *water salinity* (practical salinity scale PSS-78; Fofonoff, 1985), and *water depth* using a Conductivity Temperature Depth (CTD) probe (Sea and Sun Technology CTD75M memory probe) with a sampling interval of 0.1 s;

iii) *sea ice draft* observations were derived using an altimeter (Tritech PA500/6-E), which was incorporated into the CTD (0.1 s sampling interval), CTD *depth* measurements, and corrected by using *pitch* and *roll* measurements from the ADCP;

iv) water column (i.e., pelagic phytoplankton) *chl a* concentrations using a fluorometer (Turner Cyclops), which was also incorporated into the CTD (0.1 s sampling interval);

v) *under-ice light* levels using Ramses spectral radiometers (Trios GmbH, Rastede, Germany), processing and methods described in section 1.2: Lange et al. (submitted);

vi) *ice-algal chl a* were derived from the Ramses spectral radiometers processing and methods described in section 1.2: Lange et al. (submitted).

All data processing was conducted using R software Version 2.15.2 (R-Development-Core-Team, 2012). Excel was used to examine each file to ensure consistent naming protocol and column lengths, which was required for data import of the processing scripts.

The ADCP and CTD sensors sampled at different rates, 1 s and 0.1 s, respectively, and it was not possible to always steam at a constant speed. Therefore, we needed to re-sample and interpolate the data to a common and representative sampling interval, chosen to be 0.5 m. One of the most important tasks during deployments was to ensure the time of each sensor was synchronized to the ships time before each haul. Using synchronized time to join data ensured precise and accurate joining of coincident data from different sensors.

The CTD and ADCP required pressure calibration before sensor deployments to account for varying atmospheric pressure between deployments. CTD pressure data were examined to ensure calibration was conducted and if not was accounted for by subtracting the atmospheric pressure value observed while the sensor was on deck (e.g., typically around 0.1 dbar or ~0.1 m water depth). The ADCP pressure sensor, however, undergoes signal drift throughout the haul and therefore needed to be corrected. The drift of the ADCP pressure sensor was accounted for in each haul's data separately by linear interpolating between the atmospheric pressure (i.e., pressure measured on deck) before the haul and the atmospheric pressure after the haul. The drift was assumed to be linear over time and therefore the linear equation describing pressure drift as a function of time was then subtracted from the entire ADCP pressure data. Each haul was manually examined before and after drift correction to ensure accurate results. This method of drift correction was validated by comparing the ADCP corrected pressure with the CTD pressure, which resulted in accurate pressure observations showing a constant offset approximately equal to the vertical distance between the CTD and ADCP.

GPS coordinates were acquired from the ship-based GPS receiver and extracted for the duration of each SUIT haul. The ADCP data and GPS data were temporally interpolated to the 0.1 s interval spacing of the CTD data based on the synchronized data acquisition time. The raw data and interpolated data were plotted and compared for each haul to ensure an accurate fit of the interpolation method. Here we used the "smooth.spline" function in the *stats* package. All data were then spatially

interpolated to a 0.5 m spacing using the same method but based on distance from the GPS data. Sea ice draft data, however, did not have an accurate fit using this method due to the large variability of measurements and in some cases measurement drop-outs of the altimeter measurements, which caused large discrepancies between the raw data and interpolated results. Therefore, sea ice draft were first calculated on the data before spatial interpolation (section 1.2.2) then were re-sampled using a moving average where each point was the mean of all sea ice draft measurements within 0.5 m ahead of the point and 0.5 m behind the point, i.e., each point represented the mean sea ice draft over a distance of 1 m with the point centered in the middle. For the first point and last point of the haul the sea ice draft values represented the mean of the 0.5 m after the point (first point) and 0.5 m before the point (last point), respectively, (i.e., these points represented the mean draft over a distance of only 0.5 m). This method resulted in the best fit between the raw and re-sampled sea ice draft data based on manual inspections for each haul.

Each variable was summarized for each haul by mean, standard deviation and mode (Table 1). These summarized data, for selected SUIT hauls, were presented and used for ecological statistical analyses in combination with under-ice fauna catch data by (David et al., 2015b).

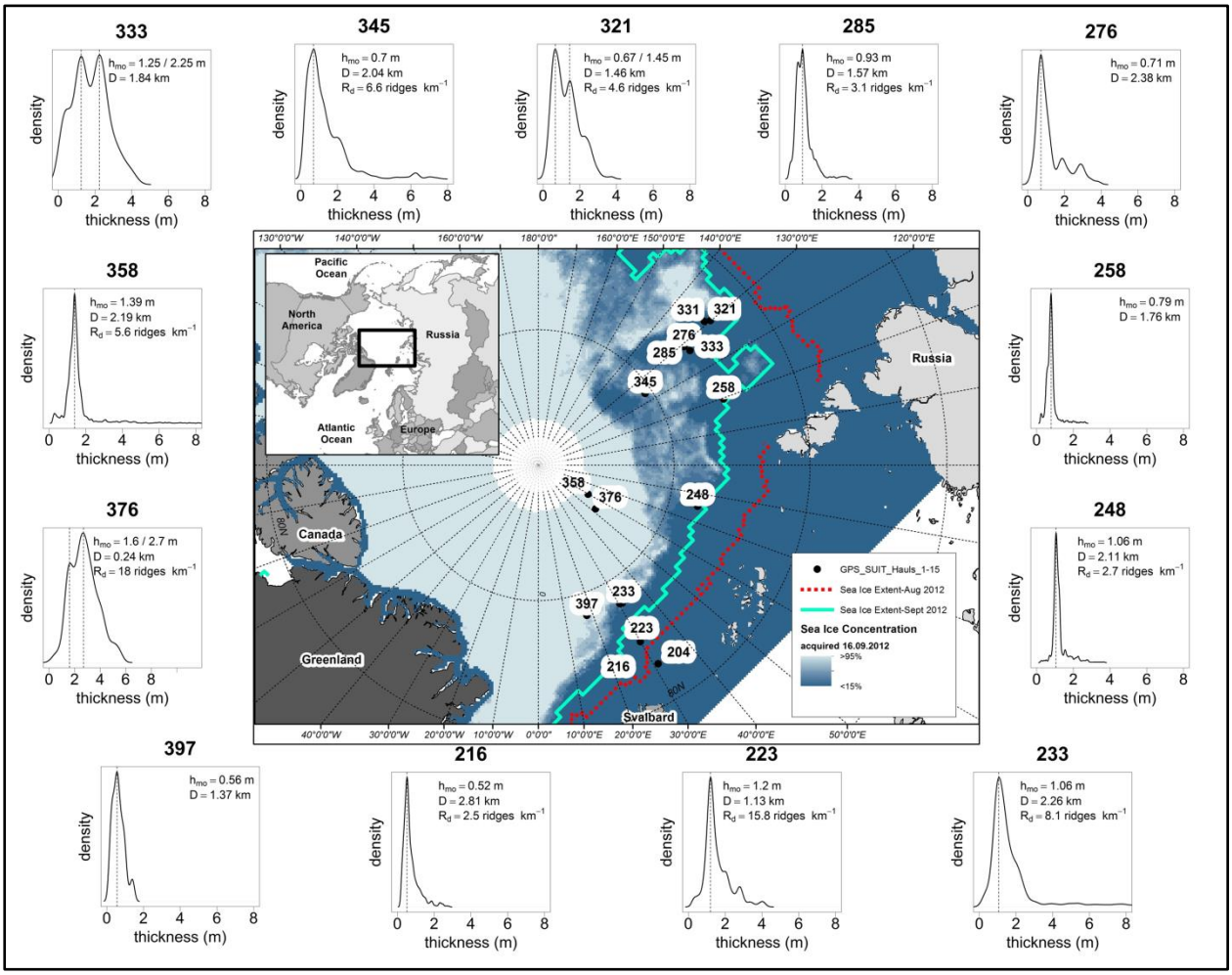

Figure 2. Map of the central Arctic Ocean showing the positions of SUIT haul stations conducted during *RV Polarstern* cruise PS80. Ice thickness (i.e., draft divided by ice density of 0.834 determined from ice cores) density distributions for each station excluding open water stations. Sea ice concentration data acquired from www.meereisportal.de according to algorithms in Spreen et al. (2008). Sea ice extent correspond to monthly means during August and September (extent data acquired from NSIDC; Fetterer et al., 2002, udpated 2011)**.**

Table 1. Summary of environmental parameters measured using the SUIT-mounted environmental sensor array. Summaries are for each haul deployed during the *RV Polarstern* cruise PS80.3. Where applicable values correspond to mean +/- standard deviation with the modal values in parentheses.

Stn	H	Date (M/DD/YYYY)	Lat	Lon	Bath (m)	Dist. (m)	Speed ($m\ s^{-1}$)	Depth (m)	Temperature (°C)	chl *a* ($mg\ m^{-3}$)	Salinity[a]	Pitch (°)	Roll (°)	CTD draft (m)	ADCP draft (m)
204	1	8/5/2012	81.5	31.1	423	2457	1.8 +/- 0.4 (1.6)	2.8 +/- 2 (1.3)	0.9 +/- 0 (0.9)	-	31.8 +/- 0 (31.8)	-10.1 +/- 2.4 (-10.5)	5.6 +/- 4 (7)	0 +/- 0.1 (0)	0 +/- 1.1 (0.2)
216	2	8/7/2012	82.5	30.0	3610	2812	1.8 +/- 0.2 (1.8)	1.7 +/- 0.4 (1.7)	-1.1 +/- 0.1 (-1.1)	-	30.9 +/- 0 (30.9)	-6 +/- 3.2 (-7.5)	1.6 +/- 3 (1)	0.6 +/- 0.7 (0.5)	0.6 +/- 0.5 (0.8)
223	3	8/9/2012	84.1	30.4	4016	1134	1.4 +/- 0.3 (1.6)	2.2 +/- 0.9 (2.3)	-1.5 +/- 0.2 (-1.7)	-	32 +/- 1.4 (33.3)	-4.9 +/- 4.4 (-7.5)	-0.5 +/- 4.5 (-2.5)	1.4 +/- 1.7 (1.2)	1.2 +/- 1 (1.2)
233	4	8/11/2012	84.0	31.3	4011	2258	1.6 +/- 0.4 (1.9)	4.3 +/- 4.9 (1.5)	-1.6 +/- 0.1 (-1.6)	0.1 +/- 0 (0.1)	32.8 +/- 0.6 (32.8)	-10.9 +/- 9.1 (-7.5)	19.1 +/- 12.3 (7.5)	1.1 +/- 4.7 (2.4)	1.4 +/- 0.7 (0.6)
248	5	8/16/2012	83.9	75.5	3424	2105	-	-	-	-	-	-	-	-	1.3 +/- 0.8 (0.8)
258	6	8/20/2012	82.7	109.6	3575	1760	1.2 +/- 0.3 (1.3)	1.8 +/- 0.4 (1.7)	-1.6 +/- 0 (-1.6)	0.2 +/- 0 (0.1)	32.6 +/- 0.2 (32.7)	-4.5 +/- 3.1 (-2.5)	-0.6 +/- 3.2 (-2.5)	0.9 +/- 0.9 (0.8)	0.9 +/- 0.4 (0.8)
276	7	8/25/2012	83.1	129.1	4188	2378	1.3 +/- 0.4 (1)	1.2 +/- 0.1 (1.1)	-1.4 +/- 0 (-1.4)	0.3 +/- 0 (0.2)	30.2 +/- 0.2 (30.3)	-9 +/- 1.4 (-10.5)	3.7 +/- 4.2 (7.5)	0 +/- 0 (0)	0.8 +/- 1.1 (0.9)
285	8	8/26/2012	82.9	129.8	4174	1573	1.1 +/- 0.2 (1.2)	1.9 +/- 0.5 (1.9)	-1.6 +/- 0 (-1.6)	0.3 +/- 0 (0.3)	30.7 +/- 0.2 (30.8)	-4.4 +/- 3 (-2.5)	-2.9 +/- 3.7 (-2.5)	1.1 +/- 1.2 (1)	0.9 +/- 0.5 (1)
321	9	9/4/2012	81.7	130.0	4011	1461	1.1 +/- 0.3 (0.9)	1.7 +/- 0.8 (1.3)	-1.6 +/- 0 (-1.6)	0.3 +/- 0.1 (0.2)	29.2 +/- 2.6 (30.3)	-5.9 +/- 4.1 (-7.5)	-1.7 +/- 5.1 (-2.5)	0.7 +/- 1.2 (0.7)	0.6 +/- 1 (0.9)
331	10	9/5/2012	81.9	130.9	4036	1570	-	-	-	-	-	-	-	-	-
333	11	9/6/2012	83.0	127.1	4187	1844	1.2 +/- 0.2 (1.2)	1.2 +/- 0.5 (1.3)	-1.2 +/- 0 (-1.2)	0.2 +/- 0 (0.2)	30.1 +/- 0 (30.1)	-8.4 +/- 2.2 (-7.5)	0.7 +/- 3.5 (-2.5)	0.2 +/- 0.4 (0.1)	1.4 +/- 1.1 (0.9)
345	12	9/9/2012	85.3	123.8	4354	2042	1.2 +/- 0.2 (1.1)	1.9 +/- 1.1 (1.3)	-1.6 +/- 0 (-1.6)	0.4 +/- 0 (0.4)	30.1 +/- 0.1 (30.2)	-6.2 +/- 5.6 (-7.5)	-7.6 +/- 7.2 (-7.5)	0.9 +/- 1.5 (0.8)	0.8 +/- 1.2 (1)
358	13	9/19/2012	87.9	59.7	4384	2190	1.5 +/- 0.4 (1.3)	3.1 +/- 1.6 (2.3)	-1.8 +/- 0 (-1.8)	0.3 +/- 0.1 (0.3)	33.1 +/- 0.2 (33.1)	59.7 +/- 0 (59.6)	5.5 +/- 1.4 (5.5)	-	-
376	14	9/25/2012	87.3	52.6	3509	239	1.1 +/- 0.5 (1.3)	3.4 +/- 1.3 (3.3)	-1.8 +/- 0 (-1.8)	0.3 +/- 0.1 (0.3)	33.1 +/- 0.5 (33.5)	-0.2 +/- 13.7 (-2.5)	6.9 +/- 15.4 (5)	1.7 +/- 3.3 (2.9)	1.6 +/- 1.7 (2.3)
397	15	9/29/2012	84.2	17.9	4028	1372	1.2 +/- 0.3 (1.3)	1.3 +/- 0.4 (1.2)	-1.8 +/- 0 (-1.8)	0.3 +/- 0 (0.3)	32.2 +/- 0.4 (32.8)	-7 +/- 2.4 (-7)	-8.7 +/- 4.4 (-9)	0.3 +/- 0.4 (0.2)	1.6 +/- 1.7 (2.3)

[a] (practical salinity scale PSS-78; Fofonoff, 1985)

1.2.2 Sea ice draft calculations

We start our derivation of sea ice draft (h_d) with a simplified calculation only applicable if the SUIT is travelling exactly parallel to the water surface (Figure 3 a) and takes the form:

$$\boldsymbol{h_d = h_w - h_z - h_a} \quad \textbf{(1)}$$

we changed two parameters (h_z and h_a) in equation 1, which needed to be corrected for due to variable pitch and roll angles of the SUIT relative to the water surface (Figure 3 b). Equation 1 then becomes:

$$\boldsymbol{h_d = h_w - h_z' - h_a'} \quad \textbf{(2)}$$

where h_z' is calculated as (Figure 3 c):

$$\boldsymbol{h_z' = h_z \times \cos\beta \times \cos\emptyset} \quad \textbf{(3)}$$

and h_a' is calculated as (Figure 3 d):

$$\boldsymbol{h_a' = c \times \sin[\propto + \beta]} \quad \textbf{(4)}$$

Combining equations 2, 3 and 4 we get the corrected sea ice draft as:

$$\boldsymbol{h_d = h_w - [h_z \times \cos\beta \times \cos\emptyset] - [c \times \sin[\propto + \beta]]} \quad \textbf{(5)}$$

all parameters are listed and described in Figure 3 d with detailed diagrams of the sensor locations, distance measurements and derived distances shown in Figure 3 a–d.

During three SUIT hauls (stations: 248, 331, and 358) there were problems with the CTD (e.g., low batteries, configuration issues), which resulted in unusable data. Therefore, we developed an ice draft proxy based on the pressure sensor from the ADCP to estimate ice draft for hauls with missing data. Theoretically, the top side of the SUIT should ride along the under-side of the ice with a constant distance to the ice bottom and thus with a constant distance to the ADCP pressure sensor (distance between top of SUIT, where altimeter is located, and ADCP = 1.21 m), which theoretically could be used to derive sea ice draft (h_d'') in the form:

$$\boldsymbol{h_d'' = h_{w,ADCP} - 1.21} \quad \textbf{(6)}$$

where $h_{w,ADCP}$ is the ADCP measured water depth. However, in reality it is slightly more complicated because the SUIT does not ride perfectly along the under-side of the sea ice and undergoes large vertical movements in the water column due to variability of the bottom-ice topography, primarily influenced by features such as sea ice ridges. From the SUIT hauls where we have CTD data, we examined how the SUIT rides along the under-side of the sea ice and found a constant offset between the altimeter and ice bottom of 0.25 m for level ice regions. Adjusting the theoretical equation (6) by this constant, we get:

$$\boldsymbol{h_d'' = h_{w,ADCP} - 1.46} \quad \textbf{(7)}$$

To test if this is an appropriate assumption we took all coincident CTD-derived (corrected) sea ice draft observations and coincident interpolated ADCP depth observations and applied a linear regression (Figure 4). The data were first filtered to eliminate measurements conducted during abrupt movements of the SUIT (e.g., at ridges) by setting thresholds for the pitch (±10 º) and roll (±7º). The linear regression resulted in a good fit to the data (N= 19,216; adjusted $R^2 = 0.78$; $p < 0.001$) and more importantly was very similar to the theoretical equation 7. The fitted linear regression equation has the form:

$$\boldsymbol{h_d'' = 0.95 \times h_{w,ADCP} - 1.41} \quad \textbf{(8)}$$

These ADCP measured water depth data were then used to fill the gaps of data for the SIT hauls without reliable CTD data using equation 8. However, this fitted model is only valid for the level ice and will have larger uncertainty for regions around sea ice ridges. Nevertheless, identification of

ridges was still possible using the ADCP-derived sea ice draft, however, the accuracy of sea ice ridge properties (e.g., thickness and width) is less certain (see section 1.2.4).

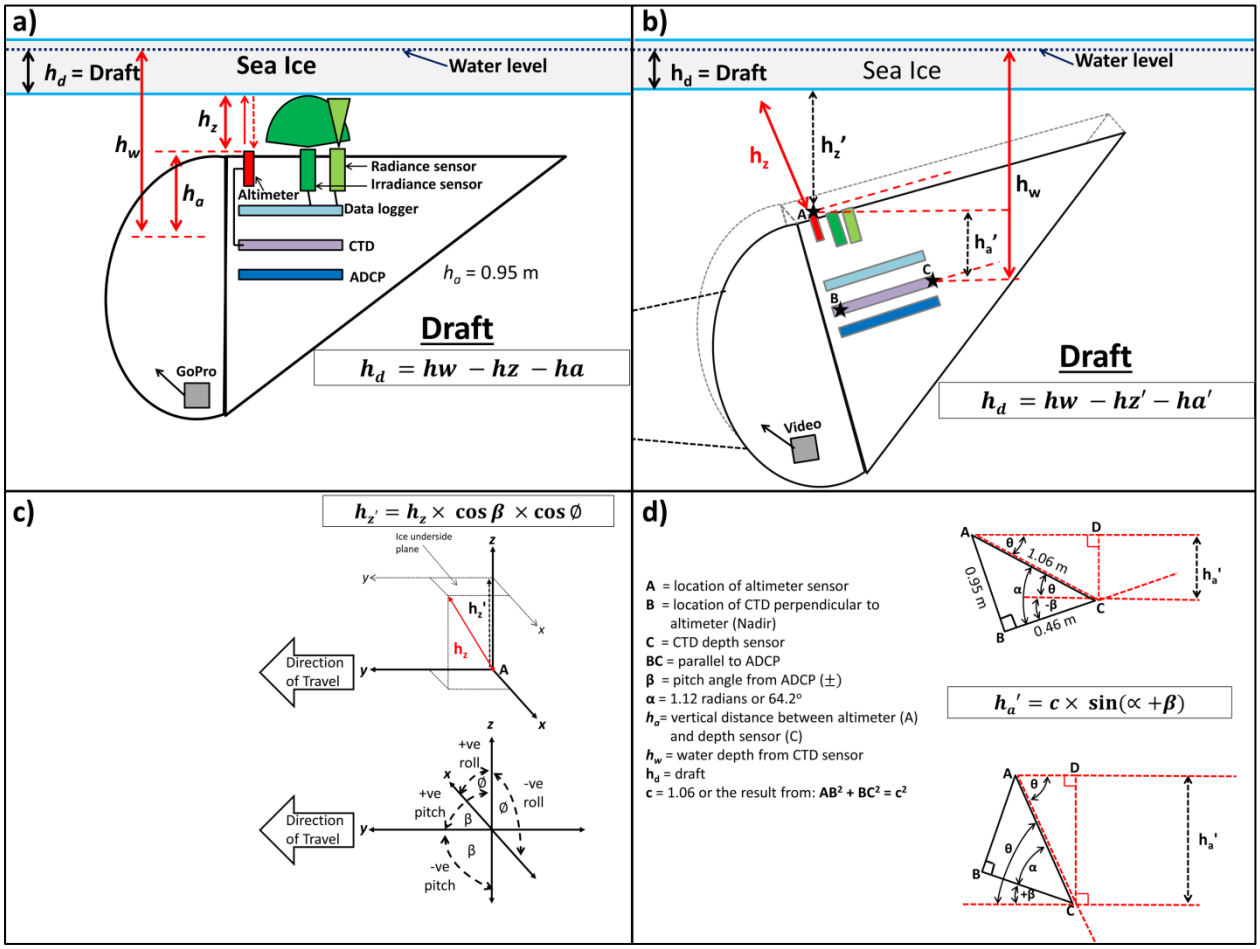

Figure 3. Sea ice draft calculations showing: **a)** sensor locations, and distance measurements and derived distances required for the simplified version of the sea ice draft calculations, applicable only if the SUIT travelled perfectly horizontal (i.e., parallel to the water surface); **b)** same as in "**a)**" but a realistic situation with the SUIT travelling at an angle relative to the water surface with the different distances actually measured by the sensors and what is needed for a corrected calculation of the sea ice draft; **c)** correction of the measured altimeter distance to the perpendicular (relative to water surface) distance to the ice bottom and showing the angles (i.e., pitch and roll) required for the correction measured by the ADCP; **d)** vertical distance correction required between the altimeter and CTD depth sensor due to differential offset at different pitch angles.

1.2.3 Sea ice ridge identification

Sea ice ridges were identified from the SUIT ice draft profiles using the Rayleigh criteria, following procedures described by: Castellani et al. (2014); and Rabenstein et al. (2010) for the sea ice surface topography, and Castellani et al. (2015) for the sea ice bottom profile. Ice draft local minima (e.g., thicker ice as draft is negative) identified along the SUIT profile with a threshold of 1.5 m deeper than the surrounding ice, following Castellani et al. (2015), were selected as potential ridges. Moreover, adjacent minima needed a separation distance between points which was less than half the depth of the first minima in order to be identified as two single elements not belonging to the same ridge. Ridge depth and width were measured in order to calculate ridge density (ridges km^{-1}) and percent coverage of ridges. We calculated ridge width as the ridge width at half maximum depth.

1.2.4 Ship-based and ice station-based observations

In order to assess if the SUIT-based observations improved the representativeness of sampling the under-ice environmental properties we compared the summarized data to ship-based and ice station-based observation of ice thickness, and surface water chl *a* , salinity and temperature. Ship-based surface water properties were measured using a CTD probe with a carousel water sampler (CTD sampling details provided in Boetius et al., 2013; David et al., 2015b). Coincident CTD stations closest in time and space to the SUIT stations were compared. Ship-based observations of ice thickness were conducted visually every hour, while in ice-covered waters, from the bridge of the *RV Polarstern* during PS80.3 (Hendricks et al., 2012).

Under-ice surface water CTD casts were conducted through a hole in the ice at each ice station (Fernández-Méndez et al., 2015). Ice thickness surveys were conducted at each ice station using an EM-31 electromagnetic induction sounding device (data presented in Boetius et al., 2013).

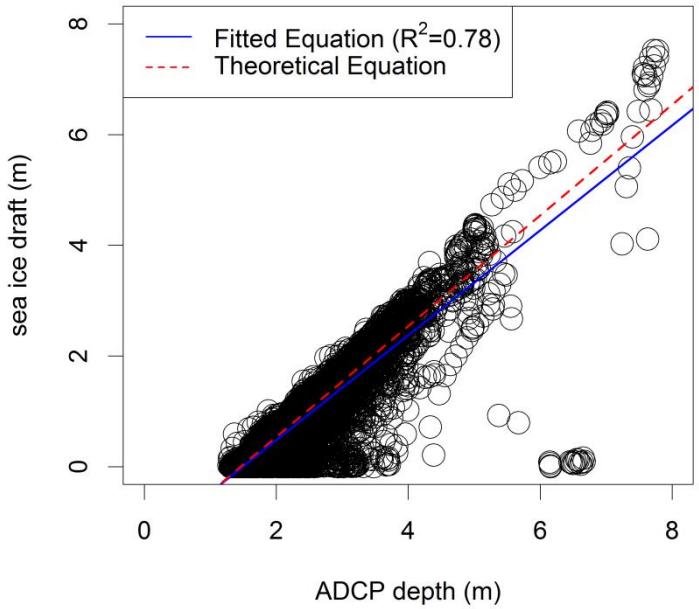

Figure 4. Linear regression of CTD-derived and corrected sea ice draft (m) versus ADCP depth (m) and showing the fitted equation line (solid blue; equation 8) and theoretical equation line (dashed red; equation 7).

1.2.5 CTD fluorometer chl *a* calibration

The CTD fluorometer chl *a* concentrations ($chla_{CTD}$) were calibrated using water samples obtained from under the sea ice during ice stations, briefly described in (David et al., 2015b) and used in (Fernández-Méndez et al., 2015). Chl *a* concentrations were determined for water samples by high-performance liquid chromatography (HPLC; i.e., observed chl *a* in mg m^{-3} Figure 3). Calibration coefficients were determined using linear regression between the observed water sample chl *a* concentrations and the uncalibrated CTD chl *a* concentrations ($chla_{CTD}$; n = 2484; adjusted R^2 = 0.63; $p < 0.001$; Figure 3). The coefficients were used in the following linear equation to derive the calibrated CTD chl *a* concentrations in mg m^{-3} ($chla_{cal}$):

$$\boldsymbol{chla_{cal} = 0.385 \times chla_{CTD} + 0.013} \qquad \textbf{(6)}$$

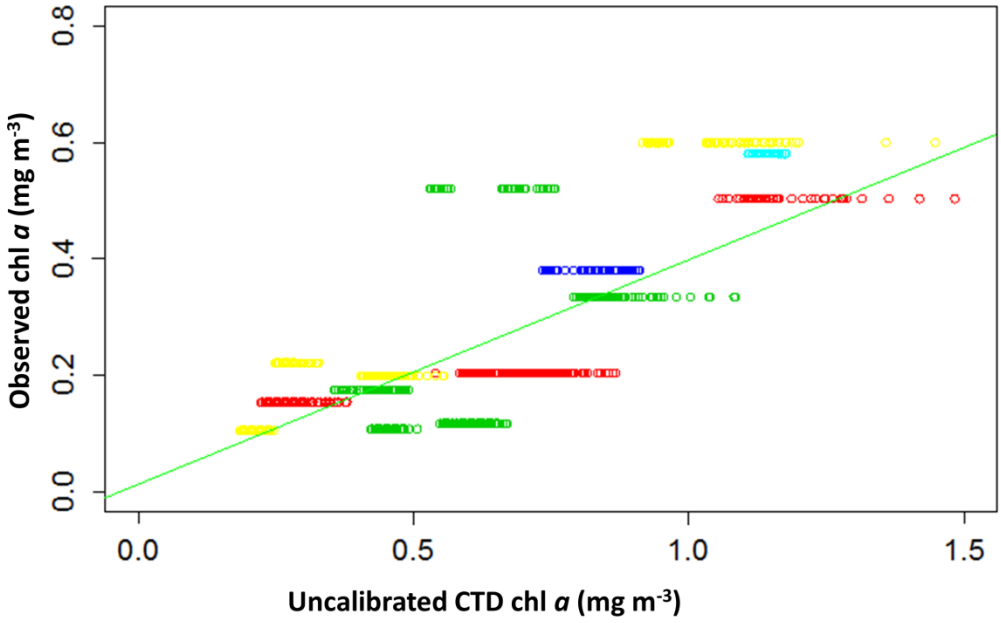

Figure 5. Regression of the observed chl *a* concentrations derived from High-Performance Liquid Chromatography of water samples (HPLC) versus the coincident uncalibrated chl *a* concentrations (mg m^{-3}) derived from the CTD fluorometer. Points are colour coded by depth. Green line is the linear regression (n = 2484; adjusted $R^2 = 0.63$; $p < 0.001$).

1.3 Results and Discussion

A detailed examination of surface water and sea ice horizontal spatial variability is beyond the scope of this paper. Nevertheless, we do assess if the environmental sensor array improved the spatial representativeness of observed environmental parameters compared to using nearby ship-based or ice station observations.

1.3.1 Salinity

The linear regression between the SUIT CTD-derived salinity with the ship-based and ice station salinity observations showed good, significant fits ($R^2 = 0.86$ and 0.77, respectively; Figure 5). Nearly all ship-based and ice station salinity observations were higher than the SUIT-based salinity (Figure 5) and the discrepancy was larger at lower salinities. We attributed this to the presence of fresher water pockets near the water surface or under-ice surface resulting from melting sea ice. This fresher water has lower density and thus floats to the surface, which is apparent from the horizontal SUIT haul data summarized into vertical depth profiles (Figure 6 b) where the upper surface has the highest variability of salinity. The SUIT salinity values for each haul showed high variability in the direction of lower salinity compared to the ship-based (vertical dotted lines; Figure 6 b) and ice station-based (vertical dashed lines; Figure 6 b) salinity values. Obvious features of relatively fresh water are shown for two SUIT stations (258 and 285; Figure 8). At station 258 the fresh water pockets appeared to be related to the presence of open water regions between ice floes (Figure 8 a). Whereas at station 285 the features appeared to be related to both open water regions and the presence of sea ice ridges (Figure 8 b). Accumulation of fresher water in the regions between ice floes likely occurred due to its lower density and the movement of lower density to the surface, which in this case was the open water between the ice floes. The relationship of fresher water pockets with sea ice ridges was likely due to formation of dome-shaped features along the under-side of the sea ice, typically adjacent to ridges,

which can trap fresher water where they are sheltered from currents and have no path to surface open water regions.

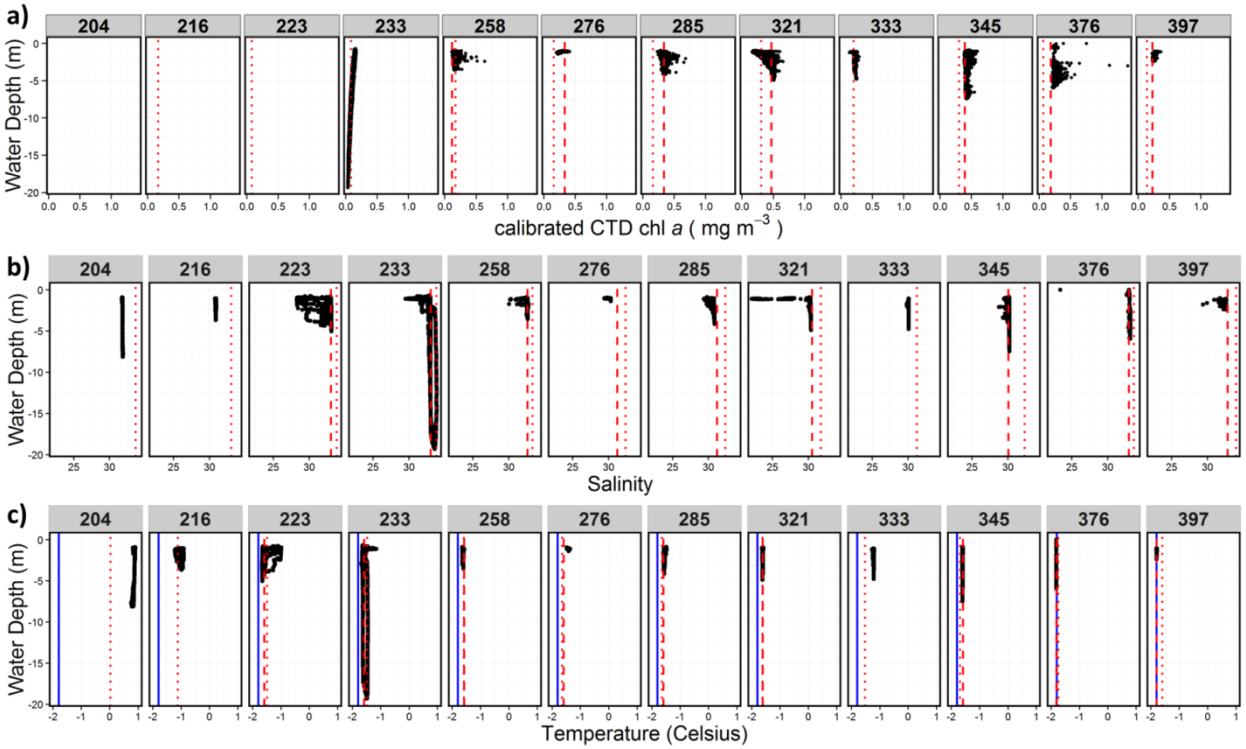

Figure 6. Depth profiles of the horizontal SUIT hauls showing: a) calibrated CTD chl a (mg m-3); b) salinity (practical salinity scale PSS-78; Fofonoff, 1985); and c) temperature (ºC), the vertical solid blue line corresponds to the freezing point of sea water of ~ -1.8 ºC. The ice station CTD-derived values are depicted by the dashed red lines and ship-based CTD-derived values by dotted red lines.

This demonstrates that ice station or ship-based observations do not capture these freshwater features. If these features are important to biological activity can only be assessed if we can actually observe these features, however, using ship or ice station based methods it is less likely to capture them since the ship disturbs the water, particularly the surface water due to mixing from the propeller and thrusters. Capturing fresh water features at ice stations is more likely than ship-based observations since there is no disturbance, however, based on the SUIT profiles these features are not predictable and therefore would require more extensive sampling through the ice, which is logistically demanding and time consuming. On ice stations it would also be advisable to sample from the ice edge to increase the likelihood of sampling fresh water pockets from undisturbed water between ice floes. It would remain difficult, however, to capture the freshwater pockets that may be associated with sea ice ridges and dome shaped under-ice features since this would require CTD casts at multiple locations on the ice floe, which may not be feasible.

1.3.2 Temperature

Temperature values had relatively low horizontal variability at most stations except for at station 223 and 233 (Figure 6 c). At these stations the variability of temperature coincided with changes in salinity showing an inverse relationship between the variables (Appendix A-2: Supplementary Material Figure A1-2 and A1-2). The inverse relationship between temperature and salinity was also observed in other profiles although were less drastic (Figure 8). Coldest surface water temperatures ~-1.8 ºC were observed at stations 376 and 397 (Figure 6 c) and were indicative of the onset of freezing conditions. Overall, the mean SUIT-based temperature had a good and significant fit with both the ship-based and ice station surface water temperature values (R^2 = 0.80 and 0.95, respectively; $p < 0.05$). This can be attributed to the small degree of horizontal variability within the SUIT-based temperature data.

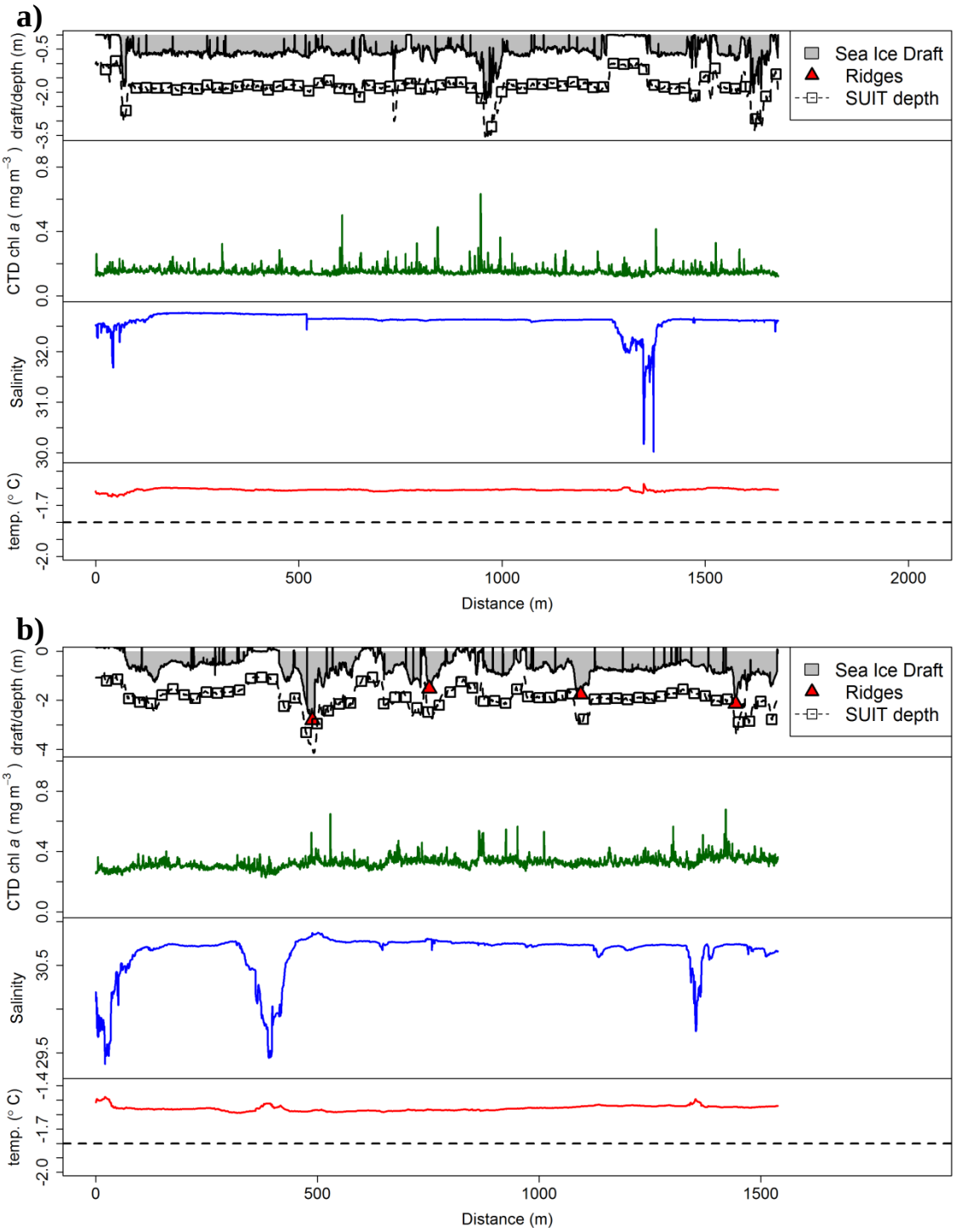

Figure 8. Surface and under-ice trawl (SUIT)-mounted sensor arrays profiles of sea ice draft, surface water chl *a* (mg m^{-3}), salinity (practical salinity scale PSS-78; Fofonoff, 1985), and temperature (ºC) for stations: a) 258; and b) 285.

1.3.3 Surface water chlorophyll a

Surface water chl *a* showed a moderately good and significant fit between the SUIT- and ship-based CTD mean chl *a* values (R^2 = 0.49; $p < 0.05$; Figure 7 a). A non-significant and relatively poor fit was found between the SUIT- and ice station-based CTD mean chl *a* values (R^2 = 0.28; $p > 0.05$; Figure 7

a). SUIT-based chl *a* showed generally large horizontal variability, particularly at stations 258, 285, 321, 376 (Figure 6 a). Overall, the SUIT-based chl *a* were higher than ice station CTD observations (Figure 7 a) likely because the SUIT was able to capture the large horizontal variability and included high chl *a* concentration regions whereas the ice station was only one cast under the ice. The ship-based observations did not show any directional bias compared to the mean SUIT chl *a*. This may be coincidental or could due to vertical and horizontal mixing creating a more homogeneous surface layer.

In contrast to the salinity profiles, the horizontal variability of SUIT-based chl *a* appeared to be more erratic and varied at smaller scales (Figure 8). We observed no obvious relationships with the under-ice topography, however, some patches of high chl *a* concentrations were observed adjacent to ridges (Figure 8). This could be the result of less turbulent waters adjacent to ridges, forming isolated pockets similar to the freshwater pockets. This is likely not the case since there was no relationship of high concentration patches with the freshwater patches, which may be expected if the former were true, and because patches were observed in regions of relatively smooth ice and open water. Therefore, a more detailed analysis of the horizontal patchiness of under-ice chl *a* concentrations is required in order to explain possible mechanisms responsible for the observed patchiness. This is particularly important since under-ice phytoplankton blooms have been identified as important features in the Arctic Ocean in terms of carbon export and ecological significance (Arrigo et al., 2012).

1.3.4 Sea ice draft / thickness

Ice thickness had poor, non-significant regression fits between the SUIT-based ice thickness and ship-based and ice stations observations (Figure 7). The poor fit with ship-based ice thickness values was the result of two stations 376 and 333, which had large deviations from the SUIT ice thickness data (Figure 7 c). This was likely due to the inability of visual observations to accurately capture the spatial variability of the sea ice thickness. These visual observations are good at characterizing the general ice conditions but are perhaps less accurate at assessing and characterizing the spatial variability of sea ice thickness. Furthermore, the ship tends to travel in open water leads and along the edges of ice floes. Ice floe edges typically experience enhanced melt compared to the interior regions of the ice floes (Perovich et al., 2003) and therefore may introduced a bias towards thinner ice thickness observations if only ice edges were characterized during the ship-based observations.

The poor fit between the SUIT-based and ice station ice thickness observations was the result of three stations (248, 321 and 345), which had substantially thicker corresponding ice station thickness observations (Figure 7 c). The selection of these three suitable ice floes to work on may have introduced a bias towards thicker sea ice, particularly in regions of thinner sea ice, since an ice floe needs to have certain characteristics to ensure a safe working platform. Typically, large level ice floes were selected and therefore could be assumed to be thicker than the surrounding area because they were able to withstand the compressive forces without breaking apart.

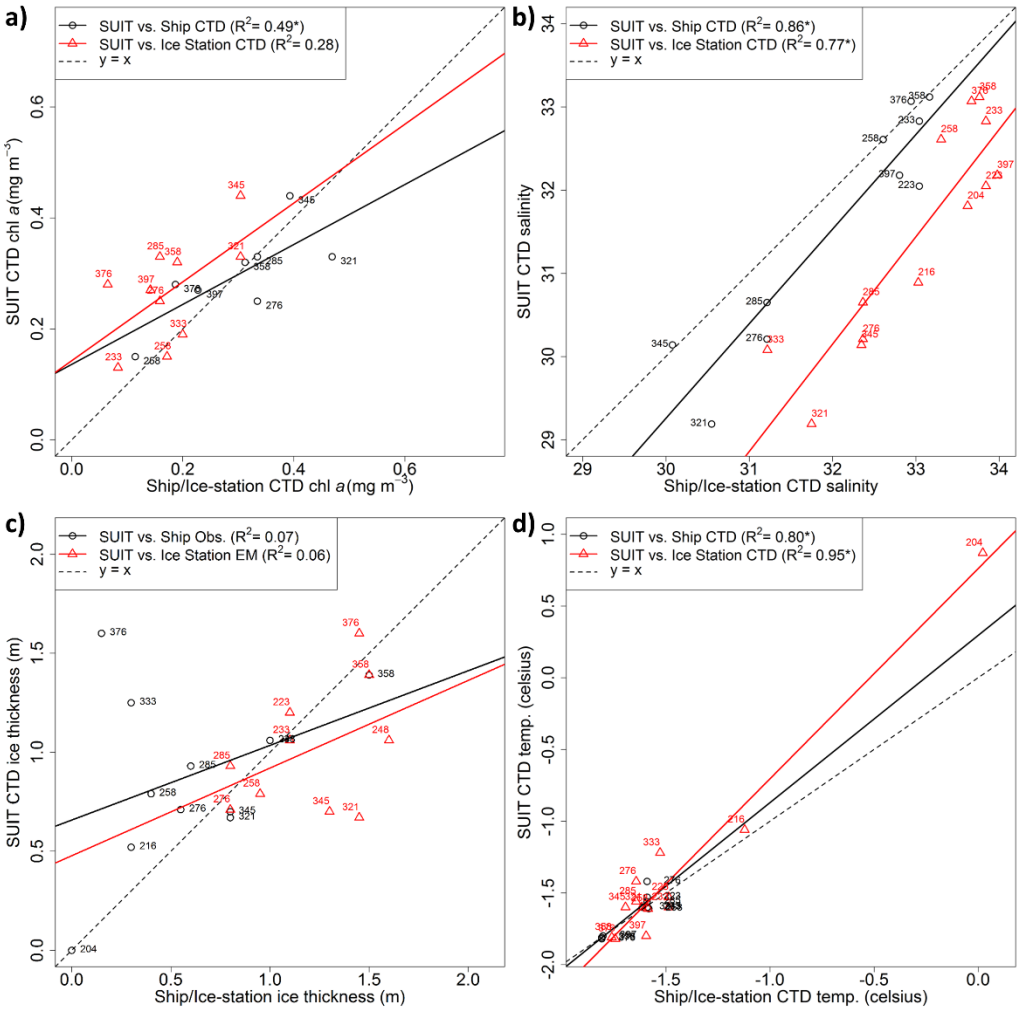

Figure 7. Linear regressions and comparisons of the SUIT CTD-derived observations versus the nearest ship-based observations and nearest ice station observations for: a) water column chl *a* (mg m^{-3}); b) salinity (practical salinity scale PSS-78; Fofonoff, 1985); c) ice thickness (m), SUIT ice thickness calculated from modal draft divided by density of ice (0.834 determined from ice cores), ice station thickness values are from (Boetius et al., 2013) and ship-based ice thickness are observations from the bridge by a person; and d) temperature (ºC). "*" following the R^2 value denotes significant linear regression at $p < 0.05$.

1.4 Conclusions

Overall, ice thickness, salinity and under-ice surface water chlorophyll *a* showed high horizontal spatial variability, which was not represented well with the nearby ship-based or ice station observations. Temperature, however, showed a good agreement between methods due to lower spatial variability. These results suggest that conducting ecological modelling with environmental data, which are not-coincident to the sampling location, may result in non-representative or false assessments of the Ecosystem. Nevertheless, because many of the observations were in agreement, we suggest that using non-coincident environmental data may be suitable although should be done with caution and limited to cases where there is no alternative option and/or to fill essential data gaps.

David et al., showed that ice thickness and surface water properties played an important role in structuring the under-ice communities. This means that if other environmental data were used (e.g., nearby vertical CTD casts of chl *a*, which showed a poor fit to the SUIT CTD chl *a*) a drastically different statistical relationship would likely have resulted. These results demonstrate the sensitivity of ecological modelling, in particular, to how environmental properties are characterized.

Acknowledgements

We thank Captain Uwe Pahl, the crew, and scientific cruise leader Antje Boetius of RV Polarstern expedition PS80.3 (ARK27-3; IceArc), for their excellent support and guidance with work at sea. We thank Jan Andries van Franeker (IMARES) for kindly providing the Surface and Under-Ice Trawl (SUIT) and Michiel van Dorssen for technical support. SUIT was developed by IMARES with support from the Netherlands Ministry of EZ (project WOT-04-009-036) and the Netherlands Polar Program (project ALW 866.13.009). This study is part of the Helmholtz Association Young Investigators Group Iceflux: Ice-ecosystem carbon flux in polar oceans (VH-NG-800). We also acknowledge the Alfred-Wegener-Institut, Helmholtz-Zentrum für Polar- und Meeresforschung for essential financial and logistical support. All data are available from the PANGAEA database doi.org/XX.XXXX/PANGAEAXXXXXX.

References

Arrigo, K.R., Perovich, D.K., Pickart, R.S., Brown, Z.W., van Dijken, G.L., Lowry, K.E., Mills, M.M., Palmer, M.A., Balch, W.M., Bahr, F., Bates, N.R., Benitez-Nelson, C., Bowler, B., Brownlee, E., Ehn, J.K., Frey, K.E., Garley, R., Laney, S.R., Lubelczyk, L., Mathis, J., Matsuoka, A., Mitchell, B.G., Moore, G.W.K., Ortega-Retuerta, E., Pal, S., Polashenski, C.M., Reynolds, R.A., Schieber, B., Sosik, H.M., Stephens, M., Swift, J.H., 2012. Massive Phytoplankton Blooms Under Arctic Sea Ice. *Science*, 336, 1408.

Boetius, A., Albrecht, S., Bakker, K., Bienhold, C., Felden, J., Fernández-Méndez, M., Hendricks, S., Katlein, C., Lalande, C., Krumpen, T., Nicolaus, M., Peeken, I., Rabe, B., Rogacheva, A., Rybakova, E., Somavilla, R., Wenzhöfer, F., Party, R.P.A.-.-S.S., 2013. Export of Algal Biomass from the Melting Arctic Sea Ice. *Science*, 339, 1430-1432.

David, C., Lange, B., Krumpen, T., Schaafsma, F., van Franeker, J.A., Flores, H., 2015a. Under-ice distribution of polar cod Boreogadus saida in the central Arctic Ocean and their association with sea-ice habitat properties. *Polar Biology*.

David, C., Lange, B., Rabe, B., Flores, H., 2015b. Community structure of under-ice fauna in the Eurasian central Arctic Ocean in relation to environmental properties of sea-ice habitats. *Marine Ecology Progress Series*, 522, 15-32.

David, C., Schaafsma, F.L., van Franeker, J.A., Lange, B., Brandt, A., Flores, H., 2016. Community structure of under-ice fauna in relation to winter sea-ice habitat properties from the Weddell Sea. *Polar Biology*.

Fernández-Méndez, M., Katlein, C., Rabe, B., Nicolaus, M., Peeken, I., Bakker, K., Flores, H., Boetius, A., 2015. Photosynthetic production in the Central Arctic during the record sea-ice minimum in 2012. *Biogeosciences Discussions*, 12, 2897-2945.

Fetterer, F., Knowles, K., Meier, W., Savoie, M., 2002, udpated 2011. Sea Ice Index. Boulder, CO: National Snow and Ice Data Center. Digital Media.

Flores, H., van Franeker, J.-A., Cisewski, B., Leach, H., Van de Putte, A.P., Meesters, E., Bathmann, U., Wolff, W.J., 2011. Macrofauna under sea ice and in the open surface layer of the Lazarev Sea, Southern Ocean. *Deep Sea Research Part II: Topical Studies in Oceanography*, Vol. 58 (pp. 1948-1961).

Flores, H., van Franeker, J.A., Siegel, V., Haraldsson, M., Strass, V., Meesters, E.H., Bathmann, U., Wolff, W.J., 2012. The Association of Antarctic Krill *Euphausia superba* with the Under-Ice Habitat. *PLoS ONE*, Vol. 7 (p. e31775): Public Library of Science.

Fofonoff, N.P., 1985. Physical properties of seawater: A new salinity scale and equation of state for seawater. *Journal of Geophysical Research*, 90, 3332.

Hendricks, S., Nicolaus, M., Schwegmann, S., 2012. Sea ice conditions during POLARSTERN cruise ARK-XXVII/3 (IceArc). Alfred Wegener Institute, Helmholtz Center for Polar and Marine Research, Bremerhaven.

Kohlbach, D., Graeve, M., Lange, B.A., David, C., Peeken, I., Flores, H., 2016. The importance of ice algae-produced carbon in the central Arctic Ocean ecosystem: food web relationships revealed by lipid and stable isotope analyses. *Limnol. Oceanogr*.

Lange, B.A., Katlein, C., Nicolaus, M., Peeken, I., Flores, H., submitted. Spectrally-derived sea ice-algal chlorophyll a concentrations using under-ice horizontal profiling platforms. *Journal of Geophysical Research*.

Perovich, D.K., Grenfell, T.C., Richter-Menge, J.A., Light, B., Tucker III, W.B., Eicken, H., 2003. Thin and thinner: Sea ice mass balance measurements during SHEBA. *Journal of Geophysical Research*, Vol. 108 (p. 8050).

R-Development-Core-Team, 2012. R: A Language and Environment for Statistical Computing. *R Foundation for Statistical Computing, Vienna, Austria.*

Schaafsma, F.L., David, C., Pakhomov, E.A., Hunt, B.P.V., Lange, B.A., Flores, H., van Franeker, J.A., 2016. Size and stage composition of age class 0 Antarctic krill (Euphausia superba) in the ice–water interface layer during winter/early spring. *Polar Biology*.

Spreen, G., Kaleschke, L., Heygster, G., 2008. Sea ice remote sensing using AMSR-E 89-GHz channels. *Journal of Geophysical Research*, 113, C02S03.

van Franeker, J.A., Flores, H., van Dorssen, M., 2009. The surface and under ice trawl (SUIT). Frozen desert alive—the role of sea ice for pelagic macrofauna and its predators. *PhD thesis, University of Groningen,Groningen*.

Paper 2. Spectrally-derived sea ice-algal chlorophyll a concentrations using under-ice horizontal profiling platforms

Paper currently under review in *Journal of Geophysical Research: Oceans*

NOTE: Supplementary Material for this paper is found in Appendix A3

Benjamin A. Lange, Christian Katlein, Marcel Nicolaus, Ilka Peeken, and Hauke Flores

Key Points

- Ice-algal chl a best estimated from large-scale spectral data using EOF-approach because it accounts for varying environmental conditions
- Accounting for variability of incoming light produced most reliable ice-algal biomass estimates
- Insufficient spatial representativeness of sea ice-algal biomass can cause biases in large-scale ice algal biomass and PP estimates

Abstract

Multi-scale sea ice algae observations are fundamentally important for projecting changes to sea ice ecosystems, as the physical environment continues to change. In this study we developed upon previously established methodologies for spectrally-deriving sea ice-algal chlorophyll *a* concentrations (chl *a*), and applied these to larger-scale spectral surveys. We developed models based on ice core chl *a* and coincident spectral measurements conducted during two cruises to the central Arctic Ocean in 2011 and 2012. We conducted four different under-ice spectral measurements: irradiance; radiance; transmittance; and transflectance, and applied three statistical approaches: Empirical Orthogonal Functions (EOF); Normalized Difference Indices (NDI); and multi-NDI. These reference models were ranked based on two criteria: mean robustness R^2; and true prediction error estimates. The EOF approach performed better than the NDI, due to its ability to account for the high variability of environmental properties experienced over large areas. Based on robustness and true prediction error, the best three models, EOF-transmittance, EOF-transflectance and NDI-transmittance, were applied to two remotely operated vehicle (ROV) and two Surface and Under-Ice Trawl (SUIT) surveys. In these larger-scale chl *a* estimates, EOF-transmittance showed the best fit to ice core chl *a*. Ice core chl *a*, and ROV and SUIT EOF-based chl *a* estimates demonstrated higher chl *a* at higher latitude stations, which was attributed to lower melt rates. Application of our best model, EOF-transmittance, to an ROV station revealed large differences compared to published biomass estimates from the same site with important implications for projections of Arctic-wide ice-algal biomass and primary production.

2.1 Introduction

Many of the most pronounced changes in the Arctic Ocean have been observed in the physical sea ice environment, as these properties are easily monitored from satellites and air-borne sensors. Such changes include: dramatic reductions in sea ice extent [*Serreze et al.*, 2007; *Stroeve et al.*, 2012] and thickness [*Kwok and Rothrock*, 2009; *Haas et al.*, 2008]; replacement of multi-year ice (MYI) by first-year ice (FYI) and the loss of thick, old ice [*Maslanik et al.*, 2011]; increased light transmittance through the summer sea ice cover [*Nicolaus et al.*, 2012], decreased summer sea ice albedo [*Riihela et al.*, 2013]; and increased melt-pond coverage [*Rösel and Kaleschke*, 2012]. These changes to the Arctic sea ice cover are likely to continue unabated into the future, having profound ecological consequences [*AMAP*, 2011; *IPCC*, 2013].

Satellite observations have already indicated increased pelagic production within the Arctic Ocean due to decreased ice cover and a longer open water season [*Arrigo et al.*, 2008; *Arrigo and van Dijken*, 2011]. A recent study in the Central Arctic Ocean also suggested that sea ice related primary production has increased and will continue to increase in the Central Arctic due to more light penetrating through the ice [*Fernández-Méndez et al.*, 2015]. Overall, changes to ice-associated production are difficult to evaluate due to a lack of studies in the Central Arctic [*Wassmann et al.*, 2011]. Monitoring sea ice ecosystems remains a challenge due to logistical constraints and the difficulty of remotely sensing biological processes in and under the ice cover. As sea ice algae are a major source of energy for many key marine organisms in the Arctic [*Budge et al.*, 2008; *Kohlbach et al.*, in press; *Søreide et al.*, 2013; *Wang et al.*, 2015], multi-scale sea ice algae observations are of particular interest in order to address potential changes to the sea ice ecosystem as the physical environment continues to change.

There is growing interest in extending sea ice algal observations by developing larger-scale observation systems and methodologies that can capture the spatial distribution of sea ice algae at multiple scales. Although sea ice coring will remain an essential method for any ice-related research, point measurement coring is time consuming and logistically demanding, making it an unlikely candidate for large-scale ice-algal observation systems. Other devices such as the slurp-gun [*Gosselin et al.*, 1990] or underwater pulse-amplitude-modulated fluorometer (Diving-PAM)[*Rysgaard et al.*, 2001] have shown promise, however, they require the deployment by divers, which is also logistically demanding and time intensive.

New developments of Autonomous Underwater and Remotely Operated Vehicles (AUV/ROV) give promising new opportunities to study the underside of ice [*Wadhams*, 2012]. Currently these platforms have mainly been used to observe physical [e.g., *Katlein et al.*, 2015; *Nicolaus and Katlein*, 2013; *Nicolaus et al.*, 2012] and biological [e.g., *Ambrose et al.*, 2005; *Katlein et al.*, 2014a] processes within and under the ice at larger scales and with relatively minimal logistical requirements, in terms of spatial coverage compared to other methods (e.g., 8 hours for 100 to 500 m transects). ROVs deployed with mounted digital imagery systems have been used to document the distribution of sub-ice algal aggregates [e.g., *Ambrose et al.*, 2005; *Gutt*, 1995; *Katlein et al.*, 2014a]. Digital imagery is limited to 2-dimensional space and therefore abundance estimates may have high uncertainty. Using image analysis, *Katlein et al.* [2014a] showed that ice-algal aggregate distribution is mainly controlled by under-ice topography with the accumulation of aggregates along the edges of ridges and in dome-shaped ice features.

Under-ice spectral measurements can be used to derive chlorophyll *a* concentrations in sea ice using bio-optical models. Until now, however, these models have not been applied to larger scale under-ice ROV spectral measurements. ROVs have recently been deployed, with mounted spectral radiometers, to measure under-ice spectral irradiance [e.g., *Katlein et al.*, 2015; *Katlein et al.*, 2014b; *Nicolaus and Katlein*, 2013; *Nicolaus et al.*, 2012], but focused primarily on physical processes and energy budgets. Spectral radiometers have also been mounted on Surface and Under-Ice Trawls (SUIT, van Franeker et al. 2009), a potential horizontal profiling platform for monitoring ice algal concentration in combination with the abundance of under-ice grazers over profiles up to 3 km in length [e.g. *David et al.*, 2015]. The development of under-ice horizontal profiling platforms for observing spectral

properties of sea ice, among other properties, has resulted in and will continue to result in larger amounts of under-ice spectra. These spectral observations, both from the past and future, could be used to estimate the temporal evolution and spatial variability of ice-algal chl *a*. However, this requires the development of robust and reliable methodologies that can be applied to datasets with variable temporal and spatial coverage, and with a large range of environmental conditions.

Spectrally-derived ice-algal chl *a* concentrations have been estimated using a normalized difference index method (NDI), introduced by *Mundy et al.* [2007] and applied in other field studies [e.g., *Campbell et al.*, 2014]. This method has proved useful during springtime to detect under-ice spectral variations near the 440 nm chl *a* absorption peak in order to estimate chl *a* concentrations. The second chl *a* absorption peek at ~ 670 nm, however, did not provide an accurate bio-optical model due to the stronger influence of snow in the same wavelength range [*Mundy et al.*, 2007].

Alternatively, Empirical Orthogonal Function (EOF) analysis has been used to identify variations within underwater spectral measurements and estimate water column concentrations of chl *a* [*Craig et al.*, 2012] and phycoerythrin [*Taylor et al.*, 2013]. *Melbourne-Thomas et al.* [2015] compared several statistical approaches, including: NDI, EOF, ratios of spectral irradiance, and scaled band area, to estimate ice-algal biomass from under-ice spectra measured during winter and spring expeditions in the ice-covered Southern Ocean. Their results indicated that the NDI method was most robust for their dataset, but the EOF also provided reliable model results.

Previous work on spectrally-derived concentrations of chl *a* and pigments have demonstrated essential methodological advancements and applications [e.g., *Campbell et al.*, 2014; 2015; *Craig et al.*, 2012; *Melbourne-Thomas et al.*, 2015; *Mundy et al.*, 2007; *Taylor et al.*, 2013]. The application of spectrally-derived ice-algal chl *a* estimates, however, remains limited to local point measurements, with limited spatial coverage and during a period dominated by the influence of snow cover on light attenuation. In addition, previous ice-related work has focused on under-ice irradiance, which does not account for variations of the incoming solar radiation. Variability of incoming radiation and more importantly variations of the solar elevation angle not only produce variations in magnitude but also variations in spectral shape, which may introduce variability (i.e., artificial chl *a* absorption signals) within spectral regions of maximum chl *a* absorption.

The main motivation for this work is to find a reliable bio-optical model for estimating the variability of ice-algal chl *a* under highly heterogeneous environmental conditions that can be applied to larger scale spectral measurements using under-ice horizontal profiling platforms (e.g., ROV and SUIT). We accomplished this by developing upon previously established bio-optical methodologies and statistical approaches. We determined the best ranked bio-optical model for estimating ice-algal biomass by comparing: *i)* different statistical approaches: NDI and EOF, including a newly introduced multi-NDI method that takes advantage of both chl *a* absorption peaks; and *ii)* different spectral measurements, including: under-ice irradiance, under-ice radiance, under-ice transmittance and under-ice transflectance. We applied a selected best set of models to larger scale spectral surveys for additional model assessment and comparison, in addition to a preliminary analysis of the spatial distribution of ice-algae based on a short transect extracted from a selected ROV survey.

2.2 Materials and Methods

2.2.1 Study Area

Field observations and sampling for this study were conducted during two summer research cruises to the Central Arctic Ocean onboard the German icebreaker R/V *Polarstern*: *i) TransArc* (PS78.3, hereafter referred to as PS78) conducted from 4 August to 7 October 2011 (Figure 1); and *ii) IceArc* (PS80.3, hereafter referred to as PS80) conducted from 4 August to 8 October (Figure 1). Measurements and ice core samples were acquired from a total of 6 ice stations during the 2011 PS78 cruise, and from 9 ice stations, one helicopter ice landing and two Surface and Under-Ice Trawl profiles (SUIT; with mounted sensor array) during the 2012 PS80 cruise.

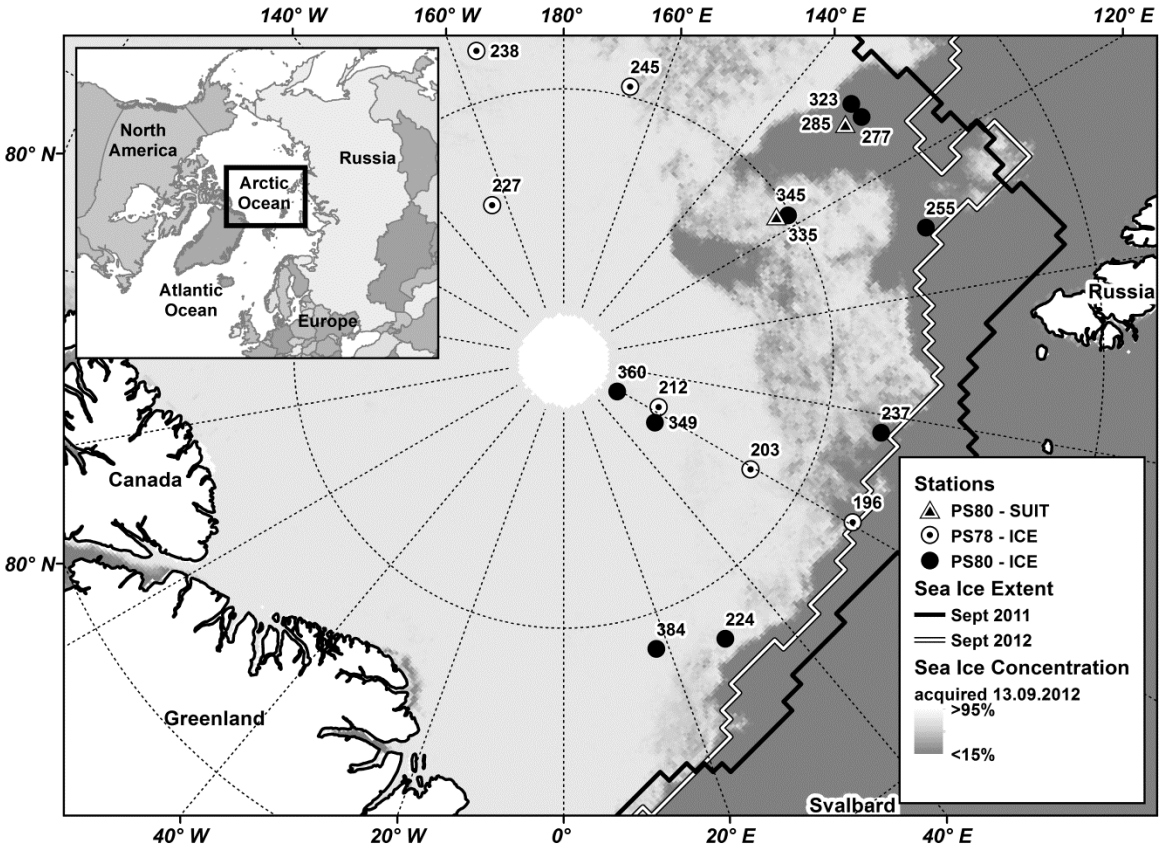

Figure 1. Map of the study region with ice stations conducted during expeditions PS80 and PS78, and the two selected SUIT sampling sites. Sea ice concentration data acquired from www.meereisportal.de according to algorithms in [*Spreen et al.*, 2008]. Sea ice extent correspond to monthly means during September for both cruise years [extent data acquired from NSIDC; *Fetterer et al.* 2002, udpated 2011].

2.2.2 Spectral measurements

Spectral radiance and irradiance measurements were acquired using Ramses spectral radiometers (Trios GmbH, Rastede, Germany) with a wavelength range from 350 to 920 nm and a resolution of 3.3 nm, which were subsequently interpolated to a 1 nm grid following *Nicolaus et al.* [2010]. Incident solar radiation (E_S) and under-ice irradiance (E_T) were measured using an irradiance sensor (RAMSES-ACC) containing a cosine receptor with a180º field-of-view (FOV. Under-ice radiance (I_T) measurements were acquired using a radiance sensor (RAMSES-ARC) with a 9º FOV. All spectral measurements are presented for the photosynthetically active radiation range (PAR) between 400 to 700 nm, unless stated otherwise. Additional details about the sensors and spectral data processing were described by *Nicolaus et al.* [2010]. Spectral transmittance (T_E) is defined as the ratio of under-ice irradiance (E_T) to incident solar radiation (E_S), as described by *Nicolaus et al.* [2010].

$$\boldsymbol{T_E(\lambda) = \frac{E_T(\lambda)}{E_s(\lambda)}} \quad (1)$$

with wavelength λ within the PAR range (400:700 nm). Spectral transflectance (T_I), introduced by *Nicolaus and Katlein* [2013], is defined as the ratio of under-ice radiance (I_T) to incident solar radiation (E_S).

$$\boldsymbol{T_I(\lambda) = \frac{I_T(\lambda)}{E_s(\lambda)}} \quad (2)$$

Transmittance and transflectance are dimensionless, however, following the SI-system to use steradian for solid angles, we use sr^{-1} as the unit for transflectance [e.g., *Nicolaus and Katlein* 2013].

Under-ice spectral measurements were conducted using: i) an under-ice L-arm sensor system; ii) a remotely operated vehicle (ROV), V8Sii-ROV (Ocean Modules, Åtvidaberg, Sweden), with mounted sensor array; and iii) a Surface and Under Ice Trawl (SUIT)[*van Franeker et al.*, 2009] with mounted sensor array, as described by *David et al.,* [2015]. Simplified diagrams and images showing the deployment of all under-ice profiling platforms are presented in Figure 2. The under-ice L-arm sensor system (Figure 2 a and e), previously described in [*Melbourne-Thomas et al.*, 2015; *Mundy et al.*, 2007], was deployed below the ice through a ~14 cm diameter vertical hole drilled using a Kovacs Mark II 9 cm internal diameter corer (Kovacs Enterprise, Roseburg, USA). Once the L-arm was below the ice, the lower ~1.2 m of the aluminum bar setup, with mounted radiometer, was extended horizontally, and then slowly raised so the sensor was ~10 cm from the ice bottom. To minimize shading by the system equipment and operator, the sensor was positioned directly south of the L-arm hole at ~1.2 m distance. Coincident incoming irradiance measurements were conducted above the ice for all under-ice L-arm measurements. The snow/ice surface directly south of the L-arm hole was kept undisturbed during spectral measurements. Ice cores were then sampled coincident to the spectral measurement location (see Section 2.3; and Figure 2 a and b).

A detailed description of the ROV (Figure 2 c and f) spectral measurements, calibration and calculations, and ROV operation during PS78 was provided by *Nicolaus and Katlein* [2013]. Some minor modifications to the ROV system were made for the PS80 cruise and are described in *Katlein et al.* [2014a]. ROV spectral measurements, calibration, and calculations during PS80 were consistent to those used during PS78 and conducted as described in *Nicolaus and Katlein* [2013]. Under-ice ROV spectral surveys (Figure 2 a) were performed over perpendicular *x-y* transects with *x* and *y* transect lengths between 50 and 150 m. Incident solar radiation (E_S) measurements, for the calculation of spectral transmittance and transflectance, were performed using an irradiance sensor mounted on a tripod positioned on the sea ice nearby the ROV operation tent (Figure 2 a). Stationary spectral measurements were conducted directly (~0 to 10 cm) under the ice at 10 m intervals along the *x-y* transects. When the ROV spectral surveys were complete, ice cores were extracted at pre-determined locations coincident to selected spectral measurement locations (Figure 2 a).

The Surface and Under Ice Trawl (SUIT) [*van Franeker et al.* 2009] is a net used to sample sea ice fauna, zooplankton and micronekton in the upper 2 m of the water column under the ice (Figure 2 d, g, and h). A detailed description of the SUIT is provided as supplementary material in *Flores et al.* [2012]. During PS80 the sensor array was specifically enhanced to target the variability of sea ice algae. The new sensor package included an Acoustic Doppler Current Profiler (ADCP), a Conductivity Temperature Depth probe (CTD) with built-in fluorometer, an altimeter, one irradiance sensor (RAMSES-ACC), one radiance sensor (RAMSES-ARC) and a video camera (Figure 2 h; previously described in *David et al.* [2015]). The sensor array provides measurements of pitch and roll, depth and distance to ice, which were used to calculate ice draft, and under-ice spectral measurements.

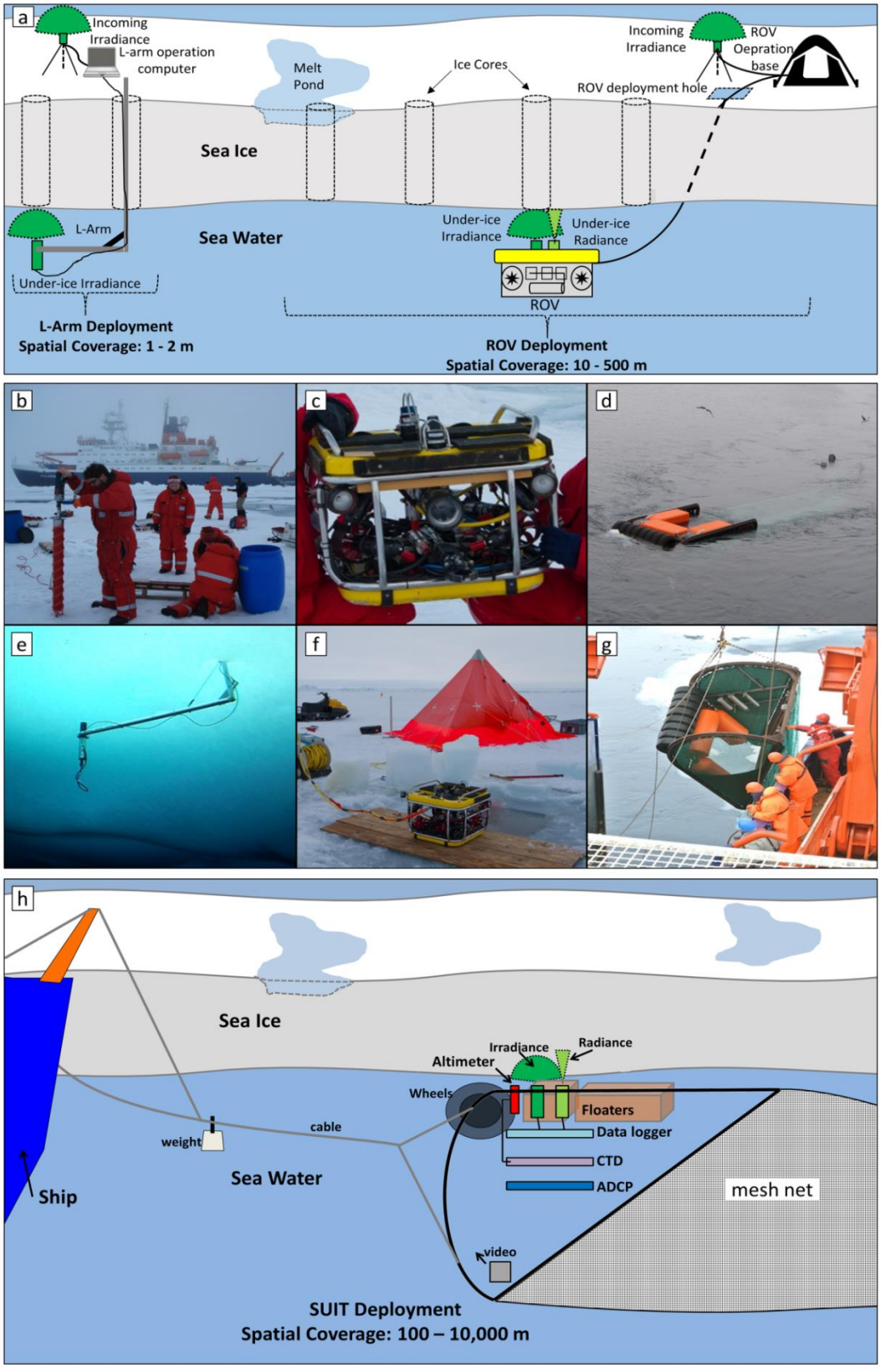

Figure 2. Diagrams and images showing under-ice horizontal spectral profiling platforms and sea ice sampling. a) simplified diagram showing ice station work, which included deployment of the L-arm and remotely operated vehicle (ROV), and ice core extraction; b) image showing ice coring; c) image of the ROV; d) image of the surface and under-ice trawl (SUIT) floating in the water; e) image of the L-arm deployed under the ice with a mounted radiance sensor; f) image of the ROV adjacent to the

deployment hole and operation tent; g) image of the SUIT being lifted back onto Polarstern, with sensor array on portside wing; and h) simplified diagram of the SUIT, with mounted sensor array, being towed behind a ship. NOTE: a) and h) are not to scale.

2.2.3 Spectral Quality control of under-ice profiling platforms

SUIT and ROV cover different distances and were operated at various depths under the ice along the profiles. Therefore, the data needed to be filtered to get suitable spectra for the bio-optical prediction models. Pitch and roll, and distance to ice measurements were used to filter the spectra in order to minimize the influence of light extinction in water on the spectra. The integration time of the spectral radiometers varies with the strength of the received radiation, which is highly variable under sea ice. Therefore, ADCP measurements (1 Hz) and distance to ice (10 Hz) were averaged over the integration time interval of each spectral measurement. The footprint of each measurement was dependent on the distance to the ice bottom, the field-of-view (FOV) of the sensor, and the horizontal speed of the sensor platform. Best spectral quality results from ROV operation at a constant depth [*Nicolaus and Katlein*, 2013]. However, variations of distance to ice and orientation of the ROV are difficult to minimize and therefore the measurement footprints during ROV surveys were highly variable. We minimized the influence of light extinction by water on the spectral signal and limited variability of the footprint size by selecting only measurements that had a distance to the ice bottom of < 1.5 m, and pitch and roll between -10º and +10º [*Nicolaus and Katlein*, 2013]. Similar to the ROV, SUIT haul measurements were also filtered by a distance to ice bottom of < 1.5 m, and pitch and roll between -15º and +15º. At a distance of <1.5 m the influence of water extinction was assumed to be minimal. Because the ROV was operated at slow speeds (< 0.2 m s^{-1}) the footprint size had minimal horizontal variability due to movement (e.g., across-track and along-track spatial footprint were equal).The faster horizontal operation speeds of the SUIT (~1.5 m s^{-1}), however, resulted in an along-track spatial footprint dependent on the integration time of the sensor. Footprint size variability was accounted for by using the footprint as a weighting factor when conducting statistical analyses.

2.2.4 Ice coring and Chlorophyll *a* measurements

Sea ice cores were extracted using a 9 cm inner diameter ice corer powered by an electric drill . At each core location, we measured snow depth or surface scattering layer depth, ice thickness, core length, and freeboard. Here the scattering layer is defined as an unconsolidated surface layer of large ice granules (~1 to 5 mm). Ice cores were placed in acid-cleaned barrels, and then immediately transported to the ship and melted at 4 ºC in the dark. During PS78, ice cores were cut in three parts (the upper and lower 20 cm, and the remaining middle part of the core), placed in separate barrels and processed separately (i.e., three samples for each core). During PS80, each entire ice core was placed in one acid-cleaned barrel for melting and processing (i.e., one sample for each core). When extracting cores from melt ponds, melt pond water was added to the sample with a volume approximately equal to a 9 cm diameter cylinder (e.g., core barrel) with a height equal to the depth of the melt pond.

Sub-samples from each melted sample were filtered onto 25 mm Whatmann GF/F filters, placed in liquid nitrogen then stored in a -80 ºC freezer until analyses were conducted back at the laboratory in Bremerhaven, Germany. Chl *a* concentrations were measured on each filter using high-performance liquid chromatography (HPLC) as described in *Tran et al.* [2013]. All chl *a* concentrations are reported as vertically-integrated units (mg chl *a* m^{-2}).

2.2.5 Statistical Methods and Approaches

All statistical analyses were conducted using R software Version 2.15.2 [*R-Development-Core-Team*, 2012] with all relevant packages listed after the corresponding analysis description.

To avoid large negative numbers in log space due to the presence of near-zero chl *a* concentrations, raw chl *a* (*chla*) values were adjusted by a constant value so that the minimum chl *a* ($chla_{min}$) value was set to 1 mg chl *a* m^{-2}, as follows:

$$\boldsymbol{chla_{adj} = chla + (1 - chla_{min})} \quad (3)$$

where $chla_{adj}$ is the adjusted chl *a* value used in all the models.

2.2.5.1 Empirical Orthogonal Function (EOF)

The large dimensionality of spectral data (e.g., 301 wavelengths) was reduced by applying Empirical Orthogonal Function (EOF) analyses (also referred to as principal component analyses - PCA). Spectra were first standardized by subtracting the mean then dividing by the standard deviation [*Taylor et al.*, 2013]. Standardizing the spectra minimizes any variability due to magnitude and allows for a more detailed examination of spectral shape [*Craig et al.*, 2012; *Taylor et al.*, 2013]. The resulting standardized spectra formed an $N \times M$ matrix X consisting of N observations and M wavelengths = 301 (PAR: 400 to 700 nm, 1 nm resolution). Using the 'R' function *cov*, a covariance matrix C was calculated from X:

$$\mathbf{C} = \frac{\mathbf{1}}{\boldsymbol{M}}\mathbf{X^T X} \quad (4)$$

We then used the 'R' function *eigen*, to conduct an Eigen decomposition of the covariance matrix C:

$$\mathbf{C = S\Lambda S^T} \quad (5)$$

where S ($N \times N$) Eigenvectors, hereafter referred to as EOFs, contains the loadings for each sample (N) by mode (N). Λ (diagonal matrix with dimensions N) contains the Eigenvalues, which explain the variance of each EOF mode. The first EOF mode, captures the largest proportion of variability within the spectra, with each subsequent mode capturing progressively less of the variability. Each selected EOF mode can be represented as a mode of oscillation in the data (spectra) by calculating the EOF expansion coefficients Z. Z was calculated by projecting the spectral matrix X onto S:

$$\mathbf{Z = XS} \quad (6)$$

where Z ($M \times N$) contains the loadings for each wavelength (M) by mode (N).

To create predictor models for chl *a* concentrations in sea ice, we applied Generalized Linear Models (GLM) [*McCullagh and Nelder* 1989] of the log-transformed chl *a* ($chla_{adj}$: response variable) versus EOF modes (predictor variables). Sample size (N) varied depending on data subset and spectral measurement combination. For $N \geq 9$, we selected the first 9 EOF modes, and for $N < 9$, we selected the first N EOF modes as predictor variables for the GLM analyses. In addition, each selected EOF mode was squared and included as predictor variables in the GLM analyses. The GLM models have the form:

$$\boldsymbol{\ln[E(chla_{adj})] = \alpha + \beta_1 s_1 + \beta_2 s_2^2 + \cdots + \beta_m s_m + \beta_n s_n^2} \quad (7)$$

where $s_{1,2,\ldots,n.m}$ are the EOF modes or the EOF modes squared from S determined from the GLM model selections, α is the intercept and $\beta_{1,2,\ldots,m,n}$ are the regression coefficients. Following *Taylor et al.* [2013], we assumed a Gaussian error distribution and applied a log-link function for the prediction of chl *a*, i.e., $E(chla_{adj})$.

2.2.5.2 Normalized Difference Index (NDI)

We constructed a spectral correlation surface matrix between chl *a* concentrations and all possible NDI combinations of two wavelengths within the photosynthetically active radiation (PAR) wavelength range between 400 and 700 nm, as described by *Mundy et al.* [2007]. Correlation surfaces were constructed for each bio-optical model combination (all combinations of bio-optical models are described in Section 2.5.4 and visualized in Figure 3). We applied a moving average to the correlation surfaces by taking the mean of a 3 x 3 nm grid centered at each value to ensure maximum chl *a*-NDI correlations were not chosen at the edge of regions of high correlation.

Two maximum chl *a*-NDI correlations were chosen from each correlation surface: NDI_{440}, which corresponds to the wider ~440 nm chl *a* absorption peak and has at least one NDI wavelength within the range 400 to 480 nm; and NDI_{670}, which corresponds to the narrower ~670 nm chl *a* absorption

peak and has at least one NDI wavelength between 655 to 685 nm. We then applied a GLM to chl *a*, adjusted according to Equation 3 ($chla_{adj}$: response variable) and NDI (*NDI*: predictor variables) values in the form:

$$\ln[E(\mathbf{chla}_{adj})] = \alpha + \beta(NDI) \quad (8)$$

where α is the intercept and β the regression coefficient (i.e., slope). *NDI* corresponds to either the maximum chl *a*-NDI correlation NDI_{440} or NDI_{670}. To maintain consistency between statistical approaches, which is important for inter-comparison, we applied a log-link function for all statistical approach models, i.e., $E(chla_{adj})$.

2.2.5.3 Multi-NDI

In order to take advantage of both chl *a* absorption peaks we incorporated both NDIs (e.g., NDI_{440} and NDI_{670}) into one model. The two maximum NDI correlations for each bio-optical model combination (all combinations described in section 2.5.4 and visualized in Figure 3) were used as predictor variables in GLMs with chl *a*, adjusted according to Equation 3 ($chla_{adj}$) as the response variable:

$$\ln[E(chla_{adj})] = \alpha + \beta_{440}(NDI_{440}) + \beta_{670}(NDI_{670}) \quad (9)$$

where α is the intercept and $\beta_{440,\,670}$ are the regression coefficients.

2.2.5.4 Selection criteria of bio-optical reference models

To visualize the selection process from a large number of possible model combinations we provided a flowchart illustrating the model selection and ranking process following the selection path of one model (Figure 3). Bio-optical models to estimate ice-algal chl *a* were constructed using GLMs based on four different statistical approaches: 1) Empirical Orthogonal Function analysis (EOF); 2) NDI_{440}; 3) NDI_{670}; and 4) multi-NDI (Figure 3 a). These statistical approaches were applied to four different spectral measurements: a) Under-ice Irradiance (E_T); b) Under-ice Radiance (I_T); c) Transmittance (T_E); and d) Transflectance (T_I; Figure 3 a). These 16 "statistical approach-spectral measurement" combinations were applied to 1) the full dataset (*all*); 2) PS78 cruise (*PS78*); 3) PS80 cruise (*PS80*); 4) high-latitude MYI sites from PS80 (*PS80-MYI*); 5) low chl *a* (*low*: < 2 mg m^{-2}); and 6) high chl *a* (*high*: > 2 mg m^{-2}; Figure 3 a).This resulted in 96 "statistical approach-spectral measurement-data subset" combinations, of which 72 were based on the NDI approaches, and 24 were based on the EOF approach.

Within each of these 96 combinations there were multiple potential reference model possibilities of wavelength combinations (NDI) or EOF mode combinations (EOF; Figure 3 a). From the many possible NDI-based GLMs, which have various potential combinations of wavelengths, the NDI-wavelength combination with the highest spearman correlation coefficients (Figure 3) was selected as the NDI predictor variable (NDI_{440} or NDI_{670}) or variables (multi-NDI) for fitting the reference model of each 72 corresponding NDI-based approach-spectral measurement-data subset combinations.

For each of the 24 EOF-based spectral measurement-data subset combinations, there were a large number of EOF mode combinations as potential predictor variables in the GLMs. With 9 modes, 9 squared-modes, and up to 5 predictor variables, this resulted in over 500,000 different combinations of EOF modes in the GLMs. We used the 'R' package *glmulti* [*Calcagno and de Mazancourt*, 2010], to select the 'best' 100 GLMs from all possible unique combinations of predictor variables based on a predefined model evaluation criterion. Here we used the Bayesian Information Criterion (BIC), because it includes a penalty for the number of variables included in the GLM [*Schwarz*, 1978]. Out of these 100 'best' potential models (GLMs) for each of the 24 EOF-based spectral measurement-data subset combinations, we selected one reference model, which had the lowest BIC and in which all coefficients were significant ($p \leq 0.05$) (Figure 3 a).

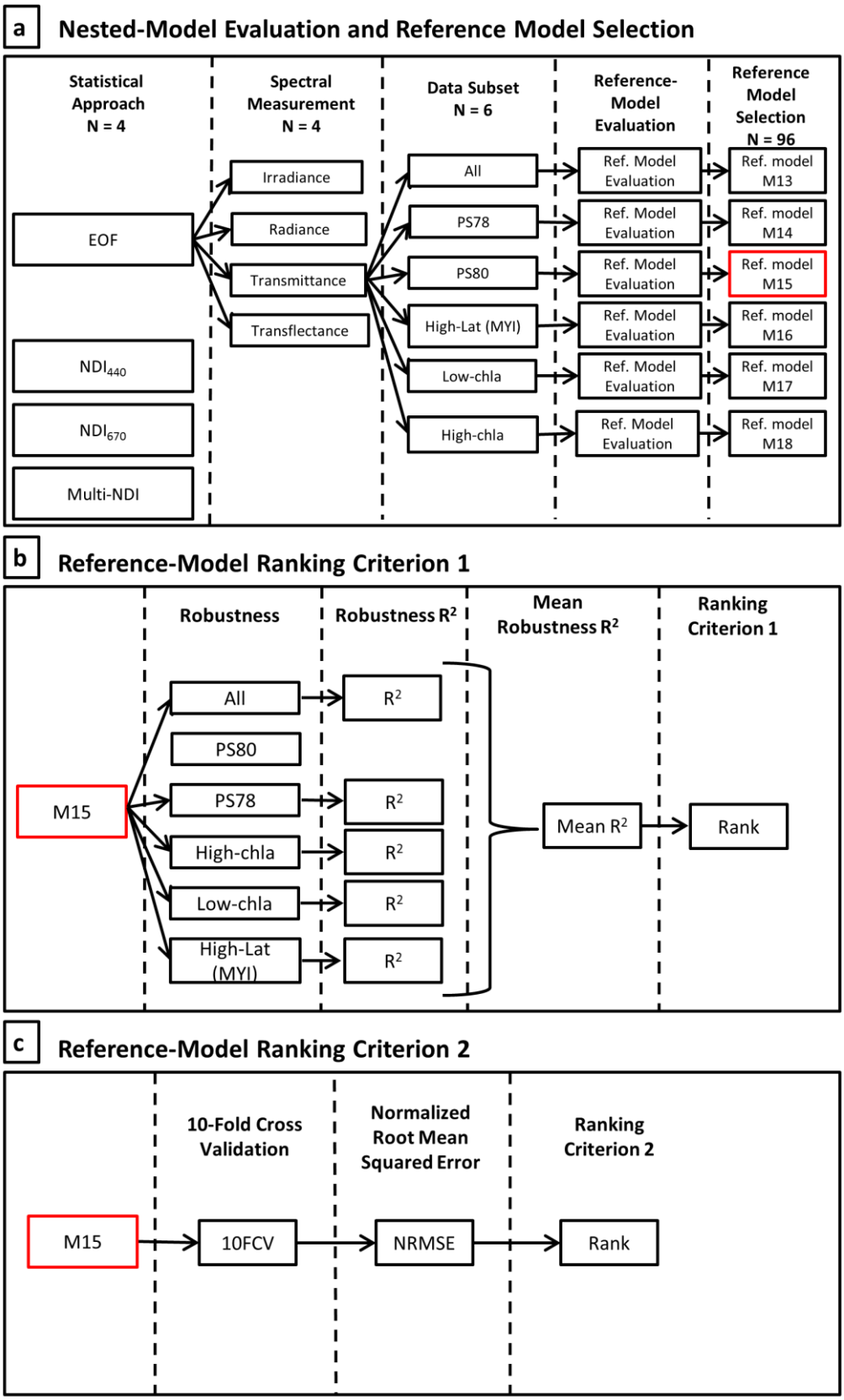

Figure 3. Flowcharts of: a) Reference model evaluation and selection process; b) reference model ranking criterion 1 based on the mean robustness R2; and c) reference model ranking criterion 2 based on the normalized root mean squared error (NRMSE). a) is performed first and results in the selection of one bio-optical model for each of the 96 statistical approach-spectral measurement-data subset combinations. b) and c) occur independently in parallel and rank the reference models as a means of

model inter-comparison. The "best" (i.e., most reliable) models were than ranked based on the average of b) and c). For simplicity, the flowchart only follows the pathway of the top ranked model (M15, referred to in text as EOF-Transmittance).

2.2.5.5 Comparing reference models and identifying predictive models

The previous selection process identified the 'best' reference model for each of the 96 statistical approach-spectral measurement-data subset combinations (Figure 3 a). In order to assess the reliability of these reference models to predict ice-algal chl *a* concentrations in larger spectral datasets such as from under-ice profiling platforms (e.g., ROV and SUIT), we ranked the 96 reference models based on two criteria (Figure 3 b and c) then, based on the average of both rankings, we selected the top 5 models as the set of potential 'predictive models' for further comparison.

For the first ranking criterion (Figure 3 b), we assessed model robustness, applying an adapted procedure used by *Melbourne-Thomas et al.* [2015]. Each of the 96 reference models was applied to the 5 data subsets not used to fit the respective reference model. We then calculated the predicted chl *a* versus observed chl *a* coefficient of determination (R^2) for each reference model applied to each of the 5 data subsets, which we refer to as the robustness R^2. We calculated the mean of the robustness R^2 values for each data subset. The mean robustness R^2 provides an estimate of how well the models perform when applied to "new" spectral data (e.g., larger-scale ROV or SUIT spectra) and may also identify variability in how the models fit different cruises (PS80 vs. PS78) or chl *a* concentrations (high vs. low). The mean robustness R^2 values were ranked from highest to lowest and used as the first criterion for selecting the top 5 potential predictive models. One limitation of this ranking criterion is that subsets were pre-selected by non-random factors, which may introduce bias. This is why we included an additional ranking criterion, which uses random data subsets to evaluate predictive power of the models.

Models are optimized for the data they are fitted to (i.e., training data); therefore the error of the model applied to new data (true prediction error) is usually higher than when the model is applied to the training data (training error). It is common to use training error estimates (e.g., trained model residuals) for the selection of models or to report confidence intervals for predicted data (e.g., *Taylor et al.* [2013]). This can result in the selection of inferior models or an inaccurate estimate of the true prediction error. Taking these considerations into account, we implemented a second model ranking criterion in order to select the predictive models. The second ranking criterion is based on 10-Fold Cross-Validation (10FCV) to estimate the true prediction error of each model. K-fold cross validation is a commonly used method to assess the performance of predictive models by providing accurate estimates of the true prediction error [e.g., *Mahmood and Khan* 2009]. In 10FCV the data are first subset into 10 folds (i.e., data subsets). Model fitting and error estimation are repeated 10 times. Each time a different set of 9 folds are combined to train/fit the model. Each model is then applied to the 10^{th} fold of "new" spectral data (i.e., holdout data). The root mean square error (RMSE) is calculated for the "new" predicted chl *a* data, which provides an estimate of the true prediction error. The 10 error estimates (RMSE) are averaged to provide a more robust RMSE estimate for each 10FCV run. Since the data are subset randomly, the 10FCV process is repeated 100 times to ensure more representative sub-sampling of the data and a more representative estimate of the true prediction error (RMSE). The 10FCV procedure results in one estimate of the true prediction error for each model, which we term the cross-validation RMSE ($RMSE_{CV}$). The $RMSE_{CV}$ is used as an indicator for the quality of the model, with lower $RMSE_{CV}$ values corresponding to models with a higher predictive performance. The $RMSE_{CV}$ is also used to provide model uncertainty estimates when models are applied to new spectral data (e.g., ROV and SUIT).

In order to compare between models with different sample sizes and range of values we normalized the $RMSE_{CV}$ by the range (minimum and maximum) of observed chl *a* values ($chla_{obs,min}$ and $chla_{obs,max}$) used to train the model. $NRMSE_{CV}$ was calculated as:

$$\boldsymbol{NRMSE_{CV}} = \frac{\boldsymbol{RMSE_{CV}}}{\boldsymbol{chla_{obs,max} - chla_{obs,min}}} \quad (10)$$

$NRMSE_{CV}$ values were ranked from lowest to highest and used as the second criterion for selecting the top 5 potential predictive models. The rankings of the mean robustness R^2 (first criterion) and $NRMSE_{CV}$ (second criterion) were then averaged and ranked to arrive at the top 5 ranked potential predictive models. Robustness of statistical assumptions in these 5 predictive GLMs were visually assessed based on validation plots. Because we have limited data points in the high chl *a* range, particular attention was given to the leverage of each point and identification of potential model fit outliers. Following procedures described in *Aguinis et al.*, [2013], we first identified potential model fit outliers using a Cook's *D* cutoff value equal to the *F*-statistic (~0.92). Second, we fitted the models with removal of the identified potential outliers and assessed the change in model fit statistics: R^2, BIC, and model significance [*Aguinis et al.*, 2013]. Model fit outliers were only reported if statistically significant changes in model fit were observed. Model significance was assessed with an analysis of variance (ANOVA) using the *F*-test.

Further quality assessments were conducted on the top 5 predictive models in order to ensure these models were acceptable for application to larger scale spectral data. This included: *i)* investigating any potential relationships between environmental properties and chl *a*, which may influence model performance; *ii*) evaluating the biases of the model, and the model applied to high- and low-chl *a*, e.g., if the model over-estimates (positive bias) or under-estimates (negative bias) the predicted data; *iii)* applying the potential predictive models (excluding any models identified as unreliable from the previous two steps) to larger-scale spectral profiles and comparing general performance between predictive models for all profiles; and *iv)* assess predictive performance of each potential predictive model along a short 85 m ROV transect and compare to ice core chl *a* observations along the same transect.

2.2.5.6 Predicting ice-algal chl a

We applied the selected best predictive models to independent spectral measurements from two SUIT stations and two ROV stations conducted during the *PS80* cruise. These included high-latitude stations PS80/358 (SUIT) and PS80/360 (ROV ice station), and lower-latitude stations PS80/285 (SUIT) and PS80/323 (ROV ice station; Figure 1). These stations were selected in order to compare the predictive models applied to independent data from different regions and different environmental conditions.

The application of NDI models to independent spectral measurements required first to calculate the $NDI_{\lambda 1:\lambda 2}$ using the wavelength combinations (e.g., λ1 and λ2) from NDI-based predictive models. The *NDI* values were then incorporated into Equation 8 (NDI model) or Equation 9 (multi-NDI model) along with the α and β values predetermined by the predictive models to derive the corresponding chl *a* concentrations.

Predictions of chl *a* concentrations on new spectral data using the EOF method were conducted as described in Taylor et al., 2013. The independent spectral measurements were first standardized, as described previously. The independent standardized spectral data Y, a $J \times M$ matrix with J the number of independent spectral measurements and M the number of wavelengths, was then projected onto the EOF expansion coefficients Z in the form:

$$\mathbf{F} = (\boldsymbol{Z}^{-1}\mathbf{Y})^{\boldsymbol{T}} \quad (11)$$

where F, the EOFs, is a $J \times J$ matrix providing the loadings by mode (J) for each sample (J), as with S. Predicted ice-algal chl *a* values were calculated using the EOF-based predictive models' GLM formula and the new EOFs, F, in the form:

$$\ln[\boldsymbol{E}(\boldsymbol{chla}_{\mathbf{pred}})] = \boldsymbol{\alpha} + \boldsymbol{\beta}_1 \boldsymbol{f}_1 + \boldsymbol{\beta}_2 \boldsymbol{f}_2^2 + \cdots + \boldsymbol{\beta}_n \boldsymbol{f}_n + \boldsymbol{\beta}_m \boldsymbol{f}_m^2 \quad (12)$$

where $f_{1,2,\ldots,n.m}$ are the EOF modes or modes squared from F, which correspond to the selected modes from S (e.g., $s_{1,2,\ldots,n,m}$) used as response variables in Equation 7, α is the intercept and $\beta_{1,2,\ldots,n,m}$ the regression coefficients from Equation 7.

The $chla_{pred}$ values were re-adjusted by subtracting (1 - $chla_{min}$) to account for the pre-model adjustment of the chl *a* values (Equation 3). Due to the range of observed chl *a* values (~0 to 12 mg chl *a* m^{-2}), the predicted chl *a* were limited to a range of 0 to 20 mg chl *a* m^{-2} by excluding all other values. We set these limits because the models were fitted to a certain range of values and predicting values significantly outside this range only increases uncertainty in the predicted data. Setting an upper limit to 20 mg chl *a* m^{-2} is unlikely to result in under-estimated predictions of chl *a* values since our 73 ice core chl *a* values, and literature chl *a* values [e.g., *Gosselin et al.* 1997; *Lund-Hansen et al.* 2015] from our sampling region and season were below 20 mg chl *a* m^{-2}.

2.3 Results and Discussion

2.3.1 Environmental properties

Both expeditions covered large geographical regions and were conducted during the transition from late-melt to the onset of freeze-up, and thus encountered a large range of sea ice conditions. Sea ice conditions during all ice stations were summarized in Table 1. Information about individual ice core samples was summarized in Supplementary Material Table S1. During PS78, sea ice stations were conducted from the Eurasian shelf edge to the Canadian Basin and back again. This sampling effort captured the transition from ice-edge through first-year ice and into the multi-year pack-ice. During ice stations PS78/198, PS78/203, and PS78/212 the surrounding sea ice was in an advanced state of melt with no snow cover and open melt ponds. Freeze-up conditions were first observed on 22 August, characterized by the presence of a light snow cover and surface freezing of melt ponds, and continued during the remaining ice stations PS78/227, PS78/238, and PS78/245.

During PS80, the first two ice stations, PS80/224 and PS80/237, were situated in dense first-year ice. Ice stations PS80/255, PS80/277, and PS80/323 were conducted in a region dominated by rotten sea ice with ice thicknesses < 1.0 m. A thin snow cover was first observed at station PS80/323 and was present at the remaining stations, but did not exceed 0.1 m. Station PS80/335 was situated in an area of mixed FYI and MYI with no obvious signs of advanced melt or freeze-up, indicating it was in transition from melt to freeze-up conditions. Freeze-up conditions were first observed at station PS80/349, characterized by ice forming on the surface of melt ponds, and continued for the remaining stations. Ice stations PS80/349 and PS80/360 were conducted within the heavy pack-ice consisting of predominantly MYI with thicknesses > 1.5 m. The first ice station PS80/224 was revisited as station PS80/384 and was then characterized by fall freeze-up and an ice thickness of ~ 1 m.

All observations were made in late summer at the end of the productive season. Thus, algal biomass was relatively low during both cruises. Of the 14 bio-optical cores collected during PS78, none of the samples exceeded 1.0 mg chl *a* m^{-2} (Table 1). Of the 59 bio-optical cores collected during PS80, however, samples exceeded 1.0 mg chl *a* m^{-2} at 6 out of the 10 ice stations (PS80/237, PS80/255, PS80/335, PS80/349, PS80/360, and PS80/384). Maximum chl *a* concentrations were observed at MYI station PS80/360, with three ice cores ranging between 6.4 and 11.8 mg chl *a* m^{-2} (Table 1). Also noteworthy was MYI station PS80/349, which had the next highest chl *a* concentrations with two cores at 3.5 and 5.6 mg chl *a* m^{-2} (Table 1).

Table 1. Summary of environmental properties and bio-optical cores for each ice station.

Cruise/Station	Ice Station [a]	Date [dd/mm/yy]	Latitude	Longitude	Ice Type	[b]SIC	[b] Modal ice thickness	[c]E_S (PAR)	[c]E_T (PAR)	[d]T_E (PAR)	[c]I_T (PAR)	[d]$T_{I\,(PAR)}$	N	Core length [m]	Snow [m]	Scatt. [m]	mg chl *a* m^{-2}
PS78/196	Ice-1	11/08/11	83.84	60.50	FYI	-	-	53.9	2.8	0.05	-	-	1	0.90	0.00	0.05	0.17
PS78/203	Ice-2	14/08/11	85.97	59.35	NEW	-	-	37.0	-	0.06	-	-	1	0.05	-	-	0.05
PS78/212	Ice-4	19/08/11	88.02	59.45	FYI	-	1.2	35.5 ± 5.8	14.0 ± 6.3	0.29 ± 0.2	-	-	3	0.93 ± 0.20	-	-	0.57 ± 0.27
PS78/227	Ice-7	29/08/11	86.86	-155.05	FYI	-	1.1	18.6 ± 4.4	1.7 ± 1.8	0.10 ± 0.11	1.1 ± 0.8	0.07 ± 0.05	3	1.92 ± 1.43	0.00	0.02 ± 0.02	0.18 ± 0.18
PS78/239	Ice-10	06/09/11	84.072	-164.19	MYI	-	0.8	42.8 ± 11.9	1.4 ± 0.9	0.03 ± 0.02	0.6 ± 0.6	0.01 ± 0.01	3	1.64 ± 0.79	-	-	0.40 ± 0.27
PS78/245	Ice-11	08/09/11	84.81	166.22	FYI	-	1.2	39.3 ± 16.7	1.0 ± 0.1	0.04 ± 0.03	0.8 ± 0.6	0.02 ± 0.02	3	0.82 ± 0.62	-	-	0.17 ± 0.15
PS80/224	Ice-1	10/08/12	84.00	30.00	FYI	80	1.0	50.7 ± 2.1	-	-	2.4 ± 2.2	0.04 ± 0.04	8	1.33 ± 0.41	0.00	0.09 ± 0.17	0.38 ± 0.22
PS80/237	Ice-2	15/08/12	83.95	76.85	FYI	80	1.3	77.7 ± 10.6	5.2 ± 7.6	0.07 ± 0.11	3.6 ± 4.2	0.04 ± 0.05	12	1.54 ± 0.55	0.00	0.04 ± 0.03	0.82 ± 0.58
PS80/255	Ice-3	20/08/12	82.86	109.86	FYI	70	0.9	35.0 ± 1.4	4.7 ± 0.5	0.13 ± 0.01	2.4 ± 0.5	0.06 ± 0.01	4	0.76 ± 0.17	0.00	0.03 ± 0.02	1.03 ± 0.66
PS80/277	Ice-4	26/08/12	82.89	129.78	FYI	80	-	-	-	-	-	-	5	0.63 ± 0.29	0.00	0.03 ± 0.04	0.19 ± 0.20
PS80/323	Ice-5	05/09/12	82.88	130.76	FYI	60	0.8	91.4 ± 9.1	2.9 ± 0.6	0.04 ± 0.02	1.6 ± 0.5	0.02 ± 0.02	6	0.73 ± 0.58	0.04 ± 0.02	0.00	0.16 ± 0.13
PS80/335	Ice-6	08/09/12	85.06	122.52	FYI	50	0.7	69.2 ± 8.4	2.7 ± 2.4	0.03 ± 0.03	1.4 ± 1.7	0.02 ± 0.02	6	1.07 ± 0.49	0.07 ± 0.07	0.00	0.96 ± 0.91
PS80/349	Ice-7	19/09/12	87.93	60.95	MYI	100	1.6	14.4 ± 1.3	1.0 ± 1.0	0.09 ± 0.09	0.8 ± 0.8	0.05 ± 0.06	7	0.89 ± 0.56	0.01 ± 0.01	0.00	1.62 ± 2.09
PS80/360	Ice-8	22/09/12	88.83	58.53	MYI	100	1.8	8.0 ± 0.5	0.2 ± 0.1	0.02 ± 0.01	0.2 ± 0.1	0.01 ± 0.01	4	1.11 ± 0.36	0.04 ± 0.03	0.00	6.59 ± 4.91
PS80/384	Ice-9	29/09/12	84.35	17.73	FYI	100	1.2	9.9 ± 0.5	0.2 ± 0.1	0.02 ± 0.02	0.1 ± 0.0	0.01 ± 0.01	4	1.07 ± 0.65	0.04 ± 0.02	0.00	0.40 ± 0.49
PS80/HELI-64	-	27/09/12	-	-	NEW	-	-	23.1± 2.7	-	0.54 ± 0.09	-	0.25 ± 0.02	3	0.05 ± 0.01	0.00 ± 0.00	0.00	0.03 ± 0.01

[a] Added for easy cross reference to other publications using this naming protocol [e.g., *Boetius et al*., 2013; *Fernández-Méndez et al.*, 2015; *Katlein et al*., 2014a]
[b] Data presented in *Nicolaus and Katlein* [2013] for PS78 and *Katlein et al*. [2014a] for PS80.
[c] $E_{S\,(PAR)}$ incident solar radiation; $E_{T\,(PAR)}$ under-ice irradiance; and $I_{T\,(PAR)}$ under-ice radiance were integrated over PAR wavelengths 400 to 700 nm.
[d] $T_{E\,(PAR)}$ spectral transmittance; and $T_{I\,(PAR)}$ spectral transflectance are mean over PAR. "-" represent no data

2.3.2 Spectral Measurements

Incident solar radiation (E_S) steadily decreased during both cruises and also decreased with latitude, which was evident by the strong negative correlations of E_S with Julian day and latitude (Table 2). Incident solar radiation was typically over 35 W m^{-2} except at stations PS78/227, PS80/349, PS80/360, and PS80/384, which fell below 20 W m^{-2} (Table 1). These values were expected for the sampling season and regions. ROV-derived spectral properties of the sea ice were presented and discussed in *Nicolaus and Katlein* [2013] and *Nicolaus et al.* [2012] for PS78, and in [*Katlein et al.*, 2014b] for PS80. Of the 73 bio-optical core locations, under-ice irradiance (E_T) and transmittance (T_E) spectra from 49 core locations, and under-ice radiance (I_T) and transflectance (T_I) spectra from 50 core locations were deemed of high quality and used for the development of bio-optical models (Supplementary Material Table S1).

Table 2. Pearson correlation coefficient matrix for all combinations of bio-optical core location bio-environmental variables.

	snow	**Scat.**	**ice**	**julian**	**lat**	E_S	E_T	T_E	I_T	T_I
chla	0.05	-0.07	0.08	0.27*	**0.47***	-0.28*	-0.22	-0.17	-0.22	-0.15
snow	-	-0.20	0.08	0.37*	0.10	0.05	-0.30*	-0.29*	-0.31*	-0.33*
Scat.	-	-	0.23	**-0.40***	-0.18	0.14	-0.16	-0.22	-0.08	-0.14
ice	-	-	-	-0.26*	0.03	0.11	-0.37*	**-0.47***	-0.33*	**-0.51***
julian	-	-	-	-	**0.46***	**-0.56***	-0.20	0.09	-0.25	0.13
lat	-	-	-	-	-	**-0.68***	-0.12	0.19	-0.32*	0.03
E_S	-	-	-	-	-	-	0.14	-0.21	0.29*	-0.18
E_T	-	-	-	-	-	-	-	**0.82***	**0.94***	**0.78***
T_E	-	-	-	-	-	-	-	-	**0.65***	**0.97***
I_T	-	-	-	-	-	-	-	-	-	**0.73***

***** indicates significant correlation at $p \leq 0.05$

Bold values indicate strong correlations ≥ 0.4

During summer, snow effects can generally be neglected due to a lack of snow [*Nicolaus et al.*, 2012], which is applicable to both cruises as the presence of snow never exceeded 0.1 m. Strong negative correlations were observed for ice thickness with T_E and T_I (Table 2). The strong correlation of ice thickness with T_E and T_I is a result of the large range of ice thicknesses sampled (e.g., 0.05 to 3.53 m) in combination with the strong influence of ice on light transmittance. The observed highly variable ice conditions had a large influence on light transmission, which showed horizontal variability of one to two orders of magnitude on the same ice floe for both FYI and MYI [*Nicolaus et al.*, 2012]. Overall, FYI showed higher transmittance than MYI during PS78 [*Nicolaus et al.*, 2012], which was also the case for PS80. The observed difference between MYI and FYI is mainly influenced by melt-pond coverage since relatively similar transmittance values were observed during PS78 when compared between white (not ponded) MYI (0.01) and white FYI (0.04), and between ponded MYI (0.15) and ponded FYI (0.22) [*Nicolaus et al.*, 2012]. FYI has a larger areal coverage of melt ponds compared to MYI, which causes FYI to have nearly a threefold greater total transmittance value (0.11) compared to MYI (0.04) [*Nicolaus et al.*, 2012].

Critical minimum under-ice irradiance, E_T, levels for algal growth have been reported between 0.4 and 2.0 W m^{-2} (2 to 9 µmol photons m^{-2} s^{-1}; e.g., [*Gosselin et al.*, 1985; *Gosselin et al.*, 1986; *Horner and Schrader*, 1982; *Lange et al.*, 2015]). Stations PS80/360 and PS80/384 had mean E_T values below this critical range (< 0.4 W m^{-2}); stations PS78/227, PS78/238, PS78/245, and PS80/349 had mean E_T values within this critical range (0.4 to 2.0 W m^{-2}); and all other stations were above this critical range (Table 1). Even though the high-latitude stations PS80/360 and PS80/349 had mean E_T values below or within the critical range these stations still had the highest mean ice core chl *a* concentrations compared to the other stations. Loss of algal biomass in summer is primarily the result of losses due to ice melt [e.g., *Grossi et al.* 1987], and substantial loss of ice algal biomass had likely occurred prior to our sampling in 2012 [*Boetius et al.*, 2013]. The higher latitude and dominance of thicker MYI at stations PS80/360 and PS80/349 probably resulted in lower melt rates, due to less internal energy

absorption by MYI compared to FYI [*Nicolaus et al.*, 2012], and subsequently less algal biomass loss due to melt before our sampling.

2.3.3 Model performance

2.3.3.1 Comparison of statistical approaches

The two highest-ranking predictive models were based on an EOF approach, and had considerably higher R^2 values (≥ 0.9) and lower RMSE values (< 0.8) than all other predictive models (Table 3). The two NDI-based predictive models in our selection were based on the 'high chl *a*' data subset, using radiance data (rank 3) and transmittance data (rank 5), respectively. Only the EOF models ranked first and fourth, however, combined large data subsets (n = 38 and n = 50, respectively) with spectral measurements that take into consideration the incoming solar radiation, indicating a wide applicability under varying environmental conditions (Table 3).

Based on the model biases, there appear to be no obvious trends between statistical approaches of the five 'best' predictive models, with all values near zero (Table 3). However, the biases of the models applied to the high-chl *a* and low-chl *a* data demonstrate that the NDI-based approaches underestimate the high-chl *a* data while overestimating the low-chl *a* data. The EOF-based approaches demonstrated low model biases and low biases when applied to both high- and low-chl *a* data.

A complete list summarizing all 96 reference models for each combination of spectral measurement with a statistical approach and a data subset was provided in Supplementary Material Table S2. Based on the model R^2 values, the EOF-based models performed generally better than the three NDI-based approaches (Supplementary Material Table S2). Among the NDI-based approaches, multi-NDI and NDI_{670} performed best. The good performance of the multi-NDI approach was probably driven by good relationships in the NDI_{670} values because overall the NDI_{440} models demonstrated the lowest R^2 values.

Similar studies have provided no model error estimate (e.g., [*Melbourne-Thomas et al.*, 2015]) or provided the model RMSE (e.g., [*Campbell et al.*, 2014; *Taylor et al.*, 2013]) as a measure of model uncertainty, which is always an underestimate of the true prediction error. The true prediction error estimate is particularly important to assess the uncertainty of predictions made using new (spectral) data. Here we provided an assessment of the true prediction error for the models using $RMSE_{CV}$ values (Table 3), which are often over double the model RMSE values (Table 3). For our predictive models, these values appear to be in an acceptable range considering the variability of environmental conditions. For comparison, all predictive models true prediction error estimates, $RMSE_{CV}$ (Table 3), were lower than the model RMSE provided by [*Campbell et al.*, 2014].

All 5 selected predictive models demonstrated high variability in predicting low-chl *a* values of the low chl *a* subset and the *PS78* data subset (i.e., < 2 mg m^{-2}; Table 3). This is expected, since with low chl *a* concentrations there is less absorption of light by algal biomass, which enhances the relative influence of other environmental properties on the transmitted spectra. The two selected predictive models based on NDI_{670} had relatively large positive biases when applied to low-chl *a* (Table 3), suggesting that the NDI_{670} models applied to independent data may also result in overestimation of low-chl *a* regions. This is not surprising since these two NDI-based predictive models were fitted to high-chl *a* data. Even though the EOF models also had large errors associated with predicting the variability of low-chl *a*, these models had practically no directional bias when applied to low- and high-chl *a* (Table 3), suggesting that these EOF models can correctly differentiate between low, medium, and high chl *a* concentrations, and are less likely to result in over- or under-estimations when applied to independent spectral data.

An overall better performance of models using an EOF-based approach can be attributed to the fact that the EOF method accounted for a larger range of spectral variability by including multiple regions of the spectra, which were represented by the different EOF modes. In ocean color remote sensing, increasingly complex algorithms have been developed to include more spectral bands in order to account for the many variables that influence ocean optics other than phytoplankton chl *a* [e.g., *Craig et al.*, 2012]. In the ocean, this is mostly CDOM or other particles, but for sea ice the snow and ice

matrix generally have a much larger influence on light penetration than any single variable in the ocean. The variability of under-ice and incoming spectra was particularly important during our study due to the large range of environmental properties experienced in terms of latitude, ice thickness, state of melt and melt pond coverage. In comparison, previous studies were performed in more uniform ice properties over a smaller latitudinal range [e.g., *Campbell et al.*, 2014; 2015; *Melbourne-Thomas et al.*, 2015; *Mundy et al.*, 2007].

Table 3. Summary of the top 5 predictive models.

Model ID		EOF-Transmittance	EOF-Radiance	NDI_{670}-Irradiance	EOF-Transflectance	NDI_{670}-Transmittance
N		38	15	15	50	15
Equation: $\ln[E(chl\ a_{adj})] =$		$0.7 - 3.0s_2 + 1.1s_4 + 2.4s_6 - 6.5s_7^2 + 3.9s_9^2$	$2.0 + 2.7s_4 - 1.7s_5 - 1.0s_6 - 2.3s_2^2 - 10.0s_8^2$	$2.2 + 10.8NDI_{669:683}$	$0.3 + 1.5s_2 - 1.7s_4 + 2.0s_7 + 3.2s_9 + 8.6s_9^2$	$1.2 - 11.1NDI_{678:684}$
Model	R^2	0.90	0.95	0.73	0.74	0.70
	RMSE	0.77	0.66	1.58	1.12	1.65
	bias	-0.02	-0.08	0.02	-0.12	0.06
Bias of Model applied to subset:	High-chla	-0.01	-0.08	0.02	-0.01	0.06
	Low-chla	0.00	0.00	2.09	0.00	1.96
R^2 of model applied to subset:	All	0.88	0.56	0.54	NA	0.63
	PS78	-0.11	NA	-0.08	NA	0.01
	PS80	NA	0.55	0.60	0.74	0.64
	MYI	0.94	0.55	0.68	0.76	0.62
	Low-chla	-0.01	-0.02	0.07	0.00	0.06
	high-chla	0.93	NA	NA	0.82	NA
	mean[a]	0.53	0.41	0.36	0.58	0.39
Cross Validation	RMSE	1.81	1.81	1.89	2.46	2.01
	NRMSE[b]	0.15	0.17	0.18	0.21	0.19
Ranking	R^2 mean[a]	4	9	13.5	2	11
	NRMSE[b]	6	7	8	23	14
	Mean	1	2	3	4.5	4.5

[a] and [b] depict the matching model statistic and corresponding ranking criterion variable.

The modes of oscillation (Figure 4) show the signatures of change within the spectral measurements due to different variables that influence the transmission of light through sea ice. Mode 1 alone explained most of the variability (~95 %), but was not selected in any reference model. This is not surprising, since the shape of the mode of oscillation closely resembles that of the spectral extinction coefficient curves for snow and ice [*Grenfell and Maykut*, 1977]. Furthermore, mode 1 had a significant medium-to-strong correlation with the presence of melt ponds, indicating that melt ponds had a large influence on spectral variability. This is expected since melt ponds are known to transmit more light [e.g., *Katlein et al.*, 2015; *Light et al.*, 2008; *Nicolaus et al.*, 2012].

For each of the modes included in the EOF-transmittance model (modes 2, 4, 6, 7 and 9) there is at least one local maximum or minimum corresponding to one of the maximum chl *a* absorption regions (Figure 4). Accordingly, four out of five modes, for both EOF-based predictive models, have medium to strong significant correlations with chl *a*, and two of the five modes for the EOF-Transmittance model (s_6 and s_9^2) and one of five modes used in the EOF-Transflectance model (s_7) have strong significant correlations with only chl *a* (Table 4). The modes that have strong correlations with only chl *a* also are associated with high changes in BIC when the term is removed from the model.

The proportion of variance explained by the modes used in the selected "best" EOF-based predictive models was relatively low compared to those found in other studies [e.g., *Craig et al.*, 2012; *Melbourne-Thomas et al.*, 2015]. *Taylor et al.* [2013] included modes 5 to 9 in their analyses and

showed that even subordinate modes which explained smaller proportions of the spectral variance still had an important influence on the models based on change in the Akaike Information Criterion (AIC). Their study related spectral radiance to phycoerythrin concentrations, which is an accessory pigment and therefore has a smaller influence on light absorption compared to chl *a*. This could explain why the subordinate modes were important in the model, since they capture the smaller variations caused by the spectrally less influential phycoerythrin pigment [*Taylor et al.*, 2013]. Similarly, during our study, ice-algal chl *a* concentrations had a smaller influence on spectral light transmission relative to e.g. ice thickness, melt ponds, incoming light and solar inclination. Because the physical properties of the snow and ice matrix dominate the influence of light transmission, the variability of chl *a* concentrations in sea ice appears to be best represented by subordinate modes explaining a smaller part of the EOF variability compared to approaches estimating chl *a* concentrations in water.

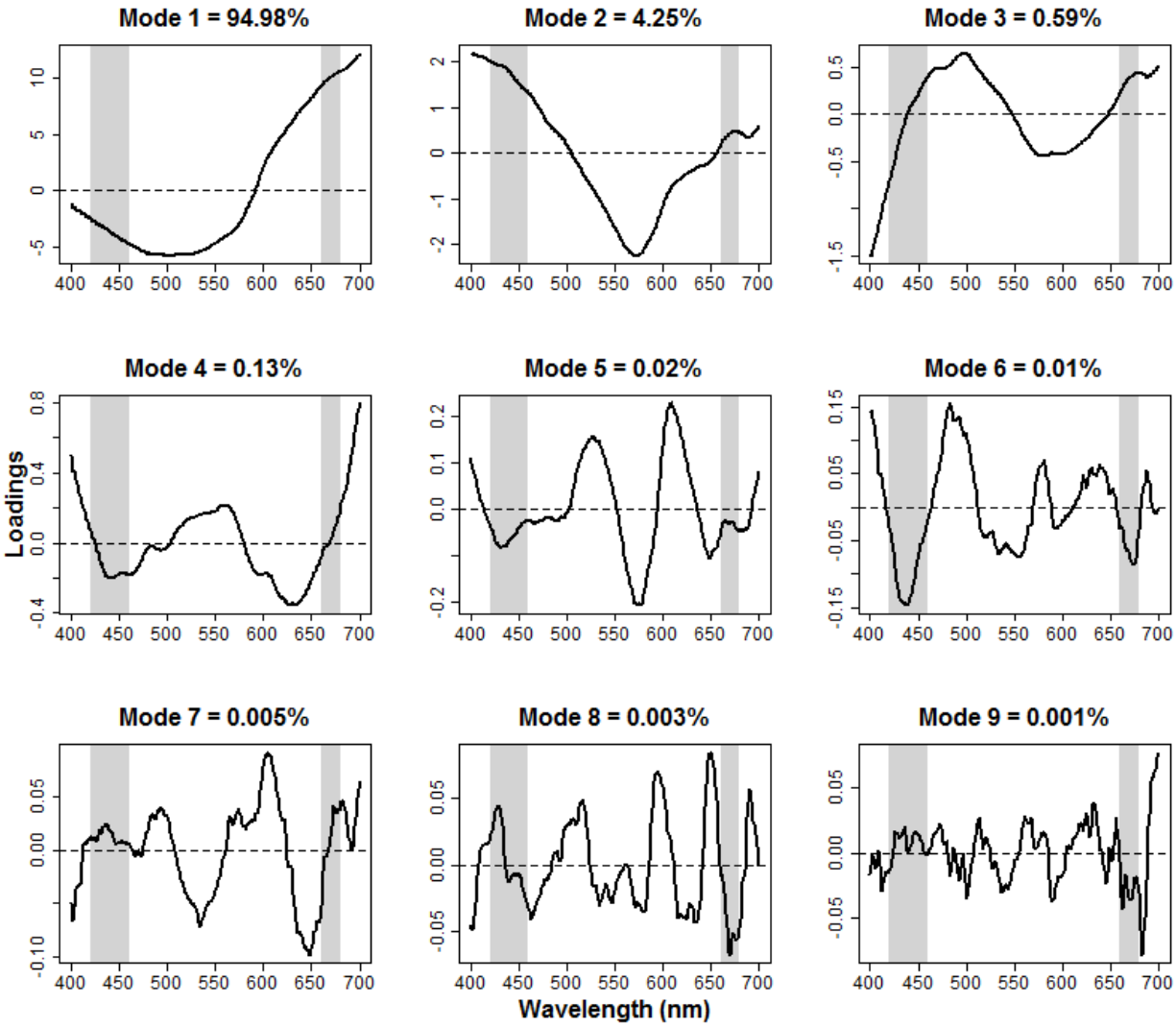

Figure 4. EOF modes represented as modes of oscillation in the entire standardized spectral Transmittance dataset. The modes of oscillation were calculated by projecting the spectral matrix (X) onto the EOF matrix (S), showing the loadings for each wavelength by mode. Included is the proportion of variance explained by each corresponding mode. Grey shaded areas represent the maximum chl a absorption regions centered at 440 and 670 nm.

Table 4. Correlation matrix between EOF modes ($s_1 - s_9$, $s_1^2 - s_9^2$) and bio-environmental properties for the three best EOF models. Model terms show only the modes used as terms in the corresponding model.

Model	Variable	s_1	s_2	s_3	s_4	s_5	s_6	s_7	s_8	s_9	s_1^2	s_2^2	s_3^2	s_4^2	s_5^2	s_6^2	s_7^2	s_8^2	s_9^2
EOF-Transmittance	Model Terms		s_2		s_4		s_6										s_7^2		s_9^2
	Chl *a*	0.28	-0.35*	-0.08	0.33*	-0.04	0.49*	0.18	-0.04	-0.36*	-0.28	0.29	-0.04	0.08	0.04	0.63*	0.21	0.06	0.59*
	Melt pond	0.38*	-0.32*	-0.40*	-0.10	-0.25	-0.15	-0.20	0.14	-0.12	-0.38*	0.37*	0.36*	0.18	-0.03	0.12	0.36*	0.32	-0.10
	snow	-0.07	-0.13	0.49*	0.08	0.55*	-0.10	0.18	0.11	-0.16	0.06	-0.08	0.28	0.03	0.37*	-0.07	0.02	-0.14	0.06
	Scatt.	-0.15	0.33*	-0.13	0.19	0.03	0.10	-0.26	-0.37*	0.25	0.16	-0.16	-0.16	-0.07	-0.26	-0.25	-0.22	-0.10	-0.04
	ice	-0.15	0.43*	-0.10	0.53*	0.40*	-0.06	-0.06	-0.18	0.03	0.15	-0.16	-0.01	-0.15	-0.13	-0.15	-0.22	-0.17	0.17
EOF-Transflectance	Model Terms		s_2		s_4			s_7		s_9									s_9^2
	Chl *a*	0.25	0.31*	0.00	-0.32*	-0.10	0.01	0.36*	0.27	0.34*	-0.24	0.24	-0.07	0.16	0.18	0.20	0.41*	0.03	0.13
	Melt pond	0.39*	0.28*	0.42*	-0.10	-0.27	0.17	-0.21	-0.03	-0.04	-0.40*	0.40*	-0.02	0.16	-0.06	0.45*	-0.04	0.02	0.03
	snow	-0.07	0.19	-0.53*	0.05	0.43*	-0.15	0.18	0.03	0.32*	0.06	-0.09	0.45*	0.00	0.33*	-0.12	0.17	-0.16	-0.04
	Scatt.	-0.04	-0.29*	0.04	-0.14	-0.07	-0.06	-0.01	-0.32*	-0.28	0.03	-0.02	-0.13	-0.06	-0.11	-0.11	-0.17	0.30*	0.03
	ice	-0.16	-0.52*	-0.24	-0.47*	0.25	-0.05	-0.18	0.07	-0.13	0.16	-0.17	0.24	-0.11	-0.10	-0.26	0.15	0.02	-0.01
EOF-Radiance	Model Terms				s_4	s_5	s_6					s_2^2						s_8^2	
	Chl *a*	0.19	0.15	-0.04	0.63*	-0.23	0.05	-0.25	0.18	-0.38	-0.19	0.20	-0.14	0.28	0.03	-0.23	0.30	-0.19	0.05
	Melt pond	0.55*	-0.53*	0.31	0.39	-0.57*	-0.10	-0.03	-0.26	0.10	-0.53*	0.52*	0.32	0.15	0.56*	0.25	-0.34	0.28	-0.21
	snow	0.17	-0.32	-0.61*	0.10	0.51	-0.30	-0.06	0.11	-0.14	-0.21	0.21	0.27	-0.42	0.04	0.00	0.46	-0.12	-0.23
	Scatt.	-0.40	0.14	0.46	-0.70*	0.16	0.06	-0.17	-0.16	0.20	0.42	-0.42	-0.26	0.33	-0.28	-0.37	-0.50	-0.23	0.44
	ice	-0.13	0.24	0.00	-0.10	0.89*	-0.08	0.10	0.02	0.11	0.11	-0.10	-0.21	-0.15	-0.46	-0.15	-0.03	-0.07	0.00

* Refers to significant correlations at $p \leq 0.05$

2.3.3.2 Comparison of Spectral Measurements

Significant correlations of ice core chl *a* with latitude and ice core chl *a* with solar radiation (Table 4) suggest that care is needed when interpreting models that do not account for the variability of incoming solar radiation (i.e., under-ice irradiance and radiance). Of the 5 selected predictive models, the lowest-ranking NDI_{670} model uses under-ice irradiance for the high-chl *a* data subset. In this data subset there was a significant negative correlation between chl *a* and incoming solar radiation ($r = -0.58$, $n = 15$, $p = 0.02$), and a trend between chl *a* and under-ice irradiance ($r= -0.46$, $n=15$, $p = 0.08$). No correlation was observed between chl *a* and integrated transmittance for the high-chl *a* data subset. Based on these correlations it is unclear if under-ice irradiance- or radiance-based models are actually predicting chl *a* based on a spectral signal influenced by chl *a* biomass, or if the relationship between chl *a* biomass and the strength of the incoming light field influences the apparent predictive performance of these models. Because we cannot be certain to what extent the performance of the irradiance- and radiance-based models were influenced by variations within the incoming solar irradiance, we excluded the two selected predictive models using under-ice radiance and irradiance data (e.g., EOF-radiance and NDI_{670}-irradiance) from further analyses.

Previous studies presented reliable models for estimating ice-algal chl *a* concentrations using under-ice irradiance, which do not account for variations of incoming solar radiation. These studies covered small local study regions during early-spring [*Mundy et al.*, 2007] and spring-summer transition [*Campbell et al.*, 2014; 2015], and had a comparably lower latitudinal range during austral spring [*Melbourne-Thomas et al.*, 2015], and therefore had less variability in the incoming light field. These studies were also conducted during a time when snow had a dominant influence on light transmittance. This together with the generally better performance of transmittance and transflectance models suggests that incoming solar radiation should always be measured and accounted for in bio-optical predictive models extending over a large spatial and/or temporal range. The additional time and logistical requirements incurred by operating an additional sensor is minimal making it all the more realistic to incorporate this important methodological advancement in future field programs.

2.3.4 Bio-Optical Predictive Model Up-scaling

The aim of model development and selection was to derive a predictive model that is best at estimating ice-algal chl *a* concentrations from independent spectral data over large spatial scales collected by an ROV and a SUIT. The EOF-Transmittance (PS80 data subset) model was chosen as the 'best' predictive model based on the ranking of the mean robustness R^2 and the NRMSE (Table 3). We excluded the EOF-radiance predictive model (ranked 2nd) and NDI_{670}- irradiance predictive model (ranked 3rd; Table 3) due to correlations of chl *a* with incoming light and under-ice irradiance, which leaves the EOF-Transflectance (*All* data subset) predictive model and the NDI_{670}-Transmittance (hereafter referred to as NDI-Transmittance) predictive model for further analyses and 34comparison. These three predictive models were applied to spectral data collected during two ROV stations (PS80/360 high-latitude site; PS80/323 lower-latitude site) and two SUIT stations (PS80/358 high-latitude site; PS80/285 lower-latitude site).

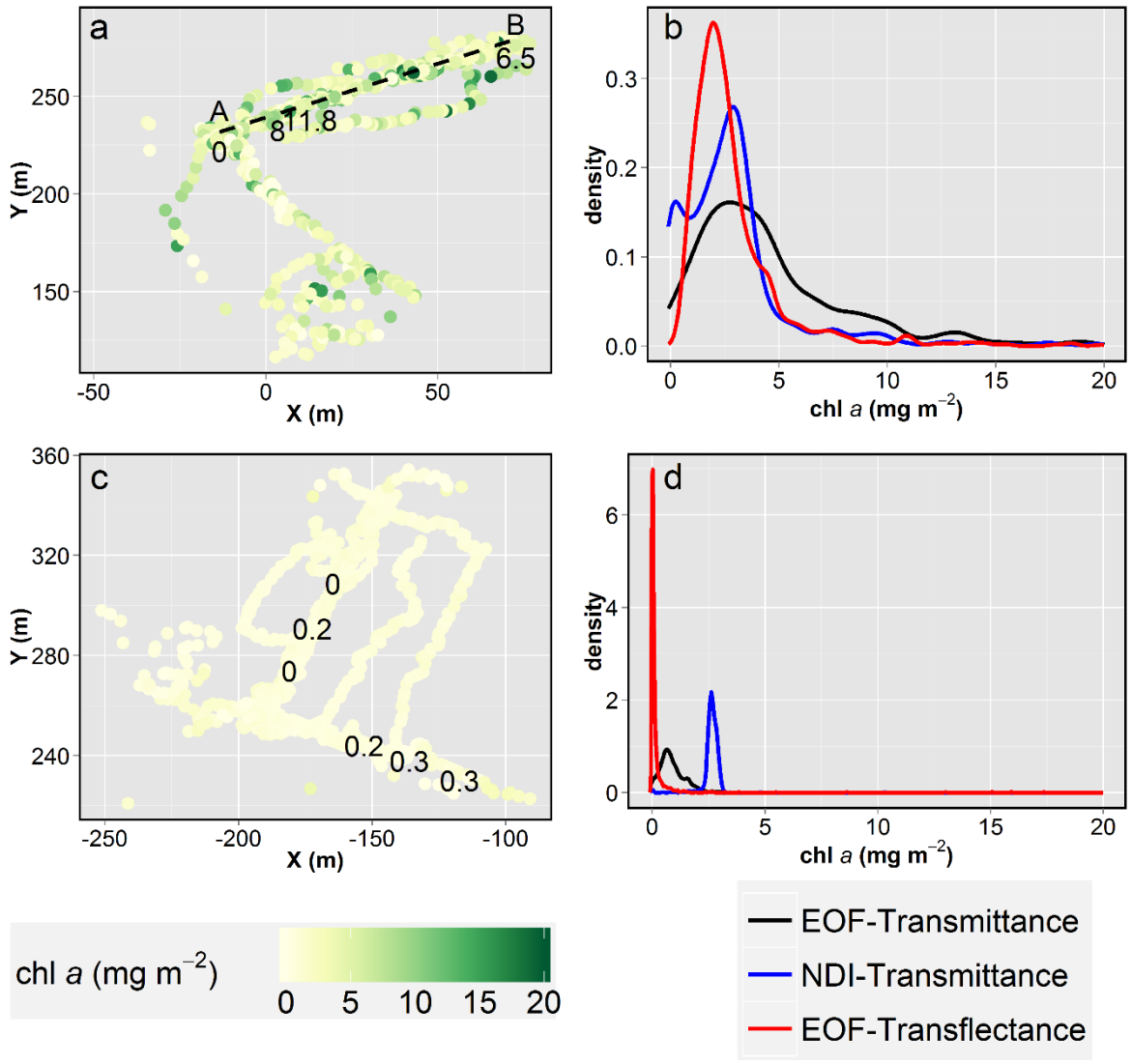

Figure 5. Remotely Operate Vehicle (ROV) spectrally-derived sea ice algal chl *a* estimates for high-latitude station PS80/360 a) and b); and for low-latitude station PS80/323 c) and d). a) and c) show the spatial distribution of EOF-Transmittance model chl *a* estimates and ice core chl *a* concentrations overlaid at corresponding grid locations. Positions in a) and c) are given in a floe fixed coordinate system relative to the ship's GPS receiver. Transect-AB is depicted in a) by a dashed line. b) and c) show weighted (based on point footprint size) density distributions of estimated chl *a* from the top 3 predictive models EOF-Transmittance, EOF-Transflectance, and NDI-Transmittance.

At the high-latitude ROV and SUIT stations (PS80/360 and 345), the NDI-Transmittance predicted values were generally in good agreement with EOF-Transmittance and EOF-Transflectance predicted values when comparing the density distributions (Figure 5 b and Figure 6 b), and median and range of values (Table 5). However, the NDI-Transmittance predicted values had low variability within and between all SUIT and ROV stations in comparison to the EOF-based predicted models and ice core chl *a* values (Table 5; Figure 5 d and Figure 6 c). At the low-latitude SUIT (PS80/285) and ROV (PS80/323) stations it was apparent that the NDI-Transmittance predictive model over-estimated low-chl *a* values compared to the EOF-based predictive models. This was particularly evident from the substantially higher values observed within chl *a* density distributions for the NDI-Transmittance predicted values compared to EOF-based predicted values (Figure 5 d and Figure 6 d). Furthermore, there was a large difference between the low-latitude station summaries of NDI-Transmittance predicted chl *a* values and ice core chl *a* concentrations (Table 5). Since the over-estimation of low-chl *a* values and low variability appears to be a constant feature of the NDI-Transmittance predictive model, we suggest it was a less reliable predictive model compared to the EOF-based predictive

models when applied to larger-scale independent spectral data. Although uncertainty is also high for low chl *a* values for the EOF-Transmittance and EOF-Transflectance models, the biases are low (almost zero) and therefore over larger-scales should result in minimal over-/under-estimation biases of ice-algal chl *a*.

Table 5. Summary of ice core chl a and spectrally-derived chl a from the selected under-ice horizontal profiling platform stations. ROV: Remotely Operated Vehicle; and SUIT: Surface and Uunder-Ice Trawl. Ice core and predicted chl a values represent the median (50th percentile), interquartile range (25th – 75th percentiles), and sample size [N].

Region	Platform -Station	Distance, Spacing (m) [a]	Footprint (m^2) [b]	Core chl *a* (mg m^{-2})	EOF-Transmittance Predicted chl *a* (mg m^{-2})	EOF-Transflectance Predicted chl *a* (mg m^{-2})	NDI-Transmittance Predicted chl *a* (mg m^{-2})
High-latitude	ROV-PS80/360	180, 0.9	3.0 / 0.02	7.25 (4.86 – 8.99) [4]	3.7 (2.1 – 5.9) [821]	2.3 (1.6 – 3.3) [960]	2.6 (1.2 – 3.5) [927]
	SUIT-PS80/345	625, 24	3.5 / 0.11	-	3.2 (0.0 – 5.0) [23]	2.1 (1.1 – 4.9) [26]	3.0 (2.6 – 3.3) [34]
Low-latitude	ROV-PS80/323	180, 0.5	2.6 / 0.02	0.17 (0.06 – 0.23) [6]	0.8 (0.5 – 1.1) [1568]	0.01 (0.00 – 0.11) [1667]	2.7 (2.5 – 2.8) [1569]
	SUIT-PS80/285	1500, 14	1.6 / 0.05	-	0.4 (0.0 – 1.5) [102]	1.6 (0.9 – 2.5) [110]	2.7 (2.5 – 3.0) [118]

[a] Distance refers to the distance covered by the profiling platform (e.g., maximum distance between any two points) and spacing is the mean spacing between all adjacent points.
[b] Footprint is the mean of all point footprints for Transmittance / Transflectance, respectively.

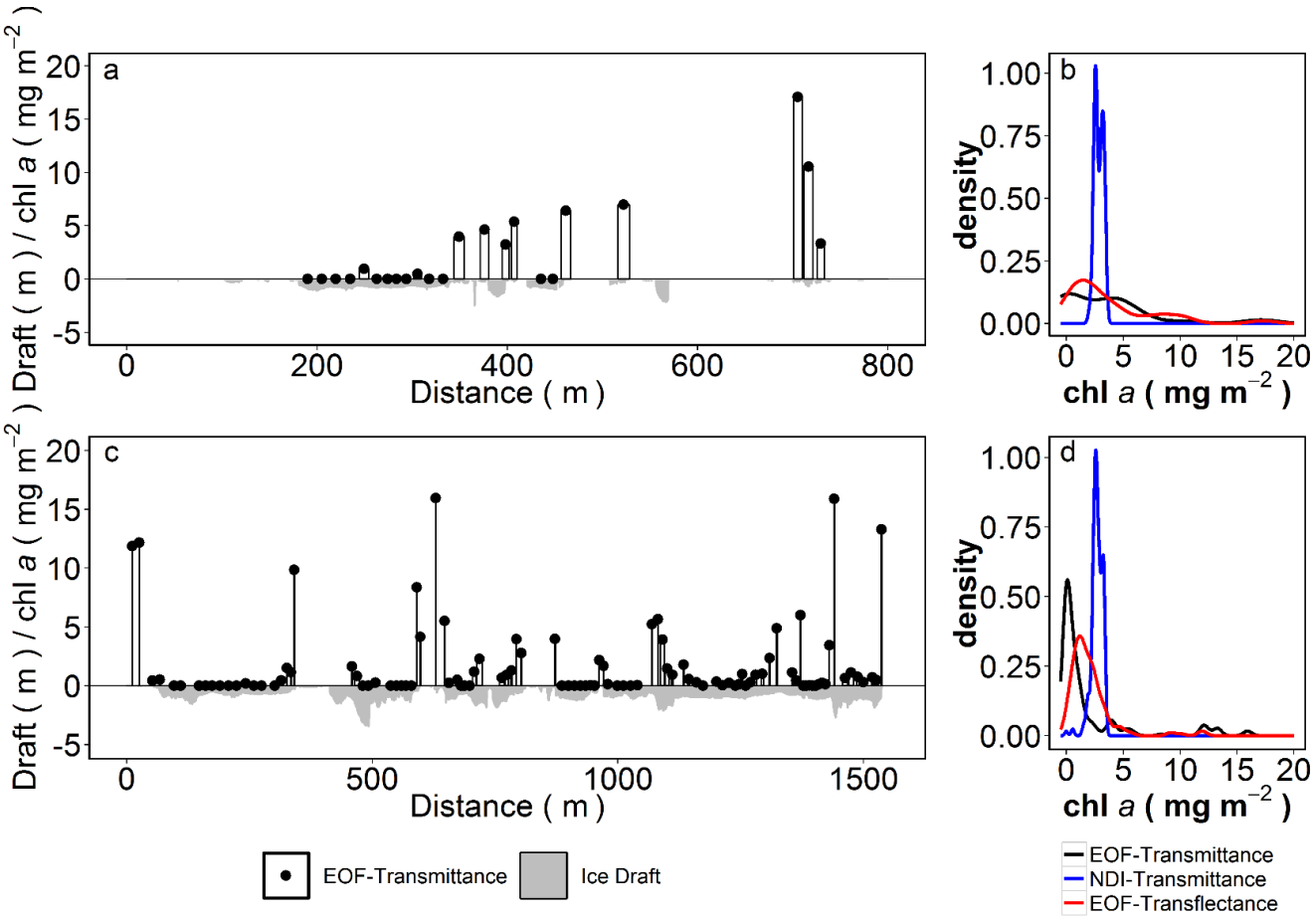

Figure 6. Surface and Under-Ice Trawl (SUIT) spectrally-derived sea ice algal chl a estimates for high-latitude station PS80/345 a) and b); and for low-latitude station PS80/285 c) and d). a) and c) show the horizontal profile of the EOF-Transmittance model chl a estimates and sea ice draft over the trawled distance, values > 0 correspond to chl a (mg m-2) and values < 0 correspond to draft (m). The horizontal widths of the bars in a) and c) depict relative along-track footprint size. Note the difference in trawled distance in a) and c). b) and c) show weighted (based on point footprint size) density distributions of estimated chl a from the top 3 predictive models EOF-Transmittance, EOF-Transflectance, and NDI-Transmittance.

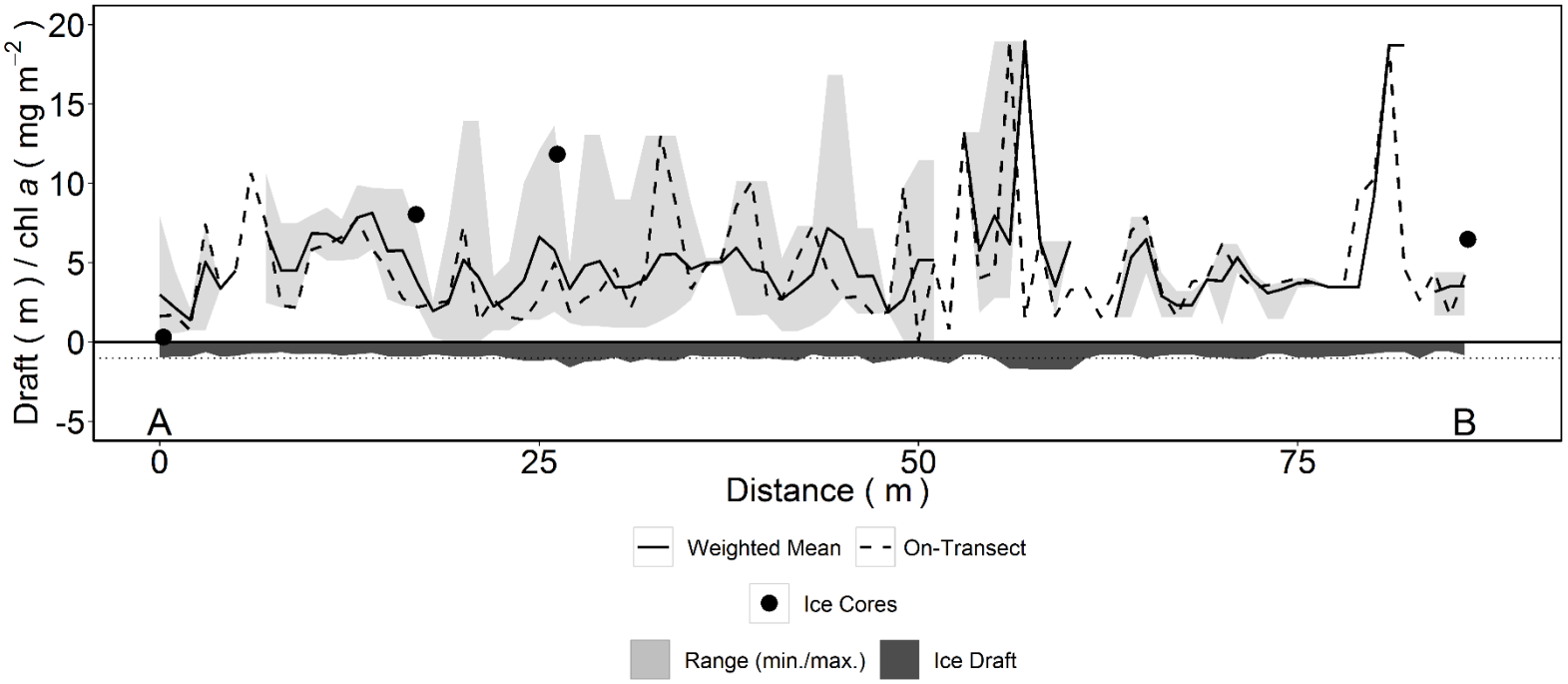

Figure 7. Sea ice-algal chl *a* concentrations along Transect-AB (depicted in Figure 6) extracted from ROV station PS80/360. Shown are ice draft (m), ice core chl *a* values (points) at corresponding locations along the transect, and EOF-Transmittance predictive model chl *a* estimates along the transect. Model predicted chl *a* values correspond to: exactly on the transect (on-transect), and weighted (based on footprint size) mean and range of values within 1.5 meters of the transect. Y-axis values > 0 correspond to chl *a* (mg m^{-2}) and values below zero correspond to draft (m). Stippled horizontal line depicts draft of -1 m.

The EOF-based predictive models both showed comparable median and range of chl *a* values at the same stations (Table 5). Hence, both EOF-based models showed similar regional differences in chl *a* concentrations with higher values at the higher latitude stations (Table 5), which is also in agreement with the general trend of our ice core chl *a* concentrations. Overall, however, there was little correlation between the EOF-Transmittance and EOF-Transflectance predictive models' estimated chl *a* values. This can be explained by their different mean footprint size, which was 1.5 m for the irradiance sensor, and 0.15 m for the radiance sensor.

In order to account for ROV position uncertainty and the variable footprint size of spectral measurements when comparing independent spectrally-derived chl *a* to ice core chl *a* concentrations, we took the weighted (based on footprint of each spectral measurement) mean of all bio-optical chl *a* estimates that were within 1.5 m of each 1 m bin along an 85 m transect (transect-AB Figure 5 a and Figure 7). Points within 2 adjacent overlapping bin areas were assigned to only the closest bin location. Transect-AB includes four ice core sample locations, with the ice core chl *a* concentration values overlaid on the ROV measurement grids (Figure 5 a and c). The first three ice core chl *a* observations were within the range of values predicted by the EOF-Transmittance model, for the 1.5 m region surrounding the core locations. The estimated chl *a* value at the end of the transect (~85 m), however, was lower than the corresponding ice core value, but still within the model uncertainty ($RMSE_{CV}$ of 1.8 mg chl *a* m^{-2}; Figure 7). The EOF-Transmittance model showed a better fit to the ice core chl *a* observations compared to the EOF-Transflectance and NDI-Transmittance predictive models, which further confirms that the EOF-Transmittance model performs best as a predictive model also indicated by the final model ranking.

A tentative assessment of the spatial variability of ice-algal chl *a* concentrations indicates that large-scale estimates of ice algal biomass and primary production are sensitive to the choice and number of ice cores analyzed compared to continuous spectral profiles, which capture the variability of ice algal chl *a* concentrations over larger distances. Based on the up-scaled (SUIT and ROV) EOF-Transmittance predictive model results (Figure 5 a, c, and Figure 6 a, c) and the extracted 85 m transect-AB from the ROV station PS80/360 (Figure 7) it is apparent that ice-algae biomass has a patchy distribution, which is well-known. Regardless of the patchy distribution, Arctic-wide sea ice primary production estimates, which integrated standing stock chl *a* biomass, used only one to three core samples per location [e.g., *Fernández-Méndez et al.*, 2015; *Gosselin et al.*, 1997]). The four bio-optical cores sampled along transect AB had an average chl *a* concentration of 6.6 mg m^{-2}. The range of the four cores (~0 to 12 mg chl *a* m^{-2}), however, indicates that basing large-scale estimates on a small number of ice cores carries large uncertainties in biomass and subsequent derived primary production estimates. Based on one ice core sample with an ice-algal biomass of 8 mg chl *a* m^{-2}, *Fernández-Méndez et al.* [2015] estimated that ice-algae contributed up to 60 % of the total primary production at ice station PS80/360. Along transect AB chl *a* concentrations of sea ice estimated by our best bio-optical predictive model (EOF-Transmittance; Figure 7 a) yielded a considerably lower weighted median and interquartile range of 4.0 (2.8 to 6.4) mg chl *a* m^{-2}, which was also evident from the full ROV survey values for that site (Table 5). A potential difference of over 50% between ROV spectrally-derived chl *a* concentration estimates compared to published chl *a* values based on ice core measurements at the same location emphasizes the importance of high-resolution measurements to capture the spatial variability of ice algal biomass for large-scale biomass and primary production estimates. In order to conduct detailed spatial analyses of ice-algal chl *a*, however, further geospatial processing of the data is required and is beyond the scope of this study.

2.4 Conclusions

With this first large-scale bio-optical summer study in the Arctic Ocean, we demonstrated the suitability of different combinations of statistical approaches with four spectral measurements for deriving ice-algal chl *a* concentrations in sea ice, and their application to larger scale spectral measurements. For these late-summer Arctic data, the EOF models performed better than the NDI models, particularly at differentiating between low, medium and high chl *a* concentrations. We attributed this to the ability of the EOF models to account for the high variability of environmental properties by incorporating variability from multiple regions of the spectra. Compared to the more

complex EOF-based approach, the NDI-based approach may be more easily applied and often suitable, depending on the variability of light conditions, sea ice properties, and sea ice-algal chl *a* concentrations. Regardless of the statistical approach taken, accounting for incoming solar radiation by calculating transmittance and transflectance resulted in superior models compared to simply using under-ice irradiance or radiance. This is particularly important for studies covering large spatial and temporal scales, and therefore a wide range of incident light conditions. Considerable discrepancy between mean chl *a* concentrations derived from our 'best' bio-optical model applied to a 85 m spectral transect in comparison to published chl *a* values based on ice core measurements at the same location highlights the need of high-resolution measurements to capture the true variability of ice algal biomass in the context of large-scale estimates and modeling studies. The increasing use of ROVs and AUVs equipped with spectral sensors means that spectral data for making large-scale chl *a* estimates will become more widespread with continued technological advancements. This study provides the first concise analysis of the potentials and limits of predicting chl *a* content in sea ice from spectral data under variable environmental conditions, and a toolbox for studies extending over large spatial and/or temporal scales, using e.g. autonomous vehicles or moored sea ice observatories.

Acknowledgements

We thank Martin Schiller for his technical expertise and operational support during ROV deployments. We thank Captain Uwe Pahl and Captain Stefan Schwarze, the crews, and scientific cruise leaders Antje Boetius and Ursula Schauer and RV Polarstern expeditions PS80.3 (ARK27-3; IceArc) and PS78.3 (Ark26-3; TransArc), respectively, for their excellent support and guidance with work at sea. We thank Jan Andries van Franeker (IMARES) for kindly providing the Surface and Under-Ice Trawl (SUIT) and Michiel van Dorssen for technical support. SUIT was developed by IMARES with support from the Netherlands Ministry of EZ (project WOT-04-009-036) and the Netherlands Polar Program (project ALW 866.13.009). We acknowledge the collaboration and technical support by Ocean Modules, Sweden for development and deployment of the ROV. Sea ice concentration data from September 13, 2012 were obtained from http://www.meereisportal.de (grant: REKLIM-2013-04). This study is part of the Helmholtz Association Young Investigators Group *Iceflux*: Ice-ecosystem carbon flux in polar oceans (VH-NG-800). We also acknowledge the Alfred-Wegener-Institut, Helmholtz-Zentrum für Polar- und Meeresforschung for essential financial and logistical support. All data are available from the PANGAEA database doi.org/XX.XXXX/PANGAEAXXXXXX.

References

Aguinis, H., R. K. Gottfredson, and H. Joo (2013), Best-Practice Recommendations for Defining, Identifying, and Handling Outliers, Organizational Research Methods, 16(2), 270-301, doi:10.1177/1094428112470848.

AMAP (2011), Snow,water, ice and permafrost in the Arctic (SWIPA): Climate change and the cryosphere., Scientific Rep., Gaustadalléen 21, N-0349 Oslo, Norway (www.amap.no).

Ambrose, W. G., C. von Quillfeldt, L. M. Clough, P. V. R. Tilney, and T. Tucker (2005), The sub-ice algal community in the Chukchi sea: large- and small-scale patterns of abundance based on images from a remotely operated vehicle, Polar Biol., 28(10), 784-795.

Arrigo, K. R., G. van Dijken, and S. Pabi (2008), Impact of a shrinking Arctic ice cover on marine primary production, Geophys. Res. Lett., 35(19), L19603, doi:10.1029/2008GL035028.

Arrigo, K. R., and G. L. van Dijken (2011), Secular trends in Arctic Ocean net primary production, J. Geophys. Res., 116(C9), C09011, doi:10.1029/2011JC007151.

Boetius, A., et al. (2013), Export of Algal Biomass from the Melting Arctic Sea Ice, Science, 339(6126), 1430-1432, doi:10.1126/science.1231346.

Budge, S. M., M. J. Wooller, A. M. Springer, S. J. Iverson, C. P. McRoy, and G. J. Divoky (2008), Tracing carbon flow in an arctic marine food web using fatty acid-stable isotope analysis, Oecologia, 157(1), 117-129, doi:10.1007/s00442-008-1053-7.

Calcagno, V., and C. de Mazancourt (2010), glmulti: An R Package for Easy Automated Model Selection with (Generalized) Linear Models, Journal of Statistical Software, 34(12), 1-29.

Campbell, K., C. J. Mundy, D. G. Barber, and M. Gosselin (2014), Remote Estimates of Ice Algae Biomass and Their Response to Environmental Conditions during Spring Melt, Arctic, 67(3), 375, doi:10.14430/arctic4409.

Campbell, K., C. J. Mundy, D. G. Barber, and M. Gosselin (2015), Characterizing the sea ice algae chlorophyll a–snow depth relationship over Arctic spring melt using transmitted irradiance, J. Mar. Syst., 147, 76-84, doi:10.1016/j.jmarsys.2014.01.008.

Craig, S. E., C. T. Jones, W. K. W. Li, G. Lazin, E. Horne, C. Caverhill, and J. J. Cullen (2012), Deriving optical metrics of coastal phytoplankton biomass from ocean colour, Remote Sens. Environ., 119, 72-83, doi:http://dx.doi.org/10.1016/j.rse.2011.12.007.

David, C., B. Lange, B. Rabe, and H. Flores (2015), Community structure of under-ice fauna in the Eurasian central Arctic Ocean in relation to environmental properties of sea-ice habitats, Mar. Ecol. Prog. Ser., 522, 15-32, doi:10.3354/meps11156.

Fernández-Méndez, M., C. Katlein, B. Rabe, M. Nicolaus, I. Peeken, K. Bakker, H. Flores, and A. Boetius (2015), Photosynthetic production in the Central Arctic during the record sea-ice minimum in 2012, Biogeosci. Disc., 12(3), 2897-2945, doi:10.5194/bgd-12-2897-2015.

Fetterer, F., K. Knowles, W. Meier, and M. Savoie (2002, udpated 2011), Sea Ice Index, edited, Boulder, CO: National Snow and Ice Data Center. Digital Media.

Flores, H., J. A. van Franeker, V. Siegel, M. Haraldsson, V. Strass, E. H. Meesters, U. Bathmann, and W. J. Wolff (2012), The Association of Antarctic Krill Euphausia superba with the Under-Ice Habitat, PLoS ONE, 7(2), e31775, doi:10.1371/journal.pone.0031775.

Gosselin, M., L. Legendre, S. Demers, and R. G. Ingram (1985), Responses of Sea-Ice Microalgae to Climatic and Fortnightly Tidal Energy Inputs (Manitounuk Sound, Hudson Bay), Can. J. Fish. Aquat. Sci., 42(5), 999-1006, doi:10.1139/f85-125.

Gosselin, M., L. Legendre, J.-C. Therriault, and S. Demers (1990), Light and nutrient limitation of sea-ice microalgae (Hudson Bay, Canadian Arctic), J. Phycol., 26(2), 220-232, doi:10.1111/j.0022-3646.1990.00220.x.

Gosselin, M., L. Legendre, J. C. Therriault, S. Demers, and M. Rochet (1986), Physical control of the horizontal patchiness of sea-ice microalgae, Mar. Ecol. Prog. Ser., 29(3), 289-298, doi:10.3354/meps029289.

Gosselin, M., M. Levasseur, P. A. Wheeler, R. A. Horner, and B. C. Booth (1997), New measurements of phytoplankton and ice algal production in the Arctic Ocean, Deep Sea Res II, 44(8), 1623-1644, doi:10.1016/S0967-0645(97)00054-4.

Grenfell, T. C., and G. A. Maykut (1977), The optical properties of ice and snow in the Arctic Basin, J Glaciol, 18(80), 445-463.

Grossi, S., S. Kottmeier, R. Moe, G. Taylor, and C. Sullivan (1987), Sea ice microbial communities. 6. Growth and primary production in bottom ice under graded snow cover, Mar. Ecol. Prog. Ser., 35(1-2), 153-164.

Gutt, J. (1995), The occurrence of sub-ice algal aggregations off northeast Greenland, Polar Biol., 15, 247-252.

Haas, C., A. Pfaffling, S. Hendricks, L. Rabenstein, J.-L. Etienne, and I. Rigor (2008), Reduced ice thickness in Arctic Transpolar Drift favors rapid ice retreat, Geophys. Res. Lett., 35(17), L17501, doi:10.1029/2008GL034457.

Horner, R., and G. C. Schrader (1982), Relative Contributions of Ice Algae, Phytoplankton, and Benthic Microalgae to Primary Production in Nearshore Regions of the Beaufort Sea, Arctic, 35(4).

IPCC (2013), Climate Change 2013: The Physical Science Basis. Contribution of Working Group I to the Fifth Assessment Report of the Intergovernmental Panel on Climate ChangeRep., 1535 pp, Cambridge, United Kingdom and New York, NY, USA.

Katlein, C., et al. (2015), Influence of ice thickness and surface properties on light transmission through Arctic sea ice, Journal of Geophysical Research: Oceans, 120(9), 5932-5944, doi:10.1002/2015jc010914.

Katlein, C., M. Fernández-Méndez, F. Wenzhöfer, and M. Nicolaus (2014a), Distribution of algal aggregates under summer sea ice in the Central Arctic, Polar Biol., doi:10.1007/s00300-014-1634-3.

Katlein, C., M. Nicolaus, and C. Petrich (2014b), The anisotropic scattering coefficient of sea ice, J. Geophys. Res., 119(2), 842-855, doi:10.1002/2013JC009502.

Kohlbach, D., M. Graeve, B. A. Lange, C. David, I. Peeken, and H. Flores (in press), The importance of ice algae-produced carbon in the central Arctic Ocean ecosystem: food web relationships revealed by lipid and stable isotope analyses, Limnol. Oceanogr, accepted.

Kwok, R., and D. A. Rothrock (2009), Decline in Arctic sea ice thickness from submarine and ICESat records: 1958–2008, Geophys. Res. Lett., 36(15), L15501, doi:10.1029/2009GL039035.

Lange, B. A., C. Michel, J. F. Beckers, J. A. Casey, H. Flores, I. Hatam, G. Meisterhans, A. Niemi, and C. Haas (2015), Comparing springtime ice-algal chlorophyll a and physical properties of multi-year and first-year sea ice from the Lincoln Sea, PLoS One, 10(4), e0122418, doi:10.1371/journal.pone.0122418.

Light, B., T. C. Grenfell, and D. K. Perovich (2008), Transmission and absorption of solar radiation by Arctic sea ice during the melt season, J. Geophys. Res., 113(C3), C03023, doi:10.1029/2006JC003977.

Lund-Hansen, L. C., S. Markager, K. Hancke, T. Stratmann, S. Rysgaard, H. Ramløv, and B. K. Sorrell (2015), Effects of sea-ice light attenuation and CDOM absorption in the water below the Eurasian sector of central Arctic Ocean (>88°N), Polar Res., 34(0), doi:10.3402/polar.v34.23978.

Mahmood, Z., and S. Khan (2009), On the Use of K-Fold Cross-Validation to Choose Cutoff Values and Assess the Performance of Predictive Models in Stepwise Regression, The International Journal of Biostatistics, 5(1), doi:10.2202/1557-4679.1105.

Maslanik, J. A., J. C. Stroeve, C. Fowler, and W. Emery (2011), Distribution and trends in Arctic sea ice age through spring 2011, Geophys. Res. Lett., 38, L13502, doi:10.1029/2011GL047735.

McCullagh, P., and J. A. Nelder (1989), Generalized linear models, Chapman and Hall, London, United Kingdom.

Melbourne-Thomas, J., K. M. Meiners, C. J. Mundy, C. Schallenberg, K. L. Tattersall, and G. S. Dieckmann (2015), Algorithms to estimate Antarctic sea ice algal biomass from under-ice irradiance spectra at regional scales, Mar. Ecol. Prog. Ser., 536, 107-121, doi:10.3354/meps11396.

Mundy, C. J., J. K. Ehn, D. G. Barber, and C. Michel (2007), Influence of snow cover and algae on the spectral dependence of transmitted irradiance through Arctic landfast first-year sea ice, J. Geophys. Res., 112(C3), C03007, doi:10.1029/2006JC003683.

Nicolaus, M., S. R. Hudson, S. Gerland, and K. Munderloh (2010), A modern concept for autonomous and continuous measurements of spectral albedo and transmittance of sea ice, Cold Regions Science and Technology, 62(1), 14-28.

Nicolaus, M., and C. Katlein (2013), Mapping radiation transfer through sea ice using a remotely operated vehicle (ROV), The Cryosphere, 7(3), 763-777, doi:10.5194/tc-7-763-2013.

Nicolaus, M., C. Katlein, J. Maslanik, and S. Hendricks (2012), Changes in Arctic sea ice result in increasing light transmittance and absorption, Geophys. Res. Lett., 39, 2699–2700, doi:10.1029/2012GL053738.

R-Development-Core-Team (2012), R: A Language and Environment for Statistical Computing, R Foundation for Statistical Computing, Vienna, Austria.

Riihela, A., T. Manninen, and V. Laine (2013), Observed changes in the albedo of the Arctic sea-ice zone for the period 1982-2009, Nature Clim. Change, 3(10), 895-898, doi:10.1038/nclimate1963.

Rösel, A., and L. Kaleschke (2012), Exceptional melt pond occurrence in the years 2007 and 2011 on the Arctic sea ice revealed from MODIS satellite data, J. Geophys. Res., 117(C5), doi:10.1029/2011jc007869.

Rysgaard, S., M. Kühl, R. N. Glud, and J. W. Hansen (2001), Biomass, production and horizontal patchiness of sea ice algae in a high-Arctic fjord (Young Sound, NE Greenland), Mar. Ecol. Prog. Ser., 223, 15-26.

Schwarz, G. (1978), Estimating the Dimension of a Model, The Annals of Statistics, 461-464, doi:10.1214/aos/1176344136.

Serreze, M. C., M. M. Holland, and J. Stroeve (2007), Perspectives on the Arctic's shrinking sea-ice cover, Science, 315, 1533-1536.

Søreide, J. E., M. L. Carroll, H. Hop, W. G. Ambrose, E. N. Hegseth, and S. Falk-Petersen (2013), Sympagic-pelagic-benthic coupling in Arctic and Atlantic waters around Svalbard revealed by stable isotopic and fatty acid tracers, Mar. Biol. Res., 9(9), 831-850, doi:10.1080/17451000.2013.775457.

Spreen, G., L. Kaleschke, and G. Heygster (2008), Sea ice remote sensing using AMSR-E 89-GHz channels, J. Geophys. Res., 113(C2), C02S03, doi:10.1029/2005JC003384.

Stroeve, J. C., V. Kattsov, A. Barrett, M. Serreze, T. Pavlova, M. Holland, and W. N. Meier (2012), Trends in Arctic sea ice extent from CMIP5, CMIP3 and observations, Geophys. Res. Lett., 39(16), L16502, doi:10.1029/2012GL052676.

Taylor, B. B., M. H. Taylor, T. Dinter, and A. Bracher (2013), Estimation of relative phycoerythrin concentrations from hyperspectral underwater radiance measurements—A statistical approach, Journal of Geophysical Research: Oceans, 118(6), 2948-2960, doi:10.1002/jgrc.20201.

Tran, S., B. Bonsang, V. Gros, I. Peeken, R. Sarda-Esteve, A. Bernhardt, and S. Belviso (2013), A survey of carbon monoxide and non-methane hydrocarbons in the Arctic Ocean during summer 2010, Biogeosciences, 10(3), 1909-1935, doi:10.5194/bg-10-1909-2013.

van Franeker, J. A., H. Flores, and M. van Dorssen (2009), The surface and under ice trawl (SUIT). Frozen desert alive—the role of sea ice for pelagic macrofauna and its predators, PhD thesis, University of Groningen,Groningen.

Wadhams, P. (2012), The use of autonomous underwater vehicles to map the variability of under-ice topography, Ocean Dynamics, 62(3), 439-447, doi:10.1007/s10236-011-0509-1.

Wang, S. W., S. M. Budge, K. Iken, R. R. Gradinger, A. M. Springer, and M. J. Wooller (2015), Importance of sympagic production to Bering Sea zooplankton as revealed from fatty acid-carbon stable isotope analyses, Mar. Ecol. Prog. Ser., 518, 31-50, doi:10.3354/meps11076.

Wassmann, P., C. M. Duarte, S. Agusti, and M. K. Sejr (2011), Footprints of climate change in the Arctic marine ecosystem, Global Change Biol., 17(2), 1235-1249, doi:10.1111/j.1365-2486.2010.02311.x.

Chapter 3: Linking Sea Ice Algae Spatial Variability to Summertime Carbon Demand

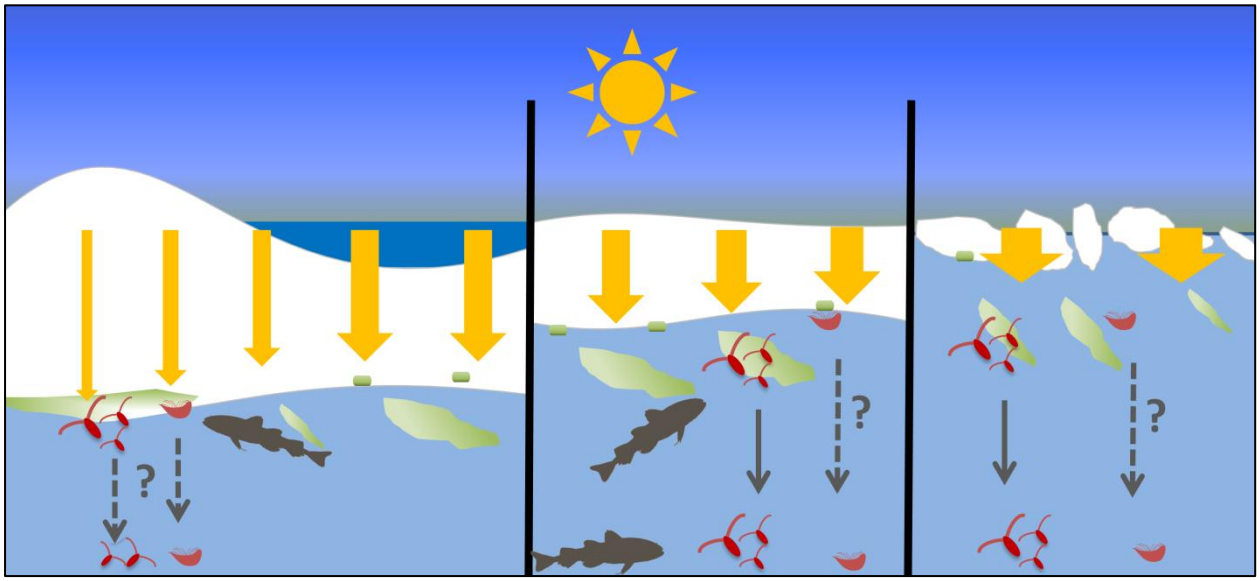

Conceptual diagram of the spatial distribution of sea ice algae at the bottom of different ice types during late-summer with under-ice organisms grazing on the ice-algae. Thicker ice has lower melt rates and lower melt-induced algal losses.

Paper 3. On improving the spatial representativeness of sea ice algae chlorophyll *a* biomass and primary production estimates

in preparation for submission to: *Geophysical Research Letters*

NOTE: Supplementary Material for this paper is found in Appendix B1

Benjamin A. Lange, Christian Katlein, Giulia Castellani, Mar Fernández-Méndez, Marcel Nicolaus, Ilka Peeken, and Hauke Flores

Key Points

- Ice-core based ice-algal chl *a* and NPP estimates were not representative of up-scaled estimates
- Grouping ice cores improved representativeness but still high risk of non-representative estimates
- Sea ice ridges identified as potentially high ice-algal biomass features with relatively high NPP

Abstract

The spatial representativeness of sea ice algal biomass and primary production remains a key issue in sea ice sampling. To address this issue, we presented two novel approaches to up-scale ice-algal biomass and net primary production (NPP) estimates combining ice core-based methods and under-ice horizontal spectral profiling platform observations. We conducted a multi-scale comparison of ice-core based ice-algal biomass and NPP estimates with the up-scaled estimates. Our results showed that ice core-based estimates of summertime ice-algal biomass and NPP do not representatively capture the spatial variability compared to the up-scaled estimates, which carries similar uncertainties for pan-Arctic estimates based on ice core observations alone. Grouping sea ice cores based on region or ice type improved the representativeness, however, with only a small sample size there remains a high risk of obtaining non-representative estimates. Furthermore, we identified sea ice ridges as potentially high biomass and high NPP features, which should receive more dedicated research.

3.1 Introduction

There is mounting evidence for an overall increase in Arctic-wide net primary production (NPP) as a result of the declining sea ice cover and increasing duration of the phytoplankton growth season (Arrigo & van Dijken, 2011; Arrigo & van Dijken, 2015; Fernández-Méndez et al., 2015). It remains uncertain how sea ice algae NPP will respond to continued changes of the sea ice environment. It has been suggested that a thinning Arctic sea ice cover and increased light transmittance will result in increased sea ice algae primary production (PP) rates due to more available photosynthetically active radiation (PAR) (Nicolaus et al., 2012).

In the central Arctic Ocean sea-ice algae has been documented to contribute up to 60% of the NPP during summer (Fernández-Méndez et al., 2015; Gosselin et al., 1997). Overall, however, sea ice-related PP is relatively low accounting for 1 to 10 % of total PP in the Arctic Ocean (Arrigo & van Dijken, 2015; Dupont, 2012). Regardless of the overall low contribution of ice-related PP, sympagic (ice-associated) and pelagic organisms both showed a high dependency on ice-algae produced carbon within the central Arctic Ocean (Kohlbach et al., 2016). The key role of sea ice algae in Arctic foodwebs, particularly in terms of reproduction and growth of key Arctic organisms (Michel et al., 1996; Søreide et al., 2010), highlights the importance of timing and duration of ice algal growth, and the availability of algal biomass throughout different times of the year.

Spatial variability of springtime ice-algal biomass has been related to the distribution of snow on FYI, due to the large influence of snow on light transmission, with patch sizes in the ranges of 5 – 10 m (Rysgaard et al., 2001) and 20 – 90 m (Gosselin et al., 1986; Granskog et al., 2005; Søgaard et al., 2010). The undulating surface topography of MYI plays an important role in the distribution of snow, which has been linked to the presence of high ice-algal biomass at the bottom of thick MYI hummocks with little or no snow cover (Lange et al., 2015). In summer when the snow is mostly melted, light availability has a smaller influence on the spatial distribution of ice algal biomass with other factors such as melt rates having a stronger influence (Grossi et al., 1987; Lavoie et al., 2005). The spatial distribution of ice algal biomass during summer, however, remains poorly understood and under-sampled.

The high spatial and temporal variability of sea ice algae, in addition to sparse sampling, results in poorly constrained sea ice-algal biomass and PP estimates for the central Arctic Ocean (Miller et al., 2015). Large-scale estimates of sea ice algal biomass and PP are limited to modelling studies as satellites are unable to observe the underside of sea ice. Lee et al. (2015) demonstrated that pelagic phytoplankton PP models for the Arctic Ocean were highly sensitive to uncertainties in chlorophyll *a* (chl a) and performed best with *in situ* chl *a* data. *In situ* ice algal chl *a* used in models, however, are typically based on a small number of ice core observations (e.g., Fernández-Méndez et al., 2015). A recent study comparing ice core chl *a* biomass to floe-scale (~200 m) ROV-based spectrally derived ice-chl *a* biomass showed large differences, which could carry high uncertainties for large-scale estimates based on these data (Lange et al., submitted).

Furthermore, (Miller et al., 2015) reviewed the different methods for primary production measurements with spatial sampling resolution on the order of 0.01 m for ice coring-based *in vitro* incubations (e.g., Fernández-Méndez et al., 2015; Gosselin et al., 1997; Gradinger, 2009) or *in situ* incubations (e.g., Gradinger, 2009; Mock & Gradinger, 1999), and at larger scales the under-ice eddy covariance method integrates primary production over an area of 100 m^2 (Long et al., 2012). Thus there is a large gap in spatial coverage between the 0.01 to 100 m^2 scales, which is not resolved by these methods. It is within this spatial range that many environmental properties can vary, which can have a large influence on light availability, ice melt and growth, and the spatial distribution of ice algae. Typical patch sizes of snow have been reported in the range 20 to 25 m (Gosselin et al., 1986; Steffens et al., 2006). Surface properties such as albedo have patch sizes of approximately 10 m (Katlein et al., 2015; Perovich et al., 1998) and sea ice draft can vary at scales of around 15 m (Katlein et al., 2015).

Here we have presented a novel approach to fill this important spatial gap of ice-algal chl *a* biomass and primary production estimates by combining *in vitro* ice coring-derived photosynthetic parameters

with spectrally derived chl *a* biomass and under-ice light measurements. Furthermore, we investigated the spatial patterns of biomass and NPP estimates, and evaluated potential discrepancies between the up-scaled and core-based estimates.

3.2 Materials and Methods

3.2.1 Spectrally derived ice-algal biomass estimates

Under-ice profiling platform-based spectral measurements were made using an under-ice remotely operated vehicle (ROV) and surface and under-ice trawl (SUIT), with mounted sensor arrays, described in (David et al., 2015). All surveys were conducted during the *RV Polarstern* expedition PS80 to the central Arctic Ocean in August and September 2012. ROV spectral surveys were conducted at seven ice stations (Figure 1). SUIT spectral surveys were conducted at 9 stations (Figure 1). Incoming solar radiation observations were measured on-ice for ROV based spectral measurements, and from a ship-based sensor for SUIT-based spectral measurements. To ensure high quality spectra, data were limited to observations at a distance to ice-bottom of ≤ 1 m and with a pitch and roll between -10º and 10º, as suggested by (Nicolaus & Katlein, 2013). SUIT spectral surveys were manually inspected to identify good spectral measurements at sea ice ridges. Since the SUIT behaves more erratic near ridges we needed a less strict threshold and in some cases measurements were included with a distance to the ice bottom of up to 2 m.

Sea ice draft was calculated based on sensor measurements of depth and distance to ice bottom, and corrected for pitch and roll angles as described in Lange et al. (submitted) and David et al. (2015). Sea ice ridges were identified from the SUIT ice draft profiles using the Rayleigh criteria, following procedures described by: Castellani et al. (2014); and Rabenstein et al. (2010) for the sea ice surface topography and Castellani et al. (2015) for the sea ice bottom profile. Ice draft local minima (e.g., thicker ice as draft is negative) identified along the SUIT profile with a threshold of 1.5 m deeper than the surrounding ice, following Castellani et al. (2015), were selected as potential ridges. Moreover, adjacent minima needed a separation distance between points which was less than half the depth of the first minima in order to be identified as two single elements not belonging to the same ridge. Ridge depth and width were measured in order to calculate ridge density (ridges km^{-1}) and percent coverage of ridges. Here ridge depth was calculated as the width at half maximum. During one SUIT haul (station 358) there were no altimeter measurements. Because the SUIT generally travels directly under the ice, the depth measurements can be used to reliably ($R^2 = 0.78$) derive level ice draft using a simple linear model, previously presented in David et al. (2015). Draft measurements at ridges are less accurate and therefore not used, however, the identification of ridges from the derived draft was still possible.

Ice-algal chl *a* biomass estimates were derived from under-ice profiling platform-based spectral transmittance observations using empirical orthogonal function (EOF) analysis combined with generalized linear models (GLM), as described in (Lange et al., submitted). GLMs were fitted using ice core chl *a* concentrations (response variable) and EOF modes (predictor variables). The combination of spectral transmittance, calculated according to Nicolaus et al. (2010), and the EOF approach resulted in the most reliable predictive model with a true prediction error estimate, 10-Fold cross validated root mean squared error ($RMSE_{CV}$), of 1.8 mg chl *a* m^{-2} (Lange et al., submitted). In addition, the selected predictive model showed good agreement between chl *a* estimates derived from independent spectral data (spectra not used to fit the model) and ice core chl *a* concentrations for the same location.

We resampled the data in order to account for potential spatial sampling biases (e.g., multiple or overlapping measurements at the same location), and the variable footprint size of the under-ice ROV spectral measurements. Data were resampled to a grid (x, y) of equally spaced 1 m diameter circles (grid circles) with the same overall grid dimensions as the corresponding ice station. A grid of circles was created for the ROV measurements (ROV circles) with each circle's center location determined by the measurement location (x, y) and the diameter determined by the footprint of the measurement (e.g., distance to ice bottom multiplied by 2, as described in (Lange et al., submitted). For each grid

circle with only one overlapping ROV circle, which had an overlapping area ≥ 0.2 m^2 (25% of the 1 m circle), the corresponding ROV-based transmittance and chl *a* were assigned to that grid circle. For each grid circle that had more than one overlapping ROV circle, of which at least one ROV circle had an overlapping area ≥ 0.2 m^2, the weighted means of the corresponding ROV-based transmittance and chl *a* were assigned to the grid circle. Weighting factors were calculated as the overlapping area of each ROV circle with the corresponding grid circle divided by the sum of all overlapping areas for that grid circle. For a detailed diagram outlining the resampling process refer to Supplementary Figure S1.

3.2.2 ROV-based Net Primary Production estimates

Up-scaled daily ice-algal net primary production (NPP) estimates, *P* (mg C m^{-2} d^{-1}), were calculated using the photosynthesis equation from (Platt et al., 1980):

$$\boldsymbol{P = \int_t \left[\left(P_s^B \left[1 - e^{-\propto I_t / P_s^B} \right] e^{-\beta I_t / P_s^B} \right) chla \right]}$$

where P^B_s is the chl *a*-normalized maximum fixation rate with no photoinhibition (mg C [mg chl *a*]$^{-1}$ h^{-1}); α is the initial slope of the saturation curve (mg C [mg chl *a*]$^{-1}$ h^{-1} [µmol photons m^2 s^{-1}]$^{-1}$); and β is strength of photoinhibition (same units as α). P^B_s, α, and β correspond to the photosynthetic parameters determined by Fernández-Méndez et al. (2015) based on ice core samples collected from the same seven ice stations. Derivation of the photosynthetic parameters was conducted for upper and lower portions of the sea ice. We used the bottom ice parameters measured for ice sampled at each corresponding ice station as we used only biomass estimates for the lower portion where 75 % of the total biomass was observed. The 75% was calculated from the mean of all chl *a* profile cores. *chla* represents the bottom-ice algae chl *a* concentrations derived from ROV-based spectral transmittance measurements. ROV-based chl *a* correspond to the total biomass within the entire ice column therefore we multiplied by 0.75 to get the appropriate fraction of the total chl *a* in the bottom ice portion. I_t is the hourly-averaged available transmitted PAR (µmol photons m^2 s^{-1}) at the ice-water interface, converted to bottom-ice scalar irradiance according to Katlein et al. (2014), and calculated for each hour (*t*) over a 24 hour period (*t* =1, 2,..24) by multiplying the ROV spectral (PAR) transmittance by hourly-averaged (*t*) incoming PAR (µmol photons m^2 s^{-1}) measured during each corresponding ice station.

Net primary production estimates were only calculated and compared for the bottom ice portions because previous *in situ* incubations demonstrated bottom-ice had the highest primary production rates, despite lower irradiance levels, which was attributed to replenishment of nutrients from the surface waters (Mock & Gradinger, 1999). Furthermore, because sea ice algal biomass typically accumulates in the bottom-ice portion it is safe to assume a large majority of the primary production also occurs in the bottom-ice.

Comparison of ice core chl *a* with ROV- and SUIT-based spectrally derived chl *a* estimates were conducted using Student's *t* test on the log-transformed chl *a* values. Weighted mean and weight standard deviation were used for the log-transformed SUIT chl *a* as these data were not re-sampled. Similarly, NPP estimates were log-transformed for comparisons; however, these comparisons were conducted between ROV-based estimates for level sea ice and sea ice ridges at station 224 only.

Ice core chl *a* data used for comparison were presented in Fernández-Méndez et al. (2015), hereafter referred to as "FM" cores (1 core per station); and Lange et al. (submitted), hereafter referred to as "LA" cores (4 – 12 cores per station). Student's *t* tests were performed using the FM and LA cores grouped together as *t* tests require a sample size greater than one. Since the FM-cores were used to characterize the NPP for each ice station we do, however, assess the representativeness of the single cores compared to the up-scaled ROV and SUIT surveys of chl *a* biomass and NPP. FM-cores were considered representative of the area if they were within the interquartile range (IQR; 25 – 75 percentiles) of the up-scaled ROV and SUIT estimates.

The relative importance of each variable (*chla* and I_t), in terms of explaining the variance of NPP for each ROV station, was assessed using the coefficient of determination (R^2) for all up-scaled NPP estimates (P_t) vs. chl *a* (*chla*) estimates (i.e., explained variance due to chl *a*), and NPP estimates (P_t) vs. bottom-ice light (I_t) observations (i.e., explained variance due to light). The R^2 was calculated for each hour (***t***) of the 24 hour period to assess the diurnal variability of light conditions. Values provided in Table 1 correspond to the daily mean R^2.

3.3 Representativeness of ice-algal biomass estimates

Sea ice cores had significantly lower chl *a* biomass than ROV estimates at station groups B, C, D, and F, which were all generally lower-biomass stations (Figure 1 and Table 1). Ice cores also had significantly lower biomass than ROV-based biomass estimates at group G where biomass was slightly higher (Figure 1 and Table 1). No significant differences were observed at groups H and I, which were relatively higher-biomass stations (Figure 1 and Table 1). The FM-cores were representative (i.e., within the IQR) of the up-scaled SUIT-based chl *a* biomass estimates at only station group B and were only slightly larger than the 75th percentile of the ROV-based estimates. FM-cores were not representative of the larger scale chl *a* biomass estimates at all other stations groups. FM-cores at station groups C, H, and I, over-estimated chl *a* biomass compared to the up-scaled estimates, and at station groups D, E, F, and G the FM-cores under-estimated chl *a* biomass compared to the up-scaled surveys (Table 1). All gridded ROV surveys of chl *a*, sea ice draft, transmittance and NPP are shown in Supplementary Figures S2 to S9. SUIT profiles of chl *a*, sea ice draft, and identified ridges are shown in Supplementary Figures S10 to S17.

These results demonstrate the difficulty to capture the larger-scale variability of ice algal biomass using only coring-based methods. In general, ice coring under-estimated ice-algal biomass at the relatively lower-biomass stations. While at the higher-biomass stations the ice cores appeared to accurately capture the variability of ice-algal biomass. The higher-biomass observed was likely the result of less melt-induced algal losses due to thicker ice and lower melt rates at these higher latitudes stations (Lange et al., submitted). Sampling biases could have also resulted at the advanced melt stations, which may have had a higher chance of losing biomass from the ice-bottom during coring due to drainage or ice loss. Another explanation could be that relatively higher-biomass regions (e.g., patches) at lower-biomass stations had a lower probability to be sampled compared to higher biomass stations and were not accurately represented at the lower-biomass stations. We must not overlook the possibility that the up-scaled estimates over-estimated the biomass; however, this is unlikely because the model for spectrally deriving chl *a* biomass had no directional bias and some of the cores had comparable values to the up-scaled chl *a* estimates (Lange et al., submitted).

The higher-biomass station 360 (group I) showed no significant difference between the cores and ROV-based biomass estimates, however, of the individual core values (0.05, 6.46, 8.03, 8.00, and 11.83 mg chl *a* m^{-2}) only one core was within the IQR (2.96 – 6.70 mg chl *a* m^{-2}) albeit at the high range. One core with near-zero biomass resulted in an overall mean biomass (log-transformed) that was not significantly different even though many cores over-estimated the biomass in comparison to the up-scaled values. This was also apparent at station 349 (group H), which also showed no significant difference, but also had only one core within the IQR of the up-scaled biomass estimates. Even at stations with the largest sample sizes of 8 (group B) and 12 (group C) there were significant differences between the cores and up-scaled biomass estimates. This further emphasizes the issue of accurately representing the variability of ice-algal biomass by strictly using ice core-based methods even if the sample size was large.

The discrepancy between the ice core-based and up-scaled biomass estimates in combination with the lack of autocorrelation (i.e., patch size identification; not shown here) indicates the ice-algal biomass was highly variable at small scales (< 2 m), which was difficult to capture with average measurement footprints between 1 – 2 m for ROV and SUIT surveys. The up-scaled estimates were therefore the averages over a larger area and are less likely to capture small patches of high-biomass or low-biomass (i.e., values in the range 8 to12 mg chl *a* m^{-2} or with near-zero biomass) unless the RO V was in close proximity to the ice bottom or the patches were on the order of the footprint size. These

discrepancies identify two important sampling constraints: first, the cores do not capture the large-scale variability; and second, the up-scaled surveys do not capture small-scale variability. Therefore, these results highlight the potential uncertainties in making assumptions about the spatial representativeness of ice-algal biomass estimates. Since little is known or has been reported on summertime spatial variability of ice-algal biomass we propose that observations from both core-based and under-ice spectral profiling systems should be combined when making assumptions about multi-scale spatial variability of ice-algal biomass.

When chl *a* estimates were grouped into FYI and MYI stations for each gear, we observed no significant differences between the FM-cores and the ROV or SUIT chl *a* estimates (supplementary Table S 1). This demonstrates a suitable approach taken by Fernández-Méndez et al. (2015), used to increase the representativeness of the biomass samples for up-scaling. However, sample sizes were small (N = 3 and 5) for ice cores of each ice type and the median and IQR values had large differences between the cores and ROV or SUIT. Similar to the LA-cores from station 360, two of the MYI FM-cores had high biomass (8 mg chl *a* m^{-2}) while one had very low biomass (0.4 mg chl *a* m^{-2}), which resulted in the mean value being largely influenced by one low value. Although in this case the mean MYI FM-core biomass values were not significantly different, each MYI FM-core value was higher or lower than the IQR of the larger-scale estimates. A similar pattern was observed with the FYI grouping comparison although not as drastic because the values were overall smaller particularly the range of values. Combining the ice cores based on ice type was an improvement in terms of representative sampling; however, there remained a high risk of estimating a non-representative mean (or median) and variance (range or IQR) of ice algal chl *a* biomass.

Table 1. Summary of incoming and bottom-ice light, chl *a* biomass, net primary production (NPP), and explained variance of NPP per station groupings (shown in Figure 1 inset) and sampling method (gear): ice cores (FM or LA), remotely operated vehicle (ROV) and surface and under-ice trawl (SUIT).

Group	Gear [a]	Sample Size	Station	Incoming PAR [b]	Scalar PAR (I) [b]	Chl *a* [c]	NPP [c]	Explained Variance (R^2) of NPP by	
				µmols photons m^{-2} s^{-1}		mg m^{-2}	mg C m^{-2} d^{-1}	I	Chl *a*
A	SUIT	46	216	–	–	0.9 (0.7 – 1.1)	–	–	–
B	FM	1	224	249 ± 90	40.8 ± 14.7	1.2	10.16	–	–
	LA	8	224	–	–	0.34 (0.20 – 0.48) *R; *S	–	–	–
	ROV	468	224	211 ± 72	51.3 ± 25.1	1.04 (0.97 – 1.18)	8.5 (5.6 – 12.3)	0.65 (0.53 – 0.71)	0.12 (0.08 – 0.20)
	SUIT	43	223	–	–	1.6 (1.1 – 1.7)	–	–	–
	SUIT-2	45	233	–	–	1.2 (1.0 – 1.5)	–	–	–
C	FM	1	237	174 ± 90	28.5 ± 14.7	1.7•(+)	0.56•(-)	–	–
	LA	12	237	–	–	0.63 (0.46 – 1.07) *R	–	–	–
	ROV	156	237a	137 ± 59	28.8 ± 23.2	0.96 (0.76 – 1.17) •	0.6 (0.3 – 1.0)	0.61 (0.34 – 0.84)	0.12 (0.03 – 0.25)
	ROV-2	1378	237b	137 ± 59	18.7 ± 8.1	1.26 (1.10 – 1.50) •	0.9 (0.6 – 1.0) •	0.60 (0.37 – 0.79)	0.08 (0.03 – 0.17)
D	FM	1	255	104 ± 71	26.7 ± 18.2	0.6•(-)	0.62•(-)	–	–
	LA	4	255	–	–	0.79 (0.67 – 1.16) *R	–	–	–
	ROV	186	255	93 ± 60	36.3 ± 20.3	1.42 (1.37 – 1.54) •	1.7 (1.5 – 1.9) •	0.11 (0.0 – 0.24)	0.71 (0.53 – 0.93)
E	FM	1	277	101 ± 57	25.9 ± 14.6	0.4•(-)	0.45	–	–
	SUIT	91	285	–	–	1.2 (0.8 – 2.0) •	–	–	–
F	FM	1	323	81 ± 63	24.2 ± 18.8	0.3• (-)	0.02•(-)	–	–
	LA	6	323	–	–	0.17 (0.05 – 0.23) *R	–	–	–
	ROV	1145	323	67 ± 49	7.7 ± 8.6	1.53 (1.36 – 1.74) •	0.14 (0.10 – 0.19) •	0.87 (0.77 – 0.91)	0.17 (0.14 – 0.22)
	SUIT	63	321	–	–	1.6 (0.6 – 2.7) •	–	–	–
G	FM	1	335	49 ± 43	5.9 ± 5.2	0.4•(-)	0.05•(-)	–	–
	LA	6	335	–	–	0.91 (0.38 – 1.07) *R	–	–	–
	ROV	762	335m	46 ± 39	3.0 ± 7.6	2.36 (1.89 – 2.83) •	0.13 (0.07 – 0.22) •	0.93 (0.89 – 0.95)	0.01 (0.01 – 0.02)
	ROV-2	302	335f	46 ± 39	2.3 ± 2.7	2.73 (2.3 – 3.16) •	0.13 (0.08 – 0.24) •	0.69 (0.68 – 0.69)	0.08 (0.07 – 0.10)
	SUIT	18	345	–	–	1.4 (0.4– 5.3)	–	–	–
H	FM	1	349	25 ± 15	1.4 ± 0.9	8•(+)	1.00•(+)	–	–
	LA	7	349	–	–	0.58 (0.25 – 2.26)	–	–	–
	ROV	282	349	23 ± 13	2.4 ± 1.5	1.32 (1.17 – 1.51) •	0.14 (0.09 – 0.21) •	0.18 (0.12 – 0.24)	0.60 (0.53 – 0.67)
	SUIT	101	358	–	–	1.9 (1.4 – 2.5) •	-	–	–
I	FM	1	360	13 ± 7	0.9 ± 0.5	8•(+)	0.39•(+)	–	–
	LA	4	360	–	–	7.25 (4.86 – 8.98)	–	–	–
	ROV	647	360	10 ± 5	0.4 ± 0.4	4.36 (2.86 – 6.70) •	0.07 (0.05 – 0.12) •	0.79 (0.77 – 0.79)	0.16 (0.15 – 0.17)

•corresponds to not-representative, i.e., FM-core estimate outside of interquartile range of ROV and/or SUIT. (+) indicates over-estimate; (-) under-estimate compared to larger-scale data. *R corresponds to a significant difference between ice cores (FM and LA cores combined) and ROV; and *S significant difference between ice cores and SUIT ($p < 0.05$).

[a] "FM" corresponds to FM-cores from Fernández-Méndez et al. (2015); "LA" correspond to LA-cores from (Lange et al., submitted); "ROV" correspond to the up-scaled remotely operated vehicle estimates; and "SUIT" correspond to the up-scaled surface and under-ice trawl estimates.

[b] Incoming PAR and bottom ice scalar PAR (I) are presented as mean ± sd to maintain consistency with Fernández-Méndez et al. (2015)

[c] Chl *a* and NPP are presented as median (interquartile range).

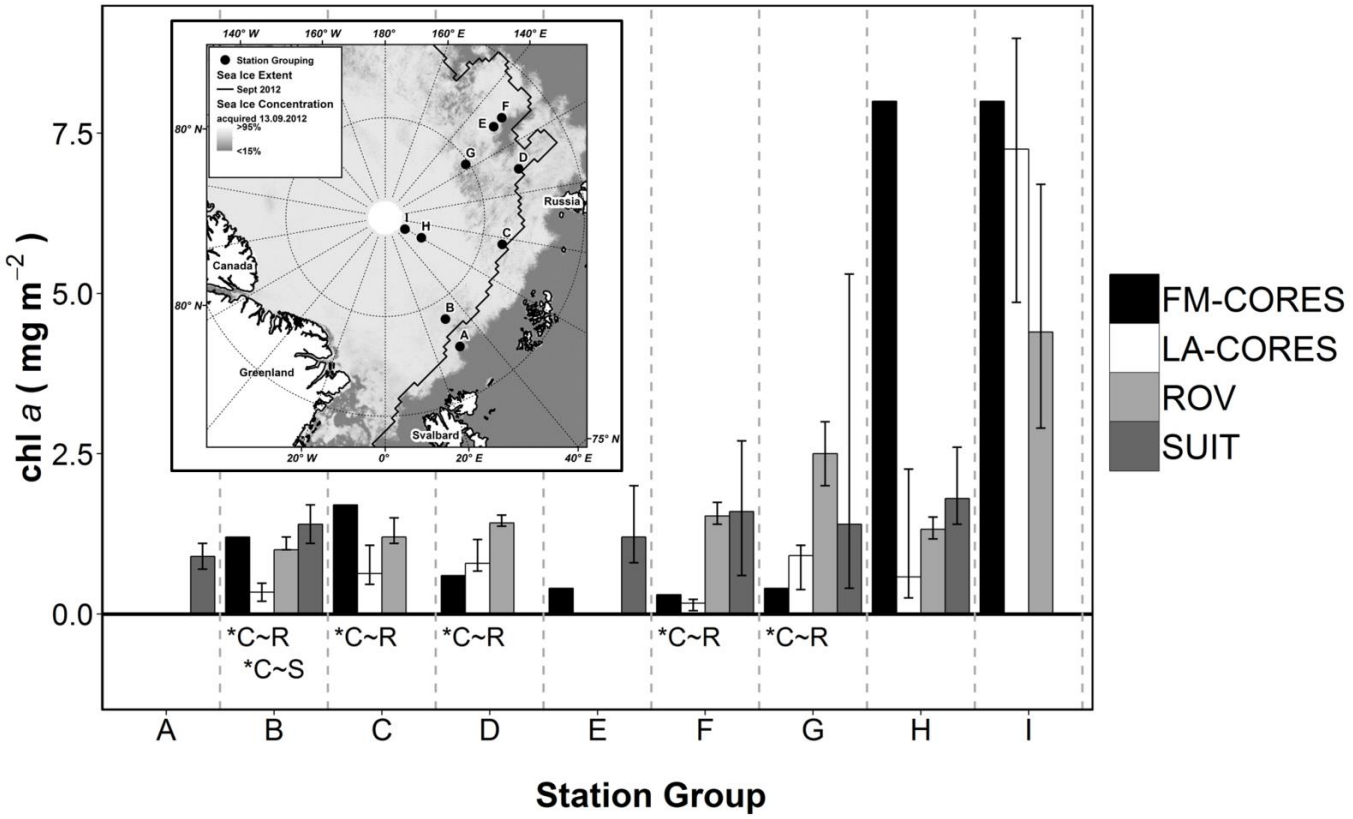

Figure 1. Bar graph showing an inter-method and regional comparison of ice-algae chl *a* biomass based on single ice cores from each station (FM-CORES), data from Fernández-Méndez et al. (2015); multiple ice cores from each station (LA-CORES), data from Lange et al. (submitted); and spectrally derived chl *a* from under-ice ROV and SUIT surveys. FM-CORES bars represent a single value whereas the other bars represent median (50th percentile) with error bars representing the 25th and 75th percentiles. "*" depicts significant *t* test ($p < 0.05$) results performed between: CORES and ROV (C~R); or CORES and SUIT (C~S). CORES correspond to LA-CORES and FM-CORES grouped together. Inset map of the Arctic Ocean with sea ice extent and concentration data, and the locations of the corresponding station groupings conducted during the 2012 PS80 cruise (station numbers for each grouping are listed in Table 1). Sea ice concentration data acquired from www.meereisportal.de according to algorithms in Spreen et al. (2008). Sea ice extent correspond to the 2012 September monthly mean (extent data acquired from NSIDC, Fetterer et al. (2002, udpated 2011)).

3.4 Up-scaled in situ ice-algal net primary production

During spring, ice algae are typically light limited and therefore have higher biomass where light levels are higher (e.g., Gosselin et al., 1986), assuming there is no photo-inhibition. During our summer sampling period, however, we found no strong correlations between the up-scaled chl *a* estimates and available under-ice light (i.e., maximum spearman correlation coefficient, r = 0.22). This means the under-ice light and chl *a* varied independent of each other, which is likely because in late-summer biomass losses due to high melt rates (Lange et al., submitted) had a dominant influence on bottom-ice biomass. For example, bottom-ice with higher light levels may also have had higher melt rates due to more internal ice absorption, which could not have sustained a bottom-ice algal community, and therefore even if light conditions were suitable for high primary production rates the net primary production would have been almost zero if no algae were present. With an additional variable (i.e., melt), which can influence NPP, the spatial distribution of NPP may be more complex in late-summer than during the spring to summer transition making it even more important to understand and account for the spatial variability of both chl *a* biomass and the bottom-ice light field.

We accounted for the spatial variability of NPP by combining the variability of both chl *a* and bottom-ice light in the calculations of the larger-scale NPP estimates then determined the explained variance of NPP by each variable individually. All gridded ROV surveys of NPP are shown in Supplementary Figures S2 to S9. At station groups B, C, F, G and I, the spatial variability of bottom-ice light explained most of the spatial variability of the up-scaled NPP estimates, whereas at station groups D and H, chl *a* explained most of the spatial variability of NPP (Table 1 and supplementary Figure S18). These results emphasize the importance of accounting for both the spatial variability of ice-algal biomass and the bottom-ice light field in order to make representative NPP estimates.

The largest diurnal variability of the explained variances was observed at stations with the largest bottom-ice light levels, which also had larger diurnal variability of light levels (Table 1 and supplementary Figure S2). At all stations, the explained variance of chl *a* was inversely related to light, which is expected since NPP is a function of both variables and chl *a* estimates were constant over the diurnal cycle while only light varied. The inter-station differences regarding which variable (chl *a* or light) explained most of the variance in NPP cannot be stated for certain as we observed no significant correlations between the explained variance for each station and any other station variable (e.g., nutrients, median and IQR chl *a* or bottom-ice light). However, there was a non-significant but strong positive correlation (r = 0.46) between explained variance of NPP by chl *a* with sea ice NO_3 concentrations (data from Fernández-Méndez et al., 2015), and a non-significant but strong negative correlation between explained variance of NPP by bottom-ice light with sea ice NO_3 concentrations. These correlations were likely not significant due to the small sample size (N=9), nevertheless, in the absence of other correlations, it does provide some indication that the sea ice nutrient regime could have also had some influence on the relative (inter-station) importance of chl *a* biomass and light on NPP.

FM-core NPP estimates were representative (i.e., within the IQR) of the up-scaled estimates at station group B and one ROV survey at station group C (Table 1). FM-cores under-estimated NPP at station groups C, D, F, and G, and over-estimated NPP at station groups H and I compared to the up-scaled ROV-based NPP estimates (Table 1). The differences between methods were likely the result of differences in chl *a* and/or light. Station group B had similar chl *a* biomass and NPP for both the FM-core and up-scaled estimates (Table 1, Figures 1 and 2). Station groups D, F, and G had higher up-scaled chl *a* biomass and NPP estimates compared to FM-core estimates (Table 1). Conversely, station groups H and I had lower up-scaled chl *a* biomass and NPP estimates compared to FM-core estimates (Table 1). The same directional difference of chl *a* biomass and NPP observed between up-scaled and FM-core estimates for all station groups, except group C, suggests the differences between the FM-cores and up-scaled NPP estimates were driven by the differences in chl *a* biomass with the exception of station group C. This was further confirmed by the fact that the bottom-ice light levels used for each method were comparable for all stations (Table 1).

Only station group C had higher chl *a* biomass but lower NPP estimates for the FM-cores compared to the up-scaled estimates (Table 1; Figures 1 and 2). Furthermore, light levels were comparable (237a)

or slightly higher (237b) for the FM-core derived NPP estimates compared to the ROV surveys (Table 1). This suggests that the spatial variability of both the chl *a* biomass and bottom-ice light derived from the group C ROV surveys had a combined influence on the observed differences that is not apparent from the overall survey estimates.

Station group B had similar NPP estimates for the FM-core and up-scaled observations (Table 1 and Figure 2), which we attributed to the similar chl *a* biomass estimates (Table 1 and Figure 1). Even though light levels and chl *a* biomass were only slightly larger at station group B compared to groups C and D, group B had NPP estimates almost and order of magnitude larger than groups C and D. This was attributed to the substantially higher value of the photosynthetic parameter P^B_s determined for this station (Fernández-Méndez et al., 2015), compared to all other stations. This further emphasizes the need for larger samples sizes for ice core-based estimates and that the combination of data from several stations, an approach described by Fernández-Méndez et al. (2015), is necessary not only to account for the spatial variability of light and chl *a* but also the potential variability of the derived photosynthetic parameters.

We observed no significant differences between the FM-cores and the up-scaled NPP estimates when they were grouped into FYI and MYI stations (Table 2). However, the median and IQR values had large differences between sampling methods for the MYI stations and the mean values, although they were similar, were largely the result of only one or two extreme values. These results suggest grouping ice core samples as an acceptable approach to improve the representativeness of the estimates but with only a small number of samples this approach can still carry high risk of obtaining non-representative or false estimates.

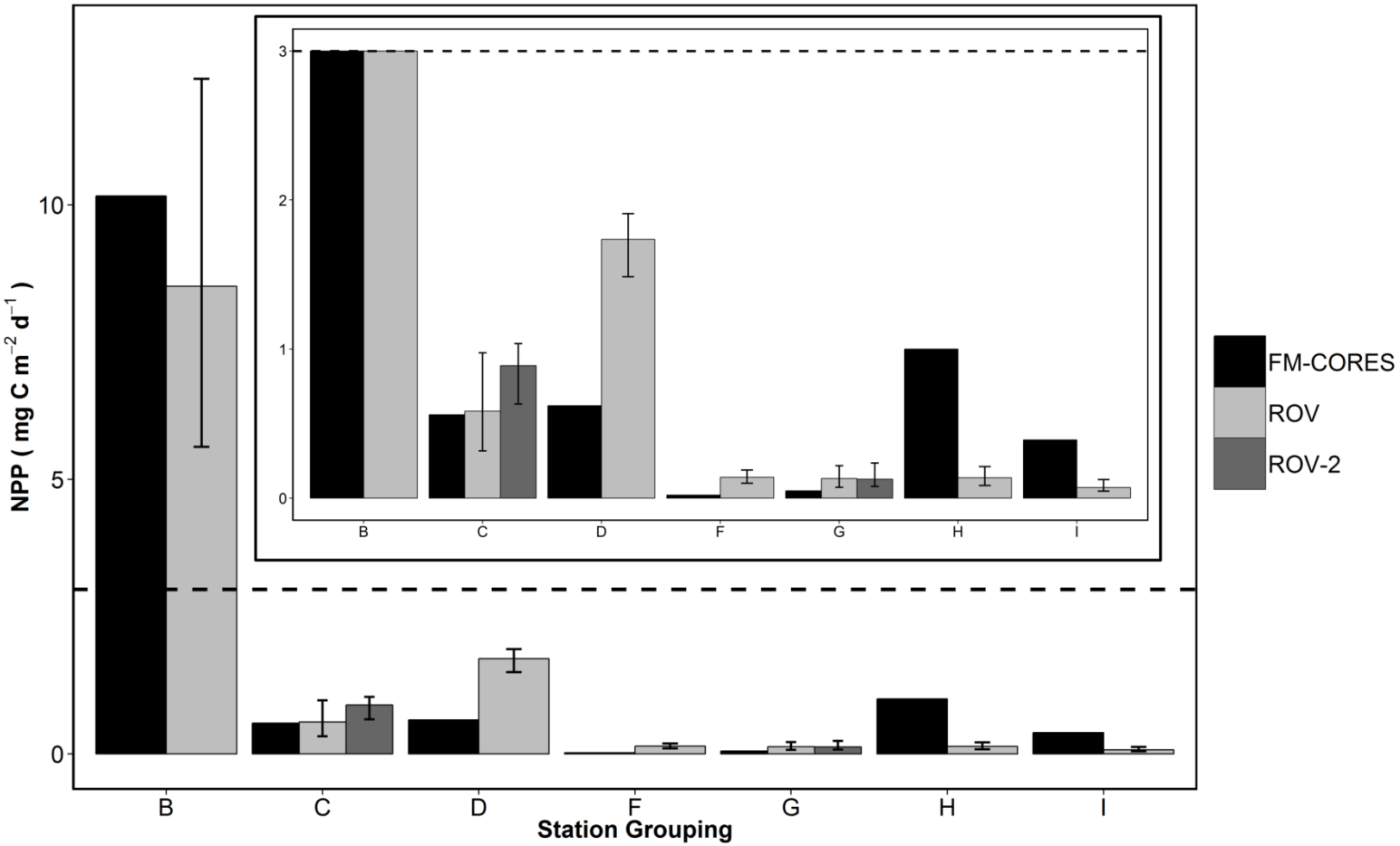

Figure 2. Bar graph showing a comparison of net primary production (NPP) estimates based on ice core samples (FM-CORES) and up-scaled NPP estimates based on ROV measurements of spectral transmittance and spectrally-derived chl *a*. Inset is a magnified version of full bar graph, to better show the low values, with y-axis maximum corresponding to the dashed line on the full bar graph. At some ice stations two ROV surveys were conducted at different locations on the ice floe (e.g., ROV and ROV-2).

3.5 Sea ice ridges have high biomass and net primary production

Sea ice algae are generally an under-sampled component of sea ice. Sea ice ridges are even more under-sampled due to the difficulty of sampling this type of ice. Despite this fact, sea ice ridges have been reported to host high abundances of sea ice fauna during advanced melt (Gradinger et al., 2010). Therefore, we specifically investigated sea ice ridges with the hypothesis that they could host high abundances of ice algae during advanced melt, due to lower melt rates in these locations, which could indicate that sea ice ridges are an important high biomass region during advanced melt.

At ice station 224 we identified two ridges based on the ROV draft measurements (Figure 3a). Both ridges had significantly higher ice-algal chl *a* biomass than the level ice ($p < 0.05$) (Supplementary Table S 2; Figure 3 b). Despite the higher biomass at the ridges, ridge 2 had significantly lower NPP compared to level ice, whereas ridge 1 had similar NPP to the level ice (Supplementary Table S 2; Figure 3 b). This difference was attributed to the lower bottom-ice light at ridge 1. Bottom-ice light was significantly higher for level ice compared to both ridges ($p < 0.05$; Supplementary Table S 2) indicating that the variability of ice-algal chl *a* biomass was more important than the bottom-ice light levels in determining NPP at ridge 1 since NPP was not different between ridge 1 and the level ice. Chl *a* biomass and bottom-ice light explained comparable amounts of the level ice NPP variance, however, chl *a* biomass explained relatively more variance compared to bottom-ice light at ridges 1 and 2 (Supplementary Table S 2). Chl *a* biomass explained between 58 – 91 % of the NPP variance when ridges and level ice were examined separately. However, chl *a* only explained 12 % of the NPP variance for the entire ROV survey (Supplementary Table S 2). This exemplifies the complex relationship between chl *a* biomass and available PAR for NPP estimates and that during late summer (i.e., advanced melt) both the variability of bottom-ice light levels and the variability of chl *a* biomass are required to make representative large-scale NPP estimates. Furthermore, sea ice features such as ridges can play an important role in biomass and NPP but have a different and perhaps more complex relationship between available light and biomass than the surrounding sea ice. Bottom-ice scalar irradiance values, *I*, were higher at the bottom of ridge 1 even though draft values were thicker. This indicates high variability of the attenuation of light under ridges and that further investigations are required to understand these processes, particularly in regards to potential for NPP on larger scales.

In addition, high biomass sea ice ridges were identified within four SUIT stations (223 Figure 3 e; 285, 358 supplementary Figure S2). The number of high biomass ridges per SUIT haul were too small and ridge sampling was biased therefore a statistical comparison was not conducted. Nevertheless, identified high biomass ridges had chl *a* biomass estimates in the range 2 – 9 mg chl *a* m^{-2} (Figure 3 and supplementary Figure S10 to S17), which is larger than the overall SUIT haul median values in the range 1.2 – 1.9 mg chl *a* m^{-2} (Table 1). This suggests that sea ice ridges can have a significant contribution to overall ice-algal biomass and NPP and therefore should also be more accurately sampled and included in large-scale models.

Based on the ridge identification analysis for all SUIT stations we calculated a mean (min–max) ridge density of 7.5 ridges km^{-1} (2.5 – 18.0), mean ridge width of 68.7 m (47.6 – 100.3), and a mean percent total ice coverage by ridges of 9.2 % (2.5 – 15.4 %). Ridge analysis summaries for each SUIT station are shown in Supplementary Table S 3 and SUIT profiles with identified ridges are shown in Supplementary Figures S10 to S17. These results demonstrate that sea ice ridges can make up a substantial portion of the sea ice environment and therefore should not be overlooked in terms of their contribution to overall Arctic sea ice algal biomass and NPP.

We must also note that both the ROV and SUIT surveys do not representatively sample sea ice ridges and therefore remains an under-sampled component of the overall sea ice system. Movement of the SUIT is guided by the under-ice topography and therefore at ridges the SUIT contacts the ridge and diverts downward causing larger distances to the ice and/or large pitch and roll therefore the sensors may not "see" the ice bottom. This constraint would be difficult to overcome since the most obvious option would be to decrease the towing speed. However, the chosen haul speeds are required to ensure representative fauna catches. Another option could be to do "sensor" dedicated hauls where haul speeds are reduced and the main focus would be to conduct representative sampling of ridges, which

would have the added bonus of decreasing the along track footprint resulting in higher resolution measurements.

ROV sites are typically chosen to avoid ridges because operation in close proximity to ridges is risky due to the possibility of tangling the cable. Dedicated ROV dives under sea ice ridges could be accomplished with experienced operators, however, this would be more time consuming in order to minimize the risk of losing or damaging the ROV. Nevertheless, dedicated ROV surveys and ice core sampling of ridges should be a priority in future campaigns.

It is possible that sea ice ridges have different optical properties, which were not accounted for by the model and therefore resulted in higher chl *a* biomass estimates for these features. However, this is unlikely since not all ridges that fit the manual inspection showed the same pattern of high biomass. We suggest that further work on modelling the optical properties of sea ice ridges and to include coincident ice core chl *a* biomass with spectral measurements are required in order to better understand the potential for high ice-algal biomass at sea ice ridges.

3.6 Conclusions

We presented two novel approaches to estimate ice-algal biomass and net primary production, which have demonstrated substantial improvements regarding representative sea ice algae observations. We provided, for the first time, a detailed multi-scale comparison of ice-core based ice-algal biomass and NPP estimates with up-scaled spectrally-derived estimates. Our results showed that ice core-based estimates of summertime ice-algal biomass and NPP do not representatively capture the spatial variability compared to the up-scaled estimates. This may carry similar uncertainties for pan-Arctic estimates based on ice core observations alone. We showed that grouping ice core samples, an approach used by Fernández-Méndez et al. (2015), can improve the representativeness of biomass and NPP estimates but with only a small number of samples there is still a high risk of obtaining non-representative estimates. Therefore, we recommend that future sea ice sampling should combine ice-core based methods to estimate ice-algal biomass and NPP with the larger-scale under-ice spectral profiling approaches presented and described here and in Lange et al. (submitted).

We also identified high biomass ridges within several up-scaled surveys. Although more work is needed to representatively sample these features and to confirm ridges as high biomass and potentially high primary production regions, these results do support previous findings on the potential importance of sea ice ridges for under-ice fauna during advanced melt (Gradinger et al., 2010). Further dedicated sea ice ridge studies are warranted particularly in terms of ice algal biomass, nutrients, primary production and bio-optical properties.

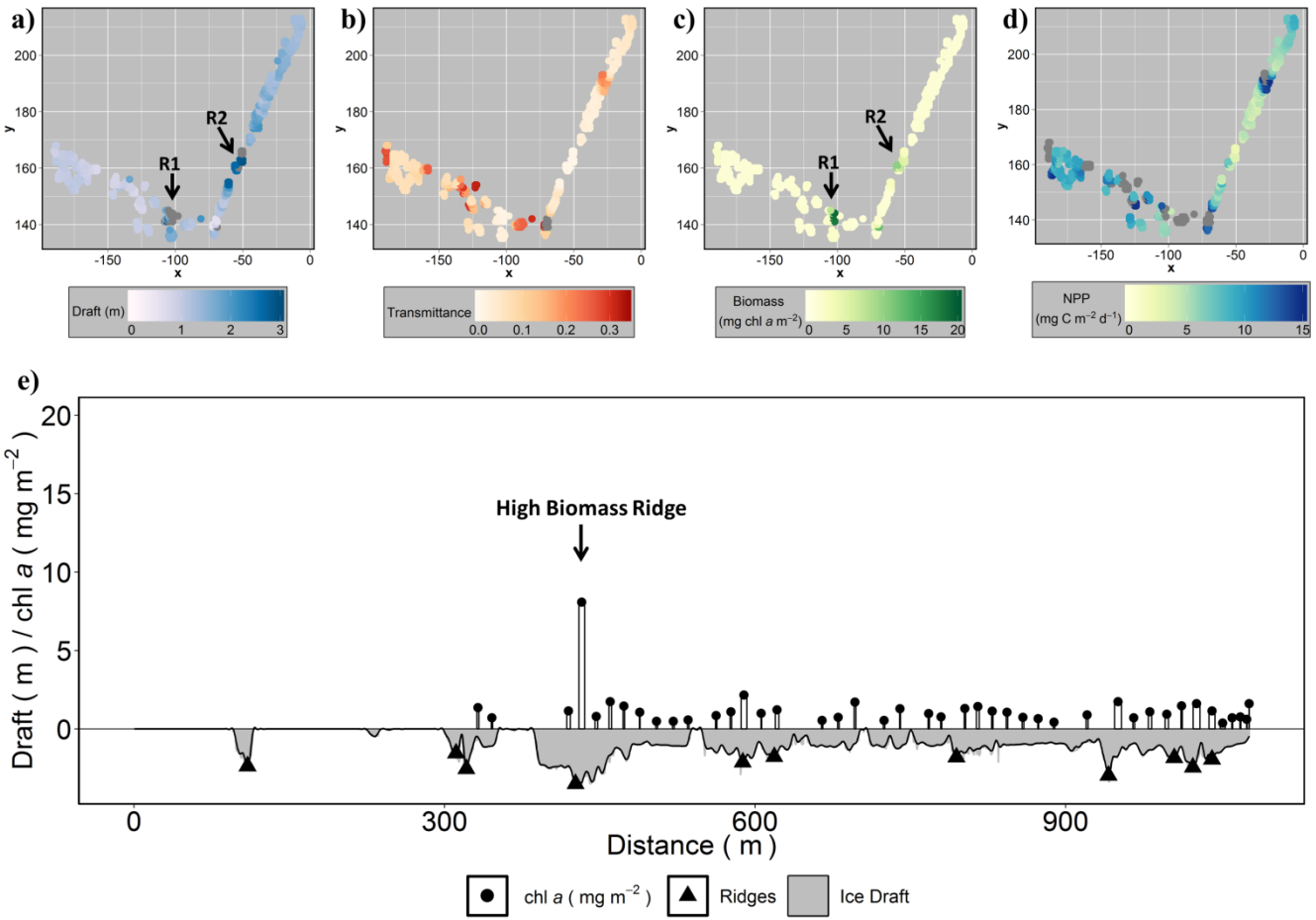

Figure 3. Identified high biomass ridges at remotely operated vehicle (ROV) station 224 showing a) draft (m); b) transmittance; c) spectrally-derived chl *a* biomass (mg m^{-2}); and d) net primary production-NPP (mg C m^{-2} s^{-1}). R1 and R2 depict ridge 1 and ridge 2, respectively. Grey circles represent values above the scale maximum value. e) High biomass ridge identified at Surface Under-Ice Trawl (SUIT) station 223 showing sea ice draft, identified ridges and spectrally-derived chl *a* biomass.

Acknowledgments and Data

We thank Martin Schiller for his technical expertise and operational support during ROV deployments. We thank Captain Uwe Pahl, the crew, and scientific cruise leader Antje Boetius of RV Polarstern expedition PS80.3 (ARK27-3; IceArc), for their excellent support and guidance with work at sea. We thank Jan Andries van Franeker (IMARES) for kindly providing the Surface and Under-Ice Trawl (SUIT) and Michiel van Dorssen for technical support. SUIT was developed by IMARES with support from the Netherlands Ministry of EZ (project WOT-04-009-036) and the Netherlands Polar Program (project ALW 866.13.009). We acknowledge the collaboration and technical support by Ocean Modules, Sweden for development and deployment of the ROV. This study is part of the Helmholtz Association Young Investigators Group Iceflux: Ice-ecosystem carbon flux in polar oceans (VH-NG-800). We also acknowledge the Alfred-Wegener-Institut, Helmholtz-Zentrum für Polar- und Meeresforschung for essential financial and logistical support. All data are available from the PANGAEA database doi.org/XX.XXXX/PANGAEAXXXXXX.

References

Arrigo, K.R., van Dijken, G.L., 2011. Secular trends in Arctic Ocean net primary production. *Journal of Geophysical Research*, 116, C09011.

Arrigo, K.R., van Dijken, G.L., 2015. Continued increases in Arctic Ocean primary production. *Progress in Oceanography*, 136, 60-70.

Castellani, G., Lüpkes, C., Hendricks, S., Gerdes, R., 2014. Variability of Arctic sea-ice topography and its impact on the atmospheric surface drag. *Journal of Geophysical Research: Oceans*, 119, 6743-6762.

David, C., Lange, B., Rabe, B., Flores, H., 2015. Community structure of under-ice fauna in the Eurasian central Arctic Ocean in relation to environmental properties of sea-ice habitats. *Marine Ecology Progress Series*, 522, 15-32.

Dupont, F., 2012. Impact of sea-ice biology on overall primary production in a biophysical model of the pan-Arctic Ocean. *Journal of Geophysical Research*, Vol. 117.

Fernández-Méndez, M., Katlein, C., Rabe, B., Nicolaus, M., Peeken, I., Bakker, K., Flores, H., Boetius, A., 2015. Photosynthetic production in the Central Arctic during the record sea-ice minimum in 2012. *Biogeosciences Discussions*, 12, 2897-2945.

Fetterer, F., Knowles, K., Meier, W., Savoie, M., 2002, udpated 2011. Sea Ice Index. Boulder, CO: National Snow and Ice Data Center. Digital Media.

Gosselin, M., Legendre, L., Therriault, J.C., Demers, S., Rochet, M., 1986. Physical control of the horizontal patchiness of sea-ice microalgae. *Marine Ecology Progress Series*, 29, 289-298.

Gosselin, M., Levasseur, M., Wheeler, P.A., Horner, R.A., Booth, B.C., 1997. New measurements of phytoplankton and ice algal production in the Arctic Ocean. *Deep Sea Research Part II: Topical Studies in Oceanography*, 44, 1623-1644.

Gradinger, R., 2009. Sea-ice algae: Major contributors to primary production and algal biomass in the Chukchi and Beaufort Seas during May/June 2002. *Deep Sea Research Part II: Topical Studies in Oceanography*, 56, 1201-1212.

Gradinger, R., Bluhm, B., Iken, K., 2010. Arctic sea-ice ridges—Safe heavens for sea-ice fauna during periods of extreme ice melt? *Deep Sea Research Part II: Topical Studies in Oceanography*, 57, 86-95.

Granskog, M.A., Kaartokallio, H., Kuosa, H., Thomas, D.N., Ehn, J., Sonninen, E., 2005. Scales of horizontal patchiness in chlorophyll a, chemical and physical properties of landfast sea ice in the Gulf of Finland (Baltic Sea). *Polar Biology*, 28, 276-283.

Grossi, S., Kottmeier, S., Moe, R., Taylor, G., Sullivan, C., 1987. Sea ice microbial communities. 6. Growth and primary production in bottom ice under graded snow cover. *Marine Ecology Progress Series*, 35, 153-164.

Katlein, C., Arndt, S., Nicolaus, M., Perovich, D.K., Jakuba, M.V., Suman, S., Elliott, S., Whitcomb, L.L., McFarland, C.J., Gerdes, R., Boetius, A., German, C.R., 2015. Influence of ice thickness and surface properties on light transmission through Arctic sea ice. *Journal of Geophysical Research: Oceans*, 120, 5932-5944.

Katlein, C., Nicolaus, M., Petrich, C., 2014. The anisotropic scattering coefficient of sea ice. *Journal of Geophysical Research*, 119, 842-855.

Kohlbach, D., Graeve, M., Lange, B.A., David, C., Peeken, I., Flores, H., 2016. The importance of ice algae-produced carbon in the central Arctic Ocean ecosystem: food web relationships revealed by lipid and stable isotope analyses. *Limnol. Oceanogr*.

Lange, B.A., Katlein, C., Nicolaus, M., Peeken, I., Flores, H., submitted. Spectrally-derived sea ice-algal chlorophyll a concentrations using under-ice horizontal profiling platforms. *Journal of Geophysical Research*.

Lange, B.A., Michel, C., Beckers, J.F., Casey, J.A., Flores, H., Hatam, I., Meisterhans, G., Niemi, A., Haas, C., 2015. Comparing springtime ice-algal chlorophyll a and physical properties of multi-year and first-year sea ice from the Lincoln Sea. *PLoS ONE*, 10, e0122418.

Lavoie, D., Denman, K., Michel, C., 2005. Modeling ice algal growth and decline in a seasonally ice-covered region of the Arctic (Resolute Passage, Canadian Archipelago). *Journal of Geophysical Research*, 110, C11009.

Lee, Y.J., Matrai, P.A., Friedrichs, M.A.M., Saba, V.S., Antoine, D., Ardyna, M., Asanuma, I., Babin, M., Bélanger, S., Benoît-Gagné, M., Devred, E., Fernández-Méndez, M., Gentili, B., Hirawake, T., Kang, S.-H., Kameda, T., Katlein, C., Lee, S.H., Lee, Z., Mélin, F., Scardi, M., Smyth, T.J., Tang, S., Turpie, K.R., Waters, K.J., Westberry, T.K., 2015. An assessment of phytoplankton primary productivity in the Arctic Ocean from satellite ocean color/in situ chlorophyll-a based models. *Journal of Geophysical Research: Oceans*, 120, 6508-6541.

Long, M.H., Koopmans, D., Berg, P., Rysgaard, S., Glud, R.N., Søgaard, D.H., 2012. Oxygen exchange and ice melt measured at the ice-water interface by eddy correlation. *Biogeosciences*, 9, 1957-1967.

Michel, C., Legendre, L., Ingram, R.G., Gosselin, M., Levasseur, M., 1996. Carbon budget of sea-ice algae in spring: Evidence of a significant transfer to zooplankton grazers. *Journal of Geophysical Research: Oceans*, 101, 18345-18360.

Miller, L.A., Fripiat, F., Else, B.G.T., Bowman, J.S., Brown, K.A., Collins, R.E., Ewert, M., Fransson, A., Gosselin, M., Lannuzel, D., Meiners, K.M., Michel, C., Nishioka, J., Nomura, D., Papadimitriou, S., Russell, L.M., Sørensen, L.L., Thomas, D.N., Tison, J.-L., van Leeuwe, M.A., Vancoppenolle, M., Wolff, E.W., Zhou, J., 2015. Methods for biogeochemical studies of sea ice: The state of the art, caveats, and recommendations. *Elementa: Science of the Anthropocene*, 3, 000038.

Mock, T., Gradinger, R., 1999. Determination of Arctic ice algal production with a new in situ incubation technique. *Marine Ecology Progress Series*, 177, 15-26.

Nicolaus, M., Hudson, S.R., Gerland, S., Munderloh, K., 2010. A modern concept for autonomous and continuous measurements of spectral albedo and transmittance of sea ice. *Cold Regions Science and Technology*, 62, 14-28.

Nicolaus, M., Katlein, C., 2013. Mapping radiation transfer through sea ice using a remotely operated vehicle (ROV). *The Cryosphere*, 7, 763-777.

Nicolaus, M., Katlein, C., Maslanik, J., Hendricks, S., 2012. Changes in Arctic sea ice result in increasing light transmittance and absorption. *Geophysical Research Letters*, 39, 2699–2700.

Perovich, D.K., Roesler, C.S., Pegau, W.S., 1998. Variability in Arctic sea ice optical properties. *Journal of Geophysical Research: Oceans*, 103, 1193-1208.

Platt, T., Gallegos, C., Harrison, W., 1980. Photoinhibition of photosynthesis in natural assemblages of marine phytoplankton. *Journal of Marine Research*, 38, 103-111.

Rysgaard, S., Kühl, M., Glud, R.N., Hansen, J.W., 2001. Biomass, production and horizontal patchiness of sea ice algae in a high-Arctic fjord (Young Sound, NE Greenland). *Marine Ecology Progress Series*, 223, 15-26.

Søgaard, D.H., Kristensen, M., Rysgaard, S., Glud, R.N., Hansen, P.J., Hilligsøe, K.M., 2010. Autotrophic and heterotrophic activity in Arctic first-year sea ice: seasonal study from Malene Bight, SW Greenland. *Marine Ecology Progress Series*, 419, 31-45.

Søreide, J.E., Leu, E.V.A., Berge, J., Graeve, M., Falk-Petersen, S., 2010. Timing of blooms, algal food quality and Calanus glacialis reproduction and growth in a changing Arctic. *Global Change Biology*, Vol. 16 (pp. 3154–3163).

Spreen, G., Kaleschke, L., Heygster, G., 2008. Sea ice remote sensing using AMSR-E 89-GHz channels. *Journal of Geophysical Research*, 113, C02S03.

Steffens, M., Granskog, M., Kaartokallio, H., Kuosa, H., Luodekari, K., Papadimitriou, S., Thomas, D., 2006. Spatial variation of biogeochemical properties of landfast sea ice in the Gulf of Bothnia, Baltic Sea. *Annals of Glaciology*, 44, 80-87.

Paper 4. Community structure of under-ice fauna in the Eurasian central Arctic Ocean in relation to environmental properties of sea-ice habitats

published in: *Marine Ecology Progress Series 522:15-32 doi: 10.3354/meps11156*

Carmen David, **Benjamin Lange**, Benjamin Rabe, Hauke Flores

Key Points

-

Abstract

Arctic sea-ice decline is expected to have a significant impact on Arctic marine ecosystems. Ice-associated fauna play a key role in this context because they constitute a unique part of Arctic biodiversity and transmit carbon from sea-ice algae into pelagic and benthic food webs. Our study presents the first regional-scale record of under-ice faunal distribution and the environmental characteristics of under-ice habitats throughout the Eurasian Basin. Sampling was conducted with a Surface and Under Ice Trawl, equipped with a sensor array recording ice thickness and other physical parameters during trawling. We identified 2 environmental regimes, broadly coherent with the Nansen and Amundsen Basins. The Nansen Basin regime was distinguished from the Amundsen Basin regime by heavier sea-ice conditions, higher surface salinities and higher nitrate + nitrite concentrations. We found a diverse (28 species) under-ice community throughout the Eurasian Basin. Change in community structure reflected differences in the relative contribution of abundant species. Copepods (*Calanus hyperboreus* and *C. glacialis*) dominated in the Nansen Basin regime. In the Amundsen Basin regime, amphipods (*Apherusa glacialis*, *Themisto libellula*) dominated. Polar cod *Boreogadus saida* was present throughout the sampling area. Abrupt changes from a dominance of ice-associated amphipods at ice-covered stations to a dominance of pelagic amphipods (*T. libellula*) at nearby ice-free stations emphasised the decisive influence of sea ice on small-scale patterns in the surface-layer community. The observed response in community composition to different environmental regimes indicates potential long-term alterations in Arctic marine ecosystems as the Arctic Ocean continues to change.

4.1 Introduction

The Arctic Ocean is experiencing some of the most pronounced effects of global climate change (Arctic Climate Impact Assessment 2004). During the past 4 decades, reductions in sea-ice concentration and thickness and in the duration of the melting season have been recorded in the Arctic Ocean (Kwok and Rothrock 2009; Markus et al. 2009; Overland and Wang 2013; Rigor and Wallace 2004; Shimada et al. 2006; Stroeve et al. 2012) and are predicted to continue in the future (Johannessen et al. 2004; Polyakov et al. 2005; Stroeve et al. 2007). The Arctic Ocean is changing from a perennial multi-year ice (MYI)-dominated system to a seasonal first-year ice (FYI) system (Maslanik et al. 2011). In 2012, the sea-ice extent was reduced to approximately half of the mean for the past four decades, resulting in large open-water areas (Parkinson and Comiso 2013).

These changes are expected to result in modifications of the biological systems in the Arctic Ocean. Reduction in the extent and thickness of sea ice leads to more light availability in the water column, which has been hypothesised to induce a net increase in primary production (Arrigo et al. 2008; Arrigo and van Dijken 2011). This may be true on the shelves where nutrient supply by advection or vertical mixing can be extensive. Over the basins, however, primary production can be nutrient-limited due to strengthened stratification by ice melt (Tremblay and Gagnon 2009). Sea-ice loss will lead to a decrease in ice algal production, which can account for up to 50% of the primary production in the central Arctic Ocean (Gosselin et al. 1997). Ice algae are considered a high-quality food source for Arctic marine food webs (Søreide et al. 2013; Søreide et al. 2006). How these changes in primary production will impact marine fauna is an open question. The number of documented changes in Arctic planktonic systems is low, and the number reported from the central Arctic Ocean even lower is (Wassmann et al. 2011). Lack of biological baseline data makes it impossible to estimate the effect of recent environmental changes on the biological system (Kosobokova and Hirche 2000). Increasing efforts have been made in recent years to investigate zooplankton distribution at different scales (Hopcroft et al. 2005; Hunt et al. 2014; Matsuno et al. 2012; Pomerleau et al. 2014). Only recently, have zooplankton data from different Arctic cruises been compiled into a large-scale analysis, providing a first baseline to monitor the influence of environmental change on the Arctic pelagic system (Kosobokova and Hirche 2009). It should be born in mind, however, that this dataset dates from the 1990s, a period when environmental change in the Arctic Ocean was already on-going.

Most affected by environmental changes are the organisms living in association with sea ice. Ice-associated fauna have been described as those species that complete their entire life cycle within the sea ice or spend only part of their life cycle associated with sea ice (Melnikov and Kulikov 1980). Many uncertainties still remain in understanding the association of these organisms with sea-ice habitats. Community structure of ice-associated fauna is assumed to be related to ice age, density and under-ice topography (Hop and Pavlova 2008; Hop et al. 2000). Ice-associated species may prefer a certain type of ice, e.g. MYI or FYI (Hop et al. 2000). Some, such as the large amphipod *Gammarus wilkitzkii*, are found associated with ridges, which provide shelter during the melting season (Gradinger et al. 2010; Hop and Pavlova 2008). The widely distributed amphipod *Apherusa glacialis* prefers flat ice floes (Hop and Pavlova 2008), or ice edges (Beuchel and Lønne 2002; Hop et al. 2000).

Crucial for the functioning of the Arctic ecosystem is the role of ice-associated fauna in the energy transfer to higher trophic levels (Budge et al. 2008). The dominance of diatom fatty acid trophic markers in the lipids of calanoid copepods and ice-associated amphipods underpins the importance of sea-ice algae as a critical carbon source in Arctic food webs (Budge et al. 2008; Falk-Petersen et al. 2009). Feeding extensively on calanoid copepods (Benoit et al. 2010; Scott et al. 1999) and amphipods (Matley et al. 2013), polar cod *Boreogadus saida* in turn represents a preferential prey for seabirds and marine mammals (Bradstreet and Cross 1982; Finley and Gibb 1982; Welch et al. 1992). As a key species of the Arctic system, the polar cod is believed to account for up to 75% of the energy transfer between zooplankton and vertebrate predators (Welch et al. 1992). Ice algae–copepods/amphipods–polar cod–top predators represents probably one of the most efficient pathways in energy flux through the Arctic food web, yet all its components are closely related with sea ice (Harter et al. 2013; Hop and Gjøsæter 2013; Scott et al. 1999). Changes in composition, abundance,

size and energy content of ice-associated communities will influence the energy flux through the Arctic marine ecosystem and, hence, the growth and survival of top predators (Laidre and Heide-Jørgensen 2005; Mehlum and Gabrielsen 1993). Therefore, an accurate quantification of ice-associated fauna on large spatial scales is crucial to understand the functioning of Arctic sea-ice-dependent ecosystems and their future fate. The sea-ice-covered Arctic Ocean, however, is difficult to access. In particular, sampling under the sea ice is challenging. Most commonly, ice-associated macrofauna have been sampled by divers (Arndt and Pavlova 2005; Hop et al. 2011). This method is excellent in describing the small-scale structure of ice habitats during sampling, yet the spatial variability of the organism distributions may not be covered representatively. Ice floes which appear biologically poor are not sampled due to limited time at ice stations, while it is impossible to obtain all organisms from ice floes with rich fauna (Hop and Pavlova 2008). A new sampling gear used in the Southern Ocean for the first time, the Surface and Under Ice Trawl (SUIT) (van Franeker et al. 2009), overcomes the spatial limitation of observations by divers (Flores et al. 2012). SUIT enables large-scale horizontal sampling of the 0–2 m surface layer both under sea ice and in open water.

The aim of the present study is to describe the association of macrofaunal communities in the surface layer (0–2 m) under ice and in open water, with habitat properties of the sea ice and the underlying water column. In particular we address the following objectives:

1. We identify key environmental variables of sea ice and water column that structure under-ice habitats.
2. We provide a basin-wide inventory of under-ice fauna in the Eurasian central Arctic Ocean and to highlight key species defining the under-ice communities.
3. We investigate the role of under-ice habitat properties in structuring the under-ice community.

4.2 Materials and methods

4.2.1 Study area and sampling technique

Sampling was performed during RV *Polarstern* expedition ARK XXVII/3, between 2 August to 29 September 2012, across the ice-covered Eurasian part of the Arctic Ocean deep-sea basin, from 82° to 89°N, and 30° to 130°E (Fig. 1). Thirteen horizontal hauls were performed under different ice types (MYI, FYI), and in open water. Sampling was performed with an improved version of the Surface and Under Ice Trawl (SUIT) (van Franeker et al. 2009). The improved SUIT consisted of a steel frame with a 2 x 2 m opening and 2 parallel 15 m long nets attached: (1) a 7 mm half-mesh commercial shrimp net, lined with 0.3 mm mesh in the rear 3 m of the net, covered 1.5 m of the opening width and (2) a 0.3 mm mesh zooplankton net covered 0.5 m of the opening width. Floats attached to the top of the frame kept the net at the surface or the sea-ice underside. To enable sampling under undisturbed ice, an asymmetric bridle forces the net to tow off at an angle of approximately 60º to starboard of the ship's track, at a cable length of 150 m. A detailed description of the SUIT sampling performance is provided as supplementary material by Flores et al. (2012). Depending on the ice conditions, SUIT haul durations varied between 3 and 38 min, with a mean of 24 min.

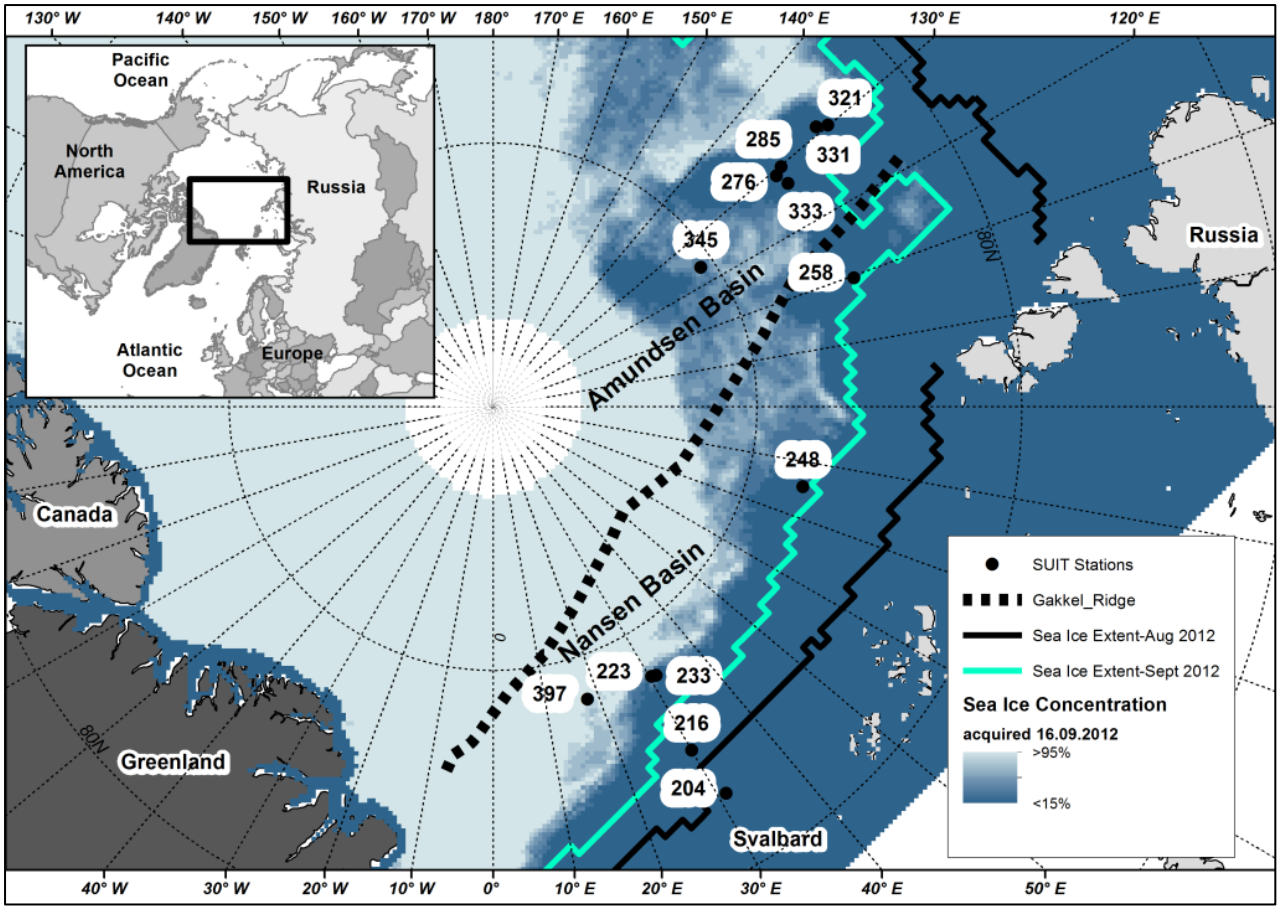

Figure 1. SUIT (Surface and Under Ice Trawl) station map during RV 'Polarstern' expedition IceARC (ARK XXVII/3). Sea-ice concentration on 16 September 2012 (data acquired from Bremen University; www.iup.uni-bremen.de:8084/amsr/) and mean sea-ice extent for August and September 2012 are represented on the map (data acquired from NSIDC Fetterer et al. 2002, updated daily). Number codes next to sampling locations indicate station numbers

4.2.2 Environmental data

A sensor array was mounted in the SUIT frame, consisting of an Acoustic Doppler Current Profiler (ADCP), a Conductivity Temperature Depth probe (CTD) with built-in fluorometer, an altimeter, 2 spectral radiometers, and a video camera. Water inflow speed was estimated using a Nortek Aquadopp® ADCP. Three acoustic beams operating at a frequency of 2 MHZ allowed constructing 3-dimensional profiles of the currents in the net opening. The ADCP measured the current velocity at 3 locations across the SUIT opening. The ADCP was also equipped with sensors for pressure, pitch, role, and heading. These data were used to reconstruct the position of the SUIT in the water during each haul as an indicator of the catch performance. Temperature and salinity profiles were obtained with a Sea and Sun CTD75M probe. The Practical Salinity Scale (PSS-78) was used for salinity values (Fofonoff 1985). A built-in Turner Cyclops fluorometer was used to estimate under-ice chlorophyll concentration. Calibration of fluorometric chlorophyll *a* concentrations was done from water samples obtained during stationary sea ice work. The calibration coefficients were derived from the linear relationship between chlorophyll *a* concentrations of water samples (measured with High Pressure Liquid Chromatography) with fluorometric chlorophyll *a* concentrations of the corresponding 1 m depth range ($n = 2484$; adj. $r^2 = 0.63$; $p < 0.001$). Data gaps in the CTD measurements caused by low battery voltage were filled using complementary datasets from the ADCP data (pressure) and the shipboard sensors (temperature and salinity), using correction factors determined by linear regression. An altimeter Tritech PA500/6-E connected to the CTD probe measured the distance between the net and the sea-ice underside. Sea-ice draft was calculated as the difference between the depth of the net relative to the water level, measured by the CTD pressure

sensor, and the distance to the sea-ice underside, measured by the altimeter, and corrected for pitch and roll angles. Draft was then converted into ice thickness by using a sea ice density value of 834 kg m^{-3}, determined from sea-ice core samples.

During each haul, changes in ship speed, ice concentration (%) and irregularities were estimated visually by an observer on deck. GPS waypoints were recorded by the observer when the SUIT was deployed and hauled in, when it behaved abnormally, or when the environment changed, e.g. when the SUIT entered or exited the sea ice. The distance sampled over ground was estimated by multiplying the amount of time the SUIT was in the water (s) with the average speed in water (m s^{-1}). The distance sampled under ice was estimated in an analogue way for the period during which the SUIT was under ice. The distance sampled under ice was then expressed as percentage ice coverage of the total distance sampled over ground.

Gridded daily sea-ice concentrations for the Arctic Ocean derived from SSMIS satellite data using the algorithm specified by Spreen et al. (2008), were downloaded from the sea-ice portal of the University of Bremen (www.meereisportal.de).

A CTD probe with a carousel water sampler was used to collect environmental parameters from the water column near SUIT stations. The CTD (Seabird SBE9+) was equipped with a seafloor altimeter (Benthos), a fluorometer (Wetlabs FLRTD), a dissolved oxygen sensor (SBE 43) and a transmissiometer (Wetlabs C-Star). Details of the CTD sampling procedure were provided in Boetius et al. (2013). Data are available online in the PANGEA database (Rabe et al. 2012). Among all CTD stations, the closest in time and space to the SUIT stations were chosen (Table 1). Nutrients were analysed in an air-conditioned laboratory container with a continuous flow auto analyser (Technicon TRAACS 800) following the procedure described in Boetius et al. (2013). Measurements were made simultaneously on 4 channels: PO_4, Si, NO_2 + NO_3 together and NO_2 separately.

The depth of the upper mixed-layer was calculated from the ship CTD profiles after Shaw et al. (2009), who define the depth of the mixed layer as the depth of the profile where the density difference to the surface exceeds 20% of the density difference between 100 m and the surface.

The relative light intensity was calculated by dividing the solar elevation angle during the SUIT haul by the solar elevation angle at solar maximum for the corresponding location. Solar elevation angles were calculated using the National Oceanic and Atmospheric Administration's (NOAA) online solar calculator with latitude, longitude, date and time as inputs (www.esrl.noaa.gov/gmd/grad/solcalc/).

Table 1. Station table of Surface and Under Ice Trawls (SUITs) and the corresponding conductivity-temperature-depth (CTD) stations; NB is Nansen Basin and AB is Amundsen Basin

		SUIT					CTD			
Haul	Basin	Station code	Station date (mo/d/yr)	Latitude (°N)	Longitude (°E)	Bottom depth [m]	Station code	Station date	Latitude (°N)	Longitude (°E)
1	NB	204	8/5/2012	81.45	31.10	423	208	8/6/2012	81.46	31.04
2	NB	216	8/7/2012	82.48	30.03	3610	215	8/7/2012	82.49	30.00
3	NB	223	8/9/2012	84.07	30.43	4016	227	8/9/2012	84.02	31.22
4	NB	233	8/11/201	84.04	31.30	4011	227	8/9/2012	84.02	31.22
5	NB	248	8/16/201	83.93	75.50	3424	242	8/16/2012	83.90	76.07
6	NB	258	8/20/201	82.74	109.63	3575	254	8/20/2012	82.69	109.12
7	AB	276	8/25/201	83.07	129.12	4188	281	8/26/2012	82.89	129.82
8	AB	285	8/26/201	82.89	129.78	4174	281	8/26/2012	82.89	129.82
9	AB	321	9/4/2012	81.71	130.03	4011	324	9/4/2012	81.92	131.12
10	AB	331	9/5/2012	81.90	130.86	4036	324	9/4/2012	81.92	131.12
11	AB	333	9/6/2012	82.99	127.10	4187	333	9/6/2012	83.00	127.18
12	AB	345	9/9/2012	85.25	123.84	4354	342	9/9/2012	85.16	123.35
13	NB	397	9/29/201	84.17	17.92	4028	387	9/28/2012	84.37	17.52

4.2.3 Biological data

The catch was partially sorted on board. Polar cod and ctenophores were immediately extracted from samples. The remaining samples from the shrimp and the zooplankton nets were then each equally divided into 2 parts with a plankton splitter (Motoda 1959). From each sample, part of the material was immediately preserved in 4% formaldehyde/seawater solution for quantitative analysis. After the cruise, the quantitative samples were analysed for species composition and density at the Alfred Wegener Institute in Bremerhaven, Germany. Macrofauna (> 0.5 cm) densities were derived from the analysis of the shrimp net samples. Copepod densities were derived from analysis of the zooplankton net samples. With few exceptions, all animals were identified to the species level and, in copepod species, to developmental stage and sex. The adult copepods and their larger juvenile stages (the copepodites CV and CIV) were both considered in density calculations. Densities were calculated dividing the total number of animals per haul by the trawled area. The trawled area was calculated by multiplying the distance sampled in water, estimated from ADCP data (Flores et al. 2011), with the net width (0.5 m for the zooplankton net and 1.5 m for the shrimp net).

4.2.4 Data analysis

Scatter plots between each possible combination of 2 environmental variables were used to identify pairs of datasets with high colinearity (Zuur et al. 2007). In pairs with Spearman's rank correlation coefficients >0.7, only one variable was chosen for subsequent analysis based on the ecological relevance to the scientific objectives of this study and the comparability with other studies. From a total of 30 variables analysed, 12 were retained for further statistical analysis (Table 2). A Principal Component Analysis (PCA) (Mardia et al. 1979) was applied on the environmental dataset to reveal patterns in habitat typologies according to properties of the sea ice and the underlying water column.

In order to investigate patterns of diversity over the sampling area, 3 diversity indices were calculated for the whole biological dataset, as well as for sub-groupings derived from environmental data analysis: (1) species richness (the number of species observed at each station) (*S*); (2) the Shannon index (*H*) (Shannon 1948); and (3) Pielou's evenness index (*J*). Species accumulation curves were plotted to assess the impact of sampling effort on species diversity. To assess the statistical difference between sub-groupings, the Mann-Whitney-Wilcoxon test was performed on diversity indices and on cumulated species densities at stations (Mann and Whitney 1947).

Species density data were analysed using Non Metric Multidimensional Scaling (NMDS) (Kruskal 1964) based on a Bray-Curtis similarity matrix (Bray and Curtis 1957). NMDS is commonly regarded as the most robust unconstrained ordination method in community ecology (Minchin 1987). Square-root transformations and Wisconsin double standardization were applied to the data to gradually down-weight the dominant taxa. The performance of the NMDS was assessed with Shepard plots and stress values (Clarke and Warwick 2001; Legendre and Legendre 2012). ANOSIM (Clarke & Ainsworth 1993) was used to test for significant differences in the community structure between *a priori* defined groupings, e.g. ocean basins and sea-ice regimes.

Table 2. Environmental variables characterising sea-ice habitats

Variable (abbreviation)	Unit	Value range
Sampled ice coverage during SUIT hauls (Coverage)	%	0 to 100
Modal ice thickness (Thickness)	m	0 to 1.25
Standard deviation of ice thickness (SD)	m	0 to 0.88
Surface-water temperature (Temperature)	°C	-1.76 to -1.06
Surface-water salinity (Salinity)		29.38 to 32.87
Chlorophyll *a* concentration at the surface (Chla-surface)	mg m^{-3}	0.06 to 0.24
Chlorophyll *a* concentration at the depth of the chlorophyll *a* maximum (Chla)	mg m^{-3}	0.15 to 0.63

Silicate concentration at the depth of the chlorophyll *a* maximum (Si)	µmol l^{-1}	1.17 to 4.80
Combined nitrate + nitrite concentration at the depth of the chlorophyll *a* maximum	µmol l^{-1}	0.12 to 6.84
Phosphate concentration at the depth of the chlorophyll *a* maximum (PO_4)	µmol l^{-1}	0.20 to 0.55
Relative daylight intensity (Relative light)	-	0 to 0.91
Mixed layer depth (MLD)	m	9 to 25

The association of the community structure with the physical environment was evaluated with a Mantel test (Mantel 1967). The Mantel test relates 2 distance matrices, one from the biological and one from the environmental dataset, using Pearson correlation (Smouse et al. 1986). The bootstrapping procedure was applied with 999 iterations. Afterwards, the association of the community structure with all possible combinations of environmental variables was evaluated with the BioEnv analysis (Clarke and Ainsworth 1993). The BioEnv analysis estimates the subset of environmental variables that has the highest correlation with the biological data. The best subset was found using the Spearman's rank correlation coefficient between a Bray-Curtis similarity matrix of the species density data and a Euclidean dissimilarity matrix of the environmental variables.

For all analyses, R software Version 3.1.2 was used with the libraries vegan, FactoMineR, plyr and MASS (R Core Team 2015).

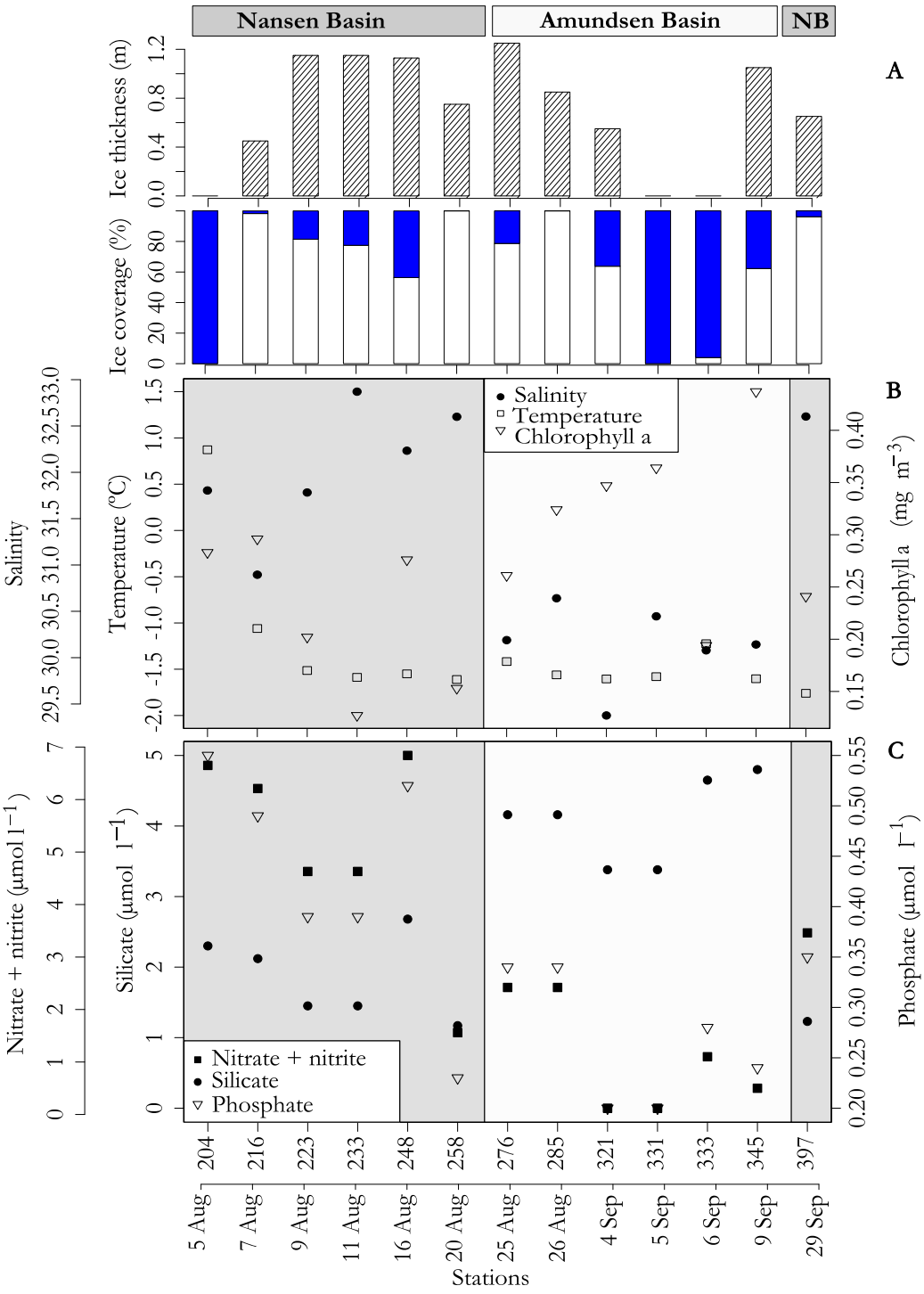

Figure 2. Environmental variables recorded at sampling stations. (A) sea-ice thickness (upper panel) and sea-ice coverage (lower panel). White portion of bars: percentage of sea-ice coverage at each station; grey portion of bars: remaining percentage of open water at each station. (B) Temperature, salinity and chlorophyll a concentration in the 0–2 m surface layer. (C) Nutrient concentrations at the depth of the chlorophyll *a* maximum. Nansen Basin stations are shown on dark grey background and Amundsen Basin stations on light grey background

4.3 Results

4.3.1 Environmental conditions

Across the Eurasian Basin 13 stations were sampled. Seven stations were located in the Nansen Basin, and 6 stations in the Amundsen Basin. Six of the Nansen Basin stations were sampled during the first half of August, and the Amundsen Basin stations during late August to mid-September.

The last station was sampled in the Nansen Basin on 29 September 2012 at the onset of winter (Table 1). All stations had water depths > 3400 m, except Stn 204 in the Nansen Basin, which was located in open waters over the continental slope at a depth of 423 m. Because oceanographic conditions at the slope station differed markedly from those in the rest of the sampling area, it was not included in the multivariate analysis, but is discussed separately. Besides Stn 204 in the Nansen Basin, 2 of the Amundsen Basin stations were nearly ice-free. At all other stations sea ice was present, ice concentrations ranging from 56 to 100% (Fig. 2A). Modal ice thickness ranged from 0.45 to 1.25 m. Within the deep-sea basins, surface temperatures ranged between –1.8 and –1°C. The surface temperature at the slope station 204 was 0.8°C (Fig. 2A).

In the PCA of physical variables, 63.6% of the variance in the dataset was explained on the first 2 axes (Fig. 3). The first axis explained 36.6% of the variance and was mainly driven by gradients of nutrients, salinity and sea-ice properties. Along this axis a clear distinction was evident between 2 environmental clusters that corresponded to the stations situated in the Nansen Basin and the Amundsen Basin, respectively.

Because the environmental gradients in our dataset represent not only spatial patterns, but also an often inseparable temporal signal over the 2 month sampling period, the clusters are referred to as spatio-temporal ‘regimes’, roughly corresponding to the 2 ocean basins. Sea-ice concentration and thickness gradients increased towards the Nansen Basin regime. The 2 open-water stations in the Amundsen Basin were clearly distinguished from all other stations, and were associated with the lowest sea-ice concentration and thickness values. Furthermore, the Nansen Basin regime was associated with high values of salinity and nitrate + nitrite, and low values of silicate and chlorophyll *a* concentrations in the 0–2 m surface layer. Conversely, the Amundsen Basin regime was associated with high chlorophyll *a* concentrations, high silicate concentrations, and low values of salinity and nitrate + nitrite. The second axis explained 26.94% of the variance and was mainly associated with gradients of temperature, chlorophyll *a* concentration at the chlorophyll maximum depth and relative light intensity. Along this axis, 2 stations were distinguished from the Nansen Basin regime cluster. Stn 216 had 100% ice coverage, high surface water temperatures and high chlorophyll *a* concentrations at the chlorophyll maximum depth (Fig. 2). Stn 397 had the lowest surface-water temperatures and lowest relative light intensity. The open-water station (Stn 333) was distinguished along the second axis from the cluster of the Amundsen Basin regime by high surface-water temperatures and high chlorophyll *a* concentrations at the chlorophyll maximum depth.

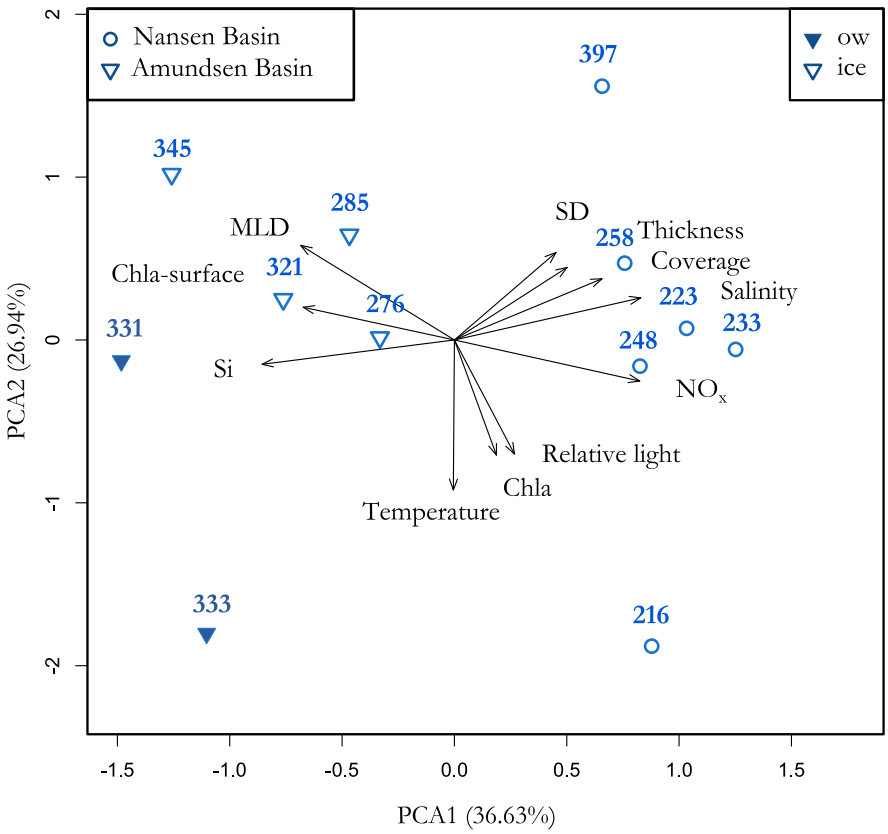

Figure 3. Principal Component Analysis of environmental variables at the sampling stations. Variable labels as defined in Table 2. Nansen Basin stations are represented by circles; Amundsen Basin stations are represented by triangles; ice: under-ice stations; ow: open-water stations. Percentage values on the axes represent the explained variance on the first (PCA 1) and second (PCA 2) dimensions.

When single environmental parameters were compared between the 2 regimes, surface salinity was significantly higher in the Nansen Basin regime (30–33) than in the Amundsen Basin regime (29–31) (Wilcoxon test: W = 0, *p*-value < 0.01) (Fig. 2B). The mixed layer depth (MLD) was shallowest at the first ice station (Stn 216; 9 m), which was situated at the ice edge. At the beginning of the cruise in the Nansen Basin regime, the MLD was around 15 m deep and increased with time, reaching up to 30 m in the Amundsen Basin regime. At the last station sampled in the Nansen Basin regime (Stn 397), the MLD was again shallower. High average values of nitrate + nitrite (4.8 µmol l^{-1}), and phosphate (0.4 µmol l^{-1}), and low values of silicate (1.7 µmol l^{-1}) characterised surface waters of the Nansen Basin regime (Fig. 2C). The opposite conditions were encountered in the Amundsen Basin regime, with low values of nitrate + nitrite (1.4 µmol l^{-1}), and phosphate (0.2 µmol l^{-1}), and high values of silicate (3.5 µmol l^{-1}). The differences between the 2 regimes in nutrient concentration were statistically significant (Wilcoxon test NO_x: W = 2, *p*-value < 0.01; PO_4: *W* = 4, *p*-value < 0.05; Si: *W* = 36, *p*-value < 0.01). At the station positioned over the Gakkel Ridge (Stn 258), all nutrients had very low concentrations. In the 2 open-water stations in the Amundsen Basin regime (Stns 331 and 333), nitrate + nitrite and phosphate were depleted in the surface waters. The averaged surface chlorophyll *a* concentration over the entire sampling area was 0.27 mg m^{-3}, ranging between 0.12 and 0.43 mg m^{-3}. The surface chlorophyll *a* concentrations were slightly higher in the Amundsen Basin regime than in the Nansen Basin regime (Wilcoxon test: *W*=30, *p*-value < 0.1). The highest value was found at Stn 345 in the Amundsen Basin regime (Fig. 2B).

4.3.2 Taxonomic composition

In total, 28 species belonging to 10 phyla were identified in our samples (Table 3). Copepods had the highest densities, accounting for 69% of the mean relative density over all stations, followed by amphipods with 28% (Fig. 4). The balance between copepods and amphipods, however, was markedly different between the 2 environmental regimes: in the Nansen Basin regime, copepods accounted for >82% of the mean density, whereas, in the Amundsen Basin regime, copepods contributed only 53%. Here the amphipods co-dominated the species composition, accounting for 43% of the mean density (Fig. 4). Appendicularians contributed 1.3% to the overall density, but this value was driven by extremely high densities at only 2 stations. Ctenophores had a high frequency of occurrence over the entire sampling area, but with highly variable densities. At 2 stations ctenophores heavily dominated the biomass of the samples. The other taxonomic groups accounted for <1% of the density.

Table 3. List of species with mean densities and frequency of occurrence over the sampling area; SD: standard deviation

Taxon	Mean density (ind. 100 m^{-2})	SD	Range	Frequency of occurrence
CTENOPHORA				
Beroe spp. Fabricius, 1780	2.11	4.75	0 – 15.79	0.85
Mertensia ovum Fabricius, 1780	0.19	0.38	0 – 1.35	0.85
MOLLUSCA				
Clione limacina Phipps, 1774	0.69	0.87	0 – 2.76	0.69
Limacina helicina Phipps, 1774	1.13	2.89	0 – 10.64	0.62
ANNELIDA				
Unidentified polychaete	<0.01	0.02		0.23
ARTHROPODA				
Apherusa glacialis Hansen, 1888	58.19	70.48	0.33 – 221.84	1.00
Eusirus holmi Hansen, 1887	0.19	0.22	0 – 0.62	0.69
Gammaracanthus loricatus Sabine, 1821	<0.01	0.01	0 – 0.04	0.15
Gammarus wilkitzkii Birula, 1897	0.10	0.18	0 – 0.71	0.92
Onisimus glacialis Sars, 1900	1.12	1.34	0 – 3.97	0.85
Onisimus nanseni Sars, 1900	0.35	0.57	0 – 1.66	0.46
Themisto abyssorum Boeck, 1871	0.75	1.07	0 – 3.13	0.69
Themisto libellula Lichtenstein, 1822	20.14	25.69	0.11 – 85.36	1
Euphausiacea				
Thysanoessa inermis Kroyer, 1861	0.03	0.07	0 – 0.25	0.31
Unidentified euphausid	<0.01	0.01	0 – 0.04	0.08
Copepoda				
Calanus finmarchicus Gunnerus, 1765	52.40	187.39	0 – 676.04	0.23
Calanus glacialis Jaschnov, 1955	641.27	1078.52	3.78 – 3052.83	1
Calanus hyperboreus Kroyer, 1838	104.08	174.46	0 – 494.62	0.85
**Pseudocalanus* spp. Boeck, 1872	24.60	33.29	0 – 109.22	0.92
Metridia longa Lubbock, 1854	172.47	619.49	0 – 2234.26	0.31
Paraeuchaeta glacialis Hansen, 1886	0.08	0.17	0 – 0.44	0.23
**Unidentified harpacticoid	0.32	0.69	0 – 1.96	0.31
**Tisbe spp.*	20.13	20.26	0 – 68.26	0.92
Ostracoda				
Boroecia borealis Sars, 1866	<0.01	0.01	0 – 0.04	0.08
CHAETOGNATHA				

Eukrohnia hamata Möbius, 1875	11.01	36.3	0 – 131.76	0.69
Parasagitta elegans Verrill, 1873	0.15	0.28	0 – 1.01	0.54
CHORDATA				
Oikopleura vanhoeffeni Lohmann, 1896	47.37	145.39	0 – 526.54	0.31
VERTEBRATA				
Boreogadus saida Lepechin, 1774	0.41	0.42	0 – 1.2	0.77

*values might be underestimated due to small size of the organisms relative to the mesh size used

4.3.3 Variability in species diversity, density and distribution

The highest number of species (20) was encountered at Stn 285 in the Amundsen Basin regime. Three other stations, 2 situated in the Nansen Basin regime and one in the Amundsen Basin regime, had 19 species each. The lowest species richness (*S*), Shannon diversity (*H*) and evenness (*J*) were encountered at the slope Stn (204), where only 8 species were found (Table 4.). The highest Shannon and evenness indices were encountered at an open-water station (Stn 331) in the Amundsen Basin regime. Species richness and Shannon diversity showed no significant difference between the 2 environmental regimes (Wilcoxon test *S*: $W = 29$, p-value > 0.1; *H*: $W = 32$, p-value < 0.1), while species evenness (*J*) was significantly higher in the Amundsen Basin than in the Nansen Basin (Wilcoxon test: $W = 34$, p-value < 0.05).

Table 4. Diversity indices calculated at each sampling station

Station code	Richness	Shannon	Evenness
204	8	0.04	0.02
216	13	1.30	0.51
223	17	1.68	0.59
233	13	0.74	0.29
248	19	1.21	0.41
258	19	1.16	0.40
276	18	1.61	0.56
285	20	1.43	0.48
321	16	1.78	0.64
331	19	2.02	0.69
333	18	1.52	0.53
345	18	1.76	0.61
397	17	0.45	0.16
Nansen Basin	24	0.94	0.34
Amundsen Basin	24	1.69	0.58
Total	28	1.28	0.45

Cumulated densities of all species ranged from 0.3 ind. m^{-2} at Stn 216 to 69 ind. m^{-2} at Stn 248 (Fig. 5). Overall densities were significantly higher in the Nansen Basin regime than in the Amundsen Basin regime (Wilcoxon test: $W = 6$, p-value < 0.05) (Fig. 5). This difference between the 2 environmental regimes remained relevant even when Stn 248, which had the highest abundance, was excluded from statistical analysis (Wilcoxon test: $W = 6$, p-value < 0.05). The most abundant species were the copepods *Calanus hyperboreus* and *C. glacialis*. The low density exception at Stn 216 was

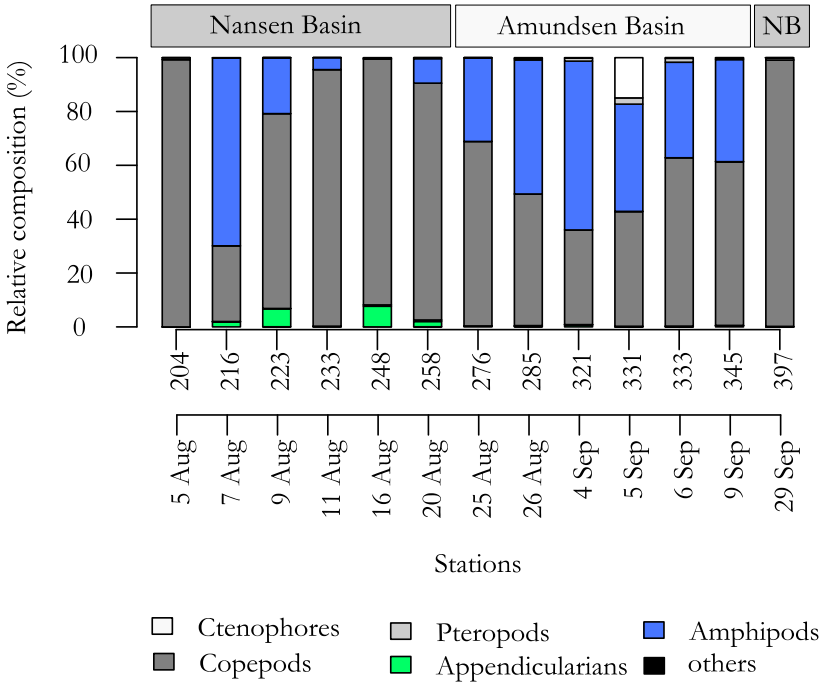

Figure 4. Relative density of taxonomic groups at the sampling stations (numbers on the x-axis). NB: Nansen Basin

caused by exceptionally low numbers of copepods. Stn 248 was unique in its species composition. Only at this station, did *C. finmarchichus* dominate numerically, and high densities of the appendicularian *Oikopleura vanhoeffeni* and the chaetognats *Eukrohnia hamata* and *Parasagitta elegans* were encountered. The biomass composition at this station was heavily dominated by ctenophores and tunicates. The last station (Stn 397) in the Nansen Basin regime differed from all other stations by a dominance of *Metridia longa* over all other copepod species. Among the amphipods, the ice-associated species *A. glacialis* was numerically dominant at all stations, except the 2 open-water stations (Stn 331 and 333) in the Amundsen Basin. Here, the amphipod *Themisto libellula* was most abundant, though also present throughout the sampling area. Polar cod was present over the survey area with few exceptions: the open water slope-station (Stn 204), a station (Stn 233) at which technical trawling problems probably affected the catch efficiency of the net for fast-swimming fish, and the early winter station (Stn 397). The density of polar cod ranged from 0.3 to 1.2 ind. 100 m^{-2}, with highest densities at Stn 285 and 345 in the Amundsen Basin regime. In contrast to nearby under-ice stations, polar cod densities at the 2 open-water stations in the Amundsen Basin (331 and 333) were close to zero.

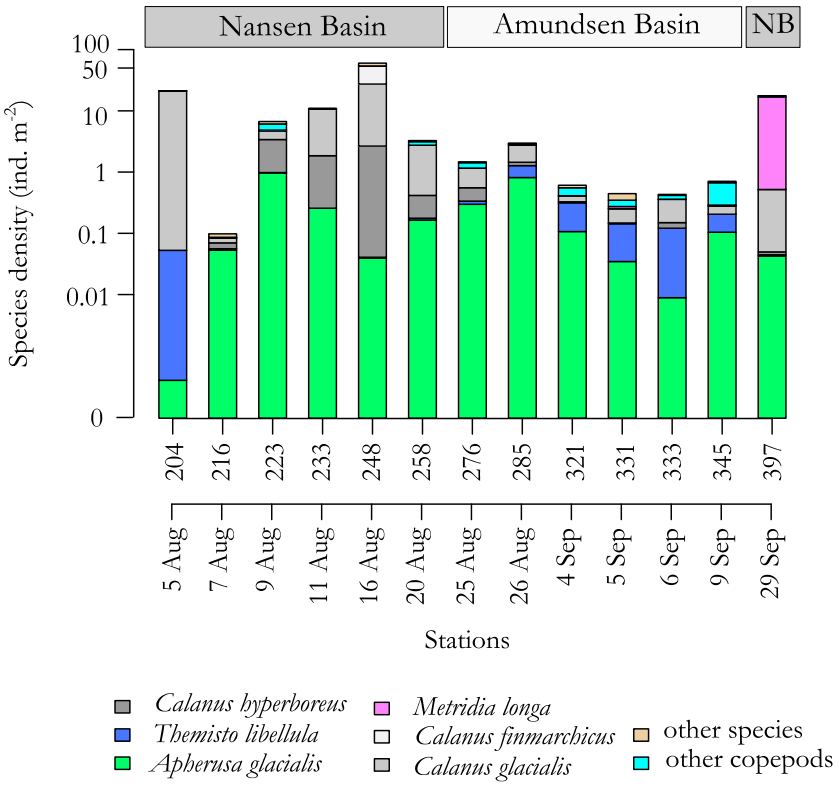

Figure 5. Species' cumulated density at the sampling stations (numbers on the x-axis). Densities are shown in log scale. Only dominant taxa are represented in the legend. NB: Nansen Basin

4.3.4 The association of environment and biota

The NMDS ordination of the community resembled the gradients of environmental variables of the PCA. In the NMDS ordination, stations grouped mainly according to the 2 environmental regimes of the Nansen and Amundsen Basins (ANOSIM: R = 0.38, p-value = 0.016) (Fig. 6). The copepods *C. hyperboreus* and *C. glacialis* and the amphipod *Eusirus holmii* were associated with the Nansen Basin regime. Polar cod and the amphipods *Onisimus nanseni* and *T. libellula* were associated with the Amundsen Basin regime. Stn 216 in the Nansen Basin grouped closer to the Amundsen Basin regime due to its high density of polar cod and *O. nanseni* and low copepod density. The amphipods *A. glacialis*, *G. wilkitzkii* and *Onisimus glacialis* grouped in the centre of the NMDS plot, indicating equal association with Nansen Basin regime and Amundsen Basin regime stations. The stations from the Amundsen Basin regime were more homogenous, presenting smaller distances between stations' positions in the NMDS ordination than those in the Nansen Basin regime. The 2 open-water stations, however, grouped clearly apart from the other stations in the Amundsen Basin regime. They were associated with the pelagic amphipod *T. libellula.*

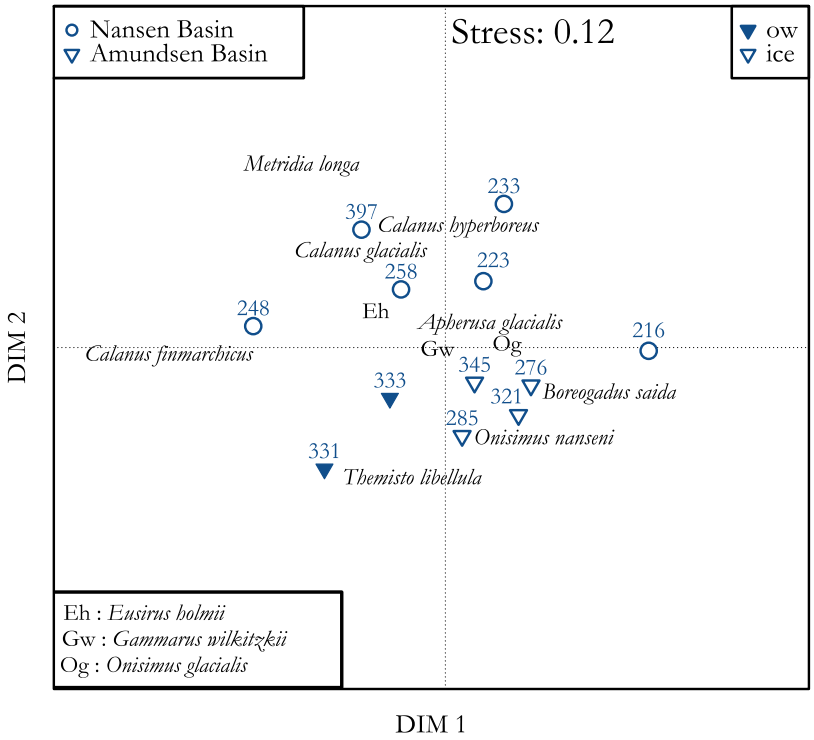

Figure 6. Non-Parametric Multi-Dimensional Scaling (NMDS) plot of the under-ice community structure. Station symbols (circles: Nansen Basin; triangles: Amundsen Basin; ow: open water; ice: under-ice) indicate the relative position of the community composition at each sampling location in the NMDS ordination. Species names indicate the relative position of polar cod and numerically dominant species in the NMDS ordination. DIM 1 & 2: NMDS dimension axes

The Mantel test and BioEnv analysis both showed a strong positive correlation between the environmental and biological datasets (Mantel test: Pearson correlation coefficient = 0.65, $p < 0.001$). In the BioEnv, nitrate + nitrite concentration in the surface layer had the highest correlation of a single environmental variable (0.60) with the variability of density-based species distribution (Table 5). The highest correlation (0.75) with the variability of density-based species distribution was achieved by a combination of nitrate + nitrite concentration, surface-water temperature and salinity, ice thickness, mixed-layer depth and surface chlorophyll *a* concentration (Table 5).

4.4 Discussion

4.4.1 Under-ice habitat properties

During summer 2012 the Arctic Ocean experienced a historical minimum sea-ice extent (Parkinson and Comiso 2013). Polarstern cruise ARK XXVII/3 sampled in the high central Arctic during that time, first across the Nansen Basin during early August, and then across the Amundsen Basin during late August–early September, almost reaching the North Pole at 87.87°N, 59.65°E. Daily sea-ice concentration data, from passive microwave satellite measurements, were >90% in the Nansen Basin during August and approximately 70% in the Amundsen Basin during September (data source: www.meereisportal.de University of Bremen). These values were in good agreement with the range of sea-ice concentrations determined from SUIT sensors. At only one station (Stn 216) did these observations differ from the SUIT sensor-derived ice coverage of 100%, whereas satellite-derived ice

coverage was 40%, averaged over 350 km^2, placing this station in the marginal ice zone. Our sampling area was mainly covered with FYI (>95%), with only small fractions of MYI (Boetius et al. 2013). In our ice-thickness profiles, modal ice thicknesses ranged from 0.45 to 1.25 m. In general, modal ice thickness was higher and more variable in the Nansen Basin regime than in the Amundsen Basin regime. Modal ice thicknesses from our SUIT hauls resembled the general pattern of airborne ice thickness measurements carried out in the survey area during ARK XXVII/3 (Lange & Hendricks pers. comm.). Electromagnetic airborne sea-ice thickness measurements confirm this range as mainly FYI (Haas et al. 2008). Therefore, our local sampling profiles largely resembled the general regional-scale situation in terms of sea ice concentration, age class and thickness.

Apart from sea-ice properties, our PCA results indicated that a variety of other environmental parameters structured our sampling stations into 2 regimes, which were broadly coherent with the 2 ocean basins sampled. These differences could in part be explained by seasonal processes, such as the melting of sea ice or the deepening of the mixed layer in the Amundsen Basin in late summer. We acknowledge the difficulty of disentangling spatial from temporal trends over our sampling area. We sampled within the pack ice, first in the Nansen Basin during early August, when a more compact sea-ice cover was present. At the end of August, while sampling in the Amundsen Basin, the pack ice began to loosen and ice was thinning, leaving locally large open-water areas, for example at Stns 331 and 333. Therefore, gradients of sea-ice properties were highly associated with the seasonal progression towards the end of summer, until the minimum sea-ice extent occurred on 16 September (Parkinson and Comiso 2013). Break-up of sea ice by early September likely allowed more light to penetrate into the water column. This favoured the increased chlorophyll *a* concentration we observed in the Amundsen Basin regime, locally depleting nutrients in the surface layer. This was demonstrated by the association of the open water stations with higher chlorophyll *a* concentrations (Fig. 2). Our last station sampled at the onset of winter in the Nansen Basin (Stn 397), however, had typical 'Nansen regime' values again, i.e. high salinity and low silicate concentrations at the depth of the chlorophyll *a* maximum (Fig. 2). This indicates that there was a strong regional component structuring the 2 regimes, besides some undoubtedly present seasonal trends.

The regional differences between the 2 regimes can largely be explained by water mass properties and circulation patterns. The Eurasian Basin is a permanently ice-covered basin with depths >4000 m. The Gakkel Ridge subdivides this basin into the nearly equally sized Nansen and Amundsen Basins. The Transpolar Drift current crosses both basins, transporting Polar Surface Water and sea ice from the Siberian shelf through the central Arctic Ocean towards the Fram Strait. A portion of the sea ice cover is recirculated within the anti-cyclonic Beaufort Gyre in the central and western Arctic Ocean, contributing to the formation of MYI (Rigor and Wallace 2004). A considerable portion of the marginal sea ice, however, is advected out of the Arctic Ocean through the Fram Strait (Kwok et al. 2004).

Nutrient-rich Atlantic Water is advected into the Eurasian Basin by 2 main branches: the Fram Strait branch and the Barents Sea branch. The Fram Strait branch of warm Atlantic Water is largely recirculated within the Nansen Basin, whereas the remaining Arctic Ocean basins, including the Amundsen Basin, are dominated by the Barents Sea branch (Rudels et al. 2013). This branch experiences water exchange by advection from the Laptev Sea continental margin, which is enriched in silicate (Bauch et al. 2014). Consequently, we found high silica and low nitrate + nitrite and phosphate concentrations in the Amundsen Basin regime, and the opposite situation in the Nansen Basin regime. Generally, Eurasian Basin regions with higher salinity indicate a higher Atlantic influence and can have surface nitrate concentrations in excess of 5 µmol l^{-1} even in summer (Codispoti et al. 2013). During our sampling, high salinities, high nitrate + nitrite, and high phosphate concentrations were present in the surface water of the Nansen Basin regime. Two stations, Stns 204 and 248, were exceptionally rich in nitrate + nitrite, with values at the chlorophyll maximum depth reaching up to 6.8 µmol l^{-1}. Stn 204 was situated on the Svalbard slope, near the inflow of Atlantic Water into the Arctic Ocean. Stn 248 was located near a convergent front formed by the Atlantic Water boundary current (Lalande et al. 2014). Nearby surface salinity and temperature profiles suggest freezing occurred prior to our arrival. The mixing due to haline convection during freezing

could have added nutrients to the mixed layer from below, explaining the higher nitrate + nitrite and chlorophyll *a* concentrations.

Table 5. Combinations of environmental variables selected by BioEnv analysis. Variables were ranked according to their correlation coefficients with the biological dataset. *r*: Spearman correlation coefficient; other abbreviations see Table 2

No of variables	Environmental variables	*r*
1	NO_x	0.60
11	NO_x + Temperature + Salinity + Thickness + SD + Coverage + MLD + Chla-surface + Chla + Relative light + Si	0.67
2	NO_x + Temperature	0.69
3	NO_x + Temperature + Salinity	0.69
10	NO_x + Temperature + Salinity + Thickness + SD + MLD + Chla-surface + Chla + Relative light + Si	0.69
5	NO_x + Temperature + Salinity + Thickness + MLD	0.72
9	NO_x + Temperature + Salinity + Thickness + SD + MLD + Chla-surface + Chla + Relative light	0.72
4	NO_x + Temperature + Salinity + Thickness	0.73
6	NO_x + Temperature + Salinity + Thickness + Chla-surface + Chla	0.73
7	NO_x + Temperature + Salinity + Thickness + SD + MLD + Chla	0.75
8	NO_x + Temperature + Salinity + Thickness + SD + MLD + Chla-surface + Chla	0.75

4.4.2 Under-ice community composition

We identified a total of 28 species in the upper 2 m of the mostly ice-covered water column. In terms of species numbers, amphipods and copepods equally dominated the community with 8 species each (Table 3). Our overall species richness was low compared to previous, geographically more extended studies on Arctic epipelagic fauna (Auel and Hagen 2002; Kosobokova and Hirche 2000; Kosobokova et al. 2011; Kosobokova and Hopcroft 2010). Such comparisons are, however, complicated by differences in net type, mesh sizes and sampled depth interval. Most Arctic zooplankton studies integrated the epipelagic community over at least the upper 50 m. The species composition from those studies is thus much more influenced by pelagic fauna, mostly dominated by the often deeper dwelling copepods (Kosobokova and Hirche 2000). Considering ice-associated species reported from the northern Barents Sea, Svalbard, Laptev Sea, or Greenland Sea (Hop et al. 2000; Werner and Arbizu 1999; Werner and Auel 2005; Werner and Gradinger 2002), our study found the highest species richness compared to any individual study. This might be due to a larger under-ice surface area of approximately 4 km^2 sampled per station in our study. Sampling effort in previous under-ice studies was spatially limited to single ice floes and was mainly performed by divers with pumps or estimates made from video surveys (Hop et al. 2011; Hop and Pavlova 2008; Werner and Gradinger 2002). These studies described ice-associated species related to ice concentration and topography (Hop et al. 2000; Werner and Gradinger 2002). But sea-ice properties vary greatly from one ice floe to another, as does the ice-associated fauna. Using the SUIT enabled us to integrate both floes with low faunal densities and floes with high faunal densities. This approach can representatively capture the meso-scale variability of the under-ice environment and facilitate large-scale density estimates if other error sources are minimal. Such error sources may be the low efficiency of the SUIT to sample

animals from crevices and wedges in the ice, or the ability of polar cod to avoid or escape the net. Reported habitat preferences and behaviour of the species sampled in this study indicate that underestimation due to preference of crevices may apply to single predatory species (e.g. *G. wilkitzkiii*), but not to those species clearly dominant in density in our and other under-ice studies, such as *A. glacialis* or *O. glacialis* (Gradinger et al. 2010; Gradinger and Bluhm 2004; Hop and Pavlova 2008). Videos from the SUIT camera show no indication of escape or avoidance of the net by polar cod, but the loss of fish through behavioural response cannot be assessed with certainty. The omnipresence of Polar cod in under-ice catches rather indicated that the sluggish lifestyle of this species (Gradinger and Bluhm 2004) may have worked in favour of sampling this species with a net that is relatively ineffective for catching fast-swimming fish.

We found higher densities of under-ice fauna in the Nansen Basin regime than in the Amundsen Basin regime. This pattern was mainly driven by high densities of large calanoid copepods. In the central Arctic Ocean, the mesozooplankton community in the surface 50 m is known to be dominated by *Calanus spp.* (Auel and Hagen 2002). The big herbivorous *C. hyperboreus* and *C. glacialis* dominated in our samples, contributing on average 9 and 38%, respectively, to the total density of the surface-layer community. *C. glacialis* largely dominated the surface community at the slope station (Stn 204), with 99%. The Atlantic water species *C. finmarchichus* appeared in high numbers at only one station in the Nansen Basin (Stn 248). Situated near a convergence front, a freezing event prior to our arrival is believed to have caused convective mixing and entrainment of nutrients from the subsurface Atlantic Water at that station (Lalande et al. 2014). More nutrients added to the euphotic layer could have favoured increased productivity and subsequent immigration of grazers from the deeper Atlantic Water layer.

Besides the 3 *Calanus* species, *M. longa* and the smaller copepods *Pseudocalanus* spp. are important contributors to the surface community, in both the eastern (Kosobokova et al. 2011) and the western Arctic Ocean (Matsuno et al. 2012). A switch in dominance occurred at our last station, at the onset of freezing. Coincident with the migration of *Calanus spp.* into deeper layers (Darnis and Fortier 2014; Fortier et al. 2001; Hirche 1997; Madsen et al. 2001), *M. longa* largely dominated the surface community (Fig. 5). This species is known to remain active year-round (Ashjian et al. 2003), but seldom occurs above depths <25 m (Fortier et al. 2001) (Table 3). Low competition, avoidance of visual predators, and food availability at the ice underside might explain their rise to the ice-water interface at Stn 397. Also active year-around are the small copepods of the genus *Pseudocalanus* (Fortier et al. 2001). They were widespread across the 2 basins without any seasonal or regional patterns. The year-round active copepods might represent a nutritious food source for polar cod and other predatory members of the under-ice community during Arctic winter.

Six species of ice-associated amphipods were found in our study area. Our results are in agreement with numerous under-ice studies in finding that *A. glacialis* dominates the ice-amphipod community in FYI-dominated environments (Werner and Auel 2005). Where MYI and ridges are more prevalent, *G. wilkitzkii* occurs in higher abundances (Beuchel and Lønne 2002; Lønne and Gulliksen 1991). Whereas *A. glacialis* is found mainly in the water just below the ice, *G. wilkitzkii* stays mainly attached to the under-side of ice and hides in ice cracks (Hop and Pavlova 2008; Hop et al. 2000). We found only few *G. wilkitzkii* individuals at each station, but consistently over both basins. Ice thickness was highly variable, with ridges at all ice-covered stations, even though we sampled mainly under FYI. Interestingly, we found young *G. wilkitzkii* juveniles just released from the brood pouch in September, whereas the release period was previously documented to occur between April and May in the northern Barents Sea (Poltermann et al. 2000). One female of the rare ice-amphipod *Gammaracanthus loricatus* and a few *Onisimus spp.* females were also observed carrying juveniles in their pouches. Such a difference in the timing of juvenile release could be related to sea-ice seasonal dynamics and consequently food availability. Near Svalbard and in the Barents Sea, ice melting starts earlier. The spring bloom usually occurs in April, followed by high abundances of *Calanus* spp. This spring to summer succession in the food chain is regarded as an important factor for releasing the amphipods' young (Dalpadado 2002).

Swarms of the pelagic amphipod *T. libellula* have been reported to rise under landfast-ice (Gulliksen 1984). We noticed high numbers of *T. libellula* juveniles under the ice in the Amundsen Basin regime.

At 2 locations, we observed a distinct change in community structure between nearby open-water and under-ice sampling locations. The difference in ice coverage was accurately mirrored by a clear dominance of the ice-associated amphipod *A. glacialis* in ice-covered waters, versus a dominance of the pelagic amphipod *T. libellula* in the surface community of ice-free waters. This pattern suggests that habitat partitioning between sympagic and pelagic species is abrupt, creating a small-scale pattern in the surface-layer community according to sea-ice conditions.

4.4.3 Two environmental regimes

In terms of species' presence, we found similar under-ice community compositions in the Nansen Basin and Amundsen Basin regimes. When the relative community structure was considered, however, gradual changes in community composition were ordered according to the 2 environmental regimes (Fig. 6). The Nansen regime was characterised by heavier sea ice, which can be considered as a compact, stable habitat. Both ice thickness and its standard deviation (an expression of sea-ice underside roughness) were correlated with the under-ice community structure. Around Svalbard, ice thickness was found to be the key variable impacting ice-associated faunal variability (Hop and Pavlova 2008).

Copepods (*Calanus* spp.) and the large ice-associated amphipod *E. holmii* were associated with the Nansen Basin regime (Fig. 6). In the water column, low chlorophyll *a* concentrations under a compact ice cover may indicate limited food availability due to light limitation, attracting copepods capable of under-ice grazing to the ice-water interface layer (Runge and Ingram 1991). In the more open Amundsen Basin regime, under-ice feeding was probably less important for *Calanus* spp., causing them to disperse in the water column. The Amundsen Basin was sampled 2 weeks after the Nansen Basin and was characterised by autumn conditions with loose sea-ice coverage, indicating a decaying sea-ice habitat with low nutrient concentrations but with higher chlorophyll *a* concentrations in the water column. Under-ice faunal densities in the Amundsen Basin regime were lower, but had higher diversity than in the Nansen Basin regime (Table 4). The density of adult copepods in the surface layer was considerably lower than in the Nansen Basin regime. There were, however, high numbers of *Calanus* spp., stages CI to CIII, present. These stages were not included in our density calculations, because the numbers caught did not represent true abundances due to our 0.3 mm mesh zooplankton net. These findings agree with the general patterns of seasonal vertical migration of *Calanus* spp. (Darnis and Fortier 2014). Migration of *Calanus* spp. starts in August in the Amundsen Gulf (Beauford Sea) (Darnis and Fortier 2014) and Fram Strait (Auel et al. 2003). At the end of summer, most copepods and their smaller stages have stored lipids, accounting for up to 50% of their body weight (Scott et al. 1999), to prepare for diapause (Auel et al. 2003). Only the juvenile stages CI to CIII of C. hyperboreus were noted to remain in the surface layer (Darnis and Fortier 2014). The progressive reduction of copepod numbers in our samples suggests that emigration from the surface layer might have gradually started at the end of August. With the decreased copepod density in the Amundsen Basin regime, the amphipods numerically co-dominated the under-ice community. Particularly, the carnivorous amphipod *T. libellula* was more abundant in the Amundsen Basin regime than in the Nansen Basin regime (Fig. 5). As a preferred prey of *T. libellula* (Auel et al. 2002; Noyon et al. 2009), the small copepodites could have attracted *T. libellula* to the surface layer. Overall, the Amundsen Basin regime appeared to support more carnivorous fauna, with a higher proportion of larger animals, such as *T. libellula*, *O. nanseni*, and polar cod. Higher sinking fluxes of detritus in the Amundsen Basin caused by melting sea ice (Lalande et al. 2014) indicate that additional food became available in the ice-water interface layer for opportunistic feeders, such as the amphipods *O. glacialis*, *O. nanseni* and *G. wilkitzkii* (Werner 1997).

A high degree of heterotrophy in the food web is supported for the entire Eurasian Basin by a tentative comparison of primary production versus food demand of the dominant grazers during our sampling period. In ice-covered waters of the Eurasian Basin, the integrated (median) primary production rate measured at the time of our sampling was 0.7 mg C m^{-2} d^{-1} in sea ice, and 18 mg C m^{-2} d^{-1} in the water column (Fernández-Méndez 2014). Experimentally derived mean ingestion rates range between 2.8 and 8.4 µg C $ind.^{-1}$ d^{-1} for *C. hyperboreus*, and between 6.0 and 18.0 µg C $ind.^{-1}$ d^{-1} for *C. glacialis* (Olli et al. 2007). For the herbivorous amphipod *A. glacialis*, the mean ingestion rate is

about 13 µg C ind.$^{-1}$ d^{-1} (Werner 1997). Based on the mean densities of these species found in the ice-water interface layer (Table 3), their cumulative mean carbon demand ranged from about 0.1 to 0.2 mg C m^{-2} d^{-1}. Only a fraction of the carbon produced by ice algae, however, is available for grazers at the ice underside. This implies that the production of ice algae could have barely matched the food demand of under-ice grazers during the sampling period. Locally, however, they may have benefited from feeding on biomass-rich algal aggregates floating under the sea ice (Fernández-Méndez et al. 2014). In the water column, 0-200 m integrated densities of *C. hyperboreus* and *C. glacialis* derived from multinet sampling during the same cruise (B. Niehoff & J. Ehrlich unpubl. data) imply a mean carbon demand range of 9.5 to 28.4 mg C m^{-2} d^{-1} based on copepod ingestion rates according to Olli et al. (2007). In sea ice and the water column combined, a nearly 1:1 ratio of primary production versus grazer food demand could have contributed significantly to the low overall chlorophyll *a* concentrations in sea ice and water during our sampling period. It further indicates that peak production levels generating zooplankton growth had passed at most sampling locations before our sampling. This scenario agrees well with the mass export of algal biomass to the sea floor observed by Boetius et al. (2013) at several ice-sampling stations during our cruise, suggesting a major production peak in the investigation area prior to our sampling. At the time of sampling, the increased populations of zooplankton and under-ice fauna resulting from this bloom relied more on heterotrophic carbon sources than on autotrophic production.

4.5 Conclusions

This first large-scale survey of under-ice fauna in the Arctic deep-sea shows that a variety of species, including amphipods and polar cod, are present virtually everywhere in the Eurasian Basin, in spite of its presumed low productivity. Although under-ice faunal densities were relatively low compared to sea-ice habitats on the shelf, the omnipresence of animals in the vast deep-sea basins highlights the large-scale importance of the under-ice habitat in the Arctic Ocean.

Differences in sea-ice properties and nutrient concentrations were the key factors separating the sampled environments into the Nansen and Amundsen Basin regimes. The separation of these 2 regimes had both a seasonal and a strong regional component related to water-mass distribution, ice drift and current patterns. The under-ice community structure followed this environmental gradient, indicating a decisive role of both sea-ice and water-column characteristics for the distribution of species in the surface layer. Abrupt changes in the dominance of ice-associated amphipods at ice-covered stations versus pelagic amphipods at nearby ice-free stations emphasised a distinct influence of sea ice on small-scale patterns in the surface-layer community.

With respect to the decades of sea-ice decline before 2012, it is likely that the situation encountered in our study reflected a snapshot of a system in transition. Whether the past central Arctic under-ice community was more or less abundant, or differed in diversity and composition, is impossible to assess in the absence of appropriate baseline data. In the future, the central Arctic under-ice community will be exposed to continuing changes, including a further shortening of the ice-covered season, the complete disappearance of multi-year ice and changes in stratification and nutrient regimes. Due to their position around the North Pole, the central Arctic basins may constitute a critical refuge for the specifically ice-adapted biota of the Arctic Ocean for several decades. Whether or not the central Arctic Ocean can fulfil this function will depend on the many direct and indirect changes affecting the Arctic pack-ice and the resilience of individual ice-associated species. The subtle response of the under-ice community to many of these changing parameters suggests that changes already have impacted Arctic under-ice communities and will continue to do so in the future. Monitoring the course of changes in Arctic biodiversity and ecosystem structure will be key requirements for successful resource and conservation management in an Arctic Ocean in transition.

Acknowledgements

We thank Captain Uwe Pahl and the crew of RV Polarstern expedition IceArc (ARK XXVII-3) for their excellent support with work at sea. We thank Jan Andries van Franeker (IMARES) for kindly providing the Surface and Under Ice Trawl (SUIT) and Michiel van Dorssen for technical support with work at sea. We thank Karel Bakker for kindly providing the nutrient data. We thank Ilka Peeken for chlorophyll a measurements used for the calibration of under-ice fluorescence data. SUIT was developed by IMARES with support from the Netherlands Ministry of EZ (project WOT-04-009-036) and the Netherlands Polar Program (project ALW 866.13.009). This study is part of the Helmholtz Association Young Investigators Group Iceflux: Ice-ecosystem carbon flux in polar oceans (VH-NG-800). We thank the three anonymous reviewers for their helpful suggestions and comments that contributed significantly to the improvement of the manuscript.

References

Arctic Climate Impact Assessment, ACIA (2004) Impacts of a Warming Arctic. Cambridge University Press, Cambridge, UK

Arndt CE, Pavlova O (2005) Origin and fate of ice fauna in the Fram Strait and Svalbard area. Mar Ecol Progr Ser 301:55-66. doi:10.3354/meps301055

Arrigo KR, van Dijken G, Pabi S (2008) Impact of a shrinking Arctic ice cover on marine primary production. Geophys Res Lett 35. doi:10.1029/2008GL035028

Arrigo KR, van Dijken GL (2011) Secular trends in Arctic Ocean net primary production. J Geophys Res-Oceans 116. doi:10.1029/2011JC007151

Ashjian CJ, Campbell RG, Welch HE, Butler M, Van Keuren D (2003) Annual cycle in abundance, distribution, and size in relation to hydrography of important copepod species in the western Arctic Ocean. Deep-Sea Res Pt I 50:1235-1261. doi:10.1016/S0967-0637(03)00129-8

Auel H, Hagen W (2002) Mesozooplankton community structure, abundance and biomass in the central Arctic Ocean. Mar Biol 140:1013-1021. doi:10.1007/s00227-001-0775-4

Auel H, Harjes M, da Rocha R, Stübing D, Hagen W (2002) Lipid biomarkers indicate different ecological niches and trophic relationships of the Arctic hyperiid amphipods *Themisto abyssorum* and *T. libellula*. Polar Biol 25:374-383. doi:10.1007/s00300-001-0354-7

Auel H, Klages M, Werner I (2003) Respiration and lipid content of the Arctic copepod *Calanus hyperboreus* overwintering 1 m above the seafloor at 2,300 m water depth in the Fram Strait. Mar Biol 143:275-282. doi:10.1007/s00227-003-1061-4

Bauch D, Torres-Valdes S, Polyakov I, Novikhin A, Dmitrenko I, McKay J, Mix A (2014) Halocline water modification and along slope advection at the Laptev Sea continental margin. Ocean Science 10:141-154

Benoit D, Simard Y, Gagné J, Geoffroy M, Fortier L (2010) From polar night to midnight sun: photoperiod, seal predation, and the diel vertical migrations of polar cod (*Boreogadus saida*) under landfast ice in the Arctic Ocean. Polar Biol 33:1505-1520. doi:10.1007/s00300-010-0840-x

Beuchel F, Lønne OJ (2002) Population dynamics of the sympagic amphipods *Gammarus wilkitzkii* and *Apherusa glacialis* in sea ice north of Svalbard. Polar Biol 25:241-250. doi:10.1007/s00300-001-0329-8

Boetius A et al. (2013) Export of Algal Biomass from the Melting Arctic Sea Ice. Science 339:1430-1432. doi:10.1126/science.1231346

Bradstreet MSW, Cross WE (1982) Trophic Relationships At High Arctic Ice Edges. Arctic 35:1-12

Bray JR, Curtis JT (1957) An ordination of the upland forest communities of southern Wisconsin. Ecol Monogr 27:325-349

Budge SM, Wooller MJ, Springer AM, Iverson SJ, McRoy CP, Divoky GJ (2008) Tracing carbon flow in an arctic marine food web using fatty acid-stable isotope analysis. Oecologia 157:117-129. doi:10.1007/s00442-008-1053-7

Clarke K, Ainsworth M (1993) A method of linking multivariate community structure to environmental variables. Mar Ecol Progr Ser 92:205-205

Clarke KR, Warwick RM (2001) Change in marine communities: an approach to statistical analysis and interpretation, 2nd edition. PRIMER-E Limited, Plymouth Marine Laboratory, UK

Codispoti LA et al. (2013) Synthesis of primary production in the Arctic Ocean: III. Nitrate and phosphate based estimates of net community production. Prog Oceanogr 110:126-150. doi:10.1016/j.pocean.2012.11.006

Dalpadado P (2002) Inter-specific variations in distribution, abundance and possible life-cycle patterns of *Themisto spp*. (Amphipoda) in the Barents Sea. Polar Biol 25:656-666. doi:DOI 10.1007/s00300-002-0390-y

Darnis G, Fortier L (2014) Temperature, food and the seasonal vertical migration of key arctic copepods in the thermally stratified Amundsen Gulf (Beaufort Sea, Arctic Ocean). J Plankton Res 36:1092-1108. doi:10.1093/plankt/fbu035

Falk-Petersen S, Mayzaud P, Kattner G, Sargent J (2009) Lipids and life strategy of Arctic Calanus. Mar Biol Res 5:18-39. doi:10.1080/17451000802512267

Fernández-Méndez M (2014) Primary productivity in Arctic sea ice and ocean. PhD dissertation. University of Bremen, Bremen, Germany

Fernández-Méndez M, Wenzhöfer F, Peeken I, Sørensen HL, Glud RN, Boetius A (2014) Composition, Buoyancy Regulation and Fate of Ice Algal Aggregates in the Central Arctic Ocean. Plos One 9:e107452

Fetterer F, Knowles K, Meier W, Savoie M (2002, updated daily) Sea Ice Index. Monthly Mean Sea Ice Extent. Boulder, Colorado USA: National Snow and Ice Data Center. doi:10.7265/N5QJ7F7W

Finley KJ, Gibb EJ (1982) Summer diet of the narwhal (*Monodon monoceros*) in Pond Inlet, northern Baffin Island. Canadian Journal of Zoology 60:3353-3363. doi:10.1139/z82-424

Flores H et al. (2011) Macrofauna under sea ice and in the open surface layer of the Lazarev Sea, Southern Ocean. Deep-Sea Res Pt II 58:1948-1961

Flores H et al. (2012) The Association of Antarctic Krill *Euphausia superba* with the Under-Ice Habitat. PLoS ONE 7. doi:10.1371/journal.pone.0031775

Fofonoff N (1985) Physical properties of seawater: A new salinity scale and equation of state for seawater. J Geophys Res-Oceans 90:3332-3342

Fortier M, Fortier L, Hattori H, Saito H, Legendre L (2001) Visual predators and the diel vertical migration of copepods under Arctic sea ice during the midnight sun. J Plankton Res 23:1263-1278. doi:10.1093/plankt/23.11.1263

Gosselin M, Levasseur M, Wheeler PA, Horner RA, Booth BC (1997) New measurements of phytoplankton and ice algal production in the Arctic Ocean. Deep-Sea Res Pt II 44:1623-1644. doi:10.1016/S0967-0645(97)00054-4

Gradinger R, Bluhm B, Iken K (2010) Arctic sea-ice ridges—Safe heavens for sea-ice fauna during periods of extreme ice melt? Deep-Sea Res Pt II 57:86-95. doi:10.1016/j.dsr2.2009.08.008

Gradinger RR, Bluhm BA (2004) In-situ observations on the distribution and behavior of amphipods and Arctic cod (*Boreogadus saida*) under the sea ice of the High Arctic Canada Basin. Polar Biol 27:595-603. doi:10.1007/s00300-004-0630-4

Gulliksen B (1984) Under-ice fauna from Svalbard waters. Sarsia 69:17-23. doi:10.1080/00364827.1984.10420585

Haas C, Pfaffling A, Hendricks S, Rabenstein L, Etienne J-L, Rigor I (2008) Reduced ice thickness in Arctic Transpolar Drift favors rapid ice retreat. Geophys Res Lett 35:L17501. doi:10.1029/2008GL034457

Harter BB, Elliott KH, Divoky GJ, Davoren GK (2013) Arctic Cod (*Boreogadus saida*) as Prey: Fish Length-Energetics Relationships in the Beaufort Sea and Hudson Bay. Arctic 66:191–196

Hirche HJ (1997) Life cycle of the copepod *Calanus hyperboreus* in the Greenland Sea. Mar Biol 128:607-618. doi:10.1007/s002270050127

Hop H, Gjøsæter H (2013) Polar cod (*Boreogadus saida*) and capelin (*Mallotus villosus*) as key species in marine food webs of the Arctic and the Barents Sea. Mar Biol Res 9:878-894. doi:10.1080/17451000.2013.775458

Hop H, Mundy C, Gosselin M, Rossnagel A, Barber D (2011) Zooplankton boom and ice amphipod bust below melting sea ice in the Amundsen Gulf, Arctic Canada. Polar Biol 34:1947-1958. doi:10.1007/s00300-011-0991-4

Hop H, Pavlova O (2008) Distribution and biomass transport of ice amphipods in drifting sea ice around Svalbard. Deep-Sea Res Pt II 55:2292-2307. doi:10.1016/j.dsr2.2008.05.023

Hop H, Poltermann M, Lonne OJ, Falk-Petersen S, Korsnes R, Budgell WP (2000) Ice amphipod distribution relative to ice density and under-ice topography in the northern Barents Sea. Polar Biol 23:357-367. doi:10.1007/s003000050456

Hopcroft RR, Clarke C, Nelson RJ, Raskoff KA (2005) Zooplankton communities of the Arctic's Canada Basin: the contribution by smaller taxa. Polar Biol 28:198-206. doi:10.1007/s00300-004-0680-7

Hunt BPV et al. (2014) Zooplankton community structure and dynamics in the Arctic Canada Basin during a period of intense environmental change (2004 to 2009). J Geophys Res-Oceans 119:2518-2538. doi:10.1002/2013jc009156

Johannessen OM et al. (2004) Arctic climate change: observed and modelled temperature and sea-ice variability. Tellus A 56:328-341. doi:10.1111/j.1600-0870.2004.00060.x

Kosobokova K, Hirche H-J (2009) Biomass of zooplankton in the eastern Arctic Ocean – A base line study. Prog Oceanogr 82:265-280. doi:10.1016/j.pocean.2009.07.006

Kosobokova K, Hirche HJ (2000) Zooplankton distribution across the Lomonosov Ridge, Arctic Ocean: species inventory, biomass and vertical structure. Deep-Sea Res Pt I 47:2029-2060. doi:10.1016/S0967-0637(00)00015-7

Kosobokova K, Hopcroft R, Hirche H-J (2011) Patterns of zooplankton diversity through the depths of the Arctic's central basins. Mar Biodiv 41:29-50. doi:10.1007/s12526-010-0057-9

Kosobokova KN, Hopcroft RR (2010) Diversity and vertical distribution of mesozooplankton in the Arctic's Canada Basin. Deep-Sea Res Pt II 57:96-110. doi:10.1016/j.dsr2.2009.08.009

Kruskal JB (1964) Nonmetric multidimensional scaling: A numerical method. Psychometrika 29:115-129. doi:10.1007/bf02289694

Kwok R, Cunningham GF, Pang SS (2004) Fram Strait sea ice outflow. J Geophys Res-Oceans 109:C01009. doi:10.1029/2003jc001785

Kwok R, Rothrock DA (2009) Decline in Arctic sea ice thickness from submarine and ICESat records: 1958-2008. Geophys Res Lett 36:L15501. doi:10.1029/2009gl039035

Laidre KL, Heide-Jørgensen MP (2005) Arctic sea ice trends and narwhal vulnerability. Biological Conservation 121:509-517

Lalande C, Nöthig EM, Somavilla R, Bauerfeind E, Shevchenko V, Okolodkov Y (2014) Variability in under-ice export fluxes of biogenic matter in the Arctic Ocean. Global Biogeochem Cy 28:571-583. doi:10.1002/2013GB004735

Legendre P, Legendre L (2012) Numerical ecology. vol 24. Third edition edn. Elsevier

Lønne OJ, Gulliksen B (1991) Sympagic macro-fauna from multiyear sea-ice near Svalbard. Polar Biol 11:471-477. doi:10.1007/bf00233082

Madsen SD, Nielsen TG, Hansen BW (2001) Annual population development and production by *Calanus finmarchicus*, *C. glacialis* and *C. hyperboreus* in Disko Bay, western Greenland. Mar Biol 139:75-93. doi:10.1007/s002270100552

Mann HB, Whitney DR (1947) On a test of whether one of two random variables is stochastically larger than the other. Ann Math Stat:50-60

Mantel N (1967) The detection of disease clustering and a generalized regression approach. Cancer research 27:209-220

Mardia KV, Kent J, Bibby J (1979) Multivariate analysis (probability and mathematical statistics). London: Academic

Markus T, Stroeve JC, Miller J (2009) Recent changes in Arctic sea ice melt onset, freezeup, and melt season length. J Geophys Res-Oceans 114:C12024. doi:10.1029/2009jc005436

Maslanik J, Stroeve J, Fowler C, Emery W (2011) Distribution and trends in Arctic sea ice age through spring 2011. Geophys Res Lett 38:L13502. doi:10.1029/2011gl047735

Matley J, Fisk A, Dick T (2013) The foraging ecology of Arctic cod (*Boreogadus saida*) during open water (July–August) in Allen Bay, Arctic Canada. Mar Biol 160:2993-3004. doi:10.1007/s00227-013-2289-2

Matsuno K, Yamaguchi A, Shimada K, Imai I (2012) Horizontal distribution of calanoid copepods in the western Arctic Ocean during the summer of 2008. Polar Science 6:105-119. doi:10.1016/j.polar.2012.01.002

Mehlum F, Gabrielsen GW (1993) The diet of high-arctic seabirds in coastal and ice-covered, pelagic areas near the Svalbard archipelago. Polar Res 12:1-20. doi:10.1111/j.1751-8369.1993.tb00417.x

Melnikov I, Kulikov A (1980) The cryopelagic fauna of the central Arctic basin. Biology of the central Arctic Basin Nauka, Moscow:97-111

Minchin PR (1987) An evaluation of the relative robustness of techniques for ecological ordination. In: Prentice IC, van der Maarel E (eds) Theory and models in vegetation science. Springer, pp 89-107

Motoda S (1959) Devices of simple plankton apparatus. Memoirs of the Faculty of Fisheries Hokkaido University 7:73-94

Noyon M, Gasparini S, Mayzaud P (2009) Feeding of *Themisto libellula* (Amphipoda Crustacea) on natural copepods assemblages in an Arctic fjord (Kongsfjorden, Svalbard). Polar Biol 32:1559-1570. doi:10.1007/s00300-009-0655-9

Olli K et al. (2007) The fate of production in the central Arctic Ocean – top–down regulation by zooplankton expatriates? Prog Oceanogr 72:84-113. doi:10.1016/j.pocean.2006.08.002

Overland JE, Wang M (2013) When will the summer Arctic be nearly sea ice free? Geophys Res Lett 40:2097-2101

Parkinson CL, Comiso JC (2013) On the 2012 record low Arctic sea ice cover: Combined impact of preconditioning and an August storm. Geophys Res Lett 40:1356-1361. doi:10.1002/grl.50349

Poltermann M, Hop H, Falk-Petersen S (2000) Life under Arctic sea ice - reproduction strategies of two sympagic (ice-associated) amphipod species, *Gammarus wilkitzkii* and *Apherusa glacialis*. Mar Biol 136:913-920. doi:10.1007/s002270000307

Polyakov IV et al. (2005) One more step toward a warmer Arctic. Geophys Res Lett 32:L17605. doi:10.1029/2005gl023740

Pomerleau C, Nelson RJ, Hunt BPV, Sastri AR, Williams WJ (2014) Spatial patterns in zooplankton communities and stable isotope ratios (δ13C and δ15N) in relation to oceanographic conditions in the sub-Arctic Pacific and western Arctic regions during the summer of 2008. J Plankton Res 36:757-775. doi:10.1093/plankt/fbt129

R Core Team (2015) R: A language and environment for statistical computing. R Foundation for Statistical Computing, Vienna, Austria URL http://www.R-project.org/

Rabe B, Wisotzki A, Rettig S, Somavilla Cabrillo R, Sander H (2012) Physical oceanography during POLARSTERN cruise ARK-XXVII/3 (IceArc). *Alfred Wegener Institute, Helmholtz Center for Polar and Marine Research, Bremerhaven*. doi:10.1594/PANGAEA.802904

Rigor IG, Wallace JM (2004) Variations in the age of Arctic sea-ice and summer sea-ice extent. Geophys Res Lett 31. doi:10.1029/2004gl019492

Rudels B, Schauer U, Björk G, Korhonen M, Pisarev S, Rabe B, Wisotzki A (2013) Observations of water masses and circulation in the Eurasian Basin of the Arctic Ocean from the 1990s to the late 2000s. Ocean Science Discussions 9:147-169. doi:10.5194/os-9-147-2013

Runge JA, Ingram RG (1991) Under-ice feeding and diel migration by the planktonic copepods *Calanus glacialis* and *Pseudocalanus minutus* in relation to the ice algal production cycle in southeastern Hudson Bay, Canada. Mar Biol 108:217-225. doi:10.1007/bf01344336

Scott CL, Falk-Petersen S, Sargent JR, Hop H, Lønne OJ, Poltermann M (1999) Lipids and trophic interactions of ice fauna and pelagic zooplankton in the marginal ice zone of the Barents Sea. Polar Biol 21:65-70. doi:10.1007/s003000050335

Shannon C (1948) A mathematical theory of communication. Bell Sys Tech J 27:379-423

Shaw W, Stanton T, McPhee M, Morison J, Martinson D (2009) Role of the upper ocean in the energy budget of Arctic sea ice during SHEBA. J Geophys Res-Oceans 114. doi:10.1029/2008JC004991

Shimada K et al. (2006) Pacific Ocean inflow: Influence on catastrophic reduction of sea ice cover in the Arctic Ocean. Geophys Res Lett 33. doi:10.1029/2005gl025624

Smouse PE, Long JC, Sokal RR (1986) Multiple Regression and Correlation Extensions of the Mantel Test of Matrix Correspondence. Systematic Zoology 35:627-632. doi:10.2307/2413122

Søreide JE, Carroll ML, Hop H, Ambrose WG, Hegseth EN, Falk-Petersen S (2013) Sympagic-pelagic-benthic coupling in Arctic and Atlantic waters around Svalbard revealed by stable isotopic and fatty acid tracers. Mar Biol Res 9:831-850. doi:10.1080/17451000.2013.775457

Søreide JE, Hop H, Carroll ML, Falk-Petersen S, Hegseth EN (2006) Seasonal food web structures and sympagic–pelagic coupling in the European Arctic revealed by stable isotopes and a two-source food web model. Prog Oceanogr 71:59-87. doi:10.1016/j.pocean.2006.06.001

Spreen G, Kaleschke L, Heygster G (2008) Sea ice remote sensing using AMSR-E 89-GHz channels. J Geophys Res-Oceans 113:C02S03. doi:10.1029/2005jc003384

Stroeve J, Holland MM, Meier W, Scambos T, Serreze M (2007) Arctic sea ice decline: Faster than forecast. Geophys Res Lett 34:L09501. doi:10.1029/2007gl029703

Stroeve J, Serreze M, Holland M, Kay J, Malanik J, Barrett A (2012) The Arctic's rapidly shrinking sea ice cover: a research synthesis. Climatic Change 110:1005-1027. doi:10.1007/s10584-011-0101-1

Tremblay J-É, Gagnon J (2009) The effects of irradiance and nutrient supply on the productivity of Arctic waters: a perspective on climate change. In: Nihoul JJ, Kostianoy A (eds) Influence of Climate Change on the Changing Arctic and Sub-Arctic Conditions. NATO Science for Peace and Security Series C: Environmental Security. Springer Netherlands, pp 73-93. doi:10.1007/978-1-4020-9460-6_7

van Franeker JA, Flores H, Van Dorssen M (2009) Surface and Under Ice Trawl (SUIT). In: Flores H (2009) Frozen Desert Alive -The role of sea ice for pelagic macrofauna and its predators: implications for the Antarctic pack-ice food web. Dissertation, University of Groningen, Groningen, Netherlands

Wassmann P, Duarte CM, AgustÍ S, Sejr MK (2011) Footprints of climate change in the Arctic marine ecosystem. Global Change Biology 17:1235-1249. doi:10.1111/j.1365-2486.2010.02311.x

Welch HE et al. (1992) Energy Flow through the Marine Ecosystem of the Lancaster Sound Region, Arctic Canada. Arctic 45:343-357

Werner I (1997) Grazing of Arctic under-ice amphipods on sea-ice algae. Mar Ecol Progr Ser 160:93-99

Werner I, Arbizu MP (1999) The sub-ice fauna of the Laptev Sea and the adjacent Arctic Ocean in summer 1995. Polar Biol 21:71-79. doi:10.1007/s003000050336

Werner I, Auel H (2005) Seasonal variability in abundance, respiration and lipid composition of Arctic under-ice amphipods. Mar Ecol Progr Ser 292:251-262. doi:10.3354/meps292251

Werner I, Gradinger R (2002) Under-ice amphipods in the Greenland Sea and Fram Strait (Arctic): environmental controls and seasonal patterns below the pack ice. Mar Biol 140:317-326

Zuur AF, Ieno EN, Smith GM (2007) Analysing ecological data. vol 680. Springer New York, United States of America

Paper 5. The importance of ice algae-produced carbon in the central Arctic Ocean ecosystem: food web relationships revealed by lipid and stable isotope analyses

Published in: *Limnology and Oceanography*, doi:10.1002/lno.10351.

NOTE: Supplementary Material for this paper is found in Appendix B2

Doreen Kohlbach, Martin Graeve, **Benjamin A. Lange**, Carmen David, Ilka Peeken, and Hauke Flores

Key Points:

-

Abstract

To better predict ecological consequences of changing Arctic sea ice environments, we aimed to quantify the contribution of ice algae-produced carbon (α_{Ice}) to pelagic food webs in the central Arctic Ocean. Eight abundant under-ice fauna species were submitted to fatty acid (FA) analysis, bulk stable isotope analysis (BSIA) of nitrogen ($\delta^{15}N$) and carbon ($\delta^{13}C$) isotopic ratios, and compound-specific stable isotope analysis (CSIA) of $\delta^{13}C$ in trophic marker FAs. A high mean contribution α_{Ice} was found in *Apherusa glacialis* and other sympagic (ice-associated) amphipods (BSIA: 87 to 91 %, CSIA: 58 to 92 %). The pelagic copepods *Calanus glacialis* and *C. hyperboreus*, and the pelagic amphipod *Themisto libellula* showed substantial, but varying α_{Ice} values (BSIA: 39 to 55 %, CSIA: 23 to 48 %). Lowest α_{Ice} mean values were found in the pteropod *Clione limacina* (BSIA: 30 %, CSIA: 14 to 18 %). Intra-specific differences in FA compositions related to two different environmental regimes were more pronounced in pelagic than in sympagic species. A comparison of mixing models using different isotopic approaches indicated that a model using $\delta^{13}C$ signatures from both diatom-specific and dinoflagellate-specific marker FAs provided the most conservative estimate of α_{Ice}. Our results imply that ecological key species of the central Arctic Ocean thrive significantly on carbon synthesized by ice algae. Due to the close connectivity between sea ice and the pelagic food web, changes in sea ice coverage and ice algal production will likely have important consequences for food web functioning and carbon dynamics of the pelagic system.

5.1 Introduction

Arctic sea ice coverage and thickness have significantly decreased in the past decades (Johannessen et al. 2004; Kwok et al. 2009; Maslanik et al. 2011). This has been accompanied by a dramatic loss of old, thick multi-year sea ice and a transition to a seasonal ice-dominated Arctic Ocean with more open water during summer (Kwok 2007; Lindsay et al. 2009; Maslanik et al. 2011). The loss of summer sea ice has consequences for ice algae that depend on sea ice as habitat and represent an important carbon source in high Arctic regions. Estimates of ice algal primary production range from 3 to 25 % of the total primary production within Arctic marine systems (Subba Rao and Platt 1984; Legendre et al. 1992) to as high as 50 to 57 % in high Arctic regions (Gosselin et al. 1997; Fernández-Méndez et al. 2015). Climate change is expected to have dramatic consequences in terms of timing, magnitude, and spatial distribution of both ice-associated and pelagic primary production, with a subsequent direct and indirect impact on higher trophic organisms such as zooplankton (Wassmann et al. 2006; Søreide et al. 2013).

The declining sea ice extent could lead to changes in the reproduction and growth cycles of some Arctic zooplankton, such as copepods, that adapt their life cycles to food availability between ice-associated and pelagic blooms (Søreide et al. 2010). Consequently, these changes at the lower trophic level may affect pelagic and benthic food webs. In order to understand how the loss of sea ice and potential changes in primary production may affect zooplankton, we need to gain insight on the importance of sea ice algae carbon to Arctic zooplankton. So far, the contribution of ice algal biomass to higher trophic levels compared to pelagic phytoplankton is scarcely investigated, particularly in the central Arctic basins. The few available studies focused on shelf-bound ecosystems (Hobson et al. 1995; Søreide et al. 2006; Budge et al. 2008).

Fatty acids (FAs) can be used as trophic markers to track predator-prey relationships within marine food webs (e.g. Falk-Petersen et al. 1998; Mayzaud et al. 2013). Certain FAs that are biosynthesized by primary producers are considered to be markers of those primary producers, and are assumed to be transferred conservatively through the marine food web (Graeve et al. 1994a; Bergé and Barnathan 2005; Budge et al. 2012). For example, Bacillariophyceae (simplified to diatoms), which often dominate algal communities in sea ice, express high amounts of the FAs 16:1n-7 and 20:5n-3, accompanied with high levels of C16 polyunsaturated FAs. Dinophyceae (simplified to dinoflagellates) are often more abundant in the water column and contain high amounts of the FA 22:6n-3 and C18 PUFAs (e.g. Dalsgaard et al. 2003). The fatty acid approach alone, however, cannot provide information on the proportional contribution of ice algae- versus pelagic phytoplankton-produced FAs, because the same FAs can originate from sea ice-diatoms or diatoms in the water column (Søreide et al. 2008). By combining FA biomarker analysis with stable isotope analysis of the bulk organic carbon content (e.g. Dehn et al. 2007; Feder et al. 2011; Weems et al. 2012) or specific compounds, such as FAs (e.g. Budge et al. 2008; Graham et al. 2014; Wang et al. 2015), it is possible to quantify the relative transfer of sea ice- and pelagic phytoplankton-derived organic matter to the consumers.

The isotopic signature of sea ice-produced carbon is assumed to be caused by a carbon-limiting environment of the sea ice system (e.g. Fry and Sherr 1984; Peterson and Fry 1987; Hecky and Hesslein 1995). The semi-closed system in sea ice results in a significantly higher ^{13}C enrichment in ice algae relative to pelagic phytoplankton. This difference in isotope values allows for the tracking of carbon from ice algae and pelagic phytoplankton to higher trophic levels (Hobson et al. 2002; Søreide et al. 2013). The quantification of ice algae-produced carbon based on bulk stable isotope parameters (BSIA), however, can be complicated by the effect of metabolic processes, e.g. isotopic routing (Gannes et al. 1997). Metabolic effects can be largely excluded when the variability of the stable isotope composition is considered only in FAs, which are not biotransformed in consumers. By using gas chromatography-combustion-isotope ratio mass spectrometry (GC-c-IRMS), it is possible to analyze the stable isotope composition of individual FAs (compound-specific stable isotope analysis-CSIA, see description of method in Meier-Augenstein 2002) with high sensitivity regarding both concentration of FAs and isotopic composition (Boschker and Middelburg 2002).

We analyzed FAs, bulk and FA-specific stable isotope compositions to describe the trophic relationships between phytoplankton, ice algae, and abundant under-ice fauna species throughout the Eurasian Basin of the Arctic Ocean during summer 2012. We also used this two-dimensional biomarker approach to estimate the relative contribution of carbon produced by sea ice algae versus pelagic phytoplankton in different macrofauna species at different levels of heterotrophy and ice association, and its sensitivity to the methodological approach chosen. According to David et al. (2015), two environmental regimes could be distinguished in our sampling area. During the sampling period, the Nansen Basin (NB) was characterized by higher salinities and nitrate concentrations compared to the Amundsen Basin (AB), among other properties. The community structure of under-ice faunal organisms was also separated according to these two environmental regimes (David et al. 2015). Besides the basin-wide perspective, we analyzed differences in the FA parameters between the two environmental regimes.

5.2 Materials and Methods

5.2.1 Study area and sampling

The sample collection was conducted during the RV 'Polarstern' expedition IceArc (PS80; 2 August to 7 October 2012) in the Eurasian Basin of the Arctic Ocean north of 80°N (**Figure 1, Table 1**). More detailed information on the sampling area, including ice types and properties, is given in David et al. (2015) and Fernández-Méndez et al. (2015).

Ice-associated particulate organic matter (I-POM), representative of the ice algae community, was sampled by taking ice cores at 8 sites using a 9 cm interior diameter ice corer (Kovacs Enterprises). Ice thickness of the cores varied between 0.9 and 2.0 m. Chlorophyll *a* (Chl *a*) concentrations of the entire ice cores varied between 0.4 and 6.5 mg m^{-3} (0.3 to 8 mg m^{-2}; Fernández-Méndez et al. 2015). Whole ice cores were melted in the dark at 4 °C on board the ship and filtered via a vacuum pump through pre-combusted 0.7 µm GF/F filters (3.5 to 10.5 L, Whatmann, 3 h, 550 °C).

Pelagic particulate organic matter (P-POM), representative of the phytoplankton community, was collected at 8 sites by a CTD probe (Seabird SBE9+) with a carousel water sampler. Further information about the CTD probe equipment can be found in David et al. (2015). Details of the sampling procedure are accessible in Boetius et al. (2013). The water collection was performed at the surface layer, or at the depth of the Chl *a* maximum (between 30 and 50 m). The water at the Chl *a* maximum showed Chl *a* concentrations between 0.2 and 1.2 mg m^{-3} throughout the sampling area. Depending on the P-POM biomass concentration, between 6.4 and 11.0 L of water was filtered using pre-combusted GF/F filters. All I-POM and P-POM filters were stored at -80 °C until further processing.

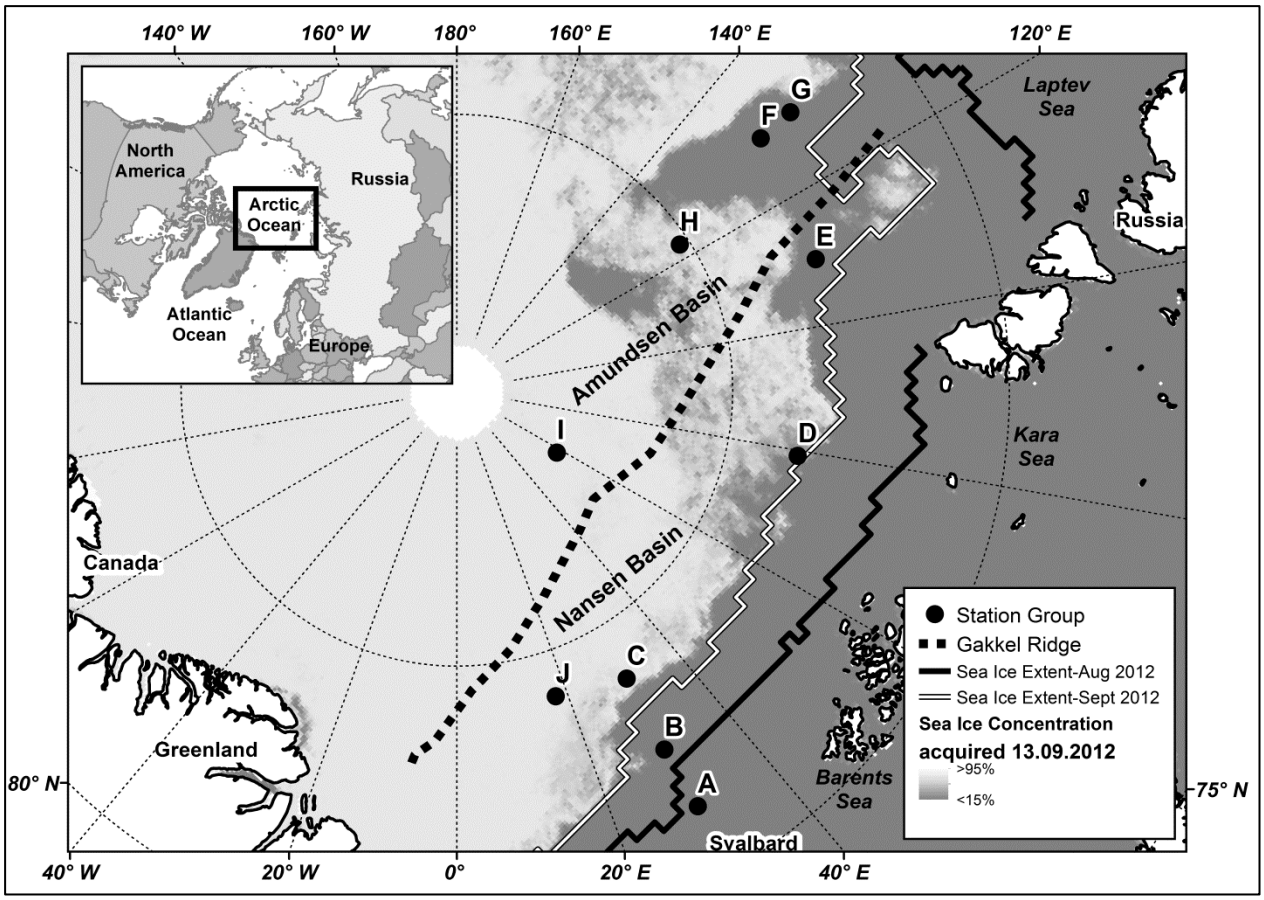

Figure 1. Map of the sampling area during RV 'Polarstern' cruise IceArc (PS80) across the Eurasian part of the Arctic Ocean. The Gakkel Ridge geographically separates the Nansen and Amundsen Basins. Sea ice concentration for 13 September 2012 (concentration data acquired from Bremen University (http://www.iup.uni-bremen.de:8084/amsr/)) and mean sea ice extent for August and September 2012 are represented on the map (data acquired from NSIDC, Fetterer et al. 2002). Letter codes correspond to sampling locations. Station information for the individual sampling sites is given in Table 1.

Samples of dominant species of the under-ice community, such as copepods, ice-associated (sympagic) amphipods, pelagic amphipods, and pteropods were collected at 14 stations, with varying ice conditions, using a surface and under-ice trawl (the SUIT, Van Franeker et al. 2009). Detailed information on the SUIT operation and sampling conditions during the expedition can be found in David et al. (2015).

The copepods *Calanus glacialis* and *C. hyperboreus* were sorted by developmental stages (CV and female). Due to the small organism size, *Calanus* spp. and *Apherusa glacialis* were pooled species-specifically (up to 27 individuals per sample) in order to obtain sufficient sample material for subsequent processing and analyses (**Table 2**). All samples were immediately frozen on board at -80 °C in pre-combusted and pre-weighed sample vials (Wheaton, 6 h, 500 °C).

Table 1. Sample information for ice-associated particulate organic matter (I-POM), pelagic particulate organic matter (P-POM), and under-ice fauna (UIF) collected in the Eurasian Basin of the Arctic Ocean during PS80 in 2012.

Location	Sample type	Date (m/dd/yyyy)	Station no.	Latitude (°N)	Longitude (°E)
A	P-POM	8/6/2012	209	81.296	30.103
B	UIF	8/7/2012	216	82.483	30.027
C	P-POM	8/8/2012	220	83.599	28.500
	UIF	8/9/2012	223	84.070	30.434
	I-POM	8/9/2012	224	84.051	31.112
	P-POM	8/11/2012	230	84.022	31.221
	UIF	8/11/2012	233	83.934	31.298
D	I-POM	8/14/2012	237	83.987	78.103
	P-POM	8/16/2012	244	83.551	75.583
	UIF	8/16/2012	248	83.934	75.500
	P-POM	8/18/2012	250	83.353	87.271
E	I-POM	8/20/2012	255	82.671	109.590
	UIF	8/20/2012	258	83.076	109.627
	P-POM	8/22/2012	263	83.476	110.899
F	UIF	8/25/2012	276	83.076	129.125
	I-POM	8/25/2012	277	82.883	130.130
	P-POM	8/26/2012	284	82.537	129.462
	UIF	8/26/2012	285	82.896	129.782
G	UIF	9/4/2012	321	81.717	130.033
	I-POM	9/4/2012	323	81.926	131.129
	UIF	9/5/2012	331	81.905	130.863
	UIF	9/6/2012	333	82.989	127.103
H	I-POM	9/7/2012	335	85.102	122.245
	P-POM	9/7/2012	341	85.160	123.359
	UIF	9/9/2012	345	85.254	123.842
I	I-POM	9/18/2012	349	87.934	61.217
	UIF	9/19/2012	358	87.341	59.653
	I-POM	9/22/2012	360	88.828	58.864
	UIF	9/25/2012	376	87.341	52.620
J	UIF	9/29/2012	397	84.172	17.922

5.2.2 Lipid class and fatty acid analyses

The analytical work was conducted at the Alfred Wegener Institute in Bremerhaven, Germany.

Prior to lipid extraction, all samples were freeze-dried for 24 h. Dry weights were determined gravimetrically (**Table 2**). The under-ice fauna samples were homogenized mechanically using a Potter-Elvehjem homogenizer. Total lipids were extracted using a modified procedure from Folch et al. (1957) with dichloromethane/methanol (2:1, v/v). The extracted lipids were cleaned with 0.88 % potassium chloride solution. The total lipid content was determined gravimetrically (**Table 2**).

Lipid classes of the under-ice fauna species were determined directly from the lipid extracts by high performance liquid chromatography using a LaChrom Elite® chromatograph (VWR Hitachi, Germany), equipped with a monolithic silica column Chromolith® Performance-Si (VWR, Germany) and an evaporative light scattering detector Sedex 75 (Sedere, France). Further information about the chromatographic method was given by Graeve and Janssen (2009). Results of the lipid class analysis were provided as supplementary content (**Table S1**).

The extracted lipids were converted into fatty acid methyl esters (FAMEs) and free alcohols derived from wax esters by transesterification in methanol, containing 3 % concentrated sulfuric acid, at 50 °C for 12 h.

After a subsequent hexane extraction, the FAMEs and alcohols were separated on an Agilent 6890N Network gas chromatograph (Agilent Technologies, USA) with a DB-FFAP capillary column (30 m, 0.25 mm I.D., 0.25 µm film thickness), equipped with a split injection and a flame ionization detector using a temperature program (160 to 240 °C). The samples were injected at 160 °C. Helium was used as a carrier gas. FAMEs were identified via standard mixtures and quantified with an internal standard (23:0) that was added prior to lipid extraction.

Fatty acids were expressed by the nomenclature A:Bn-X, where A represents the number of carbon atoms, B the amount of double bonds, and X is giving the position of the first double bond starting from the methyl end of the carbon chain. The proportions of individual FAs were expressed as mass percentage of the total FA content.

5.2.3 Bulk stable isotope analysis

Frozen samples were freeze-dried for 24 h, and under-ice fauna samples were mechanically homogenized prior to the BSIA. In order to get an adequate amount of sample material, individuals of *Calanus* spp. and *A. glacialis* were pooled species-specifically for each sampling site. The powdered material and filters were filled into tin capsules and analyzed with a continuous flow isotope ratio mass spectrometer Delta V Plus, interfaced with an elemental analyzer (Flash EA 2000 Series) and connected via a Conflo IV interface (Thermo Scientific Corporation, Germany).

According to the following equation, the isotopic ratios were conventionally expressed as parts per thousand (‰) in the δ notation (Coplen 2011):

$$(1) \qquad \delta_x = [(R_{sample}/R_{standard}) - 1]^{x} \, 1000$$

where x represents the heavy carbon isotope ^{13}C or the heavy nitrogen isotope ^{15}N. R_{sample} represents the $^{13}C/^{12}C$ or $^{15}N/^{14}N$ isotope ratio relative to the corresponding standard ($R_{Standard}$). The international Vienna Pee Dee Belemnite standard was used for carbon measurements and atmospheric nitrogen for nitrogen measurements.

Since lipids have a high turnover and are depleted in ^{13}C relative to proteins and carbohydrates (Deniro and Epstein 1977), they are often removed prior to the analysis in order to reduce the variability of $\delta^{13}C$ due to seasonal fluctuations (Tamelander et al. 2006b), and to make the C:N rations more comparable among species (Søreide et al. 2006). Previous studies, however, have shown that the extraction can cause fractionations in $\delta^{15}N$ (Pinnegar and Polunin 1999; Sweeting et al. 2006). In our study, the lipids were not removed, since the removal process might create uncertain changes in the isotopic compositions, particularly in small organisms (Madurell et al. 2008; Mintenbeck et al. 2008; Kürten et al. 2012).

The calibration of the stable isotope measurements (Brand et al. 2014) was done by analyzing the secondary reference material USGS40 (certified: $\delta^{15}N$ = -4.52 ‰, $\delta^{13}C$ = -26.39 ‰, measured: $\delta^{15}N$ = -4.46 ‰, $\delta^{13}C$ = -26.24 ‰) and USGS41 (certified: $\delta^{15}N$ = 47.57 ‰, $\delta^{13}C$ = 37.63 ‰, measured: $\delta^{15}N$ = 47.12 ‰, $\delta^{13}C$ = 37.49 ‰), provided by the International Atomic Energy Agency (IAEA, Austria). The analytical errors were indicated as ± 0.2 for nitrogen and ± 0.3 ‰ for carbon measurements for both USGS40 and USGS41 (representing the 1 SD of 7 analyses each). For the verification of accuracy and precision, the laboratory standards Isoleucine and Acetanilide were analyzed every 5 samples, with analytical errors of ± 0.1 ‰ for both Isoleucine nitrogen and carbon isotope ratios, and ± 0.1 and ± 0.2 ‰ for Acetanilide nitrogen and carbon isotope ratios, respectively (representing the 1 SD of 7 analyses each). The samples were analyzed in duplicates, and true δ values were obtained after two-point linear normalization (Paul et al. 2007).

Table 2. Dry weight, total lipid content (TLC) by dry weight, and fatty acid content (FAC) by dry weight of under-ice fauna species (mean ± 1 SD).

	Calanus glacialis	***Calanus hyperboreus***	***Apherusa glacialis***	***Onisimus glacialis***	***Gammarus wilkitzkii***	***Eusirus holmii***	***Themisto libellula***	***Clione limacina***
Ind./sample	15 ± 6	8 ± 5	12 ± 4	1	1	1	1	1
Dry weight/Ind. (mg)	0.6 ± 0.2	1.1 ± 0.7	4.2 ± 1.2	46.0 ± 33.4	103.2 ± 43.5	86.3 ± 21.1	64.6 ± 36.9	26.0 ± 20.6
TLC/dry weight (%)	40.5 ± 16.3	36.4 ± 15.3	42.3 ± 7.0	37.4 ± 7.9	26.5 ± 6.2	26.3 ± 9.7	35.7 ± 4.8	16.1 ± 8.7
FAC/dry weight (%)	16.9 ± 6.5	18.7 ± 9.2	29.1 ± 5.6	22.8 ± 5.6	16.1 ± 3.1	16.4 ± 6.0	24.7 ± 3.5	7.1 ± 4.0

Table 3. Statistical parameters of ANOVA tests and Tukey HSD post-hoc tests with significant results.

	ANOVA				
Parameter	*n*	*F*	df	p	Tukey HSD
level FA 16:1n-7	98	28.3	7, 90	< 0.001	*A. glacialis* > all amphipod species: p < 0.001 *C. limacina* < all species: p < 0.05
level FA 22:6n-3	98	39.3	7, 90	< 0.001	*Calanus* spp. > all amphipod species: p < 0.01 *C. limacina* > all species (except C. *hyperboreus*): p < 0.001

FA: fatty acid, *n*: sample size

5.2.4 Compound-specific stable isotope analysis

Prior to the CSIA, FAMEs were separated from the wax ester-derived fatty alcohols in order to avoid overlapping peaks. An insufficient baseline separation between FAMEs and alcohols can potentially cause carry-over effects and, thus, potentially lead to imprecise calculations of the FAME $\delta^{13}C$ values. For this purpose, FAMEs were isolated from the fatty alcohols via column chromatography with silica gel (6 %, deactivated). The FAME fraction was eluted with hexane/dichloromethane (9:1, v/v), fatty alcohols with hexane/acetone (1:1, v/v).

Carbon stable isotope ratios were determined for selected marker FAs using a Thermo GC-c-IRMS system, equipped with a Trace GC Ultra gas chromatograph, a GC Isolink and Delta V Plus isotope ratio mass spectrometer, connected via a Conflo IV interface (Thermo Scientific Corporation, Germany). The FAMEs, dissolved in hexane, were injected in splitless mode and separated on a DB-FFAP column (60 m, 0.25 mm I.D., 0.25 µm film thickness). The $\delta^{13}C$ values of a free FA and the corresponding FAME can differ slightly due to the added methyl group during the transesterification (e.g. Budge et al. 2011; Wang et al. 2014). However, in a previous study, we did not find significant differences between the $\delta^{13}C$ values of the free FA and the FAME (e.g. 16:0 FA: -28.56 ± 0.12 ‰, 16:0 FAME: -28.57 ± 0.16 ‰; C. Albers unpubl.). Therefore, we did not correct for these potential differences.

The $\delta^{13}C$ values of the individual FAMEs were calibrated by analyzing the certified standard FAMEs 14:0 (certified: $\delta^{13}C$ = -29.98 ‰, measured: $\delta^{13}C$ = -29.54 ‰) and 18:0 (certified: $\delta^{13}C$ = -23.24 ‰, measured: $\delta^{13}C$ = -23.29 ‰), supplied by Indiana University, every 5 samples. The analytical error was ± 0.3 ‰ for both 14:0 and 18:0 (representing the 1 SD of 10 analyses each). Furthermore, for quality assurance and analytical precision of the determined carbon stable isotope ratios, the laboratory standard 23:0 was measured intermittently during the sample runs with an analytical error of ± 0.4 % (representing the 1 SD of 10 analyses). The samples were analyzed in duplicates.

5.2.5 Data analysis

The species-specific FA proportions were used as an indicator of a consumer's carbon sources in the days and weeks before the sampling. Consumers at lower trophic levels, such as *Calanus* copepods, show a quick lipid turnover rate ranging between hours and days (Graeve et al. 2005).

The investigation of the FA composition variations was based on six marker FAs. The FAs 16:1n-7 and 20:5n-3 are mainly produced by diatoms and can therefore be treated as valid diatom-specific marker FAs (e.g. Graeve et al. 1997; Falk-Petersen et al. 1998; Scott et al. 1999). The FAs 18:4n-3 and 22:6n-3 are produced in high amounts by dinoflagellates and are therefore used as a dinoflagellate marker FAs (Viso and Marty 1993; Graeve et al. 1994b). Long-chained FAs 20:1 and 22:1 (all isomers) were used to indicate the presence of *Calanus* spp. within the diets of the investigated under-ice fauna species (e.g. Falk-Petersen et al. 1987; Søreide et al. 2013). A principal component analysis (PCA) was applied on the FA dataset to visualize inter-specific differences. Spatial variability in the FA patterns between the two environmental regimes characterized by David et al. (2015) were visualized with bar plots.

Similar to FAs, stable isotope compositions can provide dietary information over a longer period (Tieszen et al. 1983). Bulk $\delta^{13}C$ and FA-specific $\delta^{13}C$ values were determined to estimate the proportional contribution of ice algae-produced carbon (α_{Ice}) to the diet of the under-ice fauna species. Bayesian multi-source stable isotope mixing models (SIAR; Parnell et al. 2010) were used to determine the α_{Ice} estimates from both analyses, BSIA and CSIA. For the CSIA modeling, two different FA combinations were used: (a) 20:5n-3 and (b) 20:5n-3 + 22:6n-3, in order to account for the potentially overlapping compositions of the ice algae and phytoplankton communities. The diatom-specific FA 20:5n-3 was used in the model, because I-POM is typically dominated by diatoms (Horner 1985; Gosselin et al. 1997; Arrigo et al. 2010). However, diatoms can also be present in P-POM (Gosselin et al. 1997; Wang et al. 2014). The dinoflagellate-specific FA 22:6n-3 was used, because the water column can contain high amounts of dinoflagellates and flagellates (Sherr et al.

1997). Besides, sea ice systems may also be dominated by flagellates, particularly during ice melt (Tamelander et al. 2009).

The models allow the incorporation of trophic enrichment factors (TEFs) to account for isotopic turnover rates in the consumers that are tissue-specific. From lower to higher trophic level, an enrichment of the heavy carbon stable isotope between 0.1 and 1 ‰ was often observed (Deniro and Epstein 1978; Rau et al. 1983; Post 2002). Since the true value of the carbon TEFs in the under-ice fauna species is unknown, carbon TEFs for both BSIA and CSIA models were assumed to be zero (Budge et al. 2011; Wang et al. 2015).

The models also allow the incorporation of concentration dependencies to account for different levels of the investigated marker FAs in the primary producers. The discrepancy in the proportions of 20:5n-3 between I-POM and P-POM during maximum ice in 2010 reported by Wang et al. (2015) was higher than in our dataset. However, Wang et al. (2015) did not find substantial differences between the results using models with and without concentration data. Thus, we did not incorporate concentration dependencies in our models.

Due to the small sample size, the calculation of α_{Ice} was based on the mean stable isotope values, with no differentiation between the two environmental regimes, for both BSIA and CSIA data.

The ice algae-produced carbon demand of the most abundant herbivores, *C. glacialis*, *C. hyperboreus* and *A. glacialis*, was estimated by multiplying our proportional α_{Ice} derived from CSIA model b with ingestions rates (Olli et al. 2007) and observed species abundances under sea ice and in the water column (David et al. 2015; Ehrlich 2015).

All data analyses were conducted using the open-source software ‘R’, version 3.2.0 (R Core Team 2015). Intra-specific and inter-specific variations in fatty acid and stable isotope compositions were tested using 1-way ANOVAs followed by Tukey HSD post-hoc tests. Student´s t-tests were applied for comparisons between two groups. Prior to testing, the FA data were transformed applying an arcsine square root function following Budge et al. (2007) to improve normality. The statistical output reported in the text was summarized in **Tables 3** (ANOVAs) and **4** (t-tests).

5.3 Results

5.3.1 Marker fatty acid compositions

5.3.1.1 Ice-associated and pelagic particulate organic matter

The I-POM samples were dominated by the diatom-specific FA 16:1n-7, showing significantly higher levels than the P-POM samples. The proportional contributions of the second diatom-specific FA 20:5n-3 were, however, significantly lower in the I-POM samples compared to the P-POM samples. The proportions of the dinoflagellate-specific FAs 18:4n-3 and 22:6n-3 showed significantly higher values in P-POM compared to I-POM (**Figure 2**, **Tables 4** and **5**).

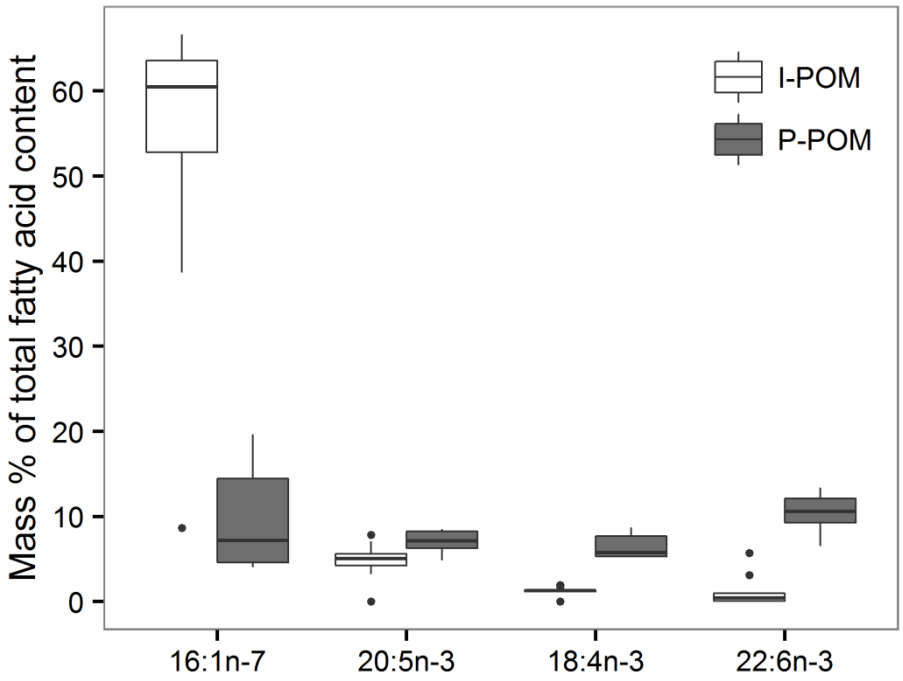

Figure 2. Relative composition of marker fatty acids (FAs) in ice-associated particulate organic matter (I-POM) and pelagic particulate organic matter (P-POM). 16:1n-7 and 20:5n-3 represent diatom marker FAs, 18:4n-3 and 22:6n-3 represent dinoflagellate marker FAs. Horizontal bars in the box plots indicate median proportional values. Upper and lower edges of the boxes represent the approximate 1st and 3rd quartiles, respectively. Vertical error bars extend to the lowest and highest data value inside a range of 1.5 times the inter-quartile range, respectively (R Core Team 2015). Outliers are represented by the dots outside the boxes. Sample size is reported in Table 5.

5.3.1.2 Under-ice fauna species

In all species, the bulk of the determined FAs were incorporated into neutral (storage) lipids, whose proportions far exceeded the levels of polar (membrane) lipids (**Table S1**, supplementary).

The largest variability among all species was observed in the diatom-specific FA 16:1n-7 and the dinoflagellate-specific FA 22:6n-3. The levels of the diatom-specific FA 20:5n-3 were comparable among all species, and the proportions of the dinoflagellate-specific FA 18:4n-3 were generally low in all species (**Figure 3**, **Table 5**).

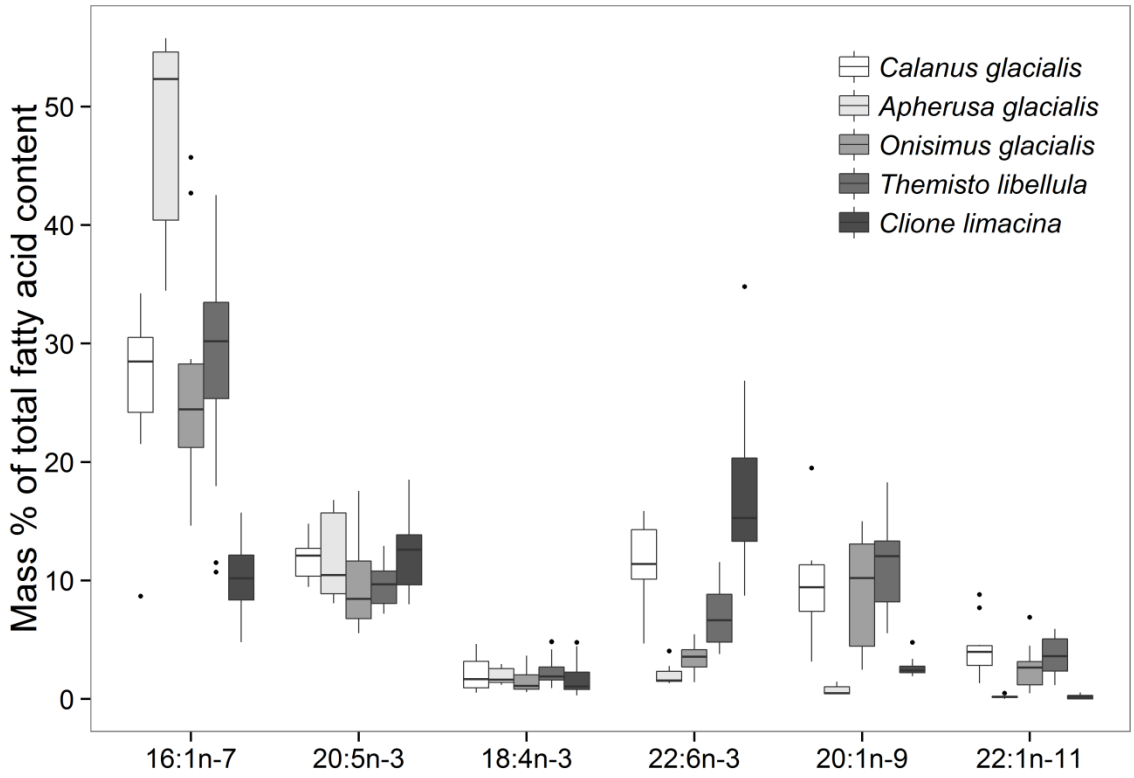

Figure 3. Relative composition of marker fatty acids (FAs) in selected under-ice fauna species. 16:1n-7 and 20:5n-3 represent diatom marker FAs, 18:4n-3 and 22:6n-3 represent dinoflagellate marker FAs, 20:1n-9 and 22:1n-11 represent Calanus-marker FAs. Box plot design as in Figure 2. Sample size is reported in Table 5.

The mean levels of 16:1n-7 in both *Calanus glacialis* and *C. hyperboreus* were lower than in all other species, except for *Clione limacina*. In contrast, their content in 20:5n-3 was high compared to the other species, with *C. hyperboreus* reaching the maximum mean value of this study. *C. glacialis* and *C. hyperboreus* contained significantly higher amounts of 22:6n-3 compared to all amphipod species (**Tables 3** and **5**). The mean level of the *Calanus*-specific FA 20:1n-9 was only higher in *Themisto libellula* relative to *Calanus* spp., and in *Onisimus glacialis* relative to *C. hyperboreus*. The second *Calanus*-specific FA 22:1n-11 was detected in generally higher amounts in both *Calanus* spp. compared to all other species. There was no significant difference found in the FA patterns between CV and female within the same *Calanus* species (t-test $p > 0.05$).

A. glacialis had a significantly higher proportion of 16:1n-7 than all other amphipod species, in addition to relatively high levels of 20:5n-3 (**Tables 3** and **5**). The levels of 20:1n-9 and 22:1n-11 were close to the detection limit in this species. *Gammarus wilkitzkii* and *Eusirus holmii* were generally similar to each other in their FA composition. *E. holmii* had the second-highest proportional content of 16:1n-7 among all amphipod species. *T. libellula* had a higher proportional content of 22:6n-3 than all other amphipods, and high levels of 20:1n-9 and 22:1n-11.

The FA 16:1n-7, which was dominant in all investigated copepods and amphipods, showed significantly lower levels in *C. limacina* compared to all other investigated species (**Tables 3** and **5**). Conversely, the proportional contribution of 22:6n-3 was significantly higher in *C. limacina* compared to all other investigated species, except for *C. hyperboreus* (**Tables 3** and **5**). The FAs 20:1n-9 and 22:1n-11 were only found in small amounts in this species.

The first two principal components of the PCA explained 69.8 % of the variance in the FA data among the samples (**Figure 4**). The first axis (PCA 1) separated the sympagic amphipods with high levels of 16:1n-7 on one side from the pelagic copepods with high levels of 22:6n-3, 20:1n-9, and 22:1n-11 on the other side. The second axis (PCA 2) emphasized the difference in the marker FA proportions

between the pelagic species *T. libellula* with higher levels of 16:1n-7 and both *Calanus*-marker FAs, and *C. limacina* with distinctly higher levels of 22:6n-3. In general, the FA profile of *C. limacina* was clearly isolated from all other species.

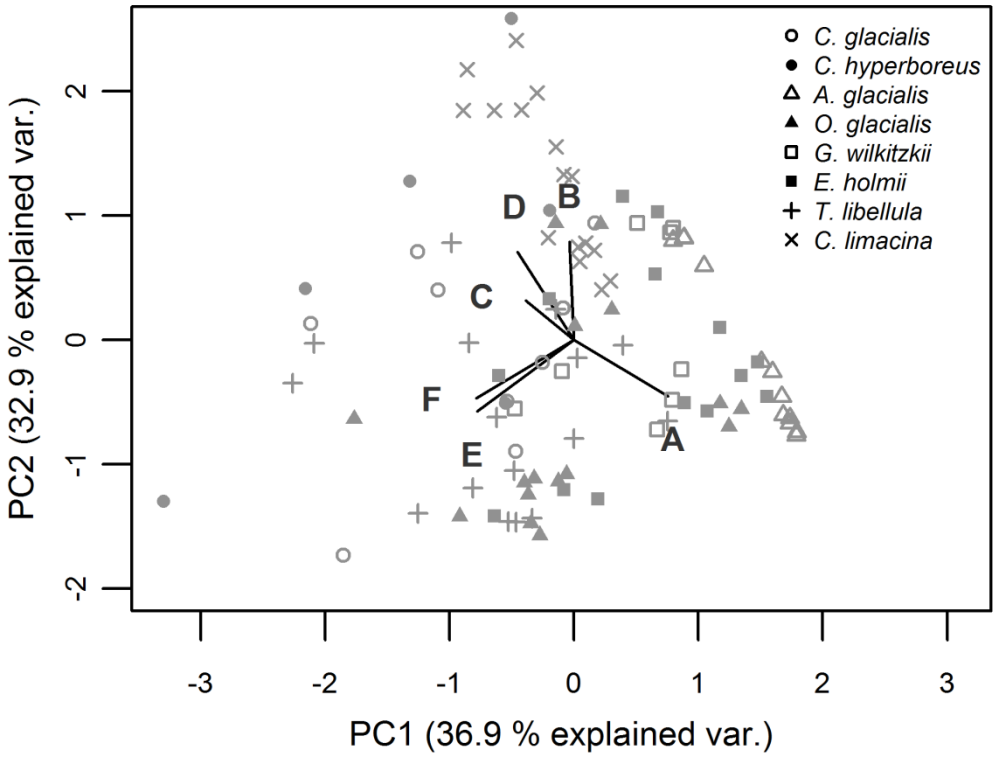

Figure 4. PCA biplot of marker fatty acid (FA) proportions in under-ice fauna species. Biplot arrows correspond to gradients of FAs in the PCA ordination. Diatom marker FAs: 16:1n-7 (A), 20:5n-3 (B); dinoflagellate marker FAs: 18:4n-3 (C), 22:6n-3 (D); Calanus-marker FAs: 20:1n-9 (E), 22:1n-11 (F). Sample size is reported in Table 5.

In addition to the differences between the species, there was an intra-specific spatial variability of certain marker FA proportions observed. SUIT station 258 was located close to the Gakkel ridge, on the border between the Nansen Basin (NB) and the Amundsen Basin (AB). In general, the FA composition of individuals from station 258 demonstrated a higher similarity to the FA profiles of the same species from the AB regime. Thus, station 258 was considered as an AB regime sample for the statistical tests. In *Calanus* spp. and all five amphipod species, the proportional amount of 16:1n-7 was higher in the AB regime samples than in the NB regime samples. This pattern was significant (t-test $p < 0.05$) in *C. hyperboreus*, *A. glacialis*, *G. wilkitzkii*, *E. holmii*, and *T. libellula*, and near-significant in *O. glacialis* ($p = 0.06$). Conversely, the levels of 18:4n-3, 20:5n-3, and 22:6n-3 were significantly higher in the NB regime in *A. glacialis*, *O. glacialis* and *G. wilkitzkii*. In *E. holmii*, the proportions of 20:5n-3 and 22:6n-3 were significantly higher in the NB regime samples compared to the AB regime samples. In *T. libellula*, the levels of 18:4n-3, 20:1n-9 and 22:1n-11 were significantly higher in the NB regime than in the AB regime (**Figure 5**). As all but one station in the AB regime were sampled later in the season than stations in the NB regime, these patterns could reflect the seasonal progression of the system (e.g. Basedow et al. 2010). In addition, the fundamental differences in the environmental characteristics of the two regimes probably played an important role. The AB regime was characterized by lower nitrate and phosphate concentrations and lower Chl *a* concentrations in the surface layer compared to the NB regime (David et al. 2015).

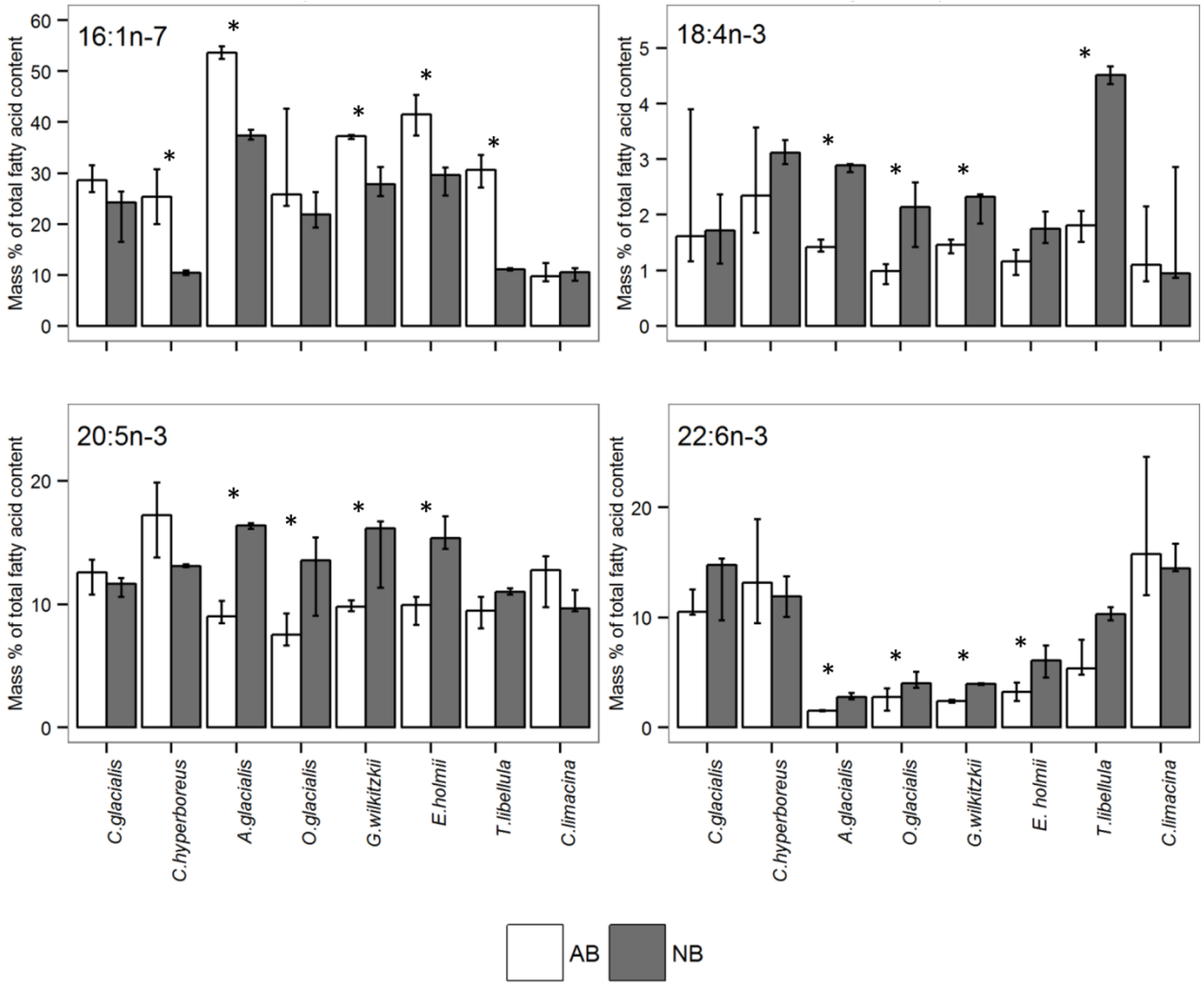

Figure 5. Intra-specific differences in the proportions of marker fatty acids (FAs) in under-ice fauna species between Nansen Basin (NB) and Amundsen Basin (AB) regimes. Columns and error bars correspond to the median and interquartile ranges, respectively. Note: y-axes have different scales. Associated bars marked with asterisk '*' represent significant differences between the regimes (t-test $p < 0.05$). Sample size is reported in Table 5.

5.3.2 Bulk stable isotope compositions

Both POM types displayed the lowest $\delta^{15}N$ values between 3.5 and 6.4 ‰ in I-POM and between 2.1 and 5.8 ‰ in P-POM, representing the trophic baseline (**Table 6**). The $\delta^{13}C$ values in I-POM varied between -22.8 and -26.8 ‰, the P-POM $\delta^{13}C$ values varied between -25.4 and -28.7 ‰.

Among the under-ice fauna species, *A. glacialis* showed the lowest $\delta^{15}N$ values between 5.0 and 5.7 ‰, *E. holmii* showed the highest $\delta^{15}N$ values between 8.9 and 12.2 ‰ (**Table 6**).

The highest carbon stable isotope values were found in *A. glacialis* (-20.0 to -23.3 ‰). The lowest $\delta^{13}C$ values were found in *Calanus* spp., *T. libellula* and *C. limacina* (-24.1 to -31.2 ‰).

A comparison of the bulk stable isotope ratios in POM and the under-ice fauna species between the two environmental regimes was provided in **Table S2** (supplementary).

5.3.3 Compound-specific stable isotope compositions

The $\delta^{13}C$ values of 18:4n-3, 20:5n-3 and 22:6n-3 were significantly higher in the I-POM samples compared to the P-POM samples (**Tables 4** and **7**). The stable isotope values of 16:1n-7 demonstrated little variation between the two source communities.

There was no significant difference in the carbon stable isotope values of the individual marker FAs between the two *Calanus* species (t-test $p > 0.05$). The mean $\delta^{13}C$ values of 18:4n-3, 20:5n-3, and 22:6n-3 were lower in both *Calanus* spp. compared to all other species, except for *T. libellula* and *C. limacina*. Among all species, *A. glacialis* displayed the highest mean $\delta^{13}C$ values of 18:4n-3, 20:5n-3 and 22:6n-3. Among the amphipods, *T. libellula* displayed the lowest mean $\delta^{13}C$ values of 18:4n-3, 20:5n-3 and 22:6n-3 (**Table 7**).

A comparison of the fatty acid-specific stable isotope ratios in POM and the under-ice fauna species between the two environmental regimes was provided in **Table S3** (supplementary).

Table 4. Statistical parameters of Student´s t-tests with significant results.

	t-test				
Parameter	*n*	*t*	df	p	
level FA 16:1n-7	19	7.1	13.6	< 0.001	I-POM > P-POM
level FA 18:4n-3	19	9.8	16.3	< 0.001	I-POM < P-POM
$\delta^{13}C$ FA 18:4n-3	12	7.3	4.7	< 0.001	I-POM > P-POM
level FA 20:5n-3	19	2.3	10.9	< 0.05	I-POM < P-POM
$\delta^{13}C$ FA 20:5n-3	13	6.4	9.9	< 0.001	I-POM > P-POM
level FA 22:6n-3	19	9.0	12.8	< 0.001	I-POM < P-POM
$\delta^{13}C$ FA 22:6n-3	11	5.9	4.4	< 0.01	I-POM > P-POM

FA: fatty acid, *n*: sample size

Table 6. Bulk stable nitrogen (δ15N) and carbon isotope values (δ13C) in ice-associated particulate organic matter (I-POM), pelagic particulate organic matter (P-POM), and under-ice fauna species (mean ± 1 SD ‰).

	n	$\delta^{15}N$	$\delta^{13}C$
I-POM	6	4.8 ± 1.3	-24.9 ± 1.6
P-POM	17	4.0 ± 1.2	-27.3 ± 0.9
Calanus glacialis	4	7.5 ± 0.9	-26.8 ± 3.1
Calanus hyperboreus	4	7.8 ± 1.4	-26.6 ± 1.1
Apherusa glacialis	4	5.4 ± 0.3	-22.3 ± 1.5
Onisimus glacialis	4	7.1 ± 1.8	-22.4 ± 1.7
Gammarus wilkitzkii	4	7.1 ± 0.6	-24.4 ± 0.4
Eusirus holmii	4	10.0 ± 1.5	-23.3 ± 0.7
Themisto libellula	4	8.8 ± 1.5	-25.7 ± 1.8
Clione limacina	4	8.6 ± 0.8	-26.9 ± 0.5

n: sample size

Table 5. Relative composition of the most abundant fatty acids (FAs) in ice-associated particulate organic matter (I-POM), pelagic particulate organic matter (P-POM), and under-ice fauna species (mean ± 1 SD mass % of total FA content) collected in the Nansen Basin (NB) and Amundsen Basin (AB). Not detected FAs are reported as '--'.

	I-POM	**P-POM**	***Calanus glacialis***	***Calanus hyperboreus***	***Apherusa glacialis***	***Onisimus glacialis***	***Gammarus wilkitzkii***	***Eusirus holmii***	***Themisto libellula***	***Clione limacina***
n_{NB}	1	7	3	2	4	7	5	5	2	3
n_{AB}	9	2	7	4	8	9	3	9	14	13
14:0	5.3 ± 1.5	6.0 ± 2.1	8.1 ± 1.2	4.6 ± 1.9	4.2 ± 0.4	3.4 ± 0.9	3.9 ± 0.5	3.8 ± 0.6	4.9 ± 1.3	2.6 ± 1.8
16:0	16.3 ± 4.1	20.3 ± 1.9	8.8 ± 1.5	7.3 ± 3.2	13.4 ± 0.5	11.5 ± 2.1	12.2 ± 0.8	12.7 ± 1.6	9.2 ± 1.3	12.1 ± 1.6
16:1n-7[a]	53.6 ± 17.9	9.8 ± 6.0	26.2 ± 7.3	20.3 ± 10.2	48.1 ± 8.1	27.0 ± 9.6	31.4 ± 5.6	36.4 ± 8.5	27.9 ± 8.5	10.3 ± 2.9
18:0	4.5 ± 7.5	5.3 ± 1.2	1.2 ± 0.5	1.6 ± 1.1	0.7 ± 0.2	0.5 ± 0.2	0.6 ± 0.1	0.6 ± 0.2	0.5 ± 0.1	2.8 ± 1.9
18:1n-9	7.0 ± 4.5	6.5 ± 2.5	3.6 ± 0.4	3.3 ± 0.6	7.9 ± 1.5	18.1 ± 4.4	16.1 ± 2.9	9.8 ± 1.4	8.1 ± 1.5	4.2 ± 1.3
18:1n-7	0.4 ± 0.4	1.8 ± 1.1	1.5 ± 0.4	1.8 ± 0.7	2.0 ± 0.5	3.4 ± 0.7	4.0 ± 0.5	3.0 ± 0.6	3.0 ± 0.7	4.6 ± 1.4
18:4n-3[b]	1.2 ± 0.5	6.4 ± 1.4	2.2 ± 1.6	3.0 ± 1.6	1.9 ± 0.7	1.5 ± 0.9	1.9 ± 0.5	1.5 ± 0.7	2.4 ± 1.3	1.8 ± 1.5
20:1n-9[c]	--	--	9.8 ± 4.3	8.7 ± 5.6	0.7 ± 0.4	8.9 ± 4.5	3.2 ± 2.1	4.9 ± 4.5	11.3 ± 4.1	2.7 ± 0.7
20:1n-7	--	--	0.5 ± 0.4	1.0 ± 0.9	0.5 ± 0.2	1.4 ± 0.6	0.7 ± 0.1	1.0 ± 0.5	1.5 ± 0.8	2.5 ± 0.6
20:5n-3[a]	4.8 ± 2.2	7.1 ± 1.3	11.9 ± 1.9	15.3 ± 3.7	11.7 ± 3.6	9.7 ± 3.8	12.8 ± 3.4	11.8 ± 3.3	9.7 ± 1.6	12.1 ± 2.9
22:1n-11[c]	--	--	4.3 ± 2.3	6.2 ± 4.8	0.2 ± 0.1	2.5 ± 1.6	2.1 ± 1.9	1.8 ± 1.8	3.7 ± 1.6	0.2 ± 0.2
22:6n-3[b]	1.2 ± 1.8	10.4 ± 2.1	11.4 ± 3.5	14.1 ± 7.8	2.0 ± 0.8	3.4 ± 1.3	3.3 ± 0.8	4.3 ± 1.8	7.1 ± 2.7	17.5 ± 7.0
Total	94.3	73.6	89.5	87.2	93.3	91.3	92.2	91.6	89.3	73.4

a: diatom marker FA, b: dinoflagellate marker FA, c: *Calanus* marker FA, *n*: sample size

Table 7. Carbon stable isotope values (δ13C) of marker fatty acids (FAs) in ice-associated particulate organic matter (I-POM), pelagic particulate organic matter (P-POM), and under-ice fauna species (mean ± 1 SD ‰). Not detected FAs are reported as '--'.

	n	16:1n-7	20:5n-3	18:4n-3	22:6n-3
I-POM	7	-24.9 ± 4.1	-26.6 ± 2.7	-28.4 ± 3.2	-23.4 ± 3.7
P-POM	7	-26.4 ± 3.4	-35.6 ± 2.3	-39.3 ± 1.1	-35.5 ± 2.3
Calanus glacialis	10	-25.0 ± 3.8	-32.2 ± 1.7	-35.6 ± 1.8	-32.0 ± 2.1
Calanus hyperboreus	6	-27.3 ± 3.6	-32.1 ± 1.2	-36.2 ± 1.1	-33.8 ± 2.3
Apherusa glacialis	10	-24.2 ± 2.6	-26.6 ± 1.3	-29.2 ± 1.9	-28.5 ± 1.6
Onisimus glacialis	8	-22.9 ± 3.0	-28.4 ± 1.6	-32.4 ± 3.6	-30.4 ± 1.0
Gammarus wilkitzkii	4	-24.8 ± 2.1	-29.0 ± 1.0	-31.2 ± 0.9	-31.3 ± 1.5
Eusirus holmii	8	-23.4 ± 2.1	-28.9 ± 1.0	-30.1 ± 1.2	-30.4 ± 1.3
Themisto libellula	7	-23.9 ± 2.3	-31.4 ± 1.4	-35.6 ± 2.2	-33.7 ± 1.8
Clione limacina	9	-28.7 ± 1.9	-34.1 ± 1.6	--	-33.8 ± 1.1

n: sample size

5.3.4 Proportional contribution of ice algae-produced carbon

All three approaches indicated that the sympagic amphipods *A. glacialis*, *O. glacialis*, *G. wilkitzkii*, and *E. holmii* showed the highest dependency on ice algal carbon, *Calanus* spp. and *T. libellula* took an intermediate position, and *C. limacina* showed the lowest dependency (**Table 8**). The results from the SIAR models using the carbon stable isotope values of FA 20:5n-3 (model a) were similar to those from the BSIA models, and were generally higher than the α_{Ice} estimates derived from model b, which combined 20:5n-3 and 22:6n-3 (**Table 8**).

A. glacialis showed the highest α_{Ice} estimates among all species, accompanied with the lowest variation between the α_{Ice} estimates derived from the BSIA model and the two CSIA models (overall mean > 85 %). Both *Calanus* spp. indicated high similarity between the estimates derived from the BSIA model and CSIA model a (BSIA: mean 43 %, CSIA model a: mean 44 %). Furthermore, all approaches provided similar α_{Ice} estimates for *O. glacialis*, *G. wilkitzkii*, and *E. holmii* (BSIA: mean ~ 90 %, CSIA model a: mean ~ 80 %, CSIA model b: mean ~ 60 %).

A high discrepancy between the BSIA model and CSIA model b was found in the pelagic species *T. libellula* (BSIA: mean 55 %, CSIA model b: 23 %) and *C. limacina* (BSIA: mean 30 %, CSIA model b: mean 14 %).

Table 8. Proportional contribution of ice algae-produced carbon (α_{Ice}) in under-ice fauna species (mean %) from SIAR mixing models based on bulk stable isotope analyses (BSIA; Table 6) and stable isotope compositions of marker fatty acids (a) 20:5n-3 and (b) 20:5n-3 + 22:6n-3 (Table 7). Ranges of α_{Ice} are shown in parentheses.

Model	BSIA	(a) 20:5n-3	(b) 20:5n-3 + 22:6n-3
Calanus glacialis	47 (10-76)	48 (20-53)	33 (26-43)
Calanus hyperboreus	39 (6-86)	40 (35-48)	25 (20-27)
Apherusa glacialis	90 (85-95)	92 (91-94)	86 (80-90)
Onisimus glacialis	87 (79-95)	77 (73-81)	61 (53-68)
Gammarus wilkitzkii	91 (88-93)	76 (63-81)	58 (48-66)
Eusirus holmii	90 (87-92)	79 (74-84)	60 (56-64)
Themisto libellula	55 (6-87)	45 (40-50)	23 (20-28)
Clione limacina	30 (16-53)	18 (13-28)	14 (10-21)

5.3.5 Ice algae-produced carbon demand

We calculated a tentative estimate of the overall demand of ice algae-produced carbon by the most abundant grazers *C. glacialis*, *C. hyperboreus* and *A. glacialis* based on the α_{Ice} values derived from CSIA model b (**Table 8**). Altogether, these species consumed between 2.9 and 8.5 mg ice algae-produced carbon m^{-2} d^{-1}. Due to its high abundance, the bulk of the ice algal carbon demand was attributed to *C. glacialis* (**Table 9**).

Table 9. Ice algae-produced carbon demand in abundant herbivores. In *Calanus* spp., only adults and CV stages were included in abundance estimates. α_{Ice} = proportional contribution of ice algae-produced carbon derived from SIAR model b (Table 8).

	α_{Ice}	Ingestion rate[1] (µg C $ind.^{-1}$ d^{-1})		Abundance (ind. m^{-2})		Ice algal carbon demand (mg C m^{-2} d^{-1})					
				Under-ice[2]	Pelagic[3]	Under-ice		Pelagic		Total	
	Mean	Min	Max	Mean	Mean	Min	Max	Min	Max	Min	Max
Calanus glacialis	0.33	6.0	18.0	6.4	1180	0.01	0.04	2.34	7.01	2.35	7.05
Calanus hyperboreus	0.25	2.8	8.4	1.0	700	0.00	0.00	0.49	1.47	0.49	1.47
Apherusa glacialis	0.86	13.0	13.0	0.6	0	0.01	0.01	0.00	0.00	0.01	0.01
Total		21.8	39.4	8.0	1880	0.02	0.05	2.83	8.48	2.85	8.53

[1]**Olli et al. (2007);** [2]**David et al. (2015);** [3]**Ehrlich (2015)**

5.4 Discussion

5.4.1 Variability in marker fatty acid compositions among algal communities and under-ice fauna species

In our study, the FA profiles of the I-POM samples suggested a diatom-dominated ice algal community. The small amounts of the dinoflagellate-specific FAs 18:4n-3 and 22:6n-3 in the I-POM samples indicated that a small part of the sea ice flora consisted of dinoflagellates, which was in agreement with the results of molecular analyses of the primary community structures (K. Hardge et

al. subm.). Based on the marker FA proportions, the phytoplankton community consisted of a mixture of both diatoms and flagellates. The dominance of dinoflagellates in the water column and a substantially higher proportion of diatoms in the sea ice community compared to the pelagic community during our sampling were also confirmed by genome sequencing (K. Hardge et al. subm.). The lower levels of the diatom-specific FA 20:5n-3 accompanied with the distinctly higher levels of the diatom-FA 16:1n-7 in the I-POM samples compared to the P-POM samples could indicate a different diatom-community in sea ice compared to the water column. Supporting our assumption, previous studies found a dominance of pennate diatoms in sea ice versus a dominance of centric diatoms in the water column (Gosselin et al. 1997; Arrigo et al. 2010).

The FA profiles of the under-ice fauna species revealed variable associations with diatom-and dinoflagellate-related marker FAs. Although it may be possible for herbivorous invertebrates to synthesize 20:5n-3 and 22:6n-3 from 18:3n-3 (Moreno et al. 1979), FA 18:3n-3 was only found in trace amounts (< 1%) in the species from this study. This indicates that biosynthesis of 20:5n-3 and 22:6n-3 likely did not occur, and these FAs were derived through the trophic chain from algal sources.

Both *Calanus* spp. are known to be key Arctic grazers, utilizing both ice algae- and pelagic phytoplankton-derived carbon (Søreide et al. 2010; Durbin and Casas 2013). There was little difference in the FA profiles between *C. glacialis* and *C. hyperboreus*, indicating that the primary carbon sources were similar for both *Calanus* species. As frequently shown, the FA composition of Arctic *Calanus* spp. was characterized by high amounts of the diatom-specific FAs 16:1n-7 and 20:5n-3 (Graeve et al. 1994b; Wang et al. 2015). Furthermore, our results showed that both copepod species contained high amounts of the dinoflagellate-specific marker FA 22:6n-3, which together suggests sources of carbon from both diatoms and dinoflagellates.

The FA composition of the amphipod *A. glacialis* indicated a diet dominated by diatom-derived carbon, evident by high proportions of the diatom-specific FAs 16:1n-7 and 20:5n-3, accompanied by low levels of the dinoflagellate-specific FA 22:6n-3. A diatom-dominated diet is in agreement with several studies showing that *A. glacialis* primarily feeds on the under-ice flora and phytodetritus (Bradstreet and Cross 1982; Scott et al. 1999; Tamelander et al. 2006a). Together with *O. glacialis* and *G. wilkitzkii*, *A. glacialis* is known to live permanently associated with the Arctic sea ice (Poltermann 2001; Gradinger and Bluhm 2004). Thus, it is not surprising that *O. glacialis* and *G. wilkitzkii* contained high levels of the diatom markers 16:1n-7 and 20:5n-3, with considerably lower levels of the dinoflagellate-specific FA 22:6n-3.

Calanus copepods are able to synthesize the long-chain FAs 20:1n-9 and 22:1n-11 in large amounts de novo. These FAs can also be used as trophic indicators for a copepod-related diet in higher consumers (Sargent et al. 1977; Wold et al. 2011). Accordingly, high values of the FA 20:1n-9 indicated a partly *Calanus*-based diet in the omnivorous amphipod *O. glacialis*. *G. wilkitzkii* has been reported to also feed extensively on copepods, primarily during adult stages (Scott et al. 2001). However, we found only small amounts of the *Calanus*-specific FAs 20:1n-9 and 22:1n-11 in this amphipod, indicating that *Calanus* may not have been important in their diets before the sampling.

Carnivorous amphipods, such as *E. holmii* and *T. libellula*, constitute important links between lipid-rich herbivores and top predators (Noyon et al. 2011). These two amphipod species also showed high levels of the diatom-specific FAs 16:1n-7 and 20:5n-3. In *T. libellula*, a higher proportion of the dinoflagellate-specific FA 22:6n-3 indicated a greater importance of dinoflagellate-derived carbon than in *E. holmii*. Both species, but particularly *T. libellula*, displayed elevated levels of the *Calanus*-specific marker FAs. Our findings are consistent with other feeding studies, which identified *T. libellula* as a part of the *Calanus*-based food web (Scott et al. 1999; Dalpadado et al. 2008; Kraft et al. 2013).

The carnivorous pteropod *C. limacina* is assumed to feed exclusively on *Limacina helicina* (Conover and Lalli 1974; Phleger et al. 2001). In our study, the FA composition of *C. limacina* was characterized by the lowest proportion of the diatom-specific FA 16:1n-7 and the highest proportion of the dinoflagellate-specific FA 22:6n-3, possibly reflecting a pelagic-based diet of diatoms and dinoflagellates in *L. helicina*. The pteropod *L. helicina* was first described as a pure herbivore, but more recent studies reported an omnivorous diet consisting of small copepods and juvenile *L. helicina*

(Gilmer 1974; Gilmer and Harbison 1991; Falk-Petersen et al. 2001). The low levels of the *Calanus*-specific FAs found in our study in *C. limacina*, however, indicated that *Calanus* copepods were not important in the *L. helicina*-based pathway of the food web during the weeks before our sampling.

Besides the expected inter-specific variations largely confirming known feeding patterns, we also found considerable intra-specific variability in the FA profiles of the investigated under-ice fauna species. All amphipod species and *Calanus* spp. from the Amundsen Basin regime had higher proportions of the FA 16:1n-7 compared to the samples from the Nansen Basin regime. Additionally, all amphipods from the AB regime showed lower proportions of all other algal FAs than those sampled in the NB regime. The FA 16:1n-7 was largely limited to I-POM samples in our dataset. Hence, the observed variability between the two environmental regimes was probably driven by variability in ice algal communities rather than phytoplankton, assuming lipid turnover rates in these herbivores were fast compared to changes in algal composition (Graeve et al. 2005). An impact of the variability of sea ice communities on the FA composition is corroborated by pronounced differences in the community composition of protists in sea ice between the two environmental regimes (K. Hardge et al. subm.), as well as by differing drift pathways of sea ice between the NB and the AB in 2012 (David et al. 2015).

5.4.2 Importance of ice algae-produced carbon to the Arctic under-ice community

In most investigated species, the α_{Ice} estimates based on BSIA were higher than those based on the single FAs. Unlike CSIA of FAs, which is limited to molecules assumed to be unchanged by metabolic processes, the interpretation of BSIA results can be more complicated. Besides the lipid components, proteins and carbohydrates are also subject to various mass-dependent metabolic processes, influencing the carbon stable isotope signal of a species. Compared to proteins and carbohydrates, lipids are more depleted in the heavy carbon stable isotope (Deniro and Epstein 1977; Søreide et al. 2006). To correct for a potential bias in the BSIA results introduced by variability in lipid content, both *a priori* lipid removal and post-analytical corrections, e.g. with the normalization algorithm proposed by McConnaughey and McRoy (1979), have been used in previous studies. Several studies showed, however, that the extraction can cause fractionations in $\delta^{15}N$ (Pinnegar and Polunin 1999; Sweeting et al. 2006; Post et al. 2007). On the other hand, there are studies indicating that normalization models do not account for different lipid levels in different species in an appropriate way (Sweeting et al. 2006; Post et al. 2007). Therefore, we based our calculations on the non-corrected data. It remains difficult to conclude to which degree and in which species BSIA-based estimates of α_{Ice} were influenced by lipid content, taxon-specific, habitat-related, and/or trophic level-related effects on metabolically active compounds. Yet, both BSIA and CSIA-derived α_{Ice} estimates yielded a consistent hierarchical order of the investigated species, ranging from a highly sea ice algae-related trophic dependency in *A. glacialis* to a considerably lower trophic dependency on sea ice algae in *C. limacina* within the food web.

Based on the CSIA results, the isotopic values of carbon in the FAs 20:5n-3 and 22:6n-3 were used to investigate the proportional contributions of sea ice algae-produced carbon α_{Ice} versus phytoplankton-produced carbon to the body tissue of abundant under-ice fauna species. Budge et al. (2008) traced the carbon flux in an Alaskan coastal ecosystem using the stable isotope values of carbon in the FA 20:5n-3, which they assumed to represent a realistic estimate of the ice algae contribution relative to all other types of phytoplankton. Wang et al. (2015) also suggested that the use of only FA 20:5n-3 could be most accurate if diatoms dominated the POM composition. Due to the mixed taxonomic composition of the primary communities in our dataset, we additionally calculated α_{Ice} using the FA 22:6n-3 in combination with 20:5n-3 to account for the contribution of the dinoflagellate-dominated pelagic communities in our samples.

To estimate the relative contribution of carbon sources to higher trophic levels, Budge et al. (2008) made several assumptions and simplifications that we also included in our study. We assumed that the major sources of FA 20:5n-3 were either ice-related diatoms or pelagic diatoms, and isotopic fractionation and routing processes were negligible. Furthermore, we assumed that our measured carbon stable isotope ratios actually reflect the ratio at the base of the food web. This means that the algae-derived lipid composition during the time of sampling was representative of the time when they

were ingested. Consumers at lower trophic levels show a quick lipid turnover rate ranging between hours and days (Graeve et al. 2005), indicating that this was indeed the case for the more herbivorous species.

The highest α_{Ice} estimates were found when only the diatom-specific FA 20:5n-3 was used (model a). The dinoflagellate-specific FA 22:6n-3 showed generally lower $\delta^{13}C$ values compared to I-POM in all under-ice fauna species. Thus, α_{Ice} estimates were considerably lower in some species when 20:5n-3 was used in combination with 22:6n-3 (model b). This indicates that the sole use of the diatom-specific FA 20:5n-3 underestimates the contribution of dinoflagellate-produced carbon when the proportion of diatoms versus dinoflagellates varies between sea ice and water column, causing a potential bias towards ice algae-produced carbon.

As expected, the sympagic amphipods showed a high trophic dependency on the ice algal production. Surprisingly, many species classified as rather pelagic also showed a considerable input of ice algae-produced carbon, further emphasizing the importance of ice algae for the entire food web. In *Calanus* spp., the estimated relative contribution of ice algae-derived carbon based on the BSIA and the CSIA profiles indicated a mix of pelagic and ice-associated carbon sources. Our results were comparable to a recent study in the Bering Sea, suggesting that the mean proportion of 20:5n-3, which originated from ice algae, was between 39 and 57 % in *Calanus* spp., depending on the ice conditions (Wang et al. 2015). The reported mean α_{Ice} values for the combination of 20:5n-3 and 22:6n-3 were somewhat higher than our values, ranging between 31 and 63 % (Wang et al. 2015). The ice algae-dependency of *Calanus* spp., however, seems to have a high variability, depending on region, season, and environmental properties. For example, Søreide et al. (2006) found a higher ice algae contribution for both *Calanus* copepods in autumn compared to spring, based on bulk stable isotope values.

Among the amphipods, *A. glacialis* showed the highest dependency on ice algal-produced carbon. *O. glacialis*, *G. wilkitzkii,* and *E. holmii* showed also high α_{Ice} values for both BSIA and CSIA, indicating a generally high trophic dependency on the ice algae production for all investigated sympagic amphipods, which is consistent with previous studies (Søreide et al. 2006; Tamelander et al. 2006a). In contrast, Budge et al. (2008) estimated the mean ice algae carbon contribution in *Apherusa sp.* near Barrow, Alaska, based on FA 20:5n-3, to be distinctly lower (61 %) than our results. The mean proportional contributions of ice algae-produced carbon in *Onisimus sp.* and *Gammarus sp*., estimated by Budge et al. (2008), were also clearly lower than our findings (*Onisimus sp*.: 36 %, *Gammarus sp*.: 46 %). These differences could be explained by a combination of regional, seasonal, or inter-annual variability. In a shelf system, pelagic production may be higher due to higher nutrient and light availability, and amphipods have better access to recycled pelagic POM. In the ice-covered high Arctic deep-sea, however, ice algae represent a highly important carbon source for species, such as *A. glacialis* or *Onisimus spp*., and pelagic production is low (Fernández-Méndez 2014).

Based on FA 20:5n-3, Wang et al. (2015) reported that *T. libellula* consumed substantial amounts of ice algae-produced FAs with a proportional contribution between 47 and 63 % in the Bering Sea, with variations according to ice conditions. These values correspond well to the results of our BSIA analysis and our model a, which is based on the same FA. Our results from model b, however, indicate that the true dependency of this species on sea ice-produced carbon was probably lower when the proportional consumption of dinoflagellate-produced FAs is considered. In fact, previous studies, based on bulk stable isotope compositions, also indicate that *T. libellula* primarily depends on pelagic carbon sources (Søreide et al. 2006).

In the pteropod *C. limacina*, we found the lowest trophic dependency on ice algae-produced carbon compared to all other species, irrespective of the method and the mixing model used. A low trophic dependency (< 20 %) on ice algae-produced carbon based on BSIA values was also found by e.g. Søreide et al. (2006). However, the subsequent loss of shelter from predators might be more pronounced in certain species than the dependency on sea ice in terms of food supply.

Altogether, a CSIA-based approach including the effect of multiple potential carbon producing taxa at the base of the food web (such as our model b) appears to be the most conservative approach to estimate the contribution of sea ice algae in food web studies.

We estimated the overall demand of ice algae-produced carbon by the most abundant herbivores *C. glacialis*, *C. hyperboreus* and *A. glacialis* (David et al. 2015). Due to its high abundance in the water column, the bulk of the ice algal carbon demand was attributed to *C. glacialis*. The outcome of this estimation should be considered as a minimum range, because the carbon demand of other abundant potential ice algal grazers, such as *Onisimus* spp. and *Oithona* spp., was not included in our tentative calculation (David et al. 2015). Because *C. glacialis* is known to constantly change its vertical position in the water column, it is unlikely that the estimate of α_{Ice} was biased by our sampling in the under-ice water layer. At an integrated (median) primary production rate by ice algae of about 0.7 mg C m^{-2} d^{-1} (Fernández-Méndez 2014), the minimum ice algal carbon demand of the three species in our study exceeded the ice algal primary production by a factor of 4 to 12 during the sampling period. To some extent, the apparent discrepancy between low sea ice primary production rates and high carbon demand of herbivores may reflect high ice algae production rates prior to our sampling, inferred by Boetius et al. (2013), who observed a high export of ice algae to the sea floor during August and September 2012. In the light of less than one day turnover times in herbivores (Graeve et al. 2005), however, minimum ice algal carbon demand rates ranging potentially an order of magnitude above measured in situ primary production rates of ice algae, indicating that the interaction between ice algal production and food web dynamics is far from understood. To improve the quantitative understanding of this interaction, efforts to quantify the spatio-temporal dynamics of both ice algal production and grazer populations must be considerably increased.

5.5 Conclusions

The results of this study showed an Arctic under-ice community with gradual differences in the dependency on sea ice algae-produced carbon, ranging from nearly 100 % in sympagic amphipods to less than 30 % in the pelagic pteropod *Clione limacina*. Particularly in ecologically important pelagic carbon transmitters, such as *Calanus* spp. and *Themisto libellula*, the dependency on sea ice algae-produced carbon was overall significant, leading to a cumulative carbon demand that considerably exceeded sea ice algae primary production estimated in the field. With a significant dependency on sea ice algae-produced carbon in almost all investigated species, our results show that the Arctic sea ice-water interface is a functional node transmitting carbon from the sea ice into the pelagic food web. Hence, the role of zooplankton and under-ice fauna in the central Arctic Ocean may change significantly in the future, as the spatio-temporal extent of sea ice declines and its structural composition changes. Our results indicate that these changes will likely first have the most pronounced impact on sympagic amphipods, but will consequently affect food web functioning and carbon dynamics of the pelagic system.

Acknowledgements

We thank the captain Uwe Pahl and the crew of the RV ‘Polarstern’ expedition IceArc (PS80) for their excellent support with work at sea. We thank Jan Andries Van Franeker (IMARES) for kindly providing the surface and under-ice trawl (SUIT) and Michiel Van Dorssen for technical support with work at sea. The SUIT was developed by IMARES with support from the Netherlands Ministry of EZ (project WOT-04-009-036) and the Netherlands Polar Program (project ALW 866.13.009). We thank Martina Vortkamp, Dieter Janssen and Sandra Murawski for support with the laboratory analyses at the Alfred Wegener Institute. We thank Maren Voss for her help with the bulk stable isotope analyses (IOW Warnemünde). We thank Stefan Frickenhaus for support with the statistical analyses. Barbara Niehoff and Julia Ehrlich provided data on pelagic zooplankton abundances. This study is part of the Helmholtz Association Young Investigators Group *Iceflux*: Ice-ecosystem carbon flux in polar oceans (VH-NG-800). We thank the editor Thomas Kiørboe and the reviewer Shiway Wang for their helpful suggestions and comments during the review process.

References

Arrigo, K. R., T. Mock, and M. Lizotte. 2010. Primary producers and sea ice, p. 283-325. *In* D. Thomas and G. Dieckmann [eds.], Sea ice. Wiley-Blackwell.

Basedow, S. L., K. S. Tande, and M. Zhou. 2010. Biovolume spectrum theories applied: spatial patterns of trophic levels within a mesozooplankton community at the polar front. J. Plankton Res. **32:** 1105-1119, doi: 10.1093/plankt/fbp110.

Bergé, J.-P., and G. Barnathan. 2005. Fatty acids from lipids of marine organisms: molecular biodiversity, roles as biomarkers, biologically active compounds, and economical aspects. Adv. Biochem. Engin./Biotechnol. **96:** 49-125, doi: 10.1007/b135782.

Boetius, A. and others 2013. Export of algal biomass from the melting Arctic sea ice. Science **339:** 1430-1432, doi: 10.1126/science.1231346.

Boschker, H. T. S., and J. J. Middelburg. 2002. Stable isotopes and biomarkers in microbial ecology. FEMS Microbiol. Ecol. **40:** 85-95, doi: 10.1111/j.1574-6941.2002.tb00940.x.

Bradstreet, M. S., and W. E. Cross. 1982. Trophic relationships at high Arctic ice edges. Arctic **35:** 1-12.

Brand, W. A., T. B. Coplen, J. Vogl, M. Rosner, and T. Prohaska. 2014. Assessment of international reference materials for isotope-ratio analysis (IUPAC Technical Report). Pure and Applied Chemistry **86:** 425-467, doi: 10.1515/pac-2013-1023.

Budge, S. M., S. N. Penney, and S. P. Lall. 2012. Estimating diets of Atlantic salmon (*Salmo salar*) using fatty acid signature analyses; validation with controlled feeding studies. Can. J. Fish. Aquat. Sci. **69:** 1033-1046, doi: 10.1139/F2012-039.

--, A. M. Springer, S. J. Iverson, and G. Sheffield. 2007. Fatty acid biomarkers reveal niche separation in an Arctic benthic food web. Mar. Ecol. Prog. Ser. **336:** 305-309.

--, S. W. Wang, T. E. Hollmén, and M. J. Wooller. 2011. Carbon isotopic fractionation in eider adipose tissue varies with fatty acid structure: implications for trophic studies. J. Exp. Biol. **214:** 3790-3800, doi: 10.1242/jeb.057596.

--, M. J. Wooller, A. M. Springer, S. J. Iverson, C. P. Mcroy, and G. J. Divoky. 2008. Tracing carbon flow in an arctic marine food web using fatty acid-stable isotope analysis. Oecologia **157:** 117-129, doi: 10.1007/s00442-008-1053-7.

Conover, R., and C. Lalli. 1974. Feeding and growth in *Clione limacina* (Phipps), a pteropod mollusc. II. Assimilation, metabolism, and growth efficiency. J. Exp. Mar. Biol. Ecol. **16:** 131-154, doi: 10.1016/0022-0981(74)90016-1.

Coplen, T. B. 2011. Guidelines and recommended terms for expression of stable-isotope-ratio and gas-ratio measurement results. Rapid Commun. Mass Spectrom. **25:** 2538-2560, doi: 10.1002/rcm.5129.

Dalpadado, P., A. Yamaguchi, B. Ellertsen, and S. Johannessen. 2008. Trophic interactions of macro-zooplankton (krill and amphipods) in the Marginal Ice Zone of the Barents Sea. Deep Sea Res. (II Top. Stud. Oceanogr.) **55:** 2266-2274, doi: 10.1016/j.dsr2.2008.05.016.

Dalsgaard, J., M. St. John, G. Kattner, D. Müller-Navarra, and W. Hagen. 2003. Fatty acid trophic markers in the pelagic marine environment. Adv. Mar. Biol. **46:** 225-340, doi: 10.1016/S0065-2881(03)46005-7.

David, C., B. Lange, B. Rabe, and H. Flores. 2015. Community structure of under-ice fauna in the Eurasian central Arctic Ocean in relation to environmental properties of sea-ice habitats. Mar. Ecol. Prog. Ser. **522:** 15-32, doi: 10.3354/meps11156.

Dehn, L.-A., G. G. Sheffield, E. H. Follmann, L. K. Duffy, D. L. Thomas, and T. M. O'hara. 2007. Feeding ecology of phocid seals and some walrus in the Alaskan and Canadian Arctic as determined by stomach contents and stable isotope analysis. Polar Biol. **30:** 167-181, doi: 10.1007/s00300-006-0171-0.

Deniro, M. J., and S. Epstein. 1977. Mechanism of carbon isotope fractionation associated with lipid synthesis. Science **197:** 261-263, doi: 10.1126/science.327543.

--, and --. 1978. Influence of diet on the distribution of carbon isotopes in animals. Geochim. Cosmochim. Acta **42:** 495-506, doi: 10.1016/0016-7037(78)90199-0.

Durbin, E. G., and M. C. Casas. 2013. Early reproduction by *Calanus glacialis* in the Northern Bering Sea: the role of ice algae as revealed by molecular analysis. J. Plankton Res. **36:** 523-541, doi: 10.1093/plankt/fbt121.

Ehrlich, J. 2015. Diversity and distribution of high-Arctic zooplankton in the Eurasian Basin in late summer 2012. Master thesis. Univ. of Hamburg.

Falk-Petersen, S., J. R. Sargent, J. Henderson, E. N. Hegseth, H. Hop, and Y. B. Okolodkov. 1998. Lipids and fatty acids in ice algae and phytoplankton from the Marginal Ice Zone in the Barents Sea. Polar Biol. **20:** 41-47.

--, --, S. Kwasniewski, B. Gulliksen, and R.-M. Millar. 2001. Lipids and fatty acids in *Clione limacina* and *Limacina helicina* in Svalbard waters and the Arctic Ocean: trophic implications. Polar Biol. **24:** 163-170.

--, --, and K. S. Tande. 1987. Lipid composition of zooplankton in relation to the sub-Arctic food web. Polar Biol. **8:** 115-120,

Feder, H. M., K. Iken, A. L. Blanchard, S. C. Jewett, and S. Schonberg. 2011. Benthic food web structure in the southeastern Chukchi Sea: an assessment using $\delta^{13}C$ and $\delta^{15}N$ analyses. Polar Biol. **34:** 521-532, doi: 10.1007/s00300-010-0906-9.

Fernández-Méndez, M. 2014. Primary productivity in Arctic sea ice and ocean. Ph.D. thesis. Univ. of Bremen.

-- and others 2015. Photosynthetic production in the central Arctic Ocean during the record sea-ice minimum in 2012. Biogeosciences **12:** 3525-3549, doi: 10.5194/bg-12-3525-2015.

Fetterer, F., K. Knowles, W. Meier, and M. Savoie. 2002. Sea Ice Index. Boulder, CO: National Snow and Ice Data Center. Digital media **6**.

Folch, J., M. Lees, and G. H. Sloane-Stanley. 1957. A simple method for the isolation and purification of total lipids from animal tissues. J. Biol. Chem. **226:** 497-509.

Fry, B., and E. B. Sherr. 1984. $\delta^{13}C$ measurements as indicators of carbon flow in marine and freshwater ecosystems. Contrib. Mar. Sci. **27:** 13-47.

Gannes, L. Z., D. M. O'Brien, and C. Martínez Del Rio. 1997. Stable isotopes in animal ecology : assumptions, caveats, and a call for more laboratory experiments. Ecology **78:** 1271-1276, doi: 10.1890/0012-9658(1997)078[1271:SIIAEA]2.0CO;2.

Gilmer, R. W. 1974. Some aspects of feeding in thecosomatous pteropod molluscs. J. Exp. Mar. Biol. Ecol. **15:** 127-144, doi: 10.1016/0022-0981(74)90039-2.

--, and G. R. Harbison. 1991. Diet of *Limacina helicina* (Gastropoda: Thecosomata) in Arctic waters in midsummer. Mar. Ecol. Prog. Ser. **77:** 125-134.

Gosselin, M., M. Levasseur, P. A. Wheeler, R. A. Horner, and B. C. Booth. 1997. New measurements of phytoplankton and ice algal production in the Arctic Ocean. Deep Sea Res. (II Top. Stud. Oceanogr.) **44:** 1623-1644, doi: 10.1016/S0967-0645(97)00054-4.

Gradinger, R., and B. A. Bluhm. 2004. In-situ observations on the distribution and behavior of amphipods and Arctic cod (*Boreogadus saida*) under the sea ice of the High Arctic Canada Basin. Polar Biol. **27:** 595-603, doi: 10.1007/s00300-004-0630-4.

Graeve, M., C. Albers, and G. Kattner. 2005. Assimilation and biosynthesis of lipids in Arctic *Calanus* species based on feeding experiments with a ^{13}C labelled diatom. J. Exp. Mar. Biol. Ecol. **317:** 109-125, doi: 10.1016/j.jembe.2004.11.016.

--, W. Hagen, and G. Kattner. 1994a. Herbivorous or omnivorous? On the significance of lipid compositions as trophic markers in Antarctic copepods. Deep Sea Res. (I Oceanogr. Res. Pap.) **41:** 915-924, doi: 10.1016/0967-0637(94)90083-3.

--, and D. Janssen. 2009. Improved separation and quantification of neutral and polar lipid classes by HPLC-ELSD using a monolithic silica phase: application to exceptional marine lipids. J. Chromatogr. B **877:** 1815-1819, doi: 10.1016/j.jchromb.2009.05.004.

--, G. Kattner, and W. Hagen. 1994b. Diet-induced changes in the fatty acid composition of Arctic herbivorous copepods: Experimental evidence of trophic markers. J. Exp. Mar. Biol. Ecol. **182:** 97-110, doi: 10.1016/0022-0981(94)90213-5.

--, --, and D. Piepenburg. 1997. Lipids in Arctic benthos: does the fatty acid and alcohol composition reflect feeding and trophic interactions? Polar Biol. **18:** 53-61, doi: 10.1007/s003000050158.

Graham, C., L. Oxtoby, S. W. Wang, S. M. Budge, and M. J. Wooller. 2014. Sourcing fatty acids to juvenile polar cod (*Boreogadus saida*) in the Beaufort Sea using compound-specific stable carbon isotope analyses. Polar Biol. **37:** 697-705, doi: 10.1007/s00300-014-1470-5.

Hecky, R. E., and R. H. Hesslein. 1995. Contributions of benthic algae to lake food webs as revealed by stable isotope analysis. J. N. Am. Benthol. Soc. **14:** 631-653, doi: 10.2307/1467546.

Hobson, K. A., W. G. Ambrose Jr., and P. E. Renaud. 1995. Sources of primary production, benthic-pelagic coupling, and trophic relationships within the Northeast Water Polynya: Insights from delta $\delta^{13}C$ and $\delta^{15}N$ analysis. Mar. Ecol. Prog. Ser. **128:** 1-10.

--, A. Fisk, N. Karnovsky, M. Holst, J.-M. Gagnon, and M. Fortier. 2002. A stable isotope ($\delta^{13}C$, $\delta^{15}N$) model for the North Water food web: implications for evaluating trophodynamics and the flow of energy and contaminants. Deep Sea Res. (II Top. Stud. Oceanogr.) **49:** 5131-5150, doi: 10.1016/S0967-0645(02)00182-0.

Horner, R. A. 1985. Sea ice biota. CRC Press.

Johannessen, O. M. and others 2004. Arctic climate change: observed and modelled temperature and sea-ice variability. Tellus A **56:** 328-341, doi: 10.1111/j.1600-0870.2004.00060.x.

Kraft, A., J. Berge, Ø. Varpe, and S. Falk-Petersen. 2013. Feeding in Arctic darkness: mid-winter diet of the pelagic amphipods *Themisto abyssorum* and *T. libellula*. Mar. Biol. **160:** 241-248, doi: 10.1007/S00227-012-2065-8.

Kürten, B., I. Frutos, U. Struck, S. J. Painting, N. V. C. Polunin, and J. J. Middelburg. 2012. Trophodynamics and functional feeding groups of North Sea fauna: a combined stable isotope and fatty acid approach. Biogeochemistry **113:** 189-212, doi: 10.1007/s10533-012-9701-8.

Kwok, R. 2007. Near zero replenishment of the Arctic multiyear sea ice cover at the end of 2005 summer. Geophys. Res. Lett. **34:** L05501, doi: 10.1029/2006GL028737.

--, G. F. Cunningham, M. Wensnahan, I. Rigor, H. J. Zwally, and D. Yi. 2009. Thinning and volume loss of the Arctic Ocean sea ice cover: 2003-2008. J. Geophys. Res. **114:** C07005, doi: 10.1029/2009jc005312.

Legendre, L. and others 1992. Ecology of sea ice biota. Polar Biol. **12:** 429-444, doi: 10.1007/BF00243114.

Lindsay, R. W., J. Zhang, A. Schweiger, M. Steele, and H. Stern. 2009. Arctic sea ice retreat in 2007 follows thinning trend. J. Climate **22:** 165-176, doi: 10.1175/2008jcli2521.1.

Madurell, T., E. Fanelli, and J. E. Cartes. 2008. Isotopic composition of carbon and nitrogen of suprabenthic fauna in the NW Balearic Islands (western Mediterranean). J. Mar. Syst. **71:** 336-345, doi: 10.1016/j.jmarsys.2007.03.006.

Maslanik, J., J. Stroeve, C. Fowler, and W. Emery. 2011. Distribution and trends in Arctic sea ice age through spring 2011. Geophys. Res. Lett. **38:** L13502, doi: 10.1029/2011gl047735.

Mayzaud, P., M. Boutoute, and S. Gasparini. 2013. Differential response of fatty acid composition in the different lipid classes from particulate matter in a high Arctic fjord (Kongsfjorden, Svalbard). Mar. Chem. **151:** 23-34, doi: 10.1016/j.marchem.2013.02.009.

McConnaughey, T., and C. P. McRoy. 1979. Food-web structure and the fractionation of carbon isotopes in the Bering Sea. Mar. Biol. **53:** 257-262, doi: 10.1007/BF00952434.

Meier-Augenstein, W. 2002. Stable isotope analysis of fatty acids by gas chromatography-isotope ratio mass spectrometry. Anal. Chim. Acta **465:** 63-79, doi: 10.1016/S0003-2670(02)00194-0.

Mintenbeck, K., T. Brey, U. Jacob, R. Knust, and U. Struck. 2008. How to account for the lipid effect on carbon stable-isotope ratio ($\delta^{13}C$): sample treatment effects and model bias. J. Fish Biol. **72:** 815-830, doi: 10.1111/j.1095-8649.2007.01754.x.

Moreno, V. J., J. E. A. De Moreno, and R. R. Brenner. 1979. Fatty acid metabolism in the calanoid copepod *Paracalanus parvus*: 1. Polyunsaturated fatty acids. Lipids **14:** 313-317.

Noyon, M., F. Narcy, S. Gasparini, and P. Mayzaud. 2011. Growth and lipid class composition of the Arctic pelagic amphipod *Themisto libellula*. Mar. Biol. **158:** 883-892, doi: 10.1007/s00227-010-1615-1.

Olli, K. and others 2007. The fate of production in the central Arctic Ocean-top-down regulation by zooplankton expatriates? Prog. Oceanogr. **72:** 84-113, doi: 10.1016/j.pocean.2006.08.002.

Parnell, A. C., R. Inger, S. Bearhop, and A. L. Jackson. 2010. Source partitioning using stable isotopes: coping with too much variation. PloS one **5:** e9672, doi: 10.1371/journal.pone.0009672.

Paul, D., G. Skrzypek, and I. Forizs. 2007. Normalization of measured stable isotopic compositions to isotope reference scales-a review. Rapid Commun. Mass Spectrom. **21:** 3006-3014, doi: 10.1002/rcm.3185.

Peterson, B. J., and B. Fry. 1987. Stable isotopes in ecosystem studies. Annu. Rev. Ecol. Syst. **18:** 293-320.

Phleger, C. F., M. M. Nelson, B. D. Mooney, and P. D. Nichols. 2001. Interannual variations in the lipids of the Antarctic pteropods *Clione limacina* and *Clio pyramidata*. Comp. Biochem. Physiol. B: Biochem. Mol. Bio. **128:** 553-564, doi:10.1016/S1096-4959(00)00356-0.

Pinnegar, J. K., and N. V. C. Polunin. 1999. Differential fractionation of $\delta^{13}C$ and $\delta^{15}N$ among fish tissues: implications for the study of trophic interactions. Funct. Ecol. **13:** 225-231, doi: 10.1046/j.1365-2435.1999.00301.x.

Poltermann, M. 2001. Arctic sea ice as feeding ground for amphipods-food sources and strategies. Polar Biol. **24:** 89-96, doi: 10.1007/s003000000177.

Post, D. M. 2002. Using stable isotopes to estimate trophic position: models, methods, and assumptions. Ecology **83:** 703-718, doi: 10.1890/0012-9658(2002)083[0703:USITET]2.0.CO;2.

--, C. A. Layman, D. A. Arrington, G. Takimoto, J. Quattrochi, and C. G. Montana. 2007. Getting to the fat of the matter: models, methods and assumptions for dealing with lipids in stable isotope analyses. Oecologia **152:** 179-189, doi: 10.1007/S00442-006-0630-x.

R Core Team. 2015. R: a language and environment for statistical computing. R Foundation for Statistical Computing, Vienna. www.R-project.org.

Rau, G. H., A. J. Mearns, D. R. Young, R. J. Olson, H. A. Schafer, and I. R. Kaplan. 1983. Animal $^{13}C/^{12}C$ correlates with trophic level in pelagic food webs. Ecology **64:** 1314-1318, doi: 10.2307/1937843.

Sargent, J. R., R. R. Gatten, and R. Mcintosh. 1977. Wax esters in the marine environment-their occurrence, formation, transformation and ultimate fates. Mar. Chem. **5:** 573-584, doi: 10.1016/0304-4203(77)90043-3.

Scott, C. L., S. Falk-Petersen, B. Gulliksen, O.-J. Lønne, and J. R. Sargent. 2001. Lipid indicators of the diet of the sympagic amphipod *Gammarus wilkitzkii* in the Marginal Ice Zone and in open waters of Svalbard (Arctic). Polar Biol. **24:** 572-576, doi: 10.1007/S003000100252.

--, --, J. R. Sargent, H. Hop, O. J. Lønne, and M. Poltermann. 1999. Lipids and trophic interactions of ice fauna and pelagic zooplankton in the marginal ice zone of the Barents Sea. Polar Biol. **21:** 65-70, doi: 10.1007/s003000050335.

Sherr, E. B., B. F. Sherr, and L. Fessenden. 1997. Heterotrophic protists in the central Arctic Ocean. Deep Sea Res. (II Top. Stud. Oceanogr.) **44:** 1665-1682, doi: 10.1016/S0967-0645(97)00050-7.

Søreide, J. E., M. L. Carroll, H. Hop, W. G. Ambrose Jr., E. N. Hegseth, and S. Falk-Petersen. 2013. Sympagic-pelagic-benthic coupling in Arctic and Atlantic waters around Svalbard revealed by stable isotopic and fatty acid tracers. Marine Biology Research **9:** 831-850, doi: 10.1080/17451000.2013.775457.

-- and others 2008. Seasonal feeding strategies of *Calanus* in the high-Arctic Svalbard region. Deep Sea Res. (II Top. Stud. Oceanogr.) **55:** 2225-2244, doi: 10.1016/j.dsr2.2008.05.024.

--, H. Hop, M. L. Carroll, S. Falk-Petersen, and E. N. Hegseth. 2006. Seasonal food web structures and sympagic-pelagic coupling in the European Arctic revealed by stable isotopes and a two-source food web model. Prog. Oceanogr. **71:** 59-87, doi: 10.1016/j.pocean.2006.06.001.

--, E. Leu, J. Berge, M. Graeve, and S. Falk-Petersen. 2010. Timing of blooms, algal food quality and *Calanus glacialis* reproduction and growth in a changing Arctic. Global Change Biol. **16:** 3154-3163, doi: 10.1111/j.1365-2486.2010.02175.x.

Subba Rao, D. V., and T. Platt. 1984. Primary production of Arctic waters. Polar Biol. **3:** 191-201, doi: 10.1007/BF00292623.

Sweeting, C. J., N. V. C. Polunin, and S. Jennings. 2006. Effects of chemical lipid extraction and arithmetic lipid correction on stable isotope ratios of fish tissues. Rapid Commun. Mass Spectrom. **20:** 595-601, doi: 10.1002/rcm.2347.

Tamelander, T., C. Kivimäe, R. G. J. Bellerby, P. E. Renaud, and S. Kristiansen. 2009. Base-line variations in stable isotope values in an Arctic marine ecosystem: effects of carbon and nitrogen uptake by phytoplankton. Hydrobiologia **630:** 63-73, doi: 10.1007/S10750-009-9780-2.

--, P. E. Renaud, H. Hop, M. L. Carroll, W. G. Ambrose Jr., and K. A. Hobson. 2006a. Trophic relationships and pelagic-benthic coupling during summer in the Barents Sea Marginal Ice Zone, revealed by stable carbon and nitrogen isotope measurements. Mar. Ecol. Prog. Ser. **310:** 33-46.

--, J. E. Søreide, H. Hop, and M. L. Carroll. 2006b. Fractionation of stable isotopes in the Arctic marine copepod *Calanus glacialis*: Effects on the isotopic composition of marine particulate organic matter. J. Exp. Mar. Biol. Ecol. **333:** 231-240, doi: 10.1016/j.jembe.2006.01.001.

Tieszen, L. L., T. W. Boutton, K. Tesdahl, and N. A. Slade. 1983. Fractionation and turnover of stable carbon isotopes in animal tissues: implications for $\delta^{13}C$ analysis of diet. Oecologia **57:** 32-37, doi: 10.1007/BF00379558.

Van Franeker, J. A., H. Flores, and M. Van Dorssen. 2009. The Surface and Under Ice Trawl (SUIT), p. 181-188. *In* H. Flores [ed.], Frozen Desert Alive-The role of sea ice for pelagic macrofauna and its predators. Ph.D thesis. Univ. of Groningen.

Viso, A.-C., and J.-C. Marty. 1993. Fatty acids from 28 marine microalgae. Phytochemistry **34:** 1521-1533, doi: 10.1016/S0031-9422(00)90839-2.

Wang, S. W., S. M. Budge, R. R. Gradinger, K. Iken, and M. J. Wooller. 2014. Fatty acid and stable isotope characteristics of sea ice and pelagic particulate organic matter in the Bering Sea: tools for estimating sea ice algal contribution to Arctic food web production. Oecologia **174:** 699-712, doi: 10.1007/s00442-013-2832-3.

--, --, K. Iken, R. R. Gradinger, A. M. Springer, and M. J. Wooller. 2015. Importance of sympagic production to Bering Sea zooplankton as revealed from fatty acid-carbon stable isotope analyses. Mar. Ecol. Prog. Ser. **518:** 31-50, 10.3354/meps11076.

Wassmann, P. and others 2006. Food webs and carbon flux in the Barents Sea. Prog. Oceanogr. **71:** 232-287, doi: 10.1016/j.pocean.2006.10.003.

Weems, J., K. Iken, R. R. Gradinger, and M. J. Wooller. 2012. Carbon and nitrogen assimilation in the Bering Sea clams *Nuculana radiata* and *Macoma moesta*. J. Exp. Mar. Biol. Ecol. **430–431:** 32-42, doi: 10.1016/j.jembe.2012.06.015.

Wold, A. and others 2011. Life strategy and diet of *Calanus glacialis* during the winter-spring transition in Amundsen Gulf, south-eastern Beaufort Sea. Polar Biol. **34:** 1929-1946, doi: 10.1007/s00300-011-1062-6.

Chapter 4: Assessing springtime spatial variability of sea ice algal habitat: MYI vs. FYI

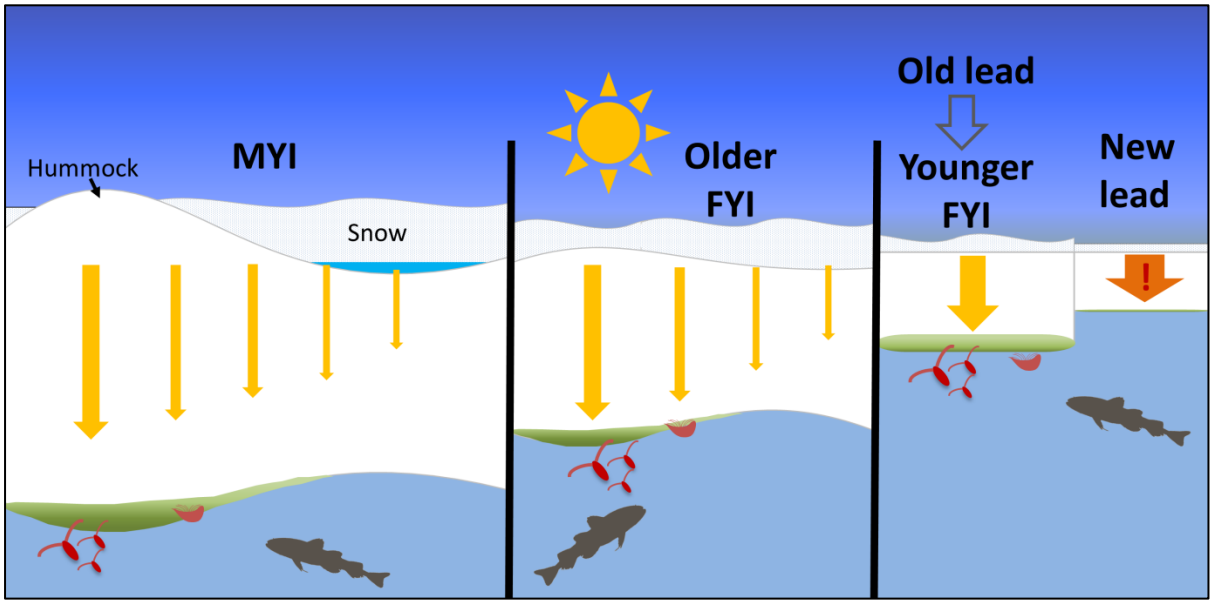

Conceptual diagram of sea ice algae distribution at the bottom of different ice types.

Paper 6. Comparing springtime ice-algal chlorophyll a and physical properties of multi-year and first-year sea ice from the Lincoln Sea

Published in: *PLoS One*, *10*(4), e0122418, doi:10.1371/journal.pone.0122418

Benjamin A. Lange, Christine Michel, Justin F. Beckers, J. Alec Casey, Hauke Flores, Ido Hatam, Guillaume Meisterhans, Andrea Niemi, Christian Haas

Abstract

With near-complete replacement of Arctic multi-year ice (MYI) by first-year ice (FYI) predicted to occur within this century, it remains uncertain how the loss of MYI will impact the abundance and distribution of sea ice associated algae. In this study we compare the chlorophyll *a* (chl *a*) concentrations and physical properties of MYI and FYI from the Lincoln Sea during 3 spring seasons (2010-2012). Cores were analysed for texture, salinity, and chl *a*. We identified annual growth layers for 7 of 11 MYI cores and found no significant differences in chl *a* concentration between the bottom first-year-ice portions of MYI, upper old-ice portions of MYI, and FYI cores. Overall, the maximum chl *a* concentrations were observed at the bottom of young FYI. However, there were no significant differences in chl *a* concentrations between MYI and FYI. This suggests little or no change in algal biomass with a shift from MYI to FYI and that the spatial extent and regional variability of refrozen leads and younger FYI will likely be key factors governing future changes in Arctic sea ice algal biomass. Bottom-integrated chl *a* concentrations showed negative logistic relationships with snow depth and bulk (snow plus ice) integrated extinction coefficients; indicating a strong influence of snow cover in controlling bottom ice algal biomass. The maximum bottom MYI chl *a* concentration was observed in a hummock, representing the thickest ice with lowest snow depth of this study. Hence, in this and other studies MYI chl *a* biomass may be under-estimated due to an under-representation of thick MYI (e.g., hummocks), which typically have a relatively thin snowpack allowing for increased light transmission. Therefore, we suggest the on-going loss of MYI in the Arctic Ocean may have a larger impact on ice–associated production than generally assumed.

6.1 Introduction

Arctic first-year sea ice (FYI), from lower latitude and shelf regions, is generally more productive than multi-year ice (MYI), which leads to the assumption that a replacement of MYI by FYI will result in an overall increase of sea ice algal biomass. Arctic sea ice has already undergone a dramatic reduction of MYI with pronounced losses of the oldest and thickest MYI (Kwok & Rothrock, 2009; Maslanik et al., 2011; Stroeve et al., 2011). In September 2012, a new record Arctic sea ice extent minimum was set, far exceeding the previous record minimum of 2007, which was itself a remarkable decline from previous years (IPCC, 2013; Parkinson & Comiso, 2013). The decline of summer sea ice has occurred concurrently with an increase in duration of the melt season and changes in the timing of melt onset and freeze-up (Howell et al., 2009; IPCC, 2013; Markus et al., 2009; Stammerjohn et al., 2012). These findings in conjunction with climate-model simulations (Massonnet et al., 2012; Overland & Wang, 2013; Stroeve et al., 2007; Stroeve et al., 2012) demonstrate that continued Arctic warming and declining Arctic sea ice, with the replacement of MYI by FYI, is likely to continue unabated into the future, having profound consequences for climate feed-backs, physical ocean processes, ecosystem linkages, and Arctic biodiversity (AMAP, 2011; IPCC, 2013).

The rapid loss of sea ice represents an equally rapid change in habitat for sea ice algae, protists, and ice-associated fauna. Sea ice algae represent an important and high quality food source, directly or indirectly, for many key organisms found in polar regions (e.g. copepods, amphipods, sea birds, polar cod, seals, polar bears; (Arrigo & Thomas, 2004; Budge et al., 2008; Søreide et al., 2013; Søreide et al., 2006)). In the Arctic, the timing of ice algal growth is important for the reproduction and growth of key grazing zooplankton species, such as copepods (Michel et al., 1996; Søreide et al., 2010). Ice algae provide food for pelagic grazers or may sink at the time of ice melt to the benthos where they are consumed by benthic communities or sequestered into the sediments (e.g., (Boetius et al., 2013)). Therefore, changes in ice algal biomass and distribution are expected to strongly impact Arctic food webs and the Arctic carbon cycle, which can have cascading impacts on global-scale ecological interactions and the global carbon budget.

Sea ice decline, thinning of Arctic sea ice, and the loss of MYI have resulted in reduced Arctic-wide sea ice albedo (Riihela et al., 2013) and more light reaching the under-ice environment in summer (Nicolaus et al., 2012). Such conditions have been suggested to be conducive to the development of under ice phytoplankton blooms, which may become more prominent in the future (Arrigo et al., 2012). Reductions in sea ice thickness and extent have also been linked to increases in primary production in coastal shelf regions (Arrigo et al., 2008; Arrigo & van Dijken, 2011). However, current and future estimates for primary production, including ice algal and phytoplankton growth, in the central Arctic Ocean remain uncertain. Even with increased light availability, primary production may be limited by nutrient supply, resulting in part from increased surface water stratification (Tremblay et al., 2012).

The development of sea ice algal communities is influenced by sea ice microstructure (e.g., salinity and temperature which influence permeability), nutrient supply, and transmitted irradiance (see recent review in (Vancoppenolle et al., 2013)). During spring, the main influences on under-ice irradiance are the snow depth distribution, with snow extinction coefficients between 4 to 80 m^{-1}(Hamre et al., 2004; Järvinen & Leppäranta, 2011; Maykut & Grenfell, 1975; Thomas, 1963), and ice thickness, to a lesser extent, with extinction coefficients between 0.8 to 1.55 m^{-1}(Grenfell & Maykut, 1977; Light et al., 2008; Nicolaus et al., 2010; Thomas, 1963). Initial growth of sea ice algae, during early spring, is primarily controlled by the snow distribution, which is typically evident by a negative relationship between chlorophyll *a* (chl *a*) and snow depth (e.g., (Campbell et al., 2014; Mundy et al., 2007)). During the progression of melt, light transmission increases due to changes in the optical properties of snow and ice (Nicolaus et al., 2010; Perovich, 1996). Consequently, ice algal growth increases and shifts to a more nutrient-limited system, which can be accompanied by a combination of other limiting factors such as: self-shading, diurnal light patterns, or ice ablation (Cota & Smith, 1991; Gosselin et al., 1990; Lavoie et al., 2005). In some instances when light transmission increases faster than algal communities can adapt, the increased light field can reduce activity and biomass of algal

communities due to photo-inhibition (Barlow et al., 1988; Michel et al., 1988). Ice algal growth and the bloom period are terminated during advanced and rapid melt (Lavoie et al., 2005).

Many studies have characterized the relationship between snow depth, transmitted irradiance, and chl *a* for FYI (e.g., (Campbell et al., 2014; Mundy et al., 2007)), however, little is known about these relationships for MYI. In general, the large majority of studies dealing with ice algae or chl *a* biomass focus on landfast FYI (e.g., (Alou-Font et al., 2013; Cota et al., 1991; Leu et al., 2011; Mundy et al., 2011; Nozais et al., 2001), see also summary in (Arrigo et al., 2010)). These limitations stem from the logistical constraints of sampling within the Arctic Ocean, particularly within regions dominated by MYI.

A summary of studies concerning Arctic MYI chl *a* biomass (Table 1) reveals the need for more recent observations within MYI-dominated regions during the onset of algal growth (e.g., April to May). The available MYI studies are all currently over nine years old with the majority covering the summer season (Table 1). The four studies conducted during the winter-spring transition were conducted within the Bering Sea, Greenland Sea, Fram Strait and Beaufort Sea (Table 1) leaving a large portion of the MYI covered Arctic with no observations during this transitional period. Of all these MYI studies (Table 1), none characterize the chl *a*-snow depth relationship or provide a detailed comparison between FYI and MYI chl *a* biomass for the same region, which could provide insight into a future Arctic Ocean with little or no MYI. Most of the MYI studies listed in Table 1, except for the three most recent studies (e.g., (Gradinger et al., 2010; Gradinger et al., 2005; Schünemann & Werner, 2005)), were conducted in a different Arctic system when the melt season was shorter (Markus et al., 2009), temperatures were colder (Screen & Simmonds, 2010), sea ice was thicker (Kwok & Rothrock, 2009), and MYI dominated (Maslanik et al., 2011). Thus, it may be stated that our current understanding of Arctic sea ice algae and chl *a* biomass is based on observations with limited spatial and temporal coverage from regions that have experienced pronounced changes. As a result, there is a need for additional MYI chlorophyll observations to fill important spatial, temporal and seasonal (i.e., spring period) gaps.

The north-eastern coast of Canada, including the Lincoln Sea, represents an important region as it is home to some of the oldest and thickest ice in the Arctic and will likely be one of the last remaining refuges for MYI in the future (Haas et al., 2006; Haas et al., 2010; IPCC, 2013; Maslanik et al., 2011). Despite the importance of this region, we are aware of only two sea ice biogeochemical studies in the Lincoln Sea, characterizing microbial communities (Hatam et al., 2014) and denitrification (Rysgaard et al., 2008).The Lincoln Sea is one of the last remaining places where baseline observations of older (>3 years) MYI biogeochemical properties are possible and a comparison between MYI and FYI would provide much needed insight into the future of Arctic marine ecosystems. Based on the limited studies of MYI and the spatial bias of FYI studies, it is difficult to estimate how Arctic sea ice algal biomass will change with a shift to a FYI dominated system.

The main goal of our study was to determine if FYI has, or has the potential for, higher chl *a* biomass than MYI in the Lincoln Sea and discuss the implications of our results in the context of a future Arctic with little or no MYI. We address our scientific question first by providing detailed analyses of the physical properties and chl *a* concentrations of sea ice (both MYI and FYI) in three consecutive spring seasons, from a region where no similar studies have been reported. Then we evaluate potential differences of ice-algal chl *a* concentrations and biophysical sea ice properties between ice types, ice ages, and texture classes. Lastly, we investigate the relationship between sea ice chl *a* concentrations and environmental properties, such as snow depth, sea ice structure, and light availability.

Table 1. Summary of relevant studies on Arctic MYI chlorophyll a biomass.

Region	Season	Year(s)	Study
Beaufort-Chukchi Seas	Year-round	1997-1998	Melnikov et al. (2002) (Melnikov et al., 2002)*
Fram Strait	Winter	1993	Thomas et al. (1995) (Thomas et al., 1995)
Fram Strait	Winter-Spring & Summer	2002 & 2003	Schünemann and Werner(2005) (Schünemann & Werner, 2005)*

Greenland Sea & FramStrait	Spring-Summer	1997	Werner and Gradinger(2002) (Werner & Gradinger, 2002)*
Bering Sea	Spring	< 1974	McRoy and Goering (1974)(McRoy & Goering, 1974)
Central Arctic Ocean	Summer	1991 & 1994	Gradinger (1999) (Gradinger, 1999);Gosselin et al. (1997) (Gosselin et al., 1997)
Beaufort-Chukchi Seas	Summer	2002 & 20032005	Gradinger et al. (2005) (Gradinger et al., 2005)Gradinger et al. (2010) (Gradinger et al., 2010)
Greenland Sea	Summer	1994 & 1995	Gradinger et al. (1999) (Gradinger et al., 1999);Werner and Zhang (2002)(Werner & Gradinger, 2002)*
Barents Sea	Summer	1993	Gradinger and Zhang (1997) (Gradinger & Zhang, 1997)

*studies conducted during multiple seasons

6.2 Materials and Methods

6.2.1 Study region

In order to conduct this research project in accordance with regulations set forth by the governing agencies responsible for the study region, all relevant research licenses and permissions were acquired from the Nunavut Research Institute (License numbers: 02-075 10R-M; 02-108 11R-M; 02 012 12R-M) and Nunavut Impact Review Board (Screening Decision Report 08YN057).

The Lincoln Sea (Fig. 1) has been called the "Last Ice Area" by the World Wildlife Fund based on recommendations from Arctic Council Assessments, indicating that the Lincoln Sea requires specific attention and research (Kovacs et al., 2011; Michel, 2013). Most studies in this region focus on physical properties (of the MYI) and have documented a slight decline in modal ice thickness since 2004 from between 4.0 and 4.5 m (pre-2008 observations) to 3.5 m (post-2008 observations), which is likely the result of less old ice along the northern coast of Canada (Haas et al., 2010; IPCC, 2013).

The Lincoln Sea is a dynamic area due to interaction with, and exchange of, sea ice with the Arctic Ocean. The Lincoln Sea ice cover is comprised of immobile landfast coastal sea ice at the southern edges and mobile pack ice at its northern extent. The landfast ice consists primarily of consolidated pack ice with smaller amounts of FYI forming in the interstitial space during freeze-up. The division between landfast ice and pack ice is not a distinct line but rather a transitional region that can be characterized by ice with limited mobility due to geographic barriers and the intermittent nature of ice export to the south through Nares Strait. Sea ice in the Lincoln Sea typically comes from the Central Arctic Ocean transported by the Beaufort Gyre and Transpolar Drift circulation patterns (Rigor & Wallace, 2004; Rigor et al., 2002). However, the origin of sea ice in the Lincoln Sea is uncertain because ice ages are typically between 2 to 5 years, with a decreasing proportion of >5 year old ice (Maslanik et al., 2011). This means that ice in this region could have originated from anywhere in the Arctic Ocean.

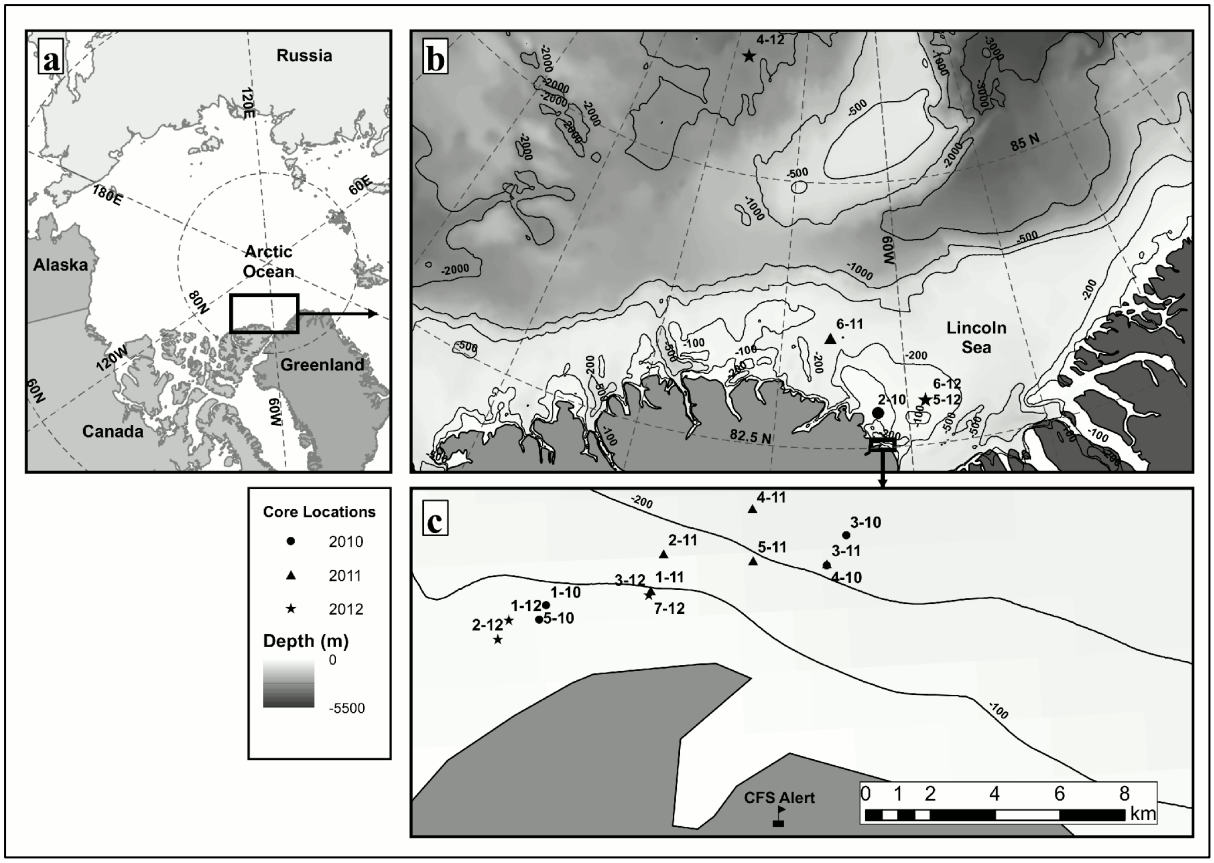

Fig 1. Overview Maps of the study region and ice coring sites. a) Map of the Arctic Ocean with an outline of the study region. b) Map of the Lincoln Sea and neighboring regions. Drifting ice sites (pack ice), ocean bathymetry, and an outline of landfast ice sites are indicated. c) Map of landfast ice coring sites, immediately offshore from CFS Alert.

6.2.2 Sampling

Sampling was conducted during spring in the first two weeks of May 2010, 2011 and 2012 in the Lincoln Sea. One site was located north of the Lincoln Sea (Fig. 1). Sea ice cores were taken at a total of 18 sites: 11 MYI sites (4 in 2010, 4 in 2011 and 3 in 2012), and 7 FYI sites (1 in 2010, 2 in 2011 and 4 in 2012), including landfast ice and mobile pack ice (Fig. 1). Landfast ice sites were visited by snowmobile, and pack ice sites were visited by helicopter or Twin Otter aircrafts.

During this time of year, when temperatures are typically below -10ºC and the low salinity MYI is very hard, coring thicker than ~3.5 m becomes exponentially more difficult. We therefore chose relatively level sites that we knew were below ~3.5 m based on pre-drilled 2 inch auger thickness holes.

At each site three ice cores were extracted within 1 m of each other using a 9 cm inner diameter ice corer (Kovacs Enterprise Mark II) and stored in sterile U-Line bags. One core was sampled for texture and bulk salinity ("Texture core"), one core for chlorophyll *a* ("chl *a* core") and one to two cores for microbial genetics (genetic methodology/protocol and results from one MYI site "1-11" presented elsewhere, see (Hatam et al., 2014)). Due to small discrepancies between core lengths at the same site, texture core lengths were adjusted to correspond to the chl *a* core length by linearly interpolating each depth value (e.g. texture class, bulk salinity, temperature and brine volume) of the texture cores proportionally. All cores were transported from the field back to the Canadian Forces Station (CFS) Alert, Nunavut, Canada (82.5 °N, 62.5 °W) and stored at -15 to -20 °C in the dark.

6.2.3 On-site measurements

At each core location, snow depth (here after referred to as core-location-snow-depth), freeboard and core length were measured. These measurements represent the local conditions (i.e., one single point) at sampling locations, which should not be confused with the larger-scale snow depth and ice thickness survey measurements. Internal ice temperatures were measured on texture cores by drilling holes and inserting a thermometer (Testo 720) immediately after core extraction. Temperatures were measured from surface to bottom at intervals of 0.1 m (cores: 1-10, 3-10 and 4-10) and 0.5 m (core 5-10). In 2012, only ice surface temperature (depth 0.1 m) was measured. For these cores the internal ice temperatures were linearly interpolated between the surface and assumed (theoretical) bottom temperature of -1.78 °C with typical surface water salinities in the Lincoln Sea of ~32 (Newton & Sotirin, 1997). During the study period daily temperature variation within the ice was minimal and based on the measured temperature profiles a linear relationship with ice depth demonstrated a good fit (R^2 = 0.94). Brine volume estimates were calculated for cores with temperature measurements using equations in (Cox & Weeks, 1983). Brine volume values are reported in parts per thousand (ppt).

Snow depth and ice thickness surveys were conducted along transects adjacent to each coring site. These measurements represent the larger-scale characteristics of the sampled ice floes, which should not be confused with the point measurements: core-location-snow-depth and core length. Snow depth was measured using a metal probe at 1 or 10 m intervals and ice thickness was measured in 2 inch augers holes drilled in the ice at 10 m intervals. The length of each transect and number of measurements were dependent on ice type and time constraints (range = 0 to 400 m, mean = 100 m). Snow density measurements were calculated for 5 snow samples collected, at site 2-10, using an Adirondack snow sampler. Additional density values from the same study region were acquired during the CryoSat Validation Experiment (CryoVEx: 11 to 18 April, 2011(Haas et al., 2011)).

Air temperature data were provided by the Environment Canada weather station located on shore at CFS Alert, Nunavut. Mean daily air temperatures during the study were on average -12.5 ^{o}C (2010 to 2012 combined), with a range between -20.3 to -7.4^{o}C, and a maximum temperature of -3.1 ^{o}C. Downwelling total solar irradiance measurements representative of the sampling area were also measured at the nearby CFS Alert weather station. Mean and range of values were calculated for the period May 1-11, 2010 to 2012 (mean = 984, range = 213 to 2313 µmol photons m^{-2} s^{-1}; data acquired from NOAA / ESRL / GMD / GRAD, the GMD-Radiation Group, ftp://aftp.cmdl.noaa.gov/data/radiation/baseline/alt/).

6.2.4 Texture cores

Texture analysis was conducted at ~ -15 ºC. Texture cores were cut into 0.10 to 0.15 m vertical sections that were further cut into vertical thick sections ~ < 5 mm thin, using an electric band saw. For each section, the ice remaining after cutting was put into plastic containers, melted and analyzed for bulk salinity using a salinometer (WTW 3300i). Bulk salinities are reported in parts per thousand (ppt). Thick sections were imaged under crossed polarizers. Analysis of the images provided a stratigraphic description of each ice core by identifying different ice texture classes and the boundaries between classes. Here we divided ice types into 7 texture classes based on grain structure and appearance, following classification systems outlined in (Eicken & Lange, 1989; Eicken et al., 1995; Lange, 1988; Lange et al., 1989)(Table 2 and Fig. 2). For each section of the chl *a* cores, the dominant texture class (i.e. the texture class with the highest areal coverage) from the corresponding texture core was assigned. For surface pieces the uppermost texture class was always assigned to the section because deteriorated ice and snow-ice are distinct layers and only located at the surface.

In MYI cores, we identified the previous year's annual layer in 7 cores by identifying peaks in bulk salinity profiles that corresponded with changes in crystal structure at the same depth, as described in (Jeffries & Krouse, 1988; Schwarzacher, 1959). Accordingly, MYI cores were divided into two groups: the sections above the annual layer (older ice) were classified as multi-year (MY) and sections below the annual layer (new ice) were classified as first-year (FY). Therefore, in later analyses ice type categories comprise MYI cores and FYI cores, whereas ice age categories comprise MY (multi-

year sections of MYI cores), FY (first-year ice sections of MYI cores) and FYI (first-year ice cores). MY portions represent ice that has survived at least one summer. The FY portions represent ice that has grown under the MY portions and typically begins to form during freeze-up in September-October (Markus et al., 2009). In general FYI and FY represent ice of similar ages (e.g. < 1 year), however, FYI can represent ice that started to form either during freeze-up or at a later stage as open water leads form and refreeze. FY also grows slower than FYI due to increased thermal insulation of the thicker ice (MY) and snow layer above it.

Table 2. Description of each sea ice texture class.

Ice Class	Description
Snow-Ice	Looks like granular but is clear in un-polarized images. Forms during flooding or with presence liquid water and snow near freezing and forms small granular crystals during rapid freezing.
Melt Pond	Fresh water, clear in appearance, at or very near the surface of the ice. Sometimes overlaid by snow-ice.
Retextured	Clear ice with unusual crystals or very large crystals, forms near surface below water level
Deteriorated	Transformed columnar or mixed ice with large brine or air pockets, near the surface usually above water level.
Granular	Consolidation of frazil ice usually near the surface (typically with mixed layer underneath). This can occur within MYI and is evidence of super-cooling, turbulent water and/or presence of adjacent re-freezing lead which creates conditions for rapid freezing and formation of frazil ice.
Mixed col./gran.	Mixture of congelation and granular ice. This class also includes intermediate congelation/granular ice because they are difficult to distinguish.
Columnar	Elongated crystals

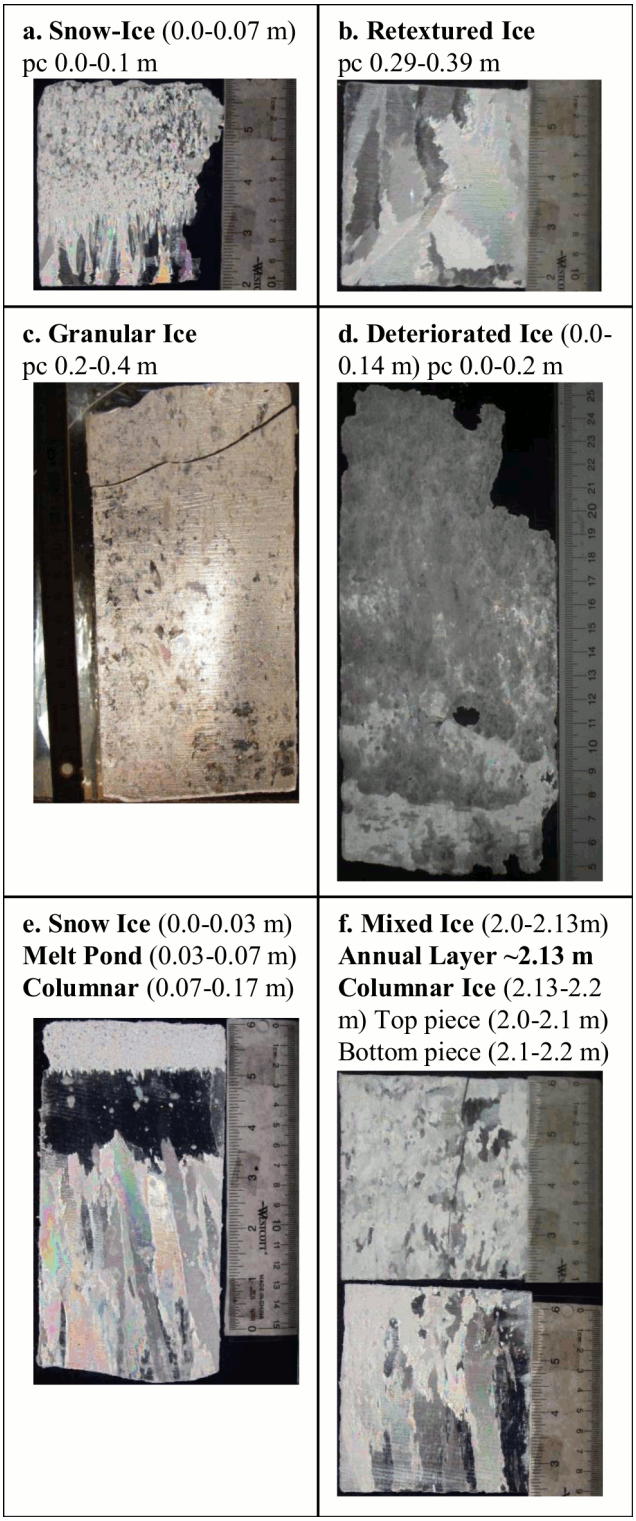

Fig 2. Cross polarized imagery of ice core thin sections showing different ice types. a) core 7-12; b) core 7-12; c) core 2-10; d) core 3-11; e) core 1-12; and f) core 7-12.

6.2.5 Chlorophyll *a* cores

In order to minimize any potential influences on the chl *a* measurements, these cores were always stored below -15 ^{o}C in the dark, for a maximum of nine days. The cores were then shipped, via air at a maximum temperature of -10^{o}C in the dark, to Resolute Bay, Nunavut, where they were stored below

-20 ^{o}C in the dark for 1 to 2 days. Cores were cut using an electric band saw (sterilized with 95% ethanol) in a -20 ^{o}C walk-in freezer. Cores were cut into 10 cm sections except for end pieces (range: 0.09 to 0.17 m), placed in sterile Whirl-Pack (NASCO) bags and melted in the dark. End pieces for 2010 and 2012 samples refer to the ice-air interface. The 2011 cores were cut in the opposite direction, therefore these end pieces refer to the ice-water interface. Core sections were melted without the addition of filtered sea water (FSW) because we were also measuring dissolved constituents (i.e. DOC, nutrients; data not presented here) in the core sections. It has been shown that for common biological analyses (e.g., chlorophyll *a* concentrations) melting without the addition of FSW is an acceptable procedure (Rintala et al., 2014).

Chl *a* concentrations were determined on sub-samples filtered onto Whatman GF/F filters, after 24 h extraction in 90% acetone at 4 ºC in the dark, using a 10AU Tuner Design fluorometer calibrated with pure chlorophyll extract from *Anacystis nidulans* (Sigma; (Parsons et al., 1989)). Chl *a* concentrations were determined using equations from (Parsons et al., 1989) and corresponding instrument calibration coefficients. Chl *a* concentrations are expressed volumetrically (mg m^{-3}) or are vertically integrated (mg m^{-2}) for the bottom 0.2 m core sections (hereafter referred to as bottom-integrated), age class core sections, or total core length.

6.2.6 Statistical analyses

Initial data exploration demonstrated that the distributions of chl *a* data were highly skewed. To achieve the normal distribution patterns required for parametric statistical analyses, log-transformations were applied to the chl *a* data. Two-sample t-tests were conducted to determine the effect of ice type (MYI & FYI) on the chl *a* concentrations of the sea ice. Variance analyses (ANOVAs) were conducted in order to determine the effect of ice age class (MY, FY & FYI); year and texture class on the chl *a* concentrations of the ice. Post-hoc tests (Tukey's HSD) were conducted when both parametric ANOVA (transformed data) and non-parametric Kruskal-Wallis (non-transformed data) analyses showed significant differences.

To investigate the potential influence of snow depth and sea ice optical properties on bottom-integrated chl *a* concentrations a logistic regression model was applied. A logistic regression was used in order to identify potential critical values (inflection point) of the independent variables (e.g., snow depth and bulk integrated extinction coefficients) that could indicate a threshold value for optimal algal growth. Logistic regression analysis required values of the dependent variable in the range 0 to 1.Therefore, bottom-integrated chl *a* values were normalized to the range 0 to 1 by dividing each chl *a* value (y_i) by the maximum value for all cores (y_{max}). The relationship between bottom-integrated chl *a* concentrations and bulk integrated extinction coefficients, for visible radiation, was analyzed in a similar manner. For all calculations we used extinction coefficients for snow: k_s = 20.0 m^{-1} (Thomas, 1963); MYI: k_m = 1.55 m^{-1}; and FYI: k_f = 1.45 m^{-1} (Grenfell & Maykut, 1977). The value of k_s, used here, was chosen from a table of k_s values (Thomas, 1963) based on a corresponding snow density comparable to measured values for our study region between 260 to 281 kg m^{-3} (see section Physical properties). The values of k_s, k_m, and k_f were integrated over the depth of the corresponding ice and snow layers for each core site resulting in "integrated extinction coefficients" (dimensionless), i.e., a value for each snow and ice layer at each site. The "bulk (snow plus ice) integrated extinction coefficient" is simply the sum of the integrated extinction coefficients for snow and ice (also dimensionless), i.e., one value for each core site. In the resulting bulk integrated extinction coefficients, larger values mean shallower penetration of light.

Results are reported as arithmetic mean ± one standard deviation ($\hat{\mu} \pm 1\sigma$).

All statistical analyses were conducted with the R software package v-2.15.2 (R-Development-Core-Team, 2012).

6.3 Results

6.3.1 Physical properties

Based on site-averaged drill hole thickness measurements, i.e., characterizing the larger scale ice properties of the sampled floes, MYI sites were more than twice as thick (3.28 ± 0.56 m) as FYI sites (1.42 ± 0.42 m). Mean MYI core length (2.62 ± 0.24 m), i.e., only characterizing local ice properties of core sampling locations, was also nearly twice as thick as FYI (1.39 ± 0.52 m), with higher variability in FYI core lengths. FYI sites represented two different kinds of ice: ice that formed during the fall when the landfast ice consolidated (i.e., older and thicker FYI with more snow); and ice that formed later in mobile ice when open leads formed and then refroze (i.e., younger and thinner ice with typically less snow).

Site-averaged snow depth at MYI sites (0.39 ± 0.10 m), in general, was thicker than at FYI sites (0.26 ± 0.15 m). Although MYI had lower variability between site-averaged snow depth values, FYI had lower variability when considering each site individually. This was illustrated by the mean of site standard deviations for FYI snow depth: 0.08 m, compared to MYI: 0.17 m. Mean snow density at site 2-10 (Fig. 1) was 260 ± 0.03 kg m^{-3} (n=5) and during CryoVex 2011 was 281 ± 0.7 kg m^{-3} (n=11 (Haas et al., 2011)).

There was no significant inter-annual difference in the mean physical properties (e.g. snow depth and ice thickness) of FYI or MYI (ANOVA, $p > 0.05$). For FYI, there were significant positive relationships between core-location-snow-depth and ice core length ($R^2 = 0.56$, $p = 0.05$, $n = 7$), and between snow depth and mean ice thickness survey measurements ($R^2 = 0.66$, $p < 0.05$, $n = 7$). For MYI, there was an inverse relationship between snow depth and ice core length ($R^2 = 0.51$, $p = 0.01$, $n = 11$), and no significant relationship between snow depth and mean ice thickness survey measurements ($R^2 = 0.12$, $p = 0.3$, $n = 11$).

Two FYI cores were exceptional (3-10 and 6-12; Table 3), exhibiting considerably lower ice thickness, snow depth and core length than the other FYI cores analyzed in this study. These 2 sites were determined to be refrozen leads that correspond to younger FYI that formed later in the season. Although core 4-11 core length was not exceptionally low, survey measurements indicated site 4-11 had the thinnest ice and snow pack (excluding sites 3-10 and 6-12; Table 3). The location was also at the edge of the landfast ice where unstable ice is likely even after freeze-up, therefore was also considered to be a younger FYI site, although older than sites 3-10 and 6-12.

Table 3. Summary of physical data for each core and core site.

Site Overview						Core Location				Ice Thickness Surveys					Snow Depth Surveys				Texture Class Lengths						
Year	**Type**	**id**	**lat**	**lon**	**bath.**	**Core**	**Snow**	**Sal**	**BV**	***μ̂***	**σ**	**d**	**N**	**fb**	***μ̂***	**σ**	**d**	**N**	**col**	**mx**	**gran**	**retex**	**mp**	**s-i**	**det**
2010	FYI	3-10	82.6	-62.0	257	0.93	0.09	6.1	189.4	0.93	-	25	4	0.07	0.08	0.0	45	10	0.88	0.03	0.02	-	-	-	-
2010	MYI	1-10	82.5	-62.6	91	2.23	0.42	3.1	88.1	3.07	0.9	100	6	0.13	0.37	0.1	100	6	0.67	1.40	-	-	0.16	-	-
	MYI	2-10	82.8	-62.3	95	2.80	0.32	3.4	-	3.49	0.4	200	9	0.23	0.33	0.2	200	42	1.94	0.19	0.27	-	0.22	0.16	-
	MYI	4-10	82.6	-62.0	199	2.54	0.50	2.0	133.0	2.45	-	0	1	0.09	0.50	-	0	1	0.73	1.00	0.72	-	-	-	0.10
	MYI	5-10	82.5	-62.6	90	3.11	0.05	2.1	73.3	3.10	0.7	200	9	0.32	0.22	0.2	200	41	0.71	0.07	2.27	-	-	-	0.05
	μ̂	-	-	-	*119*	*2.67*	*0.32*	*2.6*	*98.2*	*3.03*	*0.7*	*125*	*6*	*0.19*	*0.36*	*0.2*	*125*	*23*	*1.01*	*0.66*	*1.09*	-	*0.19*	*0.16*	*0.08*
2011	FYI	2-11	82.6	-62.3	189	1.60	0.38	4.5	-	1.67	-	0	3	0.04	0.38	-	0	1	0.23	0.06	1.32	-	-	-	-
	FYI	4-11	82.6	-62.2	242	1.52	0.17	5.5	-	1.31	0.2	40	5	0.07	0.21	-	40	5	1.40	0.11	0.01	-	-	-	-
	μ̂	-	-	-	*215*	*1.56*	*0.28*	*5.0*	-	*1.49*	*0.2*	*20*	*4*	*0.06*	*0.30*	-	*20*	*3*	*0.82*	*0.08*	*0.66*	-	-	-	-
2011	MYI	1-11	82.5	-62.4	100	2.41	0.55	3.5	-	3.85	1.1	100	10	0.29	0.36	0.2	100	10	1.51	0.24	-	0.18	0.39	0.09	-
	MYI	3-11	82.6	-62.0	199	2.96	0.32	2.1	-	2.80	0.6	100	12	0.17	0.52	0.2	100	12	1.45	0.52	0.81	-	-	-	0.17
	MYI	5-11	82.6	-62.2	159	2.53	0.32	3.9	-	4.48	1.4	100	9	0.33	0.39	0.2	100	9	1.20	-	-	1.01	0.26	0.06	-
	MYI	6-11	83.5	-66.0	260	2.59	0.30	2.4	-	3.02	0.8	100	10	0.17	0.55	0.2	100	10	2.35	0.13	-	-	-	-	0.11
	μ̂	-	-	-	*180*	*2.62*	*0.37*	*3.0*	-	*3.54*	*1.0*	*100*	*10*	*0.24*	*0.46*	*0.2*	*100*	*10*	*1.63*	*0.30*	*0.81*	*0.59*	*0.33*	*0.08*	*0.14*
2012	FYI	2-12	82.5	-62.7	57	1.77	0.20	4.4	90.4	2.00	-	100	4	0.11	0.28	0.1	100	101	1.42	0.07	0.28	-	-	-	-
	FYI	3-12	82.5	-62.4	99	1.34	0.33	3.7	-	1.51	0.1	20	2	0.05	0.33	0.1	20	21	1.25	0.04	0.05	-	-	-	-
	FYI	4-12	86.1	-78.1	2156	1.77	0.47	3.1	87.7	1.68	-	0	1	0.06	0.47	-	0	1	1.42	0.34		-	-	-	-
	FYI	6-12	82.9	-58.6	125	0.83	0.04	5.9	141.4	0.83	0.1	40	3	0.00	0.07	0.0	40	41	0.77	0.05	0.01	-	-	-	-
	μ̂	-	-	-	*609*	*1.43*	*0.26*	*4.3*	*106.5*	*1.51*	*0.1*	*40*	*3*	*0.05*	*0.29*	*0.1*	*40*	*41*	*1.21*	*0.13*	*0.11*	-	-	-	-
2012	MYI	1-12	82.5	-62.7	86	2.67	0.47	3.3	116.5	3.69	0.9	400	11	0.24	0.39	0.2	400	401	1.79	0.81	-	-	0.04	0.02	-
	MYI	5-12	82.9	-58.6	125	2.57	0.31	2.0	115.9	3.23	1.3	120	7	0.29	0.30	0.1	140	140	2.31	0.19	-	-	-	-	0.06
	MYI	7-12	82.5	-62.4	99	2.46	0.60	3.6	184.0	2.90	0.5	200	10	0.20	0.40	0.2	200	221	1.69	0.29	-	0.30	0.11	0.07	-
	μ̂	-	-	-	*103*	*2.56*	*0.46*	*3.0*	*138.8*	*3.27*	*0.9*	*240*	*9*	*0.24*	*0.36*	*0.2*	*247*	*254*	*1.93*	*0.43*	-	*0.30*	*0.07*	*0.05*	*0.06*

All measurements are in meters (m). Abbreviations and symbols: lat=latitude, lon=longitude, bath.=bathymetry, core = core length, snow = core-location-snow-depth, sal = bulk salinity (ppt), BV = core averaged brine volume (ppt), μ̂ = arithmetic mean, σ = one standard deviation, d=distance, N=sample number, fb=mean freeboard, col=columnar,mx=mixed, gran=granular, retex=retextured, mp=melt-pond, s-i=snow-ice, det=deteriorated. "-" = Not available.

In all cores, observed internal ice temperatures increased towards the ice-water interface. Surface ice temperatures ranged between -11.5 and -5 ºC. Bottom ice temperatures were consistently close to the freezing point of sea water (~ -1.78 ºC; see section On-site measurements). All FYI cores followed typical C-shaped bulk salinity curves (Fig. 3a), except for core 4-12 which showed a bulk salinity profile similar to MYI. MYI cores followed typical vertical bulk salinity profiles for MYI with low salinities (0 to 2) near the surface and a general increasing trend towards the bottom ice (Fig. 3b). Brine volume also increased with depth in most cores. Only core 1-12 had a brine volume peak at 0.57 m.

Based on the measured length of each texture class, FYI cores consisted predominantly of columnar ice (76%), with only minor proportions of granular (17%) and mixed (7%) ice. Retextured, melt pond, snow-ice and deteriorated texture classes were not identified in FYI and represented ≤ 5 % of MYI but in some instances represented up to 50% of MYI (e.g., core 5-11; Table 3). MYI cores had a lower proportion of columnar ice (57%), over twice the amount of mixed ice (17%), and approximately equal proportions of granular (14%) ice compared to FYI. Annual growth layers were identified in 7 out of 11 MYI cores (1-10, 2-10, 4-10, 5-10, 1-11, 5-12 and 7-12: Fig. 4). The FY portions (i.e., ice below the annual layer) had a mean length of 0.67 ± 0.31 m and the MY portions (i.e., ice above the annual layer) had a mean length of 1.90 ± 0.40 m. Potential annual growth layers were also identified for the remaining 4 MYI cores (1-12, 3-11, 5-11 and 6-11: Fig. 4); however, these were not assigned as annual layers in the analysis due to lack of confidence (e.g. presence of multiple layers or lack of correspondence between texture change and bulk salinity peak/change).

A summary of all sea ice physical properties is provided in Table 3.

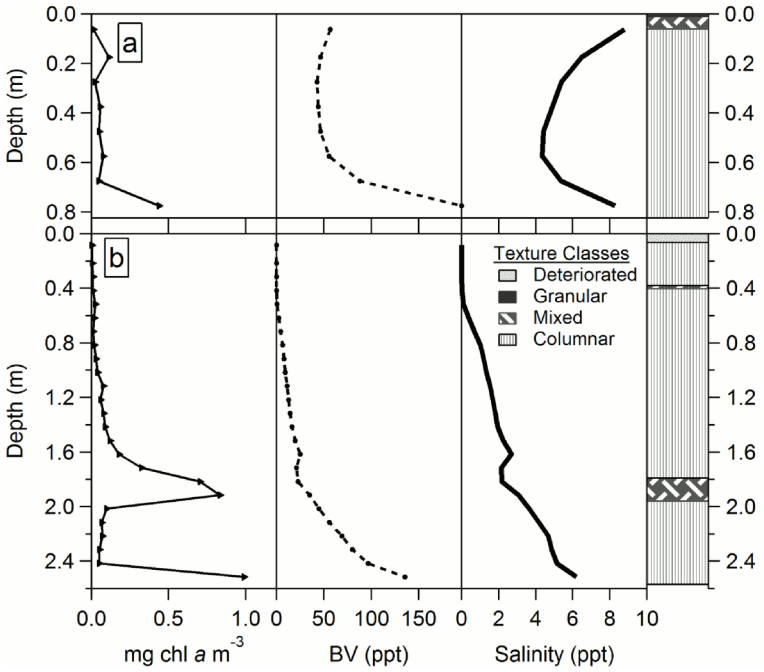

Fig 3. Example vertical profiles for MYI and FYI. Chl a, brine volume (BV), bulk salinity, and texture classes for: a) FYI core 6-12 and b) MYI core 5-12.

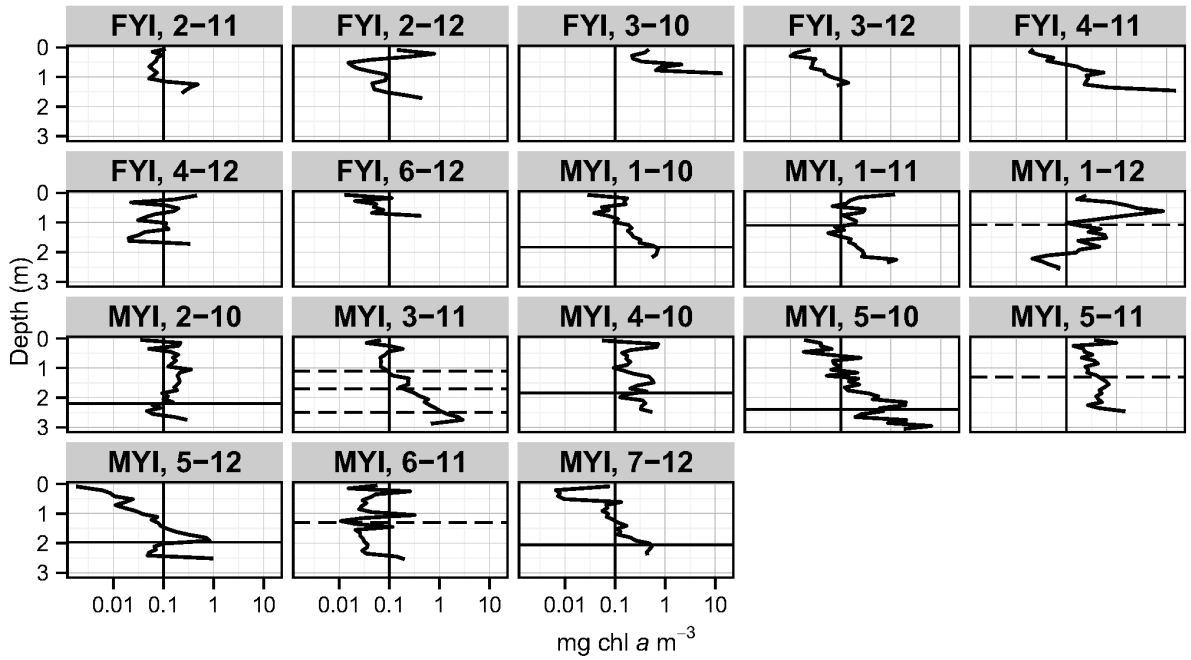

Fig 4. Vertical profiles of chl a concentrations for all cores. Solid horizontal lines represent identified annual layers used in the analyses and dashed horizontal lines represent potential annual layers not used in the analyses (x-axis is log scale).

6.3.2 Chlorophyll *a*

All ice cores, with the exception of core 1-12, had chl *a* concentration peaks or maximum values in the bottom sections (Fig. 4). Most core sections had chl *a* concentrations < 3 mg m^{-3} (Fig. 4). Two FYI cores had chl *a* concentrations > 10 mg m^{-3} in the bottom sections (~0.1 m): core 3-10 (14.1 mg m^{-3}) and 4-11 (15.4 mg m^{-3}; Fig. 4). These two FYI cores also corresponded to younger FYI sites (e.g. refrozen lead). Two MYI cores had sections with chl *a* concentrations > 5 mg m^{-3}: core 5-10 (14.1 mg m^{-3}; section midpoint 0.15 m from bottom), which corresponded to a MYI hummock with the lowest core-location-snow-depth, and core 1-12 (8.4 mg m^{-3}; section midpoint 0.57 m from surface), which had a brine volume peak at the same depth as the chl *a* peak. In all MYI cores with confirmed annual layers, peaks in chl *a* concentrations closely matched the depths of the annual layers (Figs. 3 and 4). Ice cores with re-frozen melt ponds (e.g. 1-10, 1-11, 1-12, 2-10, 5-11 and 7-12) also showed local chl *a* peaks near the surface (Fig. 4). Examples of chl *a*, bulk salinity, and brine volume profiles with coincident texture classes are shown in Fig. 3.

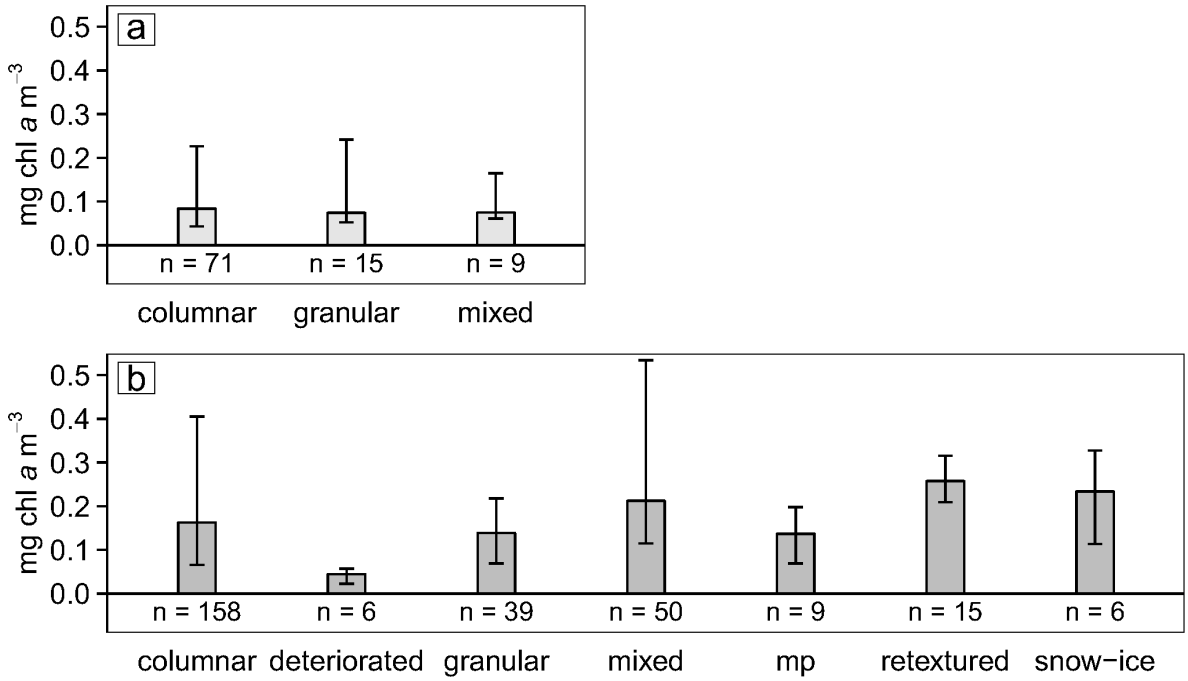

Fig 5. Chl a concentrations in each texture class. a) FYI; and b) MYI. Bars show median values with error bars delineating the 25 and 75 percentiles.

6.3.3 Comparison of ice classes

We found significantly higher bulk salinity values in FYI compared to MYI. MYI cores had higher mean core-integrated chl *a* concentrations (0.93 ± 0.68 mg m^{-2}) than FYI (0.71 ± 0.92 mg m^{-2}). These differences, however were not statistically significant (t-test, p = 0.1). We also found no significant effect of ice type on volumetric or areal chl *a* concentrations (Fig. 6). However, the relative chl *a* concentrations (e.g., fraction of the total core-integrated chl *a*) in the bottom 0.2 m were significantly higher in FYI than in MYI (Fig. 6).

One-way ANOVA tests were conducted to compare the effect of ice age (i.e., the upper multi-year portion of multi-year ice [MY]; the bottom first-year portion of multi-year ice [FY] and first-year ice cores [FYI]) on the chl *a* distribution of sea ice. There was no significant effect of the ice age portions on age class-averaged volumetric or areal chl *a* concentrations (Table 4).

Table 4: Statistical summary of results comparing chlorophyll a between ice age portions (MY, FY and FYI).

Variable	Description	FYI mean ± SD	FY mean ± SD	MY mean ± SD
chl *a*	mean (mg m^{-3})	0.58 ± 0.83	0.55 ± 0.56	0.21 ± 0.09
	integrated (mg m^{-2})	0.71 ± 0.92	0.36 ± 0.40	0.40 ± 0.20

* Indicates significant test result at $p < 0.05$

When all ice cores were compared, bottom-integrated and core-integrated chl *a* concentrations were significantly higher in landfast ice than in pack ice (Figs. 7a and c). Multi-year-landfast ice had significantly higher core-integrated chl *a* concentrations than multi-year-pack ice (Fig. 7b). No significant differences were observed when we compared first-year-landfast ice to first-year-pack ice, landfast-MYI to landfast-FYI, or pack-MYI to pack-FYI (Table 5; and Figs. 7b and d).

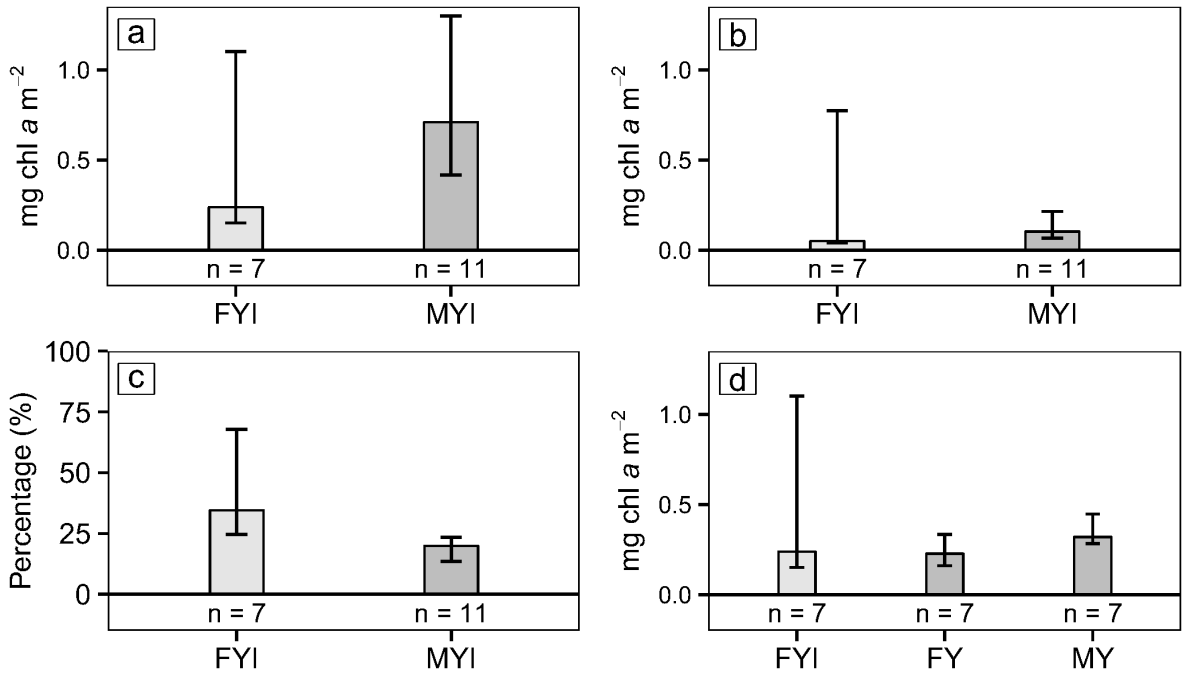

Fig 6. Summary of chl a concentrations in different ice types and age portions. Bars show median values with error bars delineating the 25 and 75 percentiles for: a) core-integrated chl a in MYI (dark-gray) and FYI (light-gray); b) bottom-integrated chl a for MYI and FYI; c) percent of the total chl a in the bottom 0.2 m for FYI and MYI; and d) chl a integrated over lengths of FYI cores (light-gray) and over age class sections for first-year (FY) and multi-year (MY) portions of MYI (dark-gray).

Table 5: Statistical summary of results comparing chlorophyll a between ice types (MYI vs. FYI and landfast ice vs. pack ice).

Variable	**Description**	**FYI mean ± SD**	**MYI mean ± SD**
Bulk **salinity (ppt)**	-	*** 4.75 ± 1.02	***2.85 ± 0.69
Percent of total **chl *a*** inbottom 0.2 m (%)	-	** 46 ± 27	** 20 ± 10
chl *a* (bottom 0. 2 m):	mean (mg m^{-3})	2.58 ± 3.76	0.89 ± 1.07
	integrated (mg m^{-2})	0.52 ± 0.75	0.18 ± 0.21
chl *a* (entire core)	mean (mg m^{-3})	0.58 ± 0.77	0.35 ± 0.22
	integrated (mg m^{-2})	0.71 ± 0.85	0.93 ± 0.64
chl *a* (bottom-integrated):	landfast ice (mg m^{-2})	0.70 ± 0.91	0.22 ± 0.25
	pack ice (mg m^{-2})	0.04 ± 0.01	0.06 ± 0.04
chl *a* (core-integrated):	landfast ice (mg m^{-2})	0.92 ± 1.02	1.16 ± 0.66
	pack ice (mg m^{-2})	0.16 ± 0.11	0.32 ± 0.14
-	-	**Landfast ice mean ± SD**	**Pack ice mean ± SD**
chl *a* (bottom-integrated):	all cores (mg m^{-2})	* 0.41 ± 0.61	* 0.05 ± 0.03
	MYI (mg m^{-2})	0.22 ± 0.25	0.06 ± 0.04
	FYI (mg m^{-2})	0.70 ± 0.91	0.04 ± 0.01
chl *a* (core-integrated):	all cores (mg m^{-2})	* 1.07 ± 0.78	* 0.26 ± 0.14
	MYI (mg m^{-2})	* 1.16 ± 0.66	* 0.32 ± 0.14
	FYI (mg m^{-2})	0.92 ± 1.02	0.16 ± 0.11

Note: entire core mean values account for the length of each section in terms of its contribution to the core mean value and therefore can be slightly different from mean values reported in text for core sections. Significant test results indicated by: * $p < 0.05$; ** $p < 0.01$; *** $p < 0.001$.

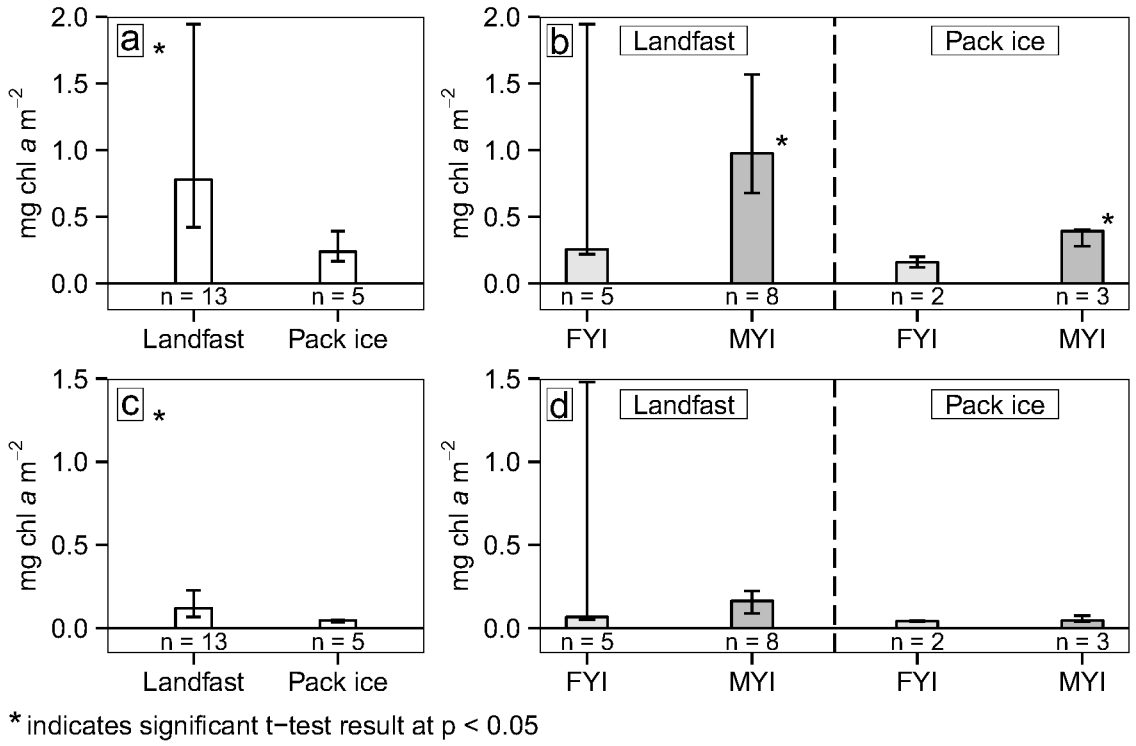

Fig 7. Summary of chl a concentrations comparing landfast ice and pack ice. a) Core-integrated chl a for all cores (MYI and FYI combined); b) core-integrated chl a categorized into FYI (light-gray) and MYI (dark-gray), then by landfast ice (left) and pack ice (right); c) bottom-integrated chl a for all cores; and d) bottom-integrated chl a categorized into FYI (light-gray) and MYI (dark-gray), then by landfast ice (left) and pack ice (right). Bars show median values with error bars delineating the 25 and 75 percentiles.

6.3.4 Relationships between chl *a*, snow depth, and bulk integrated extinction coefficients

Logistic regressions were conducted to assess the relationship of normalized bottom-integrated chl *a* concentrations with snow depth and bulk integrated extinction coefficients, respectively (Fig. 8). Core 6-12 was excluded from this analysis because it was located on a recently refrozen lead that likely experienced different growth conditions and had different snow properties (e.g., thinnest ice and snowpack compared to the other two young FYI sites 3-10 and 4-11). The logistic regression for snow depth showed a step-wise transition with an inflection point at approximately 0.17 m (Fig. 8b). The logistic regression for bulk integrated extinction coefficients shows a more abrupt step-wise transition with an inflection point at a value of 5.8 (Fig. 8c).

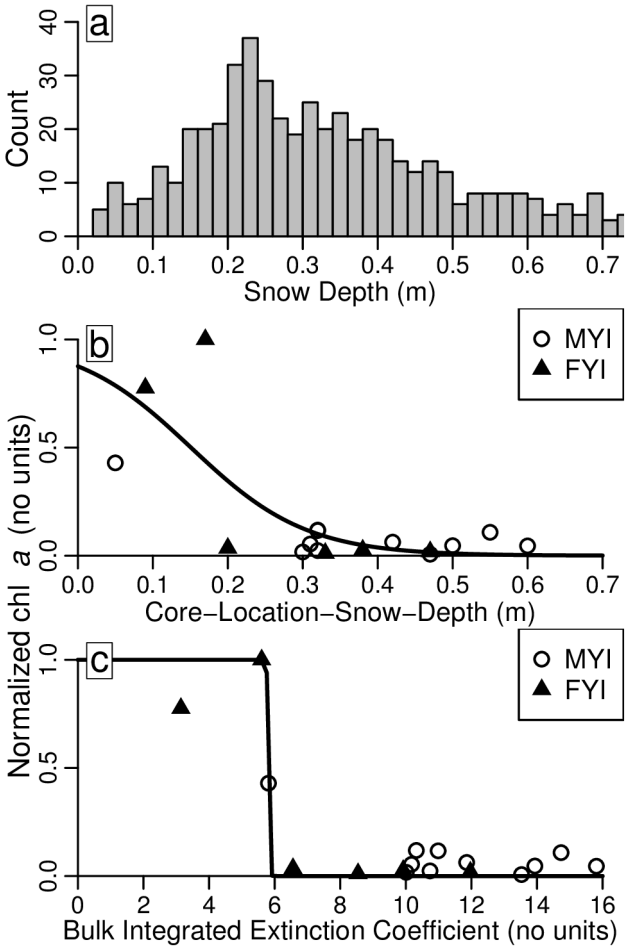

Fig 8. Snow histogram and logistic regressions. a) Histogram of snow depth survey measurements at MYI sites (n = 538). Logistic regressions of normalized bottom-integrated chl a concentrations as a function of: b) snow-depth at core locations; and c) bulk (snow plus ice) integrated extinction coefficients.

6.4 Discussion

6.4.1 Sea ice thickness

MYI in the Lincoln Sea constitutes some of the thickest sea ice remaining in the Arctic Ocean (Haas et al., 2006; IPCC, 2013). Our total thickness (snow plus ice) survey measurements (MYI: 3.0 to 4.9 m; FYI: 0.9 to 2.3 m) are in agreement with aerial and ground-based total thickness measurements conducted in the same study region, with modal total thickness values for MYI between 3.1 and 5.0 m, and for FYI between 0.9 and 2.0 m (Haas et al., 2006; Haas et al., 2010). With a range of 0.86 to 2.24 m, the total thickness (core length plus core-location-snow-depth) of core sites for FYI was in line with the larger scale survey measurements. MYI core sites, however, demonstrated slightly lower total thickness (core length plus core-location-snow-depth) values (2.65 to 3.28 m) than in the survey measurements. MYI, especially in the Lincoln Sea, has a very broad thickness distribution. Although the total thickness of the MYI cores remained within the broader thickness distribution they do not represent the thicker end of a typical ice distribution in the Lincoln Sea. This sampling bias is due to the increasing difficulty and time required for sampling as ice thickness increases.

6.4.2 Snow depth

The mean snow depth for MYI of 0.39 m (present study) was representative of the region when compared to the mean snow depth of 0.3 m found by (Haas et al., 2006). The controlling factors for

snow accumulation and distribution on MYI and FYI, however, were different. When analyzing all FYI sites together, we found a positive relationship between core snow depth and ice core length. This was surprising since on a FYI floe of uniform age a negative relationship between snow depth and ice thickness is expected due to the thermal insulating effect of snow on ice growth (Maykut & Untersteiner, 1971). Based on the variability of site-averaged FYI thicknesses, it is clear that FYI sites had formed at different times. Therefore, snow depth was rather a function of ice age: FYI that formed earlier had more time to accumulate snow, and for ice to grow, compared to newer ice. In addition, snow re-distribution and/or snow fall later in the season would have a minimal insulation effect. On MYI, snow depth and core length had a negative relationship. Apart from the thermal insulating effect, surface topography also plays an important role for snow distribution on MYI (Sturm et al., 2002). In contrast to more level FYI, MYI has an undulating surface due to accumulation of melt ponds, presence of hummocks, pressure deformation and differential melt. This subsequently promotes the accumulation of snow in thinner low spots during wind driven re-distribution, leading to the observed negative relationship between ice thickness and snow depth.

6.4.3 Annual layers

The FY portions of the MYI, and all of the FYI cores were representative of ice forming locally in the Lincoln Sea during the previous winter. FY ice portions had thicknesses between 0.4 and 0.7 m, which agrees well with reported literature values for new-ice growth at the bottom of MYI between 0.45 and 0.55 m (Maykut & Untersteiner, 1971; Perovich et al., 2003; Schwarzacher, 1959). Based on general sea ice circulation patterns (Rigor & Wallace, 2004) the MYI in our region had most likely spent a substantial portion of its life within the central Arctic Ocean. Therefore the MY portions of the MYI, were likely representative of central Arctic MYI.

Annual layers in MYI cores were identified at the transition from columnar ice texture of FY portions to granular and mixed texture in the MY portion. Local chl *a* peaks were observed to coincide with all of the identified annual layers and are probably remnants from the previous year's algal communities. A previous study (Thomas et al., 1995) also observed internal chl *a* peaks that corresponded with a transition from mixed to columnar ice types, but did not conclude it was an annual layer. The correspondence of both texture and bulk salinity profiles with local chl *a* peaks and the agreement with literature values provides strong evidence that the internal chl *a* peaks corresponded to the bottom ice algae layers from previous years.

6.4.4 Overview of chlorophyll *a* concentrations

A comparison of our maximum bottom-integrated chl *a* concentration (1.9 mg chl *a* m^{-2}) with maximum bottom-integrated chl *a* concentrations reported for different regions during spring (see summary in (Arrigo et al., 2010) and references therein) shows that our chl *a* values from the Lincoln Sea were low compared to other regions of the western Arctic Ocean. In the Canadian Arctic Archipelago, values were one to two orders of magnitude higher (14 to 340 mg chl *a* m^{-2}), and in the Baffin Bay and the Beaufort Sea they were over one order of magnitude higher (24 to 64 mg chl *a* m^{-2}). The large majority of these and other sea ice studies, however, focus primarily on FYI (Arrigo et al., 2010). Consequently a comparison with spring MYI chl *a* concentrations is limited to only a few studies. Our range of core-averaged MYI chl *a* concentrations (0.1 to 0.8 mg chl *a* m^{-3}) is in agreement with other spring MYI values (~ 0.1 to 0.65 mg chl *a* m^{-3} (Melnikov et al., 2002)), observed during a drifting study at slightly lower latitudes (75 to 80°N) in the Beaufort and Chukchi Seas. Our FYI maximum core-averaged chl *a* concentration value (2.1 mg chl *a* m^{-3}), however, was an order of magnitude higher than maximum FYI core-averaged concentrations measured during that study in April to May (~0.2 mg chl *a* m^{-3}). Melnikov et al. (2002) (Melnikov et al., 2002) reported highest MYI chl *a* concentrations during July providing some evidence that our study was conducted during the early stages of the growth season, and maximum biomass levels had not yet been reached. Spring MYI chl *a* concentration values comparable to our study were also reported from the Bering Sea with core-integrated concentrations between 0.3 to 3.0 mg chl *a* m^{-2} (McRoy & Goering, 1974), the Greenland Sea with core-integrated concentrations between 0.73 to 2.63 mg chl *a* m^{-2} (Werner &

Gradinger, 2002), and Fram Strait with section concentrations between 0.0 to 3.4 mg chl *a* m^{-3} (Schünemann & Werner, 2005).

6.4.5 Comparison of Ice Age Portions (MY, FY, FYI)

It is well documented that differences in chl *a* biomass are observed in FYI at the same location due to small scale variations in snow and ice properties (see review in (Vancoppenolle et al., 2013)). We have shown that FYI and MYI have different snow and ice properties; suggesting different under-ice light regimes. Based on FYI and FY samples that have grown in the same region (i.e., similar water properties), it might be expected to observe different ranges in chl *a* concentration values between the ice ages, due to differences in the light regimes. Our observations, on the other hand, showed similar chl *a* concentrations for FYI and for FY samples, and similar bottom chl *a* concentrations for FYI and MYI. This indicates that the range of under-ice light conditions may be similar under FYI and MYI (FY), regardless of large differences in their physical properties.

It might also be expected that the upper MY portion would have had lower chl *a* concentrations than the other ice age portions, because it experienced vertical flushing of the ice column during the previous melt season(s), and had no access to nutrient replenishment from the underlying water column. However, during our study the upper MY still had chl *a* concentration values similar to FY and FYI. This observation can be attributed to the presence of remnant communities within the previous year's bottom layers and melt ponds. Refrozen melt-ponds were identified at or near the surface of 6 out of 11 MYI cores. Each coincided with an elevated chl *a* concentration in the corresponding core section. Algal communities in surface layers of Arctic sea ice are not common. However, similar features were observed in summer sea ice by Gradinger et al., (2005), and were attributed to freshwater melt pond inhabitants (Gradinger et al., 2005).

Maintenance of the previous years' algal biomass levels in the annual layers was supported by a separation of bacterial communities in one MYI core. At MYI site 1-11, distinct bacterial assemblages were observed at different depths (i.e.., surface melt ponds, MY, and FY) based on analyses of the 16S rRNA gene from one coincident core (Hatam et al., 2014). This suggests that carbon sources were high enough and vertical exchange was sufficiently low to sustain different bacterial communities within the entire MYI column at site 1-11. Although the presence of sequences classified as closely related to cyanobacteria have been reported in Arctic summer pack ice (Bowman et al., 2011), these sequences were not observed in the MYI core from site 1-11 (Hatam et al., 2014). This suggests that the chl *a* maxima, observed throughout the core, originate from phototrophic eukaryotes (i.e. diatoms and flagellates), which is in agreement with a previous study that reported high flagellate and diatom biomass in the upper and bottom portions, respectively, of Arctic summer ice (Gradinger, 1999).

6.4.6 Chl *a*-snow/ice relationships

The relatively high bottom-integrated chl *a* concentrations at sites with the lowest snow depth and highest potential light availability indicates that the limiting factor for algal growth during this study was light availability. This is consistent with other studies that found light to be limiting algal growth during the early-spring growth season (e.g., (Lavoie et al., 2005; Riedel et al., 2006)). The difference between landfast ice and pack ice chl *a* concentrations may also suggest a limited influence of nutrient availability on algal growth during our study.

The logistic regression analysis showed that core-normalized bottom integrated chl *a* concentrations were nearly zero at snow depths > 0.17 m, or at bulk integrated extinction coefficients > 5.8 (Figs. 8b and c). Ice cores that had snow depth and bulk integrated extinction coefficients below these critical values for algal growth also had the highest bottom ice chl *a* concentrations between 6.4 and 15.4 mg m^{-3}. A similar influence of snow depth on chl *a* concentration has been reported previously by using an exponential relationship, identifying a similar threshold value for snow depth on FYI (Mundy et al., 2007). The main feature of the logistic regression is the identification of a critical threshold (inflection point). The critical value divides the snow depth and bulk integrated extinction coefficient values into two conditions, either: 1) favorable for algal growth (higher chl *a*); or 2) not favorable for algal growth (lower chl *a*).

Combining the mean downwelling incoming radiation values with the critical threshold bulk integrated extinction coefficient value (5.8) as parameters in a simplified light extinction model (equation 1 in (Grenfell & Maykut, 1977)), results in an estimated daily mean available irradiance for bottom ice algae of 3 µmol photons m^{-2} s^{-1}. This estimate is in good agreement with reported critical minimum under-ice irradiance levels to maintain algal growth between ~2 and 9 µmol photons m^{-2} s^{-1} (Gosselin et al., 1985; Gosselin et al., 1986; Horner & Schrader, 1982). The strong relationship between snow depth and bottom-integrated chl *a* concentration emphasizes the dominating effect of snow depth on light transmission and subsequent algal growth. The combined effect of snow and ice on light transmission and subsequently on chl *a* concentration in the lowermost 0.2 m of sea ice demonstrates that both parameters should be considered when comparing ice of variable thicknesses and snow depths.

Although snow typically has a dominating effect on light transmission compared to sea ice, which has typical extinction coefficients between 0.8 and 1.55 m^{-1} (e.g., (Grenfell & Maykut, 1977; Light et al., 2008; Nicolaus et al., 2010; Thomas, 1963)), extinction coefficients of snow in the visible spectrum can vary by over an order of magnitude from 4 m^{-1} for wet snow to between 40 and 80 m^{-1} for fresh snow (e.g., (Hamre et al., 2004; Järvinen & Leppäranta, 2011; Maykut & Grenfell, 1975; Thomas, 1963)). The low extinction coefficients associated with wet snow or high coefficients associated with fresh snow are likely not representative of our study region. Air temperatures were well below freezing during the study and the fresh snow extinction coefficient, as the name implies, is an intermittent property of the snow that is not representative over longer periods. Therefore, we consider the extinction coefficient for snow of 20.0 m^{-1} used here, based on the mean snow density, a realistic estimate of snow properties for the study region. Biomass in sea ice also reduces available light for other in-ice or under-ice phototrophic organisms (Mundy et al., 2007). Using observed specific absorption coefficients for sea ice algae between 0.003 and 0.010 m^{-1} [mg chl *a* m^{-3}]$^{-1}$ in the spectral range 400 to 500 nm (Arrigo et al., 1991) would amount to absorption coefficients between 0.02 and 0.15 m^{-1}, for our maximum chl *a* concentrations (6.4 to 15.4 mg m^{-3}). This suggests that light limitation and self-shading by in-ice algae would have been minimal during our study.

Based on the combined effect of snow and ice on bottom integrated chl *a* concentration, it is important to address the representativeness of the ice cores in terms of the actual ice thickness and snow distribution in the Lincoln Sea. Bottom chl *a* concentrations were highest in 2 FYI cores from refrozen leads that were likely younger than the other FYI sites based on snow depth and ice thickness survey measurements. A third core (6-12) that was also from a younger refrozen lead did not have high biomass even though it was the thinnest core and had lowest snow depth. This could be explained by higher under-ice irradiance, which would have inhibited algal colonization until light levels became more favorable or until algal cells would have had sufficient time to adapt to the light conditions (e.g., (Barlow et al., 1988; Campbell et al., 2014; Lund-Hansen et al., 2014; Michel et al., 1988)). Second, the recent or current ice growth rate may have been too rapid to establish substantial algal biomass (Legendre et al., 1991).

A common feature, which influences the formation of refrozen leads and FYI, in the Lincoln Sea is an ice arch that forms at the entrance to Nares Strait (Kwok, 2005; Kwok et al., 2010). With the presence of an ice arch and more stable ice conditions, FYI represented less than 15% of all airborne ice thickness measurements in the Lincoln Sea (Haas et al., 2006; Haas et al., 2010). However, in the absence of an ice arch FYI represented up to 20% of all airborne ice thickness measurements due to a more mobile ice pack (Haas et al., 2006). Under typical stable conditions in the Lincoln Sea (e.g., with the presence of an ice arch) newer refrozen leads would likely represent a smaller fraction of the overall FYI cover. This implies the 2 cores with highest bottom chl *a* concentrations were not representative of typical FYI in this region. However, in years with unstable conditions (e.g., no ice arch forming) in the Lincoln Sea and in a future Arctic system with a more mobile ice pack the relative coverage of refrozen leads will likely increase and perhaps become an increasingly more important component of overall sea ice algal biomass in the Lincoln Sea and Arctic Ocean (IPCC, 2013).

6.4.7 Underestimation of MYI Algal biomass

As discussed previously, there is a sampling bias towards thinner MYI in this and many other studies. In this study the core with the maximum MYI bottom chl *a* concentration was extracted from a hummock. The hummock core, 5-10, corresponded to the thickest core with shallowest snow depth and high chl *a* biomass (Table 3). This indicates the potential for relatively higher algal biomass in under-represented thick MYI hummocks, which typically have lower snow coverage. In a study from the Fram Strait (Schünemann & Werner, 2005), maximum spring bottom chl *a* concentrations were also observed in the thickest MYI core with lowest snow depth when compared to two other second-year ice cores.

From a total of 538 snow depth measurements conducted on MYI, 15% were below the critical snow depth value of 0.17 m (Fig. 8a). This value of 15% may be a good estimate for the distribution of hummocks in the region. Due to the significantly stronger influence of snow depth than ice thickness on light attenuation, these regions of thicker ice and less snow (e.g., hummocks) could be the only regions of MYI where transmitted under-ice PAR is above a threshold value for algal growth during spring. This becomes more apparent if we consider the potential bulk integrated extinction coefficients of different ice types using a range of extinction coefficients. Based on typical snow densities in the region, we use snow extinction coefficients of 20 and 25 m^{-1} combined with the full range of reported values for ice of 0.8 and 1.55 m^{-1}. These calculations result in bulk integrated extinction coefficients between 2.8 to 5.4 for a 3.5 m hummock with no snow, 4.8 to 7.9 for a 3.5 m hummock with 0.1 m of snow, and 5.6 to 8.1 for a snow covered melt pond (0.2 m of snow and 2 m of ice). Light attenuation is likely different between refrozen melt pond ice and hummocks, which is apparent when you compare the texture images for deteriorated ice (Fig. 2d), typical of hummock surface ice, and melt ponds (Fig. 2e). The corresponding spring time extinction coefficients are unknown for hummocks and melt ponds and therefore the full range of reported values were used to account for the potential variability. Although extinction coefficients for snow are highly variable we used an upper limit of 25 m^{-1} to account for some variability in snow properties and the influence of small amounts of fresh snow that may be intermittently present throughout the spring season.

The above mentioned ranges of extinction coefficients demonstrate that thick hummock ice, with little or no snow, has the potential for higher amounts of available under-ice PAR and more importantly bulk integrated extinction coefficients below the critical value of 5.8. Furthermore, this suggests that under similar nutrient and incoming solar radiation conditions, 15% of MYI, which has little or no snow coverage, has the potential for bottom algal layers similar to or greater than the observed maximum MYI chl *a* concentration of 6.4 mg m^{-3}. This value is low compared to FYI in the Canadian Arctic Archipelago where bloom values at the ice bottom can reach concentrations greater than 100 mg m^{-3} (e.g., (Alou-Font et al., 2013; Mundy et al., 2007; Smith et al., 1990)). However, taking into account that our study was conducted during the early algal growth season, we would expect to observe more algal growth and higher chl *a* concentrations later in the season. If the observed maximum MYI value was extrapolated over 15% of the thicker MYI regions (e.g., 3+ year old MYI extent for March 2011 was >1.5 x 10^6 km^2 (Maslanik et al., 2011)), taking into account the potential for higher biomass expected during bloom, these regions could represent a substantial amount in terms of chl *a* biomass and, possibly, primary production.

6.4.8 Implications for a changing Arctic (shift from MYI to FYI)

In light of the limited number of recent studies, one may argue that our current understanding of Arctic sea ice algal biomass in MYI is based on a historic Arctic that was different from today. The melt season has lengthened (Howell et al., 2009; Markus et al., 2009), and sea ice thickness, extent, and volume have undergone drastic changes (IPCC, 2013). MYI is disappearing from the Arctic at a rate faster than predicted by models, with a seasonally ice-free Arctic likely to occur before the end of this century, possibly as early as 2020 (Stroeve et al., 2012), resulting in the complete, or near complete, loss of MYI. Measurements of primary production in the central Arctic Ocean indicate that sea ice production can account for over 50% of total primary production (Gosselin et al., 1997), but it remains unclear how ice-associated production will change with a shift from MYI to FYI.

Arctic FYI studies in general have shown a higher range of bottom chl *a* biomass in FYI compared to MYI. FYI values include highly productive regions (e.g. Arctic shelves) where MYI is not present or has not been studied. Here we show that FYI and MYI in the Lincoln Sea can have comparable chl *a* biomass during the spring period (May). Previous studies have also demonstrated comparable or even slightly higher chl *a* biomass in MYI compared to FYI (Melnikov et al., 2002). In addition, maximum chl *a* biomass values have also been observed in the thickest sea ice during spring (Schünemann & Werner, 2005) and summer (Gradinger et al., 2010). Based on our results and previous studies that show generally higher, or similar, chl *a* biomass potential in MYI compared to FYI, we suggest that the general view of higher productivity in FYI than in MYI should be revisited in order to achieve a better understanding of the current and future state of the Arctic system.

If we base future estimates of ice-algal production on the fact that FYI from Arctic shelf regions is more productive than MYI in general, this would lead to the assumption that sea ice algal production would increase with a replacement of MYI by FYI during the ice-covered period. However, our results suggest only minor changes in ice algal biomass when all MYI is replaced by FYI. This considered in combination with the underestimated chl *a* biomass potential of thick MYI (hummocks) suggests the on-going loss of MYI in the Arctic Ocean may have a larger impact on ice–associated production than generally assumed.

Our results also showed that younger FYI (e.g., refrozen leads) had the highest chl *a* biomass and that the comparable values between MYI and FYI are likely driven by the higher biomass in the younger FYI. The relative proportion of younger FYI and refrozen leads in the central Arctic Ocean will likely increase with continued increases in ice drift velocities and a thinning ice pack (AMAP, 2011; IPCC, 2013; Rampal et al., 2011). The increase in younger FYI and refrozen leads will likely result in a general increase of ice algal biomass during the bloom period, the extent of which will depend on the spatial extent and regional variability of these features.

The expected higher bloom biomass of thinner FYI, however, may not result in a net increase in ice algal production over the entire growth season. Even with larger areas of thinner FYI, the expected increase in maximum ice-algal biomass may not compensate for the increased vulnerability of thinner ice to rapid changes in the light field and rapid snow/ice melt. These vulnerabilities could result in earlier termination of the ice-algal bloom due to photo-inhibition and/or rapid melt (Campbell et al., 2014; Lavoie et al., 2005). Earlier termination of the ice-algal bloom has been linked to a mismatch with the reproductive cycles of key grazers having negative consequences for the entire food web (Leu et al., 2011; Søreide et al., 2010). In addition, sea ice decline has already been linked to increased export of POC and algal aggregates to the sea floor (e.g., (Boetius et al., 2013; Lalande et al., 2009)), which indicates an associated removal of carbon and nutrients from surface waters. Higher carbon and nutrient export rates in the future may result in a situation where a rapid increase followed by a rapid decline in ice-associated primary production would not be sustainable for longer periods due to the removal of nutrients. This would be analogous to a boom-bust cycle. The MYI system, however, is less vulnerable to rapid environmental changes and therefore could be considered a more sustainable system where rapid sinking of ice-algae (i.e., carbon and nutrients) is less likely. Thus, the MYI system may have the potential to sustain biogeochemical cycles required to maintain moderate levels of algal biomass over longer periods (i.e., higher net primary production).

6.5 Conclusions

Studies comparing biogeochemical properties of first-year sea ice (FYI) with multi-year sea ice (MYI) in the high Arctic are essential to understand the potential biogeochemical changes to sea ice ecosystems in a future Arctic Ocean with little or no MYI. In light of the current limited investigations of Arctic MYI algae, the present study provides a unique multi-annual dataset comparing ice-algal chl *a* and physical properties of both FYI and MYI during spring from a high-Arctic system. The low variability in chl *a* concentrations, both within and between MYI and FYI in the coastal Arctic Ocean, suggests little or no change in algal biomass with a shift from MYI to FYI. The apparent relationship between chl *a* biomass in the bottom layer of ice and bulk integrated extinction coefficients of the snow-ice matrix, implies that an appropriate representation of areas with

low snow depths, such as MYI hummocks, is critical for a realistic estimation of the MYI contribution to overall ice algal biomass estimates in the Arctic Ocean. The potential for higher ice algal biomass in thick MYI with less snow, in conjunction with a lack of significant difference between FYI and MYI chl *a* biomass during our study suggests that the on-going loss of MYI in the Arctic Ocean may have a more negative impact on ice–associated production than generally assumed.

Acknowledgements

We thank the logistical support from Jim Milne and Al Tremblay, Defence Research and Development-Atlantic. We thank G. Stewart and all of the personnel at Canadian Forces Station Alert for their hospitality and support. Invaluable logistical support, laboratory access, and Helicopter and Twin Otter aircraft transportation were provided by the Polar Continental Shelf Program. Pilots from Universal Helicopters and Kenn Borek Air provided safe transportation throughout the project. We thank A. Reppchen, N. Fortin, K. Hille, A. Tatare and J. Wiktor for their help in the field laboratory. We acknowledge Dr. Ken Ryan and one anonymous reviewer for constructive comments that improved the manuscript.

References

Alou-Font, E., Mundy, C.J., Roy, S., Gosselin, M., Agusti, S., 2013. Snow cover affects ice algal pigment composition in the coastal Arctic Ocean during spring. *Marine Ecology Progress Series*, 474, 89-104.

AMAP, 2011. Snow,water, ice and permafrost in the Arctic (SWIPA): Climate change and the cryosphere. Gaustadalléen 21, N-0349 Oslo, Norway (www.amap.no).

Arrigo, K.R., Mock, T., Lizotte, M.P., 2010. Primary Producers and Sea Ice. In D.N. Thomas, G.S. Dieckmann (Eds.), *Sea Ice* (pp. 283-325). Oxford: Wiley-Blackwell.

Arrigo, K.R., Perovich, D.K., Pickart, R.S., Brown, Z.W., van Dijken, G.L., Lowry, K.E., Mills, M.M., Palmer, M.A., Balch, W.M., Bahr, F., Bates, N.R., Benitez-Nelson, C., Bowler, B., Brownlee, E., Ehn, J.K., Frey, K.E., Garley, R., Laney, S.R., Lubelczyk, L., Mathis, J., Matsuoka, A., Mitchell, B.G., Moore, G.W.K., Ortega-Retuerta, E., Pal, S., Polashenski, C.M., Reynolds, R.A., Schieber, B., Sosik, H.M., Stephens, M., Swift, J.H., 2012. Massive Phytoplankton Blooms Under Arctic Sea Ice. *Science*, 336, 1408.

Arrigo, K.R., Sullivan, C.W., Kremer, J.N., 1991. A bio-optical model of Antarctic sea ice. *Journal of Geophysical Research: Oceans*, 96, 10581-10592.

Arrigo, K.R., Thomas, D.N., 2004. Large scale importance of sea ice biology in the Southern Ocean. *Antarctic Science*, 16, 471-486.

Arrigo, K.R., van Dijken, G., Pabi, S., 2008. Impact of a shrinking Arctic ice cover on marine primary production. *Geophysical Research Letters*, 35, L19603.

Arrigo, K.R., van Dijken, G.L., 2011. Secular trends in Arctic Ocean net primary production. *Journal of Geophysical Research*, 116, C09011.

Barlow, R.G., Gosselin, M., Legendre, L., Therriault, J.C., Demers, S., Mantoura, R.F.C., Llewellyn, C.A., 1988. Photoadaptive strategies in sea-ice microalgae. *Marine Ecology Progress Series*, 45, 145-152.

Boetius, A., Albrecht, S., Bakker, K., Bienhold, C., Felden, J., Fernández-Méndez, M., Hendricks, S., Katlein, C., Lalande, C., Krumpen, T., Nicolaus, M., Peeken, I., Rabe, B., Rogacheva, A., Rybakova, E., Somavilla, R., Wenzhöfer, F., Party, R.P.A.-.-S.S., 2013. Export of Algal Biomass from the Melting Arctic Sea Ice. *Science*, 339, 1430-1432.

Bowman, J.S., Rasmussen, S., Blom, N., Deming, J.W., Rysgaard, S., Sicheritz-Ponten, T., 2011. Microbial community structure of Arctic multiyear sea ice and surface seawater by 454 sequencing of the 16S RNA gene. *ISME J*, 1-10.

Budge, S.M., Wooller, M.J., Springer, A.M., Iverson, S.J., McRoy, C.P., Divoky, G.J., 2008. Tracing carbon flow in an arctic marine food web using fatty acid-stable isotope analysis. *Oecologia*, 157, 117-129.

Campbell, K., Mundy, C.J., Barber, D.G., Gosselin, M., 2014. Characterizing the sea ice algae chlorophyll a–snow depth relationship over Arctic spring melt using transmitted irradiance. *Journal of Marine Systems*, , in press.

Cota, G.F., Legendre, L., Gosselin, M., Ingram, R.G., 1991. Ecology of bottom ice algae: I. Environmental controls and variability. *Journal of Marine Systems*, 2, 257-277.

Cota, G.F., Smith, R.E.H., 1991. Ecology of bottom ice algae: III. Comparative physiology. *Journal of Marine Systems*, 2, 297-315.

Cox, G.F.N., Weeks, W.F., 1983. Equations for determining the gas and brine volumes in sea-ice samples. *Journal of Glaciology*, 29, 306-316.

Eicken, H., Lange, M.A., 1989. Development and properties of sea ice in the coastal regime of the southeastern Weddell Sea. *Journal of Geophysical Research*, Vol. 94 (pp. 8193-8206).

Eicken, H., Lensu, M., Leppäranta, M., Tucker, W.B., Gow, A.J., Salmela, O., 1995. Thickness, structure, and properties of level summer multiyear ice in the Eurasian sector of the Arctic Ocean. *Journal of Geophysical Research*, 100, 22697-22710.

Gosselin, M., Legendre, L., Demers, S., Ingram, R.G., 1985. Responses of Sea-Ice Microalgae to Climatic and Fortnightly Tidal Energy Inputs (Manitounuk Sound, Hudson Bay). *Canadian Journal of Fisheries and Aquatic Sciences*, 42, 999-1006.

Gosselin, M., Legendre, L., Therriault, J.-C., Demers, S., 1990. Light and nutrient limitation of sea-ice microalgae (Hudson Bay, Canadian Arctic). *Journal of Phycology*, 26, 220-232.

Gosselin, M., Legendre, L., Therriault, J.C., Demers, S., Rochet, M., 1986. Physical control of the horizontal patchiness of sea-ice microalgae. *Marine Ecology Progress Series*, 29, 289-298.

Gosselin, M., Levasseur, M., Wheeler, P.A., Horner, R.A., Booth, B.C., 1997. New measurements of phytoplankton and ice algal production in the Arctic Ocean. *Deep Sea Research Part II: Topical Studies in Oceanography*, 44, 1623-1644.

Gradinger, R., 1999. Vertical fine structure of the biomass and composition of algal communities in Arctic pack ice. *Marine Biology*, 133, 745-754.

Gradinger, R., Bluhm, B., Iken, K., 2010. Arctic sea-ice ridges—Safe heavens for sea-ice fauna during periods of extreme ice melt? *Deep Sea Research Part II: Topical Studies in Oceanography*, 57, 86-95.

Gradinger, R., Friedrich, C., Spindler, M., 1999. Abundance, biomass and composition of the sea ice biota of the Greenland Sea pack ice. *Deep Sea Research Part II: Topical Studies in Oceanography*, 46, 1457-1472.

Gradinger, R., Meiners, K., Plumley, G., Zhang, Q., Bluhm, B.A., 2005. Abundance and composition of the sea-ice meiofauna in off-shore pack ice of the Beaufort Gyre in summer 2002 and 2003. *Polar Biology*, 28, 171-181.

Gradinger, R., Zhang, Q., 1997. Vertical distribution of bacteria in Arctic sea ice from the Barents and Laptev Seas. *Polar Biology*, 17, 448-454.

Grenfell, T.C., Maykut, G.A., 1977. The optical properties of ice and snow in the Arctic Basin. *Journal of Glaciology*, 18, 445-463.

Haas, C., Hendricks, S., Doble, M., 2006. Comparison of the sea-ice thickness distribution in the Lincoln Sea and adjacent Arctic Ocean in 2004 and 2005. *Annals of Glaciology*, 44, 247-252.

Haas, C., Hendricks, S., Eicken, H., Herber, A., 2010. Synoptic airborne thickness surveys reveal state of Arctic sea ice cover. *Geophysical Research Letters*, Vol. 37 (p. L09501).

Haas, C., Willatt, R., Beckers, J., Laxon, S., Giles, K., Davidson, M., 2011. CryoVEx 2011 Alert Sea Ice Ground Team Report. (pp. 1-53). University of Alberta, https://earth.esa.int/documents/10174/134665/CryoVEx2011_FinalReport.

Hamre, B., Winther, J.-G., Gerland, S., Stamnes, J.J., Stamnes, K., 2004. Modeled and measured optical transmittance of snow-covered first-year sea ice in Kongsfjorden, Svalbard. *Journal of Geophysical Research*, 109, C10006.

Hatam, I., Charchuk, R., Lange, B., Beckers, J., Haas, C., Lanoil, B., 2014. Distinct bacterial assemblages reside at different depths in Arctic multiyear sea ice. *FEMS Microbiology Ecology*, 1-11.

Horner, R., Schrader, G.C., 1982. Relative Contributions of Ice Algae, Phytoplankton, and Benthic Microalgae to Primary Production in Nearshore Regions of the Beaufort Sea. *Arctic*, 35.

Howell, S.E.L., Duguay, C.R., Markus, T., 2009. Sea ice conditions and melt season duration variability within the Canadian Arctic Archipelago: 1979–2008. *Geophysical Research Letters*, Vol. 36 (p. L10502).

IPCC, 2013. Climate Change 2013: The Physical Science Basis. Contribution of Working Group I to the Fifth Assessment Report of the Intergovernmental Panel on Climate Change. In T.F. Stocker, D. Qin, G.-K. Plattner, M. Tignor, S.K. Allen, J. Boschung, A. Nauels, Y. Xia, V. Bex and P.M. Midgley (eds.) (Ed.) (p. 1535). Cambridge, United Kingdom and New York, NY, USA.

Järvinen, O., Leppäranta, M., 2011. Transmission of solar radiation through the snow cover on floating ice. *Journal of Glaciology*, 57, 861-870.

Jeffries, M.O., Krouse, H.R., 1988. Salinity and isotope analysis of some multi-year landfast sea-ice cores, northern Ellesmere Island, Canada. *Annals of Glaciology*, 10, 63-67.

Kovacs, K., Lydersen, C., Overland, J., Moore, S., 2011. Impacts of changing sea-ice conditions on Arctic marine mammals. *Marine Biodiversity*, 41, 181-194.

Kwok, R., 2005. Variability of Nares Strait ice flux. *Geophysical Research Letters*, Vol. 32 (p. L24502).

Kwok, R., Rothrock, D.A., 2009. Decline in Arctic sea ice thickness from submarine and ICESat records: 1958–2008. *Geophysical Research Letters*, Vol. 36 (p. L15501).

Kwok, R., Toudal Pedersen, L., Gudmandsen, P., Pang, S., 2010. Large sea ice outflow into the Nares Strait in 2007. *Geophysical Research Letters*, Vol. 37 (p. L03502).

Lalande, C., Bélanger, S., Fortier, L., 2009. Impact of a decreasing sea ice cover on the vertical export of particulate organic carbon in the northern Laptev Sea, Siberian Arctic Ocean. *Geophysical Research Letters*, 36, L21604.

Lange, M.A., 1988. Basic properties of Antarctic sea ice as revealed by textural analysis of ice cores. *Annals of Glaciology*, 10, 95-101.

Lange, M.A., Ackley, S.F., Wadhams, P., Dieckmann, G.S., Eicken, H., 1989. Development of sea ice in the Weddell Sea. *Ann. Glaciol*, 12, 92-96.

Lavoie, D., Denman, K., Michel, C., 2005. Modeling ice algal growth and decline in a seasonally ice-covered region of the Arctic (Resolute Passage, Canadian Archipelago). *Journal of Geophysical Research*, 110, C11009.

Legendre, L., Aota, M., Shirasawa, K., Martineau, M.J., Ishikawa, M., 1991. Crystallographic structure of sea ice along a salinity gradient and environmental control of microalgae in the brine cells. *Journal of Marine Systems*, 2, 347-357.

Leu, E., Søreide, J.E., Hessen, D.O., Falk-Petersen, S., Berge, J., 2011. Consequences of changing sea-ice cover for primary and secondary producers in the European Arctic shelf seas: Timing, quantity, and quality. *Progress in Oceanography*, 90, 18-32.

Light, B., Grenfell, T.C., Perovich, D.K., 2008. Transmission and absorption of solar radiation by Arctic sea ice during the melt season. *Journal of Geophysical Research*, 113, C03023.

Lund-Hansen, L.C., Hawes, I., Sorrell, B., Nielsen, M.H., 2014. Removal of snow cover inhibits spring growth of Arctic ice algae through physiological and behavioral effects. *Polar Biology*, 37, 471-481.

Markus, T., Stroeve, J.C., Miller, J., 2009. Recent changes in Arctic sea ice melt onset, freezeup, and melt season length. *Journal of Geophysical Research*, Vol. 114 (p. C12024).

Maslanik, J.A., Stroeve, J.C., Fowler, C., Emery, W., 2011. Distribution and trends in Arctic sea ice age through spring 2011. *Geophysical Research Letters*, Vol. 38 (p. L13502).

Massonnet, F., Fichefet, T., Goosse, H., Bitz, C.M., Philippon-Berthier, G., Holland, M.M., Barriat, P.Y., 2012. Constraining projections of summer Arctic sea ice. *The Cryosphere*, 6, 1383-1394.

Maykut, G.A., Grenfell, T.C., 1975. Spectral Distribution of Light beneath 1st-Year Sea Ice in Arctic Ocean. *Limnology and Oceanography*, 20, 554-563.

Maykut, G.A., Untersteiner, N., 1971. Some results from a time-dependent thermodynamic model of sea ice. *Journal of Geophysical Research*, 76, 1550-1575.

McRoy, C.P., Goering, J.J., 1974. The influence of ice on the primary productivity of the Bering Sea. In D.W. Hood, E.J. Kelley (Eds.), *Oceanography of the Bering Sea* (pp. 403 - 421): University of Alaska, Institute of Marine Science Occassional Publications No. 2.

Melnikov, I.A., Kolosova, E.G., Welch, H.E., Zhitina, L.S., 2002. Sea ice biological communities and nutrient dynamics in the Canada Basin of the Arctic Ocean. *Deep Sea Research Part I: Oceanographic Research Papers*, 49, 1623-1649.

Michel, C., 2013. Marine Ecosystems. In H. Meltofte (Ed.), *Arctic Biodiversity Assessment - Status and Trends in Biodiversity* (pp. 486-526.): CAFF (Conservation of Arctic Flora and Fauna).

Michel, C., Legendre, L., Demers, S., Therriault, J., 1988. Photoadaptation of sea-ice microalgae in springtime: Photosynthesis and carboxylating enzymes. *Marine Ecology Progress Series*, 50, 177-185.

Michel, C., Legendre, L., Ingram, R.G., Gosselin, M., Levasseur, M., 1996. Carbon budget of sea-ice algae in spring: Evidence of a significant transfer to zooplankton grazers. *Journal of Geophysical Research: Oceans*, 101, 18345-18360.

Mundy, C.J., Ehn, J.K., Barber, D.G., Michel, C., 2007. Influence of snow cover and algae on the spectral dependence of transmitted irradiance through Arctic landfast first-year sea ice. *Journal of Geophysical Research*, 112, C03007.

Mundy, C.J., Gosselin, M., Ehn, J.K., Belzile, C., Poulin, M., Alou, E., Roy, S., Hop, H., Lessard, S., Papakyriakou, T.N., Barber, D.G., Stewart, J., 2011. Characteristics of two distinct high-light acclimated algal communities during advanced stages of sea ice melt. *Polar Biology*, 34, 1869-1886.

Newton, J.L., Sotirin, B.J., 1997. Boundary undercurrent and water mass changes in the Lincoln Sea. *Journal of Geophysical Research*, 102, 3393-3403.

Nicolaus, M., Gerland, S., Hudson, S.R., Hanson, S., Haapala, J., Perovich, D.K., 2010. Seasonality of spectral albedo and transmittance as observed in the Arctic Transpolar Drift in 2007. *Journal of Geophysical Research*, 115, C11011, doi:11010.11029/12009JC006074.

Nicolaus, M., Katlein, C., Maslanik, J., Hendricks, S., 2012. Changes in Arctic sea ice result in increasing light transmittance and absorption. *Geophysical Research Letters*, 39, 2699–2700.

Nozais, C., Gosselin, M., Michel, C., Tita, G., 2001. Abundance, biomass, composition and grazing impact of the sea-ice meiofauna in the North Water, northern Baffin Bay. *Marine Ecology Progress Series*, 217, 235-250.

Overland, J.E., Wang, M., 2013. When will the summer Arctic be nearly sea ice free? *Geophysical Research Letters*, 40, 2097-2101.

Parkinson, C.L., Comiso, J.C., 2013. On the 2012 record low Arctic sea ice cover: Combined impact of preconditioning and an August storm. *Geophysical Research Letters*, 40, 1356-1361.

Parsons, T.R., Maita, Y., Lalli, C.M., 1989. *A manual of chemical and biological methods for seawater analysis*. Toronto: Pergamon Press.

Perovich, D.K., 1996. The Optical Properties of Sea Ice. Cold Regions Research and Engineering Laboratory.

Perovich, D.K., Grenfell, T.C., Richter-Menge, J.A., Light, B., Tucker III, W.B., Eicken, H., 2003. Thin and thinner: Sea ice mass balance measurements during SHEBA. *Journal of Geophysical Research*, Vol. 108 (p. 8050).

R-Development-Core-Team, 2012. R: A Language and Environment for Statistical Computing. *R Foundation for Statistical Computing, Vienna, Austria*.

Rampal, P., Weiss, J., Dubois, C., Campin, J.M., 2011. IPCC climate models do not capture Arctic sea ice drift acceleration: Consequences in terms of projected sea ice thinning and decline. *Journal of Geophysical Research*, 116, C00D07.

Riedel, A., Michel, C., Gosselin, M., 2006. Seasonal study of sea-ice exopolymeric substances on the Mackenzie shelf: implications for transport of sea-ice bacteria and algae. *Aquatic Microbial Ecology*, 45, 195-206.

Rigor, I.G., Wallace, J.M., 2004. Variations in the age of Arctic sea-ice and summer sea-ice extent. *Geophysical Research Letters*, Vol. 31 (p. L09401).

Rigor, I.G., Wallace, J.M., Colony, R.L., 2002. Response of Sea Ice to the Arctic Oscillation. *Journal of Climate*, 15, 2648-2663.

Riihela, A., Manninen, T., Laine, V., 2013. Observed changes in the albedo of the Arctic sea-ice zone for the period 1982-2009. *Nature Clim. Change*, 3, 895-898.

Rintala, J.-M., Piiparinen, J., Blomster, J., Majaneva, M., Müller, S., Uusikivi, J., Autio, R., 2014. Fast direct melting of brackish sea-ice samples results in biologically more accurate results than slow buffered melting. *Polar Biology*, 37, 1811-1822.

Rysgaard, S., Glud, R.N., Sejr, M.K., Blicher, M.E., Stahl, H.J., 2008. Denitrification activity and oxygen dynamics in Arctic sea ice. *Polar Biology*, 31, 527-537.

Schünemann, H., Werner, I., 2005. Seasonal variations in distribution patterns of sympagic meiofauna in Arctic pack ice. *Marine Biology*, 146, 1091-1102.

Schwarzacher, W., 1959. Pack-ice studies in the Arctic Ocean. *Journal of Geophysical Research*, 64, 2357-2367.

Screen, J.A., Simmonds, I., 2010. The central role of diminishing sea ice in recent Arctic temperature amplification. *Nature*, 464, 1334-1337.

Smith, R.E.H., Clement, P., Head, E.J., 1990. Night Metabolism of Recent Photosynthate by Sea Ice Algae in the High Arctic. *Marine Biology*, 107, 255-261.

Søreide, J.E., Carroll, M.L., Hop, H., Ambrose, W.G., Hegseth, E.N., Falk-Petersen, S., 2013. Sympagic-pelagic-benthic coupling in Arctic and Atlantic waters around Svalbard revealed by stable isotopic and fatty acid tracers. *Marine Biology Research*, 9, 831-850.

Søreide, J.E., Hop, H., Carroll, M.L., Falk-Petersen, S., Hegseth, E.N., 2006. Seasonal food web structures and sympagic–pelagic coupling in the European Arctic revealed by stable isotopes and a two-source food web model. *Progress in Oceanography*, 71, 59-87.

Søreide, J.E., Leu, E.V.A., Berge, J., Graeve, M., Falk-Petersen, S., 2010. Timing of blooms, algal food quality and Calanus glacialis reproduction and growth in a changing Arctic. *Global Change Biology*, Vol. 16 (pp. 3154–3163).

Stammerjohn, S., Massom, R., Rind, D., Martinson, D., 2012. Regions of rapid sea ice change: An inter-hemispheric seasonal comparison. *Geophysical Research Letters*, 39, L06501.

Stroeve, J.C., Holland, M.M., Meier, W., Scambos, T., Serreze, M., 2007. Arctic sea ice decline: Faster than forecast. *Geophysical Research Letters*, Vol. 34 (p. L09501).

Stroeve, J.C., Kattsov, V., Barrett, A., Serreze, M., Pavlova, T., Holland, M., Meier, W.N., 2012. Trends in Arctic sea ice extent from CMIP5, CMIP3 and observations. *Geophysical Research Letters*, 39, L16502.

Stroeve, J.C., Serreze, M.C., Holland, M.M., Kay, J.E., Malanik, J., Barrett, A.P., 2011. The Arctic's rapidly shrinking sea ice cover: a research synthesis. *Climatic Change* (pp. 1-23).

Sturm, M., Holmgren, J., Perovich, D.K., 2002. Winter snow cover on the sea ice of the Arctic Ocean at the Surface Heat Budget of the Arctic Ocean (SHEBA): Temporal evolution and spatial variability. *Journal of Geophysical Research*, Vol. 107 (p. 8047).

Thomas, C.W., 1963. On the transfer of visible radiation through sea ice and snow. *Journal of Glaciology*, 4, 481-484.

Thomas, D.N., Lara, R.J., Eicken, H., Kattner, G., Skoog, A., 1995. Dissolved Organic-Matter in Arctic Multiyear Sea-Ice during Winter - Major Components and Relationship to Ice Characteristics. *Polar Biology*, 15, 477-483.

Tremblay, J.-É., Robert, D., Varela, D.E., Lovejoy, C., Darnis, G., Nelson, R.J., Sastri, A.R., 2012. Current state and trends in Canadian Arctic marine ecosystems: I. Primary production. *Climatic Change*, Vol. 115 (pp. 161-178).

Vancoppenolle, M., Meiners, K.M., Michel, C., Bopp, L., Brabant, F., Carnat, G., Delille, B., Lannuzel, D., Madec, G., Moreau, S., 2013. Role of sea ice in global biogeochemical cycles: emerging views and challenges. *Quaternary science reviews*, Vol. 79 (pp. 207-230).

Werner, I., Gradinger, R., 2002. Under-ice amphipods in the Greenland Sea and Fram Strait (Arctic): environmental controls and seasonal patterns below the pack ice. *Marine Biology*, 140, 317-326.

Paper 7. Suitable ice-algal habitat and biomass are largely underestimated over multi-year sea ice

In preparation for submission to: *Progress in Oceanography*

NOTE: Supplementary Material for this paper is found in Appendix C1

Benjamin A. Lange, Hauke Flores, Christine Michel, Justin Beckers, Anne Bublitz, J. Alec Casey, Giulia Castellani, Ido Hatam, Anke Reppchen, Svenja A. Rudolph, Christian Haas

Abstract

There is mounting evidence that multi-year sea ice (MYI) is a unique and important component of the Arctic system and it may play a more important ecological role than previously assumed. In this study we aimed to improve our understanding of the suitability of MYI as a habitat for sea ice algae by testing the hypothesis that MYI hummocks have the potential to host high biomass of bottom-ice algae due to their typically snow-free surface.

We sampled sea ice cores from MYI (2.2 – 4.1 m), first-year sea ice (FYI; 1.3 – 1.8 m) and lead ice (0.8 – 0.9 m) within the Lincoln Sea during four consecutive spring seasons. Snow depth at core locations ranged between 0.00 – 0.60 m (MYI), 0.15 – 0.47 (FYI), and 0.04 – 0.09 m (lead ice). Bottom-ice integrated chl *a* biomass ranged between 0.0 – 3.6 mg m^{-2} (MYI), 0.0 – 1.9 mg m^{-2} (FYI), and 0.1 – 1.5 mg m^{-2} (lead-ice). We sampled four MYI hummocks with a mean chl *a* biomass of 2.0 mg m^{-2}. Three of the four hummocks cored had the three highest biomass values of all cores from all ice types. MYI hummocks also had significantly higher chl *a* biomass than FYI and refrozen melt-pond MYI cores. We identified a threshold value of 6.75 for the bulk (snow plus ice) integrated light extinction coefficient (k_B), above which nearly zero biomass was observed. Snow and ice surveys were classified as not suitable ($k_B > 6.75$) or suitable ($k_B \leq 6.75$) habitat for ice algae. The coverage of suitable ice-algal habitat was < 6% for thick-MYI (> 3m), 17 – 38% for thin-MYI (≤ 3 m), 87% for FYI low-snow (< 0.20 m), 18 – 37% for FYI high-snow (> 0.20 m), and 100 % for lead-ice. Our results confirmed the hypothesis that MYI hummocks do have the potential to host substantial ice algae biomass.

We applied our habitat classification to pan-Arctic Cryosat-2 sea ice thickness and snow depth data products and showed over an order of magnitude greater percent coverage of suitable ice-algal habitat when we considered the variability of the snow and ice properties compared to a block model approach assigning one snow and one ice thickness value. A simple 1D model showed initial model conditions set for chl *a* had a larger influence on algal growth than variable light conditions between ice types. The initial chl *a* values were, however, ultimately the result of the variable light conditions experienced at the different ice types. Our case study results further emphasize the need to implement variable snow and ice conditions for up-scaling and modeling studies, in addition to improved model parametrization of initial conditions.

7.1 Introduction

The extent of multi-year sea ice (MYI) has declined dramatically in the satellite record from 75% of the total Arctic sea ice pack in the mid-1980s, to 45% in 2011(Maslanik et al., 2011). This trend is expected to continue, given large sea ice volume losses observed from satellite ice thickness data (Laxon et al., 2013) and modelling studies (Schweiger et al., 2011). Furthermore, sea ice extent has been declining in all seasons with the most pronounced rates of decline in summer (Stroeve et al., 2012; Stroeve et al., 2011). The record minimum summer sea ice extent set in September 2012 (Parkinson & Comiso, 2013), which was a remarkable decline from the previous 2007 record, demonstrates the continued vulnerability of the Arctic climate system. The Arctic ecosystem may be particularly vulnerable to climate change, however, monitoring biological and biogeochemical processes and interactions is much more difficult as these components are not easily observed from satellites or airborne systems. Of great consequence to our understanding of the Arctic sea ice system is the lack of ecologically relevant studies within the vast MYI covered region of the Arctic Ocean (Wassmann, 2011).

A disproportional amount of research effort regarding sea ice ecology has been dedicated to coastal regions dominated by first-year sea ice (FYI). In order to understand and monitor changes we need a greater understanding of the current state of the entire Arctic sea ice ecological system. This requires baseline studies of MYI covered regions of the Arctic Ocean, which is already too late in many regions due to the disappearance of a large portion of the MYI cover. From the limited number of studies conducted within MYI covered regions there is mounting evidence that MYI is a unique and important component of the entire Arctic sea ice system and that MYI may play a more important ecological role than was previously assumed. For instance, Hatam et al. (2016) suggested that a shift from a predominantly MYI to predominantly FYI sea ice cover will result in more functional instability within sea ice bacterial communities, causing a reduced capacity to adapt to environmental disturbances. This has important consequences for nutrient dynamics for the entire Arctic. Furthermore, during summer, high latitude regions dominated by MYI showed the highest proportion of ice-related primary production compared to the water column (Fernández-Méndez et al., 2015; Gosselin et al., 1997). Maximum under-ice algal aggregate biomass (Katlein et al., 2014a) and maximum in-ice algal biomass (Lange et al., in review) were also observed within MYI dominated regions compared to the lower latitude FYI dominated regions. These higher biomass observations were attributed to reduced melt, likely resulting from a combination of higher latitude and thicker sea ice. There remains a significant knowledge gap in terms of MYI algal biomass and production during spring due to the logistical constraints of sampling within this region at this time of the year.

One approach to improve our understanding of the ecology of MYI would be to identify key relationships between the algal communities and the physical sea ice environment, which can be substantially different between the two ice types. These relationships would vastly improve our ability to: i) model sea ice biogeochemical processes; and ii) develop reliable sea ice algal habitat classification systems based on critical/threshold properties that are strongly related to ice algal growth and biomass, which can be applied to pan-Arctic satellite and airborne observations.

Threshold light levels (i.e., critical light levels) for ice-algal growth have been proposed and may be determined by lab experiments (Gosselin et al., 1985; Gosselin et al., 1986). However, it is difficult to re-create the natural environmental variability using experiments, particularly for ice algae, and thus may not be representative of the natural communities. During spring, ice algae growth is primarily controlled by light availability and thus largely influenced by the physical properties of the snow and ice that control light transmittance to the bottom-ice, where the highest algae biomass is located (see review inVancoppenolle et al., 2013). Due to the influence of snow and ice on light transmission (Maykut & Grenfell, 1975; Thomas, 1963), snow and ice thickness have the potential to be used as proxies to identify regions of suitable sea ice algal habitat. Incoming solar radiation can generally be assumed to have higher temporal variability (e.g., diurnal patterns and cloud cover) than the physical snow and ice properties, which have a dominant influence on light transmittance. We must note that events such as snow storms or sea ice ridging can also influence the snow and ice light field on relatively small time-scales, however, these events can be considered less frequent and thus have a

smaller albeit important influence on light availability. Therefore, we propose the physical environment may be a robust proxy of long-term light availability for ice algae and should demonstrate some key relationships that can be used for a reliable sea ice habitat classification system.

A similar approach to identify a proxy for ice algal growth was previously suggested by Lange et al. (2015). Lange et al. (2015) conducted a multi-year study within the Lincoln Sea and demonstrated no significant differences between springtime MYI and FYI algal chl *a* biomass. However, it was proposed that MYI hummocks (i.e., relatively large surface undulations protruding ~ 1 m above the adjacent level ice) may be suitable habitat for high accumulations of algal biomass because of the low snow cover on hummocks, which could lead to higher light levels at the ice bottom, despite hummocks being thicker than the surrounding level ice. This hypothesis was proposed based on one MYI ice core that showed high bottom-ice chl *a* biomass, which was identified as a hummock post hoc. Schünemann and Werner (2005) also observed the highest springtime ice-algal chl *a* values in the bottom of the thickest ice with lowest snow cover, which may also be considered a MYI hummock. This hypothesis has potential pan-Arctic implications as hummocks are a common feature of MYI and may represent a largely under-estimated region of suitable ice algal habitat currently neglected from large-scale estimates and modelling studies.

Here we test the hypothesis that MYI hummocks have the potential for higher biomass than other ice types due to the increased transmission of light in these regions. To this end, we have extended the work presented in Lange et al. (2015), with an increased sampling effort at MYI hummock (MYI-Hum) locations. In addition, we sampled other ice types including FYI and deeper snow covered regions with relatively lower surface elevation, which we refer to here as MYI-melt ponds (MYI-MP) as these locations are commonly refrozen melt ponds due to accumulation of melt water in topographically low regions. Furthermore, we conducted under-ice light measurements to assess the variability of the under-ice light field for the different ice types and related the optical observations to ice-algal biomass. Based on the observed optical-biological relationships at the ice core locations, we classified sea ice habitats as regions "suitable" or "not-suitable" for ice-algal growth. We extrapolated this classification from the ice core locations to local scale snow and sea ice surveys to assess the coverage of "suitable" ice-algal sea ice habitats for different ice types. We applied the developed physical-biological relationships to two case studies:

1. Developed a habitat classification system and applied it to pan-Arctic satellite ice thickness (Cryosat-2) and snow depth climatology data products to demonstrate the potential importance of MYI algal biomass on pan-Artic scales.
2. Used the different habitat classes to initialize and parametrize 1D sea ice process models in order to demonstrate the importance of parameterizing different types and snow covers of ice in sea ice biogeochemical models.

7.2 Material and Methods

Here we present observations conducted in early May 2013 at two FYI stations and six MYI stations in the Lincoln Sea, north of Ellesmere Island, Canada (Figure 1). These observations are supplemented with data from 2010-2012 that were previously presented in Lange et al. (2015). All sites from 2010 – 2013 are grouped by location and shown in Figure 1. Groupings are listed in Table 1. Methods described in the present study refer to sampling conducted during the 2013 campaign unless otherwise stated. Site naming follows the same protocol as in Lange et al. (2015), in the form "SS-YY" with each 2 digit site "SS" enumerated in consecutive order starting with "01" for each (2-digit) year "YY". During the 2013 season, at some sites we sampled multiple cores from separate regions from the same site, which were classified as different ice types. We also sampled at different revisit periods of the snow removal experiments. For example: at site 06-13 we sampled a refrozen melt pond (06-13-MP) and hummock ice (06-13-Hum). In addition, we sampled the melt pond at different revisit days (t_0 = day 1 = 06-13-MPt_0; and t_3 = day 3 = 06-13-MPt_3).

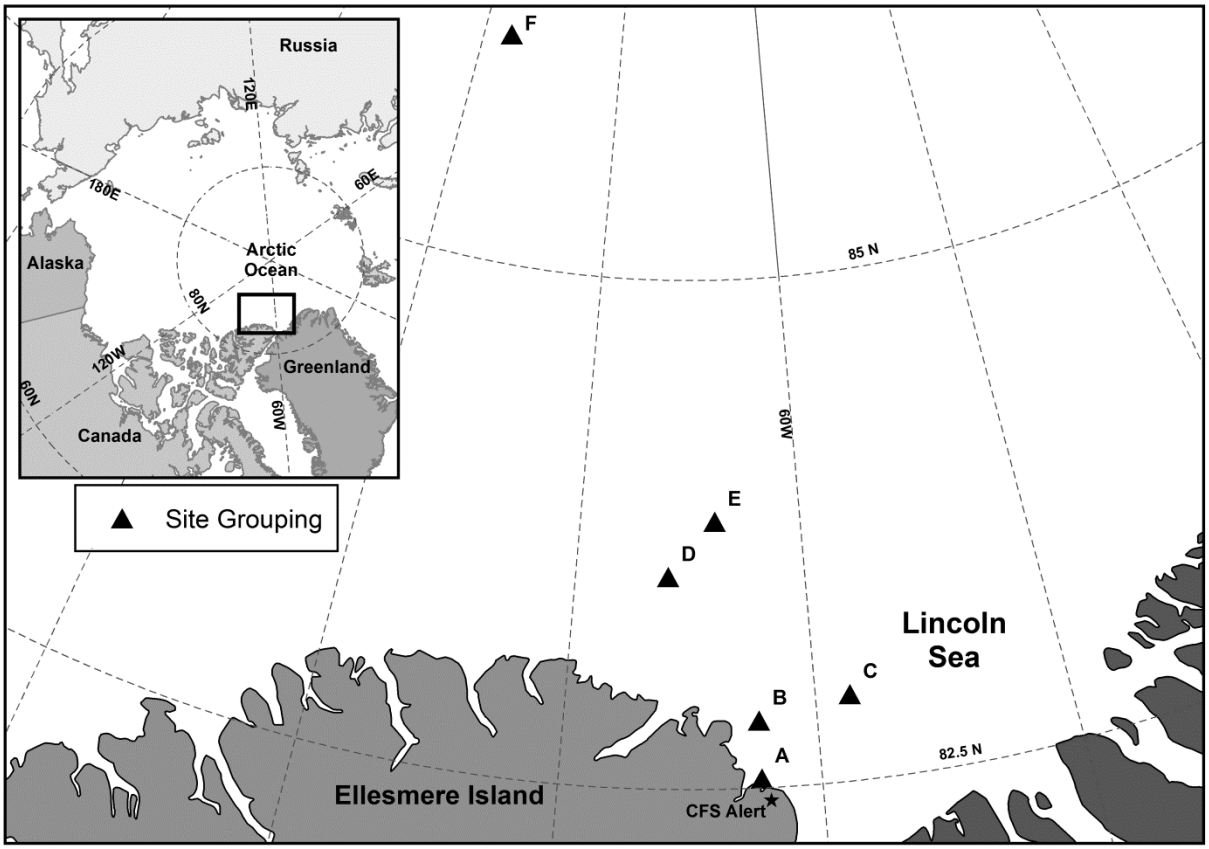

Figure 1: Map of the study region north of Ellesmere Island, Canada. Site groupings are shown, and the corresponding sites for each group are provided in Table 1.

7.2.1 Snow, sea ice and surface topography surveys

Snow depth and ice thickness surveys were conducted as described in Lange et al. (2015). In combination with the drill hole ice thickness measurements and snow depth surveys, measurements of the snow and ice surface elevation were conducted using a laser level and survey rod. The laser survey provided snow and ice surface elevation relative to the reference laser level plane and were conducted as described in Eicken and Salganek (2010). By tying these data in to sea ice freeboard measurements at the drill hole locations, the surface elevations were converted to relative elevations from the local sea surface height, i.e. the ice surface elevations represent sea ice freeboard. In 2012 the snow and ice surveys were conducted along a single transect at each site. In that year survey transects were conducted along a MYI floe (site 01-12), a FYI floe (02-12), and at one site that spanned a MYI floe and a refrozen lead (05-12). Survey data from site 05-12 was split into two separate surveys at the boundary between the MYI floe and the refrozen lead. Survey transect lengths for each site are shown in Table 1. In 2013 the snow and ice surveys were conducted on two FYI stations (02-13 and 03-13) and six MYI stations (01-13, 04-13, 05-13, 06-13, 07-13, 08-13). In 2013 the surveys were carried out along two perpendicular 100 m long transects that intersected in the middle of each transect (Table 1).

Coincident electromagnetic (EM) ice thickness surveys were conducted during the 2012 campaign using thr Geonics EM31 (9.8 kHz, 3.66 m coil spacing) obtaining ice thickness values using an exponential fit method as described by (Weissling et al., 2011). During the 2013 campaign EM thickness surveys were conducted using the EMP-400 from GSSI (9 kHz, 1.21m coil spacing). Results were obtained using a model analysis (2400 mS water conductivity) that finds the best fit between modelled and measured quadrature values, assigns the according ice thickness and averages data over 5m intervals. Thickness values were then interpolated to 1 m intervals using the spline interpolation method provided by the R software function *spline* in the "stats" package.

Bulk integrated light extinction coefficients, k_B (dimensionless; i.e., the bulk extinction of light over the entire column of snow and ice), were calculated for the snow and ice surveys based on common literature values, symbolized hereafter as $k_{B,calc}$. For all calculations we used extinction coefficients for snow $k_s = 20.0\ m^{-1}$ and sea ice $k_i = 1.55\ m^{-1}$ (Grenfell & Maykut, 1977; Thomas, 1963). The value of k_s was chosen from a table of values (Thomas, 1963) based on a corresponding snow density comparable to measured values for our study region (Lange et al., 2015). The values of k_s and k_i were integrated over the depth of the corresponding ice and snow layers to provide "integrated extinction coefficients" (dimensionless) for all measurement locations along the survey transects and for each core site. The "bulk (snow plus ice) integrated extinction coefficient" (dimensionless) was then calculated as the sum of the integrated extinction coefficients for snow and ice. In the resulting bulk integrated extinction coefficients, larger values mean shallower penetration of light.

Table 1: Summary of sea ice survey sites. Physical and optical properties of the sea ice and snow cover are provided for each site and ice type.

Site	Group	Profile[a]	Ice Type	h_i (mean)	h_i (IQR)	h_s (IQR)	fb (IQR)	rms_{fb}	$k_{B,calc}$ (IQR)	$k_{B,calc} \leq 6.75$ (%)	P_i	P_s	P_{fb}
A5-12	A	Line (50 m)	Lead-Ice	0.8	0.8 (0.8-0.8)	0.06 (0.04-0.09)	2 (-3-8)	8	2.4 (2.1-2.9)	100	-	-	-
A2-12	A	Line (100 m)	FYI	1.8	1.8 (1.7-1.9)	0.29 (0.22-0.33)	11 (8-15)	12	8.6 (7.4-9.2)	18	-	-	-
A2-13	A	Cross	FYI	1.7	1.8 (1.7-1.8)	0.17 (0.11-0.23)	11 (10-14)	12	5 (3.9-6.2)	87	31	29.5	39.0
A3-13	A	Cross	FYI	1.6	1.6 (1.5-1.7)	0.29 (0.24-0.38)	5 (2-7)	6	7.3 (6.3-9)	37	27	44.8	24.6
A1-12	A	Line (400 m)	MYI	3.4	3.4 (2.9-3.8)	0.41 (0.24-0.53)	22 (7-44)	37	13.5 (10.7-15.8)	3	-	-	-
A5-12	A	Line (130 m)	MYI	3	2.6 (2.2-3.8)	0.28 (0.21-0.36)	22 (14-44)	32	10.5 (8.4-12.1)	5	-	-	-
A1-13	A	Cross	MYI	2.9	2.7 (2.2-3.4)	0.31 (0.11-0.44)	14 (3-34)	29	8.6 (5.4-11)	38	23.5	19.6	25.2
A4-13	A	Cross	MYI	3.1	3 (2.4-3.6)	0.32 (0.14-0.43)	14 (-3-35)	27	9 (6.2-10.9)	28	21.2	24.7	23.3
A5-13	A	Cross	MYI	3.7	3.5 (3.1-4.2)	0.43 (0.29-0.64)	30 (2-43)	36	11.8 (9.3-15.6)	6	24.0	9.9	10.4
A6-13	A	Cross	MYI	2.8	2.9 (2.3-3.2)	0.28 (0.17-0.42)	23 (5-35)	27	8.2 (6.4-10.5)	30	14.9	9.4	8.3
A7-13	A	Cross	MYI	2.5	2.5 (2.3-2.8)	0.33 (0.26-0.44)	20.5 (10.5-30)	27	9 (7.5-10.8)	17	13.5	9.0	6.1
A8-13	E	Cross	MYI	2.1	1.9 (1.8-2.5)	0.33 (0.24-0.43)	11 (6-18)	17	8.4 (6.8-10.5)	25	23.4	23.6	7.8
Total			FYI		1.7 (1.6-1.8)	0.25 (0.18-0.31)			6.7 (5.4-8.3)	53			
			Lead-Ice		0.8 (0.8-0.8)	0.06 (0.04-0.09)			2.4 (2.1-2.9)	100			
			MYI		2.9 (2.4-3.5)	0.34 (0.21-0.46)			10.1 (7.5-12.5)	18			

[a]"Cross" profiles refer to surveys conducted along two perpendicular 100 m transects that intersect in the middle of each transect.

h_i is the ice thickness; h_s is the snow depth; fb is the ice freeboard; rms_{fb} the root mean squared of the ice freeboard (i.e., proxy for surface roughness); $k_{B,calc}$ is the bulk integrated light extinction coefficient calculated from the snow and ice surveys. P_i, P_s, and P_{fb} are the patch sizes determined from autocorrelation analyses (Supplementary Material Figures S 9 – S 16) of ice thickness, snow depth, and ice freeboard, respectively. Interquartile range (IQR) represents median (50^{th}) and 25^{th} – 75^{th} percentiles.

7.2.2 Under-ice light measurements

Spectral irradiance measurements were acquired using RAMSES spectral radiometers (TriOS GmbH) with a wavelength range from 350 to 920 nm and a resolution of 3.3 nm, which were subsequently interpolated to a 1 nm grid following Nicolaus et al. (2010). Incident solar radiation (E_S) and under-ice irradiance (E_T) were measured using an irradiance sensor (RAMSES-ACC) containing a cosine receptor with a 180º field-of-view (FOV). All spectral measurements are presented for the photosynthetically active radiation range (PAR) between 400 to 700 nm, unless stated otherwise. Additional details about the RAMSES sensors and spectral data processing are available in Nicolaus et al. (2010). Spectral transmittance (T_E) is defined as the ratio of E_T to E_S (Nicolaus et al., 2010).

Under-ice spectral measurements were conducted using an under-ice L-arm sensor system with a mounted irradiance sensor. The under-ice L-arm sensor system, previously described in Lange et al. (in review), was deployed below the ice through a ~14 cm diameter hole drilled using a Kovacs Mark II 9 cm internal diameter corer (Kovacs Enterprise, Roseburg, USA). Once the L-arm was below the ice, the lower ~1.2 m of the aluminum bar setup, with mounted sensor, was extended horizontally, and then slowly raised so the sensor was ~10 cm from the ice bottom. The snow-ice surface directly south of the L-arm hole was kept undisturbed during the initial snow covered spectral measurements. To minimize shading by the system equipment and operator, the spectral measurements used for further analyses were conducted with the sensor positioned directly south of the L-arm hole at a distance of ~1.2 m. Additional spectral measurements were conducted at equal intervals along a hemisphere, centered in the south direction. A total of 10 E_T measurements were taken with two measurements conducted directly south of the L-arm hole. Coincident E_S measurements were conducted above the ice directly before and directly after the under-ice survey. T_E was calculated for all combinations of under-ice spectral measurements (N=10) and above ice incoming irradiance (N=2) for a total of 20 transmittance measurements. The two incoming irradiance and 20 transmittance spectra were assessed to ensure no significant variability of the incoming light field.

A total of 6 under-ice L-arm surveys were conducted at sites with an undisturbed snow cover. Under-ice light surveys were conducted at one FYI (02-13-FY), three MYI refrozen melt pond (01-13-MP; 06-13-MP; 07-13-MP) and two MYI hummock core locations (06-13-Hum; 08-13-Hum). No surveys were conducted under lead-ice (Table 2). The 06-13-MP and 06-13-Hum L-arm sites were adjacent to each other, separated by ~ 5 m.

In addition to the undisturbed snow cover measurements, snow removal experiments were conducted at two sites, 01-13-MP and 06-13-MP. On the first day of the snow removal experiment (t_0: 01-13-MPt_0 and 06-13-MPt_0) an L-arm survey was conducted with the original undisturbed snow pack. We then measured the snow depth at 10 locations within the snow removal area. The snow was then removed from a 2 m by 2 m square area with the center of the square ~ 1.2 m directly south of the L-arm hole (i.e., directly above where the two main spectra were measured). We then repeated the L-arm survey with no snow. Finally, an ice core was extracted from the main measurement location ~ 1.2 m south of the L-arm hole to determine chlorophyll *a* concentrations (see next section 2.3).

We revisited site 01-13-MP twice, one revisit was 3 days after t_0 (t_3; 01-13-MPt_3) and the other revisit was 6 days after t_0 (01-13-MPt_6; Table 2). There was a fresh ~1 cm layer of snow covering the snow removal area on day 3 (01-13-MPt_3; Table 2). We re-cored the refrozen ice from the L-arm hole while minimizing disturbance to the fresh snow cover and conducted the first L-arm survey. The refrozen ice core (refr.) from the L-arm hole was kept and processed for chl *a*. The thin snow layer was removed and the L-arm survey was repeated with no-snow. Finally, we extracted one ice core ~1.2 m south-east of the L-arm hole (still within the snow-free area), which was processed for chl *a*. The site was snow-free when we revisited it on day 6 (01-13-MPt_6). We conducted one L-arm survey with no snow (01-13-MPt_3); no cores were extracted on this day.

Site 06-13-MP was revisited once, 4 days after t_0 (06-13-MPt_4; Table 2). No fresh snow was present at t_4 so only one snow-free L-arm survey was conducted. After the L-arm survey, we sampled the bottom 0.1 m of the L-arm hole refrozen ice core (refr.) and the bottom 0.1 m of an ice core extracted ~1.2 m south-west of the L-arm hole, which were processed for chl *a*.

We also calculated $\mathbf{k_B}$ based on the L-arm spectral surveys, symbolized hereafter as $\mathbf{k_{B,obs}}$, according to (Thomas, 1963) in the form:

$$-k_{B,obs} = \ln\left[\frac{E_T}{[1-\alpha]\,E_S}\right] \Big/ z \qquad (1)$$

where z is the total combined depth of snow and sea ice in meters, E_T is the under-ice irradiance, E_S is the incident solar radiation, and α is the surface albedo for the snow and ice types present at each L-arm survey. Here we used values of α from Perovich (1996), which are listed in Table 2.

7.2.3 Chlorophyll *a*

Sea ice core sampling and processing were conducted following procedures outlined in Lange et al. (2015). Chl *a* concentrations were determined fluorometrically using equations from Parsons et al. (1989). We vertically integrated chl *a* over the bottom section of each ice core, which varied in length between 0.1 – 0.2 m, hereafter referred to as the bottom-integrated chl *a* concentrations (mg m^{-2}). Here we used the bottom-integrated chl *a* concentrations presented in Lange et al. (2015) (N= 18) in addition to the cores collected in 2013. A total of nine bottom-ice core sections were collected from undisturbed sites during 2013.

Four additional cores were collected during later stages of the snow removal experiments (i.e., disturbed sites) and are considered separately to the undisturbed site chl *a* observations. Sea ice cores extracted at t_0 of the snow removal experiment were considered undisturbed as the cores were removed within 1 hour of the snow removal and ice-algal biomass was unlikely to be significantly influenced in such a short time. At the snow removal site 01-13-MPt_3, two cores were extracted, one from a site ~1.2 m south-east of the L-arm hole and one from the ice that had refrozen in the L-arm hole. For these two cores, the full length of the ice cores were melted (i.e., the bottom-ice was not sectioned off); therefore, the chl *a* concentrations for these cores represent the bulk integrated chl *a* (also in mg m^{-2}) and are therefore integrated over the entire length of the core and not the bottom section.

At snow removal site 06-13-MPt_4 two bottom-ice core sections were sampled, one extracted ~1.2 m south-east of the L-arm hole in the snow removal area, and one from the refrozen ice extracted from the L-arm hole. Ice coring and an L-arm survey were also conducted at an adjacent hummock (site 06-13-Hum). At this hummock site, three bottom-ice cores were sampled in order to assess the representativeness of ice cores from a MYI-hum site (06-13-Hum-a, -b, -c), which was important to test the hypothesis. We used the mean of these three cores as one sample for the statistical comparison between ice types (06-13-Hum).

7.2.4 Statistical Analyses

To test if there were significant differences in bottom-ice algal chl *a* biomass and calculated bulk integrated extinction coefficients ($k_{B,calc}$) between the different ice types (FYI, lead-ice, MYI-MP, and MYI-Hum) we used an analysis of variance (ANOVA) applied to the log-transformed chl *a* and $k_{B,calc}$ observations. Log-transformations were conducted to conform with the assumptions of statistical analyses. For a significant ANOVA test ($p < 0.05$), which indicated significant differences between ice types, we performed a post-hoc Tukey HSD test to identify which ice types were significantly different ($p < 0.05$).

The 2013 snow and ice surveys were conducted in two perpendicular directions, West-East (WE) and South-North (SN). Snow depth, ice thickness, ice freeboard, and $k_{B,calc}$ values were individually compared between the two profile directions at each site using a student's t test with a significance level of $p < 0.05$.

7.2.5 Spatial autocorrelation analyses

Spatial autocorrelation was used to investigate the horizontal variability of sea ice thickness, snow depth and sea ice surface topography (i.e., sea ice freeboard). Autocorrelation was estimated using Moran's *I* (Legendre & Fortin, 1989; Moran, 1950), which was calculated for each of the eight sites at 30 equally spaced (3.3 m) distance classes between 2.65 – 98.35 m. Individual autocorrelation coefficients or Moran's *I* estimates were plotted for each distance class in the form of a spatial correlogram (Legendre & Fortin, 1989). All analyses were conducted using the 'R' software function *correlog* from the "pgirmess" package. Autocorrelation coefficients for each distance class were assigned a two-sided p-value following methods in (Legendre & Fortin, 1989). We used a significance level of $p < 0.05$ to identify insignificant spatial autocorrelation (i.e., the null hypothesis is true at $p \geq 0.05$ indicating a random spatial distribution) or the presence of significant spatial autocorrelation (i.e., reject null hypothesis at $p < 0.05$ indicating possible pattern or patchiness). We focused on the first x-intercept of the correlogram line, which identifies the patch size (P) of the variables (Legendre & Fortin, 1989), in our case: ice thickness (P_i), snow depth (P_s), and ice surface topography (P_{fb}; i.e., sea ice surface freeboard). This methodology is consistent with spatial autocorrelation analyses used in other snow and sea ice studies to identify patch sizes of both biological and physical variables (e.g., Gosselin et al., 1986; Granskog et al., 2005; Rysgaard et al., 2001; Søgaard et al., 2010).

7.3 Results

7.3.1 Snow and sea ice properties

FYI ice sites had relatively uniform ice thicknesses, with site median thicknesses in the range 1.6 – 1.8 m, and the interquartile range (IQR) within ± 0.1 m of median thickness at each site (Table 1). Ice thickness was more variable between MYI sites, with site median thicknesses in the range 1.9 – 3.5 m, and within the individual MYI sites (IQR within ± 0.1 – 1.2 m of median; Table 1). Two MYI sites were exceptionally thick with site median thicknesses of 3.4 m (01-12) and 3.5 m (05-13; Table 1). These two sites also had the thickest snow cover with median snow depths of 0.41 m (01-12) and 0.43 m (05-13; Table 1). The median snow depth at the remaining MYI sites was consistently ~0.3 m (Table 1). One FYI site (02-13) had a noticeably thinner snow cover than the other two sites with a site median snow depth of 0.17 m compared to 0.29 m for both of the other FYI sites (Table 1). In general, the snow cover was thicker on MYI (median for all sites 0.34 m) than on FYI (median of all sites 0.25 m), however, the lower range of snow depth observations (25^{th} percentile) were comparable at 0.18 m for FYI and 0.21 m for MYI (Table 1). One survey was conducted on lead-ice (site 05-12), which consisted of very thin uniform ice 0.8 m thick (IQR within ± 0.05 m of median) and a very thin and uniform snow pack (median: 0.06; IQR: 0.04 – 0.09; Table 1).

Overall, lead-ice had the lowest survey-derived $k_{B,calc}$ (median: 2.4) and the lowest variability (IQR: 2.1 – 2.9; Table 1 and Figure 2). FYI generally had lower and more uniform survey-derived $k_{B,calc}$ than MYI, with overall median (IQR) values of 6.7 (5.4 – 8.3) for FYI and 10.1 (7.5 – 12.5) for MYI (Table 1 and Figure 2). There was high variability in the median values of $k_{B,calc}$ for both FYI sites (5.0 – 8.6) and MYI sites (8.2 – 13.5; Table 1 and Figure 2). The two MYI sites with the highest survey-derived $k_{B,calc}$ of 11.8 (site 05-13) and 13.5 (site 01-12) also had the two largest median snow depth and ice thickness values (Table 1).

ANOVA and post hoc Tukey HSD tests indicated that ice core $k_{B,calc}$ were not significantly different between FYI and MYI-Hum ice types, however, all other combinations of ice types were significantly different from each other (Table 3; Figure 3). Lead-ice cores had the lowest $k_{B,calc}$ and MYI-MP had the highest $k_{B,calc}$ (Table 3; Figure 3b). MYI-Hum and FYI $k_{B,calc}$ values were in between lead-ice and MYI-MP ice cores. MYI-Hum ice core $k_{B,calc}$ values were generally more uniform than FYI (Figure 3b) but within the range of FYI $k_{B,calc}$ values. The representativeness of ice core sampling for each ice type is indicated in Figure 4 with vertical lines depicting ice core $k_{B,calc}$ values. The probability density functions (Figure 4) are the survey-derived $k_{B,calc}$ values for all sites summarized per ice type . It is apparent from the density plots and vertical ice core lines, that the lower range of FYI $k_{B,calc}$ and the

higher range of lead-ice $k_{B,calc}$ could be better represented with more ice core samples in these regions, whereas ice cores from MYI are well represented over the full range of surveyed $k_{B,calc}$.

Each directional profile conducted in 2013 (West-East and South-North) of snow depth, sea ice thickness and surface topography combined with coincident $k_{B,calc}$ profiles are shown in the supplementary material (Figures S1–S8). The directional comparison, West-East vs. South-North, of the eight perpendicular snow and ice surveys showed significant differences for ice thickness at four sites, for snow depth at five sites, for ice freeboard at three sites, and for $k_{B,calc}$ at six sites (Table 4).

From the snow and ice survey data we found strong, significant ($p < 0.05$) negative correlations between snow depth and ice freeboard on lead-ice ($r = -0.56$), FYI ($r = -0.69$), and MYI ($r = -0.73$; Table 5). We also observed a very strong, significant correlations between snow depth and calculated bulk integrated extinction coefficients on lead-ice ($r = 1.00$), FYI ($r = 0.97$), and MYI ($r = 0.91$; Table 5).

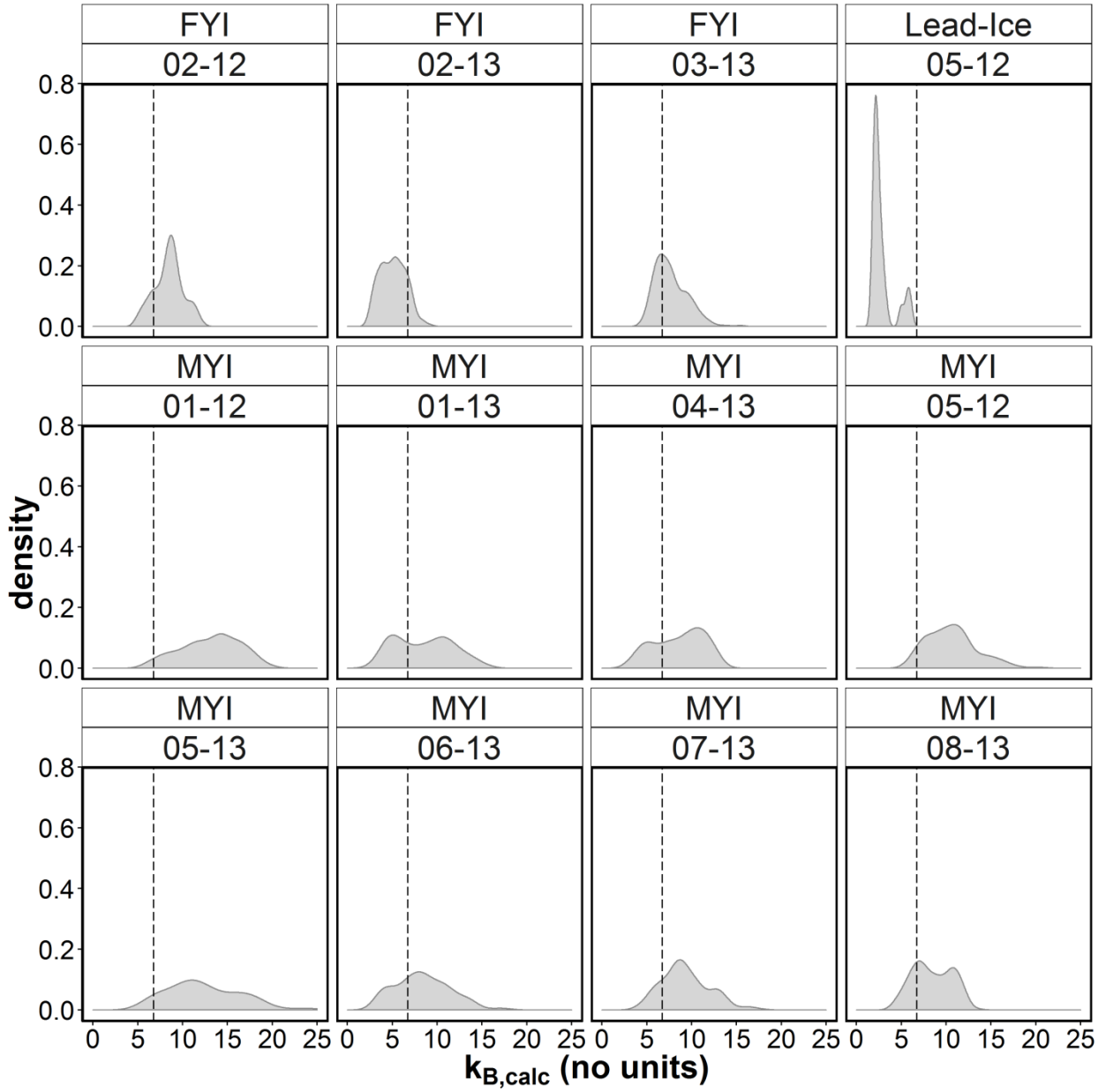

Figure 2: Probability density distributions of bulk integrated extinction coefficients ($k_{B,calc}$) calculated from the snow and ice surveys for individual sites. Dashed vertical line is the threshold $k_{B,calc} = 6.75$.

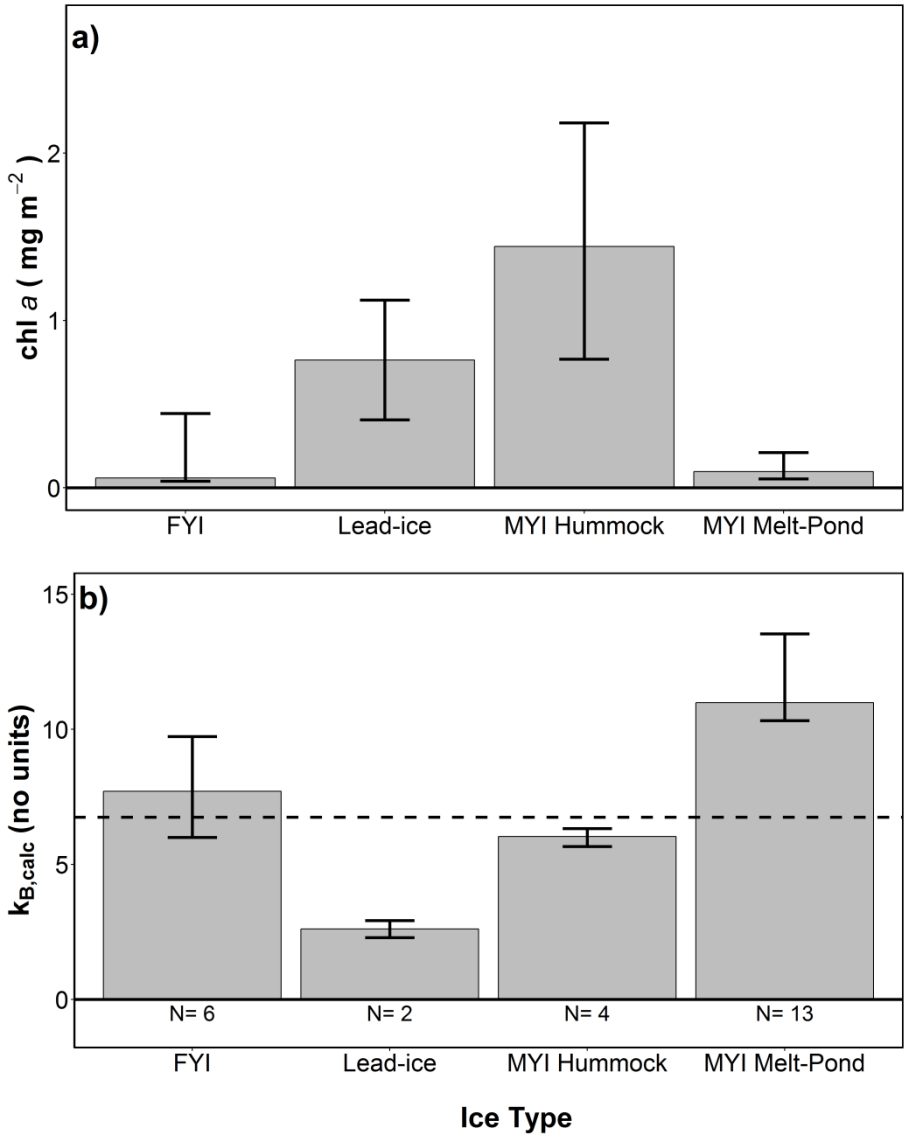

Figure 3: Comparison between ice types of a) chl *a* biomass; and b) calculated bulk integrated extinction coefficients ($k_{B,calc}$). Bars represent the median and error bars the interquartile range (25th and 75th percentiles). Dashed horizontal line in b) is the threshold $k_{B,calc}$ = 6.75.

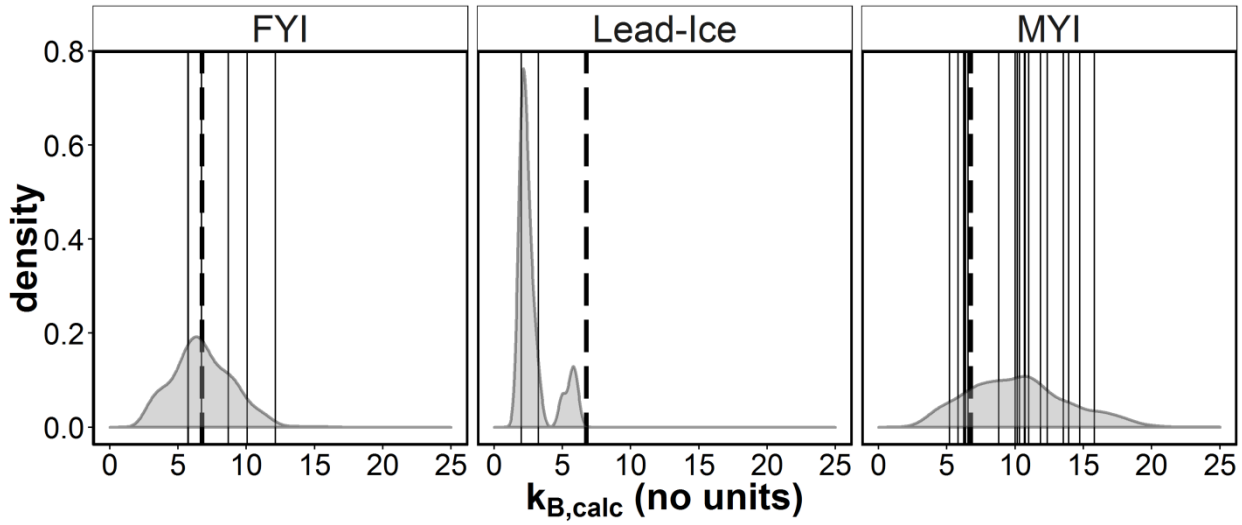

Figure 4: Density distributions of snow and ice survey-derived bulk integrated extinction coefficients ($k_{B,calc}$) shown for the combined surveys grouped by ice type. Solid vertical lines correspond to $k_{B,calc}$ of ice core locations from the corresponding ice type. Dashed vertical lines corresponds to the threshold $k_{B,calc}$ value of 6.75.

Table 3: Posthoc Tukey HSD test results showing the adjusted p-value matrix for multiple comparison of the means of the log-transformed chl *a* biomass and corresponding calculated bulk integrated extinction coefficients ($k_{B,calc}$) for the different ice types.

Variable	Ice Type	FYI	Lead-Ice	MYI-MP	MYI-Hum
Chl *a*	FYI (N=6)	-			
	Lead-Ice (N=2)	0.87	-		
	MYI-MP (N=13)	0.986	0.735	-	
	MYI-Hum (N=4)	**0.047**	0.52	**0.013**	-
$k_{B,calc}$	FYI (N=6)	-			
	Lead-Ice (N=2)	**0.00**	-		
	MYI-MP (N=13)	**0.007**	**0.00**	-	
	MYI-Hum (N=4)	0.22	**0.001**	**0.0001**	-

Bold values indicate significant difference between ice types ($p < 0.05$).

Table 2: Summary of the L-arm measurements and corresponding ice cores. Summaries are per site and revisit day (t_0, t_3, t_4, t_6) for snow removal experiments. Snow conditions indicate if the L-arm measurements were conducted under snow or no snow.

Site	Ice type	Snow Conditions	h_s	h_i	E_S	E_T	T_E	Albedo α[a]	$k_{b,calc}$	$k_{b,obs}$	Chl *a*	Core (section)
			(m)	(m)	(µmols photons m-2 s-2)		----------No units----------				mg m^{-2}	
01-13-MPt_0	MYI-MP	Snow	0.36	2.25	1019.3	0.5	0.0008	0.81	10.6	5.5	-	
01-13-MPt_0	MYI-MP	No snow	0	2.25	707.5	8.8	0.0165	0.4	3.4	3.6	-	
01-13-MPt_3	MYI-MP	Snow	0.01	2.22	996.6	12.6	0.0153	0.87	3.6	2.1	1.04	Refr. entire core
			0.01	2.21							1.12	entire core
01-13-MPt_3	MYI-MP	No snow	0	2.25	1035.7	14.5	0.0180	0.4	3.4	3.5	-	
01-13-MPt_6	MYI-MP	No snow	0	2.25	1218.0	13.9	0.0148	0.4	3.4	3.7	-	
02-13-FY	FYI	snow	0.13	1.77	1045.9	25.9	0.0297	0.81	5.3	1.9	0.57	bottom 0.16 m
06-13-Hum	MYI-Hum	No snow	0	4.09	951.2	3.0	0.0044	0.7	6.3	4.2	3.59	Hum-a bottom 0.1 m
			0	4.12							2.73	Hum-b bottom 0.1 m
			0	4.03							1.26	Hum-c bottom 0.1 m
06-13-MPt_0	MYI-MP	Snow	0.41	3.3	1380.2	1.0	0.0012	0.81	13.3	5.0	0.55	bottom 0.1 m
06-13-MPt_0	MYI-MP	No snow	0	3.3	1114.2	5.8	0.0083	0.4	5.1	4.3	-	-
06-13-MPt_4	MYI-MP	No snow	0	3.29	620.5	5.0	0.0111	0.4	5.1	4.0	1.17	Refr. (bottom 0.1 m)
			0	3.24							0.98	bottom 0.1 m
07-13-MP	MYI-MP	Snow	0.24	2.32	931.7	0.5	0.0008	0.81	8.4	5.5	0.06	bottom 0.17 m
08-13-Hum	MYI-Hum	Snow	0.1	3.07	1074.8	3.3	0.0049	0.81	6.8	3.7	0.62	bottom 0.1 m

[a] values taken from (Perovich, 1996) for corresponding snow or ice type.

Table 4. Directional comparison of snow and sea ice surveys from 2013 summarized by West-East (WE) and South-North (SN) transect directions.

Site	Ice	[a]Mean h_i (m)		[a]Median (IQR) h_i (m)		[a]Median (IQR) h_s (m)		[a]Median (IQR) fb (cm)		rms_{fb}		[a]Median (IQR) $k_{B,calc}$		$k_{B,calc}$ < 6.75 (%)	
		WE	SN	WE	SN	WE	SN	WE	SN	WE	SN	WE	SN	WE	SN
02-13	FYI	**1.7**	**1.8**	**1.7 (1.6-1.7)**	**1.8 (1.7-1.8)**	**0.20 (0.15-0.25)**	**0.13 (0.08-0.19)**	**11 (10-12)**	**12 (10-16)**	11	13	**5.6 (4.6-6.5)**	**4.3 (3.4-5.4)**	84	89
03-13	FYI	1.6	1.6	1.6 (1.6-1.7)	1.6 (1.5-1.7)	**0.28 (0.24-0.34)**	**0.31 (0.25-0.40)**	5 (3-7)	4 (1-7)	6	6	**7 (6.3-8.2)**	**7.6 (6.5-9.3)**	44	30
01-13	MYI	**2.7**	**3.1**	**2.7 (2.1-3.2)**	**2.8 (2.2-3.9)**	**0.36 (0.15-0.47)**	**0.28 (0.04-0.41)**	**11 (4-31)**	**18 (2-45)**	22	34	**9.2 (6.2-11.5)**	**7.8 (4.8-10.5)**	32	44
04-13	MYI	**3.4**	**2.7**	**3.3 (2.8-4.0)**	**2.7 (2.2-3.2)**	0.32 (0.17-0.42)	0.34 (0.1-0.45)	16 (-3-37)	11.5 (-3-33)	28	27	9.1 (7.3-10.7)	8.9 (5.1-11)	22	35
05-13	MYI	3.7	3.7	3.2 (3.0-4.1)	3.6 (3.2-4.3)	**0.44 (0.31-0.68)**	**0.41 (0.22-0.6)**	**22 (0-36)**	**33 (16-48)**	30	40	**12.5 (9.8-15.8)**	**11.5 (8.8-14.4)**	4	8
06-13	MYI	**2.6**	**2.9**	**2.5 (2.1-2.9)**	**3.2 (2.5-3.3)**	*0.26 (0.1-0.43)*	*0.28 (0.2-0.42)*	22 (4-35)	23 (15-34)	26	27	**7.7 5-10.5)**	**8.5 (7.1-10.8)**	44	17
07-13	MYI	2.6	2.5	2.6 (2.4-2.8)	2.5 (2.1-2.8)	**0.28 (0.21-0.35)**	**0.4 (0.31-0.53)**	25 (16-32)	17 (7-27)	22	31	**8.2 (6.9-9.4)**	**10.3 (8.6-12.6)**	22	13
08-13	MYI	2.1	2.1	1.9 (1.7-2.5)	2.0 (1.8-2.5)	*0.35 (0.27-0.42)*	*0.27 (0.21-0.43)*	*8 (5-14)*	*13 (6-19)*	15	19	8.6 (7.3-10.3)	7.7 (6.2-10.6)	15	35

[a]Bold values correspond to significant differences ($p < 0.05$) and italics correspond to differences with $0.05 < p < 0.1$, based on t tests comparing the WE and NS perpendicular transects.

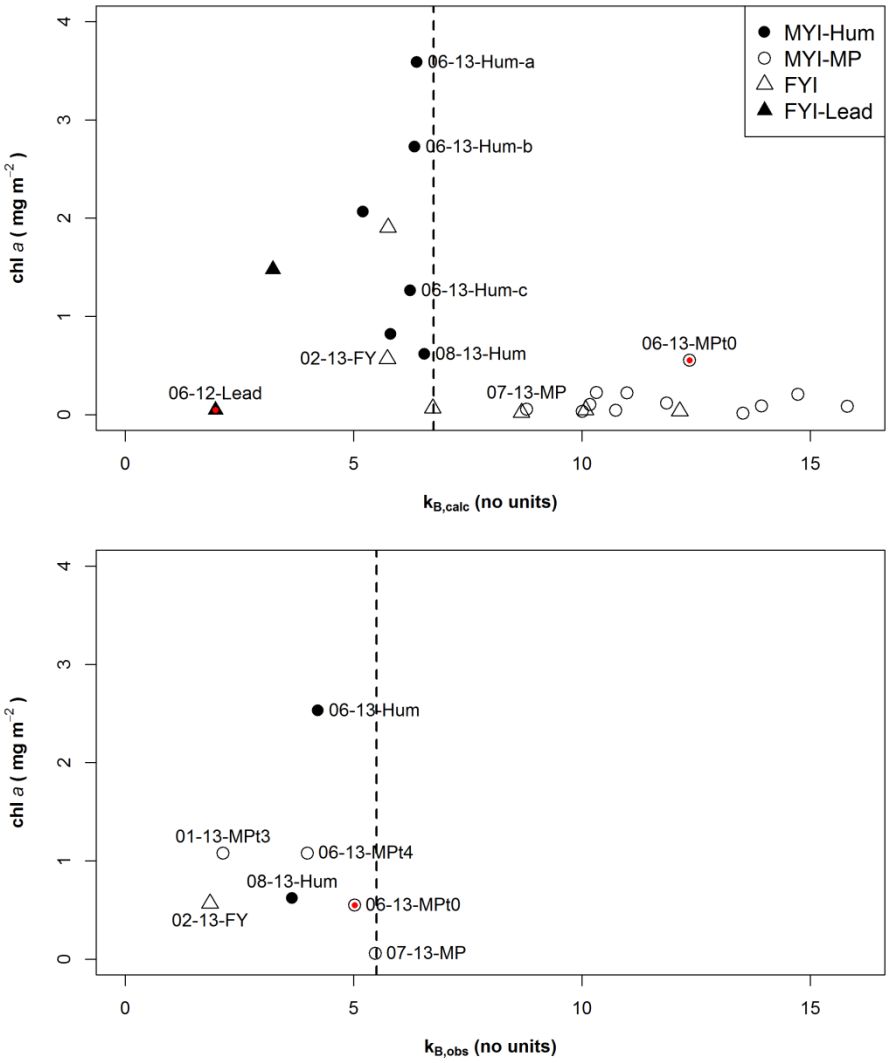

Figure 5: Ice core chl *a* biomass versus a) calculated bulk integrated extinction coefficient ($k_{B,calc}$), and b) observed bulk integrated extinction coefficients ($k_{B,obs}$) obtained during the L-arm light transmittance surveys. Red dots indicate suspicious points explained in main text. Dashed vertical lines indicate the determined critical light extinction thresholds of $k_{B,calc}$ of 6.75, and kB,obs of 5.5, which separate suitable and non-suitable sea ice algal habitats.

7.3.2 Chl *a* biomass at undisturbed sites

ANOVA and post hoc Tukey HSD tests indicated that ice core chl *a* biomass was significantly higher in MYI-Hum ice cores than FYI and MYI-MP ice cores ($p < 0.05$; Table 3 and Figure 3a). No significant differences in ice core chl *a* biomass were observed between the other ice types (Table 3 and Figure 3a). Three bottom-ice cores (triplicates) were taken from the same hummock at site 06-13 (i.1., 06-13-Hum-a, -b, -c); the mean of the triplicate core sections, 2.53 mg m^{-2}, was the maximum value used in the ANOVA and Tukey tests. Two of the triplicate cores had the highest (3.59 mg m^{-2}; 06-13-Hum-a) and second highest (2.73 mg m^{-2}; 06-13-Hum-b) biomass values of all cores (Figure 5; Table 2). The third triplicate had the sixth highest biomass (1.26 mg m^{-2}; 06-13-Hum-c; Table 2). The three other MYI hummocks sampled had the third (2.06 mg m^{-2}), seventh (0.82 mg m^{-2}) and eighth (0.62 mg m^{-2}) highest biomass of all bottom-ice cores (Figure 5). Two of the six FYI cores had relatively high biomass; the highest biomass FYI core (1.91 mg m^{-2}) had the fourth highest biomass of all cores and the second highest FYI core (0.57 mg m^{-2}) had the ninth highest biomass of all cores (Figure 5). One of the two lead-ice cores had high biomass (1.48 mg m^{-2}) while the other was near zero (0.05 mg m^{-2}; Figure 5).

Table 5: Correlation matrix between the snow and ice survey-derived properties: snow depth (h_s), ice thickness (h_i), ice freeboard (fb) and calculated bulk integrated extinction coefficients ($k_{B,calc}$).

Ice Type	Variable	h_s	fb	$k_{B,calc}$
Lead-ice	h_s	-		
	fb	**-0.56***	-	
	$k_{B,calc}$	**1.00***	**-0.54***	-
	h_i	-0.13	0.34*	-0.07
FYI	h_s	-		
	fb	**-0.69***	-	
	$k_{B,calc}$	**0.97***	**-0.56***	-
	h_i	-0.41*	**0.59***	-0.25*
MYI	h_s	-		
	fb	**-0.73***	-	
	$k_{B,calc}$	**0.91***	-0.49*	-
	h_i	-0.27*	**0.66***	0.07*

*indicate significant correlations ($p < 0.05$) and **bold** are strong correlations ($r > 0.5$).

Two suspicious ice cores were identified and depicted with small red dots (Figure 5): core 06-13-MPt_0 had anomalously high chl *a* biomass given its high $k_{B,calc}$ value and core 06-12 (labelled "06-12-lead" in Figure 5a) had anomalously low chl *a* biomass given its low $k_{B,calc}$ value (Figure 5a). Core 06-13-MPt_0, however, showed a better fit, relative to all other cores, with the $k_{B,obs}$ value (Figure 5b).

Based on the relationship between chl *a* biomass and bulk integrated light extinction coefficients ($k_{B,calc}$) we separated the samples into two habitat classes using the identified threshold $k_{B,calc}$ value of 6.75 (Figure 5a). The threshold value of $k_{B,calc}$ was visually identified at the clear division between high biomass and low biomass cores (dashed vertical line in Figure 5a). The two classes are: i) $k_{B,calc} \leq 6.75$ was classified as suitable habitat for ice-algal growth as biomass values below this threshold had the highest biomass of all cores (with the exception of one lead-ice core; Figure 5a); ii) conversely, > 6.75 was considered not-suitable habitat for ice-algal growth due to near-zero or very low biomass values above the threshold (Figure 5a). This pattern was similar based on the relationship between biomass and the observed $k_{B,obs}$ values (Figure 5b). The threshold value of $k_{B,obs}$ was slightly lower at 5.5 than the 6.75 determined for the $k_{B,calc}$ (Figure 5), however, only one low biomass core was available so this may be a less reliable threshold estimate than the $k_{B,calc}$ threshold. Nevertheless, the anomalous core 06-13-MPt_0 (Figure 5a) shows a better relationship with the $k_{B,obs}$ and the $k_{B,calc}$ was higher than th $k_{B,obs}$. This indicates that there was more available bottom-ice light than expected at the 06-13-MPt_0 site, which is likely the result of horizontal scattering from the adjacent hummock. The higher than expected light values also helps explain the higher than expected bottom-ice algal biomass.

7.3.3 Under-ice light surveys and snow removal experiments

Under-ice L-arm surveys were conducted under undisturbed snow and ice conditions at five sites (Table 2). One undisturbed site was a snow-free hummock (06-13 MYI-HUM) with a thickness of 4.08 m and transmittance of 0.004. The undisturbed snow sites were highly variable in terms of physical properties with mean snow depths (measured at 10 locations within a 2 x 2 m square centered above the light measurement) ranging between 0.13 m (02-13-FY) – 0.41 m (06-13-MPt_0), ice thicknesses between 1.77 (02-13-FY) – 3.30 m (06-13-MPt_0), and transmittance values ranging between 0.001 (01-13-MPt_0) – 0.03 (02-13-FY; Table 2).

Snow removal experiments were conducted at two sites (01-13-MP and 06-13-MP). Disturbed (no snow) L-arm surveys showed little variability with transmittance values ranging between 0.015 – 0.018 (01-MP) and 0.0083 – 0.011 (06-MP; Table 2). Revisit site 01-MPt3 had a fresh 1 cm snow layer present, which had a relatively minimal influence on the light transmittance with values of 0.0153 (with fresh snow) and 0.018 (fresh snow removed; Table 2).

The literature-based $k_{B,calc}$ values compared to the observation-based $k_{B,obs}$ values showed minimal differences for all surveys conducted with no snow cover, whether they were measurements from snow-free undisturbed sites or from disturbed (snow-removed) experiment sites (Table 2). Differences between $k_{B,calc}$ and $k_{B,obs}$ from L-arm survey measurements were greatest at snow-covered undisturbed sites 01-13-MPt_0 (difference of 5.1) and 06-13-MPt_0 (8.3; Table 2). Noteworthy differences were also found between $k_{B,calc}$ and $k_{B,obs}$ from L-arm surveys at all other undisturbed sites where a snow cover was present (Table 2).

Ice cores were extracted at the snow removal sites during the first visit (i.e., baseline chl *a* cores) and the second revisit (t_3 site 01-13-MPt_3 and t_4 site 06-13-MPt_4) after snow removal. Unfortunately, the baseline core sample from site 01-MPt0 was lost. Core 06-13-MPt_0 had a chl *a* biomass of 0.55 mg m^{-2} and the biomass at this site nearly doubled after four days with no snow; two bottom-ice cores extracted during the revisit survey (06-13-MPt_4), had chl *a* biomass values of 0.98 and 1.17 mg m^{-2} (Table 2). Entire ice cores extracted at site 01-13-MPt_3 had relatively high chl *a* biomass (note: chl a was integrated over the entire core, not the bottom section). We cannot assess the magnitude of change in chl *a* biomass during the 3 day period with no snow, from 01-13-MPt_0 to 01-13-MPt_3. However, it is likely that there was an increase in chl *a* biomass since under the original thick snow cover (0.36 m) with $k_{B,obs}$ (5.5) equivalent to the observed threshold value, we would have expected low or near zero biomass.

7.3.4 Spatial coverage of suitable sea ice algal habitats

Based on the determined $k_{B,calc}$ threshold value of 6.75, we identified the spatial coverage along each snow and ice survey with $k_{B,calc} \leq 6.75$ and classified these regions as suitable habitat for ice-algal growth. The percent coverage of suitable ice-algal habitat for all ice types showed a significant relationship with site median snow depth ($R^2 = 0.82$). Overall, lead-ice had the highest coverage of suitable habitat at 100%, with FYI second at 53 % and MYI the lowest coverage at 18 % (Table 1). However, there was high variability in the percent coverage of suitable ice-algal habitat within the FYI and MYI ice types. For FYI sites the percent coverage of suitable ice-algal habitat ranged from 18 – 87 %. For MYI sites the percent coverage of suitable ice-algal habitat ranged from 3 – 38 %. Two FYI sites (02-12 and 03-13) had suitable habitat coverages (18 and 37 %, respectively) within the range observed for MYI sites (Table 1). The thickest MYI sites (01-12 and 05-13) were among the lowest suitable habitat coverage values with 3 and 6 % suitable habitat, respectively. Site 05-12 also had low suitable habitat coverage (5%) but was not considered a thick sea ice site with a mean thickness of 3 m. All other "thin" MYI sites had higher suitable habitat coverage, ranging between 17 – 38 % (Table 1).

7.3.5 Spatial autocorrelation

Spatial autocorrelation analyses and spatial correlograms indicated larger sea ice thickness patch sizes (P_i) for FYI, with patch sizes around 30 m, than for MYI, which had patch sizes between 13.5 – 24 m (Table 1). Snow patch sizes (P_s) were generally larger for FYI (30 – 45 m) compared to MYI (9 – 25 m; Table 1). Freeboard (surface topography) patch sizes (P_{fb}) were also typically larger for FYI (25 – 40 m) than MYI (6 – 25 m); however, two MYI sites (01-13 and 04-13) had patch sizes comparable to FYI (23 – 25 m; Table 1). The other four MYI sites had surface topography patch sizes between 6 – 10 m (Table 1). Spatial correlograms are shown in supplementary material (Figures S9 to S16).

7.4 Discussion

7.4.1 Sea ice algal chl *a* biomass

Sea ice cores sampled from MYI hummocks had significantly higher chl *a* biomass than ice cores sampled from FYI and MYI-MP (Figure 3 and Table 3). To the best of our knowledge, the biomass values from our hummock bottom-ice samples in the range 0.62 – 3.6 mg chl *a* m^{-2} (6.2 – 35.9 mg chl *a* m^{-3}) are among the highest reported from Arctic springtime MYI. Melnikov et al. (2002) observed comparable maximum bottom-ice algal chl *a* concentrations of 9.32 mg m^{-3} during a

seasonal study of MYI; however, their maximum values were observed in July. Schünemann and Werner (2005) reported generally low chl *a* biomass values for all samples collected during late-winter (April) with the exception of one core, which had bottom chl *a* concentration of 3.4 mg m^{-3}. This core also was the thickest ice (2.46 m) with the thinnest snow cover (0.1 m). Lange et al. (2015) proposed that MYI hummocks are a suitable habitat for sea ice algal growth due to the typically thin snow-cover on these features. Lange et al. (2015) argued in combination with the Schünemann and Werner (2005) study that low-snow, high-biomass hummocks may be common feature of MYI. However, with only two ice cores showing the potential suitability of hummocks for ice-algal growth, further data was required to test the hypothesis that hummocks could represent a significant portion of suitable habitat for ice-algae in the Arctic. Using the results from Lange et al. (2015) together with our additional samples from MYI hummocks, we have demonstrated that these features do in fact have high sea ice algal chl *a* biomass, with higher biomass than FYI sampled from the same region within the Lincoln Sea. Furthermore, our MYI hummock biomass values are among the highest chl *a* concentrations reported for MYI in the Arctic Ocean. We can therefore confirm the hypothesis proposed by Lange et al. (2015) that MYI hummocks are a suitable habitat for sea ice algal biomass, which can be attributed to more available light due to a typically thinner snow pack than the surrounding MYI with a more uniform surface topography.

Ice core chl *a* biomass values from lead-ice were not significantly different than hummocks, however, this should be interpreted with caution since we only had two bottom-ice samples from lead-ice. One lead-ice core had high biomass, which we can also attribute to high bottom-ice light levels due to a thin, uniform snow pack. The other lead-ice core had the thinnest snow cover and thinnest sea ice of any cores considered in this study but it had near-zero chl *a* even though light levels at the bottom-ice would have been high. Lange et al. (2015) attributed the low biomass to either light levels that were too high and inhibited algal colonization (Barlow et al., 1988; Michel et al., 1988), or sea ice growth rates were too rapid to establish substantial algal biomass (Legendre et al., 1991). Regardless of the higher light levels present under lead-ice, higher chl *a* biomass was observed in three of the bottom-ice hummock samples (Figure 5), which also suggests there could be some limitation imposed on algal growth by higher light levels.

Two bottom-ice FYI samples had relatively high biomass; one was comparable to MYI-Hum bottom-ice chl *a* biomass. Our proxy for potential light availability, $k_{B,calc}$, for these two FYI cores were also comparable to the MYI-Hum core sites (Figure 5). However, if we also consider $k_{B,obs}$ for the FYI core at L-arm site 02-13-FY, the observed value is actually lower (i.e., more available light) than the MYI-hum cores $k_{B,calc}$ and $k_{B,obs}$ values (Figure 5). $k_{B,obs}$ from site 02-13-FY is actually more comparable to $k_{B,calc}$ for the high-biomass lead-ice core but has lower biomass than would be expected relative to other bottom-ice chl *a* values with similar potential light availability.

One explanation for the lower than expected chl *a* biomass from FYI sites with high potential light availability is that the snow cover is continuously being redistributed, which would result in a continuously changing light regime for the ice-algal communities at the bottom of FYI. This is a consequence of the level surface topography typical of FYI, which is apparent from the snow and ice survey at FYI site 02-12 (Figure 6a). This results in a drifted snow pack that is redistributed based on wind speed and direction and is continuously changing as there are no surface ice features (e.g., ridges or hummocks) that can "trap" the snow (Note: we are only referring to level FYI). Michel et al. (1988) showed photo-inhibition has a rapid response to increasing light conditions whereas photo-adaptive strategies to higher light conditions (i.e., adjusting photosynthetic rates to increased light conditions) have been linked to cell division time, which is on the order of a few days. The influence of a continuously changing snow cover would have resulted in intermittent periods of suitable light conditions for algal growth. Together with the lag in adaptive strategies to changing light conditions, changes in the FYI snow cover may have resulted in the diminished capacity for FYI to accumulate chl *a* biomass compared to MYI hummock ice.

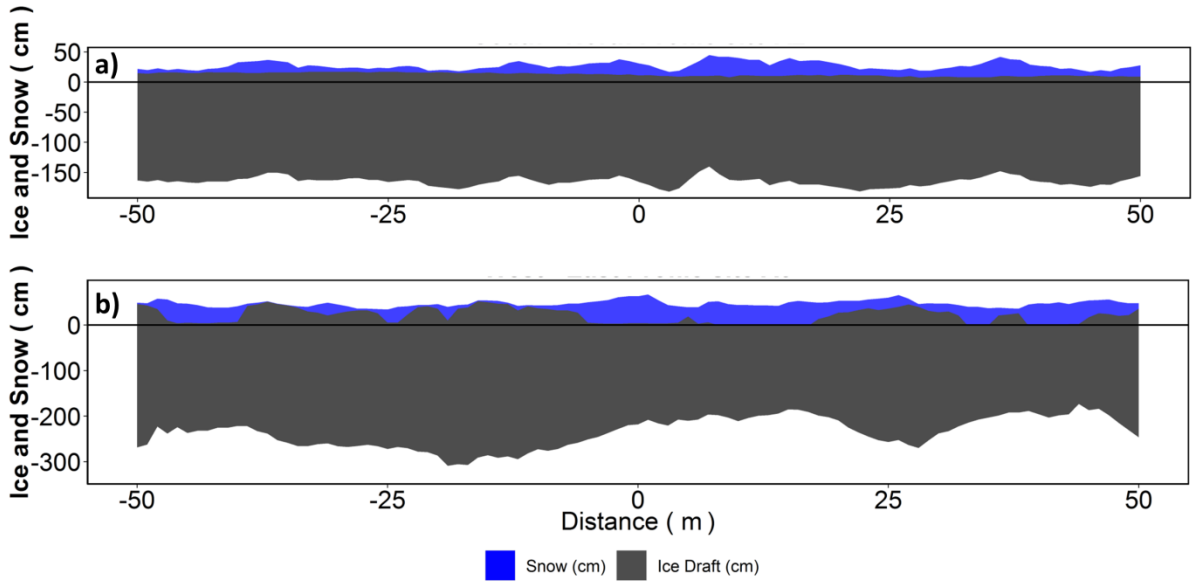

Figure 6: Snow and sea ice surveys conducted at a) FYI site 02-12 showing the South-North transect; and b) MYI site 06-13 showing the West-East transect.

Snow re-distribution likely has an important influence on ice-algal communities, however, little is known of the temporal evolution of snow on FYI and at what time-scales it varies. Therefore, another explanation could be that ice-algal biomass between the ice types was not different for the identified relatively higher biomass sites. Rather, the carbon to chl *a* ratios were different between ice types due to differences in photo-adaptation, which typically range between 20 – 40 i.e., mg C/mg chl *a* (Arrigo et al., 2010). Possible differences in photo-adaptation were supported by the large differences in observed light conditions, with an observed $k_{B,obs}$ at site 02-13-FY of 1.9, which translates to three times more light transmittance (T_E = 0.03) than the averaged snow removal site 06-13-MP ($k_{B,obs}$ = 4.15; T_E = 0.01; Table 2). Furthermore, bottom-ice chl *a* biomass of site 02-13-FY was only half the bottom-ice biomass of snow removal site 06-13-MPt_4, which had three times less light conditions during a period of four days. Snow removal site 01-13-MPt_3 also showed similar entire core-integrated chl *a* biomass and slightly higher light availability ($k_{B,obs}$ = 3.5 – 3.7; T_E = 0.015 to 0.018) compared to snow removal site 06-13-MPt_4. We assumed the entire core chl *a* biomass observations were predominantly the result of recent bottom-ice algal growth, due to higher light levels, since one core was refrozen sea water from t_0 and the other was a full core of original ice present at t_0. This excludes the possibilities that substantial biomass was incorporated into the refrozen ice core from the sea water or that the biomass was within upper portions of the sea ice because both cores showed similar biomass values.

We note that the significantly higher chl *a* biomass observed in MYI-Hum should not be interpreted as having more actual ice-algal biomass than FYI. This is due to the presence of two FYI cores that were within the range of MYI-Hum chl *a* values and may actually have higher or comparable biomass if we consider photo-adaptation (i.e., carbon to chl *a* ratio). If we assume the higher light conditions at FYI site 02-13-FY resulted in a higher carbon to chl *a* ratios (i.e., more available light requires less light harvesting chl *a* per cell) and applied the upper range of the typical sea ice algae carbon to chl *a* ratio of 40 mg C/mg chl *a* (Arrigo et al., 2010) this results in a bottom-ice carbon concentration of 22.8 mg C m^{-2}. Conversely, applying the lower range carbon to chl *a* ratio value of 20 mg C/mg chl *a* (Arrigo et al., 2010) to the three lower light condition MYI-Hum site 06-13-Hum cores (a, b, c) results in carbon concentrations in the range 25.2 – 71.8 mg C m^{-2}. Considering the possibility differential C to chl *a* ratios suggests that this particular MYI hummock (06-13-Hum) had higher bottom-ice algal biomass than FYI site 02-13-FY, however, the other hummock sites would have carbon concentrations in the range 12.4 – 41.2 mg C m^{-2}. Using the same approach for the high biomass, high light lead-ice site (4-11) results in a carbon concentration of 76.2 mg C m^{-2}, which is slightly higher than the highest biomass MYI-Hum site (06-13-Hum-a). Therefore, based on our data we cannot state

that MYI-Hum had higher algae biomass. Rather, the fact that MYI-Hum cores showed significantly higher chl *a* biomass can only confirm MYI-Hum ice as a suitable habitat for algal growth.

These results indicated a complex and dynamic relationship of potential light availability (k_B) with ice-algal biomass, which is difficult to estimate from chl *a* measurements alone, particularly from highly variable environmental conditions. Therefore, we do not assess the magnitude of the differences in actual ice-algal biomass between the ice types but rather quantify the coverage of suitable sea ice algal habitat for different ice types based on the overall observed relationship between chl *a* biomass and $k_{B,calc}$, which holds for all ice types.

7.4.2 Suitable sea ice algal habitat classification

The relationship between $k_{B,calc}$ and bottom-ice chl *a* biomass showed a consistent relationship for all ice types with a threshold at $k_B = 6.75$. This relationship was also observed between the L-arm based $k_{B,obs}$ values and chl *a* biomass, which showed a shift to low chl *a* biomass at a slightly lower $k_{B,obs}$ of 5.5 (Figure 5b), however, we had only one sample above the threshold. The small difference between the calculated ($k_{B,calc}$) and observed ($k_{B,obs}$) threshold values is likely the result of large variations in snow properties, which can have light extinction coefficients (k_s) in the range 4 – 40 m^{-1} (Perovich, 1996). The range of surface albedo values used to calculate the $k_{B,obs}$ may have also contributed to the differences as these can also have a large range of values depending environmental conditions (Perovich, 1996). Furthermore, horizontal scattering due to the snow cover was evident from the substantially larger differences between $k_{B,calc}$ and $k_{B,obs}$ for the not-disturbed L-arm surveys compared to the disturbed surveys (i.e., snow removed so light attenuation primarily influenced by ice). This emphasizes the influence of a highly varying snow pack on light conditions, which make it difficult to accurately calculate light extinction from observations (Perovich, 1996). Nevertheless, the difference of 1.25 in the threshold values identified for $k_{B,calc}$ and $k_{B,obs}$ is rather small considering the large variability of the horizontal scattering, albedo and light extinction values. Therefore, we used the $k_{B,calc}$ threshold to classify the suitability of sea ice algal habitats based on larger-scale observations of physical snow and sea ice properties.

The survey-derived percent coverage of suitable ice-algal habitat showed some general patterns between and within ice types. Overall lead-ice had the highest coverage of suitable habitat, which was attributed to the uniform and thin snow pack. FYI had the largest range of suitable habitat coverage between sites, with generally higher percent suitable habitat coverage than MYI. The range of suitable habitat on FYI was attributed to high variability of snow depth on this ice type. A thicker overall snow pack meant less suitable habitat and vice versa. It is important to note that the overall $k_{B,calc}$ (i.e., median of all survey location $k_{B,calc}$) was 5.0 on FYI site 02-13, with a median snow pack of 0.17 m and median ice thickness of 1.8 m (Table 1). Site 02-13 could therefore be classified as FYI with 100% suitable habitat if we took a "block model" approach. We define the "block model" approach as an approach in modeling or up-scaling where each grid cell, which is typically very large (on the order of 10s of kilometers), is assigned one ice thickness and one snow depth value and typically does not account for any spatial variability of these properties within the grid cell. However, on site 02-13 the observed spatial coverage of suitable habitat is not 100% but rather 87% due to the presence of snow drifts, which are features we observed at all FYI sites (see Figure 6a). Conversely, the overall $k_{B,calc}$ was 7.3 at FYI site 03-13 with median snow depth of 0.29 m and median ice thickness of 1.6 m. Therefore, site 03-13 could be classified as 0% suitable ice-algal habitat using the "block model" approach, whereas the observed spatial coverage of suitable habitat was 37% (Table 1).

Spatial heterogeneity of sea ice-algal biomass is related to the distribution of snow on FYI, due to the large influence of snow on light transmission, with snow patch sizes reported between 20 – 90 m (Gosselin et al., 1986). Our spatial autocorrelation analyses demonstrated snow patch sizes, P_s, between 30 – 45 m for snow on FYI, which we interpreted as the sizes of snow drifts. Our results also showed that the variability of suitable habitat on FYI was largely controlled by the snow pack, which is spatially re-distributed by wind creating the wave-like snow drifts with peaks (high snow) and troughs (low snow). Gosselin et al. (1986) suggested wind-induced drifting resulted in short-term variability of the snow pack, which also influenced the distribution and perhaps re-distribution or re-colonization of bottom-ice algal communities. This supports our suggestion that ice algal biomass

growth and accumulation may be limited based on the short-term temporal variability of the snow pack and hence short-term variability of available light for bottom-ice algal communities.

The overall snow distribution also had a large influence on the spatial coverage of suitable ice-algal habitat for MYI. There were distinct differences, however, between FYI and MYI as a result of the different mechanisms and features controlling the distribution of snow on MYI. Contrary to FYI, which has a snow pack in a continuous state of change due to wind-driven redistribution, the snow distribution on MYI is strongly influenced by the highly undulating ice surface topography where snow accumulates in topographic lows or regions adjacent to hummocks and is removed or has substantially less accumulation on the surface of hummocks. This relationship between snow and ice surface is apparent from the MYI snow and ice profile (Figure 6b), and was a consistent feature observed at all MYI sites (see all 2013 profiles in supplementary material Figures S1 – S8). Spatial autocorrelation analyses for MYI sites showed surface topography patch sizes mostly between 6 – 10 m, however, ~25 m patches were observed at two sites. The surface topography patch sizes were interpreted as the size of hummocks. The 6 – 10 m hummock size range was obvious from the snow and ice profiles and was the most obvious size range for the undulating surface features in all profiles with only a few larger hummocks ~25 m (Figure 6b and supplementary Figures S1 – S16). The observed distribution of snow in relation to the highly undulating MYI surface indicates that the horizontal variability of snow on MYI is also a relatively constant feature with more snow at low points (e.g., refrozen melt ponds) and adjacent to hummocks (or ridges) but no or little snow accumulation on hummocks. This snow-ice relationship on MYI was previously documented by Perovich et al. (2003) and Sturm et al. (2002) who also observed that hummocks and ridge peaks typically had the thinnest snow cover. This is an important distinction from FYI, as MYI hummocks represent a constant suitable habitat for sea ice algal growth, which are not subject to rapid changes in snow depth and bottom-ice light availability, and thus can be considered a more stan;e habitat for sea ice algae.

The quantification of typical MYI hummock sizes and FYI snow drift sizes has important implications for airborne and satellite remote sensing of snow. The common size range of snow-free/low-snow hummocks between 6 – 10 m suggests that airborne or satellite sensors would need to have at least the same spatial resolution in order to capture the variability of the snow on these features. This is also the case for FYI with our observed snow drifts ranging between 30 – 45 m and other studies between 20 – 90 m (e.g., Gosselin et al., 1986). Therefore, in order to observe the variability of snow on MYI and FYI there is a need for improved satellite and airborne sensors that can resolve these spatial scales. Currently, even the best airborne snow radar measurements have too coarse of a spatial resolution and large uncertainties to be useful for characterizing the spatial variability of snow depths at the required scale, and further improvements in snow depth observations are needed (Kurtz & Farrell, 2011) (Kwok & Haas, 2015) (Newman et al., 2014).

Suitable sea ice algal habitat for MYI had high variability between sites, which was related to overall site ice thickness (i.e., median ice thickness). Thick MYI sites (median ice thickness > 3 m) had substantially lower suitable habitat (< 6%) than thin MYI sites (median ice thickness ≤ 3 m; 17 – 38%). This was the result of thicker hummock ice with $k_{B,calc}$ values greater than the threshold value (6.75); under snow free conditions a $k_{B,calc}$ of 6.75 corresponds to an ice thickness of 4.35 m. This means that MYI sites with median ice thicknesses greater than 3 m were dominated by hummocks greater than 4.35 m that even under snow free conditions do not represent suitable ice-algal habitat.

One exception to this pattern was site 05-12, which had median ice thickness of 2.6 m but a suitable habitat coverage of only 5% (Table 1). However, the entire survey or the median ice thickness value may not be representative for two reasons: first, the IQR of ice thickness is larger than the other thin MYI sites (Table 1); and second, this survey was a single linear profile with a shorter length than any other MYI site (130 m). The shorter length and larger range of ice thickness values may indicate the profile was not representative of the surveyed floe. Furthermore, comparison between the perpendicular west-east and south-north profiles at each site indicated significant differences between all physical parameters at most sites. This demonstrates that perpendicular profiles are important to capture the variability of the snow and ice properties at each site. Gosselin et al. (1986) also showed that the orientation of survey transects was critical in identifying the spatial variability of snow on

FYI and the influence on the spatial distribution of bottom-ice algal biomass. On level FYI snow drift patterns are wave-like undulations of snow depth with uniform snow features (e.g., snow drifts or valleys) forming perpendicular to the wind direction. Therefore, it is possible to conduct single linear profiles oriented parallel to a snow drift that do not cross the snow drift. On MYI the snow drifting pattern is less likely to have a similar influence on the representativeness of the sampling. The distribution and orientation of ice surface features, however, are likely more important as they primarily control snow distribution. Though hummocks may not have direct relationship to wind direction it would still be possible to survey a single profile line, which only covers the "valley" between hummocks and does not representatively capture the undulating surface topography and snow distribution on MYI. This sampling bias is eliminated or significantly minimized when conducting perpendicular survey transects.

One limitation of the presented observation-based habitat classification approach is that it does not account for any horizontal (anisotropic) scattering of light through sea ice (Katlein et al., 2014b). Another study by Katlein (2012) showed that ~90 % of the light field received at the bottom of the ice comes from a circular footprint with a radius equal to ~2 times the ice thickness. Therefore, the spatial uncertainty in k_B on thinner FYI was likely lower than the thicker MYI. This would be particularly important for regions of high light transmittance (e.g., low snow cover). For MYI horizontal scattering would be most pronounced around hummocks with low or no snow cover. The influence of horizontal light scattering was observed at site 06-13-MPt_0 with higher than expected light transmittance values observed during the undisturbed L-arm survey. These higher than expected light levels were the result of horizontal scattering from an adjacent hummock (site 06-13-Hum) located at a distance of ~5 m. The chl *a* biomass recorded at 06-13-MPt_0 was also much higher than expected form the corresponding $k_{B,calc}$ value. However, the site 06-MPt0 $k_{B,obs}$ was substantially lower than $k_{B,calc}$, therefore, based on the $k_{B,obs}$ could be classified as suitable habitat. This suggests that regions in close proximity to hummocks may also be classified as suitable habitat or at least a transition zone between suitable and non-suitable habitat. Thus, our habitat suitability classification may under-estimate the suitable habitat coverage of MYI regions.

We also observed the influence of horizontal scattering on FYI site 02-13-FY. The $k_{B,calc}$, which was based on the mean snow depth above the L-arm survey (0.13 m), was substantially larger than the $k_{B,obs}$ value. The range of snow depth was between 0.08 – 0.15 m. There is a considerable range of light transmittance associated with this range of snow depths, with an almost tripling of light transmittance from 0.15 m of snow (0.07) to 0.08 m of snow (0.20). As a result, the available light is predominantly coming from shallow snow regions, and the median snow depth is not necessarily representative of the median light availability under the ice. This demonstrates the potential influence of snow variability on horizontal scattering and subsequently uncertainties (i.e., under-estimates) that may be present in suitable habitat coverage estimates on FYI. If horizontal scattering had a large influence on the spatial coverage of suitable habitat on FYI it would have been more likely to sample regions with relatively high snow that also had chl *a* biomass values higher than would be expected, similar to what was observed at site 06-MPt0. The small sample size of thick snow FYI cores (N=4) makes it difficult to assess this compared to MYI-MP for which 13 samples were available. The influence of horizontal light scattering on FYI algal biomass may also be minimized by the continuous re-distribution of snow (as discussed previously).

For MYI, we have demonstrated a reliable observation-based habitat classification system, which was possible due to the relatively stable pattern of snow distribution on MYI (thin snow on hummocks, thick snow on refrozen melt ponds), which was independent of overall snow depth. This also implies that upscaling such a habitat classification system to larger-scale satellite or airborne remote sensing observations would be more robust for MYI. This is due to the fact that observation systems and modelling of sea ice thickness are much more reliable and established than observations and forecasts of snow depth on sea ice (Kurtz & Farrell, 2011; Kwok & Haas, 2015; Newman et al., 2014). Modelling a static system, such as the distribution of hummocks, can be assumed to be more reliable than a dynamic system, such as wind-driven snow distribution.

For FYI we have fewer survey sites, and high variability in snow depth at the surveyed sites. With no constant sea ice surface features the snow surface and suitable habitat can vary on short time scales in

an unpredictable manor. With no concrete relationships to ice thickness, which could be used for the basis of up-scaling to larger-scale observations or in modelling studies, it may be less reliable to up-scale the habitat suitability classification system to larger-scale observations from models. That being said, we did observe a relationship between suitable habitat coverage and overall snow depth with low-snow (snow < 0.2 m) had high suitable algal habitat coverage (87%) and high-snow (snow > 0.2 m) had low suitable algal habitat coverage (18 – 37 %). Based on this, we divided FYI into two classes based on the amount of overall snow accumulation, which holds for our dataset. This provides a reliable aspect to the habitat classification that could be used to upscale based on snow climatologies or large scale models. However, there remains a strong need for more ground-truthing of snow depths on FYI in order to assess the reliability of applying the habitat classification to larger scales. Regardless of the accuracy of these estimates to identify a representative classification of suitable habitat for FYI, we have demonstrated based on observations, that any attempt at characterizing the variability of snow on FYI and MYI will likely result in more accurate representations of suitable ice-algal habitat or biomass than simply using single values for snow depth and ice thickness to describe this habitat.

7.5 Case Studies

7.5.1 Case Study 1: Application of our sea ice algae habitat classification system to Cryosat-2 data products

The main objective of this case study was to demonstrate the application of such an observation-based habitat classification system at the pan-Arctic scale using reliable sea ice thickness and snow depth data. Furthermore, we aimed to demonstrate the potential significance of MYI in terms of suitable ice algal habitat coverage, which has been generally neglected in the existing literature.

7.5.1.1 Data and methods

Here we used the Cryosat-2 sea ice thickness data product of Ricker et al. (2014). Snow depth values are included in the Ricker et al. (2014) Cryosat-2 data product and are derived using a modified version of the Warren snow water equivalent climatology (Warren et al., 1999). This included reduction of snow depth over FYI by 50% as suggested by Kurtz and Farrell (2011). Ricker et al. (2014) used sea ice type data (FYI and MYI) from the daily ice type product as described by Eastwood (2012). Snow depth corrections were conducted on the according ice type. The correction of snow depth over FYI was first introduced to Cryosat-2 data processing by Laxon et al. (2013) and is now an established standard practice. All CryoSat-2 data are averaged over an entire month, with data gridded to a 25 by 25 km grid spacing. For the habitat classification we used the data derived for April 2013 to be closest in time to our sampling period (30 April to 07 May 2013) (Figure 7). There is no Cryosat-2 data available for the month of May. Within the Cryosat-2 data there were grid cells with missing or unreliable data, which were removed from our analyses (e.g., blank regions in Figure 7). We applied a mask to the Cryosat-2 data as described by Ricker et al. (2014). Data outside this mask were excluded because the snow depth fit (Warren et al., 1999) is not valid in these regions.

We used two different approaches to classify the Cryosat-2 data products into different habitat classes based on ice type, ice thickness and snow depth:

1. **Observation-based approach**: each grid cell is assigned one of five habitat classes based on classification criteria of ice type, ice thickness and snow depth threshold values determined from in situ ice core chl *a* biomass, and snow and ice survey observations (outlined in Table 6). Each habitat class has a single value or range of values for the percent coverage of suitable habitat.
2. **"Block-Model" approach**: a single value of k_B was calculated for each grid cell integrated over the ice thickness using k_i (1.55 m^{-1}), and snow depth using k_s (20 m^{-1}). Based on the threshold k_B value of 6.75, each grid cell was assigned a habitat class of either suitable ($k_B \leq$ 6.75) or not-suitable ($k_B >$ 6.75) for ice algal growth (Table 6).

The observation-based habitat classes were based on the results and relationships determined from the in situ snow and ice surveys, as described previously. The two MYI habitat classes were separated based on the mean monthly ice thickness: thick (> 3 m) MYI (class 1; Table 6) had a lower percent coverage of suitable habitat (<6 %) compared to thin (≤ 3 m) MYI (class 2: 17 – 38 %; Table 6). FYI was separated into three habitat classes based on the modified Warren monthly climatology snow depth and ice thickness: FYI with ice thickness < 1.1 m was considered lead/new ice (class 5; Table 6) and was assigned a suitable habitat coverage of 100%; FYI ≥1.1 m was separated into thin snow covered FYI (class 4: h_s < 0.2 m; Table 6), which had a higher percent coverage of suitable habitat (87 %) than thick snow covered FYI (class 3: h_s > 0.2 m, 18 – 37 %; Table 6). These ice thickness and snow depth criteria were applied to the Cryosat-2 data products and assigned the according value or range of values for the percent coverage of suitable habitat for ice algal growth (Table 6).

7.5.1.2 Results and Discussion

Excluding missing data and grid cells outside the data mask, MYI had a total area of 1.83 x 10^6 km^2 (28 % of total ice area), FYI had a total area of 4.3 x 10^6 km^2 (67 %), and lead/new ice had a total area of 0.31 x 10^6 km^2 (4.7 %; Table 6). Thin-snow FYI (class 4) had the largest areal coverage of suitable habitat with 2.6 million km^2 (40 % of the total ice area). The areal coverage of suitable habitat for lead-ice (class 5) was 0.31 million km^2 (4.7 % of total ice), which was comparable to the thick-snow FYI (class 3) and thin-MYI (class 2) with suitable habitat coverage between 0.24 – 0.49 million km^2 (4 – 8 % of total ice) and 0.24 – 0.53 million km^2 (4 – 7.5 % of total ice), respectively (Table 6). Thick-MYI (class 1) had the lowest areal coverage of suitable habitat with 0.03 million km^2 (0.4 % of total ice; Table 6).

The observation-based approach showed comparable coverage of suitable habitat for the thick-snow FYI and thin-MYI classes. MYI accounted for ~28 % of the total ice area, with an associated suitable habitat coverage corresponding to 3.7 – 8.2 % of the total ice area. This indicates that MYI is an overlooked region in terms of potential for ice-algal growth and likely has a significant and currently under-estimated contribution to the total algal biomass and carbon budget of the Arctic Ocean.

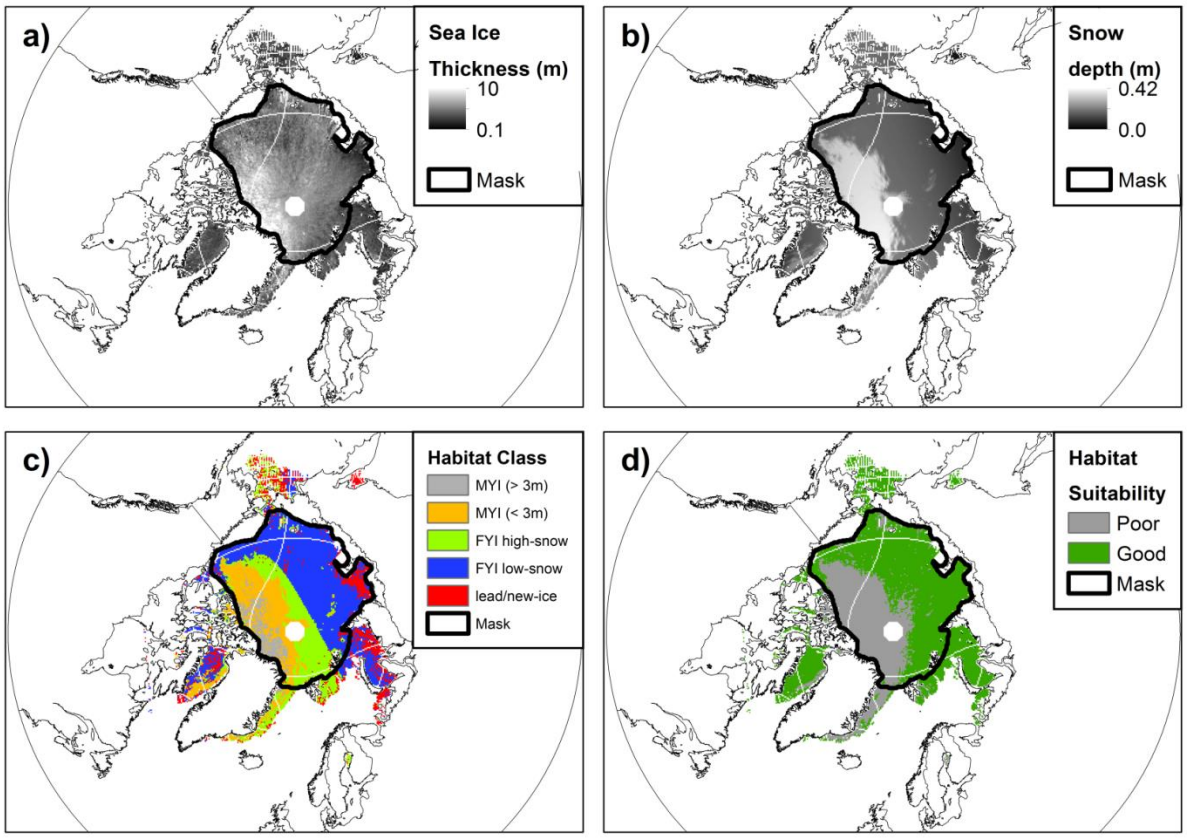

Figure 7: Maps of the Arctic Ocean showing: a) Cryosat-2 derived sea ice thickness for April 2013 (Ricker et al., 2014); b) snow depth for April 2013 based on the modified Warren snow climatology (Warren et al., 1999); and c) in situ observation-based habitat classification upscaled to sea ice thickness and snow depth from a) and b); and d) "block model" approach to assign habitat suitability using threshold k_B = 6.75 applied to classify each $k_{B,calc}$ value per 25 x 25 km Cryosat-2 grid cell calculated from one sea ice thickness and one snow depth value per cell (e.g., no variability per cell). Only sea ice thickness and snow depth data within the "Mask" outline were used in our analyses, as the data in excluded regions are not reliable (Ricker et al., 2014). Cryosat-2 data products were acquired from www.meereisportal.de.

Based on the "block model" approach MYI contributed significantly less to the overall suitable habitat compared to the observation-based approach (Figure 7 and Table 6). It is apparent from Figure 7d that a large majority of the MYI cover is classified as not-suitable for ice-algal growth, with an estimated suitable MYI habitat area of only 0.01 x 10^6 km^2 (0.14 % of total ice area; Table 6). Accounting for the variability of MYI snow and ice properties using the observation-based classification approach habitat resulted in suitable habitat coverage estimates ~26 to 55 times greater than the block-model based approach.

Table 6: Summary of the suitable ice algae habitat area derived by applying the in situ observation-based criteria and a "block model" approach to the April 2013 CryoSat-2 ice thickness and snow depth data.

Classification Approach	Habitat Class	Class Criteria	% suitable habitat	Area (% of total ice area) [x 10^6 km^2]	Suitable Habitat Area (% of total ice area)
Observation-based	1 thick-MYI	MYI > 3 m	< 6 %	0.45	0.03 (0.4 %)
	2 thin-MYI	MYI ≤ 3 m	17 – 38 %	1.39	0.24 – 0.53 (3.7 – 8.2 %)
	3 FYI high-snow	FYI ≥ 1.1 m and snow ≥ 0.2	18 – 37 %	1.31	0.24 – 0.49 (3.7 – 7.5 %)
	4 FYI low-snow	FYI ≥ 1.1 m and snow ≤ 0.2	87 %	2.99	2.60 (40.4 %)
	5 lead/new-ice	ice < 1.1 m	100 %	0.31	0.31 (4.7 %)
	MYI total			1.83 (28.4 %)	**0.26 – 0.55 (4.1 – 8.6 %)**
	FYI (excl. lead) total			4.30 (66.8 %)	**2.83 – 3.08 (44.0 – 47.9 %)**
	Total			6.44	**3.40 – 3.94 (52.8 – 61.2 %)**
Block model	1 Not-Suitable	$k_{B,calc} > 6.75$	100 %	2.54	MYI: 1.83 (28.4 %) FYI: 0.71 (11.1 %) Lead-ice: 0.001 (0.01 %)
	2 Suitable	$k_{B,calc} \leq 6.75$	100 %	3.90	**MYI: 0.01 (0.14 %)** **FYI: 3.89 (60.4 %)** **Lead-ice: 0.004 (0.06 %)**

Suitable FYI habitat largely comes from the thin-snow FYI class, which indicates that snow depth over FYI is of high importance. This means the accuracy of suitable habitat estimates for FYI is highly dependent on the accuracy of the snow depth measurements, which are currently derived from the modified Warren climatology. Of particular importance is the variability of the snow depth on FYI. We have demonstrated an important relationship between surveyed snow depth variability and overall survey snow depth; however, these are based on few surveys, which would largely benefit from more observations covering more regions to capture any regional variability. Furthermore, we have also suggested, in agreement with other studies (e.g., Gosselin et al., 1986) that the snow cover on FYI is highly variable on small time-scales, which is also an important consideration in terms of uncertainties in the FYI habitat classes. Conversely, the MYI suitable habitat estimates are independent of overall snow cover since the distribution of snow is controlled by the surface topography, which results in low or no-snow hummocks that are quasi permanent features of MYI. Thus the MYI habitat area estimates are more reliable than the FYI habitat area estimates. Regardless of the uncertainties, such an exercise is crucial to demonstrate the potential of MYI in comparison to FYI and further emphasize the importance of assessing, observing and including the variability of snow and ice properties in large-scale estimates and modelling studies.

Most of the thick MYI with low suitable habitat coverage is in the region north of the Canadian Arctic Archipelago where the thickest sea ice in the Arctic is located (Haas et al., 2006; Haas et al., 2010). Submarine sonar ice thickness measurements conducted during the period 1958–1976 had mean ice thicknesses well over the 3 m in all regions of the Arctic Ocean except the Beaufort and Chukchi Seas. Basin-wide Arctic sea ice thickness observations during winter 1980 had a mean of 3.64 m (Kwok & Rothrock, 2009). Furthermore, since the early 1990s mean ice thicknesses for all regions have been well below 3 m (Kwok & Rothrock, 2009). Based on our established threshold sea ice thickness of 3 m, we speculate that this shift from thick MYI, which dominated the Arctic Ocean up until the 1980s, to thin MYI in the 1990s resulted in a substantial increase of the suitable ice-algal habitat coverage. As MYI continues to thin and be replaced by FYI, our findings suggest that the spatial coverage of suitable ice-algal habitat will largely depend on the temporal and spatial distribution of snow on sea ice, which will be influenced by continued warming of the Arctic. Our findings for FYI suggest that with increased snow precipitation there would be similar or decreased spatial coverage of suitable ice-algal habitat. Conversely, if snow precipitation remains the same or decreases our findings suggest increased spatial coverage of suitable habitat. Regardless of the future snow situation there will be one inevitable difference. The permanent and reliable ice-algal habitat found under MYI will be replaced by a continuously varying habitat under FYI. How this will change the overall ice-algal biomass is uncertain, however, it is possible that this could have a drastic impact on under-ice organisms that rely on sea ice algae, particularly in the early spring when no other food sources are available.

The application of this habitat classification does not account for the presence of sea ice ridges, which can make-up a substantial portion of the overall ice pack (Haas et al., 2010). We did not conduct snow and ice surveys or sea ice coring on ridged ice so we cannot include these features in our analyses. Nevertheless, considering the snow distribution on MYI was largely controlled by the undulating surface, we speculate that this same process could result in extensive snow free regions on ridged sea ice. When travelling on sea ice it is common to see ridged sea ice regions with large, vertical snow-free ice chunks. Therefore, we could also speculate that light transmittance under snow-free ridges may also produce a suitable habitat in much the same way hummocks are considered a suitable habitat; however, sea ice ridges are typically thicker than hummocks, which may limit the number of ridges that are below the threshold ice thickness of 4.35 m (equivalent to kB of 6.75). Nevertheless, if we also consider the influence of horizontal scattering it is plausible that ridges could act as source of available light for adjacent undeformed ice. The study of sea ice ridges is logistically demanding, even more so than 4 m hummock ice, nevertheless, we strongly recommend physical and biological sampling of sea ice ridges in order to assess the potential of sea ice ridges as an another overlooked region of suitable ice algal habitat.

7.5.2 Case Study 2: Application of a 1D sea ice process model

The aim of this case study was to demonstrate the importance of parameterizing different types of sea ice and snow cover, particularly MYI hummocks, within a 1D sea ice process model, which can also provide insight into the implications for the more computationally expensive large-scale 3D ice-ocean models.

7.5.2.1 Model setup

We used a simple NPD model consisting of the following classes: phytoplankton (P), nutrients (N) and detritus (D). For nutrients we used Nitrate, the most abundant nutrient in sea surface waters in the Arctic. We used the following equations to describe each class:

$$\frac{dN}{dt} = -[\mu - \lambda_{up/re}]P + \lambda_{rm}D \quad (2)$$

$$\frac{dP}{dt} = -[\mu - \lambda_{up/re}]P - \lambda_{mo}P + \frac{Melt}{\delta z}P \quad (3)$$

$$\frac{dD}{dt} = \lambda_{mo}P - \lambda_{rm}D \quad (4)$$

where μ is the algal growth rate, $\lambda_{up/re}$ represents the loss of algae due to respiration/gain of nitrate due to uptake, λ_{mo} represents the algae loss due to mortality, and λ_{rm} represents the transformation of detritus into nitrate due to remineralization. These terms were taken as constant except for the growth rate (μ) which is a function of available light (Jassby & Platt, 1976) and nutrients (Monod, 1949) in the form:

$$\mu = \mu_M \frac{N}{N + k_N}\left[1 - e^{\alpha PAR/P_m}\right] \quad (5)$$

where μ_M is the maximum growth rate (constant), k_N is the half saturation constant for nitrate taken from (Sarthou et al., 2005), α is the photosynthetic efficiency, P_m is the light saturated specific photosynthetic rate (or maximum photosynthetic rate), and *PAR* is the photosynthetically active radiation (400 – 700 nm) available for bottom-ice algae. *PAR* was calculated based on equations from (Grenfell & Maykut, 1977) in the form:

$$PAR = I_o e^{-[k_i h_i + k_s h_s]} \quad (6)$$

where I_o is the incoming PAR, k_i and k_s are the literature-based bulk light extinction coefficients for snow (1.55 m^{-1}) and sea ice (20 m^{-1}), respectively (see section 2.1), and h_i and h_s are the sea ice thickness and snow depth (m), respectively (Table 7). *PAR* was converted to bottom-ice scalar irradiance according to (Katlein et al., 2014b). For the incoming radiation we used NCEP Climate Forecast System Version 2 reanalysis data. The ice thickness and snow thickness are chosen according to the mean of all ice cores for the corresponding ice types: FYI lead, FYI high-snow, FYI low-snow, MYI-MP, and MYI-Hum (Table 7). We included one observation-based modified ice type for MYI melt ponds directly adjacent (~5 m) to snow-free hummock (MYI-MP~hum) and used the observed k_B value determined from the under-ice light measurements then converted into k_i and k_s values (Table 7). The snow depth, ice thickness and light extinction values (k) were kept constant during the entire model runs. Bottom-ice algal chl *a* values were initialized using the mean of all ice core observations for the corresponding ice type (Table 7).

The first day of the model was set to 01 May 2013 and the model was run for 250 days. We focused our analyses on the first 42 days (until June 12) as this is a good approximation for the onset of melt at which point the optical properties of the snow drastically change and transmit larger amounts of light (Perovich, 1996). We limit the analyses to this period since the model does not account for variable snow and ice optical properties (e.g., k_s). The onset of melt was determined for the region based on a rapid transition from high to low backscatter observed between Advanced Scatterometer (ASCAT) satellite images acquired during the summer of 2009 (Lange, 2012). Although the year is different than our study period for the purposes of the model we assume it provides us with a good approximation for a realistic melt onset date. The shift from high to low backscatter corresponds to

the presence of liquid water in the snow, which is a good indicator of melt, and causes increased absorption of microwave energy and decreased backscatter received by the satellite (Barber et al., 2001).

7.5.2.2 Results and Discussion

The high biomass ice types (Lead-ice, FYI low-snow, MYI-hum and MYI-MP~hum) all had similar patterns of for N, P, and D in the model run (Figure 8 a, b, d, f). Initially, light conditions were not limiting as would be expected for this time of year (see review in Vancoppenolle et al., 2013), as a result of the nutrient dynamics within the model. Maximum biomass values were rather dependent on the initial chl *a* values set for the model, which were ultimately the result of actual variable light conditions experienced between the different ice types. This was evident from the minimal increase in biomass from the initial value due to the almost complete and immediate draw-down of nutrients (NO_3). The biomass began to decay as a result of initial nutrient limitation and then slowly the biomass began to level out (Figure 8 a, b, d, f). At this point, which we termed the "sustainable biomass zone", biomass was sustained by the nutrient regeneration. There were consistent ratios between the maximum biomass values and the approximate magnitude of the "sustainable biomass zone" between 2.67 to 2.75, which further emphasizes the regulation of the biomass by the initial chl *a* values.

There was another rapid drop in biomass after the "sustainable biomass zone" as light conditions rapidly declined due to decreasing incident sun angles (Figure 8 a, b, d, f). It was at this point that the different ice types showed differences in the timing of the rapid decline, which was attributed to the different light conditions cause by the snow and ice properties. An earlier decline was observed for the relatively "low-light" MYI-MP ice type (observation $k_{B,obs}$) approximately at day 125 (Figure 8 f), decline was observed around day 140 the "medium-light" FYI low-snow and MYI-hum ice types (Figure 8 b, d), and the latest decline was observed at the "high-light" FYI-lead ice type around day 160 (Figure 8 a).

Table 7: Summary of parameters used in the 1D model for case study 2, for each ice type class.

Ice Type	Chl *a*	Ice thickness (m)	Snow depth (m)	k_s	k_i	k_B
FYI Lead	3.8	0.88	0.07	20	1.55	2.61
FYI Low-Snow	6.3	1.65	0.16	20	1.55	5.75
FYI High-Snow	0.2	1.68	0.36	20	1.55	9.71
MYI-hum	16.6	3.70	0.00	20	1.55	5.73
MYI-MP	0.5	2.54	0.36	20	1.55	11.14
MYI-MP~hum	5.6	3.30	0.41	3.87 [a]	1.55 [a]	6.70 [a]

[a] k_s and k_i values were back calculated to achieve the resulting observed value of k_B =5.0 used for this ice type only.

Light extinction coefficients were set as constants for each ice type over the duration of the model run, which is likely only representative during the first 42 days before the onset of melt. However, this likely did not have a large influence because nutrients primarily regulated biomass growth and decay until the light conditions declined near the end of summer. Therefore, the decline in biomass may be later than shown in the models if we consider that there would likely be no snow cover at the end of summer.

The high biomass observed at the different ice types indicated that there were already suitable conditions for ice-algae. The fact that algal growth does not continue in the models was the result of using a closed system of nutrients and regeneration, which in reality may not be the case since there is likely nutrient exchange between the bottom-ice and the surface ocean waters resulting in highest biomass accumulations and primary production rates within bottom-ice (Mock & Gradinger, 1999). Therefore, it is difficult to assess the role of variable light conditions using such a model setup.

The low biomass ice types (FYI high-snow and MYI-MP adjacent to hummock with $k_{B,calc}$; Figure 8 c and e) had complete decay of the biomass present and no drawdown of nutrients but rather an increase

of nutrients due to the regeneration by decaying biomass. This demonstrates that at the end of summer and into polar night, when light levels cannot sustain growth, the decay of the biomass likely regenerates nutrients, which may become important for the beginning of the following growth season.

Overall, these results perhaps do not represent an extensive modelling study but rather demonstrate the implications of including different ice types and observation-based parameterizations of initial conditions. The difference between the high and low biomass ice types were the result of different initial conditions of chl *a* biomass and not directly the different light conditions, however, actual light conditions resulted in the observed chl *a* biomass so indirectly the light did have an influence but just not within the model itself. This suggests that this particular model was more sensitive to the initial chl *a* and nutrient values compared to the light levels, which emphasizes the general need for better model parameterizations of physical and biogeochemical conditions.

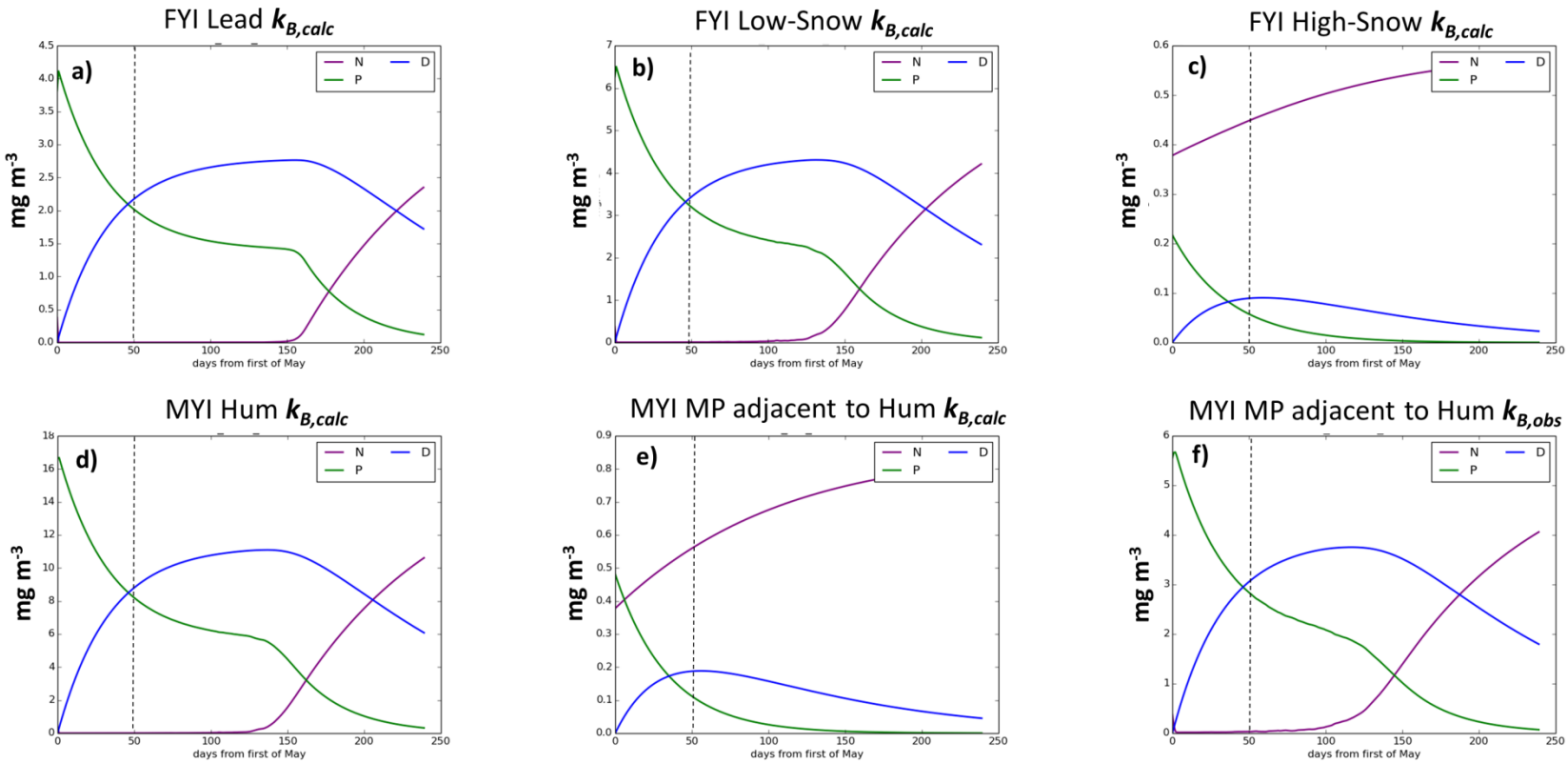

Figure 8: Sea ice algal chl *a* biomass growth results based on NDP modeling results for different snow conditions and ice types (parameters for each ice type are listed Table 7): a) FYI lead ice; b) FYI low-snow; c) FYI high-snow; d) MYI hummocks; e) refrozen melt pond on MYI adjacent to a hummock; and f) same as e) but using the observed bulk integrated light extinction coefficients $k_{B,obs}$. N refers to nutrients (NO_3 in mg m^{-3}), D refers to detritus, and P refers to chl *a* biomass (mg m^{-3}). P values were initialized based on mean observations for each ice type. N values were initialized using one value for all ice types, which was the mean of bottom-ice observed NO_3 concentrations relative to brine channel volume.

7.6 Conclusions

Our findings strongly support the hypothesis proposed by Lange et al. (2015) that MYI hummocks have the potential to support high ice-algal biomass due to the typically snow-free/low-snow surface, which results in suitable light conditions for ice-algal growth. We observed higher ice-algal chl *a* biomass in the bottom-ice of MYI hummocks than in the bottom-ice from FYI. Our MYI hummock chl *a* biomass observations were some of the highest springtime bottom-MYI chl *a* biomass observations reported in the literature. We demonstrated a reliable proxy for suitable ice-algal habitat by using the bulk integrated light extinction coefficient, which holds for all ice types and confirmed by observations. We applied this proxy to larger-scale snow and ice surveys, which showed that thin MYI (median ice thickness < 3 m) had substantial coverage of suitable ice-algal habitat. We demonstrated that the suitable habitat on MYI was the result of the typically undulating surface topography and the presence of hummocks, which are permanent snow-free/low-snow features observed on all surveyed MYI floes and represent a reliable habitat for ice algae. Over thick MYI (median ice thickness > 3 m), far less suitable habitat was observed, as hummocks were thick enough to limit the availability of light at the bottom-ice even in the absence of snow on the sea ice. In contrast to MYI, FYI has a level surface resulting in a snow cover with high temporal variability, which may induce some limitations for algal growth due to the intermittent nature of suitable light availability at the bottom-ice.

The higher spatial coverage of suitable habitat at thin MYI sites indicates that the observed shift from thick-MYI to thin-MYI, which occurred sometime in the late 1980s, likely resulted in increased coverage of suitable habitat. As MYI continues to be replaced by FYI, the subsequent changes to the sea ice ecosystem, in terms of suitable habitat coverage, may be less reliable as FYI habitat coverage is largely dependent on the snow cover, which have large uncertainties in future projections.

The up-scaled habitat classification case study showed that when the variability of snow depth on MYI is not considered the suitable habitat for sea ice algae may be drastically under-estimated by over an order of magnitude. The coupled NPD model case study did not provide obvious differences between the ice types based on the different light regimes due to limitations imposed by the nutrient dynamics of the model. The largest influence on biomass growth was rather influenced by the observation-based initial conditions set for ice-algal biomass, which were ultimately the result of different light conditions of the ice types. These results emphasize the complexity of coupled models and that the combined influence of initial conditions and parameterization of variable light conditions are important to accurately estimate sea ice algal biomass.

Overall we showed strong evidence that current springtime estimates for Arctic-wide sea ice algae biomass and primary production are likely to be drastically under-estimated. Therefore, we strongly recommend the implementation of variable snow and sea ice properties for all up-scaling and modelling studies, and better model parameterization of initial conditions.

Acknowledgements

We thank the logistical support from Jim Milne and Al Tremblay, Defense Research and Development-Atlantic. We thank G. Stewart and all of the personnel at Canadian Forces Station Alert for their hospitality and support. Invaluable logistical support, laboratory access, and Helicopter and Twin Otter aircraft transportation were provided by the Polar Continental Shelf Program. Pilots from Universal Helicopters and Kenn Borek Air provided safe transportation throughout the project. We thank N. Fortin, K. Hille, A. Tatare and J. Wiktor for their help in the field laboratory. This study is part of the Helmholtz Association Young Investigators Group *Iceflux*: Ice-ecosystem carbon flux in polar oceans (VH-NG-800). We also acknowledge the Alfred-Wegener-Institut, Helmholtz-Zentrum für Polar- und Meeresforschung for essential financial support. Processing of the CryoSat-2 (ice thickness data) is funded by the German Ministry of Economics Affairs and Energy (grant: 50EE1008). Data from April 2013 was obtained from http://www.meereisportal.de (grant: REKLIM-2013-04).

References

Arrigo, K.R., Mock, T., Lizotte, M.P., 2010. Primary Producers and Sea Ice. In D.N. Thomas, G.S. Dieckmann (Eds.), *Sea Ice* (pp. 283-325). Oxford: Wiley-Blackwell.

Barber, D.G., Yackel, J.J., Hanesiak, J.M., 2001. Sea Ice, RADARSAT-1 and Arctic Climate Processes: A Review and Update. *Canadian Journal of Remote Sensing*, 27, 51-61.

Barlow, R.G., Gosselin, M., Legendre, L., Therriault, J.C., Demers, S., Mantoura, R.F.C., Llewellyn, C.A., 1988. Photoadaptive strategies in sea-ice microalgae. *Marine Ecology Progress Series*, 45, 145-152.

Eastwood, S., 2012. OSI SAF Sea Ice Product Manual, v3.8 edn., available at: http://osisaf.met.no

Eicken, H., Salganek, M., 2010. *Field techniques for sea-ice research*: University of Alaska Press.

Fernández-Méndez, M., Katlein, C., Rabe, B., Nicolaus, M., Peeken, I., Bakker, K., Flores, H., Boetius, A., 2015. Photosynthetic production in the Central Arctic during the record sea-ice minimum in 2012. *Biogeosciences Discussions*, 12, 2897-2945.

Gosselin, M., Legendre, L., Demers, S., Ingram, R.G., 1985. Responses of Sea-Ice Microalgae to Climatic and Fortnightly Tidal Energy Inputs (Manitounuk Sound, Hudson Bay). *Canadian Journal of Fisheries and Aquatic Sciences*, 42, 999-1006.

Gosselin, M., Legendre, L., Therriault, J.C., Demers, S., Rochet, M., 1986. Physical control of the horizontal patchiness of sea-ice microalgae. *Marine Ecology Progress Series*, 29, 289-298.

Gosselin, M., Levasseur, M., Wheeler, P.A., Horner, R.A., Booth, B.C., 1997. New measurements of phytoplankton and ice algal production in the Arctic Ocean. *Deep Sea Research Part II: Topical Studies in Oceanography*, 44, 1623-1644.

Granskog, M.A., Kaartokallio, H., Kuosa, H., Thomas, D.N., Ehn, J., Sonninen, E., 2005. Scales of horizontal patchiness in chlorophyll a, chemical and physical properties of landfast sea ice in the Gulf of Finland (Baltic Sea). *Polar Biology*, 28, 276-283.

Grenfell, T.C., Maykut, G.A., 1977. The optical properties of ice and snow in the Arctic Basin. *Journal of Glaciology*, 18, 445-463.

Haas, C., Hendricks, S., Doble, M., 2006. Comparison of the sea-ice thickness distribution in the Lincoln Sea and adjacent Arctic Ocean in 2004 and 2005. *Annals of Glaciology*, 44, 247-252.

Haas, C., Hendricks, S., Eicken, H., Herber, A., 2010. Synoptic airborne thickness surveys reveal state of Arctic sea ice cover. *Geophysical Research Letters*, Vol. 37 (p. L09501).

Hatam, I., Lange, B., Beckers, J., Haas, C., Lanoil, B., 2016. Bacterial communities from Arctic seasonal sea ice are more compositionally variable than those from multi-year sea ice. *ISME J*.

Jassby, A.D., Platt, T., 1976. Mathematical formulation of the relationship between photosynthesis and light for phytoplankton. *Limnology and Oceanography*, 21, 540-547.

Katlein, C., 2012. ROV basierte Untersuchung der räumlichen Variabilität der Lichttransmission durch arktisches Meereis im Sommer. *Eberhard-Karls Universität Tübingen*, Vol. masters thesis.

Katlein, C., Fernández-Méndez, M., Wenzhöfer, F., Nicolaus, M., 2014a. Distribution of algal aggregates under summer sea ice in the Central Arctic. *Polar Biology*.

Katlein, C., Nicolaus, M., Petrich, C., 2014b. The anisotropic scattering coefficient of sea ice. *Journal of Geophysical Research*, 119, 842-855.

Kurtz, N.T., Farrell, S.L., 2011. Large-scale surveys of snow depth on Arctic sea ice from Operation IceBridge. *Geophysical Research Letters*, 38, n/a-n/a.

Kwok, R., Haas, C., 2015. Effects of radar side-lobes on snow depth retrievals from Operation IceBridge. *Journal of Glaciology*, 61, 576-584.

Kwok, R., Rothrock, D.A., 2009. Decline in Arctic sea ice thickness from submarine and ICESat records: 1958–2008. *Geophysical Research Letters*, Vol. 36 (p. L15501).

Lange, B.A., 2012. Seasonal sea ice thickness variarbility between Canada and the North Pole. *University of Alberta*, Vol. Master's Thesis.

Lange, B.A., Katlein, C., Nicolaus, M., Peeken, I., Flores, H., in review. Spectrally-derived sea ice-algal chlorophyll a concentrations using under-ice horizontal profiling platforms. *Journal of Geophysical Research*.

Lange, B.A., Michel, C., Beckers, J.F., Casey, J.A., Flores, H., Hatam, I., Meisterhans, G., Niemi, A., Haas, C., 2015. Comparing springtime ice-algal chlorophyll a and physical properties of multi-year and first-year sea ice from the Lincoln Sea. *PLoS ONE*, 10, e0122418.

Laxon, S.W., Giles, K.A., Ridout, A.L., Wingham, D.J., Willatt, R., Cullen, R., Kwok, R., Schweiger, A., Zhang, J., Haas, C., Hendricks, S., Krishfield, R., Kurtz, N., Farrell, S., Davidson, M., 2013. CryoSat-2 estimates of Arctic sea ice thickness and volume. *Geophysical Research Letters*, 40, 732-737.

Legendre, L., Aota, M., Shirasawa, K., Martineau, M.J., Ishikawa, M., 1991. Crystallographic structure of sea ice along a salinity gradient and environmental control of microalgae in the brine cells. *Journal of Marine Systems*, 2, 347-357.

Legendre, P., Fortin, M.-J., 1989. Spatial Pattern and ecological analysis. *Vegetatio*, 80, 107-138.

Maslanik, J.A., Stroeve, J.C., Fowler, C., Emery, W., 2011. Distribution and trends in Arctic sea ice age through spring 2011. *Geophysical Research Letters*, Vol. 38 (p. L13502).

Maykut, G.A., Grenfell, T.C., 1975. Spectral Distribution of Light beneath 1st-Year Sea Ice in Arctic Ocean. *Limnology and Oceanography*, 20, 554-563.

Melnikov, I.A., Kolosova, E.G., Welch, H.E., Zhitina, L.S., 2002. Sea ice biological communities and nutrient dynamics in the Canada Basin of the Arctic Ocean. *Deep Sea Research Part I: Oceanographic Research Papers*, 49, 1623-1649.

Michel, C., Legendre, L., Demers, S., Therriault, J., 1988. Photoadaptation of sea-ice microalgae in springtime: Photosynthesis and carboxylating enzymes. *Marine Ecology Progress Series*, 50, 177-185.

Mock, T., Gradinger, R., 1999. Determination of Arctic ice algal production with a new in situ incubation technique. *Marine Ecology Progress Series*, 177, 15-26.

Monod, J., 1949. The growth of bacterial cultures. *Annual Reviews in Microbiology*, 3, 371-394.

Moran, P.A., 1950. Notes on continuous stochastic phenomena. *Biometrika*, 37, 17-23.

Newman, T., Farrell, S.L., Richter-Menge, J., Connor, L.N., Kurtz, N.T., Elder, B.C., McAdoo, D., 2014. Assessment of radar-derived snow depth over Arctic sea ice. *Journal of Geophysical Research: Oceans*, 119, 8578-8602.

Nicolaus, M., Hudson, S.R., Gerland, S., Munderloh, K., 2010. A modern concept for autonomous and continuous measurements of spectral albedo and transmittance of sea ice. *Cold Regions Science and Technology*, 62, 14-28.

Parkinson, C.L., Comiso, J.C., 2013. On the 2012 record low Arctic sea ice cover: Combined impact of preconditioning and an August storm. *Geophysical Research Letters*, 40, 1356-1361.

Parsons, T.R., Maita, Y., Lalli, C.M., 1989. *A manual of chemical and biological methods for seawater analysis*. Toronto: Pergamon Press.

Perovich, D.K., 1996. The Optical Properties of Sea Ice. Cold Regions Research and Engineering Laboratory.

Perovich, D.K., Grenfell, T.C., Richter-Menge, J.A., Light, B., Tucker III, W.B., Eicken, H., 2003. Thin and thinner: Sea ice mass balance measurements during SHEBA. *Journal of Geophysical Research*, Vol. 108 (p. 8050).

Ricker, R., Hendricks, S., Helm, V., Skourup, H., Davidson, M., 2014. Sensitivity of CryoSat-2 Arctic sea-ice freeboard and thickness on radar-waveform interpretation. *The Cryosphere*, 8, 1607-1622.

Rysgaard, S., Kühl, M., Glud, R.N., Hansen, J.W., 2001. Biomass, production and horizontal patchiness of sea ice algae in a high-Arctic fjord (Young Sound, NE Greenland). *Marine Ecology Progress Series*, 223, 15-26.

Sarthou, G., Timmermans, K.R., Blain, S., Tréguer, P., 2005. Growth physiology and fate of diatoms in the ocean: a review. *Journal of Sea Research*, 53, 25-42.

Schünemann, H., Werner, I., 2005. Seasonal variations in distribution patterns of sympagic meiofauna in Arctic pack ice. *Marine Biology*, 146, 1091-1102.

Schweiger, A., Lindsay, R., Zhang, J., Steele, M., Stern, H., Kwok, R., 2011. Uncertainty in modeled Arctic sea ice volume. *Journal of Geophysical Research*, 116.

Søgaard, D.H., Kristensen, M., Rysgaard, S., Glud, R.N., Hansen, P.J., Hilligsøe, K.M., 2010. Autotrophic and heterotrophic activity in Arctic first-year sea ice: seasonal study from Malene Bight, SW Greenland. *Marine Ecology Progress Series*, 419, 31-45.

Stroeve, J.C., Kattsov, V., Barrett, A., Serreze, M., Pavlova, T., Holland, M., Meier, W.N., 2012. Trends in Arctic sea ice extent from CMIP5, CMIP3 and observations. *Geophysical Research Letters*, 39, L16502.

Stroeve, J.C., Serreze, M.C., Holland, M.M., Kay, J.E., Malanik, J., Barrett, A.P., 2011. The Arctic's rapidly shrinking sea ice cover: a research synthesis. *Climatic Change* (pp. 1-23).

Sturm, M., Holmgren, J., Perovich, D.K., 2002. Winter snow cover on the sea ice of the Arctic Ocean at the Surface Heat Budget of the Arctic Ocean (SHEBA): Temporal evolution and spatial variability. *Journal of Geophysical Research*, Vol. 107 (p. 8047).

Thomas, C.W., 1963. On the transfer of visible radiation through sea ice and snow. *Journal of Glaciology*, 4, 481-484.

Vancoppenolle, M., Meiners, K.M., Michel, C., Bopp, L., Brabant, F., Carnat, G., Delille, B., Lannuzel, D., Madec, G., Moreau, S., 2013. Role of sea ice in global biogeochemical cycles: emerging views and challenges. *Quaternary science reviews*, Vol. 79 (pp. 207-230).

Warren, S.G., Rigor, I.G., Untersteiner, N., Radionov, V.F., Bryazgin, N.N., Aleksandrov, Y.I., Colony, R., 1999. Snow Depth on Arctic Sea Ice. *Journal of Climate*, 12, 1814-1829.

Wassmann, P., 2011. Arctic marine ecosystems in an era of rapid climate change. *Progress in Oceanography*, Vol. 90 (pp. 1-17).

Weissling, B.P., Lewis, M.J., Ackley, S.F., 2011. Sea-ice thickness and mass at Ice Station Belgica, Bellingshausen Sea, Antarctica. *Deep Sea Research Part II: Topical Studies in Oceanography*, 58, 1112-1124.

Chapter 5: Discussion

D 5.1 Improving the spatial representativeness of sea ice related environmental properties

The sea ice bottom and under-ice environment remains one of the most poorly understood components of the Arctic ecosystem due to logistical constraints, limited access, and the general difficulty in sampling the bottom-ice and at the ice-water interface. The limited knowledge of this system requires methodological advancements and innovations in order to accurately and representatively sample and capture the highly heterogeneous sea ice and under-ice environments. With a more accurate and representative assessment of the sea ice environment we could develop accurate relationships of the distribution of sea ice algae and the under-ice community with important implications for large-scale estimates, up-scaling to satellite observations and pan-Arctic ecological modelling studies. As a main component of this thesis, we substantially improved the spatial representativeness of sampling methods for important sea ice-associated habitat properties, and sea ice algae carbon production and biomass using two under-ice horizontal profiling platforms: the Surface and Under-Ice Trawl (SUIT) and a Remotely Operated Vehicle (ROV).

In Chapter 2 - Paper 1, we showed that the spatial variability of sea ice and under-ice water properties, observed over ~ 1.5 km lengths using the SUIT-mounted environmental sensor array, were not accurately represented by nearby smaller-scale or local point measurements (e.g., ice station and ship-based observations). Therefore, the SUIT-mounted sensor array is a key advancement necessary to accurately and representatively sample both the sea ice environment and the under-ice community simultaneously. These results further justify the robustness of the ecological models developed by Chapter 3 – Paper 4: David et al. (2015b) and (David et al., 2015a) using these environmental observations. The fact that the sea ice environmental and under-ice community observations are coincident substantially reduces uncertainty in the representativeness of the observations and derived ecological models. This provides an ideal approach to further develop these relationships towards application in large-scale estimates using remote sensing data and pan-Arctic ecosystem models.

In addition to developing an environmental sensor array, we developed upon previous established algorithms to derive ice-algal chl *a* from under-ice spectral measurements (e.g., Campbell et al., 2014; Campbell et al., 2015; Melbourne-Thomas et al., 2015; Mundy et al., 2007) to produce a robust statistical model to spectrally-derive summertime sea ice algal chl *a* across the entire Eurasian Basin of the Arctic Ocean. We applied our statistical model to horizontal under-ice profiling platforms, the SUIT and ROV, and provided, for the first time, floe-scale (i.e., on the order of the size of a sea ice floe ~ 100 – 5000 m) estimates of ice-algal biomass (Chapter 2 - Paper 2: Lange et al., in review). The development of the SUIT-mounted environmental sensor array and processing methods was an essential first step in order to characterize the behavior of the SUIT movement and location in the water relative to the ice. This information was necessary in order to assess the quality of spectral measurements from the SUIT and to filter data based on influential features such as: open water, regions where there was a large distance of water between the sensor and the bottom of the ice and where SUIT movement was rapid and erratic.

These ROV and SUIT-based spectrally-derived estimates of ice-algal chl *a* are at scales, which are key to address the representativeness of traditional sampling methods, particularly sea ice coring, which are typically used to parameterize pan-Arctic distributions of ice-algal biomass and primary production (e.g., Fernández-Méndez et al., 2015; Gosselin et al., 1997). In Chapter 2 - Paper 2: Lange et al. (in review) we focused primarily on a methodological description of this novel approach. However, we also provided a preliminary assessment of the representativeness of ice-core chl *a* estimates (Fernández-Méndez et al., 2015) in comparison to the ROV-based spectrally-derived ice-

algal chl *a* estimates from one ice station. We demonstrated that ice coring may not accurately represent the true spatial variability of sea ice-algal biomass, which can cause subsequent biases in large-scale ice algal biomass and PP estimates.

Upon more detailed analyses of data produced using methodologies in Chapter 2 (Paper's 1 and 2) we were able to investigate the spatial representativeness of ice core-derived chl *a* and PP estimates for 7 ice stations spread across the central Arctic Ocean. We used a combined approach, which required the use of ice coring-derived photosynthetic parameters, to up-scale primary production estimates to the entire ROV surveys at each of these stations. This was only possible with the novel approach for deriving chl *a* described in Chapter 2 - Paper 2: Lange et al. (in review), which is not only a robust statistical model but can be used under highly variable environmental conditions. This was particularly important during the 2012 cruise (PS80) to the central Arctic since it covered a large geographical region and the transition period from high to low solar radiation. Our detailed comparison, provided in Chapter 3 – Paper 3, indicated that ice-core based ice-algal chl *a* and PP estimates were not representative of the up-scaled estimates derived from ROV and SUIT sensor measurements. Furthermore, we identified sea ice ridges as potentially high biomass and high PP features. This has important ecological implications for under-ice organisms particularly in the light of other studies that observed the large herbivorous amphipod, *Gammarus wilkitzkii*, in close association with sea ice ridges during advanced melt (Gradinger et al., 2010). Our results suggest that besides using ridges for shelter from environmental stress, sea ice ridges may provide an important food source with higher biomass at ridges due to lower melt-induced biomass losses. Unfortunately, ridge identification processing was not included in Chapter 3 – Paper 2: David et al. (2015b) and therefore the association of organisms with ridges could not be further assessed as suggested by Gradinger et al. (2010). However, later in this section I will introduce a brief statistical analyses, using a similar approach as in Chapter 3 – Paper 2: David et al. (2015b) and (David et al., 2016), to incorporate all variables not previously included in statistical analyses because they have been developed after these studies were completed.

Based on the presented sampling and processing methods described in Chapter 2 – Paper's 1 and 2, and applied in Chapter 3 – Paper's 3 and 4, we have demonstrated a sequence of developmental stages for the ROV- and SUIT-mounted environmental sensor array ultimately resulting in:

1. Improved representativeness of sea ice and under-ice environmental properties;
2. an essential contribution to deriving larger-scale ice-algal chl *a* biomass and PP estimates; and
3. provided key environmental properties, which were incorporated into statistical models with important ecological implications for pan-Arctic ecological modeling and large-scale distribution estimates of under-ice fauna.

In the rest of this section, we present a preliminary analyses, which combines methods and data that were not previously presented (Table 1; variables denoted by asterisk) and/or combined in order to conduct improved statistical analyses and modelling.

Table 1. Summary of variables, and environmental properties that can be observed or derived using the under-ice horizontal profiling platforms presented throughout this thesis or introduced in this section (denoted by *).

Under-ice Horizontal Profiling Platform	Sensor	Variables observed/derived
Surface and Under-Ice Trawl (SUIT)	CTD / altimeter / fluorometer	• water under-ice: chl *a*, salinity, temperature • sea ice: draft/thickness, ridge density • water depth and distance to ice-bottom • *Water under ice PP
	ADCP	• Pitch, roll, heading (ice draft correction) • draft (from depth sensor)
	Spectral radiometers	• Under-ice light • Ice-algal chl *a* • *Ice-algal PP
Remotely Operated Vehicle (ROV)	CTD	• Water Depth, salinity, temperature
	Tilt sensor	• Pitch, roll, heading
	Spectral radiometers	• Under-ice light – PAR • Ice-algal chl *a* • Ice-algal PP

Using the same approach to estimate sea ice algal PP from ROV surveys as described in Chapter 3 – Paper 3, we applied this method to the SUIT-mounted sensor array derived ice-algal chl *a* and under-ice light measurements combined with the ice-core derived photosynthetic parameters from the closest ice station (Fernández-Méndez et al., 2015). Furthermore, using a similar but somewhat modified approach we applied the same procedure to estimate water under ice primary production using photosynthetic parameters derived from under-ice water samples collected at the closest ice station (Fernández-Méndez et al., 2015) combined with the under-ice light (PAR) measurements and the CTD fluorometer chl *a* biomass observations. These values were integrated for the 2 m region under the ice because this is the approximate vertical sampling coverage of the SUIT.

For one SUIT haul we provided profiles of the sea ice properties, ice-algal chl *a* biomass, ice-algal PP, water under ice chl *a* biomass, and water under ice PP (Figure 1). Based on this one station we can see that the ice core and water sample derived PP estimates from a nearby ice station (Fernández-Méndez et al., 2015) were different compared to the SUIT-derived ice-algal PP (Figure 1 d; Table 2) and water under ice PP (Figure 1 f; Table 2). The water under the ice at the nearby ice station (360) PP of 0.1 mg C m^{-2} d^{-1} was lower than the SUIT-derived median (IQR) values of 0.23 (0.15 – 0.34) mg C m^{-2} d^{-1} (Table 2). Conversely, the ice station ice core derived ice-algal PP of 0.39 mg C m^{-2} d^{-1} was higher compared to both the ROV values of 0.07 (0.05 – 0.12) mg C m^{-2} d^{-1} and SUIT-derived NPP values of 0.09 (0.06 – 0.28) mg C m^{-2} d^{-1} (Table 2). As described in detail in Chapter 3 – Paper 3, these differences were primarily driven by differences in both ice-algal chl *a* biomass and the bottom-ice light. Based on the profiles of ice-algal chl *a* biomass, water under ice chl *a* biomass, and the under ice light regime (Figure 1 b,c,e) we can see that these properties are highly heterogeneous and therefore likely resulted in the differences of the NPP estimates compared to the ice station water under ice and ice core based estimates. These results further emphasize the need and importance of capturing the spatial variability of key environmental properties such as ice-algal biomass and NPP, and water under-ice NPP and chl *a* biomass at larger scales, as is feasible with ROV and SUIT surveys. The implications for large-scale estimates based on a limited number of ice core-based measurements may also carry the same uncertainty and therefore may not accurately represent the true spatial variability that exists within and under a highly heterogeneous habitat.

Our results have previously demonstrated relationships between environmental sea ice properties and the under-ice community as described in Chapter 3 – Paper 4: David et al. (2015b) and David et al. (2015a). These statistical analyses did not include important physical-biological properties such as:

sea ice ridge distributions, ice-algal chl *a* biomass and NPP, and water under ice NPP. Therefore, we can further develop upon these already robust ecological models with additional parameters to further improve the relationships, which can then be used in large-scale pan-Arctic ecosystem models and for up-scaling habitat

Table 2. Summary of net primary production (NPP) associated with sea ice and under-ice water at ice station 360 derived from ice cores, CTD profiles, water samples and ROV profiles, and nearby Surface and Under-Ice Trawl (SUIT) station 376;Results are given as median (interquartile range) for surveys. Single values represent single location ice station observations (FM data presented in Fernández-Méndez et al., 2015).

	Ice Station 360 (FM)	**ROV Station 360**	**SUIT Station 376**
Ice NPP (mg C m^{-2} d^{-1})	0.39	0.07 (0.05 – 0.12)	0.09 (0.06 – 0.28)
Water under ice NPP (mg C m^{-2} d^{-1})	0.1[b]	not measured	0.23 (0.15 – 0.34)[a]

[a] integrated over 2 m of water under ice; [b] integrated over euphotic zone depth (1% of incoming PAR) equal to 7 m (Fernández-Méndez et al., 2015).

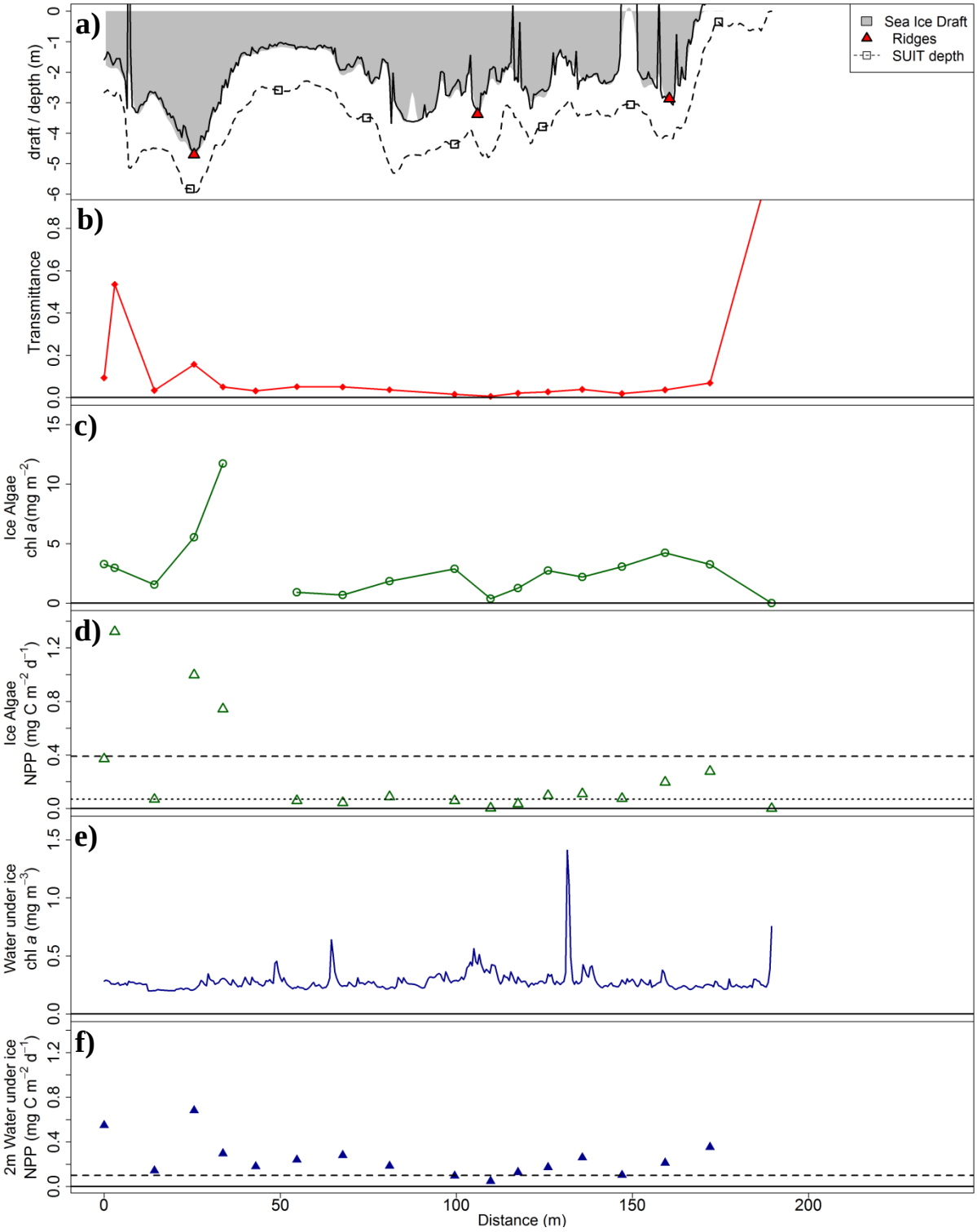

Figure 1. Surface and under-ice trawl profile at station 376 showing sensor array-measured and -derived parameters from the environmental sensor array : a) sea ice draft, identified ridges and the depth of the SUIT CTD, the black line shows the smoothed draft used for ridge detection; b) transmittance; c) spectrally-derived ice-algal chl *a*; d) ice-algal net primary production (NPP), dashed line is ice core derived NPP and dotted line ROV derived NPP (see Table 2); e) water under ice chl *a* concentrations; f) water under ice phytoplankton NPP integrated over the 2 m under-ice surface, dashed line is ice station CTD and water sample derived NPP integrated over euphotic zone depth (7 m; see Table 2).

D 5.2 Spatial variability of ice algae biomass: a synthesis

D 5.2.1 Primary production and carbon biomass availability as a food source

Our previous estimates of the food web carbon budget for the CAO based on observations during PS80 (e.g., Chapter 3- Papers 4 and 5: David et al., 2015b; Kohlbach et al., 2016) grouped all the available data for the entire cruise and quantified the total carbon budget. David et al. (2015b) estimated an approximately 1:1 ratio of total net primary production (water + sea ice) to carbon demand of the three most dominant grazer species *C. glacialis, C. hyperhoreus,* and *A. glacialis*. This estimate does not consider differences in the type of carbon source, e.g., ice algae- versus pelagic phytoplankton-derived carbon. This was addressed by the work of Kohlbach et al. (2016) who showed high dependency on ice-algae derived carbon for all three of the dominant species. Taking into account the relative contributions of ice-algae and pelagic phytoplankton derived carbon for the three dominant species, Kohlbach et al. (2016) calculated ice algal carbon demand exceeded ice-algal carbon production by a factor of 4 to 12 during our sampling period.

These approaches to estimate one compartment of the carbon budget are not without limitations. In particular, they do not account for the spatial variability of the animal communities, which were previously identified in the under-ice communities (David et al., 2015b) and pelagic zooplankton distributions observed during this cruise (Ehrlich, 2015) and other studies to the CAO (e.g., Kosobokova & Hirche, 2009). During PS80, total abundances of the three dominant species *C. glacialis, C. hyperhoreus,* and *A. glacialis* within the under-ice water (SUIT catches; David et al., 2015b) and 0 to 200 m surface layer of the water column (multi-net cacthes: Ehrlich, 2015) did not show any obvious regional differences (Table 4). This is may be contrary to Kosobokova and Hirche (2009) who found higher biomass of zooplankton in lower latitude regions (< 85ºN). We could not, however, assess whether seasonal downward migration had already occurred (Kosobokova, 1982).

Kosobokova and Hirche (2009) suggested, based on the limited studies of PP estimates for the high central Arctic that the lower PP rates, and hence lower food availability, were the reason for their lower zooplankton biomass. This may be correct, however, the estimates for PP available at that time either did not include ice-algal PP or had a limited spatial-temporal coverage. Ice-algae represent one of the dominant carbon producers within the CAO and therefore should be quantified representatively in order to assess the true estimate of the ice-algal derived carbon budget. Focusing on pelagic production, Kosobokova and Hirche (2009) suggested higher food availability and thus potentially higher zooplankton biomass if sea ice declines, neglecting the important role of sea ice algae in the diet of key Arctic zooplankton and top predators (Budge et al., 2008; Kohlbach et al., 2016; Wang et al., 2015; Wang et al., 2016).A simplistic focus on phytoplankton productivity, however, ignores the importance of timing and quality of algal blooms for zooplankton secondary production. For example, other studies demonstrated a key role of ice-algal bloom timing for zooplankton growth and development (Leu et al., 2011; Michel et al., 1996; Søreide et al., 2010). Finally, Kohlbach et al. (2016) showed that not only sympagic organisms have a high contribution of ice algae derived carbon in their diets but also abundant pelagic species, such as *Calanus* spp., strongly depend on ice-algal derived carbon. This highlights the importance of ice algae and their spatio-temporal dynamics for all domains of the Arctic ecosystem and not just the ice-associated communities.

In the central Arctic Ocean, the temporal evolution of ice algal growth from the beginning of the bloom to the end of the growth season is poorly documented so far. A temporal study by Melnikov et al. (2002) was conducted in the shelf regions of the Beaufort and Chukchi Seas, only reaching 80ºN near the end of the SEDNA drift study. They found that biomass peaked at the bottom of MYI in late July. This indicates that even at higher latitudes in the CAO, peak production is likely similar and not much later than mid-August when declining solar energy begins to limit production. During the *Polarstern* cruise PS80, conducted from mid-August to the end of September, our sampling was conducted during a post bloom period, indicated by high export of ice algal biomass to the sea floor before our arrival (Boetius et al. (2013).

Ice algal primary production represented up to 60% of the total (water + sea ice) primary production at ice stations near the north pole during the period of our sampling (Fernández-Méndez et al., 2015).

A similar proportional contribution to total PP by sea ice algae of 57 % was previously observed by Gosselin et al. (1997) within the CAO. Gosselin et al. (1997) observed maximum sea ice-algal biomass and primary production at the same high latitude station (~87ºN) while the second highest ice-algae biomass and PP was observed near the North Pole (~90 ºN). These high-latitude stations were sampled in mid-August when solar irradiance was rapidly declining. Thus, ice algal biomass and PP can be assumed to have been even higher previous to sampling. Melnikov (1997) also observed high bottom-ice-algal biomass of 22 mg chl *a* m^{-2} near the north pole in summer 1977, further indicating that high biomass and a high contribution of ice-algal PP at high latitude regions seems to be a consistent feature late in the summer, based on the limited number of studies available for high-latitude regions of the CAO. High biomass standing stocks persisting at high latitudes due to reduced melt-induced algal loses may partially compensate for the relatively low carbon assimilation rates caused by low solar radiation. In contrast, phytoplankton would not be able to maintain high biomass at lower assimilation rates, because the phytoplankton cells may sink to the sea floor at higher rates than producing new cells. This high downward particle flux of biological material is supported by Roca-Martí et al. (2016) who observed a high export efficiency of the primary produced carbon to the seafloor within the CAO. However, this is not the case for ice algae after the melt season, since the remnant community is entrained or attached to the ice-bottom and thus will likely not detach from the ice and sink.

In Chapter 3 - Paper 3 we identified regional and small-scale variability of sea ice algal biomass and primary production, which was not representatively captured using traditional ice coring observations alone (e.g., Fernández-Méndez et al., 2015). Based on the mounting evidence that sea ice algae are of key importance for many Arctic organisms, there is a need to accurately and representatively assess the ice-algae derived carbon budget. Therefore, we took a more comprehensive approach by adding an important dataset, which representatively captures the spatial variability of ice-algal carbon production and available carbon biomass standing stocks using data from Lange et al. (in review) and Lange et al., (in prep) (Chapters 2 – Paper 2 and Chapter 3 – Paper 3). These data were converted from mg chl *a* m^{-2} to mg C m^{-2} using ice-core and water-sample derived C : chl *a* ratios (mg C : mg chl *a*) from all eight ice stations. The mean (± one standard deviation) C:chl *a* ratios were 44.9 ± 0.7 mg C : mg chl *a* for sea ice algae and 41.9 ± 1.5 mg C:mg chl *a* for water column phytoplankton (I. Peeken, unpublished data). Because multi-net-, SUIT-, and ice stations were not always conducted coincident to each other we grouped stations by proximity in time and space (Table 4; Figure 2). We used these groups to investigate the spatial variability of the carbon supply and demand during our sampling period.

In previous carbon budget estimates we assessed only the carbon production rates (e.g., NPP) in terms of a carbon food supply. It may be intuitive to expect that there was lower carbon production than carbon demand because in late-summer solar energy is very low and thus production is shutting down. This is what we observed in the previous carbon budget assessments (David et al., 2015b; Kohlbach et al., 2016)**.** Similarly, **t**he overall updated estimates of ice-algal derived carbon demand were ~three times greater than ice-algal carbon production. For the lower latitude stations the supply was only 75% of the demand but with high regional variability with production to demand ratios in the range 0.03 to 3. The ratio exceeded 1 at only the first station group, which was located in a low latitude region near the ice-edge and sampled earliest in the season (Table 4). For all but one group, ice-algae carbon production was not sufficient to sustain the communities' ice-algal carbon demand. In high-latitude regions the mis-match between supply and demand was even greater with demand exceeding supply by a factor of 13, similar to estimates of (Kohlbach et al., 2016), and relatively lower variability between stations. We must also note that in order for a food supply to be sustainable the carbon supply must be much greater than a 1 to 1 ratio with carbon demand.

Phytoplankton-derived carbon demand, although difficult to compare to ice algae due to the drastically different integration depths, overall showed a generally better agreement between carbon supply and demand with a mean production to demand ratio of 2.2. The two station groups near the North Pole (H and I; Figure 2) had the lowest ratios (Table 4). The combined water column- and sea ice–derived carbon production to demand ratio was 1.6 : 1 (Table 4), again with large regional variability. The two highest latitude station groups (H and I) had by far the lowest ratios of 0.03 and

0.16 while the other groups ranged between 0.49 to 5.4 (Table 4). These results further highlight the mis-match between overall primary production and carbon demand. Furthermore, the large regional variability of these results validates the need for improved spatial representativeness of all observations.

There are important limitations of this comparison. First, water column production is integrated over a large depth and therefore appears likely greater just because of the fact that there is more water. This does not necessarily mean the density of food is higher. Rather, the availability of carbon in the water may require a lot more effort and thus energy cost to actively swim and search for this food source. Sea ice algae production is a more localized and stationary food source on a 2-dimensional plane, making it a far more attractive food source in terms of energy cost-benefit. This is more obvious if we convert the depth-integrated concentration values of ice and water PP and biomass estimates into volumetric concentrations (Table 5). Ice algae carbon concentrations (mg C m^{-3}) on average were 8 times larger than in the water column (Table 5). Similarly, the ice algal PP, expressed volumetrically, was also on average 8 times greater than in the water column (Table 5). However, to quantify the cost-benefit relationship between food sources more detailed distributions of the vertical structure of both zooplankton and primary producers are required. Furthermore, energy requirements of the zooplankton would need experimental derivations to understand how much energy it costs to search for food in the water column compared to staying at the underside of the ice and feeding there with minimal movement.

So far we have only considered primary production rates in terms of contribution to the carbon budget as a carbon food source. Production, however, shuts down early at the end of summer, particularly in higher latitude regions and thus may not be a good proxy for food availability. Therefore, we provide an additional assessment of the standing stock of carbon biomass for the ice and water column and determine how much is available for the communities and how long could these communities potentially be sustained by the standing stock of biomass alone. Taking this different approach, we found that the available standing stock of carbon biomass at high-latitude (>85 N) stations had more available ice-carbon than low-latitude stations (Figure 2 a), which may be attributed to lower melt-induced algal losses. In contrast, the lower-latitude stations had higher ice-algal carbon demand. Based on ingestion rates, this available biomass may sustain the three dominant species, *C.glacialis, C.hyperboreus, A.glacialis*, for up to ~50 additional days into polar night (Figure 2c and Table 4). Whereas at lower latitude (<85 N), lower algal biomass regions, albeit also with higher overall zooplankton biomass and higher carbon demand, the available ice-algal biomass would sustain only an additional ~15 days of feeding (Figure 2c and Table 4).

All of the sea ice algae carbon, however, may not be easily accessible to under-ice organisms because some is entrained in the upper portions of the ice (e.g., Lange et al., 2015). Based on a mean of all ice core chl *a* profiles from all stations, 75% of the chl *a* biomass was observed in the bottom portion of the ice. Nevertheless, the ice-algal carbon in the upper portions could be available to in-ice fauna, which may have limited but enough mobility within the ice to transfer carbon within different layers of the ice and perhaps to the ice bottom as food for higher trophic levels. Another question that arises is: how long will this biomass remain viable as a food source? The answer is not easy but experimental work by Zhang et al. (1998) showed that samples of autumn sea ice algae exposed to 161 days of darkness had 40% of the initial abundance remaining after the 161 day period. This was attributed to facultative heterotrophy (mixotrophy) and energy storage, which allowed the survival during the artificial polar night. This indicates that high biomass may persist well into the polar night and that algal remineralization or "decay" may not considerably limit the availability of carbon.

Table 4. Carbon budget for sea ice and water column derived carbon and the three most dominant herbivores in terms of biomass: *C. glacialis*, *C. hyperhoreus*, and *A. glacialis* caught during each station of the 2012 Polarstern cruise PS80 to the central Arctic Ocean.

Location	[a]Abundance (ind. m^{-2})	[b]Carbon Demand (mg C m^{-2} d^{-1})		Primary Production (mg C m^{-2} d^{-1})			Available chl *a* (mg chl *a* m^{-2})			[f]Available Carbon (mg C m^{-2})			Ratio Production to Demand			[g]Days of feeding	
Group	under-ice & water	ice[a]	water[a]	ice	uiw	water	[c] ice	[d] uiw	[e] water	ice	uiw	water	ice	water	total	ice	water
B	1035	3.5	9.6	10.7	1.29	25.0	1.6	0.13	3.2	**71.7**	5.4	**134.1**	**3 : 1**	**2.6 : 1**	**2.7 : 1**	20.4	14.0
C	1951	13.5	28.2	0.8	-	31.0	1.3	-	17.0	**58.4**	-	**712.3**	0.06 : 1	**1.1 : 1**	0.76 : 1	4.3	25.3
D	474	3.5	7.2	2.0	-	11.0	1.8	-	8.0	81.8	-	335.2	0.56 : 1	**1.5 : 1**	**1.2 : 1**	23.3	46.8
E	803	4.0	9.3	0.5	1.19	6.0	0.4 [d]	0.33	8.0	**18.0**	13.7	**335.2**	0.11 : 1	0.65 : 1	0.49 : 1	4.5	36.1
F	1022	4.8	11.4	0.2	4.66	60.0	1.5	0.33	11.0	**69.6**	13.7	**460.9**	0.03 : 1	**5.3 : 1**	**3.7 : 1**	14.5	40.4
G	348	2.2	3.1	0.2	6.33	28.0	2.8	0.44	17.0	**125.7**	18.3	**712.3**	0.09 : 1	**9.2 : 1**	**5.4 : 1**	58.4	233.5
H	542	2.0	2.4	0.2	**0.58**	**0.5**	1.9	0.32	3.0	**84.0**	13.5	**125.7**	0.11 : 1	0.21 : 1	0.16 : 1	42.0	52.4
I	848	5.1	4.0	0.1	**0.29**	**0.1**	5.3	0.28	1.2	**237.9**	11.7	**50.3**	0.03 : 1	0.03 : 1	0.03 : 1	47.1	12.7
mean	**877.7**	**4.8**	**9.4**	**1.8**	**2.4**	**20.2**	**2.1**	**0.3**	**8.6**	**93.4**	**12.7**	**358.2**	**0.38 : 1**	**2.15 : 1**	**1.6 : 1**	**27**	**58**

[a] cumulative abundances for *C. glacialis*, *C. hyperhoreus*, and *A. glacialis* data correspond to the cummulative data from the SUIT integrated for the 2 m of water under the ice (Chapter 3 - Paper 4: David et al., 2015b), and multi-net catches integrated for the surface 0 to 200 m water column (Ehrlich, 2015).

[b] Carbon demand calculated using the mean of the ingestions rates of 6.0 – 18 µg C $ind.^{-1}$ d^{-1} for *C. glacialis*, 2.8 – 8.4 µg C $ind.^{-1}$ d^{-1} for *C. hyperhoreus* according to Olli et al. (2007), and 13.0 µg C $ind.^{-1}$ d^{-1} for *A. glacialis* according to Werner (1997). According to values from Chapter 3 - Paper 5: Kohlbach et al. (2016) we further separate the carbon demand into water and ice derived Carbon by multiplying by the proportional contribution of ice algae derived carbon (α_{ice}; or 1 - α_{ice} for the water Carbon demand) to the diet of *C. glacialis* (α_{ice} = 0.33 for groups B-F and α_{ice} = 0.6 for groups G – I), for *C. hyperhoreus* α_{ice} = 0.25 (no regional differences), and for *A. glacialis* α_{ice} = 0.87 (no regional differences).

[c] data from Chapter 3 – Paper 3.

[d] data from SUIT presented in previous section (integrated for 0-2 m depth under ice)

[e] data from Fernández-Méndez et al. (2015) integrated for the euphotic zone (7 – 33 m).

[f] calculated using measured (samples from this cruise) Carbon to chl *a* ratios (mg C to mg chl *a*) of 44.9 ± 0.7 for sea ice algae and 41.9 ± 1.5 for phytoplankton (Peeken et al., unpublished data).

[g] Days of feeding corresponds to the number of days the available standing stocks of carbon biomass can sustain the carbon demand (based on species specific ingestion rates and species abundances)

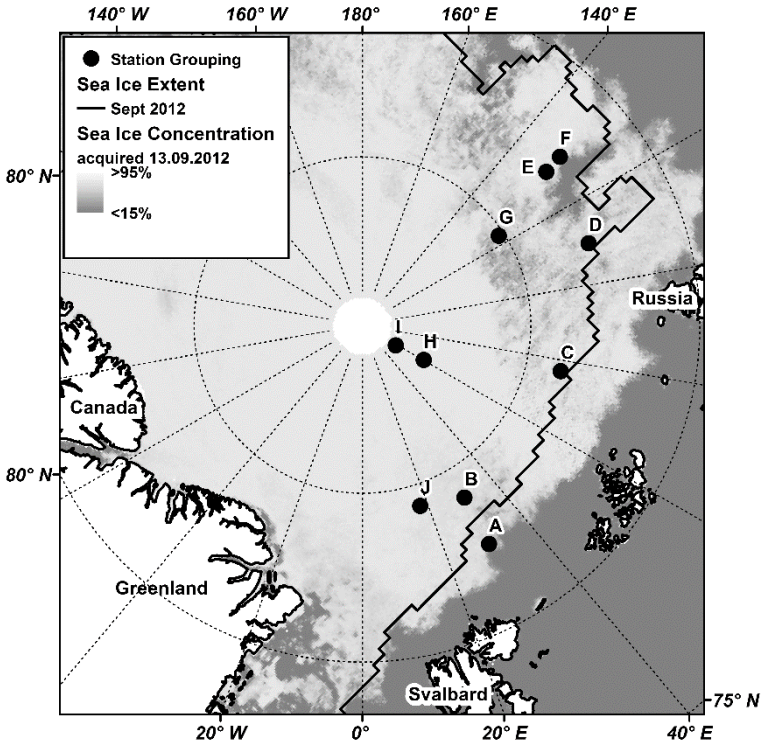

Figure 2. Map of the Arctic Ocean with sea ice extent and concentration data, and the locations of the corresponding station groupings conducted during the 2012 PS80 cruise. Sea ice concentration data acquired from www.meereisportal.de according to algorithms in Spreen et al. (2008). Sea ice extent correspond to the 2012 September monthly mean (extent data acquired from NSIDC, Fetterer et al. (2002, udpated 2011)).

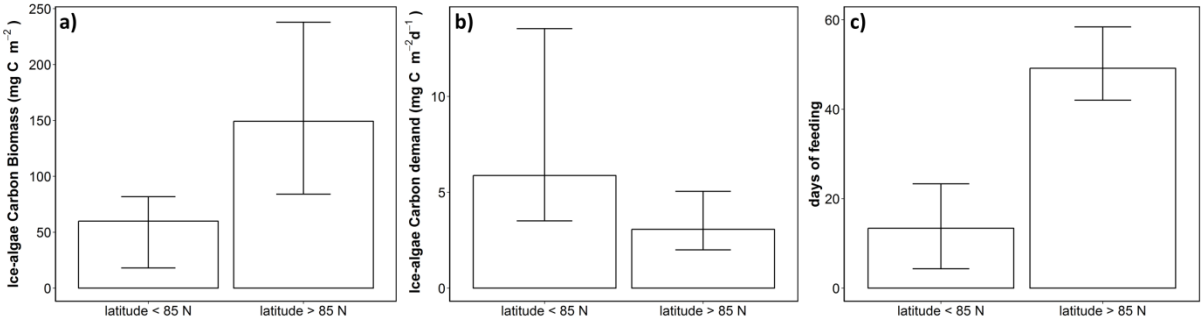

Figure 3. Ice-algae derived carbon supply and demand summarized by high latitude stations (> 85 N) and low latitude stations (< 85 N). **a)** carbon supply in terms of available ice algae carbon biomass in the sea ice (mg C m-2) converted using the C:chl *a* ratio of 44.9 mg C:mg chl *a* ; **b)** the demand of carbon from the highest biomass species (thus, ~highest carbon demand): *Calanus glacialis, Calanus hyperhoreus,* and *Apherus glacialis*. This is the total combined demand for all species at the under-ice 2 m (determined from SUIT catches) and the surface 0 to 200 m of water column (determined from multi-net catches; see Table 4?). **c)** the number of days of feeding the ice algae biomass can sustain based on the total carbon demand requirements of the three high biomass species *Calanus glacialis, Calanus hyperhoreus, and Apherus glacialis*.

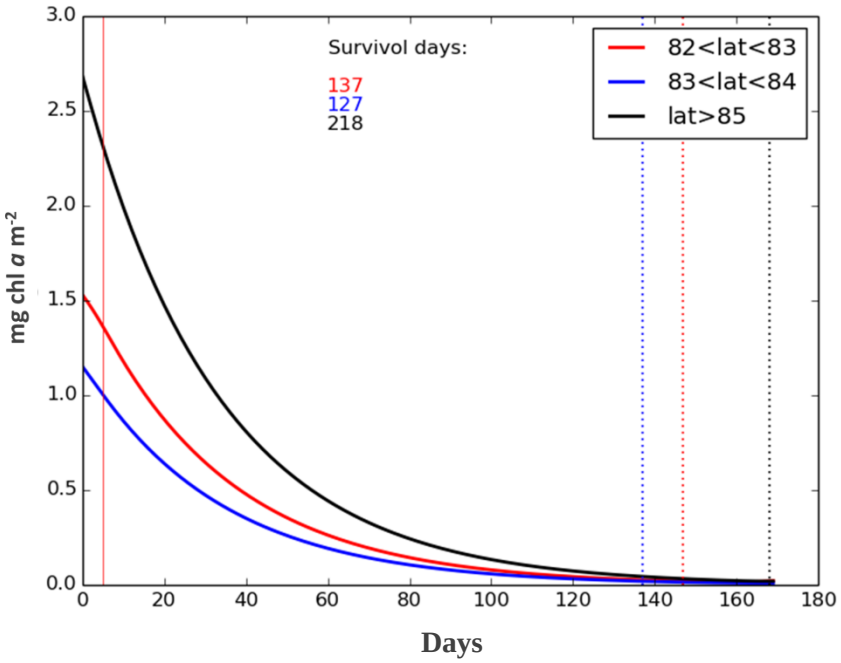

Figure 4. Days elapsed since the onset of zero light conditions of ice algae biomass within the sea ice determined from a simple 1D model (described in Chapter 4 – Paper 7) for three different latitudinal ranges. Initial chl *a* biomass was determined from the mean of all stations in the respective latitudinal range groups.

We further assessed the potential limitations imposed by a so-called algal "decay" process using established modeling parameterizations to estimate the time it would take for the ice algae to disappear and become a negligible food source. We applied the simple 1D model described in Chapter 4 - Paper 7. We used reanalysis data for downward radiation (PAR) geographically divided into the selected latitudinal ranges of 82-83ºN, 83-84ºN, and >85ºN, to correspond with the high and lower latitude classification. Initial conditions of ice thickness and chl *a* were also divided into the latitudinal groups and summarized as the mean of all stations for that class. We first defined "survival days" as the period from when the light reaches zero to when the chl *a* concentration goes under a certain limiting value. We chose the minimum value of all three latitudinal groups to be the limiting chl *a* end value of the survival period. Model results of algal biomass decay over time are shown in Figure 4. These results indicated high latitude, higher biomass stations can retain algal biomass for up to 218 days, while lower latitude, lower biomass regions can retain biomass for only 127-137 days. Figure 4 clearly shows that the retention of biomass is greater for the higher latitude stations compared to the lower latitude stations and is primarily the result of the initial biomass, which is controlled by the remaining biomass at the end of the melt season and the start of polar night. It remains unclear if this remaining biomass is used to feed the under ice fauna and in-ice fauna or fuel microbial activity. However, the potential that substantial amounts of carbon biomass remain for a considerable amount of time during a period typically characterized by zero production has significant ecological implications.

Based on this comprehensive analysis of the ice algal derived carbon component of the carbon budget, we propose the following hypothesis: *that during late-summer when primary production shuts down, the remaining ice-algal biomass in high latitude regions may represent a crucial food source to sustain ice associated organisms during the onset of polar night.* This suggests that when summer sea ice and thus remnant ice-algal biomass are absent from regions >85 N, certain organisms or entire communities may not be able to survive through the winter, with strong implications for the foodweb and winter survival.

Table 5. Primary production and available carbon biomass for the water column and bottom-ice algae, summarized volumetrically. Water column carbon concentrations given for the depth of chl *a* maximum.

group	Bottom-ice Carbon (mg C m^{-3})	Carbon @ chl *a* max. depth (mg C m^{-3})	Ice Primary Production (mg C m^{-3} d^{-1})	Water Column Primary Production (mg C m^{-3} d^{-1})
B	113.5	14.0	16.864	1.042
C	71.4	40.0	1.015	1.069
D	194.5	40.8	4.718	0.367
E	35.9	36.8	0.9	0.207
F	108.3	45.0	0.264	1.818
G	208.1	43.2	0.336	0.966
H	145.3	27.2	0.363	0.033
I	454.4	12.7	0.252	0.014

D 5.2.2 Revisiting the ecological importance of thick sea ice (features)

A common overlapping theme within this thesis for both spring ("Polar Dawn") and late-summer ("Polar Dusk") seasons in the High Arctic Ocean (>80ºN) is that thick sea ice showed some of the highest bottom-ice algal biomass levels. This challenges the view that low light is negatively associated with ice agal biomass, and conversely increased light will simply lead to increased primary production and thus biomass for the Arctic Ocean (e.g., Arrigo & van Dijken, 2015; Fernández-Méndez et al., 2015). Perhaps this is the case for pelagic phytoplankton, of which we have a far more comprehensive understanding in terms of the physiological-environmental relationships compared to sea ice algae. For ice algae in summer, thinner sea ice will ultimately lead to more light transmitted through the ice (Nicolaus et al., 2012), which will give ice algae more PAR and thus can locally increase primary production rates. However, the thinner ice is also more vulnerable to higher melt rates, meaning melt-induced algal losses will be experienced earlier in the season and thus the period of ice algal growth will likely be shortened (Lavoie et al., 2005; Lavoie et al., 2010).

In spring, sea ice algae distribution is primarily controlled by snow (Gosselin et al., 1986) (Cota & Smith, 1991; Gosselin et al., 1990), and therefore future changes to the springtime Arctic snow cover will likely determine how sea ice algae will respond to ongoing climate change during the onset of the growth season (i.e., Polar Dawn). Lavoie et al. (2010) and Leu et al. (2015) argued that ice algal growth and production will likely be hampered due to a combination of earlier snow melt and increased precipitation in the Arctic. One important factor that is commonly neglected in assessments of future springtime sea ice algal growth is the small-scale spatial distribution of the snow cover. Not only is the overall snow depth and mass balance important but how this snow is (re)distributed on the surface is one of the most important factors controlling the atmosphere-ice-ocean heat flux (Sturm et al., 2002) and the transmission of light (Grenfell & Maykut, 1977; Perovich, 1996).

During the SEDNA drift study, Melnikov et al. (2002) showed an ice algal peak in late-July during a period of no- or low-snow with an overall mean snow depth of only 3 cm by the end of June (Sturm et al., 2002). This indicated a different seasonal progression of sea ice algal growth within the central Arctic Ocean showing an ice-algal biomass peak around 100 days later than all other documented seasonal studies, albeit which were from regions characterized by seasonal sea ice (Leu et al., 2015). This suggests some clear differences between sea ice algal growth in regions characterized by seasonal sea ice compared to the High Arctic Ocean, and that these differences should be considered when assessing the future of a changing Arctic system.

In Chapter 3 we demonstrated that sea ice algal biomass was higher at higher latitude, thicker sea ice stations and occasionally also at thick sea ice ridges. The presence of high biomass observed at the bottom of ridges is not fully understood and requires further investigation. Because the ice is thicker we could assume melting may be reduced, however, Perovich et al. (2003) indicated that sea ice ridges experienced more melt than the surrounding undeformed sea ice. The higher overall melt at

ridges was partially attributed to a few very thick ridges extending deep into the water, which were experiencing melt the entire year even during winter. The temporal evolution of the melt rates revealed that ridges follow the overall mean daily bottom ice melt rates for all ice types during most of the spring season until beginning of August where only one point (representing < 1 week) is above the mean. After this one peak point the melt rates are lower than the mean and were among the lowest of all ice types for the entire month of August. In the beginning of September, ridge melt rates returned to following the mean (Perovich et al., 2003). Altogether this suggests that sea ice ridges may have overall (i.e., annual mass balance) more melt than the surrounding ice cover for the entire year but sea ice ridges can also experience some of the lowest daily melt rates during advanced melt stages, which supports our findings.

Gradinger et al. (2010) showed sea ice ridges had elevated concentrations of ice meiofauna and under-ice amphipods, which was attributed to the flushing of the sea ice and salinity stress imposed at the thinner sea ice environment. Sea ice ridges may also extend into higher salinity water compared to adjacent lower salinity water accumulations under thinner ice (Gradinger et al., 2010). These results may add additional reasons for high ice algal biomass at ridges, such as: reduced flushing and lower environmental stress. Furthermore, the presence of high algal biomass as a food source may provide an additional explanation for the observed accumulation of organisms at ridges by Gradinger et al. (2010).

Sea ice ridges represent a complex and interesting feature with an important ecological function. Therefore, the distribution of sea ice ridges is also an important parameter in order to assess its relative areal contribution of the overall ice cover. Our results from Chapter 3 – Paper 3 showed that ridges represented on average 10% (a conservative estimate) of the surveyed sea ice, a significant portion of the overall sea ice pack. The identification of high biomass ridges in addition to observed accumulations of ice-associated fauna with ridges (Gradinger et al., 2010) means these features could become even more prominent sanctuaries as sea ice continues to experience enhanced melt associated with continued sea ice thinning and declining areal coverage. Therefore, more detailed studies are required to assess how sea ice ridge distributions will change in the future and to unravel some of the uncertainties associated with the physical-ecological interactions of a highly under-sampled feature of the Arctic system.

In Chapter 4, we showed during spring that thick sea ice features also had significant contributions to overall sea ice algal biomass. We attributed this to the thin or absent snow cover observed at hummocks (Figure 4 b). This snow-ice relationship was previously shown by Perovich et al. (2003) and Sturm et al. (2002) who also observed that hummocks and ridge peaks typically had the thinnest snow cover. Furthermore, the coverage of suitable ice-algal habitat for MYI was surprisingly large and was drastically under-estimated using a block-model approach, which characterized all MYI as thick sea ice with a deep snow cover. Our main results indicated that the thick hummock sea ice features had high bottom-ice biomass and represented a stable habitat for sea ice algae. The spatial distribution of these features was relatively constant for all MYI sites, which further emphasized the importance of hummocks in terms of potential algal biomass for the entire Arctic perennial sea ice zone, which represented ~ 45% of the entire Arctic sea ice coverage in 2011 (Maslanik et al., 2011). Combined with the fact that sea ice algae are an important food source, we suggest that hummocks represent a reliable, high biomass source of carbon during the early spring when other sources are still not available in significant amounts. Furthermore, the disappearance of hummocks as a potentially reliable feeding ground and the replacement by a more temporally variable FYI snow cover may result in a more unpredictable and highly variable sea ice algal distribution with unexpected ecological consequences.

During our spring sampling we did not conduct in depth surveys over sea ice ridges. However, Perovich et al. (2003) and Sturm et al. (2002) already documented sea ice hummocks and sea ice ridge peaks as low snow regions. This suggests that the relationship between low-snow hummocks and high bottom-ice biomass may also be applied to sea ice ridges (Figure 5). Therefore, not only do sea ice ridges represent an important ecological feature during summer, as outlined in Chapter 3 – Paper 3 and e.g. by Gradinger et al. (2010), but sea ice ridges may also have important ecological implications during spring. In Chapter 4 – Paper 7, we identified an upper ice thickness limit for ice-algal biomass,

which may indicate that sea ice ridges are too thick to provide suitable light conditions at the bottom of the ice. As also identified in Chapter 4 – Paper 7, horizontal light scattering may also play an important role in creating suitable habitat in the regions surrounding hummocks. Thus, the regions surrounding sea ice ridge keels, such as the edges of the keel, may be locations of high biomass and not the keel bottom itself, due to the horizontal scattering of light from the regions of low snow at the surface of the ridge (i.e., sail; Figure 5).

The hypothesis of increased light at sea ice ridges creating suitable light conditions for high ice-algal biomass has already been applied to a modelling study (Castellani et al., in prep.). The preliminary modelling results showed that there was algae growth at the bottom of ridges; however, the biomass was less than the level ice (Castellani et al., in prep.). Another interesting feature of the model, was that the sea ice ridge algal bloom was experienced later in the season, which in terms of future sea ice decline and thinning may be able to sustain some of the carbon demand by under-ice organisms later into the season when the level ice has already experienced advanced melt-induced algal losses. Furthermore, late-summer biomass was highest in the regions with the thickest sea ice, which is consistent with our results and conclusions of higher biomass under thicker ice due to lower melt-induced algal losses (Chapter 2 – Paper 2 and Chapter 3 – Paper 3). We should also mention that because the sea ice ridges were very thick in the model runs and because the model does not account for any horizontal light scattering this may be the reason why the blooms did not occur until later during solar maximum.

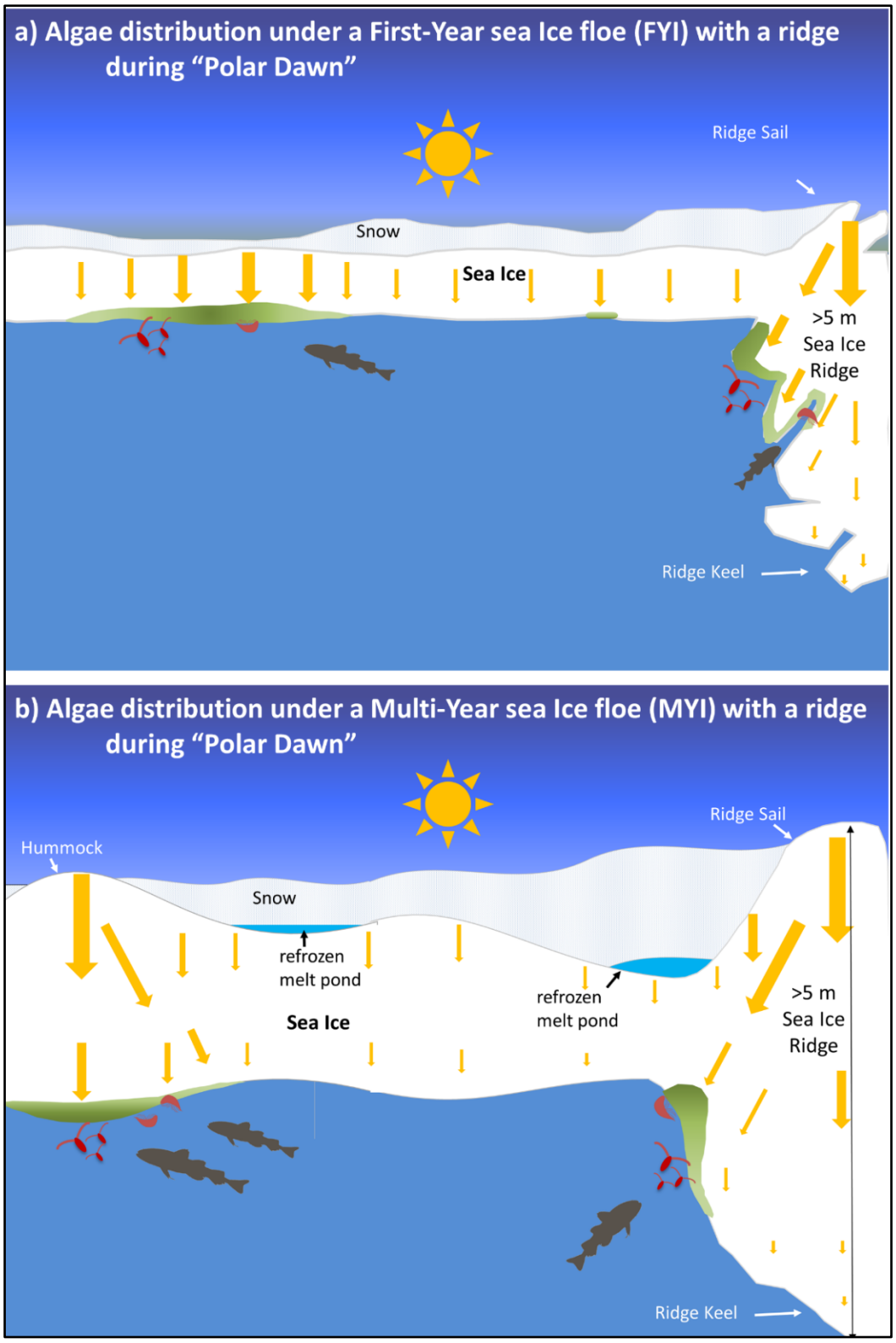

Figure 5. Conceptual diagram of sea ice algal distribution during "Polar Dawn" (i.e., onset of growth season in high latitude regions >80°N) under: a) first-year sea ice (FYI); and b) multi-year sea ice (MYI). Also shown is the presence of algal biomass at ridges.

D 5.2.3 Temporal stages of sea ice-algae variability for different ice types: implications for the future Arctic Ocean

Although a full temporal study was not conducted for ice-algal growth in the central Arctic Ocean, in the absence of other temporal studies within the CAO or high latitude regions (>80ºN) we provide some insights into the temporal stages of ice-algal growth for different ice types based on our results. The implications of our results in terms of changes to overall ice-algal biomass under different future scenarios for the Arctic Ocean are summarized in Table 6.

The temporal progression and distribution of ice algal biomass is depicted in a simplified diagram (Figure 6) covering 5 general temporal stages, which are representative of high latitude regions (>80ºN): a) end of polar night; b) "Polar Dawn" (initiation of biological production); c) "Polar Day" melt-onset coinciding approximately with solar maximum; d) "Polar Dusk" advanced melt stage; and e) the onset of "Polar Night". Within these seasonal stages we only consider the temporal evolution of sea ice algae and not phytoplankton, which we must note is also an important carbon source. As Berge et al. (2015) noted, terms like "Polar Night" and "Polar Day" characterize the light conditions whereas "winter" and "summer" are typically used in relation to temperature. In order to address any ambiguities we have classified the stages in terms of both the light regime (e.g., Polar Night vs. Polar Day) and in relation to temperature driven processes (e.g., advanced melt) where necessary. We introduced the term "Polar Dawn" to refer to the transition period between Polar Night and Polar Day with steadily increasing solar radiation, and the term "Polar Dusk" to refer to the transition period between Polar Day and Polar Night with steadily decreasing solar radiation. For the purposes of this temporal assessment, following Berge et al. (2015)'s light regime classification, we assumed minimal latitudinal variability for the high central Arctic Ocean (>80ºN) during each stage.

At the end of Polar Night (Figure 6 a) there must be algae present, in at least very small amounts, in order to seed the ice-algal community during the onset of growth (depicted by small black dots Figure 6 a). During the onset of growth MYI and older FYI (i.e., ice that likely formed during previous years freeze-up ~October) have similar biomass concentrations and areal coverage of suitable habitat (Figure 6 b) as described in Chapter 4. Old leads in transition to young FYI (i.e., ice that formed mid-to-late winter) likely have high biomass concentrations with high areal coverage due to the uniformly thinner snow cover. However, the relative difference between ice types in terms of overall biomass depends on their overall areal coverage within the Arctic Ocean.

The relative difference between MYI and FYI in terms of overall biomass contributions is difficult to assess since snow, which is poorly characterized on a pan-Arctic scale, is the main driver for the spatial distribution of suitable algae habitat on FYI. In the present state of the Arctic Ocean, MYI dominates the region between Canada, Greenland and the North Pole whereas the rest of the Arctic is dominated by FYI. Since the FYI snow cover has high spatial-temporal variability, it is difficult to compare with MYI, which has a relatively more stable snow surface even with large variations in overall snow precipitation. The older FYI forming during initial freeze-up and at higher latitudes likely has deeper snow cover (evident from the generally large snow depth values from the Cryosat-2 data products presented in Chapter 4 – Paper 7) and therefore lower spatial coverage of suitable algae habitat (Table 6). The younger FYI with thinner snow cover, found in lower latitudes, likely has larger spatial coverage of suitable algae habitat. A generalized situation with the complete replacement of MYI by FYI would result in comparable or lower overall biomass during the onset of growth in regions of older FYI with generally deeper snow cover, which is likely to dominate in regions of the high CAO (Table 6). In contrast, a shift to younger FYI with thinner snow cover will likely increase overall biomass in lower latitude regions. Some forecasts predict an Arctic-wide increase in precipitation (IPCC, 2013), which would then result in an overall decrease in ice-algae biomass during the initial growth stage (Table 6).

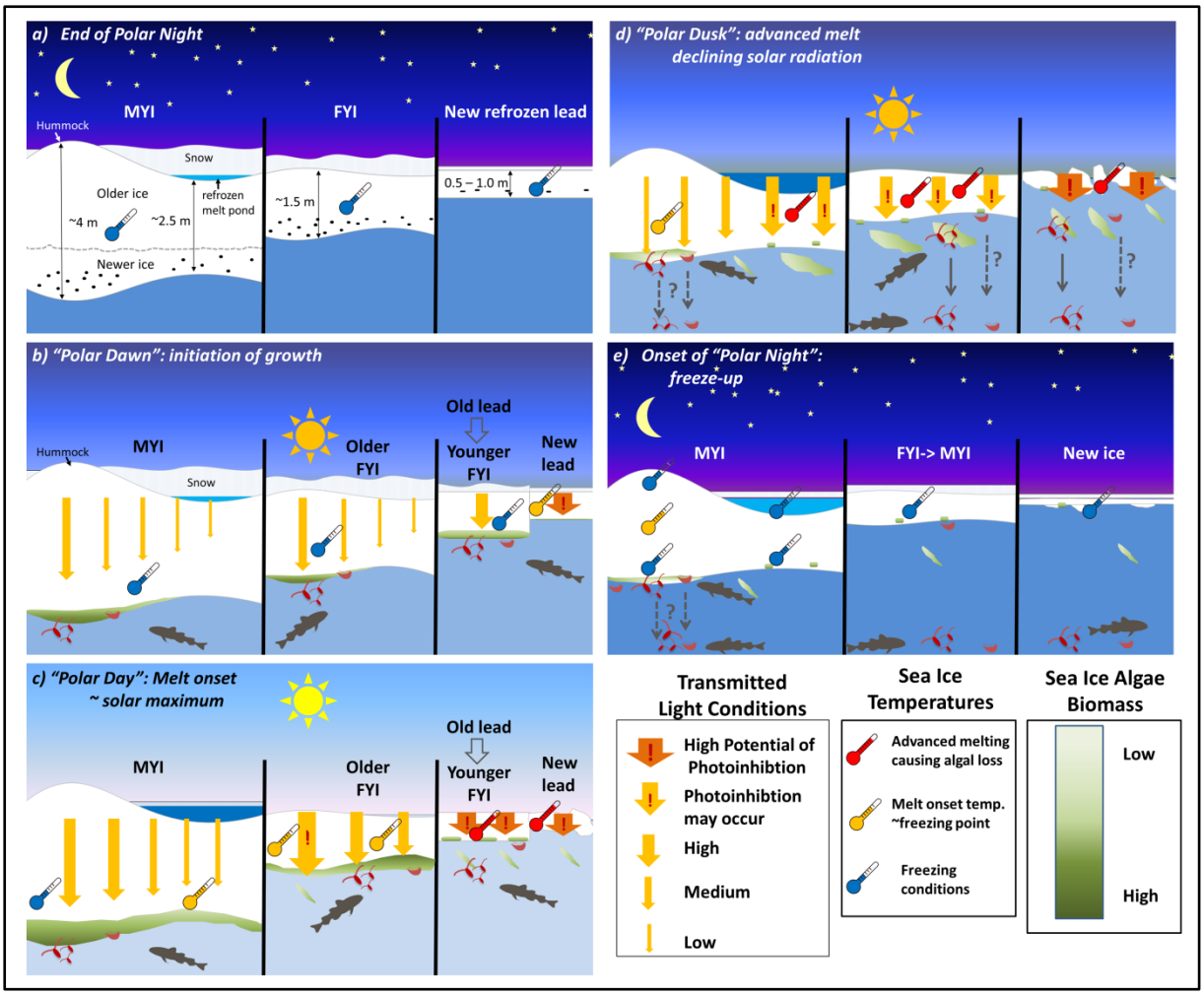

Figure 6. Conceptual diagram showing the temporal progression of ice algal biomass and distribution for different ice types summarized by seasonal stages experienced at high latitudes (>80ºN) during: a) end of polar night; b) "Polar Dawn" (initiation of growth); c) "Polar Day" melt-onset coinciding approximately with solar maximum; d) "Polar Dusk" advanced melt stage; and e) the onset of "Polar Night" and freeze-up. Green patches in the water column are ice algae expelled from the ice during melt. Grey arrows indicate the possibility of seasonal downward migration of organisms.

Although lead-ice may represent a small fraction of the overall ice cover, the potential for higher biomass likely means lead-ice is an important contributor to overall biomass during Polar Dawn and the initial growth period. The percent coverage of open water leads and new ice forming within the leads (i.e., lead-ice) also has large regional variability representing 2-3% in the CAO and 6-9% in the CAO peripheral regions (Lindsay & Rothrock, 1995), and seasonal variability with 10% in October and 3% in April (Laxon et al., 2003). The relative proportion of younger FYI and refrozen leads in the central Arctic Ocean will likely increase with continued increases in ice drift velocities and a thinning ice pack (AMAP, 2011; IPCC, 2013; Rampal et al., 2011). The increase in younger FYI and refrozen leads will likely result in a general increase of ice algal biomass during the bloom period, the extent of which will depend on the spatial extent and regional variability of these features (Table 6).

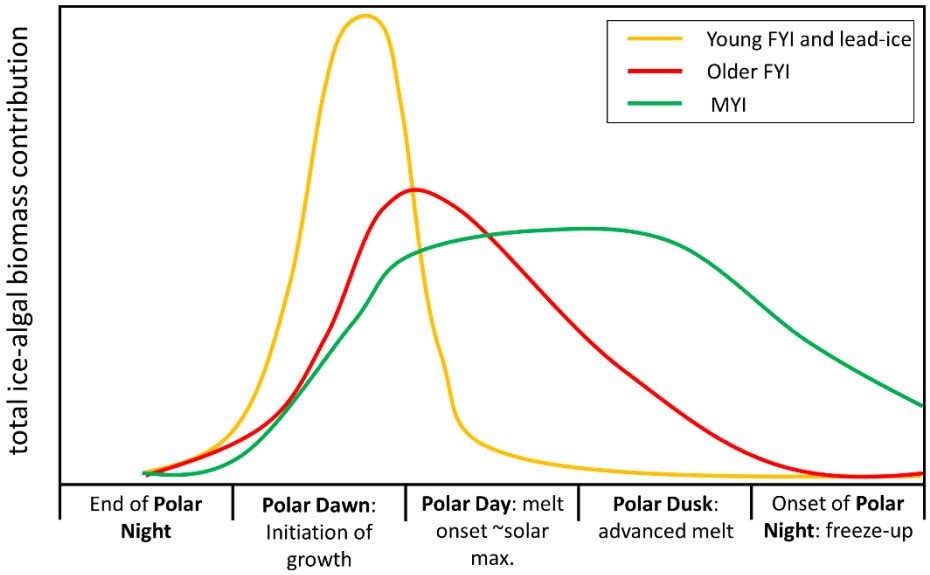

Figure 7. Conceptual progression of total ice-algal biomass (i.e., areally-averaged total biomass) over different seasonal stages (consistent with Figure 6) for the different ice types: young FYI and lead-ice; older FYI and MYI.

The expected higher bloom biomass of thinner FYI, however, may not result in a net in-crease in ice algal production over the entire growth season. During what may be called a "peak bloom" period it is less certain what is happening at the bottom of hummocks in comparison to adjacent thinner sea ice or FYI. One may expect that higher light conditions will induce higher primary production rates and thus higher biomass accumulations. This assumption although highly probable, is also likely short-lived, since the bloom period is typically terminated earlier under thinner sea ice with high light regimes due to photoinhibition (Campbell et al., 2015) and/or increased melt rates (Lavoie et al., 2005), shown in Figure 6 b, c, d and Figure 7. Hummocks and in some cases thicker ice, on the other hand, have a surface deteriorated layer present throughout the entire year, which enhances albedo and thus reduces light transmittance even when the snow (if present on hummocks) melts away (Grenfell & Maykut, 1977). This may maintain a stable and suitable light environment for algal growth during maximum solar radiation when photoinhibition is likely to occur (Figure 7). The hummock's bottom-ice biomass may also be able to persist through the advanced melt stage in late-summer due to the thicker ice, thus, resulting in stable and modest algal biomass levels through most of the growth season and into the initial stages of polar night (Figure 6 c, d, e;). This temporal progression of total ice-algal biomass in different seasonal stages for the different ice types is illustrated in Figure 7. In a future Arctic Ocean with thinner sea ice and a near-complete replacement of MYI by FYI, the presence of high biomass during advanced melt and into the onset of Polar Night is less likely due to enhanced melt. This may have important ecological implications, particularly in the high Arctic region where the growth season and available biomass is already severely limited (Table 6; Figure 6 and Figure 7).

Table 6. Possible future scenarios with predictions for changes in overall (areal) ice algal biomass in different seasonal stages and under different scenarios of snow and sea ice conditions.

Season	Scenario	Potential changes to Physical Sea Ice environment	Predicted outcome of overall sea ice algae biomass
Late-Summer "Polar-Dusk"	Su-0	Present situation: • MYI~FYI • Thick ice covering most of high latitudes	• High biomass at end of summer in high latitude, thick ice regions • Low biomass in thin ice regions of seasonal ice
	Su-1	• Thinner ice and increased melt	• Low to no biomass at the end of the year due to more extensive melt-induced algal losses
	Su-2	• Overall thinner ice and increased melt, but • Increased sea ice deformation • Larger areal coverage of ridges	• Increased biomass in regions, which at present are covered by FYI or seasonal ice • Decreased biomass for regions, which at present are covered by thick ice
	Su-3	• Almost zero sea ice in summer	• No biomass
Spring "Polar-Dawn"	Sp-0	Present situation: • MYI ~ FYI	• Biomass in: MYI ~ FYI < leads
	Sp-1	• Near-complete replacement of MYI by FYI • increased snow precipitation	• Biomass in: FYI < MYI < leads • Overall decrease in biomass, but leads may compensate if areal coverage increases
	Sp-2	• Near-complete replacement of MYI by FYI • decreased snow precipitation	• Biomass in: MYI < FYI < leads • Overall increase in biomass due to snow decrease
	Sp-3	• substantially larger areal coverage of new ice leads	• Overall biomass increase
	Sp-4	• increased sea ice deformation • larger areal coverage of ridges	• If snow increases, high biomass ridges could compensate for level ice biomass decline. • If snow decreases, more ridges may cause no change or a decrease in biomass

D 5.3 Outlook

Throughout this thesis we have addressed important issues in terms of sea ice algae distribution during different times of the year in a poorly understood region of the Arctic Ocean. Furthermore, we have identified some key questions that require further investigation in order to build upon our findings. We also developed essential tools to address these questions in future research projects.

The springtime ("Polar Dawn") use of the SUIT and ROV would substantially build upon and address some key questions from Chapter 4. In particular, the spatial-temporal variability of snow on FYI and MYI, and how this influences the light regime and growth of sea ice algae. Expeditions have already deployed the SUIT and ROV during spring ("Polar Dawn") north of Svalbard albeit from a region perhaps not representative of the CAO. The results should provide important first steps to understand these processes.

Furthermore, the identification of thick sea ice features as high ice-algal biomass regions warrants further investigations into the ecological implications of such features. Dedicated SUIT and ROV surveys should also provide more information on these features. In the past, these features were generally under-represented due to the difficulty in sampling thicker ice. Now that we know increased effort has high priority, this sampling bias should be avoided whenever possible. Specific sampling should investigate the distribution of snow around hummocks and ridges, and conduct detailed under-ice surveys of the light field and 3D under-ice topography in order to quantify 3D light scattering and the spatial variability of the under-ice light regime at these features. These results could then be

related to detailed biogeochemical samples (e.g., ice cores) from these features to assess the spatial variability of ice algae and relationship to the light regime.

During spring, access to the CAO and high Arctic regions by ice breaker is limited to low-latitude, peripheral regions with thinner sea ice. Therefore, land-based campaigns will continue to be the best way to access the CAO and the heart of the MYI covered Arctic during spring, particularly North of Canada and Greenland where the thickest sea ice in the Arctic is located (Haas et al., 2006; Haas et al., 2010). Although the SUIT cannot be deployed without a ship, deploying an ROV in addition to the standard set of field measurements (e.g., ice coring, snow ice thickness surveys) using snowmobiles or aircraft to access the MYI is a promising way to improve the spatial-temporal resolution of observations required to address some remaining key questions. These observations would then be combined with under-ice and pelagic fauna sampling to provide a comprehensive assessment of the ice-algal derived carbon budget during spring, as provided earlier in this Chapter.

Melnikov et al. (2002) demonstrated that the peak ice-algal bloom period was around the end of July within the southern extent of the CAO. This highlights the need to sample during the middle of the summer ("Polar Day") in order to capture the peak ice-algal biomass and production period and relate these to the under-ice and pelagic fauna ice-algal carbon demands.

The proposed hypothesis *that remnant ice-algal biomass in high latitude regions may represent a crucial food source to sustain ice associated organisms during the onset of polar night* is a time sensitive question that can only be addressed if observations are conducted soon before further environmental changes occur within the CAO. To test this hypothesis we would need a comprehensive field study beginning at the onset of Polar Night, on an ice floe of sufficient thickness to have remnant ice algal biomass. As many of the methodological approaches presented within this study would be limited in the absence of light we would need to develop or modify sampling strategies to assess the spatial-temporal variability of ice algae and its importance for under-ice and pelagic organisms during Polar Night.

Using the same methodologies and approaches presented throughout this thesis, in addition to new or modified approaches during Polar Night, specifically for the four identified sampling periods: 1) onset of Polar Dawn; 2) middle of Polar Day; 3) onset of Polar Dusk; and 4) onset of Polar Day, are essential steps to further our understanding of the annual ice-algal derived carbon budget and how it is likely to be modified with continued changes to the sea ice environment.

References:

AMAP, 2011. Snow,water, ice and permafrost in the Arctic (SWIPA): Climate change and the cryosphere. Gaustadalléen 21, N-0349 Oslo, Norway (www.amap.no).

Arrigo, K.R., van Dijken, G.L., 2015. Continued increases in Arctic Ocean primary production. *Progress in Oceanography*, 136, 60-70.

Berge, J., Renaud, P.E., Darnis, G., Cottier, F., Last, K., Gabrielsen, T.M., Johnsen, G., Seuthe, L., Weslawski, J.M., Leu, E., Moline, M., Nahrgang, J., Søreide, J.E., Varpe, Ø., Lønne, O.J., Daase, M., Falk-Petersen, S., 2015. In the dark: A review of ecosystem processes during the Arctic polar night. *Progress in Oceanography*, 139, 258-271.

Boetius, A., Albrecht, S., Bakker, K., Bienhold, C., Felden, J., Fernández-Méndez, M., Hendricks, S., Katlein, C., Lalande, C., Krumpen, T., Nicolaus, M., Peeken, I., Rabe, B., Rogacheva, A., Rybakova, E., Somavilla, R., Wenzhöfer, F., Party, R.P.A.-.-S.S., 2013. Export of Algal Biomass from the Melting Arctic Sea Ice. *Science*, 339, 1430-1432.

Budge, S.M., Wooller, M.J., Springer, A.M., Iverson, S.J., McRoy, C.P., Divoky, G.J., 2008. Tracing carbon flow in an arctic marine food web using fatty acid-stable isotope analysis. *Oecologia*, 157, 117-129.

Campbell, K., Mundy, C.J., Barber, D.G., Gosselin, M., 2014. Remote Estimates of Ice Algae Biomass and Their Response to Environmental Conditions during Spring Melt. *Arctic*, 67, 375.

Campbell, K., Mundy, C.J., Barber, D.G., Gosselin, M., 2015. Characterizing the sea ice algae chlorophyll a–snow depth relationship over Arctic spring melt using transmitted irradiance. *Journal of Marine Systems*, 147, 76-84.

Castellani, G., Losch, M., Lange, B.A., Flores, H., in prep. pan-Arctic sea ice algae model.

Cota, G.F., Smith, R.E.H., 1991. Ecology of bottom ice algae: II. Dynamics, distributions and productivity. *Journal of Marine Systems*, 2, 279-295.

David, C., Lange, B., Krumpen, T., Schaafsma, F., van Franeker, J.A., Flores, H., 2015a. Under-ice distribution of polar cod Boreogadus saida in the central Arctic Ocean and their association with sea-ice habitat properties. *Polar Biology*.

David, C., Lange, B., Rabe, B., Flores, H., 2015b. Community structure of under-ice fauna in the Eurasian central Arctic Ocean in relation to environmental properties of sea-ice habitats. *Marine Ecology Progress Series*, 522, 15-32.

David, C., Schaafsma, F.L., van Franeker, J.A., Lange, B., Brandt, A., Flores, H., 2016. Community structure of under-ice fauna in relation to winter sea-ice habitat properties from the Weddell Sea. *Polar Biology*.

Ehrlich, J., 2015. Diversity and distribution of high-Arctic zooplankton in the Eurasian Basin in late summer 2012., *Master thesis. Univ. of Hamburg.*

Fernández-Méndez, M., Katlein, C., Rabe, B., Nicolaus, M., Peeken, I., Bakker, K., Flores, H., Boetius, A., 2015. Photosynthetic production in the Central Arctic during the record sea-ice minimum in 2012. *Biogeosciences Discussions*, 12, 2897-2945.

Fetterer, F., Knowles, K., Meier, W., Savoie, M., 2002, udpated 2011. Sea Ice Index. Boulder, CO: National Snow and Ice Data Center. Digital Media.

Gosselin, M., Legendre, L., Therriault, J.-C., Demers, S., 1990. Light and nutrient limitation of sea-ice microalgae (Hudson Bay, Canadian Arctic). *Journal of Phycology*, 26, 220-232.

Gosselin, M., Legendre, L., Therriault, J.C., Demers, S., Rochet, M., 1986. Physical control of the horizontal patchiness of sea-ice microalgae. *Marine Ecology Progress Series*, 29, 289-298.

Gosselin, M., Levasseur, M., Wheeler, P.A., Horner, R.A., Booth, B.C., 1997. New measurements of phytoplankton and ice algal production in the Arctic Ocean. *Deep Sea Research Part II: Topical Studies in Oceanography*, 44, 1623-1644.

Gradinger, R., Bluhm, B., Iken, K., 2010. Arctic sea-ice ridges—Safe heavens for sea-ice fauna during periods of extreme ice melt? *Deep Sea Research Part II: Topical Studies in Oceanography*, 57, 86-95.

Grenfell, T.C., Maykut, G.A., 1977. The optical properties of ice and snow in the Arctic Basin. *Journal of Glaciology*, 18, 445-463.

Haas, C., Hendricks, S., Doble, M., 2006. Comparison of the sea-ice thickness distribution in the Lincoln Sea and adjacent Arctic Ocean in 2004 and 2005. *Annals of Glaciology*, 44, 247-252.

Haas, C., Hendricks, S., Eicken, H., Herber, A., 2010. Synoptic airborne thickness surveys reveal state of Arctic sea ice cover. *Geophysical Research Letters*, Vol. 37 (p. L09501).

IPCC, 2013. Climate Change 2013: The Physical Science Basis. Contribution of Working Group I to the Fifth Assessment Report of the Intergovernmental Panel on Climate Change. In T.F. Stocker, D. Qin, G.-K. Plattner, M. Tignor, S.K. Allen, J. Boschung, A. Nauels, Y. Xia, V. Bex and P.M. Midgley (eds.) (Ed.) (p. 1535). Cambridge, United Kingdom and New York, NY, USA.

Kohlbach, D., Graeve, M., Lange, B.A., David, C., Peeken, I., Flores, H., 2016. The importance of ice algae-produced carbon in the central Arctic Ocean ecosystem: food web relationships revealed by lipid and stable isotope analyses. *Limnol. Oceanogr*.

Kosobokova, K., 1982. Composition and distribution of the biomass of zooplankton in the central Arctic Basin. *Oceanology*, 22, 744-750.

Kosobokova, K., Hirche, H.-J., 2009. Biomass of zooplankton in the eastern Arctic Ocean – A base line study. *Progress in Oceanography*, 82, 265-280.

Lange, B.A., Katlein, C., Nicolaus, M., Peeken, I., Flores, H., in review. Spectrally-derived sea ice-algal chlorophyll a concentrations using under-ice horizontal profiling platforms. *Journal of Geophysical Research*.

Lange, B.A., Michel, C., Beckers, J.F., Casey, J.A., Flores, H., Hatam, I., Meisterhans, G., Niemi, A., Haas, C., 2015. Comparing springtime ice-algal chlorophyll a and physical properties of multi-year and first-year sea ice from the Lincoln Sea. *PLoS ONE*, 10, e0122418.

Lavoie, D., Denman, K., Michel, C., 2005. Modeling ice algal growth and decline in a seasonally ice-covered region of the Arctic (Resolute Passage, Canadian Archipelago). *Journal of Geophysical Research*, 110, C11009.

Lavoie, D., Denman, K.L., Macdonald, R.W., 2010. Effects of future climate change on primary productivity and export fluxes in the Beaufort Sea. *Journal of Geophysical Research C: Oceans*, 115.

Laxon, S., Peacock, N., Smith, D., 2003. High interannual variability of sea ice thickness in the Arctic region. *Nature*, 425, 947-950.

Leu, E., Mundy, C.J., Assmy, P., Campbell, K., Gabrielsen, T.M., Gosselin, M., Juul-Pedersen, T., Gradinger, R., 2015. Arctic spring awakening – Steering principles behind the phenology of vernal ice algal blooms. *Progress in Oceanography*, 139, 151-170.

Leu, E., Søreide, J.E., Hessen, D.O., Falk-Petersen, S., Berge, J., 2011. Consequences of changing sea-ice cover for primary and secondary producers in the European Arctic shelf seas: Timing, quantity, and quality. *Progress in Oceanography*, 90, 18-32.

Lindsay, R.W., Rothrock, D.A., 1995. Arctic sea ice leads from advanced very high resolution radiometer images. *Journal of Geophysical Research: Oceans*, 100, 4533-4544.

Maslanik, J.A., Stroeve, J.C., Fowler, C., Emery, W., 2011. Distribution and trends in Arctic sea ice age through spring 2011. *Geophysical Research Letters*, Vol. 38 (p. L13502).

Melbourne-Thomas, J., Meiners, K.M., Mundy, C.J., Schallenberg, C., Tattersall, K.L., Dieckmann, G.S., 2015. Algorithms to estimate Antarctic sea ice algal biomass from under-ice irradiance spectra at regional scales. *Marine Ecology Progress Series*, 536, 107-121.

Melnikov, I., 1997. *The Arctic Sea Ice Ecosystem*. Amsterdam: Gordon and Breach Science Publishers.

Melnikov, I.A., Kolosova, E.G., Welch, H.E., Zhitina, L.S., 2002. Sea ice biological communities and nutrient dynamics in the Canada Basin of the Arctic Ocean. *Deep Sea Research Part I: Oceanographic Research Papers*, 49, 1623-1649.

Michel, C., Legendre, L., Ingram, R.G., Gosselin, M., Levasseur, M., 1996. Carbon budget of sea-ice algae in spring: Evidence of a significant transfer to zooplankton grazers. *Journal of Geophysical Research: Oceans*, 101, 18345-18360.

Mundy, C.J., Ehn, J.K., Barber, D.G., Michel, C., 2007. Influence of snow cover and algae on the spectral dependence of transmitted irradiance through Arctic landfast first-year sea ice. *Journal of Geophysical Research*, 112, C03007.

Nicolaus, M., Katlein, C., Maslanik, J., Hendricks, S., 2012. Changes in Arctic sea ice result in increasing light transmittance and absorption. *Geophysical Research Letters*, 39, 2699–2700.

Olli, K., Wassmann, P., Reigstad, M., Ratkova, T.N., Arashkevich, E., Pasternak, A., Matrai, P.A., Knulst, J., Tranvik, L., Klais, R., Jacobsen, A., 2007. The fate of production in the central Arctic Ocean – top–down regulation by zooplankton expatriates? *Progress in Oceanography*, 72, 84-113.

Perovich, D.K., 1996. The Optical Properties of Sea Ice. Cold Regions Research and Engineering Laboratory.

Perovich, D.K., Grenfell, T.C., Richter-Menge, J.A., Light, B., Tucker III, W.B., Eicken, H., 2003. Thin and thinner: Sea ice mass balance measurements during SHEBA. *Journal of Geophysical Research*, Vol. 108 (p. 8050).

Rampal, P., Weiss, J., Dubois, C., Campin, J.M., 2011. IPCC climate models do not capture Arctic sea ice drift acceleration: Consequences in terms of projected sea ice thinning and decline. *Journal of Geophysical Research*, 116, C00D07.

Roca-Martí, M., Puigcorbé, V., Rutgers van der Loeff, M.M., Katlein, C., Fernández-Méndez, M., Peeken, I., Masqué, P., 2016. Carbon export fluxes and export efficiency in the central Arctic during the record sea-ice minimum in 2012: a joint 234Th/238U and 210Po/210Pb study. *Journal of Geophysical Research: Oceans*, 121, 5030-5049.

Søreide, J.E., Leu, E.V.A., Berge, J., Graeve, M., Falk-Petersen, S., 2010. Timing of blooms, algal food quality and Calanus glacialis reproduction and growth in a changing Arctic. *Global Change Biology*, Vol. 16 (pp. 3154–3163).

Spreen, G., Kaleschke, L., Heygster, G., 2008. Sea ice remote sensing using AMSR-E 89-GHz channels. *Journal of Geophysical Research*, 113, C02S03.

Sturm, M., Holmgren, J., Perovich, D.K., 2002. Winter snow cover on the sea ice of the Arctic Ocean at the Surface Heat Budget of the Arctic Ocean (SHEBA): Temporal evolution and spatial variability. *Journal of Geophysical Research*, Vol. 107 (p. 8047).

Wang, S.W., Budge, S.M., Iken, K., Gradinger, R.R., Springer, A.M., Wooller, M.J., 2015. Importance of sympagic production to Bering Sea zooplankton as revealed from fatty acid-carbon stable isotope analyses. *Marine Ecology Progress Series*, 518, 31-50.

Wang, S.W., Springer, A.M., Budge, S.M., Horstmann, L., Quakenbush, L.T., Wooller, M.J., 2016. Carbon sources and trophic relationships of ice seals during recent environmental shifts in the Bering Sea. *Ecological Applications*, 26, 830-845.

Werner, I., 1997. Grazing of Arctic under-ice amphipods on sea-ice algae. *Marine Ecology Progress Series*, Vol. 160 (pp. 93-99).

Zhang, Q., Gradinger, R., Spindler, M., 1998. Dark survival of marine microalgae in the high Arctic (Greenland Sea). *Polarforschung*, 65, 111-116.

Contributing Authors

Justin F. Beckers

Department of Earth and Atmospheric Sciences
University of Alberta
Edmonton, Alberta, Canada

Anne Bublitz

Department of Earth and Space Sciences and Engineering
York University
Toronto, Ontario, Canada

J. Alec Casey

Department of Earth and Atmospheric Sciences
University of Alberta
Edmonton, Alberta, Canada
and
Department of Earth and Space Sciences and Engineering
York University
Toronto, Ontario, Canada

Giulia Castellani

Department of Polar Biological Oceanography
Alfred Wegener Institute Helmholtz Centre for Polar and Marine Research
Bremerhaven, Germany

Carmen David

Department of Polar Biological Oceanography
Alfred Wegener Institute Helmholtz Centre for Polar and Marine Research
Bremerhaven, Germany
and
University of Hamburg
Zoological Institute and Zoological Museum, Biocenter Grindel
Hamburg, Germany

Mar Fernández-Méndez

Department of Polar Biological Oceanography
Alfred Wegener Institute Helmholtz Centre for Polar and Marine Research
Bremerhaven, Germany
and
Norwegian Polar Institute
Fram Centre
Tromsø, Norway

Hauke Flores

Department of Polar Biological Oceanography
Alfred Wegener Institute Helmholtz Centre for Polar and Marine Research
Bremerhaven, Germany
and
University of Hamburg
Zoological Institute and Zoological Museum, Biocenter Grindel
Hamburg, Germany

Martin Graeve

Department of Ecological Chemistry
Alfred Wegener Institute Helmholtz Centre for Polar and Marine Research
Bremerhaven, Germany

Christian Haas

Department of Earth and Atmospheric Sciences
University of Alberta
Edmonton, Alberta, Canada
and
Department of Earth and Space Sciences and Engineering
York University
Toronto, Ontario, Canada
and
Department of Sea Ice Physics
Alfred Wegener Institute Helmholtz Centre for Polar and Marine Research
Bremerhaven, Germany

Ido Hatam

Department of Biological Sciences
University of Alberta
Edmonton, Alberta, Canada
and
Department of Chemical and Biological Engineering
University of British Columbia
Vancouver, British Columbia, Canada

Christian Katlein

Department of Sea Ice Physics
Alfred Wegener Institute Helmholtz Centre for Polar and Marine Research
Bremerhaven, Germany

Guillaume Meisterhans

Freshwater Institute
Fisheries and Oceans Canada
Winnipeg, Manitoba, Canada

Christine Michel

Freshwater Institute
Fisheries and Oceans Canada
Winnipeg, Manitoba, Canada

Marcel Nicolaus

Department of Sea Ice Physics
Alfred Wegener Institute Helmholtz Centre for Polar and Marine Research
Bremerhaven, Germany

Andrea Niemi

Freshwater Institute
Fisheries and Oceans Canada
Winnipeg, Manitoba, Canada

Ilka Peeken

Department of Polar Biological Oceanography
Alfred Wegener Institute Helmholtz Centre for Polar and Marine Research
Bremerhaven, Germany
and
MARUM Center for Marine Environmental Sciences
University of Bremen
Bremen, Germany

Benjamin Rabe

Department of Physical Oceanography of the Polar Seas
Alfred Wegener Institute Helmholtz Centre for Polar and Marine Research
Bremerhaven, Germany

Anke Reppchen

Freshwater Institute
Fisheries and Oceans Canada
Winnipeg, Manitoba, Canada
Svenja Rudolph

Institute of Geography
University of Erlangen-Nuremberg
Erlangen, Germany

Jan Andries van Franeker

Institute for Marine Research and Ecosystem Studies
Wageningen UR (IMARES)
AG Den Helder, The Netherlands

Acknowledgements

I would like to graciously thank my supervisor, Dr. Hauke Flores, for providing me with this wonderful opportunity to develop a unique set of skills, in such an interesting field of research, and in such a fascinating region of the world. I appreciate all of your support and inspiration. I am also very grateful for your understanding and flexibility in regards to having and raising a child within the timeframe of my PhD project.

I would like to thank my supervisor Prof. Dr. Angelika Brandt for her continued support and stimulating conversations, and the time commitment to review and comment on my written thesis.

I am grateful to my POLMAR committee members Dr. Marcel Nicolaus, Dr. Ilka Peeken, and Dr. Christian Katlein for their active involvement in committee meeting throughout my PhD.

I would not have been able to move to Germany and conduct all of the field research required for this PhD project without the support from many groups and individuals. The AWI administrative support staff supported easy transition of international employees, in addition to maintaining a good working environment. The additional support provided by AWI for families was very helpful with the new addition to my family during my PhD. AWI's logitstical support staff, and the captain and crew of the *RV Polarstern* cruise PS80 to the central Arctic Ocean. Jim Milne, Al Tremblay, the PCSP logistical support team, and the Kenn Borek pilots ensured safe and reliable lodging and transport throughout many field campaigns to the Canadian Arctic.

The guidance and excellent professional development provided by the graduate school program POLMAR really made my PhD experience much better than I could have expected. The POLMAR courses and workshops were essential to develop the skills I needed to accomplish my research. Special thanks to Dr. Claudia Hanfland and Dr. Claudia Sprengel for coordinating this amazing program and for the many one-on-one information sessions.

I would like to thank all of the many friends I met during my PhD journey; you all made my PhD a fun and memorable experience.

A special thanks to Chad for moving all the way to Europe just to keep me company.

To all my friends, particularly Chad, Ken, Adam, Kurt and Dennis who have always encouraged been there for me.

From the bottom of my heart, I would like to thank my mom, dad, brother and sister. You have all always been there for me from day one. You always showed support and interest in all the different paths I have taken throughout my life. I would not have found my way here without you all.

Gramma/Gigi, your multiple visits to Germany are among the highlights of my PhD time. I also appreciate all of your support throughout all stages of my life and education life. Your fitness is an inspiration to us all.

Last but not least, my love Doreen, you have supported me through thick and thin, and grounded me when I was floating away. I cannot forget that you provided me with the greatest gift of all, Jari.

Appendix A:

A 1. SUIT sensory array deployment and processing protocols

Laptop:

1. You will want to connect to the network and setup the computer to automatically connect to network drives upon startup (there is a tutorial for this on the ship site)
2. You will also want to sync the computer time to the ship time (the instructions for this are also available on the ship website).

A 1.1 Sensor array pre- and post-deployment

Sensor PC ready!

USB-serial adapter ready and connected!

A 1.1.1 Aquadopp-ADCP (2nd priority to remove, download and/or turn off)

- Connect sensor via USB-serial adapter
- Launch Software package (AquaPro)
- Communication -> Connect
- Check battery and memory capacity by online measurement
- Load settings from standard deployment file
  - ➔ 2 MHZ
  - ➔ 4 cells, cell size 0.3 m
  - ➔ Blanking: 0.2 m
  - ➔ Measurement interval 1 s
- Start measurement. Aquadopp can run up to 1 hour before deployment.
- Mount protection cap on data-plug!
- Mount Aquadopp in SUIT protection case

A 1.1.2 CTD

- Every once in a while apply some silicon (in a tube in the CTD box) to the O-rings in the CTD probe lid (what you open to get to the batteries).
- At first operation make sure there are batteries in the unit. Use allen keys in the CTD box to open and add batteries 8 x ‘c’-cell batteries.
- After several operations check the batteries status. In the data file there is a column with the battery Voltage, if it drops under ~10 then change the batteries!
- Connect Sensor via provided serial cable (USB should work but during testing the USB did not work so we used the serial cable).
- Launch Software (SST) SDA:
  - ➔ Go to File
  - ➔ Modify and Load Project
  - ➔ Load “ARK27-3_SUIT.srj” for suit hauls and “ARK27-3_icefloe.srj” depending on where you are deploying the CTD
  - ➔ Next it will ask you to select a profile: Go to-> Arbeitplatz-> C drive -> sst_sda-> config-> select the “CTM689.prb” file
  - ➔ Select COM port 1

- Options:
  - ➔ MemoryProbe
  - ➔ CTM689
  - ➔ Start Communications
  - ➔ close
- **Calibrate** (Kalibrierung with German operating system) do this every time before you deploy so the CTD resets pressure to zero)
  - ➔ Air pressure compensation (Luftdruck Kompensation)
  - ➔ Make sure to turn the probe on with the magnet…wait until data starts showing in the window and then click "Now" check that the pressure column (far left column) is zeroed.
  - ➔ Save and Exit

  - ➔ Options->MemoryProbe->CTM689
  - ➔ Start Communications
  - ➔ Last configuration-> Continuous Mode
  - ➔ click "Configure Continuous Mode"
  - ➔ click "OK, send config to probe" (the status bar will not be complete at the top)
  - ➔ click activate and switch off probe
- The probe is now in sleep mode until activation with magnetic stick.
- Mount protection cap on data plug!

*****MAKE SURE THE CAP IS REMOVED FROM <u>THE FLUOROMETER</u>******

- When the CTD is loaded into the SUIT and you are ready to fish turn on with the magnet….the red light should turn on as a red solid light then after a few seconds will change to a **really fast blinking light (this is important because it tells you that it is working properly).**
- Shortly before SUIT launch, activate probe and mount in SUIT protection case
- Connect altimeter.

Retrieving Data:

- ➔ Options->MemoryProbe->CTM689
  - ➔ Start Communications
  - ➔ Read Out data
- ➔ Save in a folder with appropriate name and use automatic enumeration for multiple files
  - ➔ Header information is not crucial, this can be ignored. Close the header window if it opens.
  - ➔ Close the window
  - ➔ At question whether to start loggin again at reopen say **NO**
- ➔ Options-> Export Data
  - ➔ click "close", save the file, then
  - ➔ select Dataset rate "everyone" (make sure that the time is in ms)
  - ➔ Ok, show
  - ➔ Save file as .CSV (there usually will be multiple files so make sure to always keep the raw data as well as exported data). Naming "PS*cruisenumber*CTD*haulenumber*.CSV"

***Make sure to export all the data

***Make sure that the cap of the altimeter connection is clean!!!

- To make the probe ready for the next haul (but we need to make the pressure compensation before every measurement, so I would suggest to make the following procedure only if the SUIT will go in the water really soon):

Menu Extras (Zusätze)

- ➔ Memory probe (Speichersonde) –> CTM 689
- ➔ Start communication (Beginne Kommunikation)
  - Check: Memory, battery status
- ➔ Chose: Previous configuration (Letzte Konfiguration): Contin. Mode
- ➔ Chose: OK, Transmit to probe (OK, zur Sonde übertragen)
- ➔ Chose: Re-launch probe (Sonde neu starten)

- The probe is now in sleep mode until activation with magnetic stick.
- Mount protection cap on data plug!
- Shortly before SUIT launch, activate probe and mount in SUIT protection case
- Connect altimeter.

A 1.1.3 RAMSES (this should be the <u>first priority</u> to remove from SUIT)

Essential: Two RAMSES sensors must operate simultaneously during SUIT hauls (Radiance-cylindrical tip and Irradiance-conical tip)

- **Datalogger**: make sure battery is plugged in (mostly important for first time use)
  - Battery pack should have more than <u>~7.5 v</u> with nothing plugged in (this is not clear though so be careful)
- It is a good idea to keep the battery unplugged in order to avoid useless data acquiring that would simply consume the batteries.

1. Plug-in the battery of the DataLogger
2. Connect **<u>PS101</u>** to PC and Power, switch on
3. Open MSDA_XE (if not already open) should be on the desktop. Close all the windows that open automatically and leave open only the Device Manager window.
4. Connect RAMSES sensors (irradiance-conical and radiance-cylindrical) to the datalogger
5. Connect Datalogger to PS101. This should be the last step
6. Program SUIT sensors:
   a. If Device manager window not open go to Devices->Device Manager
   b. If Devices do not show up press “Scan” in top right of Device Manager window
   c. The devices should show up in COM1 and there should be the datalogger “DSP_E03A” and under that there should be the two RAMSES sensors (may have different IDs depending on the sensor used) Irrad sensor should be SAMIP_5080 (SAM_83D1)

IMPORTANT: it could happen that in the device manager window only the DataLogger is visible and not the sensor. In this case disconnect all, unplug the battery of the DataLogger and redo all the steps from 1 to 5 in the exact order as it is written. (So far I could not find a better solution to this problem)

d. Note: You need to import the calibration files "*.ini" if you are using a new sensor that has not been used before (see manual in Help, chapter 2.2 "How to import device files") you may have to ask physics group for the calibration files and put them in the "config" folder on the desktop. Other config files are on the desktop in "ANT29_6-9_Software->RAMSES->RAMSES_config". When installing the config files you need to import the 3 "*.dat" files for each sensor from the Database->Import Device. Then you need to go to the Device Manager window and click "import" and select the "*.ini" files for the devices you need.
e. Highlight DSP_E03A and click Control
f. New window will appear, click the advanced tab.
g. Click "sync with PC"
h. Click "consumption" to see how much data is on the datalogger or you can also use this function to test if the sensor it taking measurements.
i. If you are certain the data has been downloaded then you can "erase" from the datalogger
j. The "Logging Active" tab should have a green circle and the Mode-"Profiling" tab should also have a green circle.
k. Press the "Prepare autarchic usage"
l. Data Logger configuration window will appear….press Ok to continue
m. The "Run" tab at the top of the window should now have a green circle
n. Now you can disconnect the PS101 from the datalogger and put the water cap on the datalogger plug. Now you are good to go. (Keep the sensors attached to the DataLogger)

7. Post-Haul
    a. You can disconnect the sensors from the datalogger directly after the haul but remember that the datalogger is still using power until you connect and turn it off.
    b. Connect the datalogger to the PS101 (the sensors do not need to be plugged into the datalogger to download the data)
    c. You want to press the "scan" tab in either the Device Manager window or the Control window (wait for the system to recognize the datalogger because this can take a minute or so).
    d. In the control window go to the "Import" tab (Press "import" from the control run and not from the Devide manager window)
    e. Name the file by clicking the "…" tab beside the "File" name (Naming PS*cruisenumber*RAM*haulnumber*_logger.dat)
    f. Click "Read logger data and store in file" tab and wait for it to read all measurements…this can take a long time depending on the length of the haul
    g. Now click "Read file and import into database"…this also takes quite a long time
    h. Go into the Database table by clicking Database->Data in the main window dropdown menu
    i. The data will be at the end of the table and you can usually search by date/time to highlight only the data from the most recent haul.
    j. To highlight the data select the last record in the table by clicking the square to the left of the entry then scroll up to the first entry of the haul (you can tell this by the date/time) hold the select button and press the square at the left of the first entry this should highlight all entries for that haul in pink.
    k. At the bottom of the table click the "Comments.." tab (this may take a minute)

l. Now fill in the first field (C0) with the haul identifier e.g. “PS80RAM13” (this will take a minute for all of the fields to be filled in).
m. Make sure the data from the haul are still highlighted and click the disk with red arrow icon “export selected data to file” (Naming PS*cruisenumber*RAM*haulnumber*.dat)
n. Make sure at the top the “TriOS Format” tab is selected and the “Single” tab on the left is selected then click the “…” tab beside the filename and you probably want to save this on the network or on the laptop and on the network, using the same filename as before e.g. “PS80RAM13” (PS## is the polarstern cruise, RAM is for RAMSES and 13 is the haul number).
o. To ensure minimal power usage make sure to unplug the battery in the datalogger after you are finished downloading the data (this is done because on the previous cruise there was some unexpected datalogger acquisitions and power consumption even when it was thought to be turned off).
p. Now you can calibrate the data (follow pg. 37 of the Manual)

A 1.1.4 GoPro

- Check battery and memory
- Mount camera in protective housing on SUIT frame
- Shortly before launch: Press “rec” button

A 1.1.5 Sensor Recovery

Recover sensors:

- Aquadopp-ADCP
- CTD (switch off with magnetic rod)
- RAMSES (SUIT sensor + DSP logger + ship sensor + RAMSES-PC and PS101)
- Camera (rinse while in water-proof case)
- rinse all sensors immediately after haul then dry with towel and store safely in drylab before further processing

Sensor Checklist:

Aquadopp-ADCP

- Clean sensor
- Connect to sensor-pc via usb-serial adapter
- Download data
- Check battery status – if necessary, change batteries (when down to ca. 9 v)
- Check memory – if necessary, erase memory
- Convert data and save as .csv files
- Prepare for next measurement
- Disconnect sensor
- Store safely in case
- Copy data on external hard disk and on ship’s network server

CTD

- Clean CTD
- Connect to sensor-pc via usb-cable
- Download data
- Check battery status – if necessary, change batteries
- Check memory – if necessary, erase memory
- Prepare for next measurement
- Disconnect sensor

- Store safely in case, or mount back in SUIT protection case for next use
- Copy data on external hard disk and on ship's network server

RAMSES

- Clean all parts
- Consecutively connect SUIT and ship sensors to PS101 and download data
- Check memory – if necessary, erase memory
- Prepare for next measurement
- Store safely in case, or mount SUIT sensor and ISP back in SUIT protection case for next use
- Copy data on external hard disk and on ship's network server

GoPro Video camera

- Open Camera housing and check for leakages
- Bring Camera to drylab
- Download video files from sd card
- Prepare for next measurement
- Mount back in SUIT protection case
- Copy data on external hard disk and on ship's network server

A 1.2 Data preparation for processing scripts

A 1.2.1 Pressure correction

- This should be done first because then you can implement the offset when you import the data by setting "press.offset" = TRUE or FALSE accordingly.
- This needs to be done manually because you need to look at the profiles and select the range of values you want to use to average the pressure values for the offset. This is done because before and after the haul the sensors are on the deck for different periods of time and therefore the length at the start and at the end of the hauls are different.
- A look at the profiles at this stage is also good to check the quality of the data and if there appears to be anything wrong with it.
- The CTD data should be pretty good with very small correction values but if you did not calibrate to the atmospheric pressure before your haul then this calibration becomes more important.
- Look into the R script and you must load each file separately and look at the profile then select the range before it is in the water, usually about 100 points on both sides, but keep the number the same before and after (e.g. n = 100 before in water and n =100 after in water).
- With the ADCP the pressure correction is more important because there appears to be some drift in the pressure values during the haul. There usually is some discrepancy between the before and after pressure means but for these purposes the mean offset from the two (before and after) should be adequate.
- You may have to change the sep = "," or sep = ";" when loading the different .csv files. The other scripts change this automatically but here it doesn't.
- Also you must be careful with the column names because if for some reason one of the files has a different number of columns then the plotting will look different. These values are loaded into an "offsets" dataframe which are then exported into a .txt file into the main directory after for use with the main scripts.

A 1.2.2 Importing Data

- Make sure all data are in ".csv" file formats and you do not manipulate them after they have been exported from the sensor or sensor software into the ".csv" format
- When exporting data make sure to use ";" or "," as column delimiters
- Name files with the following convention **"PS80CTD01.csv"**
    - "PS80" refers to the cruise number

  - "CTD" refers to sensor (ADP = ADCP, RAM = Ramses) use only 3 letters for the sensor
  - "01" is the haul number. Make sure to use the "0" in front of the single digit hauls from 1-9. This is important for keeping sequence in the naming and how the script processes the data
- Briefly take a look at the files or a few of the files and compare to the template files for each sensor provided.
- CTD data:
  - Count the number of rows to skip in the csv files and if it is not equal to 30 you must change this value in the "import_CTD.R" file
- Create a **cruise summary file** with a **minimum** of the following columns:
  - You must provide the name of this file in one of the first lines of the R script.
  - **Haul numbers**: consecutive numbering even if a haul is not included keep all integers between "Haul 1" and "Haul n"
  - Haul **Start time** column name **"start"** format **"hh:mm"** 24 hour clock, no seconds (this is important for subsetting based on time as there could be formatting issues)
  - Haul **End time** column name **"end"** format **"hh:mm"** 24 hour clock, no seconds (this is important for subsetting based on time as there could be formatting issues)

- GPS or others files: you have an issue when you are importing and there is an error ": argument if of length zero" this might mean that you have empty cells or rows at the end of the .csv file that are NAs. You must go into the .csv file and delete these rows and try again.
- Also, with the GPS data if you have consecutive lat and lon values that are the same you might get some error values when calculating distances so you should check the .csv file and correct this manually if you can.
- GPS files: there might be an instance where the lat and lon are incorrectly represented (e.g. 0.0000825 but should be 82.5 degrees) watch for this in the .csv files

A 2. Supplementary Material for Chapter 2 - Paper 1: The Surface and Under-Ice Trawl (SUIT)-mounted environmental sensor array

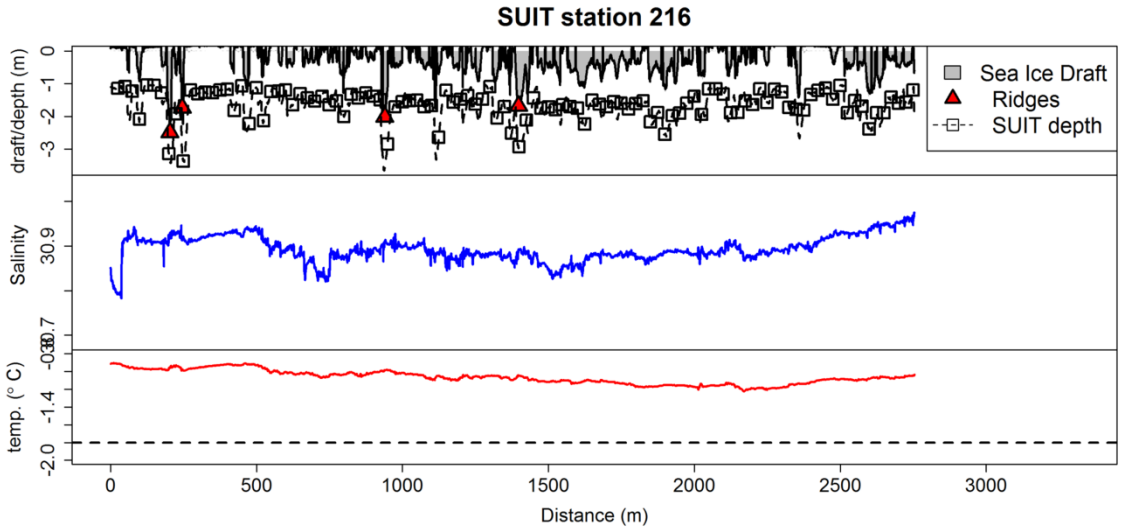

A1- 1: Surface and under ice trawl (SUIT) sensory array profile for SUIT station 216 conducted during *RV Polarstern* cruise PS80.3 showing sea ice properties, salinity and temperature (dashed line represents typical freezing point of ~-1.8ºC).

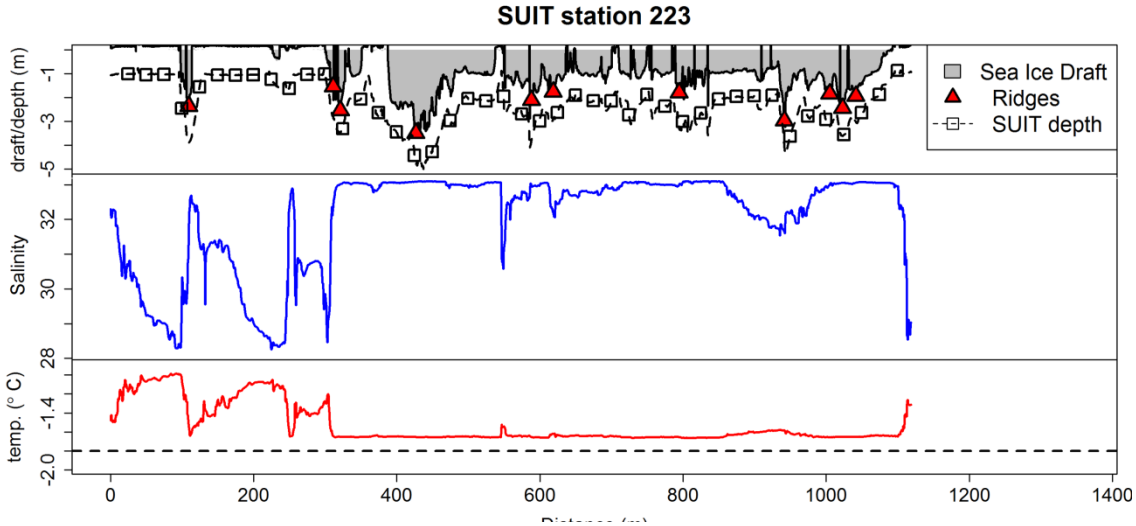

A1- 2: Surface and under ice trawl (SUIT) sensory array profile for SUIT station 223 conducted during *RV Polarstern* cruise PS80.3 showing sea ice properties, salinity and temperature(dashed line represents typical freezing point of ~-1.8ºC).

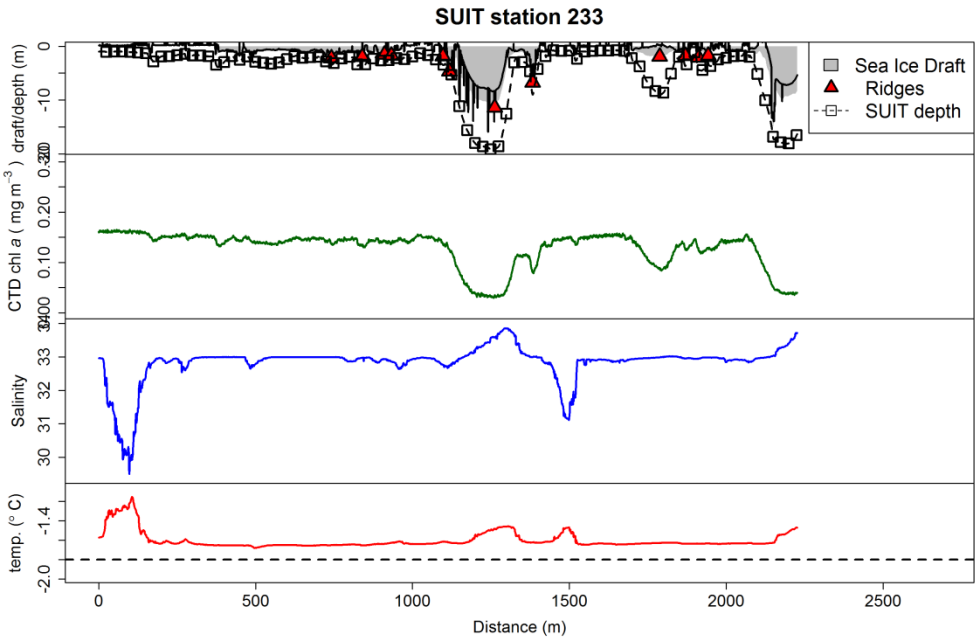

A1- 3: Surface and under ice trawl (SUIT) sensory array profile for SUIT station 233 conducted during *RV Polarstern* cruise PS80.3 showing sea ice properties, surface water chl *a*, salinity and temperature (dashed line represents typical freezing point of ~-1.8ºC).

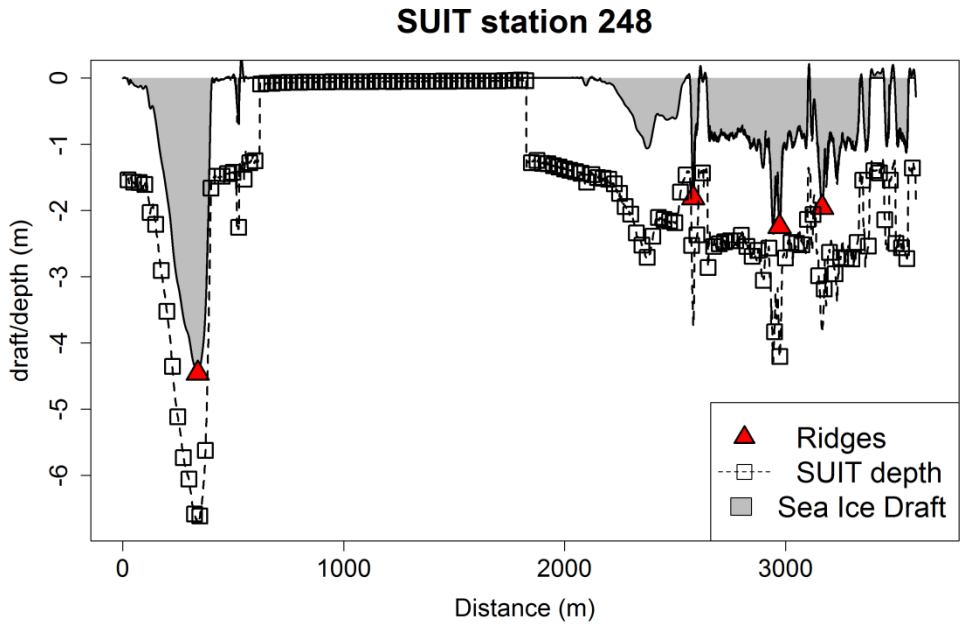

A1- 4: Surface and under ice trawl (SUIT) sensory array profile for SUIT station 248 conducted during *RV Polarstern* cruise PS80.3 showing only ADCP-derived sea ice properties because CTD data were not valid.

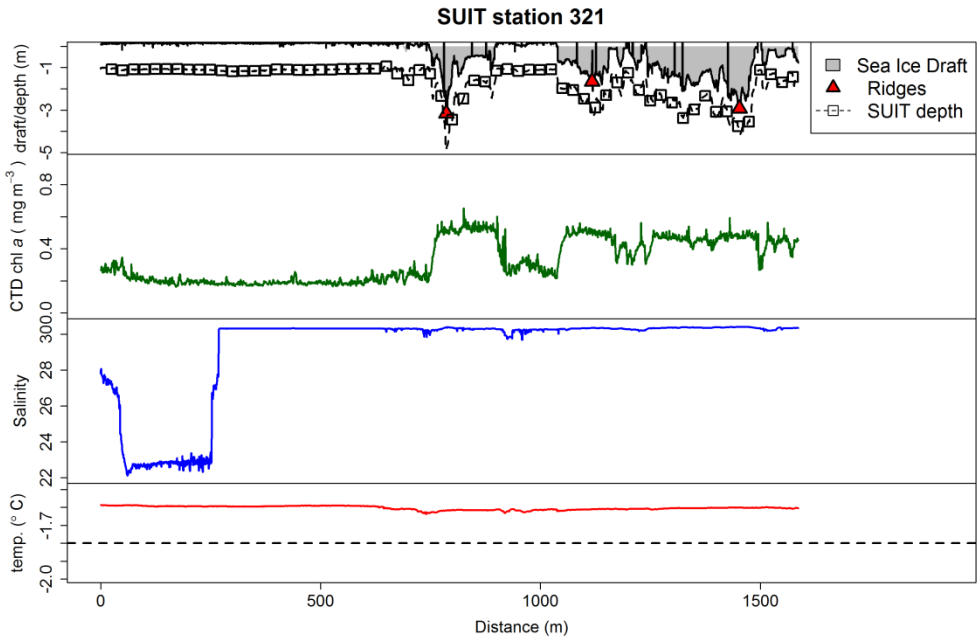

A1- 5: Surface and under ice trawl (SUIT) sensory array profile for SUIT station 321 conducted during *RV Polarstern* cruise PS80.3 showing sea ice properties, surface water chl *a*, salinity and temperature (dashed line represents typical freezing point of ~-1.8ºC).

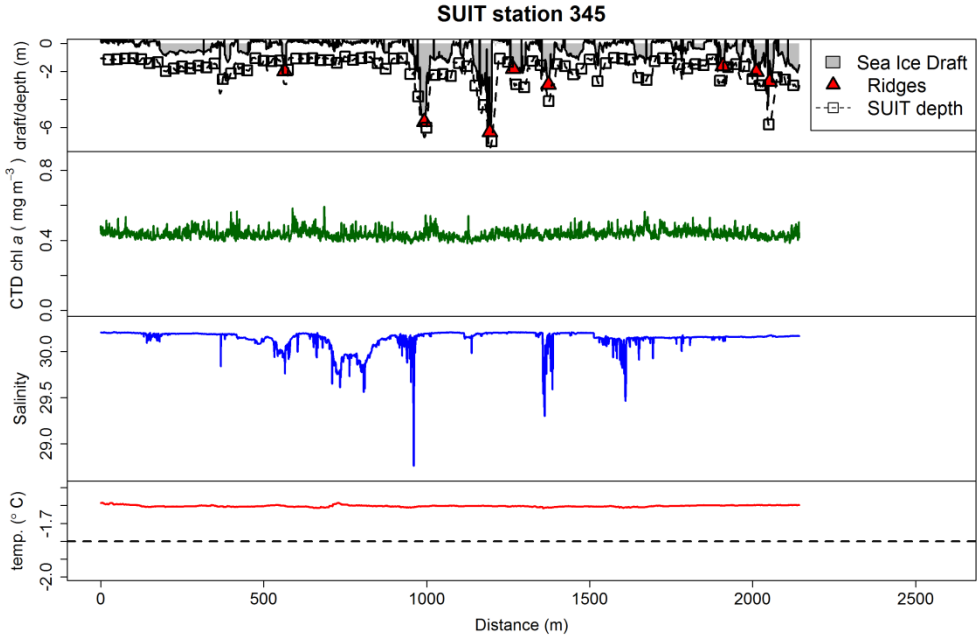

A1- 6: Surface and under ice trawl (SUIT) sensory array profile for SUIT station 345 conducted during *RV Polarstern* cruise PS80.3 showing sea ice properties, surface water chl *a*, salinity and temperature (dashed line represents typical freezing point of ~-1.8ºC).

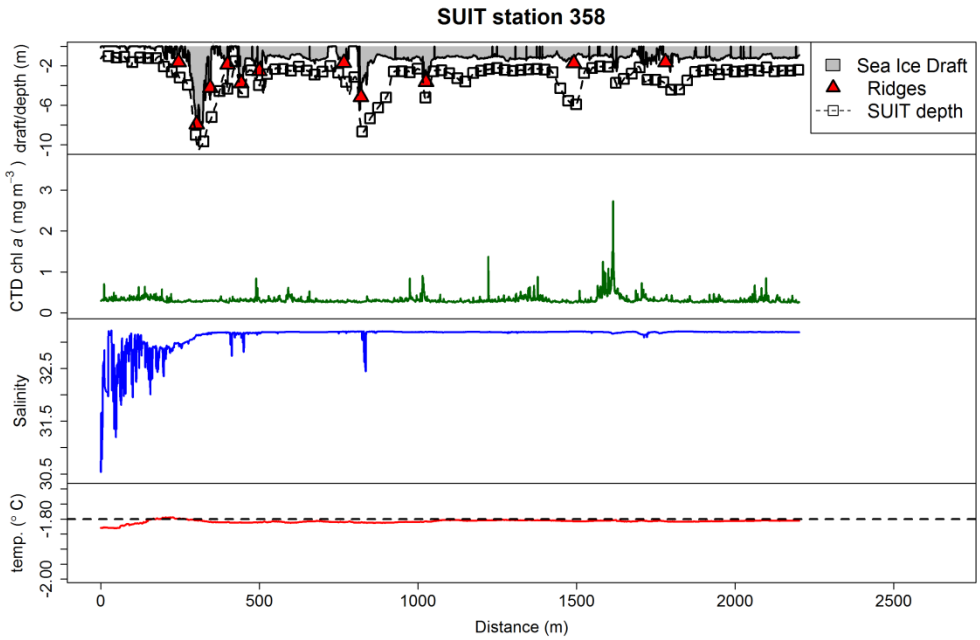

A1- 7: Surface and under ice trawl (SUIT) sensory array profile for SUIT station 358 conducted during *RV Polarstern* cruise PS80.3 showing sea ice properties, surface water chl *a*, salinity and temperature (dashed line represents typical freezing point of ~-1.8ºC).

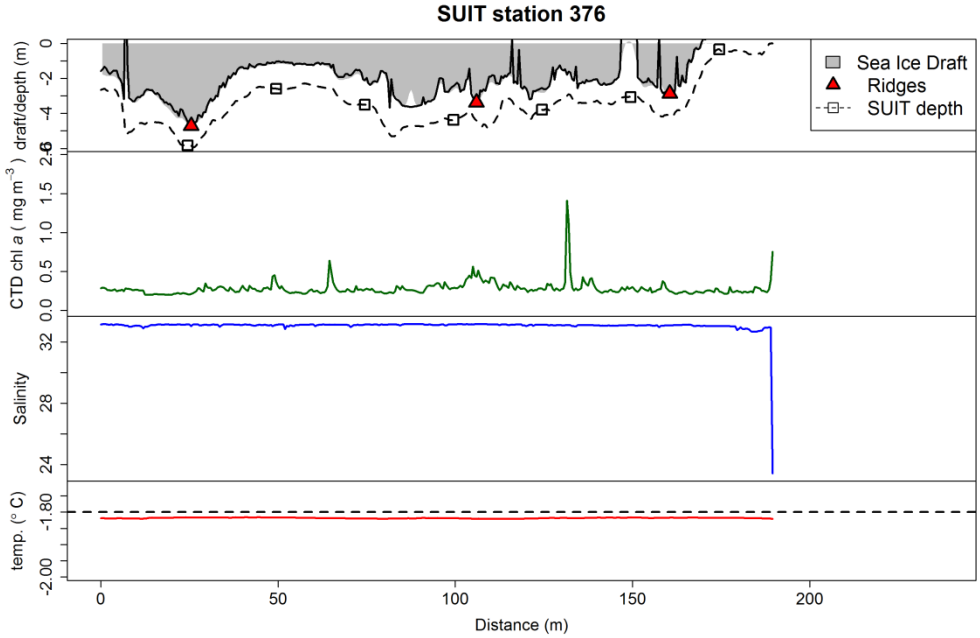

A1- 8: Surface and under ice trawl (SUIT) sensory array profile for SUIT station 376 conducted during *RV Polarstern* cruise PS80.3 showing sea ice properties, surface water chl *a*, salinity and temperature (dashed line represents typical freezing point of ~-1.8ºC).

A 3. Supplementary Material for Chapter 2 – Paper 2: Spectrally-derived sea ice-algal chlorophyll a concentrations using under-ice horizontal profiling platforms

Table S1. Overview of ice cores and coincident spectral measurements during PS78 and PS80. "Type" corresponds to the platforms used to take the spectral measurement (L-arm or ROV). "Pond" refers to if the measuremets was conducted at a melt pond (1) or not a melt pond (0; i.e., bare ice). "X" and "Y" are positions given in a floe fixed coordinate system relative to the ship's GPS receiver. "Irrad" refers to irradiance and "Rad" refers to radiance measurement conducted at the location (Yes or No). "NA" means no data are available for that location. (Table is on the following two pages).

Appendix A-3

Cruise/ Station	Date	Core-Name	Chl *a* (mg m^{-2})	Core Length (m)	Ice Thickness (m)	Snow (m)	Scattering layer (m)	Freeboard (m)	Type	Pond	X	Y	Irrad	Rad
PS78/196	11-Aug-11	110811OPT1	0.17	0.9	1.52	0	0.05	0.22	L-arm	0	-	-	yes	no
PS78/203	14-Aug-11	110814OPT1	0.05	0.05	NA	NA	NA	NA	L-arm	0	-	-	no	no
PS78/212	19-Aug-11	110819OPT1	0.6	1.04	NA	NA	NA	NA	L-arm	0	-	-	no	no
PS78/212	19-Aug-11	110819OPT2	0.83	1.04	NA	NA	NA	NA	L-arm	0	-	-	yes	no
PS78/212	19-Aug-11	110819OPT3	0.3	0.7	NA	NA	NA	NA	L-arm	1	-	-	yes	no
PS78/227	29-Aug-11	110829OPT1	0.08	1.42	1.42	0	0.04	0.1	L-arm	0	-	-	yes	yes
PS78/227	29-Aug-11	110829OPT2	0.08	0.8	0.8	0.001	0	-0.43	L-arm	1	-	-	yes	yes
PS78/227	29-Aug-11	110829OPT3	0.39	3.53	3.53	0	0.03	0.2	L-arm	0	-	-	yes	yes
PS78/238	6-Sep-11	110906OPT1	0.1	0.73	NA	NA	NA	NA	ROV	0	-	-	yes	no
PS78/238	6-Sep-11	110906OPT2	0.49	2.07	NA	NA	NA	NA	ROV	0	-	-	yes	no
PS78/238	6-Sep-11	110906OPT3	0.62	2.13	NA	NA	NA	NA	L-arm	0	-	-	yes	no
PS78/245	8-Sep-11	110908OPT1	0.01	0.11	0.29	NA	NA	NA	ROV	0	-	-	no	no
PS78/245	8-Sep-11	110908OPT2	0.32	1.18	NA	NA	NA	NA	ROV	0	-	-	yes	yes
PS78/245	8-Sep-11	110908OPT3	0.19	1.18	NA	NA	NA	NA	L-arm	0	-	-	yes	no
PS80/224	9-Aug-12	CORE-OPT-1	0.63	NA	1.7	0	0.5	0.28	ROV	0	10.3	183.5	no	yes
PS80/224	9-Aug-12	CORE-OPT-2	0.36	NA	1.11	0	0	-0.26	ROV	1	12.7	180.3	no	yes
PS80/224	10-Aug-12	CORE-OPT-1	0.75	1.12	1.08	0	0.04	0.12	ROV	0	111.7	199.6	no	yes
PS80/224	10-Aug-12	CORE-OPT-2	0.21	0.925	0.94	0	0.04	0.09	ROV	0	101.6	203.2	no	yes
PS80/224	10-Aug-12	CORE-OPT-3	0.33	0.865	0.92	0	0.06	0.17	ROV	0	73.2	212.8	no	yes
PS80/224	10-Aug-12	CORE-OPT-4	0.42	1.96	1.92	0	0.05	0.22	ROV	0	16.3	299.4	no	yes
PS80/224	10-Aug-12	CORE-OPT-5	0.18	1.74	1.72	0	0.05	0.32	ROV	0	16.4	318.8	no	yes
PS80/224	10-Aug-12	CORE-OPT-6	0.12	1.18	1.2	0	0	-0.3	ROV	1	16.4	318.8	no	yes
PS80/237	15-Aug-12	CORE-OPT-1	1.04	1.71	1.66	0	0.05	0.19	ROV	0	25.9	226.3	yes	yes
PS80/237	15-Aug-12	CORE-OPT-2	0.71	1.77	1.66	0	0.1	0.23	ROV	0	45.4	222.1	yes	yes
PS80/237	15-Aug-12	CORE-OPT-3	0.17	0.87	0.84	0	0	-0.19	ROV	1	63.8	215.2	yes	yes
PS80/237	15-Aug-12	CORE-OPT-4	1.32	1.425	1.36	0	0.05	0.16	ROV	0	82.9	208.7	yes	yes
PS80/237	15-Aug-12	CORE-OPT-5	2.25	1.425	1.39	0	0.05	0.17	ROV	0	101.6	203.2	yes	yes
PS80/237	15-Aug-12	CORE-OPT-6	0.45	1.88	1.78	0	0.04	0.19	ROV	0	15.1	249.1	yes	yes
PS80/237	15-Aug-12	CORE-OPT-7	0.56	1.66	1.61	0	0.04	0.2	ROV	0	15.9	269.6	yes	yes
PS80/237	15-Aug-12	CORE-OPT-8	0.53	1.515	1.45	0	0.05	0.18	ROV	0	15.8	290.1	yes	yes
PS80/237	15-Aug-12	CORE-OPT-9	0.98	1.27	1.26	0	0.03	0.08	ROV	0	16.3	309.9	yes	yes
PS80/237	15-Aug-12	CORE-OPT-10	1.14	1.305	1.26	0	0.06	0.16	ROV	0	16.7	329.4	yes	yes
PS80/237	16-Aug-12	CORE-OPT-11	0.25	0.72	0.71	0	0	-0.35	ROV	1	-450	130	yes	yes
PS80/237	16-Aug-12	CORE-OPT-12	0.47	2.895	2.82	0	0	-0.3	ROV	1	-415	210	yes	yes
PS80/255	21-Aug-12	CORE-OPT-1	0.55	0.765	0.71	0	0.04	0.085	ROV	0	22.2	217	yes	yes
PS80/255	21-Aug-12	CORE-OPT-2	2.01	0.89	0.89	0	0.04	0.1	ROV	0	-5.6	191.6	yes	yes

Appendix A-3

Cruise/ Station	Date	Core-Name	Chl *a* (mg m^{-2})	Core Length (m)	Ice Thickness (m)	Snow (m)	Scattering layer (m)	Freeboard (m)	Type	Pond	X	Y	Irrad	Rad
PS80/255	21-Aug-12	CORE-OPT-3	0.87	0.51	0.49	0	0	-0.1	ROV	1	-6.2	170.7	no	no
PS80/255	21-Aug-12	CORE-OPT-4	0.71	0.86	0.83	0	0.04	0.09	ROV	0	-2.3	161.9	yes	yes
PS80/277	26-Aug-12	CORE-OPT-1	0.49	0.81	0.8	0	0.08	0.17	L-arm	0	-73.2	91.5	no	no
PS80/277	26-Aug-12	CORE-OPT-2	0.05	0.31	0.25	0	0	-0.27	L-arm	1	-75.7	85.2	no	no
PS80/277	26-Aug-12	CORE-OPT-3	0.29	0.92	0.92	0	0.08	0.14	L-arm	0	-57.1	138.2	no	no
PS80/277	26-Aug-12	CORE-OPT-4	0.03	0.32	0.3	0	0	-0.16	L-arm	1	-55.2	126	no	no
PS80/277	26-Aug-12	CORE-OPT-5	0.09	0.78	0.75	0	0	-0.33	L-arm	1	-55.2	42.6	no	no
PS80/323	5-Sep-12	CORE-OPT-1	0.35	1.805	1.74	0.07	0	0.07	ROV	0	-117.3	230.1	no	no
PS80/323	5-Sep-12	CORE-OPT-2	0.25	0.71	0.68	0.05	0	0.08	ROV	0	-136.1	237.9	yes	yes
PS80/323	5-Sep-12	CORE-OPT-3	0.18	0.75	0.76	0.04	0	0.14	ROV	0	-153.1	244	yes	yes
PS80/323	5-Sep-12	CORE-OPT-4	0.01	0.17	0.17	0	0	0.04	ROV	0	-164.8	308.7	no	no
PS80/323	5-Sep-12	CORE-OPT-5	0.16	0.69	0.66	0.05	0	0.11	ROV	0	-172.5	290.7	yes	yes
PS80/323	5-Sep-12	CORE-OPT-6	0.02	0.25	0.23	0.04	0	0.05	ROV	0	-181.1	273.8	yes	yes
PS80/335	8-Sep-12	CORE-OPT-1	1.08	1.21	1.23	0.02	0	0.1	ROV	0	-14.2	389.7	yes	yes
PS80/335	8-Sep-12	CORE-OPT-2	0.03	0.25	0.91	0	0	0.01	ROV	1	-14.7	385	yes	no
PS80/335	8-Sep-12	CORE-OPT-3	0.78	1.33	1.35	0.17	0	0.05	ROV	0	-90.4	345.9	yes	yes
PS80/335	8-Sep-12	CORE-OPT-4	0.24	0.74	1.16	0	0	0.02	ROV	1	-86.5	352.3	yes	yes
PS80/335	8-Sep-12	CORE-OPT-5	1.04	1.23	1.17	0.13	0	0.11	ROV	0	-70.8	344.8	yes	yes
PS80/335	8-Sep-12	CORE-OPT-6	2.61	1.63	1.49	0.1	0	0.11	ROV	0	-30.3	339.9	yes	yes
PS80/348	19-Sep-12	CORE-OPT-1	0.58	0.2	0.18	0	0	-0.35	ROV	1	-217.3	-89	no	yes
PS80/348	19-Sep-12	CORE-OPT-2	3.47	0.38	0.18	0	0	-0.43	ROV	1	-217.3	-89	yes	yes
PS80/348	19-Sep-12	CORE-OPT-3	5.58	0.78	0.7	0	0	-0.4	ROV	1	-222.6	-118.6	yes	yes
PS80/348	19-Sep-12	CORE-OPT-4	0.25	0.77	0.93	0.01	0	0.05	ROV	0	-258.3	-69.2	yes	yes
PS80/348	19-Sep-12	CORE-OPT-5	0.18	0.78	1.02	0.01	0	0.03	ROV	0	-287.2	-43.2	yes	yes
PS80/348	19-Sep-12	CORE-OPT-6	0.26	1.64	1.64	0.02	0	0.22	ROV	0	-303.5	-31.4	yes	yes
PS80/348	19-Sep-12	CORE-OPT-7	1.04	1.65	1.58	0.02	0	0.21	ROV	0	-342	0.3	yes	yes
PS80/360	23-Sep-12	CORE-OPT-1	6.46	0.78	0.79	0.02	0	0.03	ROV	0	72.7	278.9	yes	yes
PS80/360	23-Sep-12	CORE-OPT-2	11.83	1.57	1.5	0.04	0	0.22	ROV	0	12.7	246.9	yes	yes
PS80/360	23-Sep-12	CORE-OPT-3	8.03	0.88	0.9	0	0	0.04	ROV	0	3.4	241.6	yes	yes
PS80/360	23-Sep-12	CORE-OPT-4	0.05	1.22	1.22	0.08	0	0.17	ROV	0	-13.5	230.8	yes	yes
PS80/HELI-64	27-Sep-12	CORE-OPT-1	0.02	0.05	0.05	0	0	0	L-arm	0	0	0	no	no
PS80/HELI-64	27-Sep-12	CORE-OPT-2	0.04	0.06	0.06	0	0	0	L-arm	0	20	0	no	no
PS80/HELI-64	27-Sep-12	CORE-OPT-3	0.02	0.04	0.04	0	0	0	L-arm	0	50	0	no	no
PS80/384	29-Sep-12	CORE-OPT-1	1.12	1.578	1.56	0.03	0	0.28	ROV	0	-254.4	1569.9	yes	yes
PS80/384	29-Sep-12	CORE-OPT-2	0.16	0.99	1.13	0.06	0	0.03	ROV	1	-257.6	1575.8	yes	yes
PS80/384	29-Sep-12	CORE-OPT-3	0.27	1.53	1.57	0.03	0	0.28	ROV	0	-261.3	1575.4	yes	yes
PS80/384	29-Sep-12	CORE-OPT-4	0.04	0.19	0.17	0.05	0	0	ROV	0	-326.7	1607.6	no	no

Appendix A-3

Table S2. Summary of the "Best" models from each spectral measurement-statistical approach-data subset combination (96 models). "N" refers to the sample size of data used to fit the model. "NA" refers to data that are not used in the analyses for reasons described in the manuscript or there are erroneous data based on calculation of the summary statistics (e.g., too small of a sample size). "Predictor Variables" correspond to the variables included in the generalized linear model such as: modes used from S "s#" or the squared value "s#^2" or the NDIs with wavelength combinations shown in brackets. Table continued on next page.

						Model Statistics			Bias of Model applied to subset:		R^2 of Model applied to subset:							10-Fold Cross Validation		Ranking			
Model	Statistical Approach	Spectral Measurement	Data subset	N	Predictor Variables	R^2	RMSE	Bias	high	low	All	PS78	PS80	MYI	low	high	Mean	RMSE	NRMSE	Mean-R^2	NRMSE	Mean	Final
M1	EOF	irradiance	all	49	*s4 + s5 + s7 + s7^2 + s8^2*	0.82	1.11	-0.48	-0.44	0.00	NA	-0.04	0.83	0.93	0.06	0.82	0.52	12.11	1.03	5.5	66	35.75	27
M2	EOF	irradiance	PS78	11	*s4 + s7 + s2 + s4^2 + s9^2*	0.99	0.03	0.00	-0.14	0.00	0.24	NA	0.24	0.04	0.19	0.33	0.21	0.07	0.09	24	2	13	6
M3	EOF	irradiance	PS80	38	*s4 + s5 + s7 + s7^2 + s8^2*	0.81	1.28	-0.60	-0.24	0.00	0.81	-0.06	NA	0.87	0.01	0.85	0.50	2.90	0.25	7	29	18	9
M4	EOF	irradiance	PS80-MYI	10	*s5 + s7 + s3^2 + s4^2 + s7^2*	1.00	0.25	0.01	-0.02	0.00	-0.01	0.01	-0.02	NA	0.02	-0.07	-0.01	1.69	0.14	77	5	41	40
M5	EOF	irradiance	low	34	*s4 + s8*	0.51	0.17	0.00	0.00	0.00	-0.02	0.31	-0.02	-0.12	NA	0.02	0.03	0.19	0.20	61	19	40	36
M6	EOF	irradiance	high	15	*s1 + s5 + s7 + s9 + s2^2*	0.96	0.60	-0.05	-0.05	0.00	0.17	-0.07	0.17	0.20	0.08	NA	0.11	1.44	0.13	38.5	4	21.25	11
M7	EOF	radiance	all	50	*s4 + s7 + s9 + s7^2 + s9^2*	0.59	1.53	-0.47	0.03	0.00	NA	NA	0.58	0.65	0.00	0.61	0.46	10.60	0.90	8	64	36	28
M8	EOF	radiance	PS78	NA	NA	0.00	0.98	0.00	NA	NA	NA	NA	NA	NA	NA	NA	NA	12.11	39.46	96	77.5	86.75	96
M9	EOF	radiance	PS80	46	*s4 + s5 + s7 + s8^2 + s9^2*	0.74	1.48	-0.80	-0.44	0.00	0.75	NA	NA	0.93	-0.02	0.88	0.64	4.05	0.34	1	45	23	13
M10	EOF	radiance	PS80-MYI	10	*s2 + s4 + s5 + s7 + s1^2*	0.99	0.33	-0.07	-0.35	0.00	-0.02	NA	-0.02	NA	0.07	-0.04	0.00	>50	13.70	70	75	72.5	84
M11	EOF	radiance	low	35	*s2 + s4 + s3^2 + s4^2*	0.60	0.15	0.00	-0.31	0.00	0.03	NA	0.04	-0.10	NA	0.07	0.01	0.17	0.18	65	9	37	30.5
M12	EOF	radiance	high	15	*s4 + s5 + s6 + s2^2 + s8^2*	0.95	0.66	-0.08	-0.08	0.00	0.56	NA	0.55	0.55	-0.02	NA	0.41	1.81	0.17	9	7	8	2
M13	EOF	transmittance	all	49	*s2 + s4 + s6^2 + s7^2 + s9^2*	0.88	0.77	0.01	0.02	0.00	NA	-0.09	0.88	0.86	0.06	0.89	0.52	4.14	0.35	5.5	49	27.25	14
M14	EOF	transmittance	PS78	11	*s3 + s4 + s5 + s8 + s6^2*	0.98	0.03	0.00	0.02	0.00	0.04	NA	0.02	-0.10	0.01	-0.07	-0.02	0.07	0.09	83	1	42	43
M15	EOF	transmittance	PS80	38	*s2 + s4 + s6 + s7^2 + s9^2*	0.90	0.77	-0.02	-0.01	0.00	0.88	-0.11	NA	0.94	-0.01	0.93	0.53	1.81	0.15	4	6	5	1
M16	EOF	transmittance	PS80-MYI	10	*s6 + s8 + s5^2 + s6^2 + s8^2*	1.00	0.25	-0.03	-0.15	0.00	-0.01	-0.07	-0.02	NA	-0.01	-0.07	-0.04	9.79	0.83	90	62	76	87.5
M17	EOF	transmittance	low	34	*s4 + s7 + s8 + s9 + s4^2*	0.56	0.16	0.00	-0.01	0.00	0.13	0.41	0.14	0.00	NA	0.16	0.17	0.25	0.26	28	38	33	23
M18	EOF	transmittance	high	15	*s1 + s6 + s7 + s1^2 + s4^2*	0.97	0.49	0.01	0.01	0.00	-0.02	-0.10	-0.02	0.95	-0.03	NA	0.16	>50	>50	30	82	56	57
M19	EOF	transflectance	all	50	*s2 + s4 + s7 + s9 + s9^2*	0.74	1.12	-0.12	-0.01	0.00	NA	NA	0.74	0.76	0.00	0.82	0.58	2.46	0.21	2	23	12.5	4.5
M20	EOF	transflectance	PS78	NA	NA	0.00	0.98	0.00	NA	NA	NA	NA	NA	NA	NA	NA	NA	12.11	39.46	95	77.5	86.25	95
M21	EOF	transflectance	PS80	46	*s2 + s4 + s3^2 + s6^2 + s8^2*	0.73	1.27	-0.36	0.00	0.00	0.73	NA	NA	0.69	0.07	0.78	0.57	39.58	3.35	3	72	37.5	32.5
M22	EOF	transflectance	PS80-MYI	10	*s2 + s4 + s7 + s9 + s9^2*	0.99	0.36	-0.03	-0.47	0.00	-0.02	NA	-0.02	NA	-0.03	-0.03	-0.03	1.28	0.11	87	3	45	47
M23	EOF	transflectance	low	35	*s2 + s4 + s8 + s9 + s4^2*	0.55	0.16	0.00	-0.39	0.00	0.03	NA	0.05	-0.05	NA	0.11	0.04	0.22	0.23	56.5	28	42.25	44
M24	EOF	transflectance	high	15	*s1 + s2 + s6 + s2^2 + s7^2*	0.95	0.69	-0.06	-0.06	0.00	0.29	NA	0.28	0.94	0.06	NA	0.39	2.07	0.19	11	18	14.5	7
M25	NDI-440	irradiance	all	49	*NDI (463:476)*	0.09	2.10	0.02	-1.72	0.78	NA	0.02	0.06	-0.08	0.00	-0.05	-0.01	2.20	0.19	77	15	46	48
M26	NDI-440	irradiance	PS78	11	*NDI (462:468)*	0.02	0.22	0.00	-2.68	0.04	0.09	NA	0.07	-0.08	-0.02	-0.04	0.00	0.25	0.34	70	44	57	58
M27	NDI-440	irradiance	PS80	38	*NDI (400:408)*	0.07	2.34	-0.02	-1.62	1.06	0.06	-0.06	NA	-0.08	-0.02	-0.01	-0.02	2.45	0.21	83	22	52.5	52
M28	NDI-440	irradiance	PS80-MYI	10	*NDI (426:450)*	0.40	2.90	0.25	652.70	69.62	-0.02	-0.11	-0.03	NA	0.02	-0.06	-0.04	12.51	1.06	90	67	78.5	93
M29	NDI-440	irradiance	low	34	*NDI (400:680)*	0.07	0.24	0.00	-2.99	0.00	-0.02	-0.07	-0.02	-0.11	NA	-0.07	-0.06	0.25	0.26	94	36	65	72
M30	NDI-440	irradiance	high	15	*NDI (412:418)*	0.06	2.92	0.00	0.00	2.73	0.07	-0.06	0.07	0.01	-0.03	NA	0.01	5.26	0.49	65	53	59	62.5
M31	NDI-440	radiance	all	50	*NDI (463:469)*	0.10	2.07	0.03	-1.68	0.76	NA	0.78	0.09	-0.08	0.12	-0.05	0.17	2.16	0.18	28	11	19.5	10
M32	NDI-440	radiance	PS78	4	*NDI (467:473)*	0.77	0.05	0.00	-0.04	0.02	0.06	NA	0.06	-0.10	0.15	-0.04	0.03	NA	NA	61	91	76	87.5
M33	NDI-440	radiance	PS80	46	*NDI (463:469)*	0.09	2.14	0.02	-1.63	0.81	0.10	0.78	NA	-0.08	0.12	-0.05	0.17	2.22	0.19	28	17	22.5	12
M34	NDI-440	radiance	PS80-MYI	10	*NDI (406:472)*	0.06	3.59	0.09	116.16	16.32	-0.02	-0.08	-0.02	NA	0.05	-0.05	-0.02	5.03	0.43	83	51	67	74
M35	NDI-440	radiance	low	35	*NDI (469:475)*	0.18	0.21	0.00	-2.54	0.00	0.07	0.74	0.06	-0.09	NA	-0.05	0.15	0.22	0.23	31.5	27	29.25	17.5
M36	NDI-440	radiance	high	15	*NDI (427:435)*	0.03	2.97	0.02	0.02	2.90	0.03	0.62	0.04	-0.06	-0.02	NA	0.12	3.28	0.30	35.5	43	39.25	35
M37	NDI-440	transmittance	all	49	*NDI (473:479)*	0.14	2.04	0.07	-1.63	0.82	NA	-0.08	0.12	-0.06	-0.03	0.01	-0.01	>50	43.30	77	79	78	91
M38	NDI-440	transmittance	PS78	11	*NDI (480:660)*	0.02	0.22	0.00	-3.01	-0.03	-0.02	NA	-0.03	-0.12	0.08	-0.08	-0.03	0.26	0.34	87	46	66.5	73
M39	NDI-440	transmittance	PS80	38	*NDI (473:479)*	0.13	2.26	0.07	-1.43	1.03	0.15	-0.08	NA	-0.05	-0.03	0.01	0.00	>50	>50	70	83	76.5	89
M40	NDI-440	transmittance	PS80-MYI	10	*NDI (426:449)*	0.53	2.55	0.22	63.64	14.36	-0.02	-0.11	-0.03	NA	0.01	-0.04	-0.04	5.64	0.48	90	52	71	80.5
M41	NDI-440	transmittance	low	34	*NDI (400:672)*	0.09	0.23	0.00	-2.99	0.00	-0.02	-0.02	-0.03	-0.12	NA	-0.08	-0.05	0.25	0.26	92.5	35	63.75	71
M42	NDI-440	transmittance	high	15	*NDI (474:482)*	0.05	2.95	0.04	0.04	2.58	0.20	-0.09	0.18	0.00	-0.03	NA	0.05	35.81	3.32	50.5	71	60.75	64.5
M43	NDI-440	transflectance	all	50	*NDI (460:466)*	0.13	2.03	0.06	-1.63	0.78	NA	0.93	0.13	-0.05	0.05	-0.01	0.21	4.25	0.36	24	50	37	30.5
M44	NDI-440	transflectance	PS78	4	*NDI (461:467)*	0.92	0.03	0.00	9.05	-0.14	0.06	NA	0.06	-0.10	0.08	-0.04	0.01	NA	NA	65	92	78.5	93
M45	NDI-440	transflectance	PS80	46	*NDI (460:466)*	0.13	2.10	0.06	-1.56	0.86	0.14	0.93	NA	-0.05	0.05	-0.01	0.21	4.11	0.35	24	47	35.5	25.5
M46	NDI-440	transflectance	PS80-MYI	10	*NDI (406:471)*	0.20	3.32	0.15	18.21	5.94	-0.02	0.09	-0.02	NA	0.01	-0.04	0.00	6.76	0.57	70	56	63	68
M47	NDI-440	transflectance	low	35	*NDI (402:677)*	0.02	0.23	0.00	-2.98	0.00	-0.02	0.16	-0.02	-0.12	NA	-0.08	-0.02	0.24	0.25	83	33	58	60
M48	NDI-440	transflectance	high	15	*NDI (478:484)*	0.00	3.02	0.01	0.01	2.58	0.16	-0.50	0.15	-0.04	-0.01	NA	-0.05	3.77	0.35	92.5	48	70.25	77.5

Appendix A-3

Table continued…

						Model Statistics			Bias of Model applied to subset:		R^2 of Model applied to subset:							10-Fold Cross Validation		Ranking			
Model	Statistical Approach	Spectral Measurement	Data subset	N	Predictor Variables	R^2	RMSE	Bias	high	low	All	PS78	PS80	MYI	low	high	Mean	RMSE	NRMSE	Mean-R^2	NRMSE	Mean	Final
M49	NDI-670	irradiance	all	49	*NDI (662:672)*	0.09	2.09	0.00	-1.72	0.76	NA	0.01	0.09	-0.02	0.21	-0.04	0.05	2.17	0.18	50.5	12	31.25	21
M50	NDI-670	irradiance	PS78	11	*NDI (683:700)*	0.08	0.21	0.00	-3.00	-0.03	0.07	NA	0.09	0.11	0.12	0.10	0.10	0.36	0.49	41	54	47.5	49
M51	NDI-670	irradiance	PS80	38	*NDI (661:667)*	0.14	2.25	0.05	-1.39	1.08	0.11	0.00	NA	0.00	0.12	0.01	0.05	>50	>50	50.5	90	70.25	77.5
M52	NDI-670	irradiance	PS80-MYI	10	*NDI (672:682)*	0.59	2.38	0.14	-0.23	1.73	0.50	-0.07	0.56	NA	0.04	0.63	0.33	3.23	0.27	16	41	28.5	15
M53	NDI-670	irradiance	low	34	*NDI (657:671)*	0.19	0.22	0.00	-2.90	0.00	0.04	0.01	0.04	-0.08	NA	-0.07	-0.01	0.24	0.25	77	32	54.5	54.5
M54	NDI-670	irradiance	high	15	*NDI (669:683)*	0.73	1.58	0.02	0.02	2.09	0.54	-0.08	0.60	0.68	0.07	NA	0.36	1.89	0.18	13.5	8	10.75	3
M55	NDI-670	radiance	all	50	*NDI (665:671)*	0.11	2.06	0.00	-1.75	0.75	NA	0.03	0.10	-0.01	0.05	0.00	0.03	2.15	0.18	61	10	35.5	25.5
M56	NDI-670	radiance	PS78	4	*NDI (671:677)*	0.67	0.07	0.00	-3.09	-0.10	-0.01	NA	-0.02	0.16	-0.01	0.04	0.03	NA	NA	61	93	77	90
M57	NDI-670	radiance	PS80	46	*NDI (665:671)*	0.10	2.13	0.00	-1.69	0.81	0.11	0.03	NA	-0.01	0.05	0.00	0.04	2.22	0.19	56.5	16	36.25	29
M58	NDI-670	radiance	PS80-MYI	10	*NDI (679:685)*	0.24	3.24	0.17	0.40	2.93	0.16	0.67	0.17	NA	-0.03	0.24	0.24	8.85	0.75	21.5	59	40.25	37
M59	NDI-670	radiance	low	35	*NDI (658:666)*	0.08	0.22	0.00	-2.95	0.00	0.00	0.15	0.01	-0.10	NA	-0.07	0.00	0.24	0.25	70	30	50	51
M60	NDI-670	radiance	high	15	*NDI (678:684)*	0.20	2.71	0.09	0.09	2.65	0.17	0.42	0.18	0.17	-0.03	NA	0.18	9.40	0.87	26	63	44.5	46
M61	NDI-670	transmittance	all	49	*NDI (662:672)*	0.14	2.04	0.04	-1.59	0.75	NA	0.03	0.14	-0.01	0.17	-0.01	0.06	2.20	0.19	45.5	13	29.25	17.5
M62	NDI-670	transmittance	PS78	11	*NDI (655:661)*	0.11	0.21	0.00	-2.94	0.01	0.02	NA	0.00	-0.11	0.03	-0.05	-0.02	0.52	0.70	83	58	70.5	79
M63	NDI-670	transmittance	PS80	38	*NDI (661:667)*	0.18	2.19	0.08	-1.30	1.06	0.15	0.01	NA	0.01	0.09	0.04	0.06	>50	>50	45.5	81	63.25	69.5
M64	NDI-670	transmittance	PS80-MYI	10	*NDI (672:682)*	0.54	2.52	0.14	-0.21	1.82	0.47	-0.05	0.53	NA	0.04	0.58	0.31	3.54	0.30	17.5	42	29.75	19
M65	NDI-670	transmittance	low	34	*NDI (658:671)*	0.16	0.22	0.00	-2.88	0.00	0.08	0.00	0.07	-0.08	NA	-0.05	0.00	0.25	0.26	70	37	53.5	53
M66	NDI-670	transmittance	high	15	*NDI (678:684)*	0.70	1.65	0.06	0.06	1.96	0.63	0.01	0.64	0.62	0.06	NA	0.39	2.01	0.19	11	14	12.5	4.5
M67	NDI-670	transflectance	all	50	*NDI (665:671)*	0.16	1.99	0.03	-1.62	0.73	NA	0.32	0.16	0.01	0.03	0.05	0.11	>50	>50	38.5	88	63.25	69.5
M68	NDI-670	transflectance	PS78	4	*NDI (671:677)*	0.83	0.05	0.00	-3.05	-0.08	0.00	NA	0.00	0.14	-0.01	0.10	0.05	NA	NA	50.5	94	72.25	83
M69	NDI-670	transflectance	PS80	46	*NDI (665:671)*	0.16	2.06	0.03	-1.56	0.78	0.17	0.32	NA	0.01	0.03	0.05	0.12	>50	>50	35.5	87	61.25	66
M70	NDI-670	transflectance	PS80-MYI	10	*NDI (679:685)*	0.23	3.25	0.17	0.03	2.37	0.25	0.72	0.25	NA	-0.01	0.32	0.31	8.90	0.76	17.5	60	38.75	34
M71	NDI-670	transflectance	low	35	*NDI (658:665)*	0.07	0.22	0.00	-2.94	0.00	0.03	0.33	0.04	-0.10	NA	-0.06	0.05	0.24	0.25	50.5	31	40.75	39
M72	NDI-670	transflectance	high	15	*NDI (679:685)*	0.33	2.49	0.11	0.11	2.46	0.25	0.71	0.25	0.23	-0.01	NA	0.29	5.75	0.53	20	55	37.5	32.5
M73	multi-NDI	irradiance	all	49	*NDI (463:476) + NDI (662:672)*	0.11	2.08	0.03	-1.68	0.78	NA	0.04	0.09	-0.05	0.23	-0.04	0.05	2.32	0.20	50.5	20	35.25	24
M74	multi-NDI	irradiance	PS78	11	*NDI (462:468) + NDI (683:700)*	0.12	0.21	0.00	-2.88	0.01	0.15	NA	0.13	0.14	0.07	0.02	0.10	4.78	6.41	41	74	57.5	59
M75	multi-NDI	irradiance	PS80	38	*NDI (400:408) + NDI (661:667)*	0.15	2.24	0.06	-1.39	1.09	0.12	-0.01	NA	-0.01	0.13	0.01	0.05	>50	>50	50.5	89	69.75	76
M76	multi-NDI	irradiance	PS80-MYI	10	*NDI (426:450) + NDI (672:682)*	0.59	2.37	0.10	-0.41	1.77	0.37	0.01	0.50	NA	0.00	0.63	0.30	13.55	1.15	19	69	44	45
M77	multi-NDI	irradiance	low	34	*NDI (400:680) + NDI (657:671)*	0.20	0.22	0.00	-2.86	0.00	0.05	0.02	0.04	-0.09	NA	-0.06	-0.01	0.24	0.26	77	34	55.5	56
M78	multi-NDI	irradiance	high	15	*NDI (412:418) + NDI (669:683)*	0.73	1.57	0.04	0.04	2.13	0.52	-0.09	0.58	0.69	0.09	NA	0.36	2.22	0.21	13.5	21	17.25	8
M79	multi-NDI	radiance	all	50	*NDI (463:469) + NDI (665:671)*	0.12	2.05	0.03	-1.67	0.76	NA	0.42	0.11	-0.04	0.13	-0.02	0.12	2.48	0.21	35.5	25	30.25	20
M80	multi-NDI	radiance	PS78	4	*NDI (467:473) + NDI (671:677)*	0.99	0.01	0.00	-2.26	-0.03	0.08	NA	0.07	-0.08	0.20	-0.05	0.04	NA	NA	56.5	95	75.75	86
M81	multi-NDI	radiance	PS80	46	*NDI (463:469) + NDI (665:671)*	0.11	2.12	0.02	-1.62	0.82	0.12	0.34	NA	-0.04	0.12	-0.02	0.10	2.47	0.21	41	24	32.5	22
M82	multi-NDI	radiance	PS80-MYI	10	*NDI (406:472) + NDI (679:685)*	0.24	3.23	0.15	0.19	3.14	0.03	0.91	0.05	NA	0.00	0.19	0.24	>50	24.78	21.5	76	48.75	50
M83	multi-NDI	radiance	low	35	*NDI (469:475) + NDI (658:666)*	0.28	0.20	0.00	-2.21	0.00	0.06	0.75	0.06	-0.09	NA	-0.05	0.15	0.21	0.22	31.5	26	28.75	16
M84	multi-NDI	radiance	high	15	*NDI (427:435) + NDI (678:684)*	0.26	2.61	0.06	0.06	2.41	0.16	-0.41	0.16	0.34	-0.03	NA	0.04	8.30	0.77	56.5	61	58.75	61
M85	multi-NDI	transmittance	all	49	*NDI (473:479) + NDI (662:672)*	0.16	2.02	0.07	-1.56	0.80	NA	0.06	0.14	-0.03	0.18	0.00	0.07	>50	>50	44	80	62	67
M86	multi-NDI	transmittance	PS78	11	*NDI (480:660) + NDI (655:661)*	0.20	0.20	-0.01	-1.66	0.12	0.06	NA	0.05	-0.09	-0.03	-0.03	-0.01	0.69	0.93	77	65	71	80.5
M87	multi-NDI	transmittance	PS80	38	*NDI (473:479) + NDI (661:667)*	0.20	2.17	-0.05	-1.33	1.16	0.04	-0.01	NA	0.12	0.03	0.08	0.05	>50	>50	50.5	84	67.25	75
M88	multi-NDI	transmittance	PS80-MYI	10	*NDI (426:449) + NDI (672:682)*	0.56	2.48	0.21	2.29	2.78	0.04	-0.11	0.03	NA	-0.03	-0.06	-0.03	6.95	0.59	87	57	72	82
M89	multi-NDI	transmittance	low	34	*NDI (400:672) + NDI (658:671)*	0.17	0.22	0.00	-2.81	0.00	0.09	-0.01	0.07	-0.09	NA	-0.05	0.00	0.25	0.26	70	39	54.5	54.5
M90	multi-NDI	transmittance	high	15	*NDI (474:482) + NDI (678:684)*	0.71	1.64	0.07	0.07	2.03	0.62	0.01	0.63	0.62	0.06	NA	0.39	21.62	2.00	11	70	40.5	38
M91	multi-NDI	transflectance	all	50	*NDI (460:466) + NDI (665:671)*	0.17	1.99	0.05	-1.58	0.75	NA	0.39	0.16	-0.01	0.05	0.03	0.12	>50	>50	35.5	86	60.75	64.5
M92	multi-NDI	transflectance	PS78	4	*NDI (461:467) + NDI (671:677)*	1.00	0.01	0.00	-1.80	-0.15	0.08	NA	0.07	-0.09	0.13	-0.03	0.03	NA	NA	61	96	78.5	93
M93	multi-NDI	transflectance	PS80	46	*NDI (460:466) + NDI (665:671)*	0.16	2.06	0.05	-1.52	0.81	0.17	0.41	NA	-0.01	0.06	0.03	0.13	>50	>50	33	85	59	62.5
M94	multi-NDI	transflectance	PS80-MYI	10	*NDI (406:471) + NDI (679:685)*	0.27	3.19	0.20	1.80	2.70	0.04	-0.04	0.04	NA	-0.02	-0.07	-0.01	>50	4.63	77	73	75	85
M95	multi-NDI	transflectance	low	35	*NDI (402:677) + NDI (658:665)*	0.10	0.22	0.00	-2.87	0.00	0.06	0.41	0.06	-0.10	NA	-0.05	0.08	0.25	0.26	43	40	41.5	41.5
M96	multi-NDI	transflectance	high	15	*NDI (478:484) + NDI (679:685)*	0.63	1.84	-0.07	-0.07	2.49	0.13	0.85	0.13	0.60	-0.01	NA	0.34	11.77	1.09	15	68	41.5	41.5

Appendix B:

B 1 Supplementary Material for Chapter 3 – Paper 3: On improving the spatial representativeness of sea ice algae chlorophyll a biomass and primary production estimates

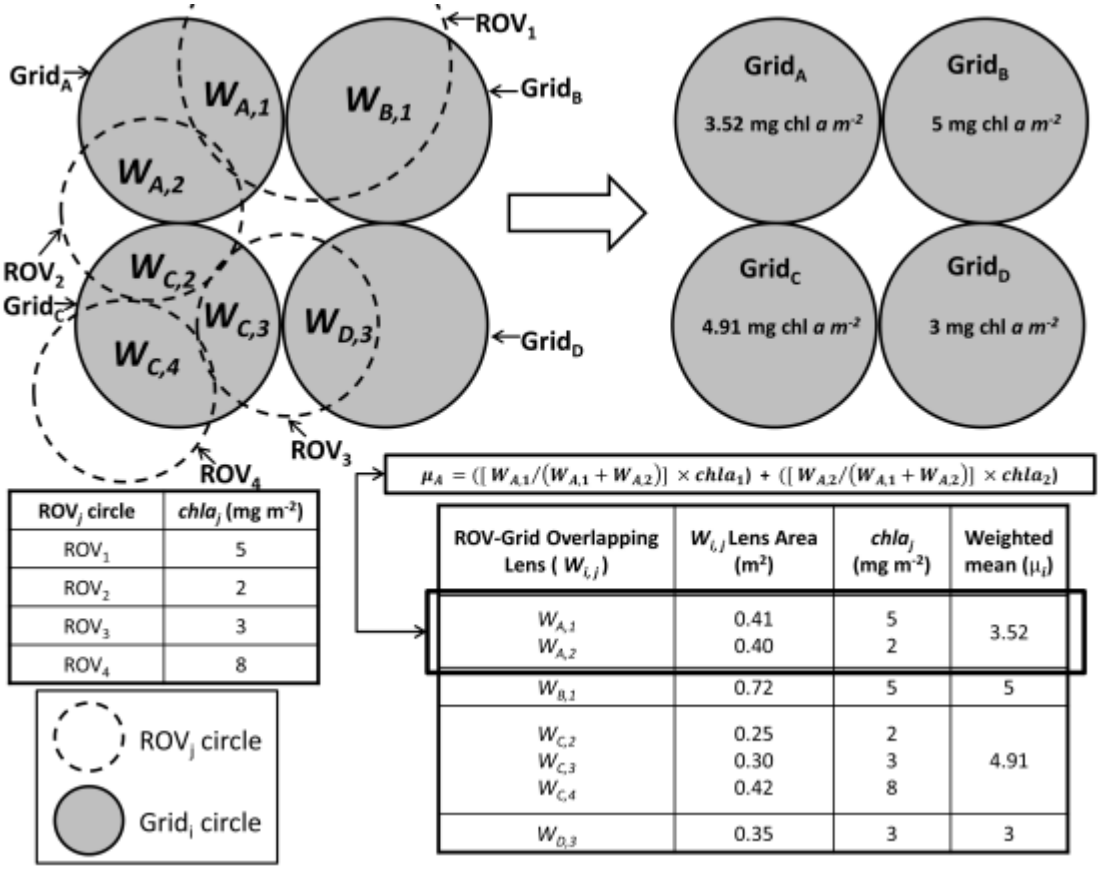

ROV$_j$ circle	$chla_j$ (mg m^{-2})
ROV$_1$	5
ROV$_2$	2
ROV$_3$	3
ROV$_4$	8

$$\mu_A = ([W_{A,1}/(W_{A,1}+W_{A,2})] \times chla_1) + ([W_{A,2}/(W_{A,1}+W_{A,2})] \times chla_2)$$

ROV-Grid Overlapping Lens ($W_{i,j}$)	$W_{i,j}$ Lens Area (m^2)	$chla_j$ (mg m^{-2})	Weighted mean (μ_i)
$W_{A,1}$	0.41	5	3.52
$W_{A,2}$	0.40	2	
$W_{B,1}$	0.72	5	5
$W_{C,2}$	0.25	2	4.91
$W_{C,3}$	0.30	3	
$W_{C,4}$	0.42	8	
$W_{D,3}$	0.35	3	3

Figure S1. Detailed diagram and example calculation of the re-sampling process described in Materials and Methods.

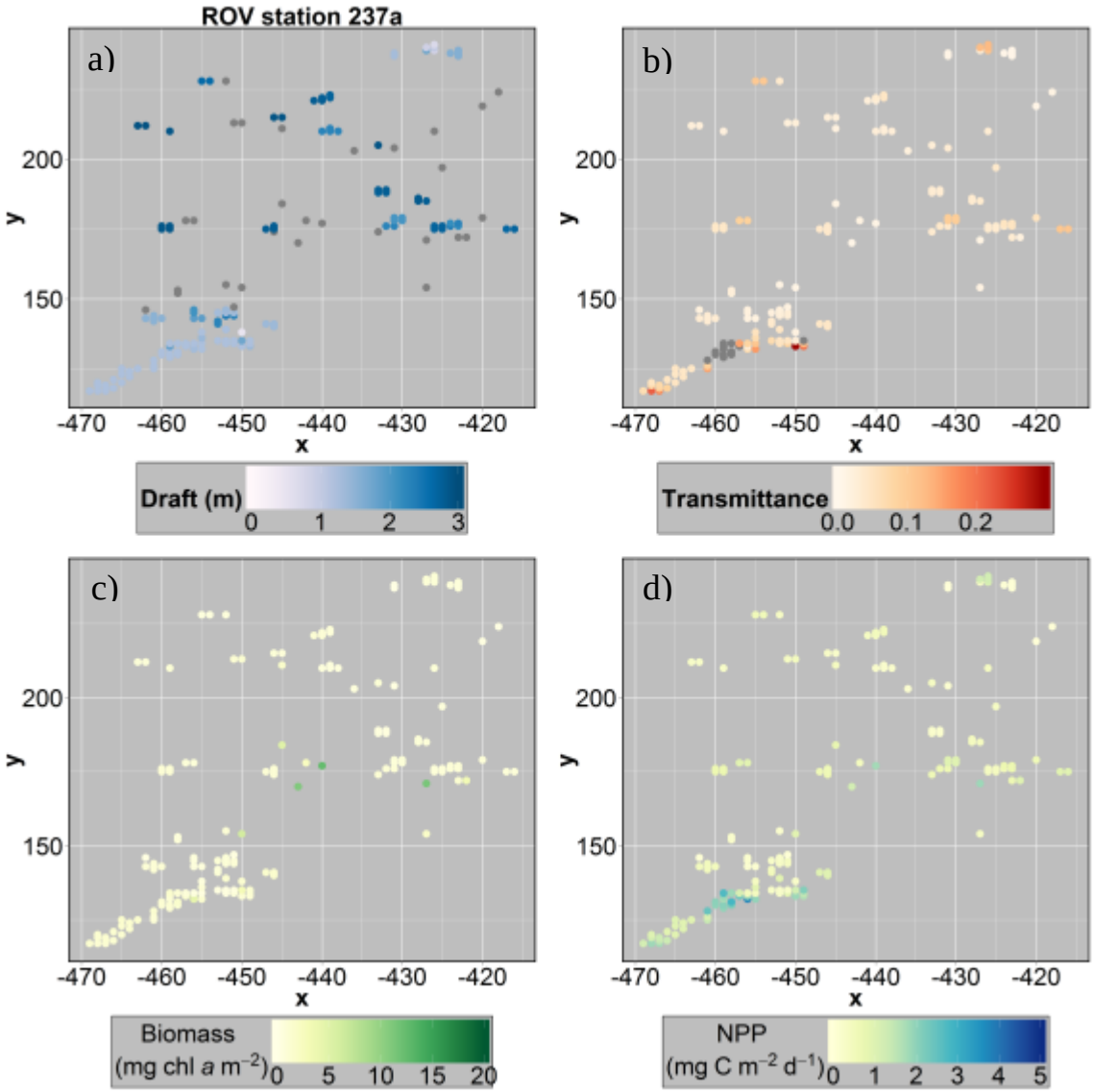

Figure S2. Gridded spatial distribution maps for ROV station 237a of: a) sea ice draft; b) transmittance; c) chl *a* biomass; and d) net primary production (NPP).

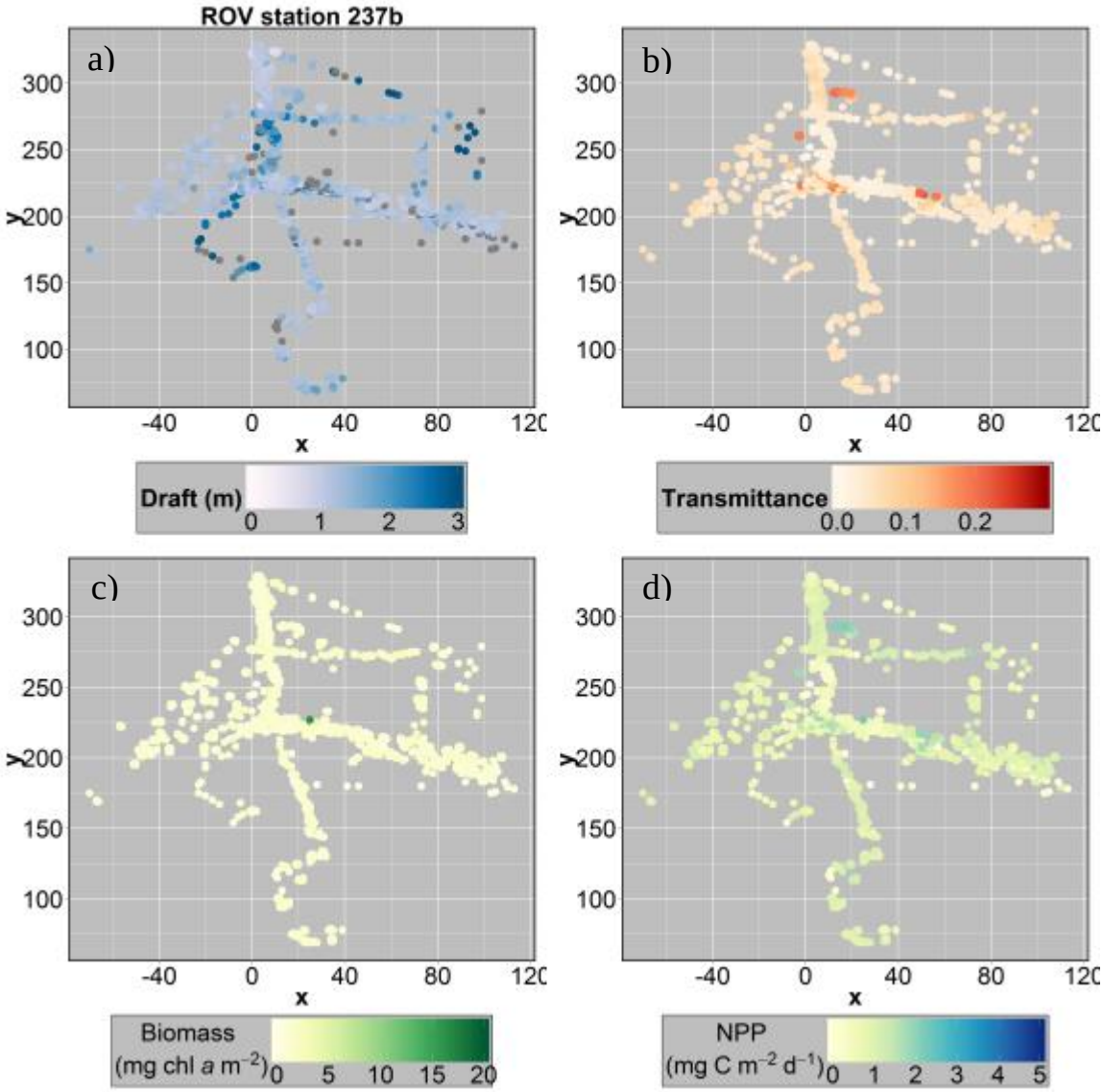

Figure S3. Gridded spatial distribution maps for ROV station 237b of: a) sea ice draft; b) transmittance; c) chl a biomass; and d) net primary production (NPP).

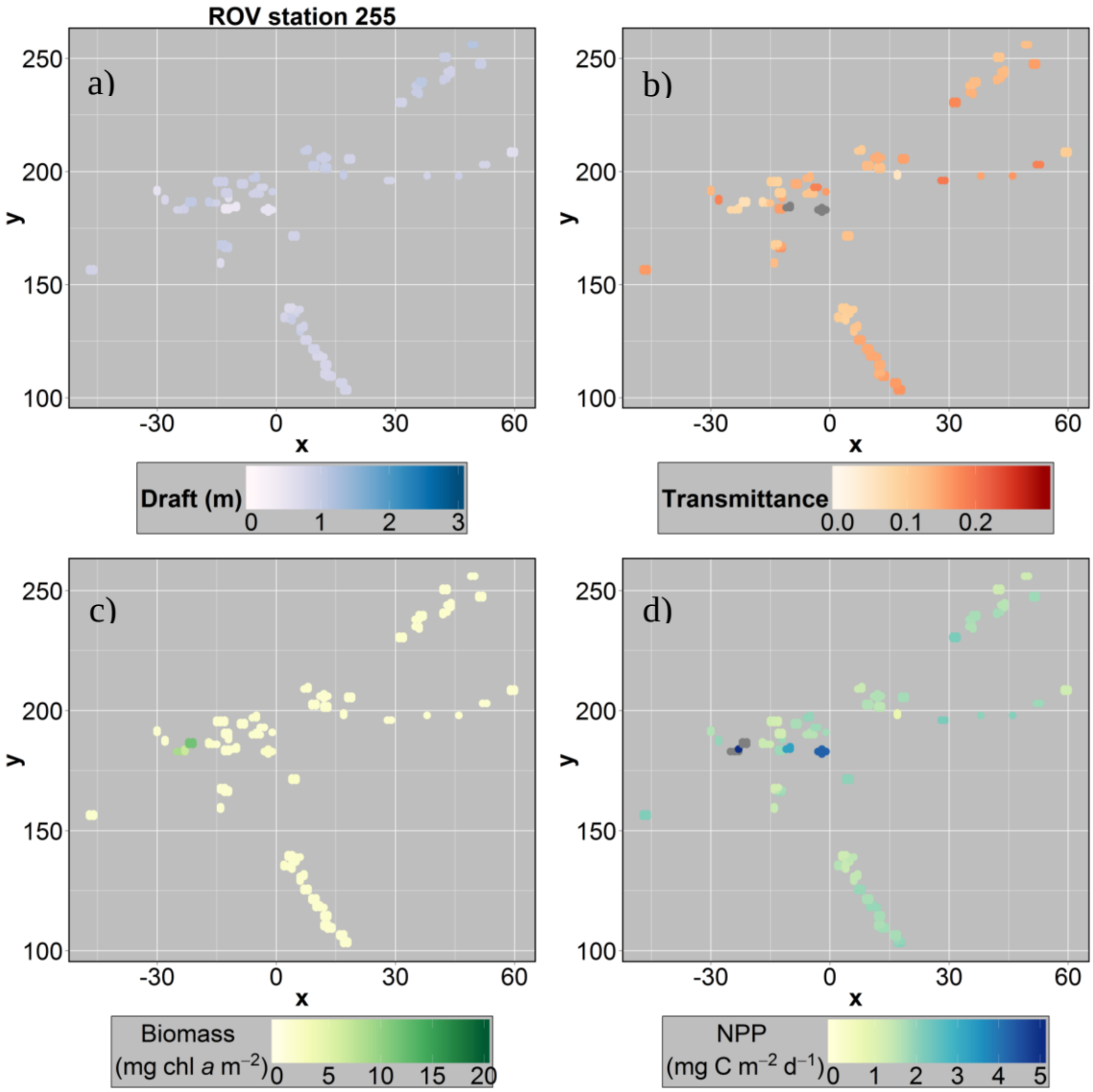

Figure S4. Gridded spatial distribution maps for ROV station 255 of: a) sea ice draft; b) transmittance; c) chl *a* biomass; and d) net primary production (NPP).

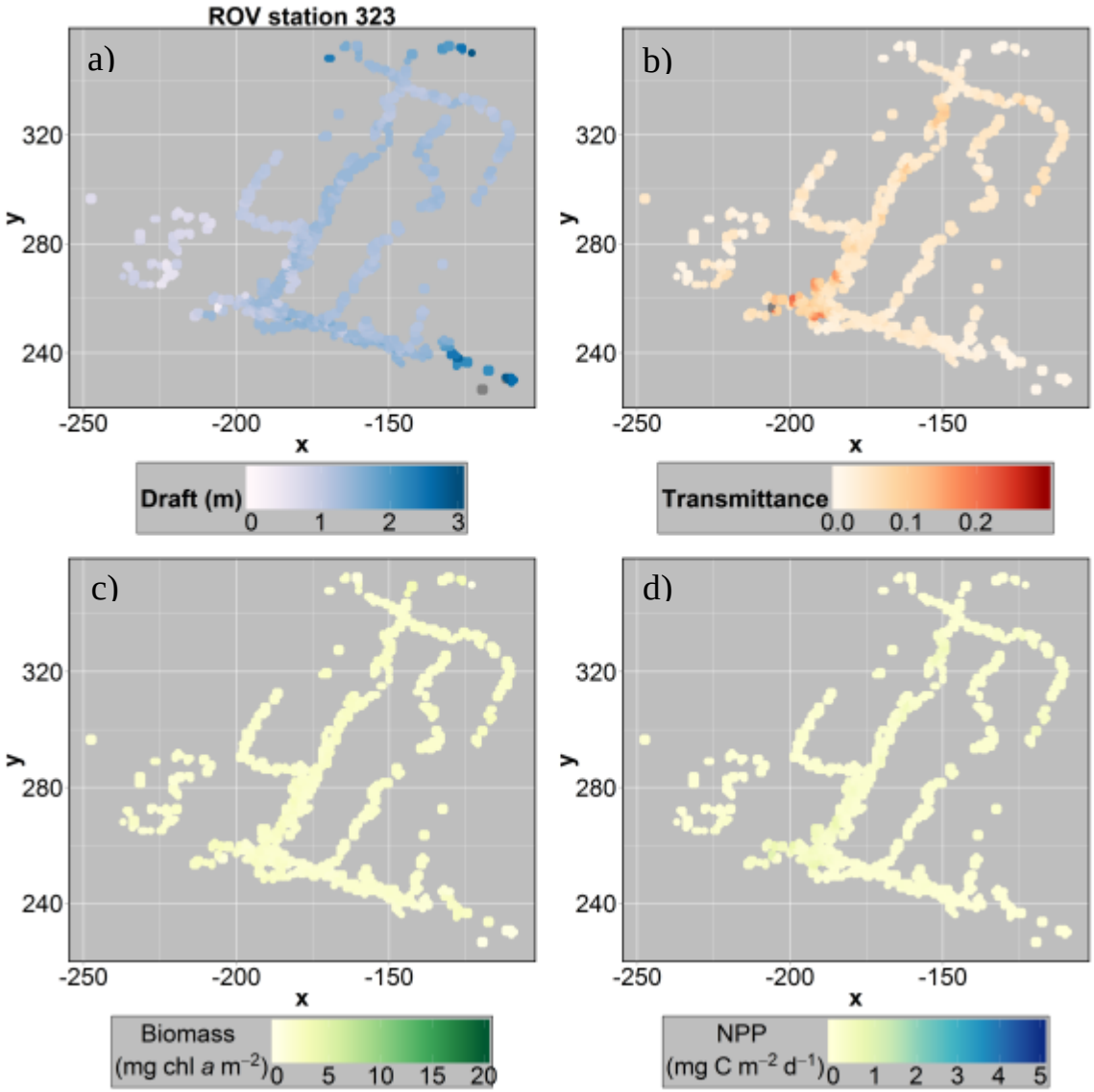

Figure S5. Gridded spatial distribution maps for ROV station 323 of: a) sea ice draft; b) transmittance; c) chl *a* biomass; and d) net primary production (NPP).

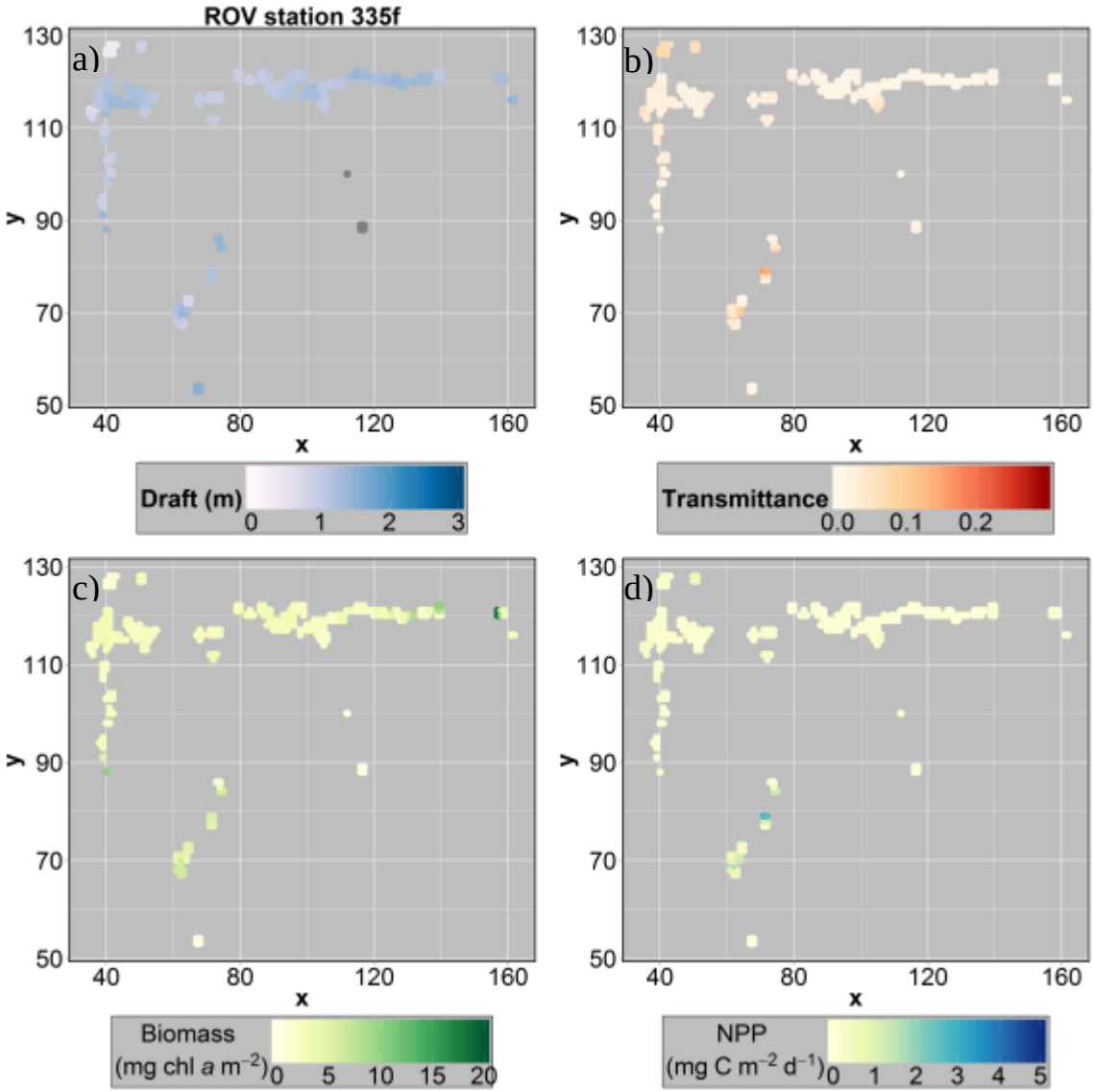

Figure S6. Gridded spatial distribution maps for ROV station 335f of: a) sea ice draft; b) transmittance; c) chl *a* biomass; and d) net primary production (NPP).

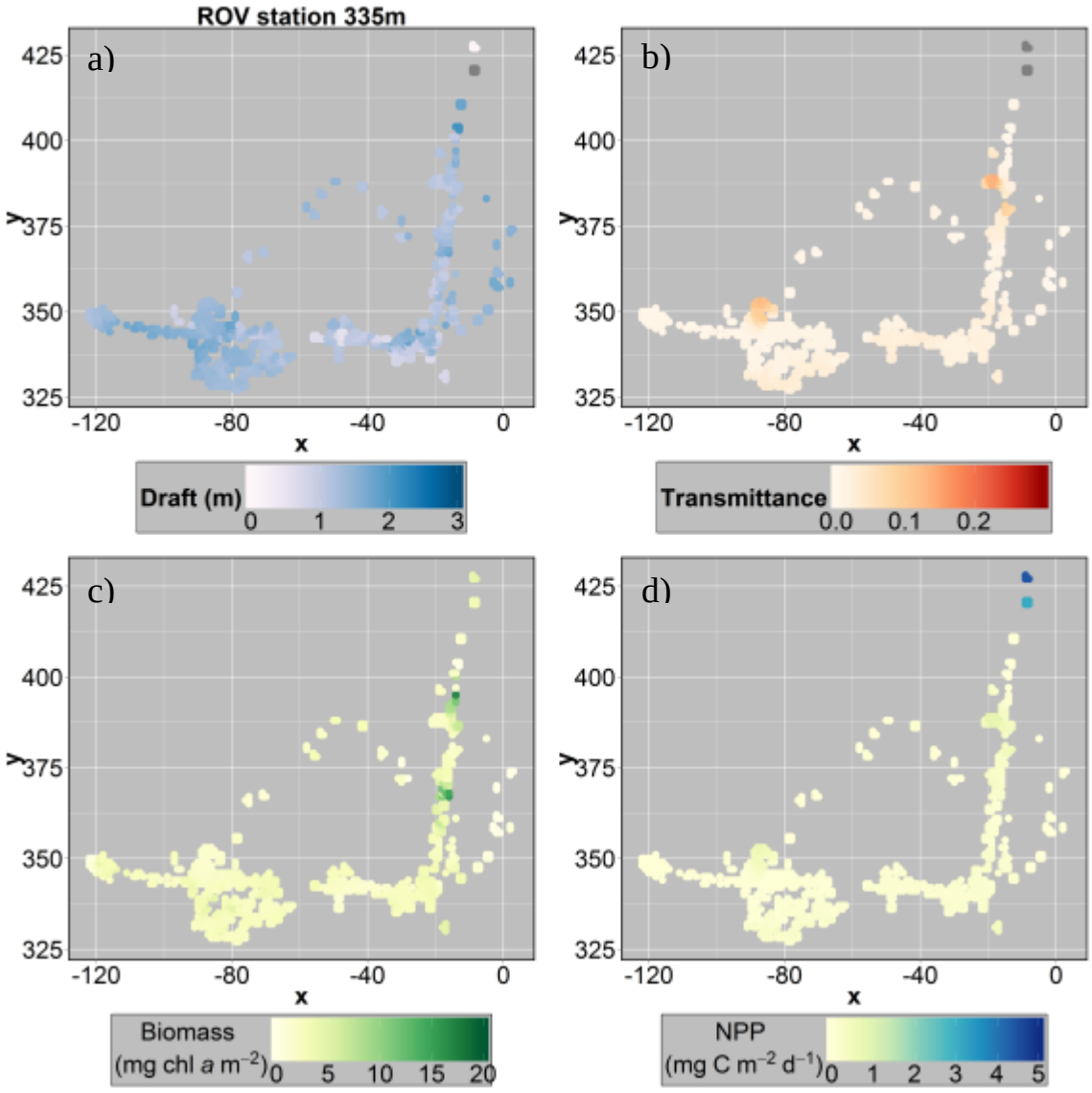

Figure S7. Gridded spatial distribution maps for ROV station 335m of: a) sea ice draft; b) transmittance; c) chl *a* biomass; and d) net primary production (NPP).

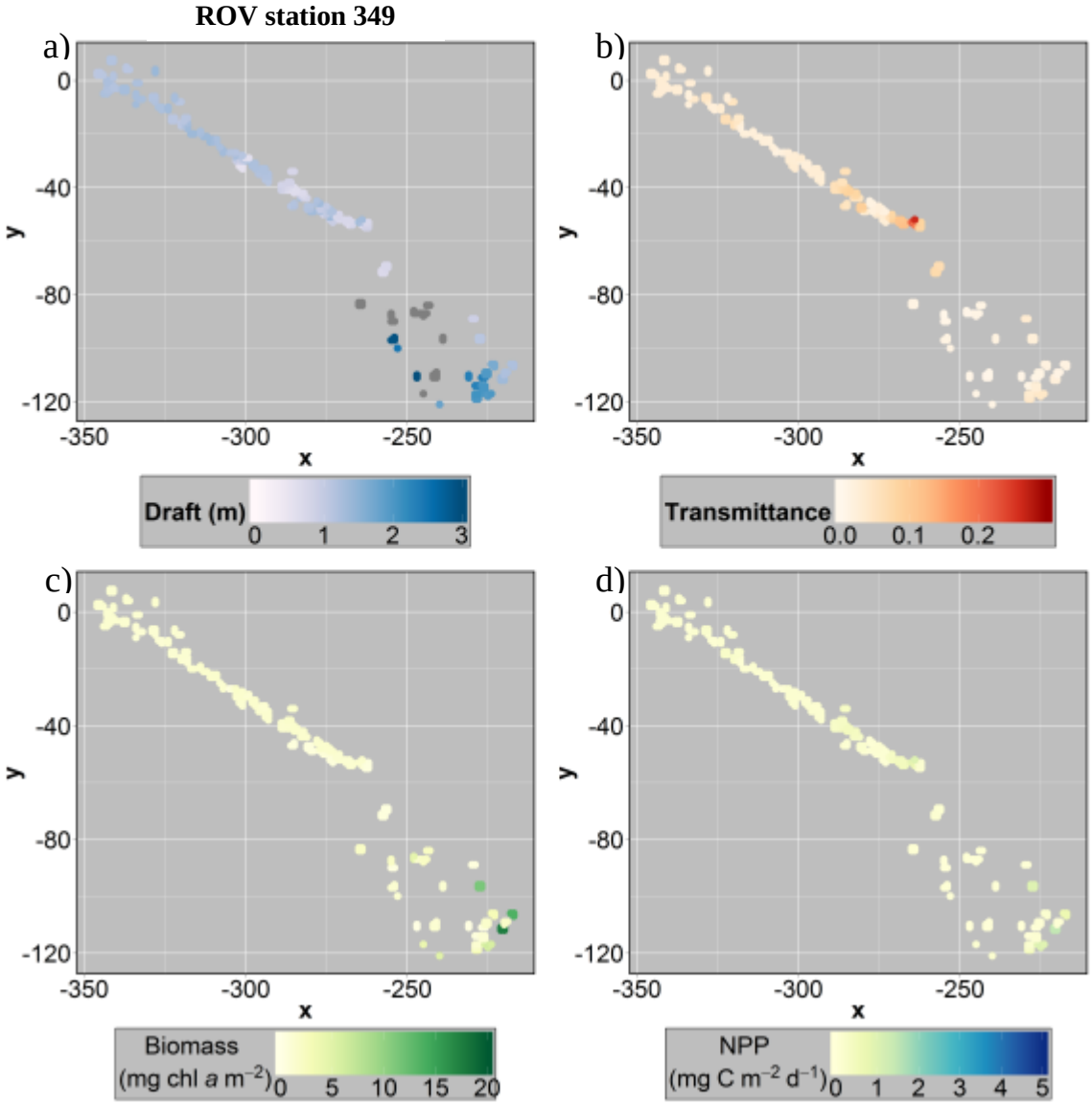

Figure S8. Gridded spatial distribution maps for ROV station 349 of: a) sea ice draft; b) transmittance; c) chl *a* biomass; and d) net primary production (NPP).

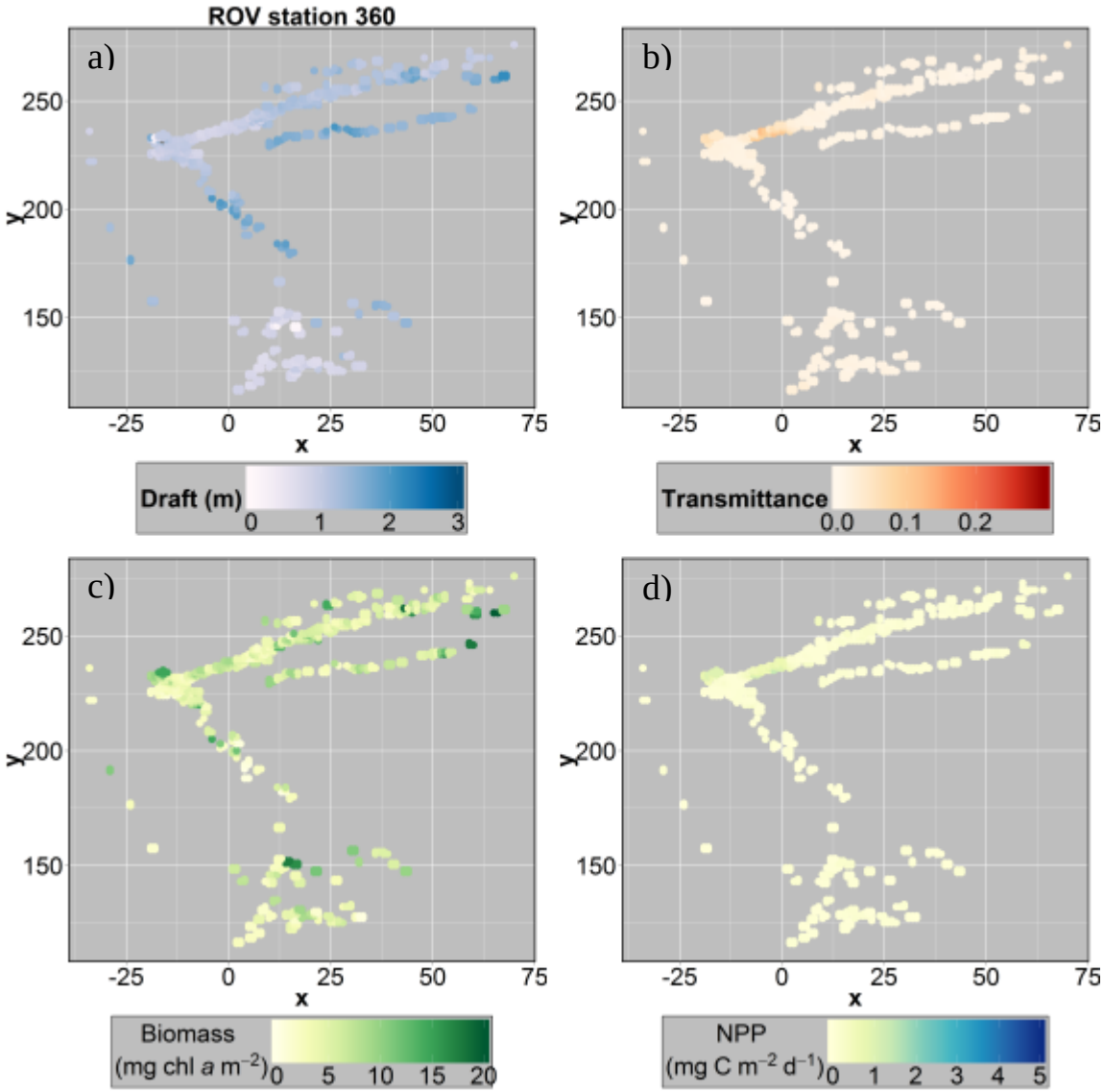

Figure S9. Gridded spatial distribution maps for ROV station 360 of: a) sea ice draft; b) transmittance; c) chl *a* biomass; and d) net primary production (NPP).

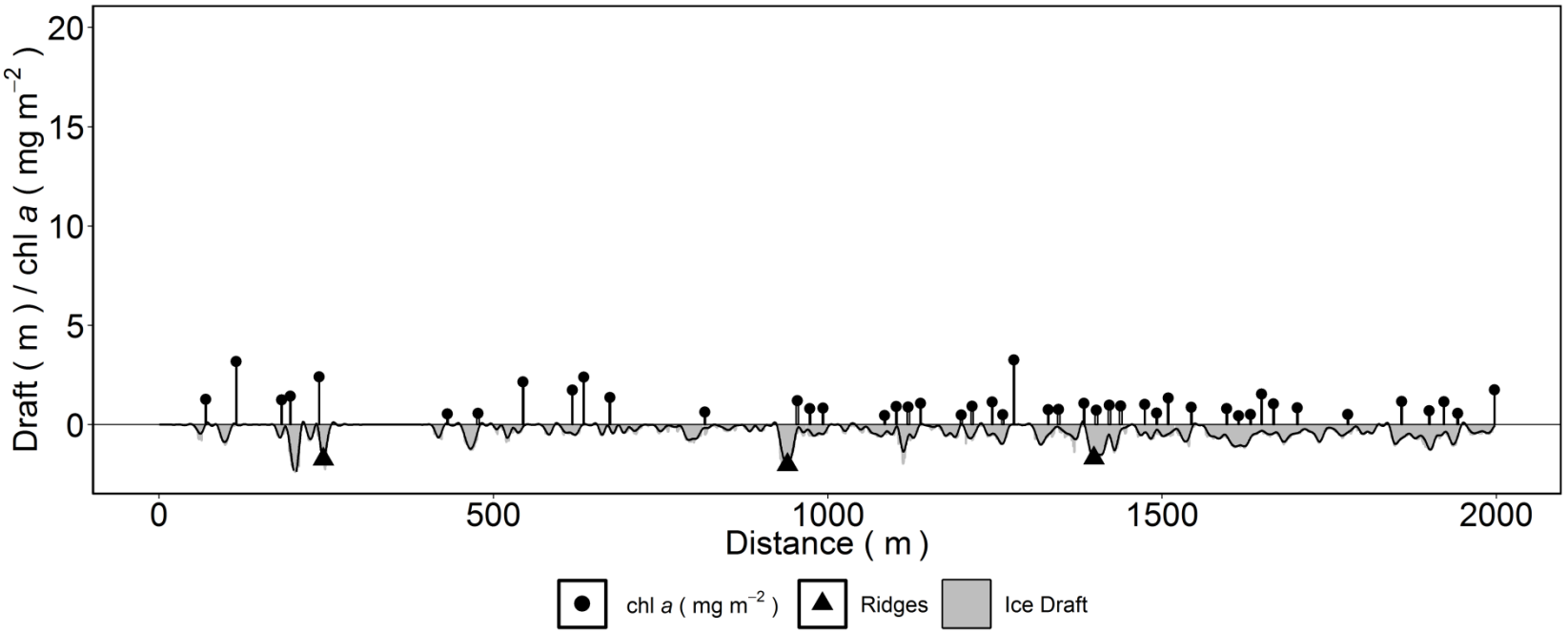

Figure S10. Surface and Under-ice trawl profile for station 216 of spectrally-derived chl *a* biomass (width of line is footprint of measurement), sea ice draft (negative values), and identified ridges. Black line represents the smoothed sea ice draft used for the identification of sea ice ridges.

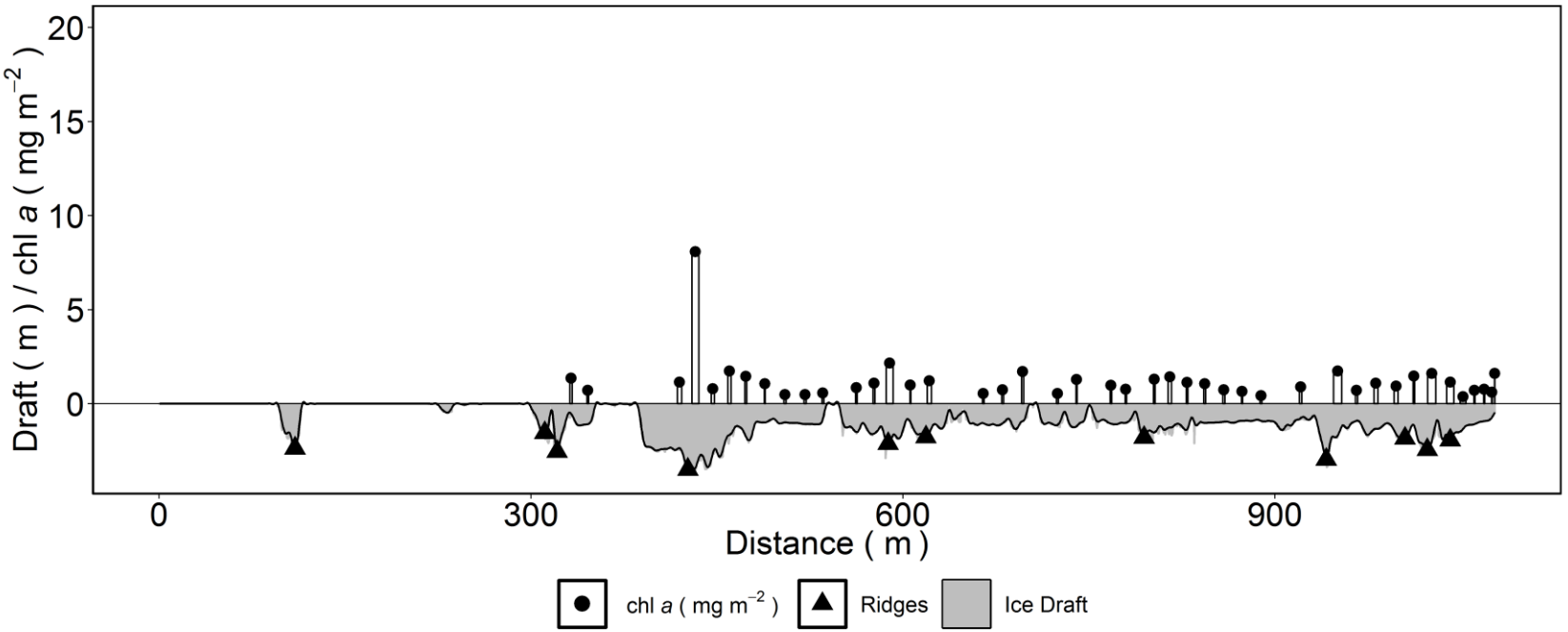

Figure S11. Surface and Under-ice trawl profile for station 223 of spectrally-derived chl *a* biomass (width of line is footprint of measurement), sea ice draft (negative values), and identified ridges. Black line represents the smoothed sea ice draft used for the identification of sea ice ridges.

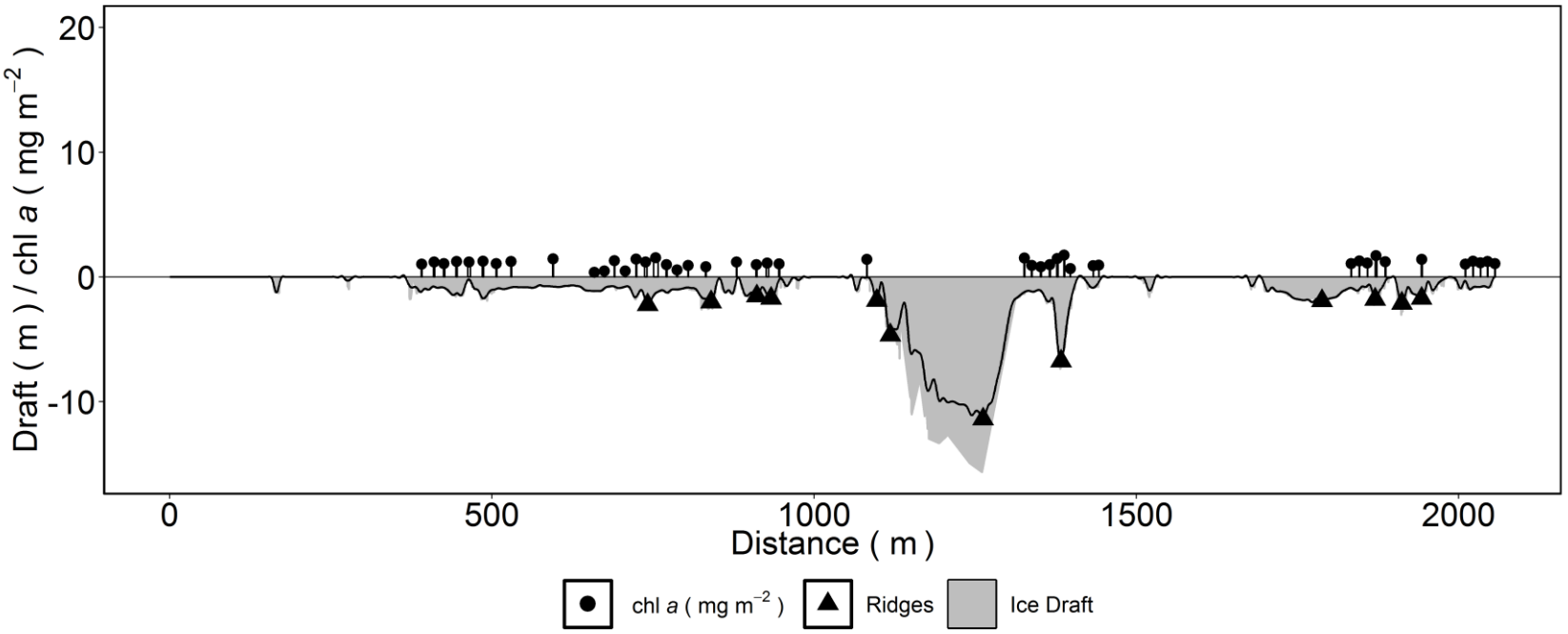

Figure S12. Surface and Under-ice trawl profile for station 233 of spectrally-derived chl *a* biomass (width of line is footprint of measurement), sea ice draft (negative values), and identified ridges. Black line represents the smoothed sea ice draft used for the identification of sea ice ridges.

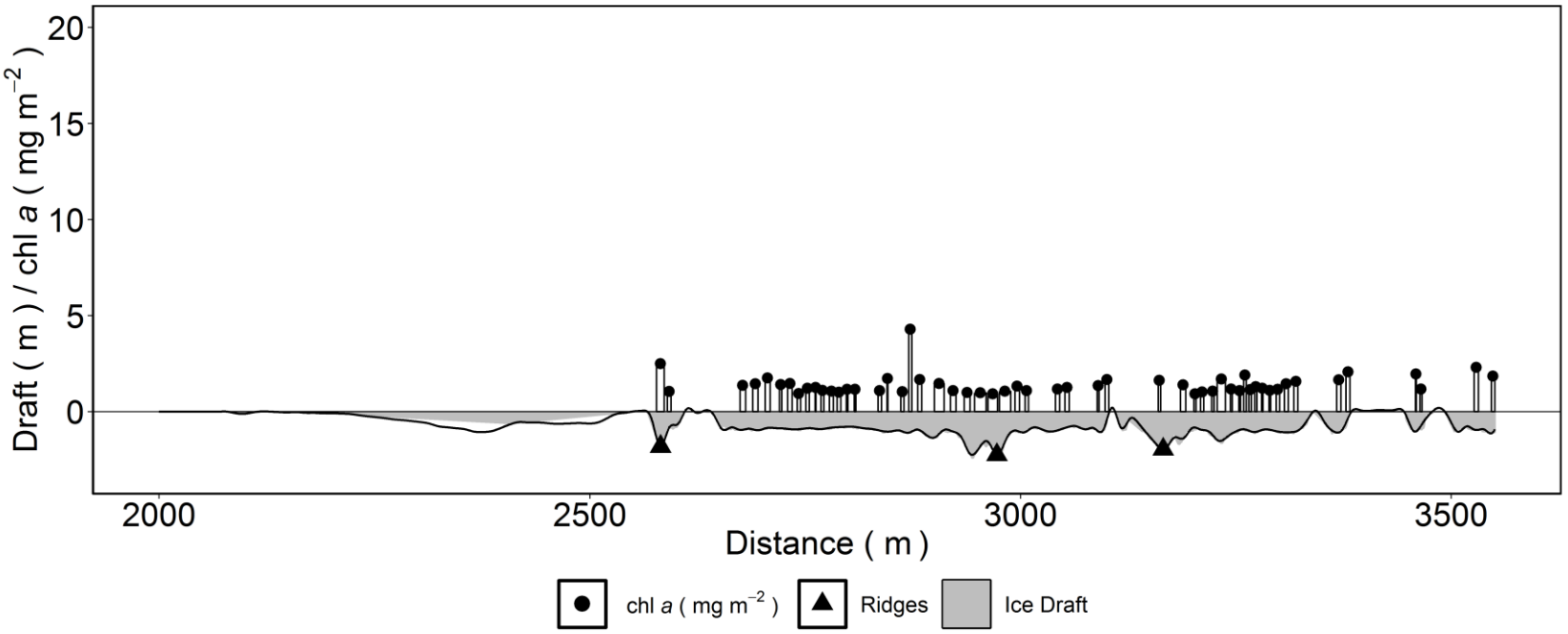

Figure S13. Surface and Under-ice trawl profile for station 248 of spectrally-derived chl *a* biomass (width of line is footprint of measurement), sea ice draft (negative values), and identified ridges. Black line represents the smoothed sea ice draft used for the identification of sea ice ridges.

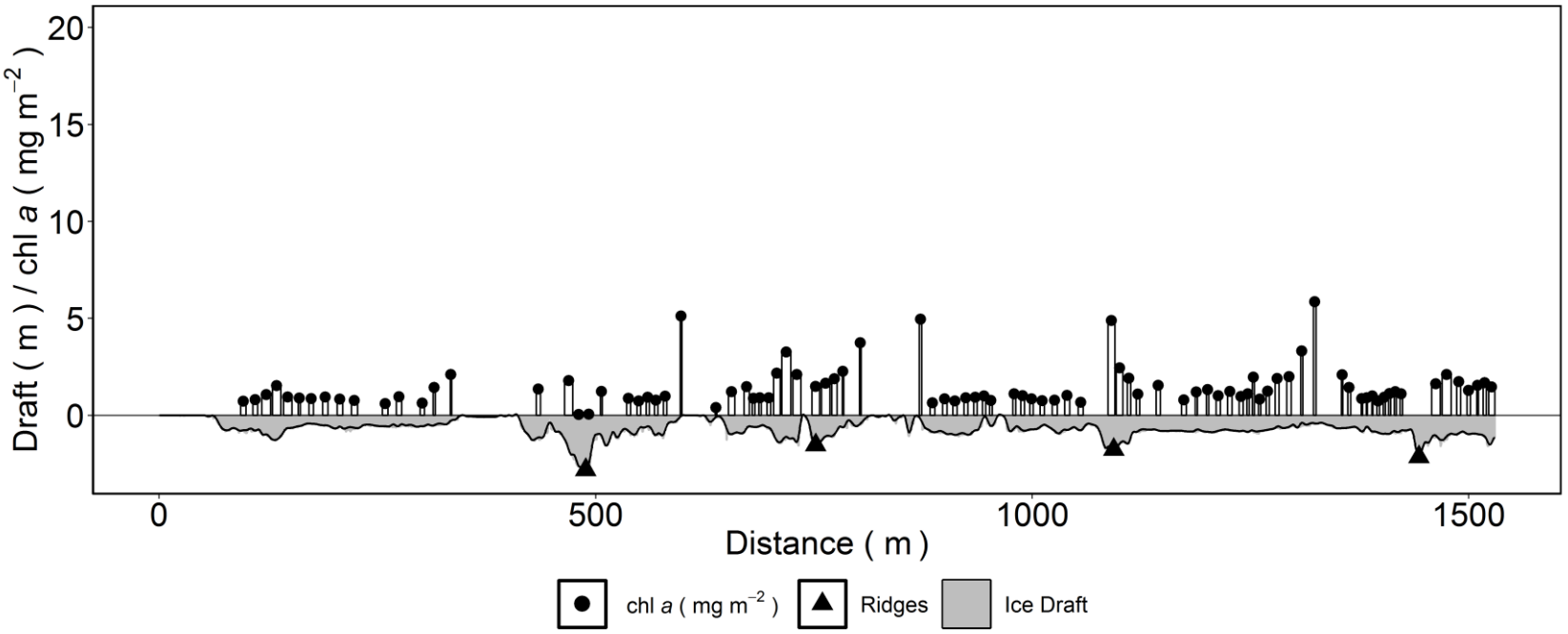

Figure S14. Surface and Under-ice trawl profile for station 285 of spectrally-derived chl *a* biomass (width of line is footprint of measurement), sea ice draft (negative values), and identified ridges. Black line represents the smoothed sea ice draft used for the identification of sea ice ridges.

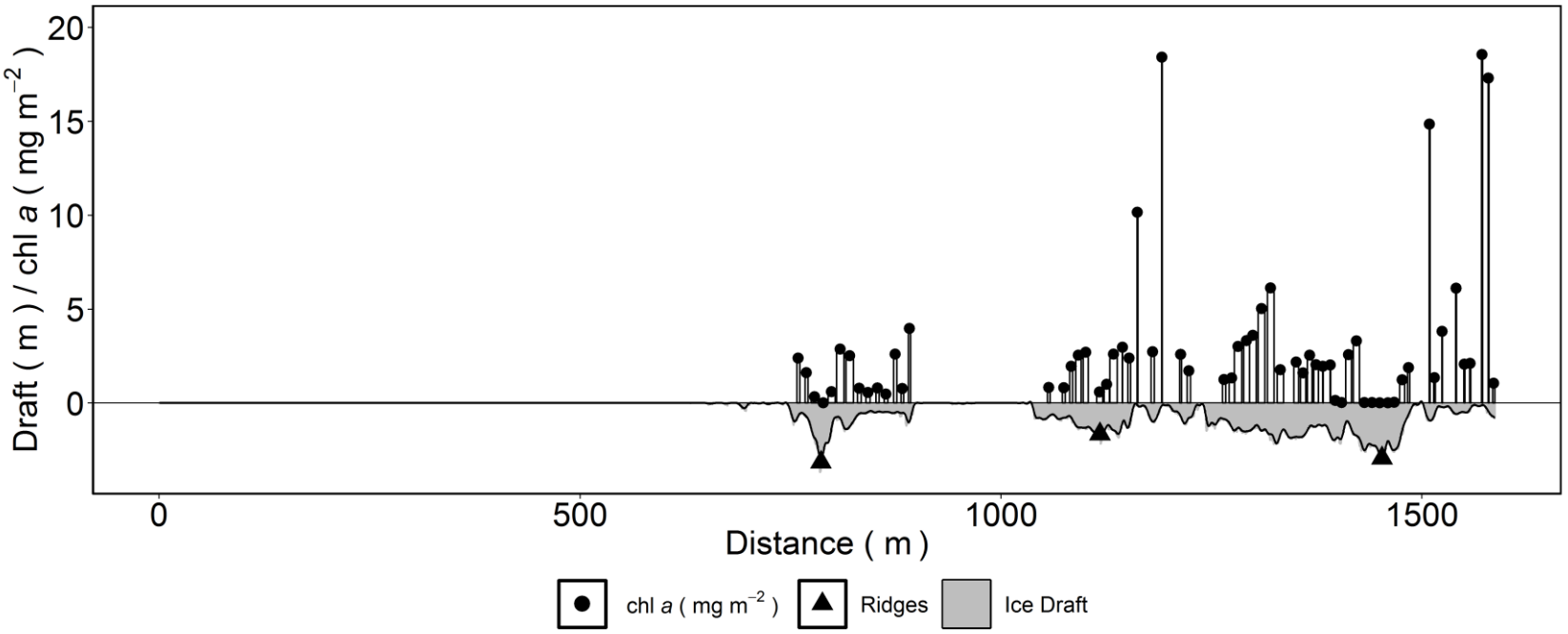

Figure S15. Surface and Under-ice trawl profile for station 321 of spectrally-derived chl *a* biomass (width of line is footprint of measurement), sea ice draft (negative values), and identified ridges. Black line represents the smoothed sea ice draft used for the identification of sea ice ridges.

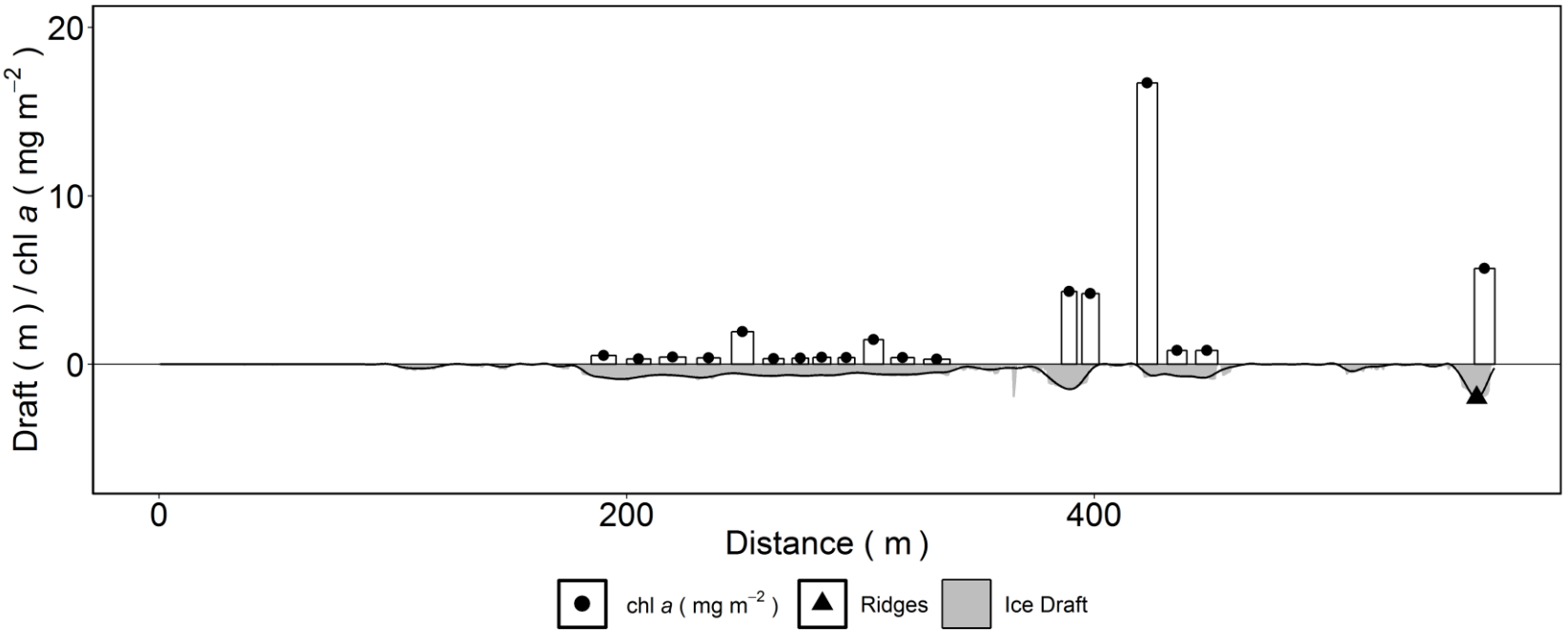

Figure S16. Surface and Under-ice trawl profile for station 345 of spectrally-derived chl *a* biomass (width of line is footprint of measurement), sea ice draft (negative values), and identified ridges. Black line represents the smoothed sea ice draft used for the identification of sea ice ridges.

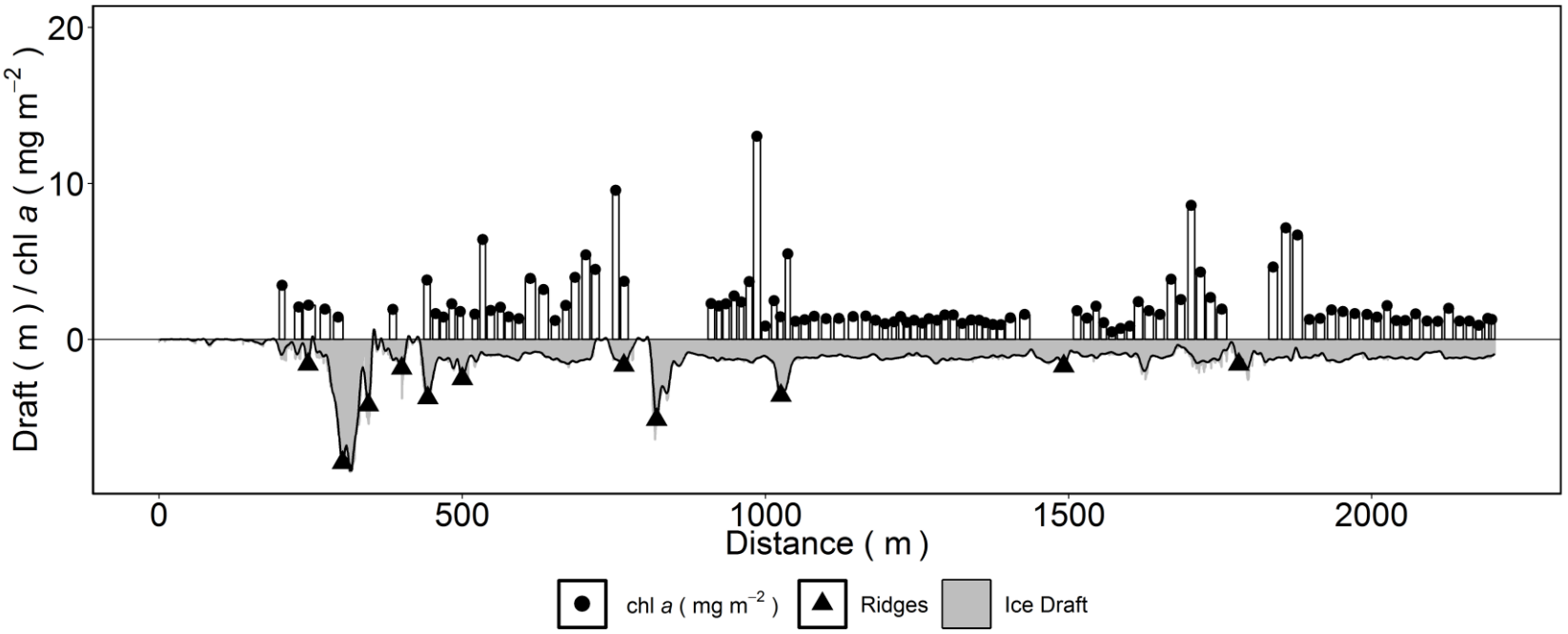

Figure S17. Surface and Under-ice trawl profile for station 358 of spectrally-derived chl *a* biomass (width of line is footprint of measurement), sea ice draft (negative values), and identified ridges. Black line represents the smoothed sea ice draft used for the identification of sea ice ridges.

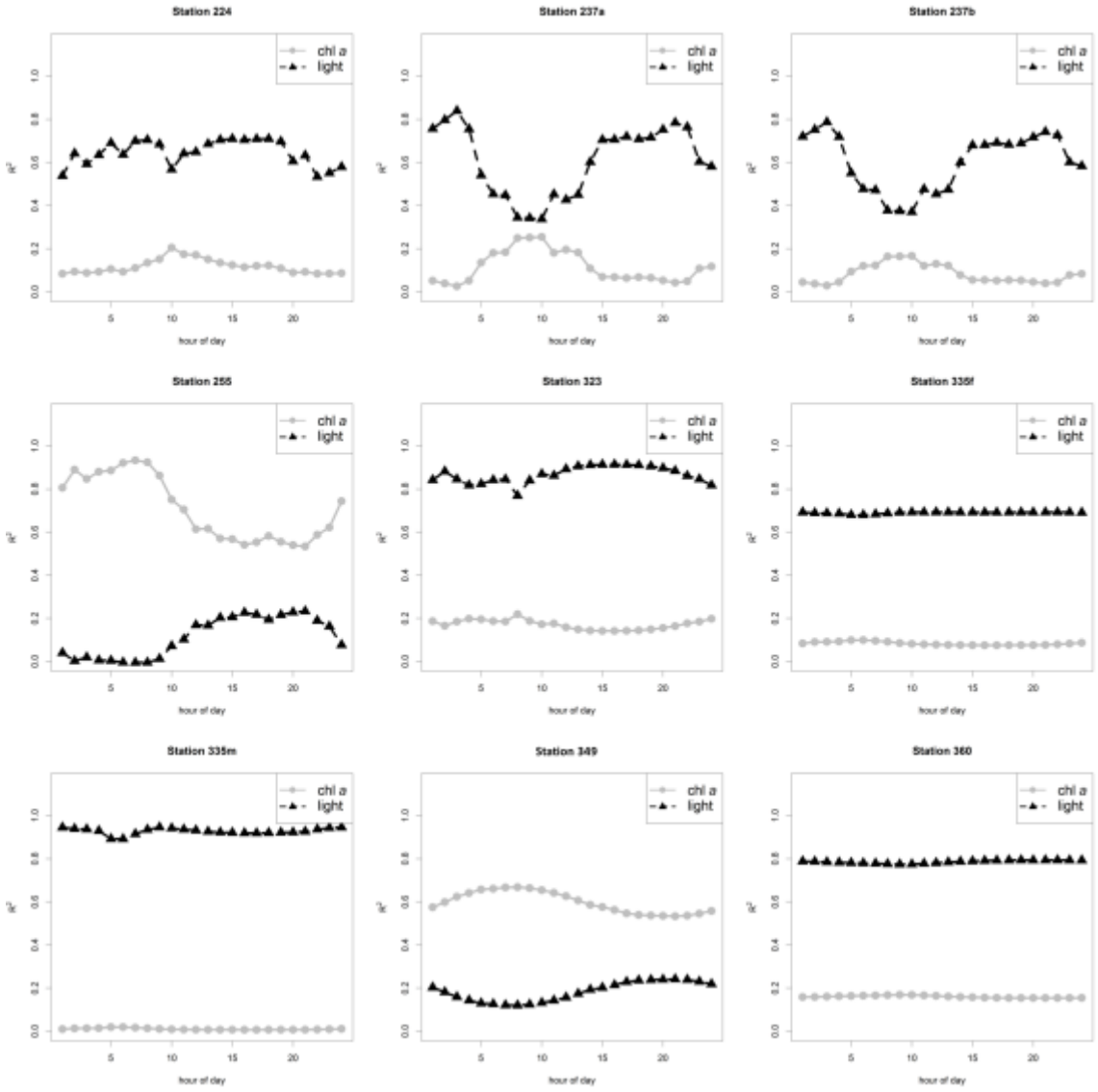

Figure S18. Explained variance (R^2) of NPP by up-scaled chl *a* and bottom-ice light per hour for each ROV station and survey listed in Table 1.

Sampling Method	**Summary statistics**	Chl *a* (mg m^{-2})		Net Primary Production (mg C m^{-2} d^{-1})	
		MYI	**FYI**	**MYI**	**FYI**
FM-CORES	Mean (range) [N]	5.5 (0.4 – 8.0) [3]	0.84 (0.3 – 1.7) [5]	0.48 (0.05 – 1.0)[3]	2.36 (0.02 – 10.16)[5]
ROV	Mean (range) [N]	3.4 (0.0 – 19.8) [1993]	1.46 (0.0 – 18.9) [3333]	0.18 (0.0 – 4.42)[1993]	2.06 (0.0 – 140) [3333]
SUIT	Mean (range) [N]	2.5 (0.3 – 16.7) [132]	1.7 (0.0 –18.5) [242]	–	–
FM-CORES	Median (IQR)	8 (4.2 – 8.0)	0.6 (0.4 – 1.2)	0.39 (0.22 – 0.70)	0.56 (0.45 – 0.62)
ROV	Median (IQR)	2.6 (1.8 – 3.9)	1.3 [1.1 – 1.6]	0.11 (0.06 – 0.20)	0.71 (0.17 – 1.17)
SUIT	Median (IQR)	1.8 (1.4 – 2.7)	1.3 (0.8 – 2.1)	–	–

Table S1. Ice-algal chl a biomass and NPP summarized for sampling gears into MYI and FYI. Means, range (min – max), and sample size [N] are provided for comparison as these are the values used in Fernández-Méndez et al. [2015] for up-scaling to the entire Arctic Ocean.

Station	**Variable**	**Ridge 1 (N=20)**	**Ridge 2 (N=21)**	**Level Ice (N=427)**
224	Draft (m)	4.5 (2.4 – 5.0)	2.8 (2.7 – 2.9)	1.1 (0.95 – 1.4)
	Chl a (mg m^{-2})	1.8 (1.7 – 17.9)* [0.91] [a]	3.4 (2.5 – 5.3)*[0.58] [a]	1.0 (0.97 – 1.1)[0.78] [a]
	NPP (mg C m^{-2})	6.9 (5.7 – 17.9)	4.0 (2.9 – 4.2)*	8.7 (5.9 – 12.3)
	I (µmol photons m^{-2} s^{-1})	11.6 (4.8 – 12.9)*[0.79] [a]	2.5 (2.2 – 5.6)*[0.0] [a]	39.0 (22.8 – 61.2)[0.71] [a]

* indicates statistically significant *t* test between the corresponding ridge and Level Ice at $p < 0.05$

[a] value within square brackets represents the explained variance of NPP by the corresponding variable and data subset of ridge or level ice.

Table S2. Comparison of chl a biomass and net primary production between sea ice ridges and level ice at station 224. Ridges are identified in Figure 3 a.

SUIT station	Ridge count	Total Distance (km)	Density (ridges km^{-1})	mean ridge width (m)	ridge coverage (% of total ice)
216	4	1.6	2.5	47.6	3.0
223	12	0.8	15.8	79.5	10.5
233	12	1.5	8.1	60.8	4.1
248	4	1.5	2.7	91.1	6.2
285	4	1.3	3.1	91.5	7.1
321	3	0.7	4.6	100.3	15.4
345	8	1.2	6.6	49.3	4.1
358	11	2.0	5.6	48.7	2.5
376	3	0.2	18.0	49.5	29.6

Table S3. Summary of ridge identification analysis from the surface and under-ice hauls conducted during PS80.3.

B 2 Supplementary Material for Chapter 3 - Paper 5:

Table S2. Bulk stable nitrogen ($\delta^{15}N$) and carbon ($\delta^{13}C$) isotope values in ice-associated particulate organic matter (I-POM), pelagic particulate organic matter (P-POM), and under-ice fauna species (mean ± 1 SD ‰). Species-specific $\delta^{15}N$ and $\delta^{13}C$ values are shown separately for Nansen (NB) and Amundsen Basin (AB) regimes.

			NB		AB	
	n_{NB}	n_{AB}	**$\delta^{15}N$**	**$\delta^{13}C$**	**$\delta^{15}N$**	**$\delta^{13}C$**
I-POM	2	5	3.7 ± 0.3	-23.2 ± 0.6	5.3 ± 0.8	-25.7 ± 1.2
P-POM	6	11	3.3 ± 0.6	-27.2 ± 0.5	4.4 ± 1.3	-27.4 ± 1.0
Calanus glacialis	2	2	7.0 ± 1.0	-29.0 ± 3.1	8.1 ± 0.2	-24.6 ± 0.2
Calanus hyperboreus	2	2	6.8 ± 1.3	-26.8 ± 0.7	8.8 ± 0.4	-26.4 ± 1.7
Apherusa glacialis	2	2	5.4 ± 0.2	-22.1 ± 0.4	5.4 ± 0.5	-21.6 ± 2.2
Onisimus glacialis	2	2	7.6 ± 2.9	-22.9 ± 0.8	6.7 ± 0.1	-21.9 ± 1.6
Gammarus wilkitzkii	3	1	7.4 ± 0.4	-24.5 ± 0.4	6.3	-24.0
Eusirus holmii	2	2	9.1 ± 0.3	-22.7 ± 0.3	10.9 ± 1.8	-23.8 ± 0.2
Themisto libellula	1	3	7.1	-28.0	9.3 ± 1.2	-25.0 ± 1.1
Clione limacina	1	3	7.4	-26.6	8.9 ± 0.5	-26.9 ± 0.5

n: sample size

Table S1. Relative composition of most abundant lipid classes in under-ice fauna species (mean ± 1 SD mass % of total lipid content).

	Calanus glacialis	***Calanus hyperboreus***	***Apherusa glacialis***	***Onisimus glacialis***	***Gammarus wilkitzkii***	***Eusirus holmii***	***Themisto libellula***	***Clione limacina***
n	2	2	6	6	6	6	6	6
WE	72.6 ± 5.4	85.6 ± 7.5	1.5 ± 1.1	16.0 ± 11.3	4.5 ± 5.0	14.9 ± 19.9	47.4 ± 18.8	1.4 ± 0.6
TAG	1.7 ± 2.4	1.9 ± 1.9	86.4 ± 4.0	73.6 ± 11.5	80.0 ± 4.8	62.7 ± 17.5	46.1 ± 18.0	61.2 ± 29.1
PE	7.9 ± 1.8	4.3 ± 3.6	3.2 ± 1.2	2.0 ± 1.1	3.2 ± 1.2	4.9 ± 1.9	1.6 ± 0.5	8.1 ± 6.2
PC	17.1 ± 7.1	7.3 ± 5.0	6.2 ± 1.3	5.9 ± 1.6	6.5 ± 1.5	11.7 ± 8.9	4.0 ± 2.0	13.3 ± 9.3
Total	99.3	99.1	97.3	97.5	94.2	94.2	99.1	84.0
NL	75.0	88.5	90.2	91.8	89.3	81.7	94.3	72.4
PL	25.0 ± 8.8	11.5 ± 8.6	9.8 ± 2.5	8.2 ± 1.5	10.7 ± 2.9	18.3 ± 9.8	5.7 ± 1.5	27.6 ± 18.0

n: sample size, NL: neutral lipid, PC: phosphatidylcholine, PE: phosphatidylethanolamine, PL: polar lipid, TAG: triacylglycerol, WE: wax ester

Table S3. Carbon stable isotope values ($\delta^{13}C$) of marker fatty acids (FAs) in ice-associated particulate organic matter (I-POM), pelagic particulate organic matter (P-POM), and under-ice fauna species (mean ± 1 SD ‰). Species-specific $\delta^{13}C$ values are shown separately for Nansen (NB) and Amundsen Basin (AB) regimes. Not detected FAs are reported as '--'.

			NB	AB	NB	AB	NB	AB	NB	AB
	n_{NB}	n_{AB}	**16:1n-7**		**20:5n-3**		**18:4n-3**		**22:6n-3**	
I-POM	1	6	-23.3	-25.2 ± 4.4	-25.8	-26.7 ± 3.0	-26.7	-28.8 ± 3.5	-21.3	-24.1 ± 4.1
P-POM	5	2	-27.3 ± 3.7	-24.1 ± 1.2	-36.3 ± 2.3	-33.8 ± 0.7	-39.2 ± 0.7	-39.6 ± 0.6	-35.7 ± 2.7	-34.7 ± 1.2
Calanus glacialis	3	7	-29.9 ± 1.9	-22.9 ± 2.0	-32.1 ± 1.2	-31.8 ± 1.4	-35.2 ± 2.2	-35.9 ± 1.6	-31.2 ± 2.1	-32.4 ± 2.2
Calanus hyperboreus	2	4	-30.8 ± 2.4	-25.5 ± 2.7	-31.6 ± 2.0	-32.3 ± 0.9	-36.0 ± 1.2	-36.3 ± 1.2	-32.7 ± 2.0	-34.3 ± 2.5
Apherusa glacialis	3	7	-26.2 ± 2.0	-23.4 ± 2.4	-27.3 ± 0.9	-26.4 ± 1.4	-31.4 ± 1.0	-28.6 ± 1.6	-30.2 ± 1.6	-27.7 ± 1.0
Onisimus glacialis	4	4	-24.8 ± 1.3	-21.1 ± 3.1	-29.3 ± 0.7	-27.5 ± 1.8	-34.5 ± 0.4	-30.3 ± 4.7	-30.6 ± 1.2	-30.1 ± 0.7
Gammarus wilkitzkii	2	2	-26.5 ± 0.8	-23.1 ± 1.1	-29.5 ± 1.3	-28.4 ± 0.1	-31.6 ± 0.9	-30.4 ± 3.5	-30.6 ± 1.4	-32.7 ± 1.0
Eusirus holmii	2	6	-25.2 ± 0.5	-22.8 ± 2.1	-29.6 ± 1.1	-28.7 ± 1.0	-30.9 ± 0.2	-29.8 ± 1.3	-31.6 ± 0.4	-29.9 ± 1.2
Themisto libellula	1	6	-28.6	-23.2 ± 1.2	-33.4	-31.1 ± 1.2	-38.5	-35.2 ± 1.9	-33.4	-33.7 ± 2.0
Clione limacina	2	7	-29.8 ± 0.5	-28.4 ± 2.1	-33.2 ± 2.0	-34.4 ± 1.5	--	--	-33.0 ± 1.5	-34.0 ± 1.0

n: sample size

Appendix C:

C 1 Supplementary Material for Chapter 4 - Paper 7: Suitable ice-algal habitat and biomass are largely underestimated over multi-year sea ice

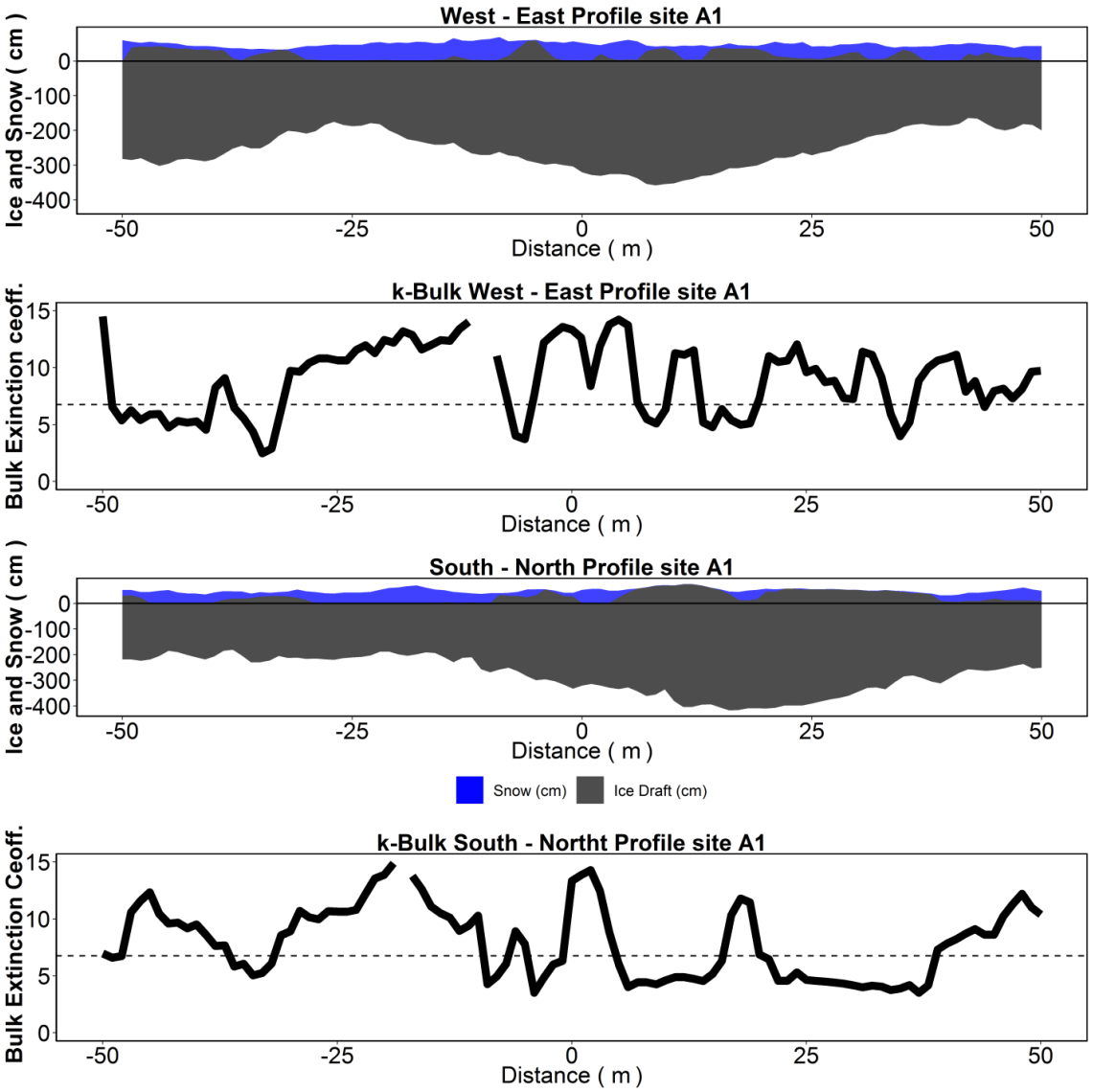

Figure S 1. Snow and sea ice profiles for MYI site 01-13 showing the different directions West-East (WE) and South-North (SN) with the corresponding calculated bulk integrated extinction coefficient ($k_{B,calc}$) profiles. Note: use of prefix "A" for sites.

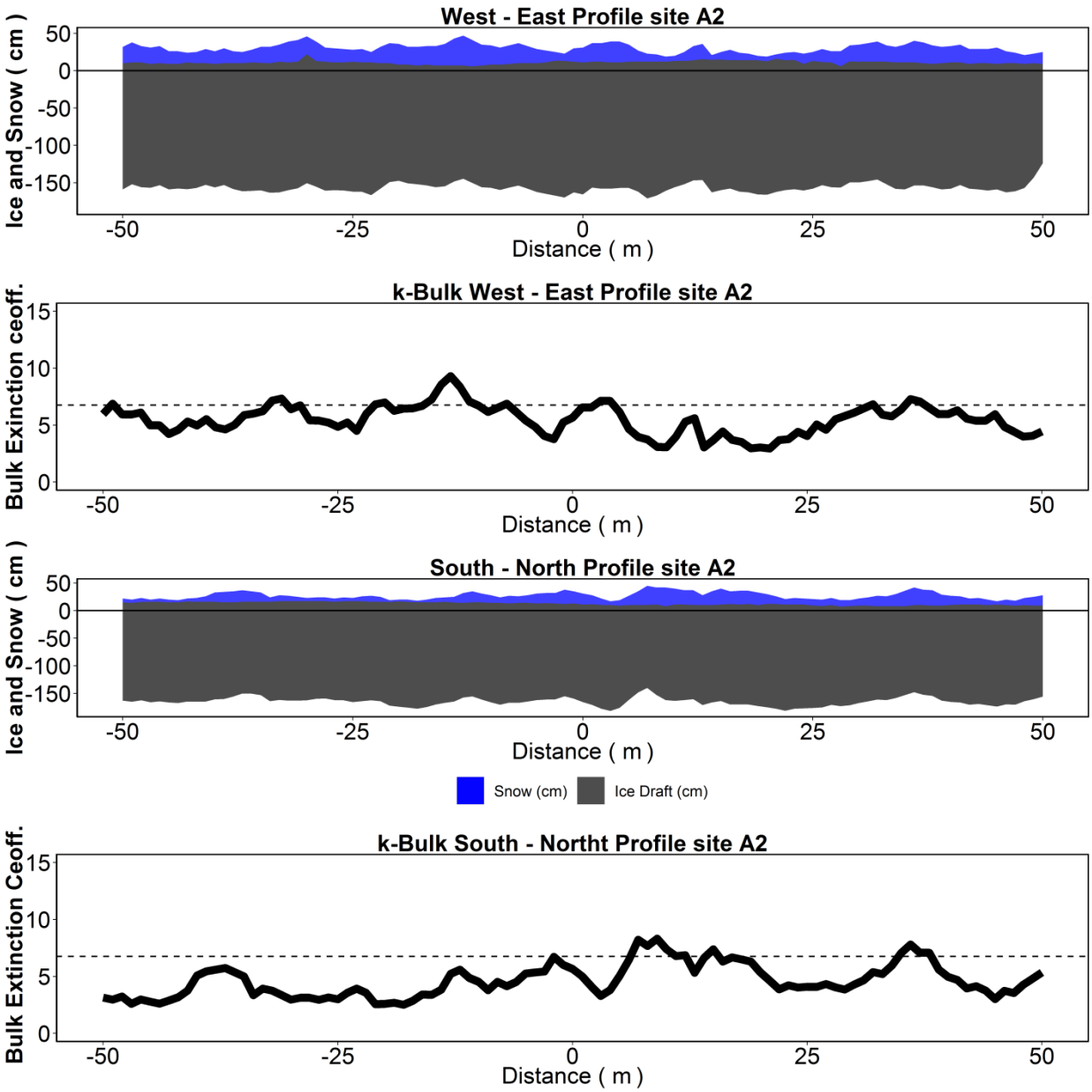

Figure S 2. Snow and sea ice profiles for FYI site 02-13 showing the different directions West-East (WE) and South-North (SN) with the corresponding calculated bulk integrated extinction coefficient ($k_{B,calc}$) profiles. Note: use of prefix "A" for site.

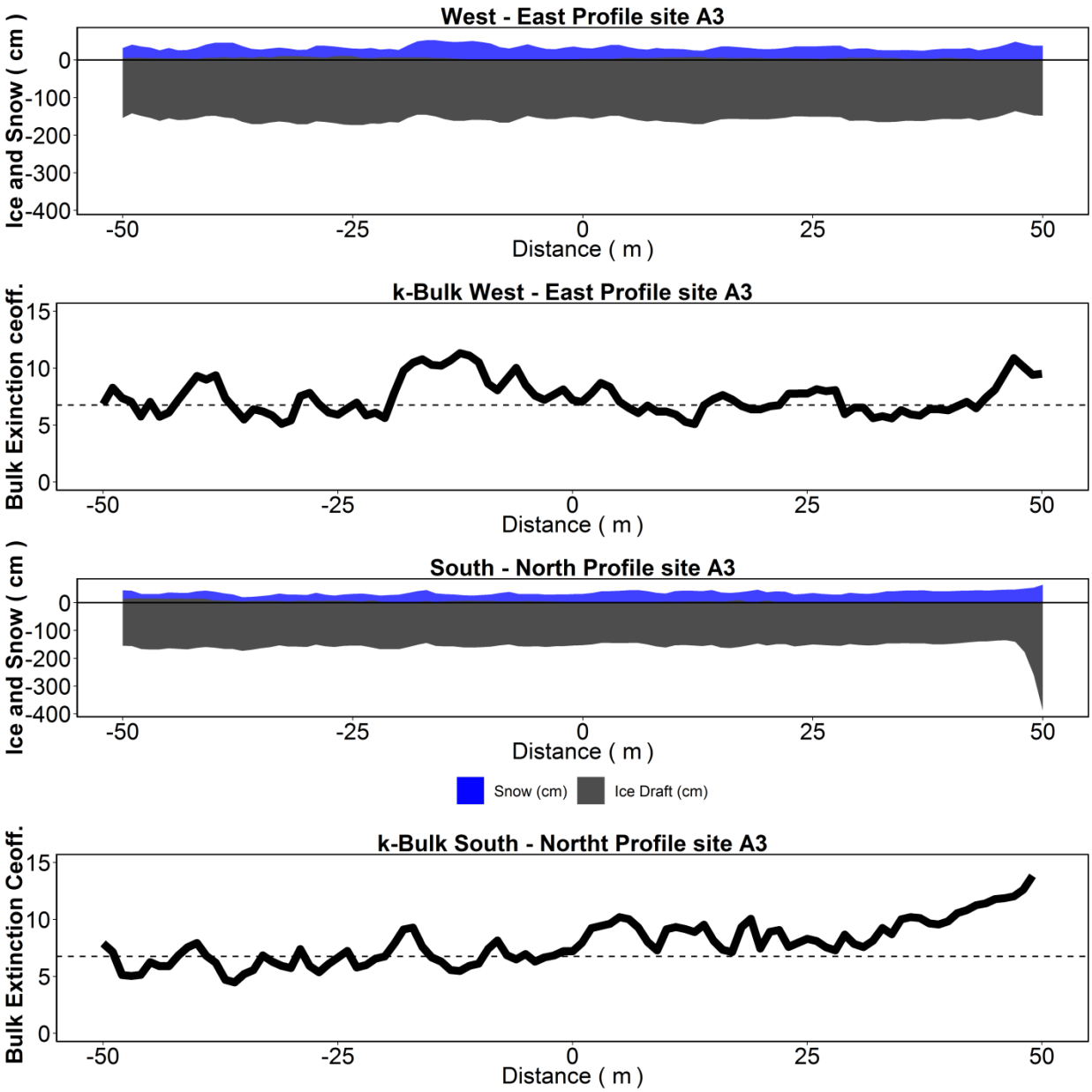

Figure S 3. Snow and sea ice profiles for FYI site 03-13 showing the different directions West-East (WE) and South-North (SN) with the corresponding calculated bulk integrated extinction coefficient ($k_{B,calc}$) profiles. Note: use of prefix "A" for sites.

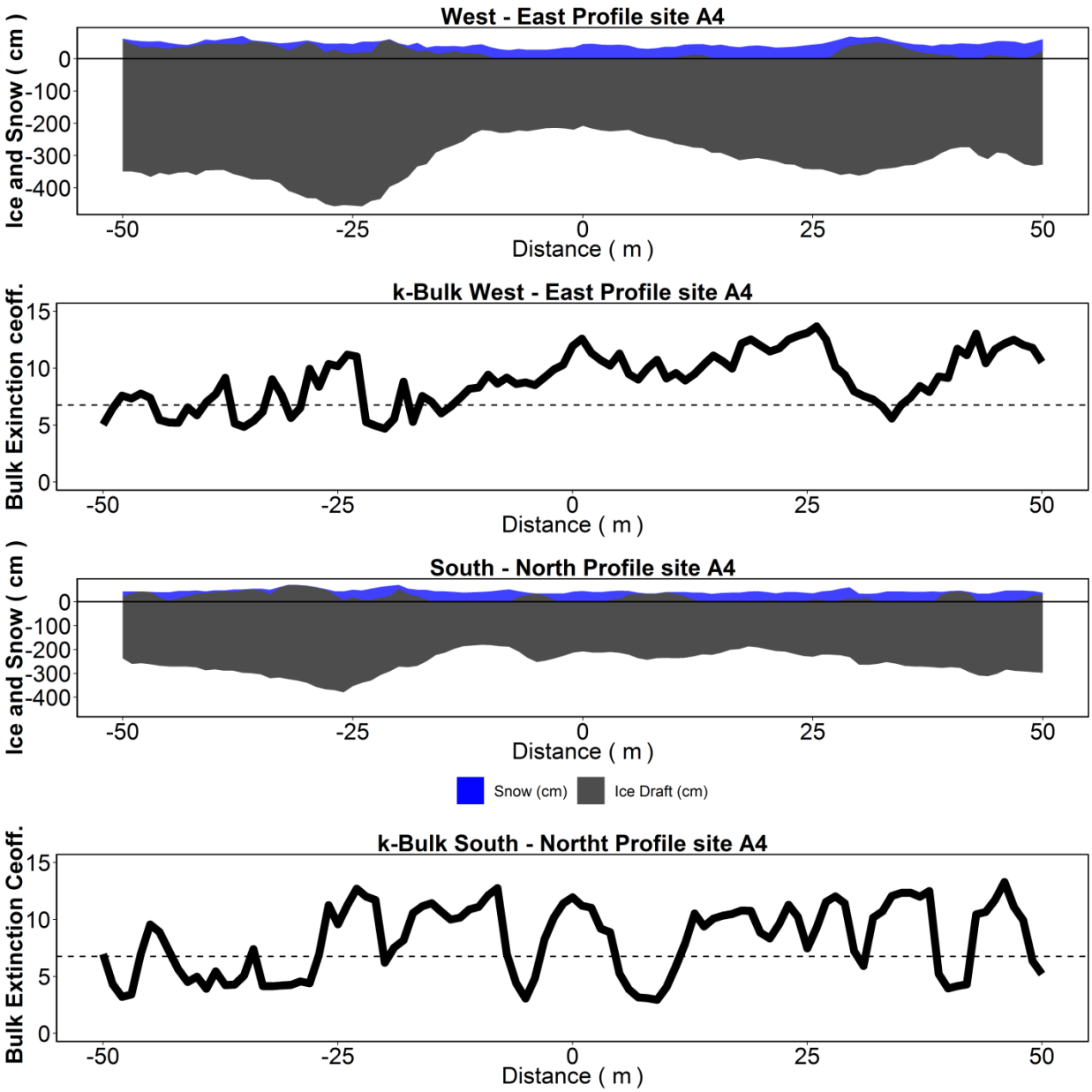

Figure S 4. Snow and sea ice profiles for MYI site 04-13 showing the different directions West-East (WE) and North-South (NS) with the corresponding calculated bulk integrated extinction coefficient ($k_{B,calc}$) profiles. Note: use of prefix "A" for sites.

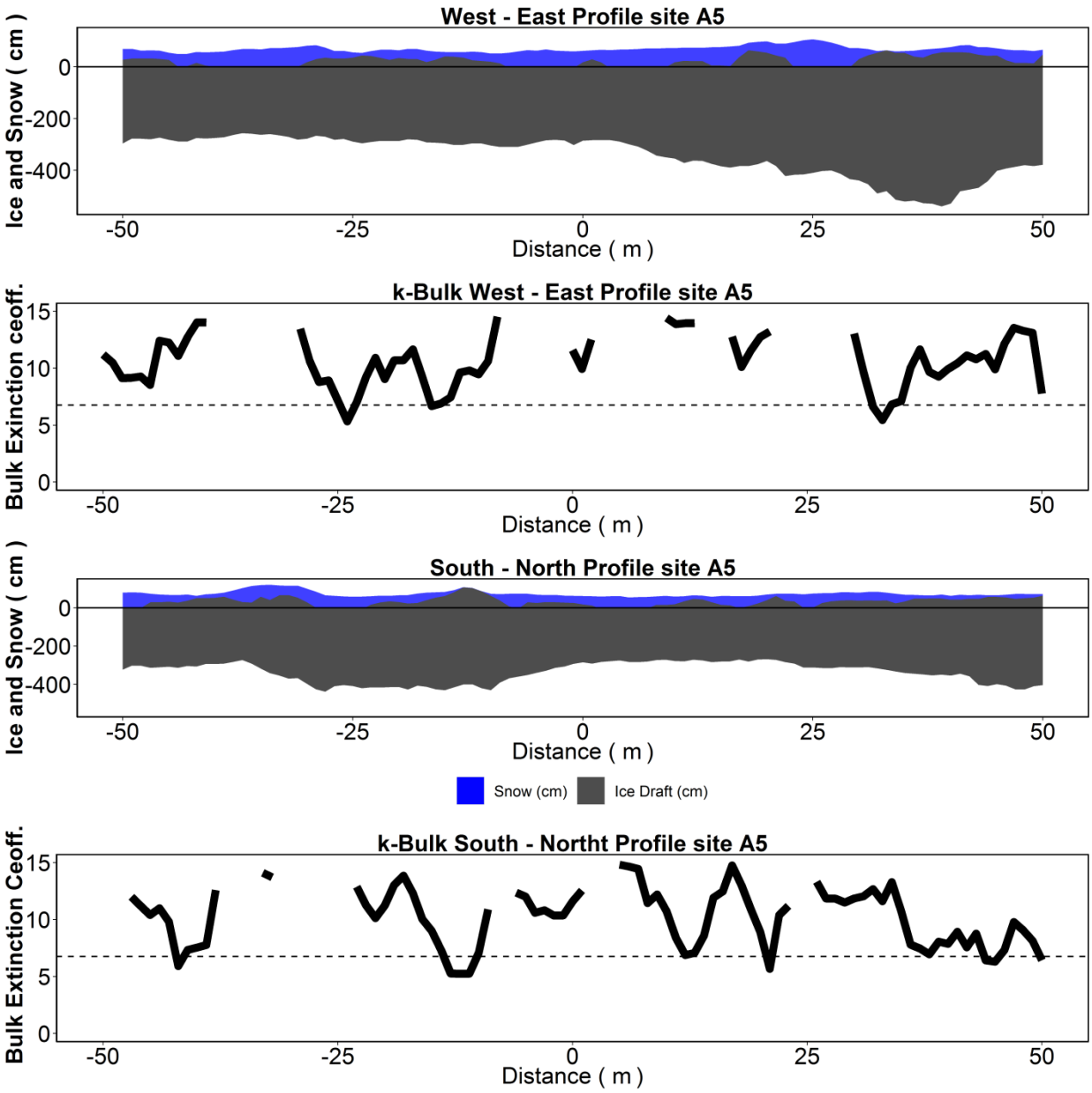

Figure S 5. Snow and sea ice profiles for MYI site 05-13 showing the different directions West-East (WE) and South-North (SN) with the corresponding calculated bulk integrated extinction coefficient ($k_{B,calc}$) profiles. Note: use of prefix "A" for sites.

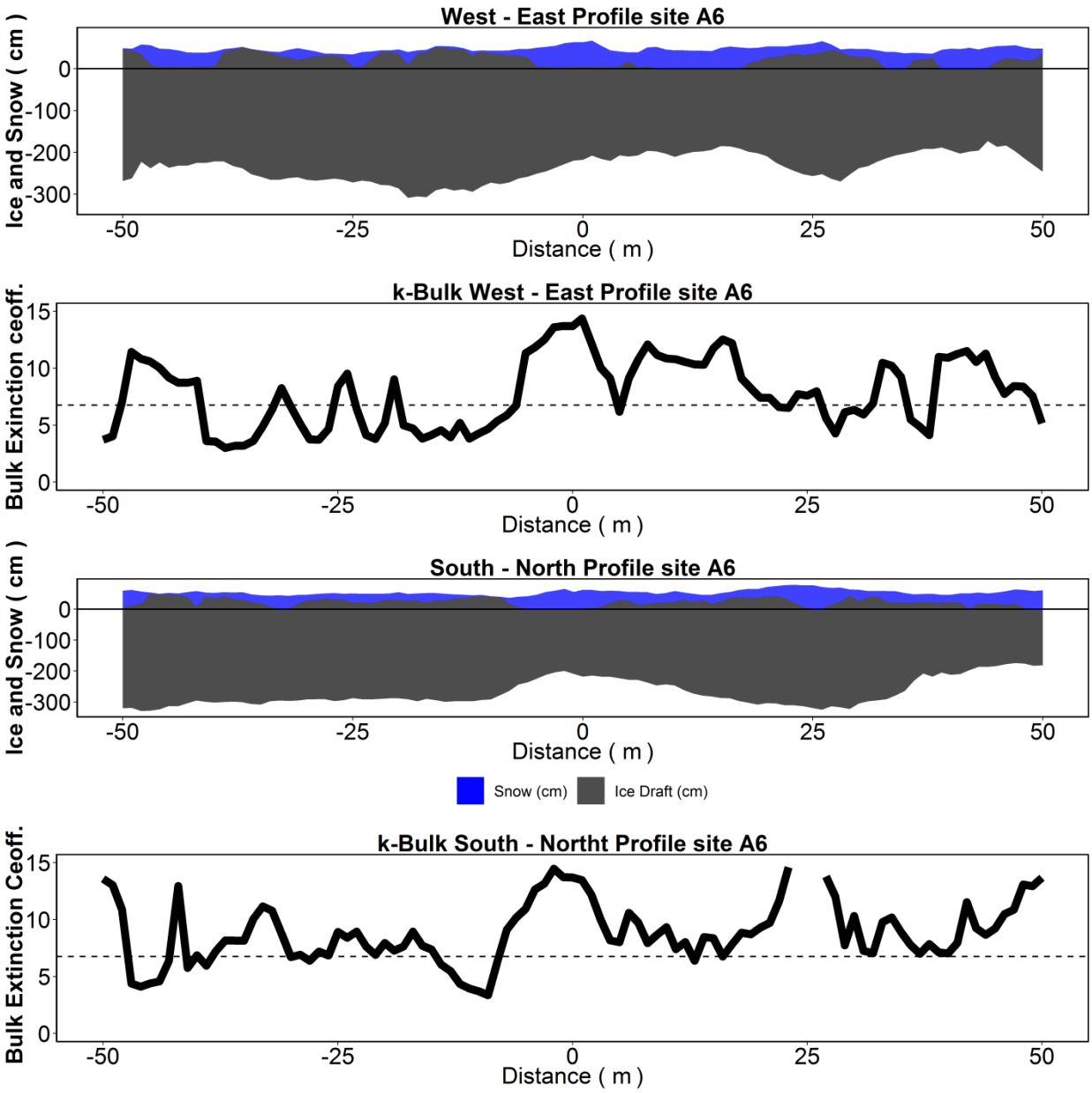

Figure S 6. Snow and sea ice profiles for MYI site 06-13 showing the different directions West-East (WE) and South-North (SN) with the corresponding calculated bulk integrated extinction coefficient ($k_{B,calc}$) profiles. Note: use of prefix "A" for sites.

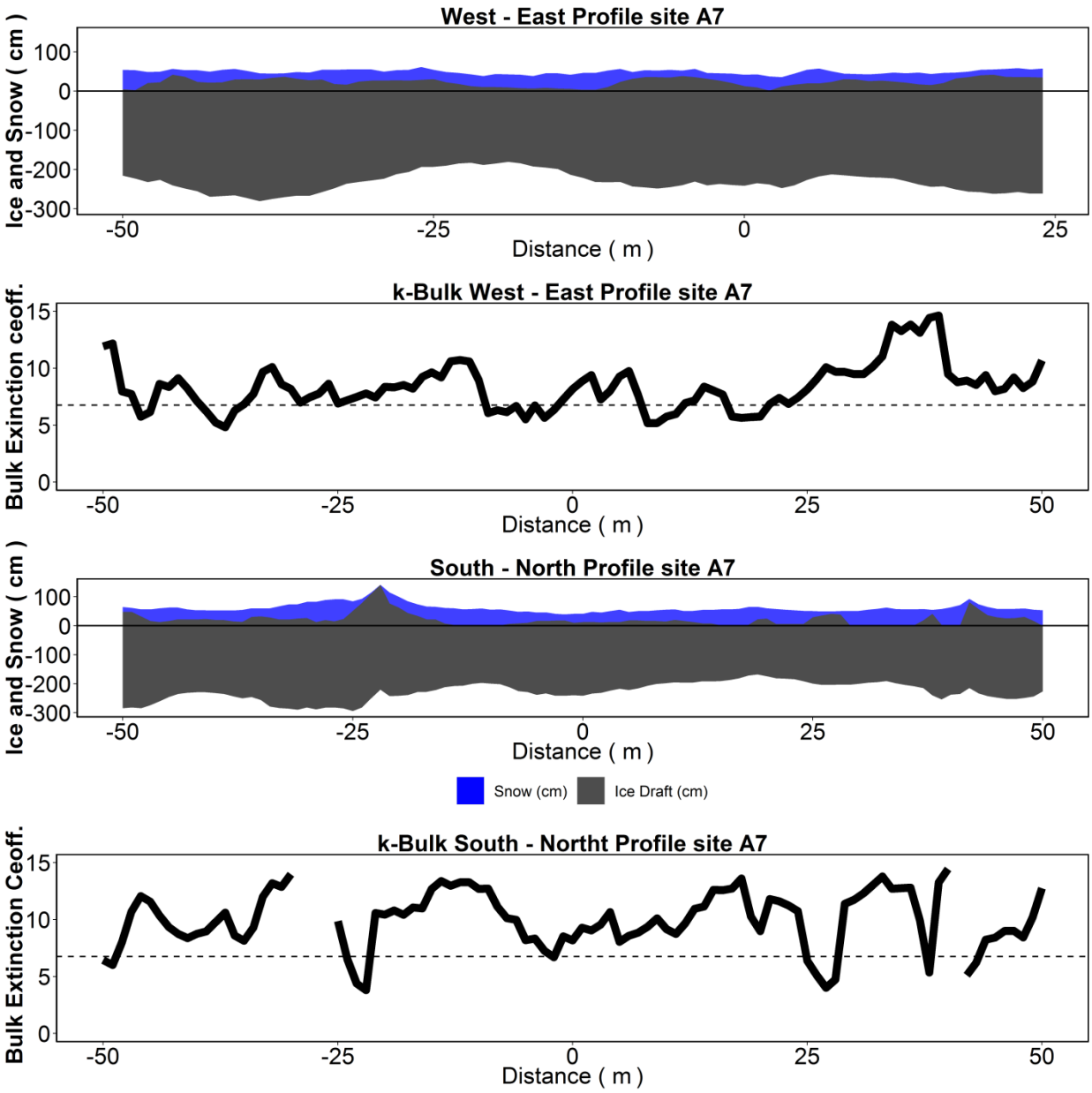

Figure S 7. Snow and sea ice profiles for MYI site 07-13 showing the different directions West-East (WE) and South-North (SN) with the corresponding calculated bulk integrated extinction coefficient ($k_{B,calc}$) profiles. Note: use of prefix "A" for sites.

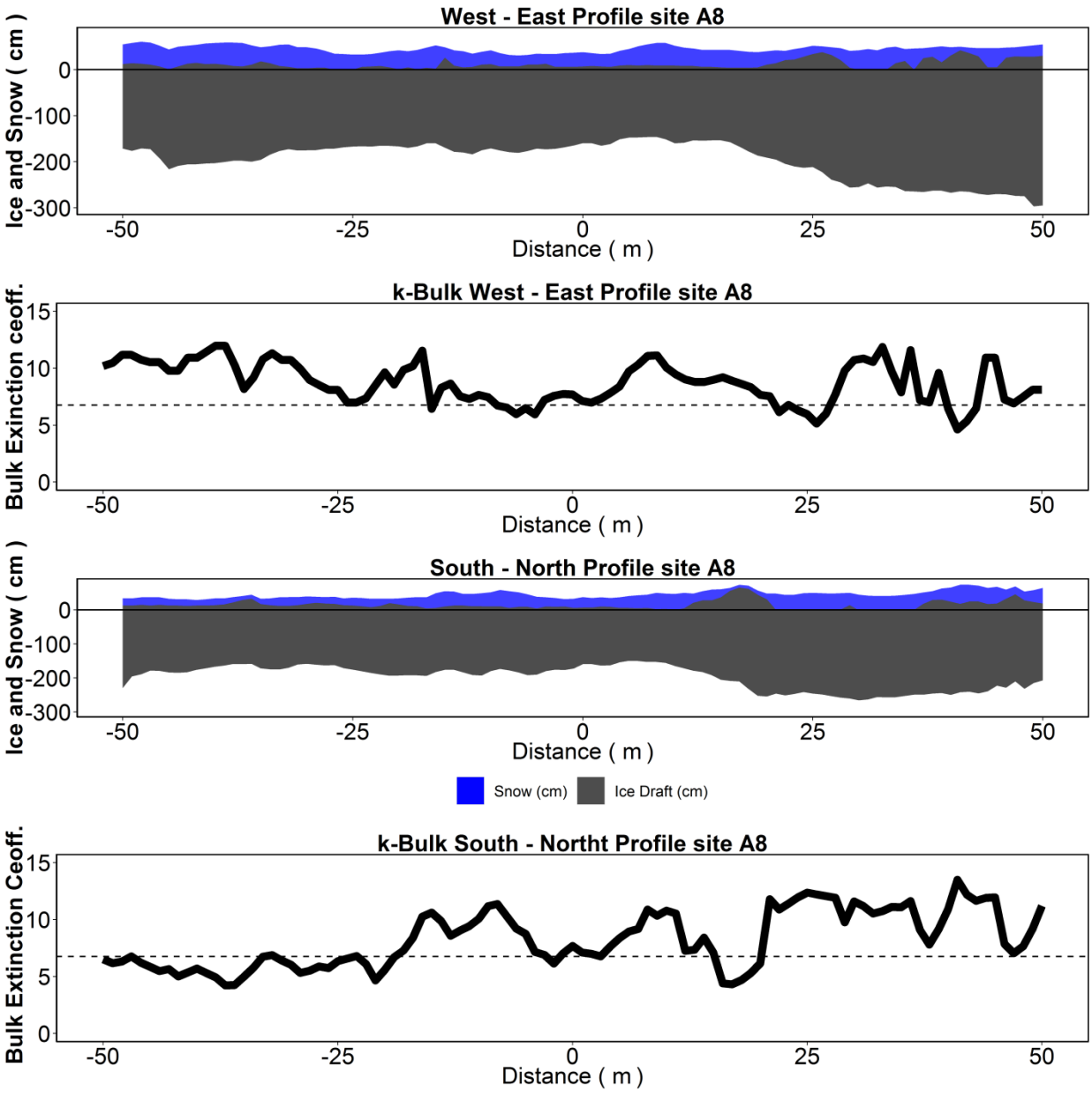

Figure S 8. Snow and sea ice profiles for MYI site 08-13 showing the different directions West-East (WE) and South-North (SN) with the corresponding calculated bulk integrated extinction coefficient ($k_{B,calc}$) profiles. Note: use of prefix "A" for sites.

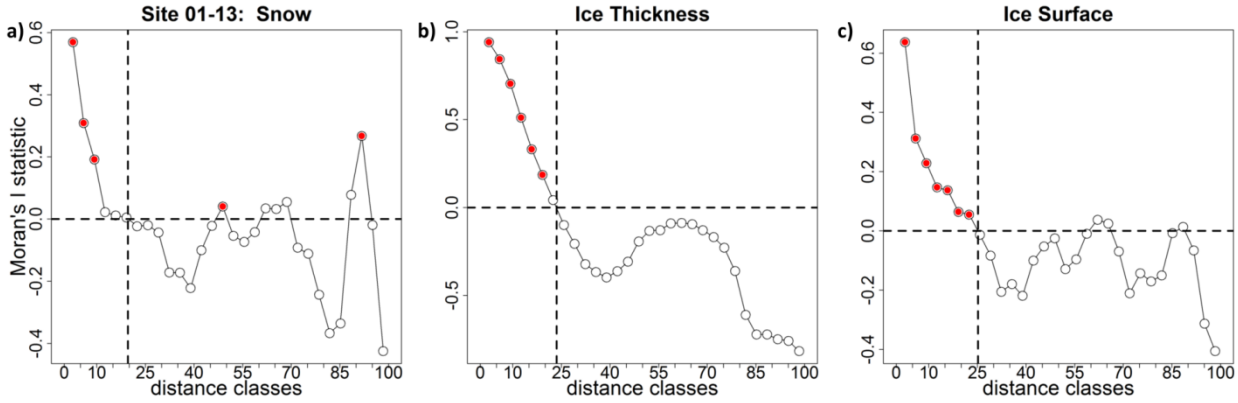

Figure S 9. Spatial correlograms showing Moran's I as a function of distance classes (meters) at MYI site 01-13 for survey measurements of: a) snow; b) ice thickness; and c) ice surface. Vertical dashed line corresponds to the identified patch size listed in Table 1. Filled red circles are significant values and open circles are non-significant values at $p < 0.05$.

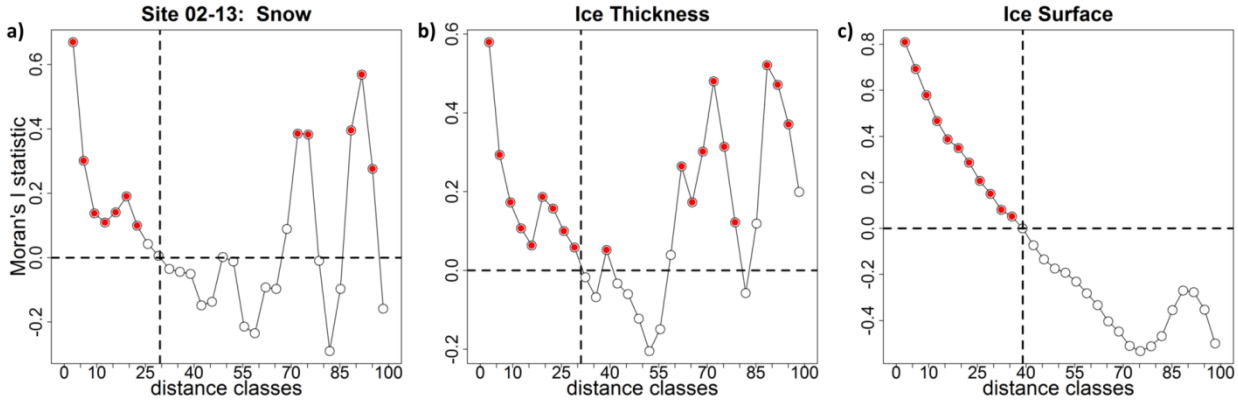

Figure S 10. Spatial correlograms showing Moran's I as a function of distance classes (meters) at FYI site 02-13 for survey measurements of: a) snow; b) ice thickness; and c) ice surface. Vertical dashed line corresponds to the identified patch size listed in Table 1. Filled red circles are significant values and open circles are non-significant values at $p < 0.05$.

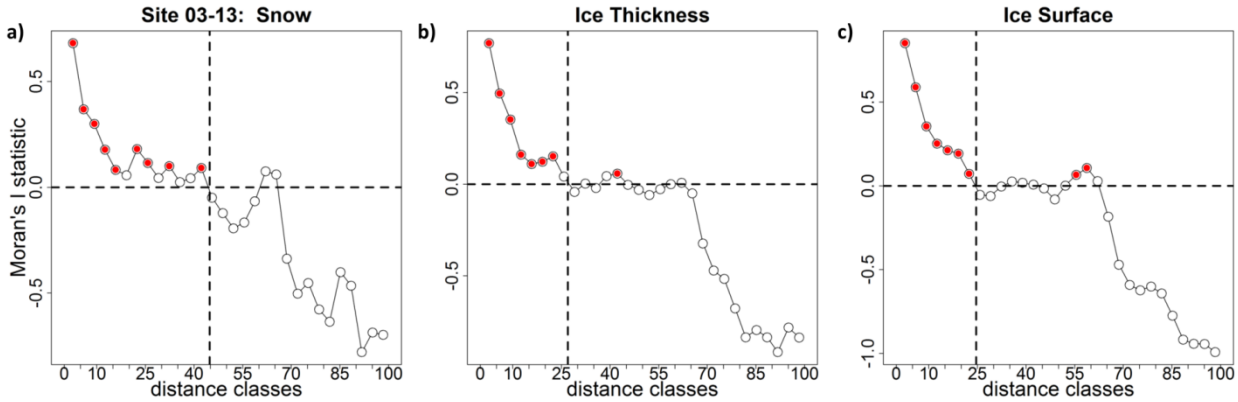

Figure S 11. Spatial correlograms showing Moran's I as a function of distance classes (meters) at FYI site 03-13 for survey measurements of: a) snow; b) ice thickness; and c) ice surface. Vertical dashed line corresponds to the identified patch size listed in Table 1. Filled red circles are significant values and open circles are non-significant values at $p < 0.05$.

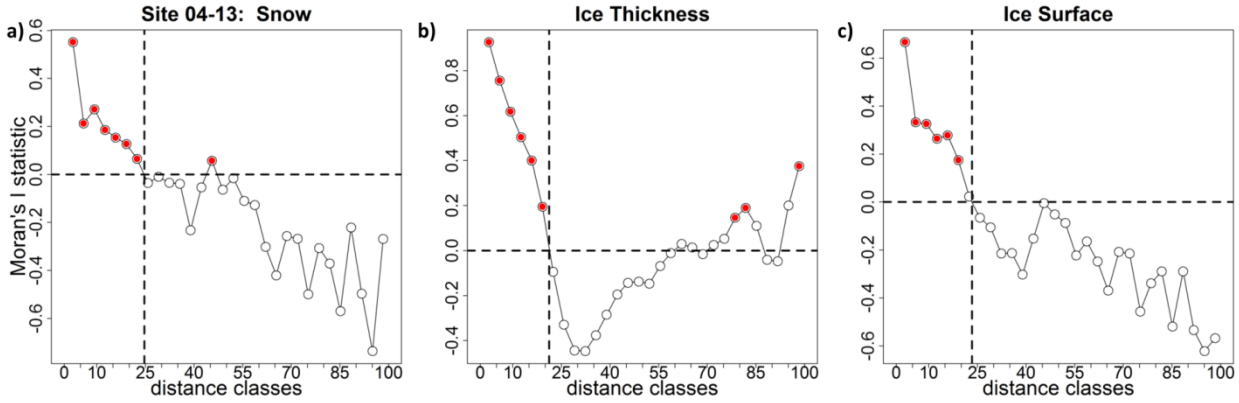

Figure S 12. Spatial correlograms showing Moran's I as a function of distance classes (meters) at MYI site 04-13 for survey measurements of: a) snow; b) ice thickness; and c) ice surface. Vertical dashed line corresponds to the identified patch size listed in Table 1. Filled red circles are significant values and open circles are non-significant values at $p < 0.05$.

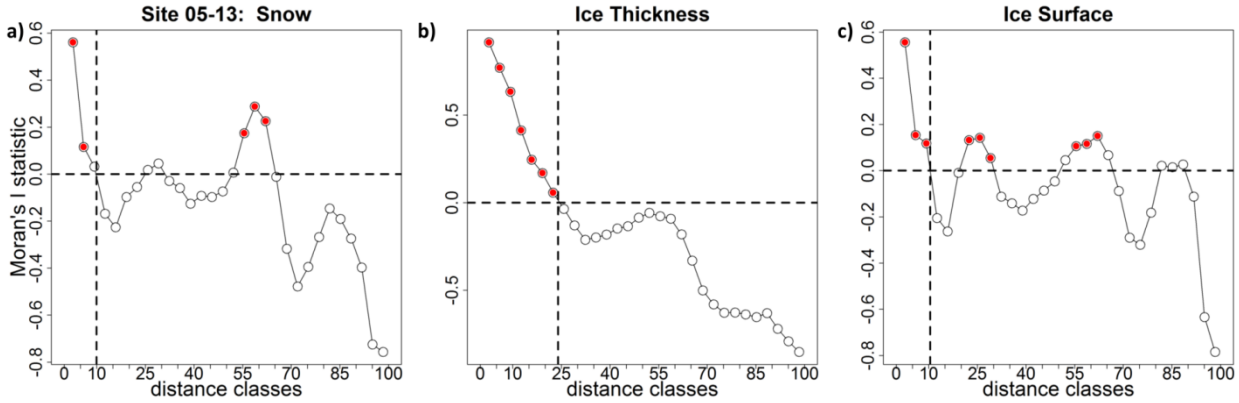

Figure S 13. Spatial correlograms showing Moran's I as a function of distance classes (meters) at MYI site 05-13 for survey measurements of: a) snow; b) ice thickness; and c) ice surface. Vertical dashed line corresponds to the identified patch size listed in Table 1. Filled red circles are significant values and open circles are non-significant values at $p < 0.05$.

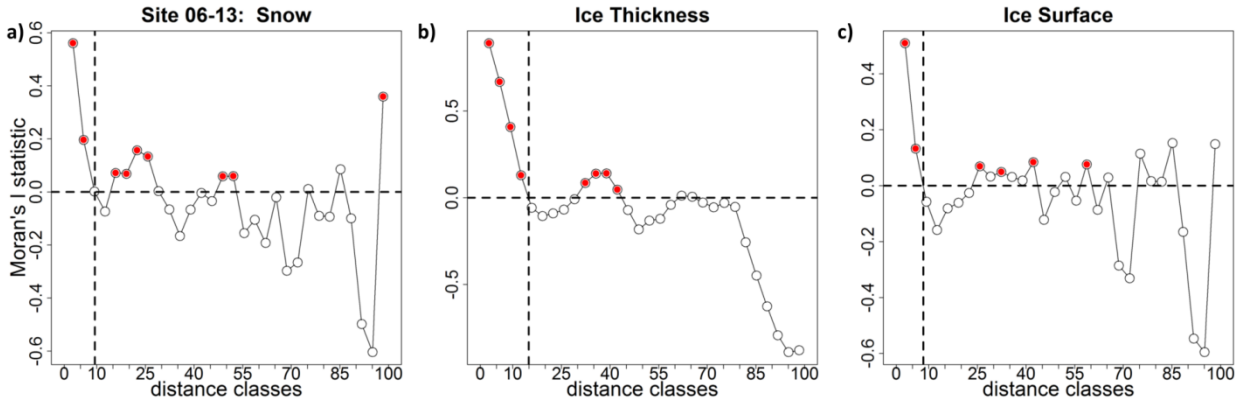

Figure S 14. Spatial correlograms showing Moran's I as a function of distance classes (meters) at MYI site 06-13 for survey measurements of: a) snow; b) ice thickness; and c) ice surface. Vertical dashed line corresponds to the identified patch size listed in Table 1. Filled red circles are significant values and open circles are non-significant values at $p < 0.05$.

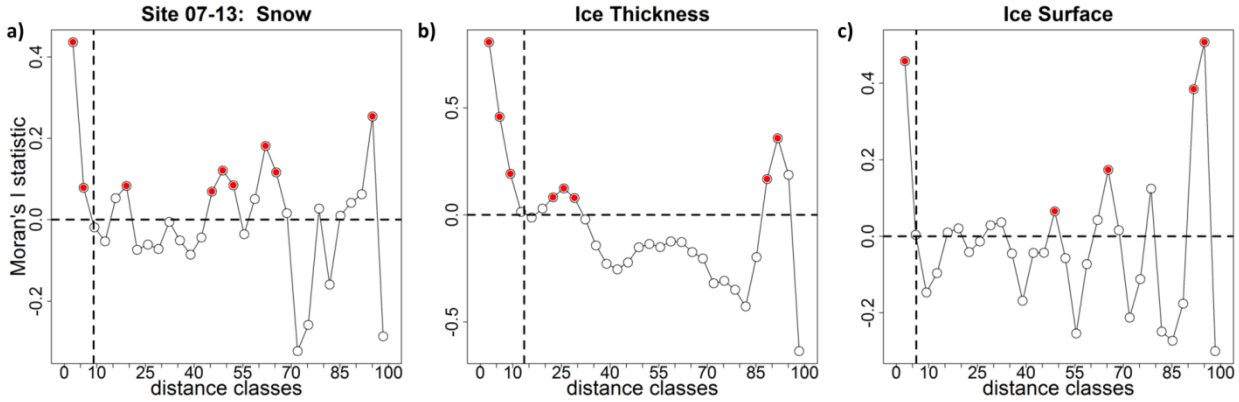

Figure S 15. Spatial correlograms showing Moran's I as a function of distance classes (meters) at MYI site 07-13 for survey measurements of: a) snow; b) ice thickness; and c) ice surface. Vertical dashed line corresponds to the identified patch size listed in Table 1. Filled red circles are significant values and open circles are non-significant values at $p < 0.05$.

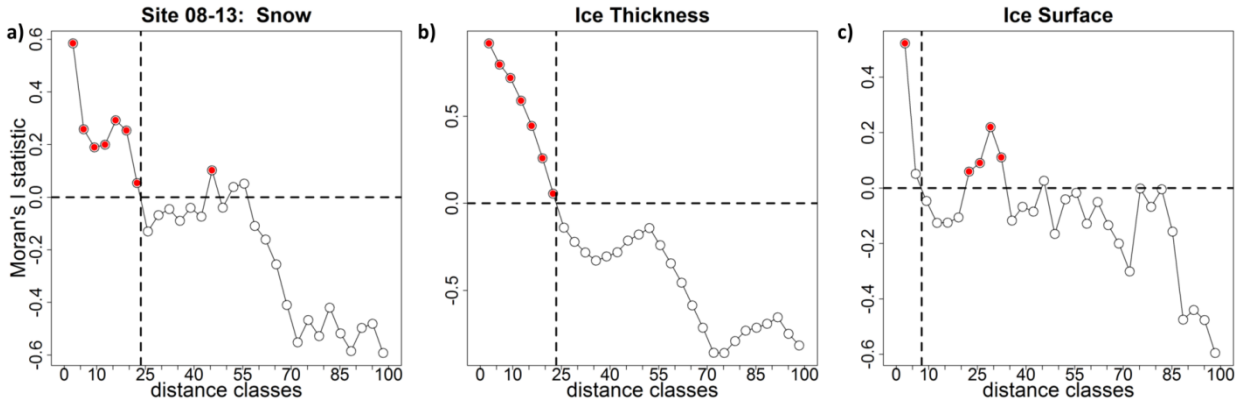

Figure S 16. Spatial correlograms showing Moran's I as a function of distance classes (meters) at MYI site 08-13 for survey measurements of: a) snow; b) ice thickness; and c) ice surface. Vertical dashed line corresponds to the identified patch size listed in Table 1. Filled red circles are significant values and open circles are non-significant values at $p < 0.05$.

Appendix C-1

Statutory Declaration

(According to § 7 (4) doctoral degree regulations of the MIN Faculty)

Eidesstattliche Erklärung

(Gem. § 7 (4) MIN – PromO)

I hereby declare, on oath, that I have written the present dissertation by my own and have not used other than the acknowledged resources and aids.

Hiermit erkläre ich an Eides statt, dass ich die vorliegende Dissertationsschrift selbst verfasst und keine anderen als die angegebenen Quellen und Hilfsmittel benutzt habe.

Benjamin A. Lange
Signature
Unterschrift

Hamburg,
Hamburg, den

05 April 2017

Paper 1

Title: *The Surface and Under-Ice Trawl (SUIT)-mounted environmental sensor array*

in preparation for submission to: *Deep-Sea Research Part I: Oceanographic Research Papers*

Author list: **Benjamin A. Lange**, Giulia Castellani, Jan Andries van Franeker and Hauke Flores

Author contributions: This study, the SUIT and sensor array were designed and developed by **B. A. Lange,** H. Flores J.A. van Franeker. Data were acquired by **B. A. Lange** and H. Flores. Data processing and protocols were developed by **B.A. Lange** with contributions from G. Castellani**.** Protocols were developed by **B. A. Lange,** G. Castellani and H. Flores. The analysis of the data was conducted by **B. A. Lange**. The manuscript first draft was written by **B. A. Lange** with contributions from all authors on the final version.

X

Benjamin Lange

X

Dr. Hauke Flores
Supervisor

Paper 2

Title: *Spectrally-derived sea ice-algal chlorophyll a concentrations using under-ice horizontal profiling platforms*

paper currently under review in *Journal of Geophysical Research: Oceans*

Author list: **Benjamin A. Lange**, Christian Katlein, Marcel Nicolaus, Ilka Peeken, and Hauke Flores

Author contributions: This study was designed by **B. A. Lange**, M. Nicolaus, I. Peeken and H. Flores. ROV data were acquired by M. Nicolaus and C. Katlein. Data processing of ROV spectra were conducted by **B. A. Lange,** M. Nicolaus and C. Katlein. SUIT sensor data were acquired and processed by **B. A. Lange,** M. Nicolaus and H. Flores. Ice core sampling and processing were conducted by **B. A. Lange** and I. Peeken. Bio-optical statistical model development was realized by **B. A. Lange**. Data analyses were conducted by **B. A. Lange** with support from C. Katlein and H. Flores. The manuscript was written by **B. A. Lange** with contributions from all authors.

Below are additional publications not included in this thesis, which have made use of the methodological advancements presented in Chapter 2 and have incorporated the environmental data as essential components of their studies:

David, C., **B. Lange**, T. Krumpen, F. Schaafsma, J. A. van Franeker, and H. Flores (2015), Under-ice distribution of polar cod *Boreogadus saida* in the central Arctic Ocean and their association with sea-ice habitat properties, *Polar Biol.*, doi:10.1007/s00300-015-1774-0.

David, C., F. L. Schaafsma, J. A. van Franeker, **B. Lange**, A. Brandt, and H. Flores (2016), Community structure of under-ice fauna in relation to winter sea-ice habitat properties from the Weddell Sea, *Polar Biol.*, doi:10.1007/s00300-016-1948-4.

Schaafsma, F. L., C. David, E. A. Pakhomov, B. P. V. Hunt, **B. A. Lange**, H. Flores, and J. A. van Franeker (2016), Size and stage composition of age class 0 Antarctic krill (*Euphausia superba*) in the ice–water interface layer during winter/early spring, *Polar Biol.*, doi:10.1007/s00300-015-1877-7.

X

Benjamin Lange

X

Dr. Hauke Flores
Supervisor

Paper 3

Title: *On improving the spatial representativeness of sea ice algae chlorophyll a biomass and primary production estimates*

in preparation for submission to: *Geophysical Research Letters*

Author list: **Benjamin A. Lange**, Christian Katlein, Giulia Castellani, Mar Fernández-Méndez, Marcel Nicolaus, Ilka Peeken, and Hauke Flores

Author contributions: This study was designed by **B. A. Lange** and H. Flores. ROV data were acquired by M. Nicolaus and C. Katlein. Data processing of ROV spectra were conducted by **B. A. Lange,** M. Nicolaus and C. Katlein. SUIT sensor data were acquired and processed by **B. A. Lange,** M. Nicolaus and H. Flores. Ice core sampling and processing were conducted by **B. A. Lange**, M Fernández-Méndez and I. Peeken. Photosynthetic parameters and ice core PP rates were determined by M Fernández-Méndez. Bio-optical statistical model and PP up-scaling approach were developed by **B. A. Lange**. Data analyses were conducted by **B. A. Lange** with support from C. Katlein, M Fernández-Méndez and H. Flores. The manuscript was written by **B. A. Lange** with contributions from all authors.

X

Benjamin Lange

X

Dr. Hauke Flores
Supervisor

Paper 4

Title: *Community structure of under-ice fauna in the Eurasian central Arctic Ocean in relation to environmental properties of sea-ice habitats*

published in *Marine Ecology Progress Series* (2015) 522:15-32

Author list: Carmen David, **Benjamin A. Lange**, Benjamin Rabe, Hauke Flores

Author contributions: This study was designed by C. David, H. Flores and **B. A. Lange**. Field sampling was performed by C. David, H. Flores and **B. A. Lange**. Species identification and counting was performed by C. David. Sensor data were processed by **B. A. Lange** H. Flores. Oceanographic data were provided by B. Rabe. The analysis of data was performed by C. David with support from **B. A. Lange** and H. Flores. Writing of the manuscript was realized by C. David with contribution from all authors.

X

Benjamin Lange

X

Dr. Hauke Flores
Supervisor

Paper 5

Title: *The importance of ice algae-produced carbon in the central Arctic Ocean ecosystem: food web relationships revealed by lipid and stable isotope analyses*

Published in: *Limnology and Oceanography*, doi:10.1002/lno.10351

Author list: Doreen Kohlbach, Martin Graeve, **Benjamin A. Lange**, Carmen David, Ilka Peeken, and Hauke Flores

Author contributions: Field sampling for this study was performed by **B. A. Lange**, H. Flores, C. David and I. Peeken. Taxonomic classification was conducted by H. Flores and C. David. Laboratory analyses were accomplished by D. Kohlbach and M. Graeve. Data analyses were performed by D. Kohlbach with support from **B. A. Lange** and H. Flores. The manuscript was written by D. Kohlbach with contribution from all authors.

X

Benjamin Lange

X

Dr. Hauke Flores
Supervisor

Paper 6

Title: *Comparing springtime ice-algal chlorophyll a and physical properties of multi-year and first-year sea ice from the Lincoln Sea*

published in: *PLoS One*, 10(4), e0122418, doi:10.1371/journal.pone.0122418

Author list: **Benjamin A. Lange,** Christine Michel, Justin F. Beckers, J. Alec Casey, Hauke Flores, Ido Hatam, Guillaume Meisterhans, Andrea Niemi, Christian Haas

Author contributions: This study was designed by **B. A. Lange**, C. Michel and C. Haas. Field sampling was performed by **B. A. Lange,** I. Hatam, J. F. Beckers, J.A. Casey and C. Haas. Sample processing was conducted **B. A. Lange**, C. Michel, G. Meisterhans and A. Niemi. Data analyses were conducted by **B. A. Lange,** J. F. Beckers, J. A. Casey, H. Flores. The manuscript was written by **B. A. Lange** with contributions from all authors.

X

Benjamin Lange

X

Dr. Hauke Flores
Supervisor

Paper 7

Title: *Suitable ice-algal habitat and biomass are largely underestimated over multi-year sea ice*

in preparation for submission to: *Progress in Oceanography*

Author list: **Benjamin A. Lange**, Hauke Flores, Christine Michel, Justin Beckers, Anne Bublitz, J. Alec Casey, Giulia Castellani, Ido Hatam, Anke Reppchen, Svenja A. Rudolph, Christian Haas

Author contributions: This study was designed by **B. A. Lange**, C. Michel and C. Haas. Field sampling was performed by **B. A. Lange**, I. Hatam, J. F. Beckers, J.A. Casey, A. Bublitz and C. Haas. Sample processing was conducted **B. A. Lange**, A. Reppchen and C. Michel. Data and statistical analyses were conducted by **B. A. Lange**, J. F. Beckers, J. A. Casey, H. Flores, A. Reppchen, S.A. Rudolph and C. Michel. The manuscript was written by **B. A. Lange** with contributions from all authors.

X

Benjamin Lange

X

Dr. Hauke Flores
Supervisor